

Tuncer Cebeci Jean Cousteix



*Modeling and Computation of Boundary-Layer Flows*  
Second Edition

**HORIZONS  
PUBLISHING**

*Long Beach, California  
Heidelberg, Germany*

Tuncer Cebeci Jean Cousteix

# **Modeling and Computation of Boundary-Layer Flows**

Laminar, Turbulent and Transitional  
Boundary Layers in Incompressible  
and Compressible Flows

Second Revised and Extended Edition

With 224 Figures, 15 Tables, 168 Problems  
and a CD-ROM



*Tuncer Cebeci*

The Boeing Company  
Long Beach, CA 90807-5309, USA  
and  
810 Rancho Drive  
Long Beach, CA 90815, USA  
TuncerC@aol.com

*Jean Cousteix*

ONERA/DMAE and SUPAERO  
2, Avenue Edouard Belin  
31055 Toulouse Cedex, France  
Jean.Cousteix@oncert.fr

ISBN 0-9668461-9-2 Horizons Publishing Inc., Long Beach  
ISBN 0-9668461-0-9 1st edition Horizons Publishing Inc., Long Beach

ISBN 3-540-24459-X Springer Berlin Heidelberg New York  
ISBN 3-540-65010-5 1st edition Springer Berlin Heidelberg New York

Library of Congress Control Number: 2005923827

All rights reserved. This work may not be translated or copied in whole or in part without the written permission of the publisher (Horizons Publishing Inc., 810 Rancho Drive, Long Beach, CA 90815, USA) except for brief excerpts in connection with reviews or scholarly analysis. Use in connection with any form of information storage and retrieval, electronic adaptation, computer software, or by similar or dissimilar methodology now known or hereafter developed is forbidden.

© Horizons Publishing Inc., Long Beach, California 1999, 2005  
Printed in Germany

The use of general descriptive names, trade names, trademarks, etc., in this publication, even if the former are not especially identified, is not to be taken as a sign that such names, as understood by the Trade Marks and Merchandise Marks Act, may accordingly be used freely by anyone.

*Please note:* All rights pertaining to the Computer Programs are owned exclusively by the authors and Horizons Publishing Inc. The publisher and the authors accept no legal responsibility for any damage caused by improper use of the programs. Although the programs have been tested with extreme care, errors cannot be excluded.

Typeset in L<sup>A</sup>T<sub>E</sub>X by the authors. Edited and reformatted by Kurt Mattes, Heidelberg, Germany.  
Printing and binding: Strauss GmbH, Mörlenbach, Germany  
Cover design: Erich Kirchner, Heidelberg, Germany

Printed on acid-free paper 5 4 3 2 1 0

# Preface

This second edition of the book, *Modeling and Computation of Boundary-Layer Flows*, extends the topic to include compressible flows. This implies the inclusion of the energy equation and non-constant fluid properties in the continuity and momentum equations. The necessary additions are included in new chapters, leaving the first nine chapters to serve as an introduction to incompressible flows and, therefore, as a platform for the extension. This part of the book can be used for a one semester course as described below.

Improvements to the incompressible flows portion of the book include the removal of listings of computer programs and their description, and their incorporation in two CD-ROMs. A listing of the topics incorporated in the CD-ROM is provided before the index. In Chapter 7 there is a more extended discussion of initial conditions for three-dimensional flows, application of the characteristic box to a model problem and discussion of flow separation in three-dimensional laminar flows. There are also changes to Chapter 8, which now includes new sections on Tollmien–Schlichting and cross-flow instabilities and on the prediction of transition with parabolised stability equations, and Chapter 9 provides a description of the rational behind interactive boundary-layer procedures.

Chapters 10 to 14 deal with compressible flows and consider, respectively, the boundary layer equations, two-dimensional laminar and turbulent flows, three-dimensional laminar and turbulent flows and stability and transition. A computer program for two-dimensional laminar and turbulent flows without separation and a computer program for three-dimensional laminar and turbulent flows, including those with separation, and related software to predict transition in three-dimensional flows are described in CD-ROMs and is available from the first author.

The above implies that the sequence of chapters is as follows. The Introduction of Chapter 1 presents two examples to demonstrate the use of inviscid and boundary-layer equations for solving engineering problems. Chapter 2 presents the conservation equations for incompressible flows, and is compara-

tively brief since detailed derivations are available elsewhere. The third Chapter discusses the boundary-layer equations. The calculation of laminar and turbulent boundary-layers and the prediction of transition in two-dimensional flows are addressed in Chapters 4 through 6. Chapter 4 considers incompressible laminar boundary-layers and their solution and includes computer programs that solve the boundary-layer equations and that are provided in two CD-ROMs (Appendices A and B).

The prediction of the onset of transition from laminar to turbulent flow has traditionally been achieved by correlations, which are known to have limited ranges of applicability. The use of the  $e^n$ -method based on solutions of the linear stability equations has been proposed as a more general approach. Thus, Chapter 5 describes the solution of the linear stability equations for incompressible flows and the prediction of transition by the  $e^n$ -method with the numerical method of Chapter 4, and a CD-ROM (Appendix B) provides a computer program that solves the Orr-Sommerfeld equation and computes transition.

Chapter 6 addresses two-dimensional incompressible turbulent boundary-layers. It begins with a physical description of turbulent boundary-layers and the empirical laws that govern them and is followed by a brief discussion of a few popular turbulence models as well as a discussion of methods for computing two-dimensional turbulent boundary-layers. Chapters 7 and 8 extend the discussions of Chapters 4 through 6 from two-dimensional flows to three-dimensional flows. Chapter 7 discusses three-dimensional laminar and turbulent boundary-layers and a CD-ROM (Appendix B) presents a computer program to solve the boundary-layer equations.

Chapter 8 extends the discussion of Chapter 5 from two- to three-dimensional flows. Unlike the occurrence of transition in two-dimensional flows, transition in three-dimensional flows can occur by different mechanisms as discussed here. The chapter also describes the solution of the linear stability equations with the numerical method of Chapter 5 as well as predicting transition with the  $e^n$ -method.

Chapter 9 provides a brief description of interactive boundary-layer theory, in which the solutions of the inviscid flow equations are coupled to those of the boundary-layer equations with an interaction approach. The viscous effects are neglected in the inviscid flow solutions, and are re-introduced with the help of the solutions of the boundary-layer equations. Applications of this approach are demonstrated for laminar and turbulent flows on a flat plate and for single and multi-element airfoils.

Chapter 10 is similar to Chapters 2 and 3 and presents the conservation equations and their reduced forms for compressible flows while Chapters 11 and 12 address the calculation of laminar and turbulent boundary layers for two-dimensional and compressible flows and a CD-ROM (Appendix B) provides a computer program that solves the boundary-layer equations for compressible

flows. Chapter 13 extends the discussions of Chapters 11 and 12 from two-dimensional to three-dimensional flows, and Chapter 14 extends the discussion of Chapter 8 from three-dimensional incompressible flows to compressible flows.

A one semester course on Modeling and Calculation of Boundary-Layer Flows for senior undergraduate students, would include a brief reading of Chapter 1 followed by Chapters 2 and 3, Sections 4.1 to 4.4 in Chapter 4, Sections 5.1 to 5.5 in Chapter 5, Sections 6.1 to 6.5 and Section 6.7 in Chapter 6. For first year graduate students, the above material might be extended to include Sections 4.5, 5.6, 6.6 that deal with the numerical methods and computer programs in Chapters 4 and 5.

A list of related and current books and solution manuals, published by Horizons and Springer-Verlag, is available on the Horizons Web site,

<http://hometown.aol.com/tuncerc>

This book is an outgrowth of work done by the authors as employees of the Boeing Company and ONERA. Their teaching responsibilities at the California State University at Long Beach (CSULB) and at the Ecole Nationale Supérieure de L'Aéronautique et de L'Espace (SUPAERO) have contributed to its organization.

The authors would like to express their appreciation to several people who have given thoughts and time to the development of this book and to people who have given encouragements and moral support. In particular, we want to thank the late A. M. O. Smith of Douglas Aircraft Company, Herb Keller of the California Institute of Technology, the late Keith Stewartson of University College, Jim Whitelaw of Imperial College, Peter Bradshaw of Stanford University and D. Arnal, B. Aupoix and R. Houdeville of ONERA. We also wish to thank Hsun H. Chen, K. C. Chang and J. P. Shao for proof reading the manuscript and making many helpful suggestions. In addition, we are indebted to many of our students who have contributed to many of the new material included in this book.

Finally, the authors wish to thank their wives, Sylvia Cebeci and Claudine Cousteix for their understanding and encouragement. Only authors of books can fully understand their contribution.

Indian Wells, California, USA  
Toulouse, France  
April 2005

*Tuncer Cebeci  
Jean Cousteix*

# Contents

<b>1. Introduction .....</b>	<b>1</b>
1.1 Skin-Friction Drag Reduction.....	3
1.1.1 Laminar Flow Control .....	4
1.1.2 Calculations for NLF and HLFC Wings .....	7
1.2 Prediction of the Maximum Lift Coefficient of Multielement Wings .....	11
References .....	16
<b>2. Conservation Equations for Mass and Momentum for Incompressible Flows .....</b>	<b>17</b>
2.1 Introduction .....	17
2.2 Navier–Stokes Equations.....	18
2.3 Reynolds-Averaged Navier–Stokes Equations .....	20
2.4 Inviscid Flow Equations .....	22
References .....	23
Problems.....	24
<b>3. Boundary-Layer Equations for Incompressible Flows .....</b>	<b>27</b>
3.1 Two-Dimensional Flows .....	27
3.1.1 Laminar Flows.....	27
3.1.2 Turbulent Flows .....	29
3.2 Axisymmetric Flows.....	30
3.3 Momentum Integral Equation .....	31
3.3.1 Two-Dimensional Flows .....	32
3.3.2 Axisymmetric Flows .....	33
3.4 Boundary and Initial Conditions .....	34
References .....	36
Problems.....	36

<b>4.</b>	<b>Two-Dimensional Incompressible Laminar Flows . . . . .</b>	43
4.1	Introduction . . . . .	43
4.2	Similar Flows: External Flows . . . . .	44
4.2.1	Similarity Concept . . . . .	44
4.2.2	Falkner–Skan Equation . . . . .	44
4.2.3	Solutions of the Falkner–Skan Equation . . . . .	48
4.3	Similar Flows: Free-Shear Flows . . . . .	53
4.3.1	Axisymmetric Jet . . . . .	53
4.3.2	Two-Dimensional Wake . . . . .	56
4.3.3	Mixing Layer Between Two Uniform Streams . . . . .	59
4.3.4	Power Laws for the Width and for the Centerline Velocity of Similar Free Shear Layers . . . . .	61
4.4	Numerical Solution of the Boundary-Layer Equations: Integral Form . . . . .	62
4.4.1	Pohlhausen Method . . . . .	62
4.4.2	Thwaites' Method . . . . .	64
4.5	Numerical Solution of the Boundary-Layer Equations: Differential Form . . . . .	66
4.5.1	Numerical Formulation . . . . .	69
4.5.2	Newton's Method . . . . .	70
4.5.3	Block-Elimination Method . . . . .	72
4.6	Applications of BLP2 to External Flows . . . . .	73
4.6.1	Airfoil Flow . . . . .	74
4.6.2	Ellipse Flow . . . . .	75
4.6.3	Prolate Spheroid Flow . . . . .	77
	References . . . . .	79
	Problems . . . . .	80
<b>5.</b>	<b>Transition in Two-Dimensional Incompressible Flows . . . . .</b>	105
5.1	Introduction . . . . .	105
5.2	Transition Process . . . . .	106
5.3	Linear Stability Theory . . . . .	109
5.3.1	Boundary Conditions . . . . .	112
5.3.2	Properties of the Orr–Sommerfeld Equation for Two-Dimensional Flows . . . . .	113
5.4	Prediction of Transition . . . . .	117
5.4.1	Empirical Correlations . . . . .	117
5.4.2	$e^n$ -Method . . . . .	119
5.4.3	$H\text{-}R_x$ Method . . . . .	121
5.5	Factors that Influence Transition . . . . .	122
5.5.1	Effects of Freestream Turbulence and Noise . . . . .	122
5.5.2	Effects of Pressure Gradient . . . . .	124

5.5.3	Effects of Heat Transfer . . . . .	127
5.5.4	Effects of Suction . . . . .	130
5.5.5	Effects of Surface Roughness . . . . .	133
5.5.6	Effects of Surface Curvature . . . . .	135
5.6	Numerical Solution of the Orr–Sommerfeld Equation . . . . .	136
5.6.1	Eigenvalue Procedure for Two-Dimensional Flows . . . . .	139
5.6.2	Eigenvalue Procedure for Transition . . . . .	143
5.7	Applications of STP . . . . .	144
5.7.1	Stability Diagrams for Blasius Flow . . . . .	145
5.7.2	Transition Prediction . . . . .	146
References	.....	149
Problems	.....	151
<b>6.</b>	<b>Two-Dimensional Incompressible Turbulent Flows . . . . .</b>	<b>163</b>
6.1	Introduction . . . . .	163
6.2	Composite Nature of a Turbulent Boundary-Layer . . . . .	163
6.2.1	The Inner Layer: Smooth Surface . . . . .	164
6.2.2	The Inner Layer: Rough Surface . . . . .	166
6.2.3	The Outer Layer . . . . .	169
6.2.4	Summary . . . . .	171
6.2.5	The Whole Layer . . . . .	171
6.3	Turbulence Models . . . . .	175
6.3.1	Zero-Equation Models . . . . .	176
6.3.2	Turbulence Models Based on Transport Equations . . . . .	179
6.4	Turbulent Boundary-Layers on Smooth and Rough Surfaces with Zero Pressure Gradient . . . . .	186
6.4.1	Smooth Flat Plate . . . . .	187
6.4.2	Rough Flat Plate . . . . .	190
6.5	Turbulent Boundary-Layers with Pressure Gradient: Integral Methods . . . . .	192
6.6	Turbulent Boundary-Layers with Pressure Gradient: Differential Methods . . . . .	195
6.7	Free Shear Layers . . . . .	196
6.7.1	Axisymmetric Jet . . . . .	196
6.7.2	Two-Dimensional Wake . . . . .	199
6.7.3	Power Laws for the Width and the Centerline Velocity of Similar Free Shear Layers . . . . .	201
References	.....	201
Problems	.....	203
<b>7.</b>	<b>Three-Dimensional Incompressible Laminar and Turbulent Flows . . . . .</b>	<b>209</b>
7.1	Introduction . . . . .	209

7.2	Boundary-Layer Equations for Three-Dimensional Flows . . . . .	210
7.2.1	Cartesian Coordinate System . . . . .	211
7.2.2	Streamline Coordinate System . . . . .	213
7.2.3	Body-Oriented Coordinate System . . . . .	215
7.3	Initial Conditions . . . . .	217
7.4	Turbulence Models . . . . .	219
7.5	Transformed Equations . . . . .	223
7.6	Numerical Solution of the Boundary-Layer Equations: Differential Form . . . . .	225
7.6.1	Flows Without Reversal: Standard Box . . . . .	228
7.6.2	Flows with Reversal: Characteristic Box . . . . .	231
7.6.3	Calculation of Geometric Parameters . . . . .	233
7.7	Evaluation of a Turbulence Model for Three-Dimensional Flows .	235
7.7.1	Infinite Swept Wing Flows . . . . .	236
7.7.2	Full Three-Dimensional Flows . . . . .	243
7.8	Boundary-Layer Program for Three-Dimensional Flows . . . . .	247
References	.....	250
Problems	.....	252
<b>8.</b>	<b>Transition in Three-Dimensional Incompressible Flows . . . . .</b>	<b>261</b>
8.1	Introduction . . . . .	261
8.2	Mechanisms of Transition . . . . .	262
8.2.1	Tollmien–Schlichting and Crossflow Instabilities . . . . .	262
8.2.2	Leading Edge Contamination . . . . .	263
8.3	$e^n$ -Method for Three-Dimensional Flows . . . . .	265
8.3.1	Eigenvalue Formulations . . . . .	265
8.3.2	The Zarf . . . . .	268
8.4	Numerical Solution of the Orr–Sommerfeld Equation for Three-Dimensional Flows . . . . .	271
8.4.1	Eigenvalue Procedure for Zarf . . . . .	272
8.4.2	Eigenvalue Procedure for Transition . . . . .	274
8.5	Application of the $e^n$ -Method with Saddle-Point Eigenvalue Formulation . . . . .	275
8.5.1	Infinite Swept Wing Data of Arnal and Juillen . . . . .	275
8.5.2	Prolate Spheroid Data of Meier and Kreplin . . . . .	278
8.6	Transition Prediction by Parabolized Stability Equations . . . . .	286
8.6.1	$n$ -Factor Calculations . . . . .	288
8.6.2	Initial Conditions . . . . .	289
8.6.3	Sample Calculations . . . . .	291
References	.....	295
Problems	.....	297

<b>9. Interactive Boundary-Layer Theory</b>	307
9.1 Introduction	307
9.2 Rational Basis of the Interactive Boundary-Layer Theory	310
9.2.1 IBL Model	310
9.2.2 Reduced Model for an Outer Irrotational Flow	313
9.2.3 Applications	313
9.3 Interaction Problem	313
9.4 Inverse Boundary-Layer Method	315
9.4.1 Transformed Equations: General Form	317
9.4.2 Numerical Method	317
9.4.3 Computer Program	320
9.5 Applications of the Inverse Boundary-Layer Method: Trailing Edge Flow of a Flat Plate	320
9.6 Applications of the Interactive Boundary-Layer Method: Airfoils	325
9.6.1 Airfoils at High Reynolds Numbers	327
9.6.2 Airfoils at Low Reynolds Numbers	329
9.7 Applications of the Interactive Boundary-Layer Method: Multielement Airfoils	333
References	335
Problems	336
<b>10. Conservation Equations for Mass, Momentum and Energy</b>	345
10.1 Introduction	345
10.2 Navier–Stokes Equations	345
10.3 Reynolds-Averaged Navier–Stokes Equations	349
10.4 Inviscid Flow Equations	350
10.5 Boundary-Layer Equations	351
10.5.1 Two-Dimensional Flows	351
10.5.2 Axisymmetric Flows	352
10.5.3 Three-Dimensional Flows	352
10.6 Integral Equations	353
10.6.1 Continuity Equation	353
10.6.2 Momentum Equation	354
10.6.3 Energy Equation	355
References	355
Problem	355
<b>11. Two-Dimensional Compressible Laminar Flows</b>	357
11.1 Introduction	357
11.2 Transformations for Compressible Flows	357
11.2.1 Falkner–Skan Transformation	358
11.2.2 Illingworth–Stewartson Transformation	359

11.3 Similar Flows .....	362
11.4 Relation Between Compressible and Incompressible Boundary-Layer Parameters .....	363
11.5 Nonsimilar Flows .....	367
11.6 Shock-Wave/Shear-Layer Interaction .....	370
11.7 Free Interaction and Upstream Influence .....	375
11.8 A Prescription for Computing Interactive Flows with Shocks ..	380
References .....	383
Problems.....	383
 <b>12. Two-Dimensional Compressible Turbulent Flows .....</b>	 387
12.1 Introduction .....	387
12.2 Turbulence Models .....	388
12.2.1 Zero-Equation Models .....	390
12.2.2 Turbulence Models Based on Transport Equations .....	391
12.3 Inner-Layer Similarity Analysis for Velocity and Temperature Profiles .....	393
12.4 Transformations for Compressible Turbulent Flows .....	395
12.5 Two-Dimensional Boundary Layers with Zero Pressure Gradient	396
12.5.1 Skin-Friction Formulas on Smooth Surfaces .....	396
12.5.2 Reynolds Analogy Factor .....	400
12.5.3 Skin-Friction Formulas on Rough Surfaces .....	401
12.6 Numerical Solution of the Boundary-Layer Equations: Differential Method .....	403
12.7 Shock-Wave/Boundary-Layer Interaction .....	408
References .....	412
Problems.....	413
 <b>13. An Interactive Boundary-Layer Method for Three-Dimensional Flows .....</b>	 417
13.1 Introduction .....	417
13.2 Governing Equations .....	418
13.2.1 Initial Conditions .....	418
13.2.2 Turbulence Models .....	420
13.3 Interaction Law .....	420
13.4 Transformed Equations .....	422
13.4.1 Attachment Line Equations .....	424
13.4.2 Quasi-Three-Dimensional Boundary-Layer Equations ..	425
13.5 Numerical Method .....	426
13.6 Modelling of Viscous Effects in Three-Dimensional Inviscid Flows .....	426
13.7 Interface Program .....	427
13.7.1 Geometric Parameters of the Coordinate System .....	430

13.7.2 Calculation of Inviscid Velocity Components for Boundary-Layer Grid . . . . .	432
13.8 Applications of the Interactive Boundary-Layer Method: Subsonic Flows . . . . .	433
13.8.1 SAAB Wing . . . . .	435
13.8.2 RAE Wing . . . . .	438
13.8.3 Multielement Wings . . . . .	442
13.9 Transonic Flows . . . . .	446
13.9.1 ONERA-M6 Wing . . . . .	448
13.9.2 Douglas Wing/Fuselage Configuration . . . . .	449
13.9.3 Challenger Wing/Body Fuselage Configuration . . . . .	450
References . . . . .	453
<b>14. Transition in Three-Dimensional Compressible Flows . . . . .</b>	455
14.1 Introduction . . . . .	455
14.2 Linear Stability Theory . . . . .	455
14.2.1 Stability Equations . . . . .	456
14.2.2 Inviscid Stability Theory . . . . .	458
14.2.3 Examples of Results . . . . .	463
14.3 Factors that Influence Transition . . . . .	468
14.3.1 Effects of Noise . . . . .	468
14.3.2 Effects of Wall Cooling . . . . .	470
14.3.3 Effects of Nose Bluntness . . . . .	470
14.3.4 Effects of Surface Roughness . . . . .	472
14.3.5 Leading Edge Contamination . . . . .	473
14.4 $e^n$ -Method for Compressible Flows . . . . .	473
14.5 Applications of the $e^n$ -Method . . . . .	476
References . . . . .	481
Problems . . . . .	482
<b>Appendix A Computer Programs on the Accompanying CD-ROM . . . . .</b>	485
<b>Appendix B Computer Programs Available from the First Author . . . . .</b>	487
<b>Appendix C A Boundary-Layer Program for Three-Dimensional Compressible Flows on Wings . . . . .</b>	489
<b>Subject Index . . . . .</b>	495

# 1

## Introduction

We are surrounded by examples of fluid dynamics phenomena; computational fluid dynamics (CFD) deals with the numerical analysis of these phenomena. Despite impressive progress in recent years it is evident that CFD remains an imperfect tool in the comparatively mature discipline of fluid dynamics, partly because electronic digital computers have been in widespread use for less than thirty years. History reminds us of ancient examples of fluid dynamics applications such as the Roman baths and aqueducts that fulfilled the requirements of the engineers who built them; of ships of various types with adequate hull designs, and of wind energy systems, built long before the subject of fluid mechanics was formalized by Reynolds, Newton, Euler, Navier, Stokes, Prandtl and others. The twentieth century has witnessed many more examples of applications of fluid dynamics for the use of humanity, all designed without the use of electronic computers. Examples include prime movers such as internal-combustion engines, gas and steam turbines, flight vehicles, and environmental systems for pollution control and ventilation.

The Navier–Stokes equations, which govern the motion of a Newtonian viscous fluid were formulated well over a century ago. The most straightforward method of attacking any fluid dynamics problem is to solve these equations for the appropriate boundary conditions. Analytical solutions are few and trivial and, even with today's supercomputers, numerically exact solution of the complete equations for the three-dimensional, time-dependent motion of turbulent flow is prohibitively expensive except for basic research studies in simple configurations at low Reynolds numbers. Therefore, the “straightforward” approach is still impracticable for engineering purposes.

Considering the successes of the precomputer age, one might ask whether it is necessary to gain a greater understanding of fluid dynamics and develop new computational techniques, with their associated effort and cost. Textbooks on fluid dynamics reveal two approaches to understanding fluid dynamics processes. The first is to device useful correlations through a progression from demonstrative experiments to detailed experimental investigations that yield additional

understanding and subsequent improvement. The second is to solve simplified versions of fluid dynamics equations for conservation of mass, momentum and energy for comparatively simple boundary conditions. There is great advantage in combining both approaches when addressing complex fluid dynamics problems, but interaction between these two approaches has been limited until recently by the narrow range of useful solutions which could be obtained by analytic methods or simple numerical computations. It is evident, therefore, that any method for increasing the accuracy of computational methods by solving more complete forms of the conservation equations than has been possible up to now is to be welcomed. The numerical approaches of CFD have, in most cases, proven much more powerful than the closed-form analytical solutions of the past. As an example, the flow through a blade passage of a gas turbine is three-dimensional, and, even if we ignore the problem of modeling the behavior of turbulence, the corresponding equations can only be solved by numerical methods; even the inviscid flow in an axisymmetric engine intake cannot be calculated by purely analytic methods. Thus, without computational fluid dynamics, we cannot calculate detailed flow characteristics essential to improving understanding and supporting the design process.

It should be recognized that both experimental and computational fluid dynamics require resources. The cost of experiments in some cases can be prohibitive as, for example, with extensive flight tests of airplanes, full-scale tests of a gas turbine, or destructive testing of expensive components. In such cases, it may be possible to reduce the number of experimental tests by using CFD, since only a relatively small number of experiments are required to check the accuracy of the CFD results. Of course, the cost of obtaining accurate numerical solutions of differential equations may also be large for a complex flow, but still are usually much less than the cost of the additional experiments that would otherwise be required. In reality, the most cost-effective approach to solving a fluid dynamics problem is likely to be a combination of measurements and calculations. Both are subject to uncertainties, but the combination of these two approaches can result in both a more cost-effective and more reliable design than by using only one approach or the other, and thus may be necessary to meet today's more stringent requirements for improved performance and reduced environmental impact, along with technical innovation and economy.

The following sections demonstrate the application of CFD techniques to solve real engineering problems by considering two examples which encompass flows which make use of the reduced forms of the conservations such as inviscid and boundary-layer equations. A more complete demonstration should also include examples of flows which make use of the time-averaged Navier–Stokes equations, but this is beyond the scope of this book. The two examples presented below are taken from the literature; additional examples, including those com-

puted by Navier–Stokes equations and by reduced Navier–Stokes equations can be found in many journal articles or conference papers.

The first example, discussed in Section 1.1, addresses the application of CFD to reduce the drag of a wing by adjustment of pressure gradient, by shaping, and by suction through slotted or perforated surfaces. The drag of an aircraft can be reduced in a number of ways to provide increased range and speed, and decreased size, cost, and decreased fuel usage. The adjustment of pressure gradient by shaping and using laminar boundary-layer control with suction are two powerful and effective ways to reduce drag. This is demonstrated with a calculation method for natural laminar flow (NLF) and hybrid laminar flow control (HLFC) wings.

The second example, discussed in Section 1.2, addresses the calculation of the maximum lift coefficient of a wing which corresponds to the stall speed, which is the minimum speed at which level flight can be maintained. A calculation method is described and used to predict the maximum lift coefficient of a high-lift system; this coefficient plays a crucial role in the takeoff and landing of an aircraft.

## 1.1 Skin-Friction Drag Reduction

There are several techniques for reducing the skin-friction drag of bodies. While the emphasis in this section is on aircraft components, the arguments apply equally to the reduction of skin-friction drag on all forms of transportation, including underwater vehicles. The importance of the subject has been discussed in a number of articles; a book edited by Bushnell and Heiner [1] summarizes the research in this area and the reader is referred to this book for an in-depth review of viscous drag reduction and for discussions of the possible savings which can occur from the reduction of the drag. As an example of the argument in support of the importance of the calculation methods used for reducing skin-friction drag, it is useful to point out that a three-percent reduction in the skin-friction drag of a typical long-range commercial transport, which burns around ten million gallons of fuel per year, at 50 cents per gallon, would yield yearly savings of around \$150,000.

There have been many suggestions for reducing the skin-friction drag on aircraft components including extension of regions of laminar flow, relaminarization of turbulent flow and modification to the turbulence characteristics of the near-wall flow. In general, these attempts to control the flow depend on changes to the wall boundary conditions including variations of longitudinal and transverse surface curvatures, the nature of the surface and heat and mass transfer through the surface. A partial exception is the use of thin airfoils (LEBUs) in the outer region of the boundary layer to break up the large eddy structure of turbulent flow [1].

In this section the discussion is limited to laminar flow control (LFC) and the reader is referred to [1] for a discussion of other techniques for reducing the skin-friction drag. In subsection 1.1.1, a brief description of laminar flow control first by “Adjustment of Pressure Gradient by Shaping,” then by “Suction Through Slotted or Perforated Surfaces” is given. This subsection is followed by a description and application of a calculation method to natural laminar flow (NLF) and hybrid laminar flow control (HLFC) wings (subsection 1.1.2).

### 1.1.1 Laminar Flow Control

#### Adjustment of Pressure Gradient by Shaping

Laminar flow on a two-dimensional or axisymmetric body (see Chapter 4) can be achieved by designing the geometry so that there are extensive regions of favorable pressure gradients. This technique is frequently referred to as natural laminar flow (NLF) control and may be implemented on a wing or a body of revolution by bringing the point of maximum thickness as far aft as possible. Typical airfoil sections designed for this purpose are shown on Fig. 1.1 and the location of the onset of transition, where laminar flow becomes turbulent flow, can be estimated by using the  $e^n$ -method discussed in Chapters 5 and 8. The success of this technique and of the calculation method also depends on factors besides the pressure gradient including surface roughness, surface waviness, freestream turbulence, and the concentration of a second phase such as rain or solid particles in water, all of which can play a role in triggering transition (Section 5.5). The influence of these factors can usually be avoided by careful design, for example by keeping the surface waviness and roughness below the allowable limits. Thus, a retractable Krueger device, which is essentially a nose flap in the leading edge of an LFC wing, can serve as a line-of-sight shield from insects and thereby help to retain a smooth surface with further benefit from spray nozzles to wet the leading edge.

A number of modern low-speed aircraft make use of extended regions of natural laminar flow on their wings [1] but transonic cruise, and the swept wings required for this configuration, introduce further complications. In particular, flow from the fuselage boundary layer can introduce instabilities which result in turbulent flow along the attachment line of the wing (Section 8.2), or a favorable pressure gradient on the upper surface can result in a shock wave which interacts with the boundary-layer to cause turbulent flow. The first problem depends on the Reynolds number, sweep angle and curvature of the leading edge and it is possible to shape the leading edge of the wing so that the attachment-line flow is laminar. In this case it is likely that, depending on the sweep angle, the flow may become turbulent away from the attachment line due to the crossflow instability discussed in Chapter 8. In subsection 1.1.2 calculations are presented for a typical NLF wing in incompressible flow to demonstrate the role of sweep

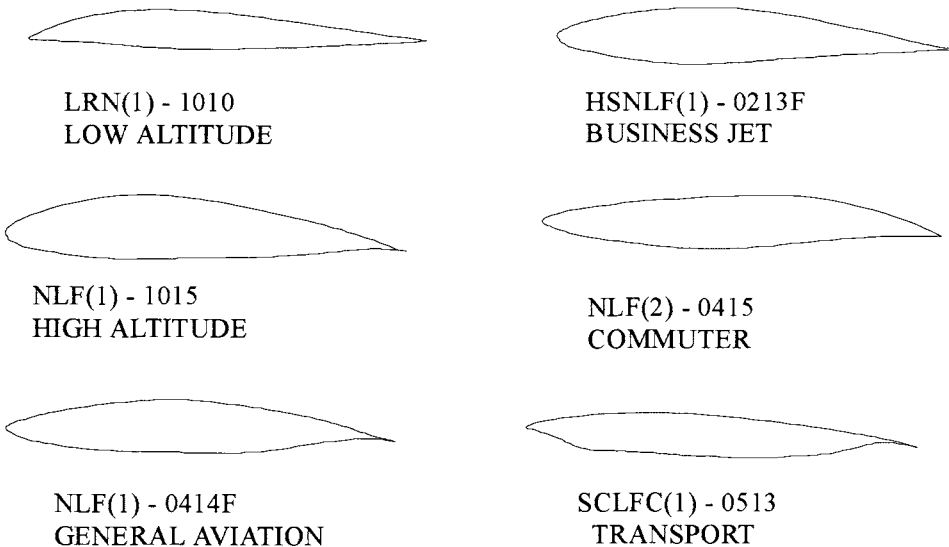


**Fig. 1.1.** Typical NLF airfoils for a wide range of applications. SCLFC denotes supercritical LFC airfoil.

angle and crossflow on transition, and the parameters that can be used to predict transition along the attachment line are discussed.

Extending the region of natural laminar flow on fuselages in order to reduce the fuselage drag is also important, as indicated by the examples of Table 1.1, relevant to transport aircraft [1]. It should be pointed out that the total skin-friction drag of a modern wide-body transport aircraft is about 40% of the total airplane drag, with approximately 3% from nacelles and pylons, 15% from fuselage, 15% from wing, and 8% from empennage. Thus, nacelles and pylons account for about 8% of the total skin-friction drag, while the fuselage, wing and empennage account for 38%, 35% and 20%, respectively. For smaller airplanes, such as the MD-80 and 737, the portion of the total skin-friction drag is usually higher than for wide bodies.

Table 1.2 shows the reduction in drag coefficient which can be achieved on an axisymmetric body by control of the location of the onset of transition: as an example, a delay of transition by 27% of the body length reduces the drag coefficient by some 30%. As in the case of wings, the onset of transition on fuselages and bodies of revolution can be estimated by an extension of the  $e^n$ -method discussed in subsection 5.4.2 from two-dimensional flows to three-dimensional flows discussed in Section 8.3.

### Suction Through Slotted or Perforated Surfaces

The attainment of laminar flow by adjustment of pressure gradient by shaping becomes increasingly more difficult as the Reynolds number increases because

**Table 1.1.** Profile drag buildup for all-turbulent transport jet and airplane with laminar lifting surfaces [1].

	All-turbulent surfaces	Laminar lifting surfaces
Nacelles and misc.	5.2%	7.6%
Fuselage	48.7%	70.2%
Empennage	14.3%	6.9%
Wing	31.8%	15.3%
Nacelle and others	0.0010	0.0010
Fuselage	0.0092	0.0092
Empennage	0.0027	0.0009
Wing	<u>0.0060</u>	<u>0.0020</u>
Total profile $C_D$	0.0189	0.0131

**Table 1.2.** Drag coefficients for an axisymmetric body with a fineness ratio 6.14 at  $\alpha = 0$ ,  $R_L = 40.86 \times 10^6$  [1].

$x_{tr}$	$C_d \times 10^2$
0.322	2.60
0.15	3.43
0.10	3.62
0.05	3.74

the boundary layer becomes relatively thinner and, as a result, more sensitive to roughness and small disturbances. Thus, there are practical limits to maintaining natural laminar flow at high Reynolds numbers because the effort spent to maintain extremely smooth surfaces may be negated by the increased sensitivity to external factors over which one has little control.

The next technique to maintain laminar flow is the use of active laminar flow control by suction which thins the boundary-layer, generates a fuller velocity profile and leads to increased boundary-layer stability. The use of suction at the leading edge of a wing, through slots or perforated material, can overcome the tendency for the cross-flow velocity to create a turbulent boundary-layer flow beginning at the attachment line [1], see also Section 11.2. The technique is referred to as hybrid laminar-flow control (HLFC) since it combines suction mass transfer with the arrangement of the airfoil (see Fig. 1.2) so as to impose a favorable longitudinal pressure gradient. This type of LFC is applicable to a wide range of small to moderate sized aircraft. The perforated plate makes use of holes of the order of 0.004 inches in diameter with a pitch-to-diameter ratio of around ten and cleaning of the holes can be accomplished by reversing the mass flow while the aircraft is stationary. Extensive wind-tunnel tests have been reported by Pfenninger [1] who made use of vertical slot widths graded

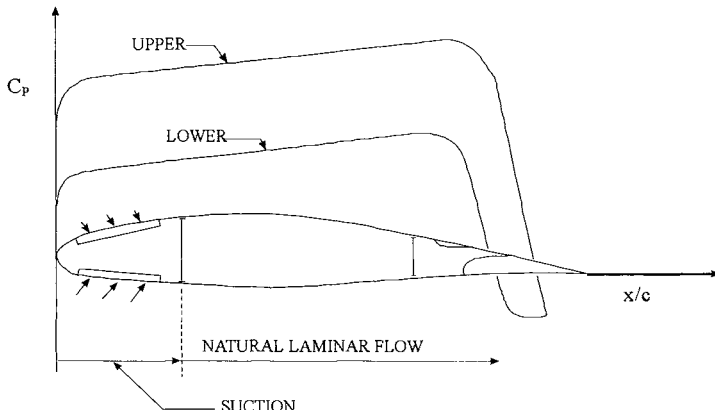


**Fig. 1.2.** A typical airfoil section for hybrid laminar flow control (HLFC).

from 0.008 to 0.003 inches depending on the thickness of the boundary-layer and a pitch which varied from 3 to 0.6 inches depending on the static pressure. Difficulties were experienced with the effective roughness created by the edges of the slots, but the system was made to operate satisfactorily so that the effects of the cross-flow velocity were removed in that the flow around the leading edge remained laminar. Again, stability (Chapter 11) and boundary-layer (Chapters 9, 10) theories can be used in the design of the HLFC wing, as discussed in the following subsection.

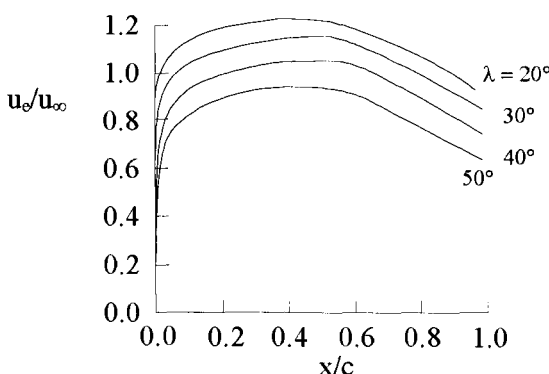
### 1.1.2 Calculations for NLF and HLFC Wings

A calculation method (Chapter 4 of [1]) based on the solutions of the panel, boundary-layer and stability equations for three dimensional flows can be used to demonstrate the effects of sweep, angle of attack, and suction on transition. A wing with a cross section of the NACA 6-series laminar flow airfoil family developed in the late thirties is chosen for this purpose. Its particular designation is NACA 65-412 where the first digit designates the airfoil series and the second indicates the extent of the favorable pressure gradient in tenths of chord on both upper and lower surfaces at design condition; the third digit gives the design lift coefficient and the last two digits denote the thickness in percent of the chord. The camber line used to generate this airfoil has the NACA designation  $a = 1.0$  which means that the additional loading due to camber is uniform along the chord. It also happens that the use of this particular camber line results in an airfoil which has its design lift coefficient at zero angle of attack and all calculations presented here were performed at this angle of attack. The results correspond to a Reynolds number of  $10^7$ , based on the total freestream velocity  $V_\infty$  and chord  $c$ , and for several sweep angles ranging from  $0^\circ$  to  $50^\circ$ . The inviscid velocity distribution was computed from the Hess panel method [2, 3].

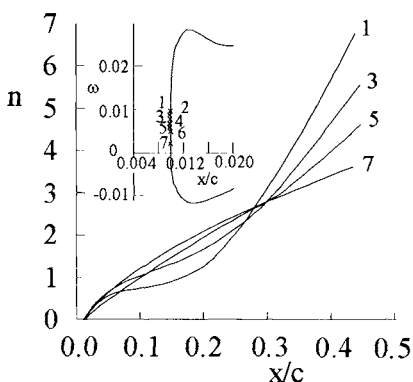
which is an extension of the two-dimensional panel method of Section 5.3 to three-dimensional flows and the boundary-layer calculations were performed again by solving the equations for an infinite swept wing (subsection 9.5.2) with the computer program similar to the one described in Chapter 10. Transition calculations are performed by using the  $e^n$ -method for three-dimensional flows developed by Cebeci and Stewartson discussed in Chapter 11.

Figure 1.3 shows the inviscid velocity distribution  $u_e/u_\infty$  for the upper surface of the wing for  $\lambda = 20^\circ, 30^\circ, 40^\circ$  and  $50^\circ$  and, as can be seen, the flow has a favorable pressure gradient up to around 50-percent chord, followed by an adverse pressure gradient. We expect that the cross-flow instability will be rather weak at lower sweep angles, so that transition will take place in the region where the flow deceleration takes place. With increasing sweep angle, however, crossflow instability (Chapter 11) will begin to dominate and cause transition to occur in the region of acceleration. The results of Fig. 1.4 for  $\lambda = 20^\circ$  confirm this expectation and indicate that the location of the critical frequencies occurs around  $x/c = 0.01$ , with amplification factors computed with different frequencies reaching values of  $n$  as high as 6.75 at  $x/c = 0.44$  but not a value of  $n = 8$  as required to indicate transition. Additional calculations show that transition occurs at  $x/c = 0.65$  and is not caused by crossflow instability. The results for  $\lambda = 40^\circ$ , shown in Fig. 1.5, however, indicate that crossflow instability makes its presence felt at this sweep angle, causing transition to occur at  $x/c = 0.08$  corresponding to a radian disturbance frequency of 0.03740. The location of the critical frequency is at  $x/c = 0.0046$ , very close to the attachment line of the wing.

Calculations performed for  $\lambda = 30^\circ, 35^\circ$  and  $50^\circ$  indicate results similar to those for  $\lambda = 40^\circ$  in that the transition location moves closer to the leading edge with increasing sweep angle, occurring at  $x/c = 0.22$  for  $\lambda = 30^\circ$ , at  $x/c = 0.12$  for  $\lambda = 35^\circ$  and at  $x/c = 0.05$  at  $\lambda = 50^\circ$ . In all cases, the location of the critical frequency is almost at the same location as for  $\lambda = 40^\circ$ , with values of critical radian frequency,  $\omega$ , becoming 0.09144, 0.09044 and 0.09952 for  $\lambda = 30^\circ, 35^\circ$  and  $50^\circ$ , respectively.



**Fig. 1.3.** Variation of inviscid velocity distribution with sweep angle for the NACA 65-412 wing.



**Fig. 1.4.** Amplification factors for several frequencies for  $\lambda = 20^\circ$ . The insert corresponds to a zarf (Section 11.3) used to identify the critical frequencies needed in the  $e^n$ -method.

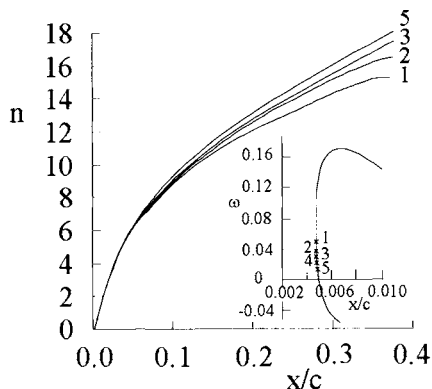


**Fig. 1.5.** Amplification factors for several frequencies for  $\lambda = 40^\circ$ .

Figures 1.6 to 1.8 show the calculated amplification factors for the same wing with suction, which is a powerful means of maintaining laminar flow over the whole wing. In practice, however, this is difficult to achieve because of the need for ailerons, flaps and openings for inspection and maintenance. Clearly a suction system adds to the complexity, weight and cost of a design. Increasing suction rates requires larger ducting system and more power so that at some point all available space in the wing may be used up and the higher suction drag will produce diminishing returns. Increased suction also makes the boundary-layer thinner, which in turn reduces the critical height of roughness that will cause transition. If suction is applied through discrete holes or slots and is not distributed over the area, increased suction velocities may cause the suction holes or slots to become critical themselves and act as sources for disturbances. It is important that the suction system must be carefully designed by calculating minimum suction rates to maintain laminar flow. In addition, the suction rate distribution must be optimum. A calculation method, such as the one described in Chapter 4 of [1], is capable of determining the minimum and optimum suction rates for the ducting system. Table 1.3 lists the suction distributions used in the calculations presented here. For simplicity, two types of suction distributions are considered: the first with uniform suction on the whole wing and the second with uniform suction over the front portion of the wing only, e.g. 5% chord from the leading edge.

Figure 1.6 shows the amplification factors for critical frequencies without suction, with the two types of suction, S1 and S4 for  $\lambda = 30^\circ$ . As can be seen, a small suction level of  $\bar{v}_w = -0.0003$  either over the whole wing, S1, or over the front 5% chord of the wing, S4, is sufficient to maintain laminar flow until

**Table 1.3.** Suction rates  $\bar{v}_w \equiv v_w/V_\infty$  used in the stability calculations. S1, S2 and S3 are applied to the whole wing while S4 to S8 are applied to the first 5% chord of the wing. S9 is applied to the first 10% of the wing.

	$\bar{v}_w \times 10^4$		$\bar{v}_w \times 10^4$
S1	-3	S5	-5
S2	-5	S6	-7
S3	-7	S7	-10
S4	-3	S8	-12
		S9	-12

separation occurs at  $x/c = 0.58$  for S4 and at  $x/c = 0.78$  for S1. The calculations for S1 produce a low value of  $n = 3$  at  $x/c = 0.34$  and indicate that the suction rate is excessive at this sweep angle.

Figure 1.7 shows the results for  $\lambda = 40^\circ$  for which case a suction level of  $\bar{v}_w = -0.0003$  for S1 yields a maximum value of  $n = 6$  at  $x/c = 0.20$  and a suction level corresponding to S2 yields a maximum value of  $n = 3$  at  $x/c = 0.12$ . Both cases eliminate transition which occurs at  $x/c = 0.08$  without suction, but the latter also eliminates the occurrence of separation while the former delays the separation until  $x/c = 0.78$ . To avoid excessive suction, two additional cases corresponding to S5 and S7 were considered and it was observed that transition takes place at  $x/c = 0.22$  for S5, and the maximum value of  $n$  is equal to 6.7 at  $x/c = 0.52$  for S7 which shows that the crossflow instabilities can be eliminated in the front portion of the wing. It is interesting to note that the small bump near  $x/c = 0.05$  along the curve for S7 shown in Fig. 1.7 is caused by the switch-off of suction at  $x/c = 0.05$ .

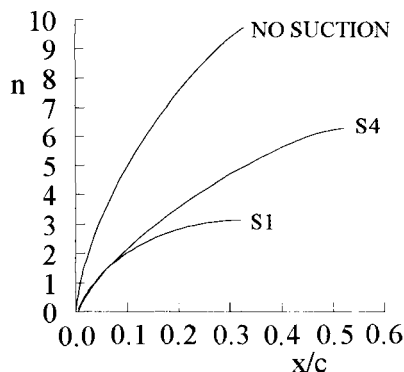


**Fig. 1.6.** Effect of suction on amplification rates for  $\lambda = 30^\circ$ .

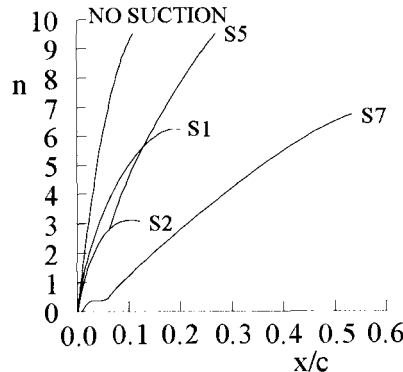


**Fig. 1.7.** Effect of suction on amplification rates for  $\lambda = 40^\circ$ .

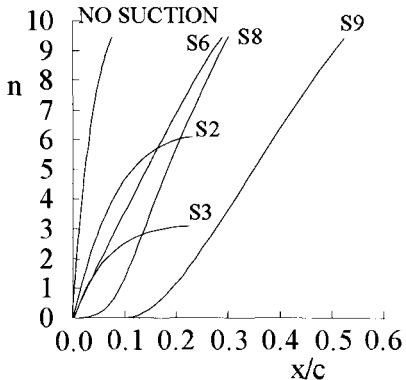


**Fig. 1.8.** Effect of suction on amplification rates for  $\lambda = 50^\circ$ .

As expected, it is more difficult to avoid the crossflow instabilities for  $\lambda = 50^\circ$  because of the high sweep, and Fig. 1.8 shows that only suction levels corresponding to S2 and S3 can eliminate transition. However, if suction is switched off at 5% chord from the leading edge, transition occurs even if a high suction level of  $\bar{v}_w = -0.0012$  is applied. In order to laminarize the flow, it is necessary to extend the range of suction at a suction level of  $\bar{v}_w = -0.0012$  for the first 10% chord of the wing, case S9, leading to transition at  $x/c = 0.48$  which is 8% upstream of the separation location. Further extensions of the suction area will eliminate transition before separation occurs. From the results corresponding to S8 and S9, it can be seen that the growth of the disturbances can be prevented only in the range over which suction is applied for  $\lambda = 50^\circ$ . Once the suction is switched off, the disturbances grow with almost constant speed and cause transition to occur downstream, indicating the difficulty of laminarizing the flow on a highly swept-back wing.

## 1.2 Prediction of the Maximum Lift Coefficient of Multielement Wings

In aircraft design it is very important to determine the maximum lift coefficient as accurately as possible, since this lift coefficient corresponds to the stall speed, which is the minimum speed at which controllable flight can be maintained. Any further increase in angle of incidence will increase flow separation on the wing upper surface, and the increased flow separation results in a loss in lift and a large increase in drag.

The high-lift system of an aircraft plays a crucial role in the takeoff and landing of an aircraft. Without high-lift devices, the maximum lift coefficient,  $(C_L)_{\max}$ , attainable by a high-aspect-ratio wing is about five times the incidence (in radians) at incidences up to stall. Typical values of  $(C_L)_{\max}$  are commonly in the range of 1.0 to 1.5. The addition of high-lift devices such as flaps and slats can more than double  $(C_L)_{\max}$  with subsequent improvement in takeoff

and landing performance. Thus, it is important to predict the performance of high-lift systems that can be designed for both  $(C_L)_{\max}$  and low drag. The lower drag also results in lower noise, which is necessary to comply with noise abatement regulations.

Despite the significant advances in CFD, our ability to predict the maximum lift coefficient of multielement wings is still not satisfactory. As shown in Fig. 1.9, the flow about multielement airfoils for high lift is very complex. The main problem is the lack of an accurate turbulence model (Section 8.3) to represent flows with extensive separation. The problem is exacerbated by inaccuracies of numerical solutions of the conservation equations (Chapter 2) at these flow conditions and difficulties in modeling flow near the trailing edge of an airfoil or wing, trailing viscous wakes that may impinge on aft elements, merging boundary-layers, and flow separation.

In this section we describe a useful design method developed by Valarezo and Chin [4]. This method, called “The Pressure Difference Rule”, for predicting the maximum lift coefficient of multielement wings is based on Hess’ panel method which is an extension of the two-dimensional panel method given in the accompanying CD-ROM, Program 4, to three-dimensional flows. The accuracy of this method, even though the solution is based on the reduced conservation equations and does not include the effects of viscosity, is then demonstrated for the high-lift systems of a transport aircraft as a function of Reynolds number. While this method is appropriate for configuration development, it cannot predict the optimum gap/overhang locations for each of the high-lift wing components; at this time the determination of these locations remains a wind-tunnel-testing task. The ability to predict these locations is one of the aims of computational fluid dynamics development efforts in high-lift research.

The Pressure Difference Rule of Valarezo and Chin [4] is based on the examination of wind tunnel data which indicates that, at a given Reynolds/Mach

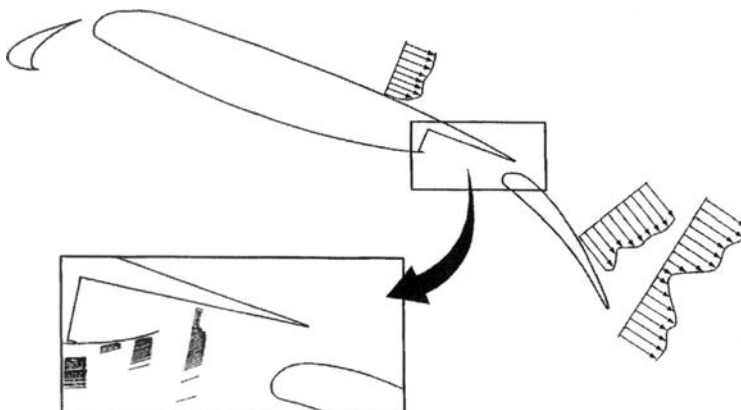


**Fig. 1.9.** A typical high-lift system

number combination, there exists a certain pressure difference  $\Delta C_p$  between the suction peak of an airfoil ( $C_p$ )<sub>min</sub> and its trailing edge ( $C_p$ )<sub>te</sub> at the maximum lift condition. For the case of a multielement airfoil, the same rule applies to whichever element (leading-edge or main) is critical at maximum lift. Thus, at a given freestream Mach number, there is a “pressure difference”  $|\Delta C_p| = |(C_p)_{\text{min}} - (C_p)_{\text{te}}|$  variation with Reynolds number (Fig. 1.10) that indicates when maximum lift is attained. This correlation applies whether or not the airfoil has an auxiliary leading-edge device.

Even though the Pressure Difference Rule is based on two-dimensional data, Valarezo and Chin assume the correlation in Fig. 1.10 to be valid also for three-dimensional flows. They determine the maximum lift coefficient of multielement transport wings by the following procedure:

1. Use a panel method to obtain flow solutions at various angles of attack for the desired geometry. While any reliable panel method can be used for this purpose, they use the Hess panel method discussed in detail in [2]. They recommend sufficient surface paneling to ensure adequate definition of the geometry at the leading and trailing edges.
2. For a given freestream Reynolds number and Mach number, construct a pressure difference  $|\Delta C_p|$  distribution vs. span based on the wing chord distribution.
3. Determine graphically at what spanwise wing station and wing lift coefficient the solutions obtained from the panel method (Step 1) match the curve constructed in Step 2.

Valarezo and Chin validated this method with RAE experimental data [5] obtained for a high-lift system. The wing had an aspect ratio of 8.35 and wing quarter-chord sweep of  $28^\circ$  with a taper ratio of 0.35. The high-lift system included a 16% chord leading-edge slat ( $\delta_S = 15^\circ, 20^\circ$  and  $25^\circ$ ) and a 34% Fowler flap ( $\delta_F = 10^\circ, 25^\circ$  and  $40^\circ$ ). The test was conducted transition-free at a Reynolds number of  $1.31 \times 10^6$  based on the mean wing chord and a

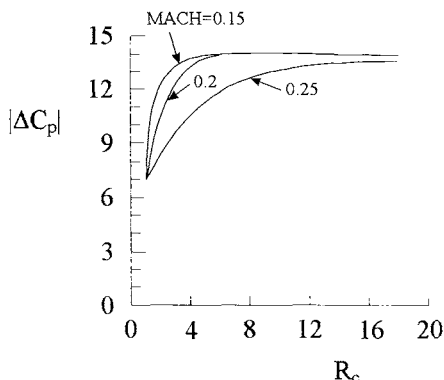
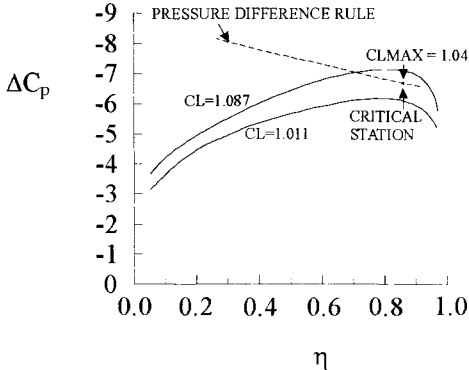


Fig. 1.10. Variation of  $|\Delta C_p|$  with chord Reynolds number  $R_c$  at maximum lift conditions.



**Fig. 1.11.** Pressure difference rule prediction of max lift for the RAE wing.

nominal Mach number was 0.22. The Pressure Difference Rule was used to predict  $(C_L)_{\max}$  for wing configurations corresponding to wing-alone, wing-flap, slat-wing and slat-wing-flap.

Figure 1.11 shows the predicted pressure difference for the wing alone. The results for  $C_L = 1.011$  and  $1.087$  correspond to the panel method solutions at angles of attack of  $11.84^\circ$  and  $12.84^\circ$ , respectively (Step 1). The allowable variation of  $\Delta C_p$  along the span was obtained from Fig. 1.10 for chord Reynolds numbers of  $1.61 \times 10^6$  and  $1.01 \times 10^6$  at spanwise stations  $\eta$  of 0.3 and 0.76, respectively, and for an interpolated  $M_\infty = 0.22$ , yielding  $|\Delta C_p| = 8.2$  at  $\eta = 0.30$  and  $|\Delta C_p| = 7$  at  $\eta = 0.76$ . The dashed straight line connecting these two points represents the boundary that predicts when  $(C_L)_{\max}$  occurs. According to Fig. 1.11, linear interpolation yields a predicted  $(C_L)_{\max}$  of 1.04 and the critical spanwise station is identified at 87% of the span.

The predictions of the Pressure Difference Rule for the RAE wing with different flap deflections are shown in Fig. 1.12 together with the experimental and calculated lift curves. The calculated viscous flow results were obtained by using the interactive boundary-layer method described in [3] and Chapter 12. The results denoted as semi-empirical were obtained from the inviscid panel method by reducing the nominal flap angle in order to account roughly for the

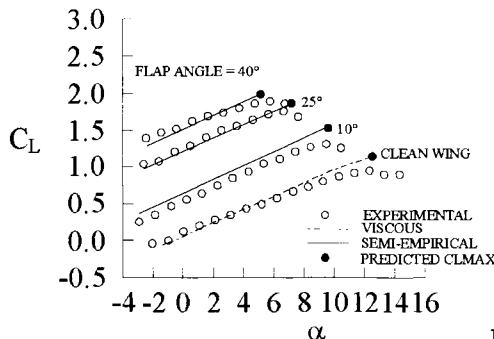


**Fig. 1.12.** Lift curves for RAE wing.

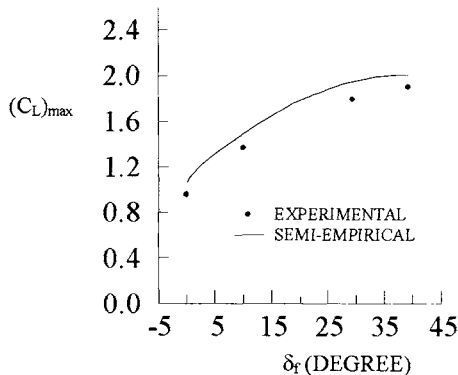


Fig. 1.13. Effect of flap deflection on maximum lift.

known decambering effect of the boundary-layer and wakes on the aft segments of a multielement wing. Agreement between experiment and prediction is seen to be very good throughout each lift curve up to and including  $(C_L)_{\max}$ . The effect of flap deflection on maximum lift for the wing-flap configuration is shown in Fig. 1.13, where the method based on the Pressure Difference Rule correctly indicates marginal lift improvements in going from  $25^\circ$  to  $40^\circ$  flaps for this particular wing. The ability to predict this is a key result since it shows that  $40^\circ$  flaps offer only a minimal improvement to lift, and therefore going from  $25^\circ$  to  $40^\circ$  flaps is not desirable given the substantial drag increase.

Further applications and validations of the Pressure Difference Rule are reported in [4] by Valarezo and Chin for several narrow-body and wide-body transport configurations. Figure 1.15 shows the results for the narrow-body transport of Fig. 1.14. The wing is configured for landing with both leading and trailing-edge devices deployed. The predicted variation of  $(C_L)_{\max}$  with Reynolds number shown in Fig. 1.15 compares very well with available wind tunnel and flight test results. As can be seen, the variation of  $(C_L)_{\max}$  with

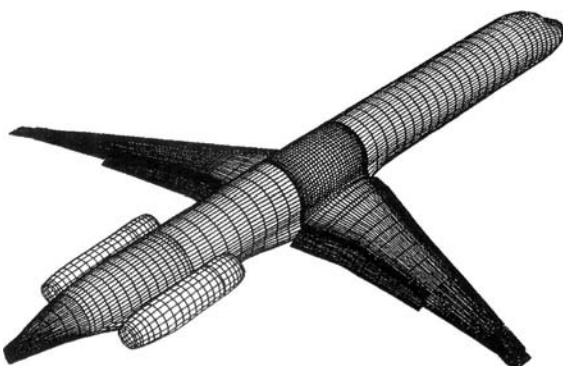
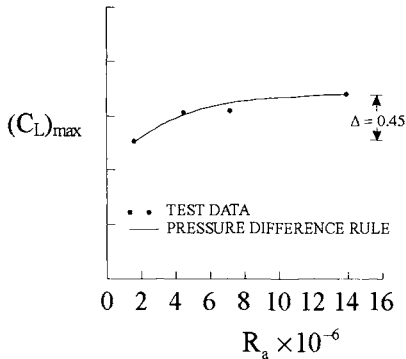


Fig. 1.14. Paneled narrow-body transport.



**Fig. 1.15.** Variation of maximum lift coefficient with Reynolds number based on mean aerodynamic chord,  $R_a$ .

Reynolds number is considerable, and the method based on the Pressure Difference Rule captures it remarkably well.

## References

- [1] Bushnell, D. M. and Heiner, J. N.: *Viscous Drag Reduction*, AIAA "Progress in Aeronautics and Astronautics" Series, 1989.
- [2] Hess, J. L.: "The Problem of Three-Dimensional Lifting Flow and Its Solution by Means of Surface Singularity Distribution," *Computer Methods in Applied Mechanics and Engineering* 4, 283–319, 1974.
- [3] Cebeci, T.: *An Engineering Approach to the Calculation of Aerodynamic Flows*. Horizons Publ., Long Beach, Calif. and Springer, Heidelberg, 1999.
- [4] Valarezo, W. O. and Chin, V. D.: "Maximum Lift Prediction for Multielement Wings," AIAA Paper No. 92-0401, Jan 1992.
- [5] Lovell, D. A.: "A Wind-Tunnel Investigation of the Effects of Flap Span and Deflection Angle, Wing Platform and a Body on the High-Lift Performance of a 28° Swept Wing", CP No. 1372, 1977.
- [6] Hess, J. L., Friedman, D. M. and Clark, R. W.: "Calculation of Compressible Flow About Three-Dimensional Inlets with Auxiliary Inlets, Slats, and Vanes by Means of a Panel Method," McDonnell Douglas Report No. MDC J3789, June 1985 (Also, AIAA Paper No. 85-119b and NASA CR-174975).

# 2 Conservation Equations for Mass and Momentum for Incompressible Flows

## 2.1 Introduction

The conservation equations for fluid flow are based on the principles of conservation of mass, momentum and energy and are known as the Navier–Stokes equations. They can be represented in both differential and integral forms. In this chapter we do not provide detailed derivations of these equations since they can be found in various textbooks such as References 1 to 5. In this book, we assume that the flow is incompressible and the temperature differences between the surface and freestream are small so that the fluid properties such as density  $\rho$  and dynamic viscosity  $\mu$  in the conservation equations are not affected by temperature. This assumption allows us to direct our attention to the conservation equations for mass and momentum and ignore the conservation equation for energy.

In this chapter we first discuss the conservation equations for mass and momentum (Section 2.2), and we shall refer to them as the Navier–Stokes equations. Since most flows are turbulent with fluctuations of velocity over a range of frequencies, the solution of the Navier–Stokes equations of Section 2.2 presents a formidable challenge and is unlikely to be achieved for the boundary conditions of real engineering flows in the foreseeable future. For this reason, it is common practice to average the equations. The resulting equations, usually called Reynolds-Averaged Navier–Stokes (RANS) equations, include correlations of fluctuation terms, as discussed in Section 2.3 and these require the models discussed in Chapter 8.

Depending on the flow conditions, it is appropriate and sometimes necessary to use the reduced forms of the Navier–Stokes equations as discussed in Section 2.4 and Chapter 3. These simplified equations, especially for inviscid flows (Section 2.4) and for boundary-layer flows (Chapter 3), reduce the complexity of solving the Navier–Stokes equations (Chapter 3), provide substantial savings of computer time and in some situations permit accurate analytical and numerical solutions to the conservation equations.

## 2.2 Navier–Stokes Equations

The Navier–Stokes equations may be obtained by using infinitesimal or finite control volume approaches, and the governing equations can be expressed in differential or integral forms, as discussed in detail in [1, 2, 5]. Here we discuss the Navier–Stokes equations in differential form obtained by using an infinitesimal control volume moving along a streamline with a velocity vector  $\vec{V}$  ( $u, v, w$ ) equal to the flow velocity at each point. For a three-dimensional incompressible flow, they are given by the following continuity and three momentum equations:

Continuity equation

$$\frac{\partial u}{\partial x} + \frac{\partial v}{\partial y} + \frac{\partial w}{\partial z} = 0 \quad (2.2.1)$$

$x$ -component of the momentum equation

$$\rho \frac{Du}{Dt} = -\frac{\partial p}{\partial x} + \left( \frac{\partial \sigma_{xx}}{\partial x} + \frac{\partial \sigma_{xy}}{\partial y} + \frac{\partial \sigma_{xz}}{\partial z} \right) + \rho f_x \quad (2.2.2)$$

$y$ -component of the momentum equation

$$\rho \frac{Dv}{Dt} = -\frac{\partial p}{\partial y} + \left( \frac{\partial \sigma_{yx}}{\partial x} + \frac{\partial \sigma_{yy}}{\partial y} + \frac{\partial \sigma_{yz}}{\partial z} \right) + \rho f_y \quad (2.2.3)$$

$z$ -component of the momentum equation

$$\rho \frac{Dw}{Dt} = -\frac{\partial p}{\partial z} + \left( \frac{\partial \sigma_{zx}}{\partial x} + \frac{\partial \sigma_{zy}}{\partial y} + \frac{\partial \sigma_{zz}}{\partial z} \right) + \rho f_z \quad (2.2.4)$$

where  $D/Dt$  represents the substantial derivative given by

$$\frac{D(\ )}{Dt} = \frac{\partial(\ )}{\partial t} + u \frac{\partial(\ )}{\partial x} + v \frac{\partial(\ )}{\partial y} + w \frac{\partial(\ )}{\partial z} = \frac{\partial(\ )}{\partial t} + \vec{V} \cdot \nabla(\ ) \quad (2.2.5)$$

Equations (2.2.2) to (2.2.4) make use of Newton's second law of motion with their left-hand sides representing mass acceleration per unit volume and their right-hand sides representing the sum of net forces per unit volume acting on the fluid which consists of surface and body forces. Typical body forces are gravity forces or electrical forces. Surface forces arise because of molecular stresses in the fluid (such as pressure,  $p$ , which is present in a fluid at rest and acts normal to a surface) and viscous stresses which act normal to a surface or tangentially (shear stress). The first term on the right-hand side of Eqs. (2.2.2)–(2.2.4) denotes the net pressure force per unit volume and the minus sign arises because, by definition, a positive pressure acts inward. The second, third and fourth terms denote the viscous forces per unit volume, and they arise as a result of the different components of normal and shear stresses shown in Fig. 2.1: the first subscript to the symbol  $\sigma$  represents the direction of the stress and the second the direction of the surface normal. By convention, an *outward*

normal stress acting on the fluid in the control volume is positive, and the shear stresses are taken as positive on the faces furthest from the origin of the coordinates. Thus  $\sigma_{xy}$  acts in the positive  $x$  direction on the visible (upper) face perpendicular to the  $y$  axis; a corresponding shear stress acts in the *negative*  $x$  direction on the invisible lower face perpendicular to the  $y$  axis.

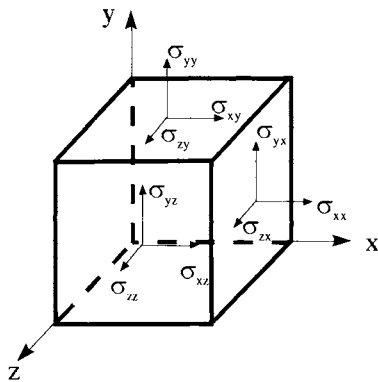


**Fig. 2.1.** Definitions of viscous stress components applied to the faces of a control volume by the surrounding fluid. Force components are stress components multiplied by areas of corresponding faces.

Sometimes it is more convenient to write the viscous terms in the momentum equations in tensor notation as

$$\frac{\partial \sigma_{ij}}{\partial x_j} \quad (2.2.6)$$

with  $i, j = 1, 2, 3$  for three-dimensional flows; for example,  $i = 1, j = 1, 2, 3$  for Eq. (2.2.2). For a constant density “Newtonian” viscous fluid, the normal viscous stresses  $\sigma_{ij}$  ( $i = j$ ) and shear stresses  $\sigma_{ij}$  ( $i \neq j$ ) are obtained from the viscous stress tensor given by

$$\sigma_{ij} = \mu \left( \frac{\partial u_i}{\partial x_j} + \frac{\partial u_j}{\partial x_i} \right) \quad (2.2.7)$$

Sometimes Eq. (2.2.7) is written as

$$\sigma_{ij} = 2\mu S_{ij}$$

where  $S_{ij}$  defined by

$$S_{ij} = \frac{1}{2} \left( \frac{\partial u_i}{\partial x_j} + \frac{\partial u_j}{\partial x_i} \right)$$

is called the rate of strain tensor.

According to Eq. (2.2.7), the normal viscous stress  $\sigma_{xx}$  and the shear stresses  $\sigma_{xy}$  and  $\sigma_{xz}$  in Eq. (2.2.2) are given by

$$\sigma_{xx} = 2\mu \frac{\partial u}{\partial x}, \quad \sigma_{xy} = \mu \left( \frac{\partial u}{\partial y} + \frac{\partial v}{\partial x} \right), \quad \sigma_{xz} = \mu \left( \frac{\partial u}{\partial z} + \frac{\partial w}{\partial x} \right) \quad (2.2.8)$$

with similar expressions for the viscous stress tensor terms in Eqs. (2.2.3) and (2.2.4).

In terms of Eq. (2.2.7), the Navier–Stokes equations can be simplified considerably so that, for example, the  $x$ -momentum equation, (2.2.2) for a Newtonian fluid becomes

$$\frac{Du}{Dt} = -\frac{1}{\rho} \frac{\partial p}{\partial x} + \nu \nabla^2 u + f_x \quad (2.2.9)$$

with similar expressions for the  $y$ - and  $z$ -components obtained from Eqs. (2.2.3) and (2.2.4). The resulting equations can be written in vector form as

$$\frac{D\vec{V}}{Dt} = -\frac{1}{\rho} \nabla p + \nu \nabla^2 \vec{V} + \vec{f} \quad (2.2.10)$$

with  $\nabla^2$  denoting the Laplacian operator

$$\nabla^2 \equiv \frac{\partial^2}{\partial x^2} + \frac{\partial^2}{\partial y^2} + \frac{\partial^2}{\partial z^2}$$

## 2.3 Reynolds-Averaged Navier–Stokes Equations

The Navier–Stokes equations of the previous section also apply to turbulent flows if the values of fluid properties and dependent variables are replaced by their instantaneous values. A direct approach to solving the equations for turbulent flows is to solve them for specific boundary conditions and initial values that include time-dependent quantities. Mean values are needed in most practical cases, so an ensemble of solutions of time-dependent equations is required. Even for the most restricted cases, this approach, referred to as direct numerical simulation (DNS) and discussed in [6], becomes a difficult and extremely expensive computing problem because the unsteady eddy motions of turbulence appear over a wide range of scales. The usual procedure is to average the equations rather than their solutions, as discussed in detail in [1, 5, 6] and briefly below.

In order to obtain the conservation equations for turbulent flows, we replace the instantaneous quantities in the equations by the sum of their mean and fluctuating parts. For example, the instantaneous values of the  $u$ ,  $v$  and  $w$  velocities and pressure  $p$  are expressed by the sum of their mean  $\bar{u}$ ,  $\bar{v}$ ,  $\bar{w}$ ,  $\bar{p}$  and fluctuating parts  $u'$ ,  $v'$  and  $w'$ ,  $p'$

$$u = \bar{u} + u', \quad v = \bar{v} + v', \quad w = \bar{w} + w', \quad p = \bar{p} + p' \quad (2.3.1)$$

where, for example,  $\bar{u}$  is the ensemble average of  $u$  defined by

$$\bar{u} = \lim_{N \rightarrow \infty} \frac{1}{N} \sum_{i=1}^N u_i$$

with  $u_i$  denoting the sample and  $N$  the number of samples.

With the help of the continuity equation, (2.2.1), one can now write the left-hand sides of the momentum equations in *conservation form* (Problem 2.1) and introduce the above relations into the continuity and momentum equations. After averaging and making use of the substantial derivatives given by Eq. (2.2.5), the Reynolds averaged Navier–Stokes (RANS) equations for three-dimensional incompressible flow can be written in the following form (Problem 2.6):

$$\frac{\partial \bar{u}}{\partial x} + \frac{\partial \bar{v}}{\partial y} + \frac{\partial \bar{w}}{\partial z} = 0 \quad (2.3.2)$$

$$\rho \frac{D\bar{u}}{Dt} = -\frac{\partial \bar{p}}{\partial x} + \mu \nabla^2 \bar{u} + \rho \bar{f}_x - \rho \frac{\partial}{\partial x} (\overline{u'^2}) - \rho \frac{\partial}{\partial y} (\overline{u'v'}) - \rho \frac{\partial}{\partial z} (\overline{u'w'}) \quad (2.3.3)$$

$$\rho \frac{D\bar{v}}{Dt} = -\frac{\partial \bar{p}}{\partial y} + \mu \nabla^2 \bar{v} + \rho \bar{f}_y - \rho \frac{\partial}{\partial x} (\overline{v'u'}) - \rho \frac{\partial}{\partial y} (\overline{v'^2}) - \rho \frac{\partial}{\partial z} (\overline{v'w'}) \quad (2.3.4)$$

$$\rho \frac{D\bar{w}}{Dt} = -\frac{\partial \bar{p}}{\partial z} + \mu \nabla^2 \bar{w} + \rho \bar{f}_z - \rho \frac{\partial}{\partial x} (\overline{w'u'}) - \rho \frac{\partial}{\partial y} (\overline{w'v'}) - \rho \frac{\partial}{\partial z} (\overline{w'^2}) \quad (2.3.5)$$

It is common to drop the overbars on  $u$ ,  $v$ ,  $w$  and  $p$ ; this results in a continuity equation identical to that given by Eq. (2.2.1), and the left-hand sides of the momentum equations, Eqs. (2.3.3) to (2.3.5), become identical to the equations for laminar flow. The right-hand sides of the momentum equations also resemble the right-hand sides of Eqs. (2.2.2) to (2.2.4) with the addition of the Reynolds normal and shear stress terms; in our previous notation the Reynolds stresses in Eq. (2.3.3) represent the turbulent contributions to a  $\sigma_{xx}$ ,  $\sigma_{xy}$  and  $\sigma_{xz}$ , respectively. The mean viscous contributions are still given by Eq. (2.2.7) and are based on the mean-velocity components. Equations (2.2.2) to (2.2.4) thus apply to both laminar and turbulent flows, provided that the so-called “stress tensor”,  $\sigma_{ij}$ , including the viscous contributions, is written as

$$\sigma_{ij} = -\rho \overline{u'_i u'_j} + \mu \left( \frac{\partial u_i}{\partial x_j} + \frac{\partial u_j}{\partial x_i} \right) \quad (2.3.6)$$

or

$$\sigma_{ij} = \sigma_{ij}^t + \sigma_{ij}^l \quad (2.3.7)$$

where now  $\sigma_{ij}^t$  denotes the Reynolds stresses so that for three-dimensional flows  $\sigma_{xx}^t = -\overline{\rho u'^2}$ ,  $\sigma_{xy}^t = \sigma_{yx}^t = -\overline{\rho u'v'}$ ,  $\sigma_{xz}^t = \sigma_{zx}^t = -\overline{\rho u'w'}$ ,  $\sigma_{yy}^t = -\overline{\rho v'^2}$ ,  $\sigma_{yz}^t = \sigma_{zy}^t = -\overline{\rho v'w'}$ ,  $\sigma_{zz}^t = -\overline{\rho w'^2}$ , and  $\sigma_{ij}^l$  is the viscous stress tensor as given by Eq. (2.2.7) for a Newtonian fluid.

The Reynolds stress terms in the momentum equations introduce additional unknowns into the conservation equations. To proceed further, additional equations for these unknown quantities, or assumptions regarding the relationship between the unknown quantities to the time-mean flow variables, are needed. This is referred to as the “closure” problem in turbulent flows: we shall discuss turbulence modeling in some detail in Chapter 6.

## 2.4 Inviscid Flow Equations

The conservation equations can be reduced to simpler forms by examining the relative magnitudes of the terms in the equations. This procedure can be applied by using the "order of magnitude" analysis or more formally by using an asymptotic expansion technique. In both cases, scales are used to evaluate the order of magnitude of the various terms in the equations. Considering the flow past a wall at high Reynolds number, typically around an airfoil, it is common to introduce two length scales  $L$  and  $\delta$  which are, respectively, parallel and normal to the wall. Near the wall, as discussed in chapter 3, as the length scale  $\delta$  normal to the wall is much smaller than the longitudinal scale, the Navier–Stokes equations reduce to the boundary-layer equations. In the wake which results from the merging of boundary-layers, the same approximation applies. Away from these regions, another approximation holds because there is only one length scale  $L$  in any direction. There, the inviscid flow approximation applies. It does not mean that the viscosity of the flow is zero in these regions, but it means that the effects of viscosity are negligible. Roughly, it can be said that the viscous stresses are small because the variations of velocity are small. The result is that the viscous forces are negligible compared to the inertia forces.

With the inviscid flow approximation, the continuity equation, Eq. (2.2.1), remains unchanged, and with the neglect of viscous forces, the Navier–Stokes equations reduce to the Euler equations,

$$\frac{D\vec{V}}{Dt} = -\frac{1}{\rho} \nabla p + \vec{f} \quad (2.4.1)$$

For a steady flow with no body forces, the Euler equations reduce to,

$$(\vec{V} \cdot \nabla) \vec{V} = -\frac{\nabla p}{\rho} \quad (2.4.2)$$

If we take the dot product of the above equation with a differential length of a streamline  $d\vec{s}$ , assume  $\rho$  constant (incompressible flow), and integrate the Euler equations along a streamline, we get (Problem 2.9)

$$p + \frac{1}{2}\rho V^2 = \text{constant} \quad (2.4.3)$$

where  $V^2 = u^2 + v^2 + w^2$ . This equation is the well known Bernoulli equation. It applies along a given streamline but, very often, the stagnation pressure  $p_i$  defined, for an incompressible flow, as

$$p_i = p + \frac{1}{2}\rho V^2 \quad (2.4.4)$$

is the same along all the streamlines when the flow is uniform at infinity. Under these conditions, the Bernoulli equation applies to the whole flow with the same constant everywhere.

Additional simplifications arise if the flow is *irrotational*, which is defined by zero vorticity

$$\vec{\omega} = \nabla \times \vec{V} = 0 \quad (2.4.5)$$

This condition implies the existence of a scalar function  $\phi$ , called the velocity potential, defined by

$$\vec{V} = \nabla \phi \quad (2.4.6)$$

In this case, for an incompressible flow, the continuity equation, can be combined with Eq. (2.4.6) to give Laplace's equation (Problem 2.10)

$$\nabla^2 \phi = 0 \quad (2.4.7)$$

which provides a good approximation to some real incompressible flows at high Reynolds numbers where the viscous effects are weak, as is sometimes the case when there is no flow separation on the body, as discussed, for example, in [3]. To be more specific, if we consider the flow around a two-dimensional airfoil at low angles of attack, the irrotational inviscid flow approximation, associated with the Kutta-Joukovski condition at the trailing edge, predicts lift coefficient well but does not predict drag which is due to viscous effects. To calculate viscous drag, it is necessary to account for the viscous effects. This can be achieved by including the boundary-layer effects in the inviscid method as discussed in Chapter 9.

## References

- [1] Anderson, J., *Fundamentals of Aerodynamics*, McGraw-Hill, 1991
- [2] Cousteix, J., *Couche Limite Laminaire*, CEPADUES, Toulouse, 1988
- [3] Anderson, D.A., Tannehill, J.C. and Pletcher, R.H., *Computational Fluid Mechanics and Heat Transfer*, Hemisphere Publishing Co., 1984
- [4] Anderson, J.D., *Computational Fluid Dynamics, The Basics with Applications*. McGraw-Hill, NY, 1995
- [5] Cebeci, T., *Convective Heat Transfer*, Horizons Publ., Long Beach, Calif. and Springer, Heidelberg, 2003.
- [6] Rai, M.M. and Moin, P., "Direct Simulations of Turbulent Flow Using Finite-Difference Schemes," *J. Comp. Phys.*, 96, p. 15, 1991
- [7] Cousteix, J., *Turbulence et Couche Limite*, CEPADUES, Toulouse, 1989
- [8] Blottner, F.G., "Significance of the Thin-Layer Navier-Stokes Approximation," In: *Numerical and Physical Aspects of Aerodynamic Flows III*, p. 184 (ed. T. Cebeci), Springer, NY, 1986

## Problems

**2-1.** Using the continuity equation, show that the substantial derivative of a scalar quantity  $f$  can be written in the form

$$\frac{Df}{Dt} = \frac{\partial f}{\partial t} + u \frac{\partial f}{\partial x} + v \frac{\partial f}{\partial y} + w \frac{\partial f}{\partial z} = \frac{\partial f}{\partial t} + \vec{V} \cdot \nabla f$$

or as

$$\frac{\partial f}{\partial t} + \frac{\partial uf}{\partial x} + \frac{\partial vf}{\partial y} + \frac{\partial wf}{\partial z} = \frac{\partial f}{\partial t} + \nabla \cdot (f \vec{V})$$

The first form is called a *nonconservation form*. The second form is called a *conservation form* or *divergence form*.

**2-2.** Write the Navier–Stokes equations for a steady, two-dimensional flow.

**2-3.** Express the continuity and momentum equations in conservation form.

**2-4.** Let  $f$  and  $g$  be two random functions and let  $\alpha$  be a non random function. The ensemble averaging process has the following properties.

$$\begin{aligned} f &= \bar{f} + f' \\ \bar{f}' &= 0 \\ \alpha &= \bar{\alpha} \\ \overline{f + g} &= \bar{f} + \bar{g} \\ \overline{\alpha f} &= \alpha \bar{f} \\ \overline{\frac{\partial f}{\partial x_i}} &= \frac{\partial \bar{f}}{\partial x_i} \\ \overline{\frac{\partial f}{\partial t}} &= \frac{\partial \bar{f}}{\partial t} \end{aligned}$$

Show that

$$\overline{fg} = \bar{f}\bar{g} + \overline{f'g'}$$

**2-5.** The instantaneous flow satisfies the continuity equation

$$\frac{\partial u_i}{\partial x_i} = 0$$

Show that the average flow and the fluctuating flow are divergence free, i.e.  $\partial \bar{u}_i / \partial x_i$  and  $\partial \bar{u}'_i / \partial x_i = 0$ . Note that the second equation is not trivial and different from  $\partial \bar{u}'_i / \partial x_i = 0$ .

**2-6.** Start from the conservation form of the Navier–Stokes equations to derive the RANS.

**2-7.** A turbulent flow is called steady if the mean flow is steady. A turbulent flow is called two-dimensional if the mean flow is two-dimensional. Simplify the RANS when the flow is steady and two-dimensional.

**2-8.** In a turbulent flow the velocity fluctuations are unsteady and three-dimensional even if the mean flow is steady and two-dimensional. Show that for a two-dimensional turbulent flow, the continuity equation for the fluctuating velocities is not the same if the averaging process is applied before or after the two-dimensional flow hypothesis is applied. Note that the averaging process must be applied to the complete Navier–Stokes equations (unsteady and three-dimensional) because the velocity fluctuations are unsteady and three-dimensional.

**2-9.** (a) Show that for an incompressible, steady inviscid flow the total pressure  $p_i = p + \rho(V^2/2)$  is constant along a streamline, but not necessarily constant throughout the flow.

(b) Defining a differential length of a streamline by  $\vec{ds}$ , which for a Cartesian coordinate system is

$$\vec{ds} = dx \vec{i} + dy \vec{j} + dz \vec{k} \quad (\text{P2.9.1})$$

and taking the dot product of Eq. (2.4.2) with (P2.9.1) and noting that  $\vec{V}$  has the same direction as  $\vec{ds}$ , show that, with  $V^2 = u^2 + v^2 + w^2$ , the left-hand side of the resulting expression can be written as

$$(\vec{V} \cdot \nabla) \vec{V} \cdot \vec{ds} = V \cdot \frac{\partial \vec{V}}{\partial s} ds = V dV = d \left( \frac{V^2}{2} \right) \quad (\text{P2.9.2})$$

and Eq. (2.4.3) follows.

**2-10.** Show that for an inviscid irrotational flow the velocity potential satisfies the Laplace equation.



# 3 Boundary-Layer Equations for Incompressible Flows

## 3.1 Two-Dimensional Flows

Another simplification of the Navier–Stokes equations occurs when the ratio of boundary-layer thickness  $\delta$  to a reference length  $L$ ,  $\delta/L$ , is sufficiently small because terms that are smaller than the main terms by a factor of  $\delta/L$  can be neglected. The resulting equations are known as the boundary-layer equations and include both laminar and turbulent flows as discussed here in this section for two-dimensional flows and axisymmetric flows in Section 3.2.

### 3.1.1 Laminar Flows

To reduce the Navier–Stokes equations to boundary-layer equations, we again use an order-of-magnitude analysis in which the gradients of a quantity such as  $u$  across a “principal flow direction”  $x$  are assumed to be at least an order-of-magnitude larger than gradients along  $x$ . This assumption permits the neglecting of some terms in the momentum (energy also as discussed in [1]) equations. While the application of the boundary-layer approximation can be demonstrated in different ways, here for simplicity and convenience, we start with the continuity and momentum equations for a two-dimensional laminar flow over a flat surface  $y = 0$ . Noting that

$$u \sim u_e, \quad p \sim \rho u_e^2, \quad x \sim L, \quad y \sim \delta \quad (3.1.1)$$

we first examine the order-of-magnitude of the normal velocity component  $v$ . It follows from the continuity equation

$$\frac{\partial u}{\partial x} + \frac{\partial v}{\partial y} = 0 \quad (3.1.2)$$

that since  $\partial u / \partial x$  is of order  $u_e / L$ ,

$$v \sim \frac{u_e \delta}{L} \quad (3.1.3)$$

The order-of-magnitude of various terms in the  $x$ -momentum Navier–Stokes equation for a two-dimensional laminar flow is

$$u \frac{\partial u}{\partial x} + v \frac{\partial u}{\partial y} = -\frac{1}{\rho} \frac{\partial p}{\partial x} + \nu \left( \frac{\partial^2 u}{\partial x^2} + \frac{\partial^2 u}{\partial y^2} \right) \quad (3.1.4)$$

$$\frac{u_e^2}{L} \quad \frac{u_e^2}{L} \quad \frac{u_e^2}{L} \quad \nu \left( \frac{u_e}{L^2} \quad \frac{u_e}{\delta^2} \right)$$

We note from the above equation that the inertia and pressure terms are of order  $u_e^2/L$  and the normal stress component of the viscous terms,  $\partial^2 u / \partial x^2$ , is small compared to the shear stress component  $\partial^2 u / \partial y^2$  and can be neglected. Rewriting the order-of-magnitude of the viscous term as

$$\nu \frac{u_e}{\delta^2} = \frac{\nu}{u_e L} \frac{u_e^2}{L} \frac{1}{(\frac{\delta}{L})^2}$$

we see that the viscous term  $\nu(\partial^2 u / \partial y^2)$  is of the same order-of-magnitude of the inertia and pressure forces (order of  $O(1)$ ) provided that

$$\frac{\delta}{L} \sim \frac{1}{\sqrt{R_L}} \quad (3.1.5)$$

where

$$R_L = \frac{u_e L}{\nu}. \quad (3.1.6)$$

Another useful way to compare the order of magnitude of various terms in the Navier–Stokes equations is to use the notion of time scales as discussed in Problem 3.14. For example, if we define convection time  $t_c$  by  $L/u_e$  and viscous time  $t_v$  by  $\delta^2/\nu$ , then the ratio of these two time scales

$$\frac{t_v}{t_c} = \frac{\delta^2}{\nu} \frac{u_e}{L} = \frac{\delta^2}{L^2} \frac{u_e L}{\nu} \quad (3.1.7)$$

which, according to the boundary-layer approximations, Eq. (3.1.7) is unity.

Applying a similar order-of-magnitude analysis to the  $y$ -momentum Navier–Stokes equation for a two-dimensional laminar flow, we find that the first and second terms on the left-hand side of this equation is  $\frac{u_e \delta}{L^2}$ . The larger of the viscous-stress terms,  $\frac{\partial^2 v}{\partial y^2}$ , is also of order  $\frac{u_e^2 \delta}{L^2}$ . This leads to the result that the pressure term in the equation  $(-\frac{1}{\rho}) \frac{\partial p}{\partial y}$ , is at most of order  $\frac{u_e^2 \delta}{L^2}$  and the change in pressure across the shear layer of thickness  $\delta$  is of order  $\rho u_e^2 (\frac{\delta}{L})^2$ . As a result of these approximations the  $y$ -momentum equation reduces to

$$\frac{\partial p}{\partial y} = 0$$

and the  $x$ -momentum Navier–Stokes equation becomes

$$u \frac{\partial u}{\partial x} + v \frac{\partial u}{\partial y} = -\frac{1}{\rho} \frac{dp}{dx} + \nu \frac{\partial^2 u}{\partial y^2} \quad (3.1.8)$$

### 3.1.2 Turbulent Flows

To discuss the boundary-layer approximations to the Reynolds-averaged Navier–Stokes equations for two-dimensional flows, we again use the same order of magnitude estimates for the mean flow given by Eqs. (3.1.1) and (3.1.3). For the fluctuating terms  $\overline{u'^2}$  and  $\overline{u'v'}$  in the  $x$ -momentum equation and  $\overline{v'^2}$  and  $\overline{v'u'}$  in the  $y$ -momentum equation, we assume that they all are of the same order of magnitude, that is,

$$\overline{u'^2} \sim \overline{v'^2} \sim \overline{u'v'}$$

Of the two-terms in the  $x$ -momentum equation

$$-\rho \frac{\partial}{\partial x}(\overline{u'^2}) - \rho \frac{\partial}{\partial y}(\overline{u'v'})$$

the first term, with  $\partial/\partial x$  being of order  $1/L$  and the second term with  $\partial/\partial y$  being of order  $1/\delta$ , is small compared to the second term and can be neglected.

Similarly, of the two terms in the  $y$ -momentum equation

$$-\rho \frac{\partial}{\partial x}(\overline{v'u'}) - \rho \frac{\partial}{\partial y}(\overline{v'^2})$$

the first term is small in comparison to the second term. Since the inertia terms on the left-hand-side of Eq. (2.3.4) together with the viscous term,  $\mu(\partial^2 v / \partial y^2)$ , are all of order  $\delta$ , we have

$$-\frac{\partial p}{\partial y} - \rho \frac{\partial}{\partial y}(\overline{v'^2}) = 0 \quad (3.1.9)$$

Consequently, the pressure variation across the boundary-layer is of  $O(\delta)$ , so that in comparison with the streamwise pressure variation, it is small and can be neglected within the boundary-layer approximations. Thus for two-dimensional flows, the Navier–Stokes equations reduce to

$$\frac{\partial u}{\partial x} + \frac{\partial v}{\partial y} = 0 \quad (3.1.2)$$

$$u \frac{\partial u}{\partial x} + v \frac{\partial u}{\partial y} = -\frac{1}{\rho} \frac{dp}{dx} + \nu \frac{\partial^2 u}{\partial y^2} - \frac{\partial}{\partial y}(\overline{u'v'}) \quad (3.1.10)$$

$$\frac{\partial p}{\partial y} = 0 \quad (3.1.11)$$

for laminar and turbulent flows with the Reynolds shear stress term  $-\overline{u'v'}$  equal to zero for laminar flows.

A comparison of Eqs. (3.1.10) and (3.1.11) with the  $x$ - and  $y$ -momentum Navier–Stokes equations for two-dimensional flows shows that with the boundary-layer approximations we have reduced some of the viscous terms in the  $x$ -momentum equation and neglected the variation of  $p$  with  $y$ . Note that, unlike

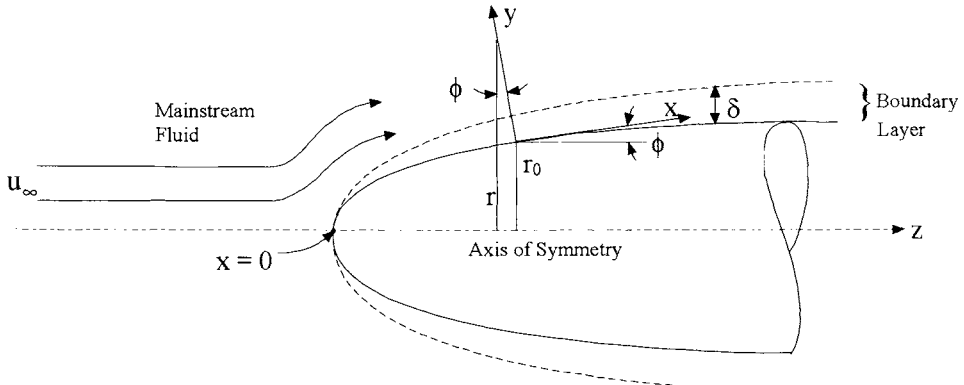


**Fig. 3.1.** The notation and the coordinate system for an axisymmetric flow.

the Navier–Stokes equations,  $p$  is no longer an unknown but has been absorbed into the boundary conditions by equating  $dp/dx$  to the value in the freestream where Bernoulli's equation applies.

$$\frac{dp}{dx} = -\rho u_e \frac{du_e}{dx} \quad (3.1.12)$$

For a two-dimensional laminar flow, with the simplification provided by Eq. (3.1.11), and without the Reynolds shear stress term, the momentum equation (3.1.10) and the continuity equation (3.1.2), are two equations for the two variables  $u$  and  $v$ . The Navier–Stokes equations, on the other hand, are three equations for three variables  $u$ ,  $v$ , and  $p$ . As we shall see in Section 3.4, boundary-layer equations are “parabolic” with disturbances propagating only downstream and not upstream. The two-dimensional Navier–Stokes equations (for  $u$ ,  $v$  and  $p$ ) are elliptic, with disturbances propagating upstream as well as downstream. The change in type is caused by the elimination of  $p$  as a variable and by the neglect of  $\partial^2 u / \partial x^2$ .

### 3.2 Axisymmetric Flows

If the flow is over an axisymmetric body so that gradients around the circumference are zero, the boundary-layer equations are similar to those for two-dimensional flows.

The continuity and momentum equations for the notation and coordinate system shown in Fig. 3.1 are

$$\frac{\partial}{\partial x}(r^k u) + \frac{\partial}{\partial y}(r^k v) = 0 \quad (3.2.1)$$

$$u \frac{\partial u}{\partial x} + v \frac{\partial u}{\partial y} = -\frac{1}{\rho} \frac{dp}{dx} + \frac{\nu}{r^k} \frac{\partial}{\partial y} \left( r^k \frac{\partial u}{\partial y} \right) + \frac{1}{r^k} \frac{\partial}{\partial y} (-r^k \bar{u}'v') \quad (3.2.2)$$

Here  $k$  denotes a “flow index” equal to unity in axisymmetric flow and zero in two-dimensional flow, so  $r^k$  is  $r$  or unity, respectively. With  $k = 0$  we recover Eqs. (3.1.2) and (3.1.10). The  $y$ -momentum equation is still given by Eq. (3.1.11).

In general,  $r$  is related to  $r_0$ , the radius of the surface  $y = 0$ , by

$$r(x, y) = r_0(x) + y \cos \phi(x) \quad (3.2.3)$$

where

$$\phi = \tan^{-1} \frac{dr_0}{dz}. \quad (3.2.4)$$

Defining

$$t \equiv \frac{y \cos \phi}{r_0} \quad (3.2.5)$$

We can write Eq. (3.2.3) as

$$\frac{r}{r_0} = 1 + t$$

Here  $t$  represents the deviation of  $r$  from  $r_0$  and is called the transverse-curvature term. In many axisymmetric flows the body radius is quite large in relation to the boundary-layer thickness, so the transverse-curvature effect is negligible. In that case, Eqs. (3.2.1) and (3.2.2) simplify and become

$$\frac{\partial}{\partial x}(r_0^k u) + \frac{\partial}{\partial y}(r_0^k v) = 0 \quad (3.2.6)$$

$$u \frac{\partial u}{\partial x} + v \frac{\partial u}{\partial y} = -\frac{1}{\rho} \frac{dp}{dx} + \nu \frac{\partial^2 u}{\partial y^2} + \frac{\partial}{\partial y}(-\bar{u}'v') \quad (3.2.7)$$

We note that Eq. (3.2.7) now has exactly the same form as Eq. (3.1.10) for two-dimensional flow. In problem 3.12, we discuss the Mangler transformation, which transforms the axisymmetric equations for small  $t$  into those of an equivalent two-dimensional flow.

In some problems, however, the body radius, while still finite, is of the same order of magnitude as the boundary-layer thickness, or even smaller. Typical examples are slender cylinders, the tail of a streamlined body of revolution, etc. In such cases the transverse curvature effect can be important and must be accounted for in the equations. For this reason, for axisymmetric flows we shall consider the more general equations given by Eqs. (3.2.1) and (3.2.2).

### 3.3 Momentum Integral Equation

The equations that result from integrating the momentum and continuity equations across the boundary-layer (i.e. from  $y = 0$  to  $y = \delta$ ) are useful in qualitative discussion and in some simplified types of calculation methods called integral methods as we shall discuss in Chapters 4 and 8. In this section we derive the equations for two-dimensional flows (Subsection 3.3.1) and then quote the equations (Subsection 3.3.2) for axisymmetric flows without proof.

### 3.3.1 Two-Dimensional Flows

We start with Eqs. (3.1.2) and (3.1.10), replacing the total shear stress  $\mu(\partial u / \partial y) - \rho \bar{u}' \bar{v}'$  by the symbol  $\tau$ , and  $-(1/\rho)(dp/dx)$  by  $u_e(du_e/dx)$ , invoking Eq. (3.1.12). For the sake of simplicity we derive the result for a boundary-layer on the surface  $y = 0$ . We have

$$\frac{\partial u}{\partial x} + \frac{\partial v}{\partial y} = 0 \quad (3.1.2)$$

$$u \frac{\partial u}{\partial x} + v \frac{\partial u}{\partial y} = u_e \frac{du_e}{dx} + \frac{1}{\rho} \frac{\partial \tau}{\partial y} \quad (3.3.1)$$

Now add  $u$  times Eq. (3.1.2) to Eq. (3.3.1)

$$\frac{\partial u^2}{\partial x} + \frac{\partial uv}{\partial y} = u_e \frac{du_e}{dx} + \frac{1}{\rho} \frac{\partial \tau}{\partial y} \quad (3.3.2)$$

and integrate with respect to  $y$  from  $y = 0$  to  $y = \delta$ . Then, with subscript  $e$  denoting boundary-layer edge,

$$\int_0^\delta \frac{\partial u^2}{\partial x} dy + u_e v_e = \int_0^\delta u_e \frac{du_e}{dx} dy - \frac{\tau_w}{\rho} \quad (3.3.3)$$

where  $\tau_w$  is the surface shear stress and

$$v_e = - \int_0^\delta \frac{\partial u}{\partial x} dy \quad (3.3.4)$$

from Eq. (3.1.2). Thus

$$\int_0^\delta \left( \frac{\partial u^2}{\partial x} - u_e \frac{\partial u}{\partial x} - u_e \frac{du_e}{dx} \right) dy = - \frac{\tau_w}{\rho}$$

or, after rearranging,

$$\int_0^\infty \left\{ -\frac{\partial}{\partial x} [u(u_e - u)] - \frac{du_e}{dx} (u_e - u) \right\} dy = - \frac{\tau_w}{\rho} \quad (3.3.5)$$

Now since  $u_e - u = 0$  for  $y \geq \delta$ , both parts of the integral contribute only for  $y < \delta$  and so are independent of  $\delta$ . Therefore, the first part of the integral can be written as

$$-\frac{d}{dx} \int_0^\delta u(u_e - u) dy$$

the  $x$ -derivative now being ordinary rather than partial because the definite integral is independent of  $y$ . With a little rearrangement and a change of sign we get

$$\frac{d}{dx} \left[ u_e^2 \int_0^\delta \frac{u(u_e - u)}{u_e^2} dy \right] + u_e \frac{du_e}{dx} \int_0^\delta \left( \frac{u_e - u}{u_e} \right) dy = \frac{\tau_w}{\rho} \quad (3.3.6)$$

We now introduce the definition of displacement thickness  $\delta^*$  which represents the distance by which the external flow streamlines are displaced in the  $y$ -direction by the presence of the boundary-layer,

$$\delta^* = \int_0^\delta \left(1 - \frac{u}{u_e}\right) dy \quad (3.3.7)$$

and the definition of momentum thickness  $\theta$ ,

$$\theta = \int_0^\delta \frac{u}{u_e} \left(1 - \frac{u}{u_e}\right) dy \quad (3.3.8)$$

The shape factor  $H$  is the ratio of displacement thickness to the momentum thickness

$$H = \frac{\delta^*}{\theta} \quad (3.3.9)$$

We now introduce the definitions of  $\delta^*$  and  $\theta$  into Eq. (3.3.6) and obtain

$$\frac{d}{dx}(u_e^2 \theta) + \delta^* u_e \frac{du_e}{dx} = \frac{\tau_w}{\rho}$$

or

$$\frac{d\theta}{dx} + (H + 2) \frac{\theta}{u_e} \frac{du_e}{dx} = \frac{c_f}{2} \quad (3.3.10)$$

where  $c_f$  is the local skin-friction coefficient defined by

$$c_f = \frac{\tau_w}{\frac{1}{2} \rho u_e^2} \quad (3.3.11)$$

Equation (3.3.10) is the momentum integral equation for two-dimensional constant density laminar or turbulent flows.

### 3.3.2 Axisymmetric Flows

In an axisymmetric flow the definition of  $\delta^*$  and  $\theta$  are

$$\delta^* = \int_0^\delta r^k \left(1 - \frac{u}{u_e}\right) dy \quad (3.3.12)$$

$$\theta = \int_0^\delta r^k \frac{u}{u_e} \left(1 - \frac{u}{u_e}\right) dy \quad (3.3.13)$$

using the “flow index” convention again ( $k = 0$  for two-dimensional flow and  $k = 1$  for axisymmetric flow). The momentum-integral equation becomes

$$\frac{d\theta}{dx} + (H + 2) \frac{\theta}{u_e} \frac{du_e}{dx} = r_0^k \frac{c_f}{2} \quad (3.3.14)$$

If  $\delta/r_0 \ll 1$ , the momentum integral equation for an axisymmetric flow is

$$\frac{d\theta}{dx} + (H + 2) \frac{\theta}{u_e} \frac{du_e}{dx} + \frac{\theta}{r_0} \frac{dr_0}{dx} = \frac{c_f}{2} \quad (3.3.15)$$

where now  $\delta^*$  and  $\theta$  are defined as in two-dimensional flow, without the  $r$  factor.

### 3.4 Boundary and Initial Conditions

The boundary-layer equations discussed in Sections 3.1 and 3.2 are parabolic partial differential equations and are much easier to solve and less costly than the Reynolds averaged Navier–Stokes equations which are elliptic. These equations are also associated with the inviscid flow equations discussed in Section 2.4. The approximations used to obtain these, however, are not valid in the same region of the flow. The boundary-layer equations apply close to the surface of a body and in wakes which form behind the body. The inviscid flow equations apply outside the boundary-layer.

For external flows, the behavior of the boundary-layer equations is similar to the behavior of the heat conduction equation (see problem 3.14). A small perturbation introduced in the boundary-layer diffuses instantaneously along a normal to the wall and is transported downstream along the local streamlines in the boundary-layer. The influence domain of a point  $P$  is limited by a line normal to the wall passing through  $P$ , by the wall and by the boundary-layer edge, see Fig. 3.2a. Therefore, if we wish to calculate the boundary-layer in a domain  $D$  shown in Fig. 3.2b, boundary or initial conditions are required along the upstream line normal to the wall, along the wall and along the outer edge which defines the domain  $D$ . This choice of boundary conditions is justified by the fact that a perturbation introduced along these bounding lines influences the flow in the calculation domain. Along the downstream boundary, no boundary condition is required because a perturbation does not influence the calculation domain, as the velocity  $u$  is positive. If  $u$  is negative, information can propagate upstream. In addition, the two-dimensional steady boundary-layer equations are singular at the point where the wall shear  $\tau_w$  vanishes. This point is defined as the separation point and the treatment of separated flow region becomes much more involved as discussed, for example briefly in Chapter 12 and in detail in [1].

In external flows, the shear layer flowing in the  $x$ -direction adjoin an effectively “inviscid” freestream extending to  $y = \infty$ . On the lower side there may be either a solid surface, usually taken as  $y = 0$  as in Fig. 3.3a, in which case the

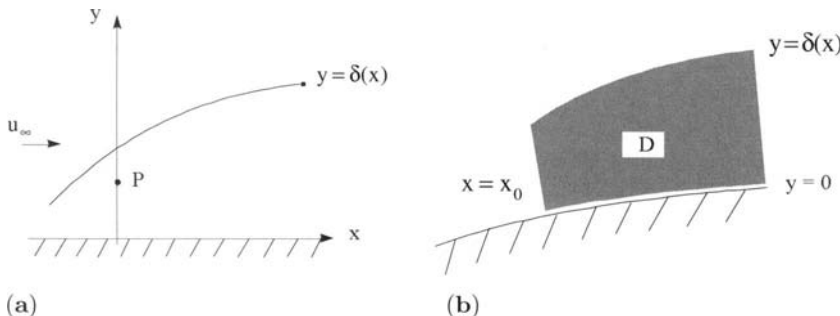


**Fig. 3.2.** Calculation domain of the boundary-layer equations for external flow.

viscous region is called a “wall shear layer”, or there may be another inviscid stream extending to  $y = -\infty$  (Fig. 3.3b), in which case the viscous region is called a “free shear layer.”

In the former case there are three boundary conditions for the velocity field that must be specified, two at the wall, and the other at the boundary-layer edge  $y = \delta$ . The conditions at the wall involve the specification of normal ( $v$ ) and tangential ( $u$ ) components of velocity, and at the edge the specification of the external velocity, that is,

$$y = 0, \quad u = 0, \quad v = v_w(x) \quad (3.4.1a)$$

$$y = \delta, \quad u = u_e(x) \quad (3.4.1b)$$

Here  $\delta$  is sufficiently large so that dimensionless  $\partial u / \partial y$  at the boundary-layer edge is small, say around  $10^{-4}$ . The transpiration velocity,  $v_w(x)$ , may be either suction or injection. On a nonporous surface it is equal to zero.

In free shear layers (Figs. 3.3b and c), the external velocity must be specified on both edges. The difficulties associated with the  $v$  boundary condition in free shear layers are less obvious. If the flow is symmetrical (Fig. 3.3a), no problem arises; the initial symmetrical velocity profile is specified and  $v$  is required to be zero on the centerline and  $u = u_e$  at one edge. If the flow is not symmetrical (Fig. 3.3b), a *boundary condition for  $v$  cannot be found* from consideration of the shear layer and the boundary-layer equations alone. In the real flow the behavior of  $v$  outside the shear layer depends on the  $v$ -component equation of motion and the continuity equation, applied throughout the flow and not merely in the shear layer. Of course, a similar problem occurs in determining  $u_e$  either

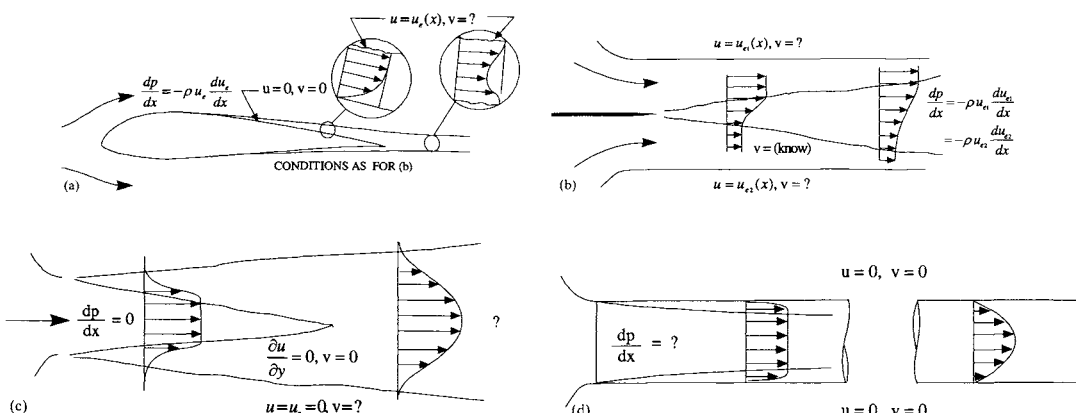


**Fig. 3.3.** Boundary conditions for shear layers. (a) Boundary-layer and wake of airfoil. (b) Mixing layer between parallel streams. (c) Merging mixing layers in jet. (d) Merging boundary-layers in internal flow.

in the boundary-layer or wake of Fig. 3.3a; the latter problem is both more familiar and less perplexing.

Internal flows (Fig. 3.3d) consist of shear layer or layers filling part or all of the space between two solid boundaries. In this case the pressure distribution is set predominantly by the displacement effect of the shear layer. It is convenient to distinguish flows in which the shear layers fill the cross section and flows such as that near the entrance to a duct (the left-hand part of Fig. 3.3d) where a region of effectively inviscid flow obeying Bernoulli's equation remains.

It is also convenient to distinguish the “entrance region,” in which the velocities change with  $x$ , and the “fully developed” region far downstream in a constant area duct, in which the velocities do not, but of course the pressure continues to decrease with  $x$ . The relevant boundary conditions in each case are similar to those for external flows, except that it is also necessary to satisfy the requirement of constant mass flow between the solid surfaces.

## References

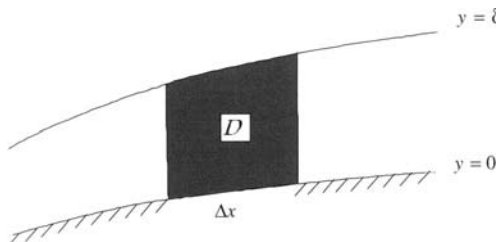
- [1] Cebeci, T., *An Engineering Approach to the Calculation of Aerodynamic Flows*, Horizons Publ., Long Beach, Calif. and Springer, Heidelberg, 1999.

## Problems

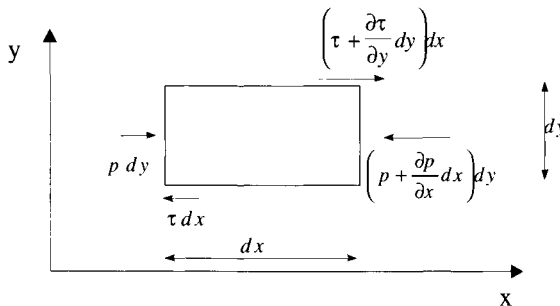
**3-1.** The momentum equation integrated on a control volume (CV) can be written as

$$\iint_s \rho \vec{V} (\vec{V} \cdot \vec{n}) ds = \sum F_{\text{ext}}$$

Here  $\vec{V}$  denotes the velocity vector,  $\vec{n}$  is the outwards unit vector normal to the surface  $S$  bounding the control volume, and  $\sum F_{\text{ext}}$  denotes the external forces acting on the control volume. Apply the integrated form of the momentum theorem to the control volume  $D$  below and derive the integral momentum equation for a boundary-layer developing between  $y = 0$  and  $y = \delta$ .



**3-2.** Show that in a boundary-layer the external forces in the  $x$ -momentum equation can be obtained by considering the pressure and shear stress acting on a control volume as shown below. Assume  $dz = 1$ .



**3-3.** Which of the stress-gradient terms in Eq. (2.3.3) are negligible according to the boundary-layer approximation? If  $d\delta/dx$  (or  $\delta/x$ ) is  $10^{-2}$ , will the ratio of a typical neglected term to a typical remaining term be of the order of  $10^{-2}$ ,  $10^{-4}$ , or  $10^{-6}$ ? Is this answer valid for laminar flow and turbulent flow or for laminar flow only?

**3-4.** Show that the shear stress,  $\tau = \mu(\partial u/\partial y) - \rho \overline{u'v'}$ , near the axis of a circular jet is proportional to the distance from the axis.

**3-5.** Show that at a solid surface in the  $xz$ -plane the tangential pressure gradient is equal to the derivative with respect to  $y$  of the component of shear stress in the direction of the pressure gradient. What is the corresponding result for two-dimensional laminar flow over a uniformly porous surface with transpiration velocity  $v_w$ ? State any assumptions that you make.

**3-6.** Consider a two-dimensional laminar boundary-layer developing on a flat plate with wall suction  $v_w < 0$  with boundary conditions  $u = u_0 = \text{const}$  at the outer edge and  $u = 0$  and  $v = v_w$  at the wall. Assume that far from the leading edge, the solution is such that

$$\frac{\partial u}{\partial x} = 0$$

(a) Show that the momentum equation is

$$v_w \frac{\partial u}{\partial y} = \nu \frac{\partial^2 u}{\partial y^2}$$

(b) Show that the solution depends on  $yv_w/\nu$  only. Calculate the displacement thickness  $\delta_1$ , the momentum thickness  $\theta$ , the shape parameter  $H$  and the skin-friction coefficient  $c_f$ . From the integrated form of the momentum equation check the relationship between the skin-friction coefficient and the suction velocity.

**3-7.** From the definitions of the displacement and momentum thicknesses, show that

$$\int_0^\delta \rho u^2 dy = \int_{\delta^* + \theta}^\delta \rho u_e^2 dy$$

This result indicates that the momentum thickness is the quantity which must be added to the displacement thickness to construct a fictitious inviscid flow having the same flux of momentum as the real flow.

**3-8.** From the global momentum equation show that the (viscous) force acting on both faces of a flat plate of length  $L$  is

$$F = 2\rho_e u_e^2 \theta_{x=L} \ell$$

Here  $\theta_{x=L}$  is the value of the momentum thickness at the trailing edge and  $\ell$  is the width of the plate.

**3-9.** Show that the integral form of the continuity equation is

$$\frac{1}{u_e} \frac{d}{dx} [u_e(\delta - \delta^*)] = \frac{v_E}{u_e} \quad (\text{P3.9.1})$$

Here  $v_E/u_e$ , with  $v_E$  denoting the component of velocity normal to the wall at the edge of the boundary-layer, is the dimensionless entrainment velocity defined by

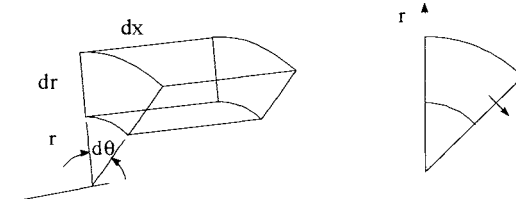
$$c_E = \frac{v_E}{u_e} = \frac{d\delta}{dx} - \frac{v_e}{u_e} \quad (\text{P3.9.2})$$

*Hint:* Integrate the continuity equation with respect to  $y$  from  $y = 0$  to  $y = \delta$ .

**3-10.** Find the mean part  $u$ , the fluctuating part  $u'$ , and the mean-square fluctuation  $\overline{u'^2}$  for the following variations of instantaneous velocity with time.

- a.  $u + u' = a + b \sin \omega t$
- b.  $u + u' = a + b \sin^2 \omega t$
- c.  $u + u' = at + b \sin \omega t$  (careful!)

**3-11.** Derive Eq. (3.2.2) by CV analysis, using the CV shown below.



**3-12.** The boundary-layer equations for two-dimensional and axisymmetric flows differ from each other only by the appearance of the radial distance  $r(x, y)$ .

For flows without transverse curvature effect, the momentum equation is the same in both cases [see Eq. (3.2.7)] and only the continuity equations differ from each other. For such flows the axisymmetric flow equations can be placed in two-dimensional flow by using the Mangler transformation. When there is transverse-curvature effect, see Eq. (3.2.5), this transformation defined by

$$d\bar{x} = \left(\frac{r_0}{L}\right)^{2k} dx \quad (\text{P3.12.1})$$

$$d\bar{y} = \left(\frac{r}{L}\right)^k dy \quad (\text{P3.12.2})$$

puts the equations into nearly two-dimensional form. Here  $(x, y)$  denotes the coordinates of the axisymmetric body.

With  $\bar{\psi}(\bar{x}, \bar{y})$  and  $\psi(x, y)$  related to each other by

$$\bar{\psi}(\bar{x}, \bar{y}) = \left(\frac{1}{L}\right)^k \psi(x, y) \quad (\text{P3.12.3})$$

show that with the Mangler transformation defined by Eqs. (P3.12.1) and (P3.12.2), the Mangler transformed continuity and momentum equations and their boundary conditions can be written as

$$\frac{\partial \bar{u}}{\partial \bar{x}} + \frac{\partial \bar{v}}{\partial \bar{y}} = 0 \quad (\text{P3.12.4})$$

$$\bar{u} \frac{\partial \bar{u}}{\partial \bar{x}} + \bar{v} \frac{\partial \bar{u}}{\partial \bar{y}} = -\frac{1}{\rho} \frac{dp}{d\bar{x}} + \frac{1}{\rho} \frac{\partial}{\partial \bar{y}} \left\{ (1+t)^{2k} \left[ \mu \frac{\partial \bar{u}}{\partial \bar{y}} - \left(\frac{L}{r}\right)^k \rho \bar{u}' \bar{v}' \right] \right\} \quad (\text{P3.12.5})$$

$$\bar{y} = 0, \quad \bar{u} = \bar{v} = 0, \quad \bar{y} = \delta(\bar{x}), \quad \bar{u} = u_e(\bar{x}) \quad (\text{P3.12.6})$$

Here

$$t = -1 + \sqrt{1 + \frac{2 \cos \phi}{L} \left(\frac{L}{r_0}\right)^2 \bar{y}}$$

where  $r_0$  and  $\phi$  are the radius and slope of the surface as shown in Fig. 3.1.

Comparison of the Mangler transformed equation (P3.12.5) with the momentum equation (3.1.10) for two-dimensional flows shows that Eq. (P3.12.5) is identical with Eq. (3.1.10) except for the presence of the transverse-curvature term,  $t$ . If this term is negligible (i.e., if  $\delta/r_0 \ll 1$ ), then we see that the Mangler transformation allows the momentum equations for axisymmetrical flows to be written exactly in the same form as the momentum equation for two-dimensional flows.

**3-13.** Show that, with mass transfer, the momentum integral equation, Eq. (3.3.36), can be written as

$$\frac{d}{dx}(u_e^2 \theta) - u_e v_w + \delta^* u_e \frac{du_e}{dx} = \frac{\tau_w}{\rho} \quad (\text{P3.13.1})$$

**3-14.** We consider a laminar flow induced by an impulsively started infinite flat plate. The  $y$ -axis is normal to the plate. The  $x$ - and  $z$ -axes form a plane parallel to the plate. The plate is defined by  $y = 0$ . For time  $t < 0$ , the plate and the flow are at rest. For  $t \geq 0$ , the velocity of the plate is parallel to the  $x$ -coordinate; its value is constant and equal to  $u_w$ . At infinity, the flow is at rest. The flow induced by the motion of the plate is independent of  $x$ .

(a) From the continuity equation, show that  $v = 0$  everywhere in the flow and the resulting momentum equation is

$$\frac{\partial u}{\partial t} = \nu \frac{\partial^2 u}{\partial y^2} \quad (\text{P3.14.1})$$

Note that this equation has the form of a diffusion equation (the same form as the heat equation).

(b) We introduce the new variables  $T$ ,  $Y$  and  $U$  such that

$$T = kt, \quad Y = k^{1/2}y, \quad U = u \quad (\text{P3.14.2})$$

where  $k$  is an arbitrary constant. In the new system of variables, the solution is  $U(Y, T)$ . The solution  $U(Y, T)$  is expressed by a function of  $Y$  and  $T$  and the solution  $u(y, t)$  is expressed by a function of  $y$  and  $t$ . Show that the functions are identical. Deduce that the solution is a function of  $y/\sqrt{t}$  only. (*Hint:* consider that  $U$  can be expressed as  $U = G(Y/T^{1/2}, T)$  and  $u$  can be expressed as  $u = g(y/t^{1/2}, t)$ . Write that  $G$  and  $g$  are the same functions for any value of  $k$  and deduce that  $G$  can not depend on  $T$ ).

(c) We introduce the variable  $\eta$  and the function  $F$  by

$$\eta = \frac{y}{2(\nu t)^{1/2}}, \quad F = \frac{u}{u_w} \quad (\text{P3.14.3})$$

From the preceding result, we have  $F = F(\eta)$ . Show that the momentum equation becomes

$$\frac{d^2 F}{d\eta^2} + 2\eta \frac{dF}{d\eta} = 0 \quad (\text{P3.14.4})$$

(d) Show that the solution of Eq. (P3.14.4) is

$$F = \frac{2}{\sqrt{\pi}} \int_{\eta}^{\infty} e^{-\eta^2} d\eta$$

We consider that the viscous effects are significant if  $F < 0.01$ . Numerically,  $F = 0.01$  when  $\eta = 1.82$ .

(e) An observer is placed at distance  $d$  from the plate. Show that the observer feels the motion of the plate after a time  $t$  of order  $d^2/\nu$ . This time is called a characteristic time of viscosity. It is the time necessary to transfer momentum by diffusion through the field.

**3-15.** Consider

$$k \frac{\partial u}{\partial y} = a^2 \frac{\partial^2 u}{\partial y^2} \quad (\text{P3.2.1})$$

with  $k < 0$ . The boundary conditions are  $u = u_0$  when  $y \rightarrow \infty$  and  $u = 0$  when  $y = 0$ . Plot the solution for  $k$  fixed and for smaller and smaller values of  $a^2$ .

For  $a = 0$  Eq. (P3.2.1) becomes

$$k \frac{\partial u}{\partial y} = 0 \quad (\text{P3.12.2})$$

To take into account the boundary condition  $u = u_0$  when  $y \rightarrow \infty$ , the solution of this equation is  $u = u_0$ . Note that the solution of the general equation for small values of  $a$  is not identical to the solution of the simplified equation. Near  $y = 0$ , a boundary-layer forms. The two solutions are close of each other outside this boundary-layer.

**3-16.** Express the boundary-layer equations for a two-dimensional laminar flow in terms of the following dimensionless quantities.

$$\bar{u} = \frac{u}{u_0}, \quad \bar{v} = \frac{v}{u_0} \sqrt{R_L}, \quad \bar{x} = \frac{x}{L}, \quad \bar{y} = \frac{y}{L} \sqrt{R_L}, \quad R_L = \frac{u_0 L}{\nu}$$

Here  $u_0$  and  $L$  denote reference quantities.

**3-17.** To study the influence of Reynolds number on the solution of the laminar boundary-layer equations given in Problem 3.16, assume that the external velocity distribution  $u_e/u_0$  is given as a function of  $x/L$  which does not change when the Reynolds number  $R_L$  changes.

Show that the solution  $\bar{u}(\bar{x}, \bar{y})$  does not depend on the Reynolds number. Knowing the solution  $u(x, y)$  for a given Reynolds number, show that the boundary-layer parameters  $\delta^*/L$ ,  $\theta/L$  and  $\tau_w/\rho u_0^2$  at another Reynolds number obey the following rules

$$\frac{\delta^*}{L} \sqrt{R_L} = F_1 \left( \frac{x}{L} \right), \quad \frac{\theta}{L} \sqrt{R_L} = F_2 \left( \frac{x}{L} \right), \quad \frac{\tau_w}{\rho u_0^2} \sqrt{R_L} = F_3 \left( \frac{x}{L} \right)$$

Here  $F_1$ ,  $F_2$  and  $F_3$  denote functions which depend on the external velocity distribution only.

**3-18.** The solution

$$f = \frac{1}{2a\sqrt{\pi T}} e^{-\eta^2}$$

of the equation

$$V \frac{\partial f}{\partial x} = a^2 \frac{\partial^2 f}{\partial y^2}$$

with

$$T = \frac{x}{V}, \quad \eta = \frac{y}{2a\sqrt{T}}$$

can be considered as the response of a system to a perturbation localized at point  $P(y = 0, t = 0)$ . Defining a domain of influence of point  $P(y = 0, t = 0)$  for  $f < 0.001$ , plot this domain in the plane  $(y, T)$ .

**3-19.** Is  $d\theta/dx$  always positive?

**3-20.** Derive Eq. (3.3.14)

**3-21.** Show that for an axisymmetric flow the entrainment velocity  $v_E$  defined in Problem 3.9 for two-dimensional flows is

$$v_E = \frac{d\delta}{dx} - \frac{v_e}{u_e} = \frac{1}{r_\delta} \frac{d}{dx} \left[ u_e \left( \delta \frac{r_0 + r_\delta}{2} \right) - \delta^* \right] \quad (\text{P3.21.1})$$

where

$$r_\delta = r_0 + \delta \cos \phi .$$

$$\delta^* = \int_0^\delta r \left( 1 - \frac{u}{u_e} \right) dy$$

# 4

## Two-Dimensional Incompressible Laminar Flows

### 4.1 Introduction

The boundary-layer equations of the previous chapter can be solved for a range of laminar and turbulent flows for the boundary and initial conditions discussed in Section 3.4. In this chapter we consider laminar flows and postpone the discussion on turbulent flows to Chapter 6. In both cases a solution can be obtained either by a “differential” method, solving the partial differential equations (3.1.2) and (3.1.10) or Eqs. (3.2.1) and (3.2.2) numerically, or by an “integral” method, solving ordinary differential equations already integrated in the  $y$ -direction, namely Eqs. (3.3.10) or (3.3.14).

Before we consider the numerical solution of the boundary-layer equations in Sections 4.4 and 4.5 in integral and differential forms, respectively, in Sections 4.2 and 4.3 we consider similar flows for external and free shear layer flows, respectively, which correspond to special flows where solutions can be obtained by solving the boundary-layer equations in differential form not as partial differential equations but as ordinary differential equations.

Similar flows were widely studied in the pre-computer era because of their comparative mathematical simplicity. In this book we use them to introduce the behavior of laminar boundary-layers because of their physical simplicity. We also show that their mathematical simplicity can be utilized as a basis for efficient calculation methods for general flows, in which the  $x$ -derivative terms resulting from nonsimilarity are either neglected or incorporated as “known” terms in a solution of the similarity equations at given  $x$ . The solutions of similar flows are also useful to check the validity and accuracy of the solutions of the boundary-layer equations for nonsimilar flows.

In this book we concentrate on external flows in general because these flows are the most common and calculation methods for them are the most highly developed. Much of the intervening material can also be applied to internal flows as discussed in Program 3 (Appendix B).

## 4.2 Similar Flows: External Flows

### 4.2.1 Similarity Concept

The similarity concept can be conveniently explained by reference to the continuity and momentum equations for laminar flows when they are applied to an external boundary-layer flow subject to the boundary conditions (3.4.1) with  $v_w = 0$ . In general, the solution of Eqs. (3.1.2) and (3.1.10) for a laminar flow with  $\nu$  and  $u_e(x)$  given, is

$$\frac{u}{u_e} = g(x, y) \quad (4.2.1)$$

where  $g$  is a general function of  $x$  and  $y$ . There are special cases in which

$$\frac{u}{u_e} = g(\eta) \quad (4.2.2)$$

where  $\eta$ , called a similarity variable, is a specific function of  $x$  and  $y$ . In such cases, the number of independent variables is reduced from two ( $x$  and  $y$ ) to one ( $\eta$ ) so that for laminar flows, Eqs. (3.1.2) and (3.1.10) become an *ordinary differential equation* for  $u$  and  $v$ . In jet flows in still air, we would replace  $u_e$  by the centerline velocity,  $u_c$ , see Problem 4.13. In wakes in a uniform stream, the similarity form of the velocity profile is expressed as

$$\frac{u_c - u}{\Delta u} = g(\eta) \quad (4.2.3)$$

where  $\Delta u$  is  $u_c - u_e$ .

### 4.2.2 Falkner–Skan Equation

There are systematic procedures for obtaining the similar forms of the laminar boundary-layer equations either for external or for free shear-layer flows as described, for example, in [1, 2]. Various coordinate transformations have been developed for reducing the boundary-layer equations into ordinary differential equations. One popular transformation for incompressible external flows is the Falkner–Skan transformation in which the similarity variable  $\eta$  is defined by

$$\eta = \sqrt{u_e/\nu x} y \quad (4.2.4a)$$

A dimensionless stream function  $f(\eta)$  is related to the stream function  $\psi(x, y)$  by

$$f(\eta) = \frac{\psi(x, y)}{\sqrt{u_e \nu x}} \quad (4.2.4b)$$

With this transformation, and with a prime denoting differentiation with respect to  $\eta$ , Eqs. (3.1.2) and (3.1.10), can be expressed as a third-order ordinary differential equation in  $\eta$ , known as the Falkner–Skan equation,

$$f''' + \frac{m+1}{2} f f'' + m[1 - (f')^2] = 0 \quad (4.2.5)$$

Here  $m$  is a dimensionless pressure-gradient parameter defined by

$$m = \frac{x}{u_e} \frac{du_e}{dx} \quad (4.2.6)$$

The velocity components  $u$  and  $v$  are related to the dimensionless stream function  $f(\eta)$  by

$$u = u_e f' \quad (4.2.7a)$$

$$v = -\sqrt{u_e \nu x} \left[ \frac{f}{\sqrt{u_e x}} \frac{d}{dx} \sqrt{u_e x} + f' \frac{\partial \eta}{\partial x} \right] \quad (4.2.7b)$$

In terms of the transformation given by Eq. (4.2.4), the boundary conditions for the continuity and momentum equations, as given by Eqs. (3.4.1), can be written as

$$\eta = 0, \quad f' = 0, \quad f = f_w = -\frac{1}{\sqrt{u_e \nu x}} \int_0^x v_w(x) dx \quad (4.2.8a)$$

$$\eta = \eta_e, \quad f' = 1 \quad (4.2.8b)$$

Here  $\eta_e$  is a transformed boundary-layer thickness,

$$\eta_e = \sqrt{u_e / \nu x} \delta \quad (4.2.9)$$

Note that nonzero  $f_w$  corresponds to surface mass transfer. For flows with suction,  $f_w$  is positive and for flows with blowing,  $f_w$  is negative.

It is clear from the definition of  $m$  and the boundary conditions that Eq. (4.2.5) can only be an ordinary differential equation if  $m$  and the boundary conditions are independent of  $x$ , that is, they are constant.

The requirement for  $m$  to be constant is satisfied if the external velocity varies with  $x$  as

$$u_e = C x^m \quad (4.2.10)$$

where  $C$  is constant.

If there is no surface mass transfer, both wall and edge boundary conditions satisfy this requirement. When there is surface mass transfer, since  $f_w$  is constant and  $u_e$  varies with  $x$  as required by Eq. (4.2.10), the variation of  $v_w(x)$  can be determined from the expression for  $f_w$  in Eq. (4.2.8a); if we assume  $v_w \sim x^n$  where  $n$  is constant, then  $f_w$  must vary with  $x$  as

$$f_w \sim x^{(2n+2-m-1)/2}$$

and that  $f_w$  becomes constant only when

$$2n + 2 - m - 1 = 0$$

that is,

$$n = \frac{m - 1}{2} \quad (4.2.11)$$

In summary, we see that for those flows in which the external velocity varies with  $x$  as prescribed by Eq. (4.2.10), the laminar boundary-layer equations given by two partial-differential equations (3.1.2) and (3.1.10) with independent variables  $x$  and  $y$  reduce to an ordinary differential equation in  $\eta$  if there is no surface mass transfer; if there is one, then the exponent of the surface mass transfer velocity  $v_w$  that is,  $n$  must vary with  $m$  as indicated by Eq. (4.2.11). These special laminar flows are called similar flows. When the constraints of the external velocity and boundary conditions are not satisfied, then the solution of the laminar boundary-layer equations cannot be obtained by solving an ordinary differential equation but either by solving the two partial differential equations given by Eqs. (3.1.2) and (3.1.10) as described in Section 4.5, or by solving the integral momentum equation, as described in Section 4.4. These flows are called nonsimilar flows.

The flows with negative pressure gradient,  $dp/dx$ , are usually referred to as favorable pressure gradient flows since the external velocity gradient,  $du_e/dx$ , is positive. Those flows in which the pressure gradient is positive are called adverse pressure gradient flows since  $du_e/dx$  is negative. When there is no pressure gradient, the external velocity is constant.

This designation of flows is useful in establishing the range of the values of  $m$  since a positive value of  $m$  refers to an accelerating (favorable pressure gradient) flow, a negative value of  $m$  to a decelerating (adverse pressure gradient) flow and  $m = 0$  to a flat-plate (zero pressure gradient) flow. If we express the wall shear in terms of the Falkner–Skan variables given by Eqs. (4.2.4), that is

$$\tau_w = \mu \left( \frac{\partial u}{\partial y} \right)_w = \mu u_e \left( \frac{\partial f'}{\partial \eta} \right)_w \sqrt{\frac{u_e}{\nu x}} = \mu u_e \sqrt{\frac{u_e}{\nu x}} f''_w \quad (4.2.12)$$

then the lower limit of negative  $m$  corresponds to one in which  $f''_w = 0$ . According to the numerical solutions of the Falkner–Skan equation with no mass transfer, this occurs for a value of  $m = -0.0904$ . The solution for this  $m$  represents a flow whose external velocity forces the boundary-layer to incipient separation at all streamwise stations. As a result, the solutions of the Falkner–Skan equation for flows with no mass transfer and separation are limited to a range of  $m$  given by

$$-0.0904 \leq m < \infty \quad (4.2.13)$$

Mass transfer at the surface has an effect similar to the pressure gradient effect on the boundary-layer equations. Mass injection to the boundary-layer reduces the wall shear of the flow without injection, and conversely suction increases the wall shear of the flow without suction. For this reason, the value

of  $m$  for which the wall shear parameter  $f_w''$  becomes negative with injection is greater than the value of  $m$  without surface mass transfer, that is,  $m > -0.0904$ .

Equation (4.2.5) was first given by Falkner and Skan [3] who also produced solutions for a range of values of  $m$ . Later, Hartree [4] studied this equation in greater detail, first eliminating  $m$  by making the linear transformation

$$Y = \left(\frac{m+1}{2}\right)^{1/2} \eta, \quad F = \left(\frac{m+1}{2}\right)^{1/2} f \quad (4.2.14)$$

so that Eq. (4.2.5) becomes

$$F''' + FF'' + \beta[1 - (F')^2] = 0 \quad (4.2.15)$$

subject to the boundary conditions

$$Y = 0, \quad F = F_w, \quad F' = 0 \quad (4.2.16a)$$

$$Y = Y_\infty, \quad F' = 1 \quad (4.2.16b)$$

In Eqs. (4.2.15) and (4.2.16), primes denote differentiation with respect to  $Y$ , and  $\beta$  is a new dimensionless pressure-gradient parameter, related to  $m$  by

$$\beta = \frac{2m}{m+1} \quad (4.2.17)$$

For positive values of  $\beta$ , Eq. (4.2.15), as Eq. (4.2.5) has unique solutions, but more than one solution exists for each negative value of  $\beta$ . Hartree calculated a range of solutions for positive values and negative values of  $\beta$  (or  $m$ ) for  $F_w'' \geq 0$ .

A second family of solutions of Eq. (4.2.15), the so-called “lower branch solutions”, was given later by Stewartson [5] and by Cebeci and Keller [6] and by others, again for negative values of  $\beta$  in the range  $-0.199 \leq \beta \leq 0$ . These solutions all have the property that  $F_w'' \leq 0$ , so that at  $y = 0$ ,  $\partial u / \partial y \leq 0$  for all  $x$ . Accordingly, these solutions represent the similarity solutions of the Falkner–Skan equation for separated laminar flows.

The solutions of Eq. (4.2.15) are sometimes referred to as “wedge-flow” solutions. The flow is diverted through an angle of magnitude  $\beta\pi/2$  (see Fig. 4.1). Thus, physically, for  $0 \leq \beta \leq 2$  the flow is past an infinite wedge whose vertex angle is  $\beta\pi$ .

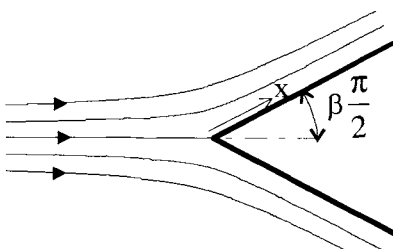


**Fig. 4.1.** Flow past a wedge. In the neighborhood of the leading edge, the external velocity distribution is  $u_e(x) = Cx^{\beta/(2-\beta)}$ .

### 4.2.3 Solutions of the Falkner–Skan Equation

If we integrate Eq. (4.2.5) across the boundary-layer and note that  $f''$  is zero at the edge of the boundary-layer, we get

$$-f_w'' + m\delta_1^* + \left(\frac{3m+1}{2}\right)\theta_1 + \frac{m+1}{2}f_w = 0 \quad (4.2.18)$$

where, with  $R_x = u_e x / \nu$ ,  $\delta_1^*$  and  $\theta_1$  denote dimensionless displacement and momentum thicknesses defined by

$$\delta_1^* = \frac{\sqrt{R_x}}{x} \int_0^\delta \left(1 - \frac{u}{u_e}\right) dy = \int_0^{\eta_e} (1 - f') d\eta = \eta_e + f_w - f_e \quad (4.2.19a)$$

$$\theta_1 = \frac{\sqrt{R_x}}{x} \int_0^\delta \frac{u}{u_e} \left(1 - \frac{u}{u_e}\right) dy = \int_0^{\eta_e} f'(1 - f') d\eta \quad (4.2.19b)$$

Eq. (4.2.18), which is the momentum integral equation (3.3.10), provides a relation between the three boundary-layer parameters  $f_w''$ ,  $\theta_1$  and  $\delta_1^*$  for a given  $m$  and can be used to obtain  $\theta_1$  without evaluating Eq. (4.2.19b) numerically.

Before we discuss the numerical solutions of Eqs. (4.2.5) and (4.2.8) for various values of  $m$ , it is useful to single out two flows that are quite common in practice. The first one corresponds to  $m = 0$  ( $\beta = 0$ ) and is the flow over a flat plate at zero incidence. In this case, the external velocity,  $u_e$ , is constant, and Eq. (4.2.5) reduces to

$$f''' + \frac{1}{2}ff'' = 0 \quad (4.2.20)$$

This equation is called the Blasius equation.

The second flow corresponds to  $m = 1$  ( $\beta = 1$ , wedge half-angle  $90^\circ$ ), which is the case of a two-dimensional stagnation flow. The external velocity is  $u_e = Cx$ , and Eq. (4.2.5) reduces to

$$f''' + ff'' - (f')^2 + 1 = 0 \quad (4.2.21)$$

This equation is called the Hiemenz equation.

The Falkner–Skan equation has been solved for different boundary conditions and for various values of  $m$ . Here we present the results for  $f_w = 0$ ,  $f'_w = 0$ , and  $f''_w \geq 0$ .

We first discuss the solution of the Blasius equation. We set  $m = 0$  in Eq. (4.2.5), specify an estimate of  $\eta_e$  ( $\eta_e = 8$  is sufficient in this case), and by the shooting method described in the accompanying CD-ROM, Program 1, calculate the functions  $f$ ,  $f'$ , and  $f''$  as a function of  $\eta$ .

The accuracy of the solutions depends on the number of  $\eta$ -points taken across the boundary-layer. To get high accuracy (say five digits) with the Runge–Kutta method used in the shooting method, we choose  $\Delta\eta = 0.10$ . For a value of  $\eta_e = 8$  this choice corresponds to 81  $\eta$ -points. In general, approximately 40

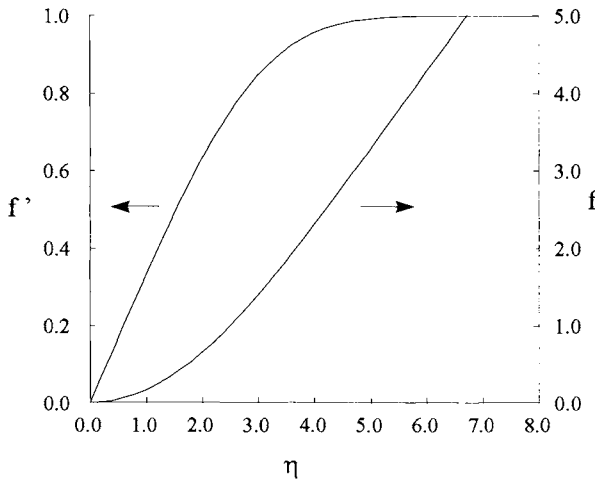


**Fig. 4.2.** The dimensionless stream function  $f$ , and velocity  $f'$ , as function of  $\eta$  for a flat-plate flow ( $m = 0$ ).

points should be sufficient to obtain four digit accuracy. Figure 4.2 shows the  $f$  and  $f'$  profiles across the boundary-layer. We note from these results that for most of the boundary-layer,  $f'$  varies almost linearly with  $\eta$ . As  $\eta$  approaches  $\eta_e$ ,  $f'$  asymptotically approaches 1.

To obtain the normal velocity component,  $v$ , from the solution of the Falkner–Skan equation, we use Eqs. (4.2.4a), (4.2.7a) in Eq. (4.2.7b) and write

$$\frac{v}{u_e} = \frac{-1}{2\sqrt{R_x}}((m - 1)\eta f' + (m + 1)f) \quad (4.2.22)$$

where  $R_x$  denotes the Reynolds number defined by

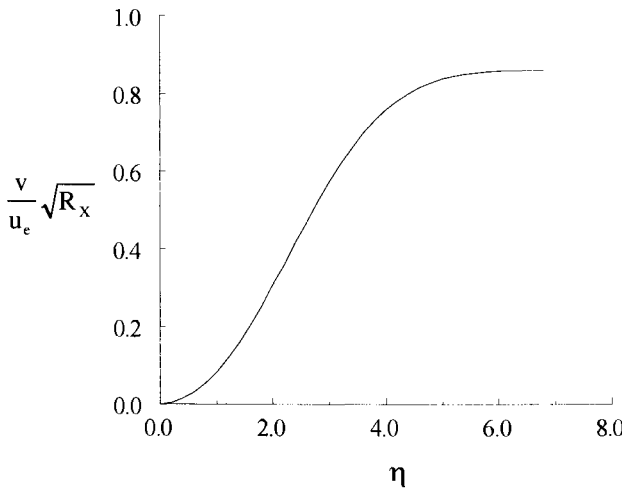
$$R_x = \frac{u_e x}{\nu} \quad (4.2.23)$$

Figure 4.3 shows the variation of  $(v/u_e)\sqrt{R_x}$  across the boundary-layer for a flat-plate flow. We note that as  $\eta$  approaches  $\eta_e$ ,  $(v/u_e)\sqrt{R_x}$  approaches a constant value (0.8604). This means that at the outer edge there is flow outward because the increasing boundary-layer thickness causes the fluid to be displaced from the wall as it flows along it. The local skin-friction coefficient and displacement thickness for a flat-plate flow can be obtained by using the definitions of Eqs. (3.3.11) and (3.3.7), and the results in Table 4.1.

$$c_f = \frac{0.664}{\sqrt{R_x}} \quad (4.2.24)$$

$$\frac{\delta^*}{x} = \frac{1.721}{\sqrt{R_x}} \quad (4.2.25)$$

We note that Eq. (4.2.18) reduces to  $\theta_1 = 2f_w''$ , while the numerical calculations give  $f_w'' = 0.33206$ ; hence



**Fig. 4.3.** The variation of dimensionless normal velocity,  $v$ , with  $\eta$  for a flat-plate flow ( $m = 0$ ). Note that at the boundary-layer edge,  $v$  reaches a constant value (= 0.8604).

**Table 4.1.** Solutions of the Falkner–Skan equation [7].

$\beta$	$m$	$R_\theta/\sqrt{R_x}$	$R_{\delta^*}/\sqrt{R_x}$	$H$	$\frac{C_f}{2}\sqrt{R_x}$
2.00000		0.00000	0.00000	2.15541	
1.00000	1.00000	0.29234	0.64789	2.21623	1.23259
0.50000	0.33333	0.42899	0.98537	2.29694	0.75745
0.28571	0.16666	0.50895	1.20511	2.36781	0.58255
0.00000	0.00000	0.66411	1.72079	2.59110	0.33206
-0.04000	-0.01961	0.69419	1.84404	2.65639	0.29052
-0.08000	-0.03846	0.72786	1.99731	2.74409	0.24512
-0.12000	-0.05660	0.76628	2.20057	2.87177	0.19351
-0.16000	-0.07407	0.81155	2.50823	3.09067	0.12981
-0.19884	-0.09043	0.86811	3.49779	4.02923	0.00000

$$\frac{\theta}{x} = \frac{0.664}{\sqrt{R_x}} \quad (4.2.26)$$

The ratio of  $\delta^*$  to  $\theta$ , the shape factor defined by Eq. (3.3.9), is

$$H = \frac{\delta^*}{\theta} = 2.591 \quad (4.2.27)$$

If  $\delta$  is defined to be the distance from the surface where  $f' = 0.995$ , this corresponds to an  $\eta$  of approximately 5.3. Then with Eq. (4.2.4a) we can write  $\delta$  as

$$\frac{\delta}{x} = \frac{5.3}{\sqrt{R_x}} \quad (4.2.28)$$

Table 4.1 shows the computed values of  $f''_w$ ,  $\delta_1^*$  and  $\theta_1$ , and Fig. 4.4 shows the velocity profiles for several values of  $m$ , including the Hiemenz value  $\beta = 1$ , the “separation” value  $\beta = -0.19884$ , where  $\tau_w = 0$  and the “lower branch” solutions. The effect of the pressure gradient on the profiles is clearly seen.

With increasing adverse pressure gradient (decelerating flow) the slope of the velocity profile near the wall decreases (even when it is plotted as  $u/u_e$  versus  $y/\delta$ ), and at  $\beta = -0.19884$  it becomes zero. The velocity profile corresponding to this value of  $m$  is called the *separating* velocity profile. On the other hand, with increasing favorable pressure gradient (accelerating flow), the slope of the velocity profile increases.

The velocity profile corresponding to an infinite value of  $m$  ( $\beta = 2$ ) cannot be obtained from Eq. (4.2.5). It can, however, be obtained from Hartree's equation (4.2.15) and gives  $H = 2.155$ . That equation in turn has problems when  $\beta$  becomes infinite, which corresponds to an accelerated stream with the external velocity given by

$$u_e = \frac{u_1}{-x} \quad (4.2.29)$$

For  $u_1 > 0$  it represents a two-dimensional flow (sometimes referred to as the sink flow) in a convergent channel. Equation (4.2.15) can be placed in a suitable form when  $\beta$  becomes infinite by defining new independent and dependent variables.

$$\zeta = \beta^{1/2} Y \quad (4.2.30)$$

$$\phi(\zeta) = \beta^{1/2} F(Y) \quad (4.2.31)$$

With these relations, Eq. (4.2.15) can be written as

$$\phi''' + \frac{1}{\beta} \phi \phi'' + 1 - (\phi')^2 = 0 \quad (4.2.32)$$

subject to the boundary conditions

$$\phi(0) = \phi'(0) = 0, \quad \phi'(\zeta_\infty) = 1 \quad (4.2.33)$$

Here the primes denote differentiation with respect to  $\zeta$ .

When  $\beta$  is infinite, Eq. (4.2.32) becomes

$$\phi''' + 1 - (\phi')^2 = 0 \quad (4.2.34)$$

A closed form solution to Eqs. (4.2.33) and (4.2.34) is

$$\phi(\zeta) = \zeta + 2\sqrt{3} - 3\sqrt{2} \tanh \left[ \frac{\zeta}{\sqrt{2}} + \tanh^{-1} \left( \frac{2}{3} \right)^{1/2} \right] \quad (4.2.35)$$

Noting that  $[\tanh^{-1}(2/3)^{1/2} = 1.146]$ , we can write the dimensionless velocity  $u/u_e$  as

$$\frac{u}{u_e} = \phi' = 3 \tanh^2 \left( \frac{\zeta}{\sqrt{2}} + 1.146 \right) - 2 \quad (4.2.36)$$

This leads to

$$H = 2.07, \quad \phi''(0) = \frac{2}{\sqrt{3}} = 1.1547 \quad (4.2.37)$$

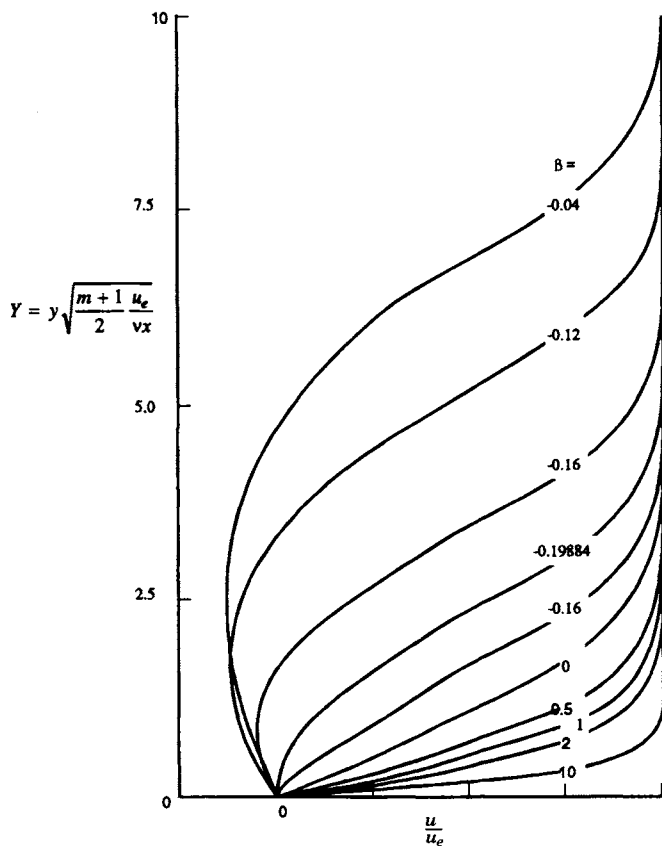


**Fig. 4.4.** The dimensionless velocity,  $f'$  profiles, as a function of  $\eta$  for various values of  $\beta$ .

The only common closed-form analytical solution for the external-flow boundary-layer equations is that for the *asymptotic suction profile*, a boundary-layer with  $v_w$  negative and independent of  $x$ . Sufficiently far downstream from the start of suction,

$$u(y) = u_e \left[ 1 - \exp \left( \frac{v_w y}{\nu} \right) \right] \quad (4.2.38)$$

independent of  $x$ . Here  $H = 2$  (compared with 2.6 for  $v_w = 0$  and  $(1/2)c_f = -v_w/u_e$  (Problem 4.11).

## 4.3 Similar Flows: Free-Shear Flows

As in the case of some external flows, the boundary-layer equations admit similarity solutions for some laminar and turbulent free shear flows. Here in this section we discuss some special free shear laminar flows shown in the sketches of Table 4.2, and later in Section 8.7 we extend the discussion to free shear turbulent flows. It should be noted that the shear layer thickness  $\delta$  used to scale the cross-stream coordinate is chosen for convenience in each case. It is not the distance from the axis at which the velocity or velocity defect is 0.005 of the maximum, analogous to  $\delta_{995}$  in boundary-layers. It should also be noted that the similarity solutions become valid only at large distances from the origin, say 20 nozzle diameters in jets or 100 body diameters in wakes because the initial profiles are not usually the similarity functions.

### 4.3.1 Axisymmetric Jet

We consider an axisymmetric jet emerging from a small circular hole and mixing with the surrounding fluid at rest. Let the  $x$ -direction coincide with the jet axis and the origin lie in the hole. Since the streamlines are nearly parallel within the jet, although the streamlines in the entraining flow are more nearly normal to the axis, the pressure variation in the jet is small and can be neglected. The boundary-layer equations follow from Eqs. (3.2.1) and (3.2.2) and can be written as

$$\frac{\partial u}{\partial x} + \frac{1}{r} \frac{\partial}{\partial r}(rv) = 0 \quad (4.3.1)$$

$$u \frac{\partial u}{\partial x} + v \frac{\partial u}{\partial r} = \frac{1}{r} \frac{\partial}{\partial r}(r\tau) \quad (4.3.2)$$

Here

$$\tau = \mu \frac{\partial u}{\partial r} - \rho \overline{u'v'} \quad (4.3.3)$$

They are subject to the boundary conditions

$$r = 0, \quad v = 0, \quad \frac{\partial u}{\partial r} = 0 \quad (4.3.4a)$$

$$r \rightarrow \infty, \quad u = 0 \quad (4.3.4b)$$

We note that Eq. (4.3.4a) follows from symmetry conditions.

Since the pressure is constant and the motion is steady, the total momentum in the  $x$ -direction is constant, that is,

$$J = 2\pi \int_0^\infty \rho u^2 r dr = \text{const.} \quad (4.3.5)$$

since  $dJ/dx = 0$ . To find the similarity solutions for the system given by Eqs. (4.3.1)–(4.3.5), valid for large distances from the orifice, we start with Eq. (4.2.2) and write it as

$$\frac{u(x, r)}{u_c(x)} = F(\eta) \quad (4.3.6)$$

where  $u_c$  is the velocity along the axis  $r = 0$ . Here  $\eta$  denotes the similarity variable defined by

$$\eta = \frac{r}{\delta(x)} \quad (4.3.7)$$

where  $\delta(x)$  is defined later in Eq. (4.3.20). We assume that the stream function  $\psi(x, r)$  is related to a dimensionless stream function  $f(\eta)$  by

$$\psi(x, r) = u_c(x)\delta^2(x)f(\eta) \quad (4.3.8)$$

With Eqs. (4.3.6) and (4.3.7) we can write Eq. (4.3.5) as

$$J = 2\pi\rho M^2 \int_0^\infty F^2 \eta d\eta \quad (4.3.9)$$

where

$$M = u_c\delta \quad (4.3.10)$$

We note that since the total momentum  $J$  is constant, then  $M$  must be constant also, since the integral in Eq. (4.3.9) is a pure number.

By using Eqs. (4.3.6), (4.3.7) and (4.3.10) and noting that  $F = f'/\eta$ , we can write Eqs. (4.3.1) and (4.3.2) as

$$\rho u_c^2 \frac{d\delta}{dx} \left[ \frac{(f')^2}{\eta} + f \left( \frac{f'}{\eta} \right)' \right] + (\tau\eta)' = 0 \quad (4.3.11)$$

In terms of similarity variables the boundary conditions [Eq. (4.3.4)] become

$$\eta = 0, \quad f = 0, \quad f' = 0 \quad (4.3.12a)$$

$$\eta \rightarrow \infty, \quad f' = 0 \quad (4.3.12b)$$

Equation (4.3.11) with  $\tau$  defined by Eq. (4.3.3) applies to both laminar and turbulent axisymmetric jets. For laminar flows, using the definition of  $\tau$ , we can write Eq. (4.3.11) as

$$\frac{M}{\nu} \frac{d\delta}{dx} \left[ \frac{(f')^2}{\eta} + f \left( \frac{f'}{\eta} \right)' \right] + \left[ \left( \frac{f'}{\eta} \right)' \eta \right]' = 0 \quad (4.3.13)$$

We see that for a circular laminar jet the system of Eqs. (4.3.1)–(4.3.5) will have a similarity solution if the coefficients of Eq. (4.3.13) are independent of  $x$ , that is, if

$$\frac{M}{\nu} \frac{d\delta}{dx} = \text{const.} = c_1 \quad (4.3.14)$$

where we expect  $c_1 > 0$ . With this restriction and with  $c_1 = 1$ , Eq. (4.3.13) becomes

$$\frac{(f')^2}{\eta} + f \left( \frac{f'}{\eta} \right)' + \left[ \left( \frac{f'}{\eta} \right)' \eta \right]' = 0 \quad (4.3.15a)$$

and can be written as

$$\left( \frac{ff'}{\eta} \right)' + \left[ \left( \frac{f'}{\eta} \right)' \eta \right]' = 0 \quad (4.3.15b)$$

Integrating Eq. (4.3.15b), we get

$$\frac{ff'}{\eta} + f'' - \frac{f'}{\eta} = \text{const.} \quad (4.3.16a)$$

To perform the integration, we note that

$$\lim_{\eta \rightarrow \infty} \frac{f'(\eta)}{\eta} = 0$$

and that as  $\eta \rightarrow \infty$ ,  $f''(\eta) \rightarrow 0$ . Therefore the integration constant in Eq. (4.3.16a) is zero. Rewriting Eq. (4.3.16a) as

$$ff' + \eta f'' - f' = 0 \quad (4.3.16b)$$

we find that its solution, subject to  $f(0) = 0$ , is

$$f(\eta) = \frac{\frac{1}{2}\eta^2}{1 + \frac{1}{8}\eta^2} \quad (4.3.17)$$

Then

$$\frac{u}{u_c} = \frac{f'(\eta)}{\eta} = \frac{1}{(1 + \frac{1}{8}\eta^2)^2} \quad (4.3.18)$$

Figure 4.5 shows the velocity profile for a circular jet according to Eq. (4.3.18) as well as the velocity profile for a two-dimensional jet (see Prob. 4-13).

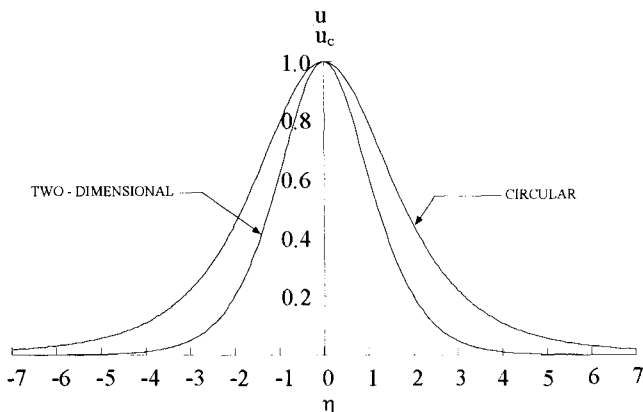


**Fig. 4.5.** Velocity profiles for laminar two-dimensional and circular jets.

Inserting Eq. (4.3.18) into Eq. (4.3.9), we find

$$M = \frac{\sqrt{3}}{2} \sqrt{\frac{J/\rho}{2\pi}} \quad (4.3.19)$$

With  $c_1 = 1$  (which defines  $\delta$ ) in Eq. (4.3.14) we find, after integration,

$$\delta = \frac{\nu x}{M} = 2.894 \left( \frac{J}{\rho} \right)^{-1/2} \nu x \quad (4.3.20)$$

where  $u/u_c$  is approximately 0.79 at  $r = \delta$ . Therefore,

$$u_c = \frac{3}{8\pi} \frac{J}{\rho} (\nu x)^{-1} = 0.119 \frac{J}{\rho} (\nu x)^{-1} \quad (4.3.21)$$

The mass flow rate,  $\dot{m} = 2\pi \int_0^\infty \rho u r dr$ , is

$$\dot{m} = 8\pi \mu x \quad (4.3.22)$$

It is interesting to note that  $\dot{m}$  is independent of  $J$  in this case.

### 4.3.2 Two-Dimensional Wake

The boundary-layer equations also admit a similarity solution for laminar and turbulent flows in the wake of a two-dimensional body. The solutions are, at best, valid only far enough downstream for the pressure disturbances introduced by the body to be negligible. In addition, the solutions are subject to the restriction that the velocity defect in the wake.

$$u_1(x, y) = u_\infty - u(x, y) \quad (4.3.23)$$

is small in comparison with the velocity of the free stream  $u_\infty$ , so that higher-order terms can be dropped. The governing equations for laminar or turbulent flows in the wake of a two-dimensional body, subject to Eq. (4.3.23), are

$$-\frac{\partial u_1}{\partial x} + \frac{\partial v}{\partial y} = 0 \quad (4.3.24)$$

$$-u_\infty \frac{\partial u_1}{\partial x} = \frac{1}{\rho} \frac{\partial \tau}{\partial y} \quad (4.3.25)$$

Here  $\tau$  is

$$\tau = -\mu \frac{\partial u_1}{\partial y} - \rho \bar{u}' v' \quad (4.3.26)$$

The boundary conditions are

$$y = 0, \quad v = 0, \quad \frac{\partial u_1}{\partial y} = 0 \quad (4.3.27a)$$

$$y \rightarrow \infty, \quad u_1 = 0 \quad (4.3.27b)$$

For simplicity let us consider flow over a flat plate. By Newton's second law, the drag of the plate,  $F$ , say, is equal to the flux of momentum defect in the wake; therefore

$$F = \rho b \int_{-\infty}^{\infty} u(u_{\infty} - u) dy \quad (4.3.28)$$

where  $b$  is the width of the plate. Substituting the definition of  $u_1$  into Eq. (4.3.28) and neglecting the second-order terms, we get

$$F = \rho b \int_{-\infty}^{\infty} u_1 u_{\infty} dy = \text{const.} \quad (4.3.29)$$

To find the similarity solution for the system of Eqs. (4.3.24)–(4.3.27) and (4.3.29), we write

$$u = u_{\infty} + u_c(x) f(\eta) \quad (4.3.30)$$

Here  $u_c(x)$  denotes the wake centerline velocity *defect* and  $f$  is negative. The definition of  $\eta$  is similar to Eq. (4.3.7).

$$\eta = \frac{y}{\delta(x)} \quad (4.3.31)$$

where  $\delta(x)$  is defined later in Eq. (4.3.37). With the definition of  $u_1$ , Eq. (4.3.30) can be written as

$$f(\eta) = -\frac{u_1}{u_c(x)} \quad (4.3.32)$$

Using Eqs. (4.3.31) and (4.3.32), we can write Eq. (4.3.25) as

$$u_{\infty} \left( f \frac{du_c}{dx} - u_c f' \frac{\eta}{\delta} \frac{d\delta}{dx} \right) = \frac{1}{\rho} \frac{\partial \tau}{\partial y} \quad (4.3.33)$$

The boundary conditions become

$$\eta = 0, \quad f' = 0, \quad \eta \rightarrow \infty, \quad f = 0 \quad (4.3.34)$$

[We shall not need the boundary condition  $v = 0$ , since Eq. (4.3.25) does not contain  $v$ , which is in fact negligibly small.]

Equation (4.3.33) applies to both laminar and turbulent flows. For laminar flows, substituting for  $\tau$  from Eq. (4.3.26) with the Reynolds stress neglected allows us to write Eq. (4.3.33) as

$$\frac{\delta^2 u_{\infty}}{\nu u_c} \frac{du_c}{dx} f - \frac{\delta u_{\infty}}{\nu} \frac{d\delta}{dx} \eta f' = f'' \quad (4.3.35)$$

We see that for a flow in the wake of a flat plate we will have a similarity solution if

$$\frac{\delta^2 u_{\infty}}{\nu u_c} \frac{du_c}{dx} = \text{const.}, \quad \frac{\delta u_{\infty}}{\nu} \frac{d\delta}{dx} = \text{const.} = c_2 \quad (4.3.36)$$

Assuming that  $c_2 = 1$  (which defines  $\delta$ ), we can integrate the second relation in Eq. (4.3.36) to obtain

$$\delta = \left( \frac{2\nu x}{u_\infty} \right)^{1/2} \quad (4.3.37)$$

In terms of similarity variables  $f$  and  $\eta$ , Eq. (4.3.29) can be written as

$$u_c \delta = - \frac{F}{\rho b u_\infty \int_{-\infty}^{\infty} f d\eta} = \text{const.} \quad (4.3.38)$$

With the definition of  $\delta$  given by Eq. (4.3.37) we find that

$$u_c = A x^{-1/2} \quad (4.3.39)$$

where  $A$  is constant.

Using Eqs. (4.3.37) and (4.3.39) we find that the constant in the first expression of Eq. (4.3.36) is  $-1$ . This, together with  $c_2 = 1$ , enables us to write Eq. (4.3.35) as

$$f'' + (\eta f)' = 0 \quad (4.3.40)$$

Integrating twice and using the boundary condition  $f'(0) = 0$ , we get

$$f(\eta) = B e^{-\eta^2/2} \quad (4.3.41)$$

Substituting Eqs. (4.3.37), (4.3.39), and (4.3.41) into Eq. (4.3.38), we find that

$$AB = - \frac{F}{\rho b} (2\nu u_\infty)^{-1/2} (2\pi)^{-1/2} \quad (4.3.42)$$

With Eqs. (4.3.39), (4.3.41) and (4.3.42), Eq. (4.3.30) becomes

$$u = u_\infty - \frac{F}{2\rho b} \left( \frac{1}{\pi\nu u_\infty} \right)^{1/2} x^{-1/2} e^{-\eta^2/2} \quad (4.3.43)$$

For the special case of a flat plate at zero incidence  $F$  (the drag on *both sides*) is, from Eq. (4.3.28) written at the trailing edge,

$$F = 2\theta_{TE} b \rho u_\infty^2 = 1.328 b \rho u_\infty^2 \sqrt{\frac{\nu \ell}{u_\infty}}$$

where  $\ell$  denotes the length of the plate. Substituting the above expression into Eq. (4.3.43) and rearranging, we get

$$\frac{u}{u_\infty} = 1 - \frac{0.664}{\sqrt{\pi}} \left( \frac{x}{\ell} \right)^{-1/2} e^{-\eta^2/2} \quad (4.3.44)$$

### 4.3.3 Mixing Layer Between Two Uniform Streams

The boundary-layer equations also admit similarity solutions for laminar and turbulent flows in which mixing takes place downstream of a splitter plate ending at  $x = 0$  between two uniform streams that move with velocities  $u_1$  and  $u_2$ . One of the velocities may be zero; in that case it is sometimes referred to as a *half jet*.

The procedure by which we can obtain the similarity solutions for this case is very similar to the procedure for the case of the two-dimensional jet (see Prob. 4-13). The governing equations are given by Eqs. (4.3.1) and (4.3.2) with the restriction that  $r = 1$  and  $\partial/\partial r = \partial/\partial y$ . The boundary conditions [Eq. (4.3.4b)] are replaced by new ones given by

$$y \rightarrow \infty, \quad u \rightarrow u_1; \quad y \rightarrow -\infty, \quad u \rightarrow u_2 \quad (4.3.45a)$$

As pointed out in Section 3.4, the  $v$  boundary condition in free shear layers depends on conditions outside the shear layer. The choice of  $v = 0$  on the centerline of symmetrical shear layers is effectively a definition of the position of the centerline in  $xy$ -space. In the asymmetrical mixing layer we define the  $x$ -axis,  $y = 0$ , as the line on which  $v = 0$ : it is in general inclined at an angle of less than  $5^\circ$  to the plane of the splitter plate. Thus

$$y \rightarrow \infty, \quad u \rightarrow u_1; \quad y \rightarrow -\infty, \quad u \rightarrow u_2 \quad (4.3.45a)$$

$$y = 0, \quad v = 0 \quad (4.3.45b)$$

To find the similarity solution, we define

$$f'(\eta) = \frac{u(x, y)}{u_1} \quad (4.3.46)$$

$$\psi(x, y) = u_1 \delta(x) f(\eta) \quad (4.3.47)$$

with  $\eta$  defined by Eq. (4.3.31). Using Eqs. (4.3.31), (4.3.46) and (4.3.47), we can write the two-dimensional boundary-layer equations (subject to the restrictions discussed above) as

$$-\frac{u_1^2}{\delta} \frac{d\delta}{dx} f f'' = \frac{1}{\rho} \frac{\partial \tau}{\partial y} \quad (4.3.48)$$

In terms of similarity variables, Eq. (4.3.45) becomes

$$\eta \rightarrow \infty, \quad f' \rightarrow 1; \quad \eta \rightarrow -\infty, \quad f' \rightarrow \frac{u_2}{u_1} \equiv \lambda; \quad \eta = 0, \quad f = 0 \quad (4.3.49)$$

Equation (4.3.48) with  $\tau$  defined by Eq. (4.3.3) ( $\partial/\partial r = \partial/\partial y$ ) applies to both laminar and turbulent flows: for laminar flows, Eq. (4.3.48) becomes

$$f''' + \frac{u_1 \delta}{\nu} \frac{d\delta}{dx} f f'' = 0 \quad (4.3.50)$$

For similarity we must have

$$\frac{u_1 \delta}{\nu} \frac{d\delta}{dx} = \text{const.} \quad (4.3.51)$$

Taking the constant equal to  $\frac{1}{2}$ , we see that

$$\delta = \left( \frac{\nu x}{u_1} \right)^{1/2} \quad (4.3.52)$$

and

$$f''' + \frac{1}{2} f f'' = 0 \quad (4.3.53)$$

No closed-form solutions are known for the system given by Eqs. (4.3.49) and (4.3.53). Several solutions obtained by numerical methods were provided by Lock [8]. The solution of Eq. (4.3.53) by using Keller's shooting method, Program 1 in the accompanying CD-ROM, can be obtained as follows. We again write Eq. (4.3.53) as a first-order system in a form similar to Eqs. (4A.1) with  $m = 0$ . The boundary conditions [Eq. (4.3.49)] become

$$f(0) = 0, \quad u(\eta_\infty) = 1, \quad u(-\eta_\infty) = \lambda \quad (4.3.54)$$

The modified shooting method solves the initial value problem for Eqs. (4A.1) with  $m = 0$ , subject to the initial conditions

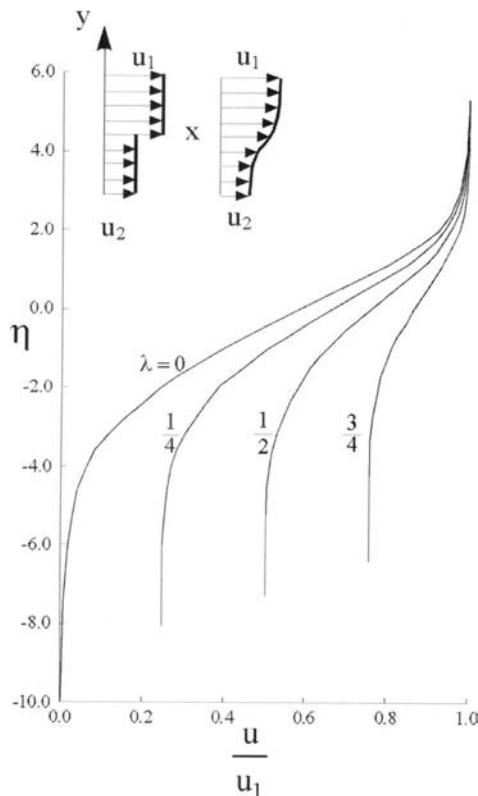


**Fig. 4.6.** Velocity profiles for the mixing of two uniform laminar streams at different velocities,  $\lambda = u_2/u_1$ .

$$f(0) = 0, \quad u(0) = a, \quad v(0) = b \quad (4.3.55)$$

Then  $a$  and  $b$  are sought to satisfy the two-edge boundary conditions

$$u(\eta_\infty, a, b) - 1 = 0, \quad u(-\eta_\infty, a, b) - \lambda = 0 \quad (4.3.56)$$

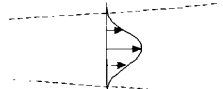
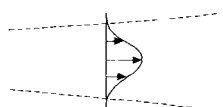
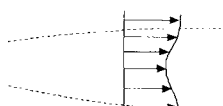
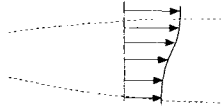
These equations are solved by Newton's method described in Program 1. Note that in this case two systems of variational equations must be solved to get the partial derivatives with respect to  $a$  and  $b$ .

Figure 4.6 shows solutions obtained by this method for  $\lambda = 0, \frac{1}{4}, \frac{1}{2}$ , and  $\frac{3}{4}$ .

#### 4.3.4 Power Laws for the Width and for the Centerline Velocity of Similar Free Shear Layers

In the previous subsections we have discussed the similarity solutions of several free shear layers for laminar flows. On the basis of similarity considerations we obtained the variations of the width ( $\delta$ ) and the centerline velocity ( $u_c$  or  $u_1$ ) of several shear layers. Table 4.2 summarizes the results.

**Table 4.2.** Power Laws for Width and for Centerline Velocity of Laminar Similar Free Shear Layers.

Flow	Sketch	Width, $\delta$	Centerline velocity, $u_c(x)$ and $u_1$
Two-dimensional jet*		$x^{2/3}$	$x^{-1/3}$
Axisymmetric jet		$x$	$x^{-1}$
Two-dimensional wake		$x^{1/2}$	$x^{-1/2}$
Axisymmetric wake*		$x^{1/2}$	$x^{-1}$
Two uniform streams		$x^{1/2}$	$x^0$

\* See Probs. 4-13 and 4-14

## 4.4 Numerical Solution of the Boundary-Layer Equations: Integral Form

In this and the following sections we discuss the numerical solution of the boundary-layer equations for nonsimilar flows which are those for which  $u/u_e$  is a function of both  $x$  and  $\eta$ . In practice these flows are more important than similar flows because  $u_e(x)$  rarely varies according to Eq. (4.2.10), as is required for similar flows, and because the surface boundary conditions may not fulfill the requirements for similarity even if  $u_e$  does.

While the differential methods discussed in the following section are more general and accurate, the integral methods are very useful in obtaining quick rough answers for some restricted flows. Of the many integral methods for laminar flows, especially popular in the pre-computer era, we first discuss the Pohlhausen method due to its simplicity (subsection 4.4.1) and the Thwaites method (subsection 4.4.2) which is still used for calculating the small initial regions of laminar flow on bodies at high Reynolds numbers before switching to turbulent flow calculations. A more accurate method is presented in Problem 4.31.

### 4.4.1 Pohlhausen Method

In this method we assume a velocity profile  $u(x, y)$  that satisfies the momentum integral equation (3.3.10) and a set of boundary conditions

$$y = 0, \quad u = 0, \quad \text{and} \quad y \rightarrow \infty, \quad u = u_e(x) \quad (4.4.1a)$$

We also use additional “boundary conditions” obtained by evaluating the momentum equation (3.1.10) at the wall with  $v_w = 0$ , that is,

$$\nu \frac{\partial^2 u}{\partial y^2} = \frac{1}{\rho} \frac{dp}{dx} = -u_e \frac{du_e}{dx} \quad (4.4.1b)$$

and also some additional “boundary conditions” obtained from differentiating the edge boundary condition with respect to  $y$ , namely,

$$y \rightarrow \infty, \quad \frac{\partial u}{\partial y}, \frac{\partial^2 u}{\partial y^2}, \frac{\partial^3 u}{\partial y^3}, \dots \rightarrow 0 \quad (4.4.1c)$$

We assume a fourth-order polynomial for the velocity profile,  $u/u_e$ , and write

$$\frac{u}{u_e} = a_0 + a_1 \eta + a_2 \eta^2 + a_3 \eta^3 + a_4 \eta^4 \quad (4.4.2)$$

where  $\eta$  is now used for  $y/\delta$ . This polynomial contains five coefficients that can be determined from the boundary conditions in Eq. (4.4.1). Using Eqs. (4.4.1a) and (4.4.1b) and the first two conditions in Eq. (4.4.1c), we get

$$\begin{aligned} a_0 &= 0, & a_1 &= 2 + \frac{\Lambda}{6}, & a_2 &= -\frac{\Lambda}{2}, \\ a_3 &= -2 + \frac{\Lambda}{2}, & a_4 &= 1 - \frac{\Lambda}{6} \end{aligned} \quad (4.4.3)$$

where  $\Lambda$  is a pressure-gradient parameter defined by

$$\Lambda = \frac{\delta^2}{\nu} \frac{du_e}{dx} \quad (4.4.4)$$

and can be interpreted physically as a typical ratio of pressure forces to viscous forces. With Eq. (4.4.3) we can write Eq. (4.4.2) as

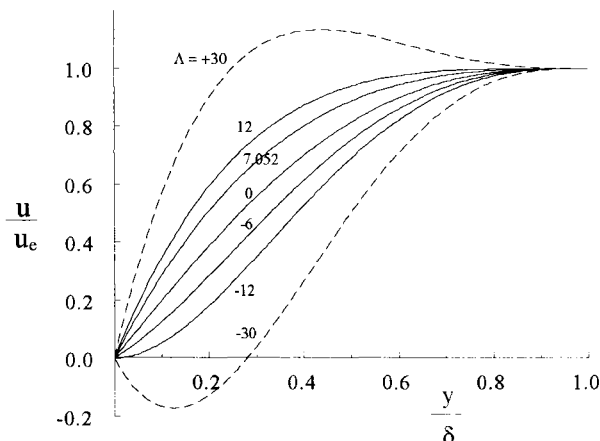
$$\frac{u}{u_e} = 2\eta - 2\eta^3 + \eta^4 + \frac{\Lambda}{6}\eta(1-\eta)^3 \quad (4.4.5)$$

Figure 4.7 shows the velocity profiles for various values of  $\Lambda$ . Here  $\Lambda = 0$  corresponds to a flat-plate flow, a negative value of  $\Lambda$  corresponds to a decelerating flow, and a positive value of  $\Lambda$  corresponds to an accelerating flow. The profile at separation corresponds to  $\Lambda = -12$ , giving  $\partial u / \partial y = 0$  at  $\eta = 0$  from Eq. (4.4.5). The positive values of  $\Lambda$  are restricted to 12, since for incompressible flows the velocity profiles cannot have overshoots within the boundary-layer. Thus  $\Lambda$  is restricted to the range  $-12 \leq \Lambda \leq 12$ .

Once the velocity profile is known, the boundary-layer parameters  $\theta$ ,  $\delta^*$ , and  $\tau_w$  or  $c_f$  appearing in the momentum integral equation (3.3.10) can be determined. From the definitions of  $\tau_w$ ,  $\delta^*$  and  $\theta$  it follows that

$$\tau_w = \frac{\mu u_e}{\delta} \left( 2 + \frac{1}{6}\Lambda \right) \quad (4.4.6)$$

$$\delta^* = \delta \left( \frac{3}{10} - \frac{1}{120}\Lambda \right) \quad (4.4.7)$$



**Fig. 4.7.** The variation of dimensionless velocity,  $u/u_e$ , across the boundary-layer according to Eq. (4.4.5).

$$\theta = \frac{\delta}{315} \left( 37 - \frac{1}{3} \Lambda - \frac{5}{144} \Lambda^2 \right) \quad (4.4.8)$$

Substituting Eqs. (4.4.6)–(4.4.8) into Eq. (3.3.10) leads to an equation of the form

$$\frac{dZ}{dx} = \frac{g(\Lambda)}{u_e} + h(\Lambda) Z^2 \frac{d^2 u_e}{dx^2} \quad (4.4.9)$$

where  $Z = \delta^2/\nu = \Lambda/(du_e/dx)$  and  $g(\Lambda)$  and  $h(\Lambda)$  are known functions of  $\Lambda$ . As usual,  $u_e$  and its derivatives are known. We note that the auxiliary relations for  $c_f$  and  $H$  that follow from Eqs. (4.4.6)–(4.4.8) are *not* differential equations: only the initial value of  $\delta$  (or  $\theta$ ) and the distribution of  $u_e(x)$  are needed to start the calculations.

Before computers became generally available, the Pohlhausen method was the most sophisticated one in general use because solution of the boundary-layer equations by a differential method was impractical. Now, it is less commonly used: for accurate work, differential solutions are preferred, while for the many cases where only the initial part of the shear layer is laminar, so that high accuracy is not needed, engineers prefer the very simple method due to Thwaites described in the following subsection.

#### 4.4.2 Thwaites' Method

Consider the momentum integral equation (3.3.10). If  $H$  and  $c_f$  are known as functions of  $\theta$  or some suitable combination of  $\theta$  and  $u_e$ , Eq. (3.3.10) can be integrated, at least by a numerical process. Such functions were found in Thwaites' method by writing the following boundary conditions for

$$y = 0, \quad \frac{\partial^2 u}{\partial y^2} = -\frac{u_e}{\theta^2} \lambda, \quad \frac{\partial u}{\partial y} = \frac{u_e}{\theta} \ell \quad (4.4.10)$$

These equations define  $\lambda$  and  $\ell$ . The variable  $\ell$  may be calculated by any particular solution of the boundary-layer equations, and it is found in all known cases to adhere reasonably closely to a universal function of  $\lambda$ , which Thwaites denoted by  $\ell(\lambda)$ . In the same way, if  $H$  is regarded as depending only on  $\lambda$ , a reasonably valid universal function for  $H$  can also be found, namely,  $H(\lambda)$ .

By putting  $y = 0$  in Eq. (3.1.10) and using Eq. (4.4.10), we find

$$\lambda = \frac{\theta^2}{\nu} \frac{du_e}{dx} \quad (4.4.11)$$

Also,

$$\frac{c_f}{2} = \frac{\tau_w}{\rho u_e^2} = \frac{\nu}{u_e^2} \left( \frac{\partial u}{\partial y} \right)_w = \frac{\nu \ell(\lambda)}{u_e \theta} = \frac{\ell}{R_\theta} \quad (4.4.12)$$

The assumptions that  $\ell$  or  $c_f$  and  $H$  are functions of  $\lambda$  only are quasi-similarity assumptions. The Falkner–Skan solutions of Section 4.2 could be used to give

$\ell(\lambda)$  and  $H(\lambda)$ . With these two results, Eq. (3.3.10) may be rewritten in the form

$$\frac{u_e}{\nu} \frac{d\theta^2}{dx} = 2\{-[H(\lambda) + 2]\lambda + \ell(\lambda)\} \equiv F(\lambda) \quad (4.4.13)$$

Here  $F(\lambda)$  is another universal function. Thwaites represents  $F(\lambda)$  chosen to fit known solutions of Eqs. (3.1.2) and (3.1.10) as well as possible by

$$F(\lambda) = 0.45 - 6\lambda = 0.45 - 6\frac{\theta^2}{\nu} \frac{du_e}{dx} \quad (4.4.14)$$

Substituting Eq. (4.4.14) into Eq. (4.4.13) and multiplying the resulting equation by  $u_e^5$ , we can write, after some rearranging,

$$\frac{1}{\nu} \frac{d}{dx} (\theta^2 u_e^6) = 0.45 u_e^5$$

which, upon integration, leads to

$$\frac{\theta^2 u_e^6}{\nu} = 0.45 \int_0^x u_e^5 dx + \left( \theta^2 \frac{u_e^6}{\nu} \right)_0 \quad (4.4.15)$$

In terms of dimensionless quantities defined by

$$x^* \equiv \frac{x}{L}, \quad u^* \equiv \frac{u}{u_{\text{ref}}}, \quad u_e^* \equiv \frac{u_e}{u_{\text{ref}}}, \quad R_L \equiv \frac{u_{\text{ref}} L}{\nu} \quad (4.4.16)$$

Eq. (4.4.15) can be written as

$$\left( \frac{\theta}{L} \right)_0^2 R_L = \frac{0.45}{(u_e^*)^6} \int_0^{x^*} (u_e^*)^5 dx^* + \left( \frac{\theta}{L} \right)_0^2 R_L \left( \frac{u_{e0}^*}{u_e^*} \right)^6 \quad (4.4.17)$$

For a stagnation-point flow ( $m = 1$ ), Eq. (4.4.17) gives

$$\left( \frac{\theta}{L} \right)_0^2 R_L = \frac{0.075}{(du_e^*/dx^*)_0} \quad (4.4.18)$$

where  $(du_e^*/dx^*)_0$  denotes the slope of the external-velocity distribution for stagnation-point flow. Note that the last term in Eq. (4.4.17) is zero in calculations starting from a stagnation point, because  $u_{e0}^* = 0$ .

Once  $\theta$  is calculated for a given external-velocity distribution, the other boundary-layer parameters  $H$  and  $c_f$  can be determined from the relations given below.

For  $0 \leq \lambda \leq 0.1$ ,

$$\begin{aligned} \ell &= 0.22 + 1.57\lambda - 1.8\lambda^2 \\ H &= 2.61 - 3.75\lambda + 5.24\lambda^2 \end{aligned} \quad (4.4.19a)$$

For  $-0.1 \leq \lambda \leq 0$ ,

$$\ell = 0.22 + 1.402\lambda + \frac{0.018\lambda}{0.107 + \lambda} \quad (4.4.19b)$$

$$H = \frac{0.0731}{0.14 + \lambda} + 2.088$$

Thwaites' method can also be used for axisymmetric boundary-layers by using the Mangler transformation. If we denote two-dimensional variables by the subscript 2 and the axisymmetric ones by 3, then according to the Mangler transformation for cases where  $\delta \ll r_0$  (no transverse curvature effect), we write

$$\theta_2 = \left(\frac{r_0}{L}\right)^k \theta_3 \quad (4.4.20a)$$

$$dx_2 = \left(\frac{r_0}{L}\right)^{2k} dx_3 \quad (4.4.20b)$$

By using Eqs. (4.4.20), Eq. (4.4.17) can be written as

$$\left(\frac{\theta_3}{L}\right)^2 R_L = \frac{0.45}{(u_e^*)^6 (r_0^*)^{2k}} \int_0^{x_3^*} (u_e^*)^5 (r_0^*)^{2k} dx_3^* + \left(\frac{\theta_3}{L}\right)_0^2 R_L \left(\frac{u_{e0}^*}{u_e^*}\right)^6 \quad (4.4.21)$$

For an axisymmetric stagnation point flow ( $m = 1/3$ ),

$$\left(\frac{\theta_3}{L}\right)^2 R_L = \frac{0.056}{(du_e^*/dx_3^*)_0} \quad (4.4.22)$$

In Eqs. (4.4.20)

$$r_0^* = \frac{r_0}{L}, \quad x_3^* = \frac{x_3}{L}$$

Once  $\theta_3$  is calculated from Eq. (4.4.21), then the variables  $\delta^*$ ,  $H$ , and  $c_f$  can be calculated from Eq. (4.4.19) and Eq. (4.4.12).

A Fortran program for predicting the laminar boundary-layer development on two-dimensional and axisymmetric bodies by Thwaites' method is given in the accompanying CD-ROM (Appendix A), Program 2.

## 4.5 Numerical Solution of the Boundary-Layer Equations: Differential Form

There are several numerical methods for solving the boundary-layer equations in differential form. The Crank–Nicolson [9] and Keller's box [10] methods are the most convenient ones as discussed in some detail in [11]. Of the two, Keller's method has significant advantages over the other, and in this section it will be used to solve the boundary-layer equations for two-dimensional flows, in Section 7.6 for three-dimensional flows, and in Section 5.6 the stability equations for two-dimensional flows and in Sections 8.4 and 14.4 for three-dimensional flows.

The continuity and momentum equations given by Eqs. (3.1.2) and (3.1.10) can be solved in the form they are expressed. They can also be solved after they are expressed as a third order equation by using the definition of stream function  $\psi(x, y)$ . Noting that

$$u = \frac{\partial \psi}{\partial y}, \quad v = -\frac{\partial \psi}{\partial x} \quad (4.5.1)$$

Eqs. (3.1.2) and (3.1.10), with a prime denoting differentiation with respect to  $y$ , and with an eddy viscosity  $\nu_t$  concept discussed in Section 6.3 and defined by

$$-\rho \overline{u'v'} = \rho \nu_t \frac{\partial u}{\partial y} \quad (6.3.1)$$

to model the Reynolds shear stress term,  $\rho \overline{u'v'}$ , discussed in Chapter 6, can be written as

$$[(\nu + \nu_t)\psi''']' + u_e \frac{du_e}{dx} = \psi' \frac{\partial \psi'}{\partial x} - \psi'' \frac{\partial \psi}{\partial x} \quad (4.5.2)$$

In either form, for given initial conditions, say at  $x = x_0$  and eddy viscosity distribution, these equations are solved subject to their boundary conditions in the interval 0 to  $\delta$  at each specified  $x$ -location greater than  $x_0$ . The boundary-layer thickness  $\delta(x)$ , however, increases with increasing downstream distance  $x$  for both laminar and turbulent flows; to maintain computational accuracy, it is necessary to take small steps in the streamwise direction.

Transformed coordinates employing similarity variables such as the one discussed in Section 4.2 provide another alternative to express the equations in a better form before solving. Such a choice can reduce the growth of transformed boundary-layer thickness and thus allow larger steps to be taken in the streamwise direction. Furthermore, in some cases, they can also be used to generate the initial conditions needed in the solution of the boundary-layer equations.

We shall advocate the use of transformed coordinates employing similarity variables in the solution of the boundary-layer equations for two and three-dimensional flows. For two-dimensional flows we will use the Falkner–Skan transformation discussed in Section 4.2. With the similarity variable defined by Eq. (4.2.4a), and the dimensionless stream function  $f$  expressed as a function of  $x$  and  $\eta$ ,

$$\psi(x, y) = \sqrt{u_e \nu x} f(x, \eta) \quad (4.5.3)$$

and using a procedure similar to that used to obtain Eq. (4.2.5), the continuity and momentum equations, Eq. (3.1.2) and (3.1.10) and their boundary conditions, Eqs. (3.4.1), can be written as

$$(bf'')' + \frac{m+1}{2} ff'' + m[1 - (f')^2] = x \left( f' \frac{\partial f'}{\partial x} - f'' \frac{\partial f}{\partial x} \right) \quad (4.5.4)$$

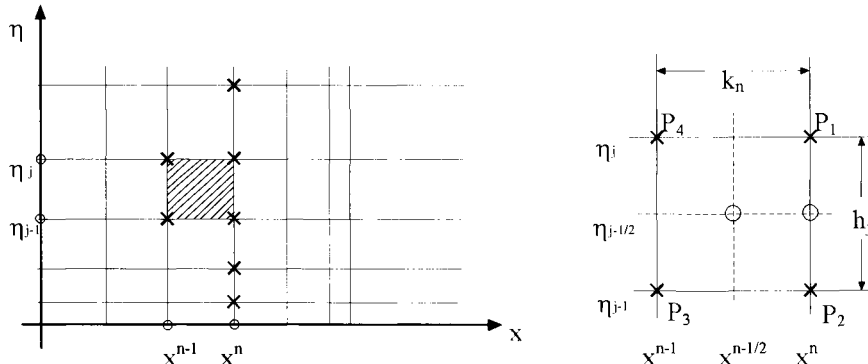


Fig. 4.8. Net rectangle for difference approximations.

$$\eta = 0, \quad f = f_w = -\frac{1}{\sqrt{u_e \nu x}} \int_0^x v_w dx, \quad f' = 0 \quad (4.5.5a)$$

$$\eta = \eta_e, \quad f' = 1 \quad (4.5.5b)$$

Here, a prime denotes differentiation with respect to  $\eta$ ; the parameter  $b$  equal to unity for laminar flows, is defined by

$$b = 1 + \nu_t^+, \quad \nu_t^+ = \frac{\nu_t}{\nu} \quad (4.5.6)$$

for laminar and turbulent flows. The velocity components  $u$  and  $v$  are now related to the dimensionless stream function  $f(x, \eta)$  by

$$u = u_e f' \quad (4.5.7a)$$

$$v = -\sqrt{u_e \nu x} \left[ \frac{f}{\sqrt{u_e x}} \frac{d}{dx} \sqrt{u_e x} + \frac{\partial f}{\partial x} + f' \frac{\partial \eta}{\partial x} \right] \quad (4.5.7b)$$

To solve Eqs. (4.5.4) and (4.5.5) with Keller's box method, which is a two-point finite-difference scheme, we first express them as a first-order system by introducing new functions to represent the derivatives of  $f$  with respect to  $\eta$  (subsection 4.5.1). The first-order equations are approximated on an arbitrary rectangular net, Fig. 4.8, with “centered-difference” derivatives and averages at the midpoints of the net rectangle difference equations. The resulting system of equations which is implicit and nonlinear is linearized by Newton's method (subsection 4.5.2) and solved by the block-elimination method discussed in subsections 4.5.3 and 5.2.6. A computer program for obtaining the solutions of the continuity and momentum equations for laminar and turbulent flows with this numerical method is given in the CD-ROM (Appendix B), Program 3.

### 4.5.1 Numerical Formulation

In order to express Eqs. (4.5.4) and (4.5.5) as a system of first-order equations, we define new variables  $u(x, \eta)$  and  $v(x, \eta)$  by

$$f' = u \quad (4.5.8a)$$

$$u' = v \quad (4.5.8b)$$

and write Eqs. (4.5.4) and (4.5.5) as

$$(bv)' + \frac{m+1}{2}fv + m(1-u^2) = x \left( u \frac{\partial u}{\partial x} - v \frac{\partial f}{\partial x} \right) \quad (4.5.8c)$$

$$\eta = 0, \quad u = 0, \quad f = f_w(x); \quad \eta = \eta_e, \quad u = 1 \quad (4.5.9)$$

We denote the net points of the net rectangle shown in Fig. 4.8 by

$$\begin{aligned} x_0 &= 0, & x_n &= x_{n-1} + k_n, & n &= 1, 2, \dots, N \\ \eta_0 &= 0, & \eta_j &= \eta_{j-1} + h_j, & j &= 1, 2, \dots, J \end{aligned} \quad (4.5.10)$$

and write the difference equations that are to approximate Eqs. (4.5.8) by considering one mesh rectangle as in Fig. 4.8. We start by writing the finite-difference approximations of the ordinary differential equations (4.5.8a,b) for the midpoint  $(x^n, \eta_{j-1/2})$  of the segment  $P_1P_2$ , using centered-difference derivatives,

$$\frac{f_j^n - f_{j-1}^n}{h_j} = \frac{u_j^n + u_{j-1}^n}{2} \equiv u_{j-1/2}^n \quad (4.5.11a)$$

$$\frac{u_j^n - u_{j-1}^n}{h_j} = \frac{v_j^n + v_{j-1}^n}{2} \equiv v_{j-1/2}^n \quad (4.5.11b)$$

Similarly, the partial differential equation (4.5.8c) is approximated by centering about the midpoint  $(x^{n-1/2}, \eta_{j-1/2})$  of the rectangle  $P_1P_2P_3P_4$ . This can be done in two steps. In the first step we center it about  $(x^{n-1/2}, \eta)$  without specifying  $\eta$ . If we denote its left-hand side by  $L$ , then the finite-difference approximation to Eq. (4.5.8c) is

$$\frac{1}{2}(L^n + L^{n-1}) = x^{n-1/2} \left[ u^{n-1/2} \left( \frac{u^n - u^{n-1}}{k_n} \right) - v^{n-1/2} \left( \frac{f^n - f^{n-1}}{k_n} \right) \right] \quad (4.5.12)$$

$$\alpha^n = \frac{x^{n-1/2}}{k_n}, \quad \alpha_1 = \frac{m^n + 1}{2} + \alpha^n, \quad \alpha_2 = m^n + \alpha^n \quad (4.5.13a)$$

$$R^{n-1} = -L^{n-1} + \alpha^n [(fv)^{n-1} - (u^2)^{n-1}] - m^n \quad (4.5.13b)$$

$$L^{n-1} \equiv \left[ (bv)' + \frac{m+1}{2}fv + m(1-u^2) \right]^{n-1} \quad (4.5.13c)$$

Eq. (4.5.12) can be written as

$$[(bv)']^n + \alpha_1(fv)^n - \alpha_2(u^2)^n + \alpha^n(v^{n-1}f^n - f^{n-1}v^n) = R^{n-1} \quad (4.5.14)$$

The identity sign introduces a useful shorthand:  $[ ]^{n-1}$  means that the quantity in square brackets is evaluated at  $x = x^{n-1}$ .

We next center Eq. (4.5.14) about the point  $(x^{n-1/2}, \eta_{j-1/2})$ , that is, we choose  $\eta = \eta_{j-1/2}$  and obtain

$$\begin{aligned} h_j^{-1}(b_j^n v_j^n - b_{j-1}^n v_{j-1}^n) + \alpha_1(fv)_{j-1/2}^n - \alpha_2(u^2)_{j-1/2}^n \\ + \alpha^n(v_{j-1/2}^{n-1}f_{j-1/2}^n - f_{j-1/2}^{n-1}v_{j-1/2}^n) = R_{j-1/2}^{n-1} \end{aligned} \quad (4.5.15)$$

where

$$R_{j-1/2}^{n-1} = -L_{j-1/2}^{n-1} + \alpha^n[(fv)_{j-1/2}^{n-1} - (u^2)_{j-1/2}^{n-1}] - m^n \quad (4.5.16a)$$

$$L_{j-1/2}^{n-1} = \left\{ h_j^{-1}(b_j v_j - b_{j-1} v_{j-1}) + \frac{m+1}{2}(fv)_{j-1/2} + m[1 - (u^2)_{j-1/2}] \right\}^{n-1} \quad (4.5.16b)$$

Eqs. (4.5.11) and (4.5.15) are imposed for  $j = 1, 2, \dots, J-1$  at given  $\eta$  and the transformed boundary-layer thickness,  $\eta_e$ , is to be sufficiently large so that  $u \rightarrow 1$  asymptotically. The latter is usually satisfied when  $v(\eta_e)$  is less than approximately  $10^{-3}$ .

The boundary conditions [Eq. (4.5.9)] yield, at  $x = x^n$ ,

$$f_0^n = f_w, \quad u_0^n = 0, \quad u_J^n = 1 \quad (4.5.17)$$

## 4.5.2 Newton's Method

If we assume  $f_j^{n-1}$ ,  $u_j^{n-1}$ , and  $v_j^{n-1}$  to be known for  $0 \leq j \leq J$ , then Eqs. (4.5.11), (4.5.15) and (4.5.17) form a system of  $3J + 3$  equations for the solution of  $3J + 3$  unknowns  $(f_j^n, u_j^n, v_j^n)$ ,  $j = 0, 1, \dots, J$ . To solve this nonlinear system, we use Newton's method; we introduce the iterates  $[f_j^{(\nu)}, u_j^{(\nu)}, v_j^{(\nu)}]$ ,  $\nu = 0, 1, 2, \dots$ , with initial value ( $\nu = 0$ ) equal to those at the previous  $x$ -station  $x^{n-1}$  (which is usually the best initial guess available). For the higher iterates we set

$$f_j^{(\nu+1)} = f_j^{(\nu)} + \delta f_j^{(\nu)}, \quad u_j^{(\nu+1)} = u_j^{(\nu)} + \delta u_j^{(\nu)}, \quad v_j^{(\nu+1)} = v_j^{(\nu)} + \delta v_j^{(\nu)} \quad (4.5.18)$$

We then insert the right-hand sides of these expressions in place of  $f_j^n$ ,  $u_j^n$  and  $v_j^n$  in Eqs. (4.5.11) and (4.5.15) and drop the terms that are quadratic in  $\delta f_j^{(\nu)}$ ,  $\delta u_j^{(\nu)}$  and  $\delta v_j^{(\nu)}$ . This procedure yields the following *linear* system (the superscript  $n$  is dropped from  $f_j$ ,  $u_j$ ,  $v_j$  and  $v$  from  $\delta$  quantities for simplicity).

$$\delta f_j - \delta f_{j-1} - \frac{h_j}{2}(\delta u_j + \delta u_{j-1}) = (r_1)_j \quad (4.5.19a)$$

$$\delta u_j - \delta u_{j-1} - \frac{h_j}{2}(\delta v_j + \delta v_{j-1}) = (r_3)_{j-1} \quad (4.5.19b)$$

$$(s_1)_j \delta v_j + (s_2)_j \delta v_{j-1} + (s_3)_j \delta f_j + (s_4)_j \delta f_{j-1} + (s_5)_j \delta u_j + (s_6)_j \delta u_{j-1} = (r_2)_j \quad (4.5.19c)$$

where

$$(r_1)_j = f_{j-1}^{(\nu)} - f_j^{(\nu)} + h_j u_{j-1/2}^{(\nu)} \quad (4.5.20a)$$

$$(r_3)_{j-1} = u_{j-1}^{(\nu)} - u_j^{(\nu)} + h_j v_{j-1/2}^{(\nu)} \quad (4.5.20b)$$

$$(r_2)_j = R_{j-1/2}^{n-1} - \begin{bmatrix} h_j^{-1}(b_j^{(\nu)} v_j^{(\nu)} - b_{j-1}^{(\nu)} v_{j-1}^{(\nu)}) + \alpha_1(fv)_{j-1/2}^{(\nu)} \\ -\alpha_2(u^2)_{j-1/2}^{(\nu)} + \alpha^n(v_{j-1/2}^{n-1} f_{j-1/2}^{(\nu)} - f_{j-1/2}^{n-1} v_{j-1/2}^{(\nu)}) \end{bmatrix} \quad (4.5.20c)$$

In writing the system given by Eqs. (4.5.19) we have used a certain order for them. The reason for this choice, as we shall see later, is to ensure that the  $A_0$  matrix in Eq. (4.5.26a) is not singular.

The coefficients of the linearized momentum equation are

$$(s_1)_j = h_j^{-1} b_j^{(\nu)} + \frac{\alpha_1}{2} f_j^{(\nu)} - \frac{\alpha^n}{2} f_{j-1/2}^{n-1} \quad (4.5.21a)$$

$$(s_2)_j = -h_j^{-1} b_{j-1}^{(\nu)} + \frac{\alpha_1}{2} f_{j-1}^{(\nu)} - \frac{\alpha^n}{2} f_{j-1/2}^{n-1} \quad (4.5.21b)$$

$$(s_3)_j = \frac{\alpha_1}{2} v_j^{(\nu)} + \frac{\alpha^n}{2} v_{j-1/2}^{n-1} \quad (4.5.21c)$$

$$(s_4)_j = \frac{\alpha_1}{2} v_{j-1}^{(\nu)} + \frac{\alpha^n}{2} v_{j-1/2}^{n-1} \quad (4.5.21d)$$

$$(s_5)_j = -\alpha_2 u_j^{(\nu)} \quad (4.5.21e)$$

$$(s_6)_j = -\alpha_2 u_{j-1}^{(\nu)} \quad (4.5.21f)$$

The boundary conditions, Eq. (4.5.17) become

$$\delta f_0 = 0, \quad \delta u_0 = 0, \quad \delta u_J = 0 \quad (4.5.22)$$

As discussed in [11], the linear system given by Eqs. (4.5.19) and (4.5.22) has a block tridiagonal structure and can be written in matrix-vector form as

$$A \vec{\delta} = \vec{r} \quad (4.5.23)$$

where

$$A = \begin{vmatrix} A_0 & C_0 \\ B_1 & A_1 & C_1 \\ \vdots & \vdots & \vdots \\ \vdots & \vdots & \vdots \\ B_j & A_j & C_j \\ \vdots & \vdots & \vdots \\ B_{J-1} & A_{J-1} & C_{J-1} \\ B_J & A_J & \end{vmatrix} \quad \vec{\delta} = \begin{vmatrix} \vec{\delta}_0 \\ \vec{\delta}_1 \\ \vdots \\ \vec{\delta}_j \\ \vdots \\ \vec{\delta}_J \end{vmatrix} \quad \vec{r} = \begin{vmatrix} \vec{r}_0 \\ \vec{r}_1 \\ \vdots \\ \vec{r}_j \\ \vdots \\ \vec{r}_J \end{vmatrix} \quad (4.5.24)$$

$$\vec{\delta}_j = \begin{vmatrix} \delta f_j \\ \delta u_j \\ \delta v_j \end{vmatrix} \quad \vec{r}_j = \begin{vmatrix} (r_1)_j \\ (r_2)_j \\ (r_3)_j \end{vmatrix} \quad 0 \leq j \leq J \quad (4.5.25)$$

and  $A_j$ ,  $B_j$ ,  $C_j$  are  $3 \times 3$  matrices defined as

$$A_0 = \begin{vmatrix} 1 & 0 & 0 \\ 0 & 1 & 0 \\ 0 & -1 & -h_1/2 \end{vmatrix} \quad A_j \equiv \begin{vmatrix} 1 & -h_j/2 & 0 \\ (s_3)_j & (s_5)_j & (s_1)_j \\ 0 & -1 & -h_{j+1}/2 \end{vmatrix} \quad 1 \leq j \leq J-1 \quad (4.5.26a)$$

$$A_J \equiv \begin{vmatrix} 1 & -h_J/2 & 0 \\ (s_3)_J & (s_5)_J & (s_1)_J \\ 0 & 1 & 0 \end{vmatrix} \quad B_j \equiv \begin{vmatrix} -1 & -h_j/2 & 0 \\ (s_4)_j & (s_6)_j & (s_2)_j \\ 0 & 0 & 0 \end{vmatrix} \quad 1 \leq j \leq J \quad (4.5.26b)$$

$$C_j \equiv \begin{vmatrix} 0 & 0 & 0 \\ 0 & 0 & 0 \\ 0 & 1 & -h_{j+1}/2 \end{vmatrix} \quad 0 \leq j \leq J-1 \quad (4.5.26c)$$

Note that the first two rows of  $A_0$  and  $C_0$  and the last row of  $A_J$  and  $B_J$  correspond to the boundary conditions [Eq. (4.5.22)]. To solve the continuity and momentum equations for different boundary conditions, only the matrix rows mentioned above need altering, as will be discussed later in subsection 5.5.3.

### 4.5.3 Block-Elimination Method

The solution of Eq. (4.5.23) can be obtained efficiently and effectively by using the block-elimination discussed by Keller [10] and described by Cebeci [11]. According to this method, the solution procedure consists of two sweeps. In the first part of the so-called *forward* sweep, we compute  $\Gamma_j$ ,  $\Delta_j$  from the recursion formulas given by

$$\Delta_0 = A_0 \quad (4.5.27a)$$

$$\Gamma_j \Delta_{j-1} = B_j \quad j = 1, 2, \dots, J \quad (4.5.27b)$$

$$\Delta_j = A_j - \Gamma_j C_{j-1} \quad j = 1, 2, \dots, J \quad (4.5.27c)$$

where the  $\Gamma_j$  matrix has the same structure as  $B_j$ . In the second part of the forward sweep, we compute  $\tilde{w}_j$  from the following relations

$$\tilde{w}_0 = \tilde{r}_0 \quad (4.5.28a)$$

$$\tilde{w}_j = \tilde{r}_j - \Gamma_j \tilde{w}_{j-1} \quad 1 \leq j \leq J \quad (4.5.28b)$$

In the so-called *backward* sweep, we compute  $\tilde{\delta}_j$  from the recursion formulas given by

$$\Delta_J \vec{\delta}_J = \vec{w}_J \quad (4.5.29a)$$

$$\Delta_j \vec{\delta}_j = \vec{w}_j - C_j \vec{\delta}_{j+1} \quad j = J-1, J-2, \dots, 0 \quad (4.5.29b)$$

The block elimination method is a general one and can be used to solve any system of first-order equations. The amount of algebra in solving the recursion formulas given by Eqs. (4.5.27) to (4.5.29), however, depends on the order of the matrices  $A_j$ ,  $B_j$ ,  $C_j$ . When it is small, the matrices  $\Gamma_j$ ,  $\Delta_j$  and the vector  $\vec{w}_j$  can be obtained by relatively simple expressions, as discussed in the accompanying CD-ROM, Program 3. However, this procedure, though very efficient, becomes increasingly tedious as the order of matrices increases and requires the use of an algorithm that reduces the algebra internally. A general algorithm, called the “matrix solver” discussed and given in the CD-ROM (Appendix B), Program 5 and Problem 4.42 can be used for this purpose.

## 4.6 Applications of BLP2 to External Flows

The boundary-layer program (BLP2) given in the accompanying CD-ROM, Program 3, can be used for both two-dimensional and axisymmetric external and internal flows. In this section we will demonstrate its use to three external flows and in the CD-ROM to an internal flow corresponding to a developing plane laminar duct flow.

For external flows, we consider two two-dimensional flows, one corresponding to a NACA 0012 airfoil (subsection 4.6.1) and one for an ellipse (subsection 4.6.2) and one axisymmetric flow corresponding to a prolate spheroid (subsection 4.6.3). For the airfoil problem, we compute its external velocity distribution with the Hess-Smith panel method (HSPM) given in the accompanying CD-ROM (Appendix A), Program 4, and for the ellipse and spheroid problems from analytical expressions based on inviscid flow theory. In all cases, the calculations are performed for a laminar flow. In general, however, the flowfield consists of both laminar and turbulent flows and requires the location of transition which is either known or calculated. We will postpone the calculation of the transition location to Chapter 5 and the calculation of the turbulent portion of the boundary layer to Chapter 6.

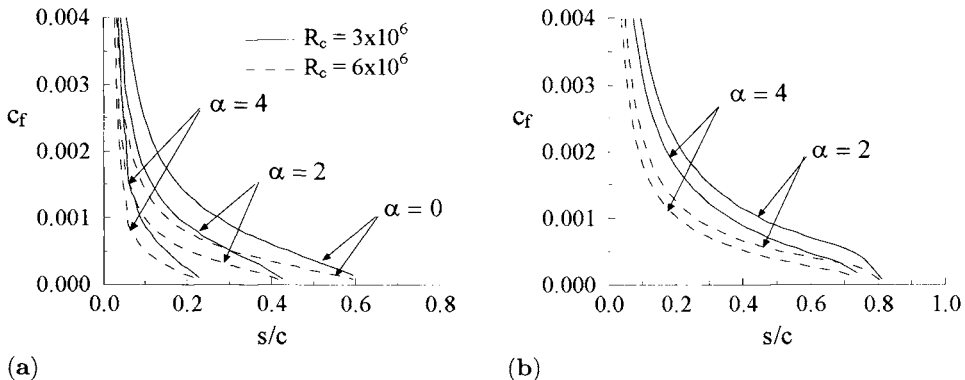


**Fig. 4.9.** Variation of the skin friction coefficient on (a) the upper surface and (b) the lower surface of the NACA 0012 airfoil at  $0^\circ$ ,  $2^\circ$  and  $4^\circ$  with surface distance.

#### 4.6.1 Airfoil Flow

For the airfoil flow, the laminar boundary layer calculations are performed for chord Reynolds numbers  $R_c$  of  $3 \times 10^6$  and  $6 \times 10^6$  at three angles of attack,  $\alpha = 0^\circ$ ,  $2^\circ$  and  $4^\circ$ . For each angle of attack, the external velocity distribution,  $u_e(x)$ , determined from HSPM, is separated into upper and lower surfaces, starting at the stagnation point up to the airfoil trailing edge. The boundary-layer calculations are then performed for each surface using the specified  $u_e(x)$  distribution as a function of surface distance. For example, at  $\alpha = 0^\circ$ , the stagnation point coincides with the leading edge and the  $u_e(x)$  distribution is read in for 92  $x$ -stations ( $NXT = 92$ ) starting at the stagnation point of the airfoil up to its trailing edge, with each  $x$ -station representing the dimensionless surface distance  $s/c$  with  $c$  corresponding to the reference length  $L$  in the definition of  $R_L$ . See Program 3 in Appendix B. We set ETAE = 8, P2(1) = 1.0 and take  $R_L$  equal to the desired chord Reynolds number. Since the calculations are performed for laminar flow, we set XCTR = 1.1 and use a uniform grid (VGP = 1.0) with DETA(1) = 0.1 which produces 81 points across the boundary layer without boundary-layer growth.

Figure 4.9 shows the variation of the local skin friction coefficient  $c_f$  with surface distance  $s/c$  on the upper and lower surfaces of the airfoil at two Reynolds numbers and for  $\alpha = 0^\circ$ ,  $2^\circ$  and  $4^\circ$ . Note that the calculations are not performed until the trailing edge of the airfoil. With flow deceleration (negative P2) flow separation occurs ( $c_f$  becomes negative), boundary-layer calculations develop singularity and the solutions do not converge. At higher angles of attack on the lower surface of the airfoil, flow accelerates and allows the calculations to be performed until the trailing-edge of the airfoil. Note that  $c_f$  decreases in the presence of an adverse pressure gradient. Note also that the location of the flow separation for both Reynolds numbers is the same. This is expected since for

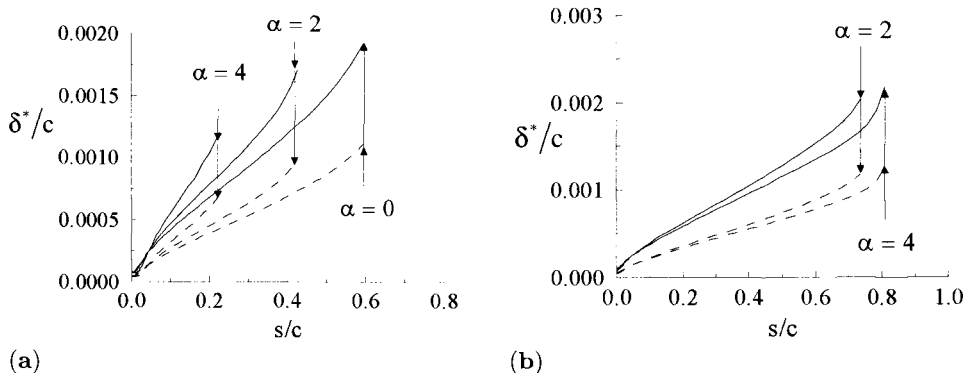


**Fig. 4.10.** Variation of the dimensionless displacement thickness,  $\delta^*/c$ , on (a) the upper surface and (b) the lower surface of the NACA 0012 airfoil at  $0^\circ$ ,  $2^\circ$  and  $4^\circ$  with surface distance.

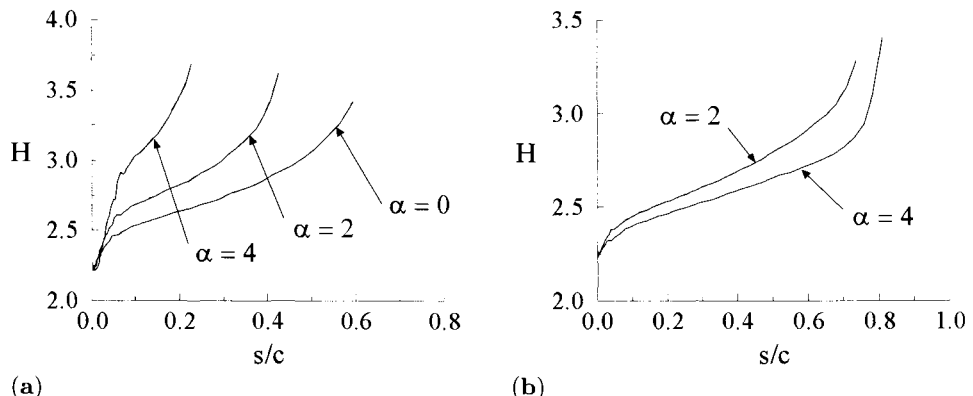


**Fig. 4.11.** Variation of the shape factor,  $H$ , on (a) the upper surface and (b) the lower surface of the NACA 0012 airfoil at  $0^\circ$ ,  $2^\circ$  and  $4^\circ$  with surface distance.

laminar flows, the flow separation is independent of the Reynolds number for a prescribed external velocity distribution.

Figures 4.10 and 4.11 show the variation of the dimensionless displacement thickness  $\delta^*/c$  and shape factor  $H$  with  $s/c$ , respectively, on the upper and lower surfaces of the airfoil, again at two Reynolds numbers. Note that  $H$  is independent of  $R_c$ .

#### 4.6.2 Ellipse Flow

The equation of an ellipse whose center is at  $(a, 0)$  can be written as

$$\frac{(x - a)^2}{a^2} + \frac{y^2}{b^2} = 1 \quad (4.6.1)$$

According to inviscid flow theory, the external velocity distribution around the ellipse is given, for zero angle of attack, by

$$u_e(s) = u_\infty(1 + t) \cos \beta \quad (4.6.2)$$

Here  $s$  denotes the surface distance,  $t$  is the thickness ratio of the ellipse ( $\equiv b/a$ ), and  $\beta$  is the angle between the line tangent to the body and the positive  $x$ -axis, that is

$$\beta = \tan^{-1} \frac{dy}{dx} \quad (4.6.3)$$

To demonstrate the application of BLP2 to this test case, we consider an ellipse of thickness ratio of 0.25 shown in Fig. 4.12 and perform laminar flow calculations at two Reynolds numbers  $R_L [\equiv (u_\infty 2a/\nu)]$  equal to  $10^6$  and  $10^7$ . The dimensionless surface distance  $s/a$  which is defined by integrating

$$\left( \frac{ds}{dx} \right)^2 = 1 + \left( \frac{dy}{dx} \right)^2 \quad (4.6.4)$$

with  $dy/dx$  given by

$$\frac{t \left( 1 - \frac{x}{a} \right)}{\left[ 2 \frac{x}{a} - \left( \frac{x}{a} \right)^2 \right]^{1/2}} \quad (4.6.5)$$

It can also be calculated by using the trapezoidal rule,

$$\left( \frac{s}{a} \right)_i = \left( \frac{s}{a} \right)_{i-1} + \sqrt{\left[ \left( \frac{x}{a} \right)_i - \left( \frac{x}{a} \right)_{i-1} \right]^2 + \left[ \left( \frac{y}{a} \right)_i - \left( \frac{y}{a} \right)_{i-1} \right]^2} \quad (4.6.6)$$

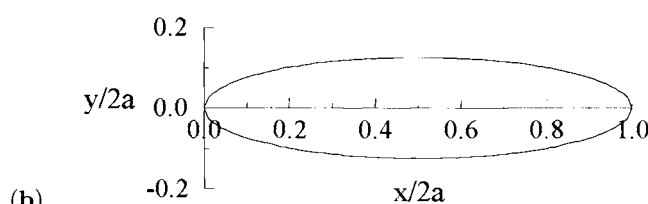
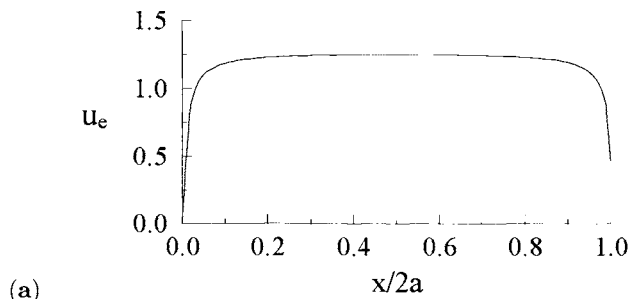


**Fig. 4.12.** (a) Inviscid velocity distribution about (b) an ellipse of thickness ratio 0.25.

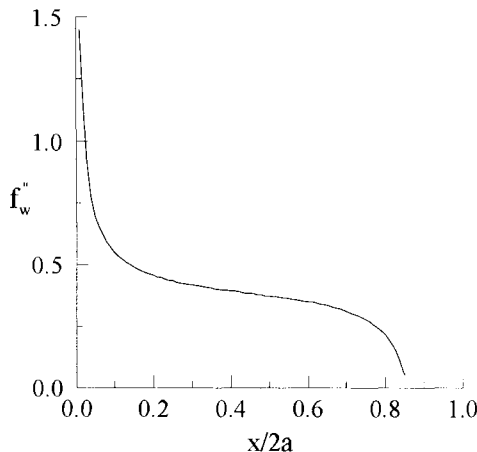


**Fig. 4.13.** Wall shear parameter,  $f_w''$ , variation on the ellipse with axial distance  $x/2a$  at  $R_{2a} (\equiv 2au_\infty/\nu) = 10^6$  and  $10^7$ .

Here we use the latter and compute  $\bar{u}_e(s)$  as a function of surface distance with  $\Delta x/2a$  increments of 0.01.

Figure 4.13 shows the variation of the wall shear parameter  $f_w'' [\equiv (c_f/2)\sqrt{R_x}]$  with axial distance  $x/2a$  at two Reynolds numbers,  $R_{2a} = 10^6$  and  $10^7$ . As can be seen, the Reynolds number has no effect on  $f_w''$  with laminar flow separation occurring at  $x/2a = 0.85$ .

#### 4.6.3 Prolate Spheroid Flow

BLP2 can also be used for axisymmetric flows by using the Mangler transformation discussed in Problems 3.12 and 4.37. This transformation places the axisymmetric boundary-layer equations in the form given by Eqs. (4.5.4) and (4.5.5) in terms of Falkner–Skan variables. If the definition of  $b$  in BLP2 is changed from

$$b = 1 + \nu_t^+ \quad (4.6.7a)$$

to

$$b = (1 + t)^{2k}(1 + \nu_t^+) \quad (4.6.7b)$$

with  $t$  defined in Eq. (P3.12.5), then BLP2 will allow the solutions of the boundary-layer equations for an axisymmetric flow provided that the input of the geometry is specified in terms of the Mangler variables  $(\bar{x}, \bar{y})$ .

To illustrate the application of BLP2 to an axisymmetric flow, we consider a prolate spheroid (see Fig. 4.14) which is an ellipsoid of revolution whose length

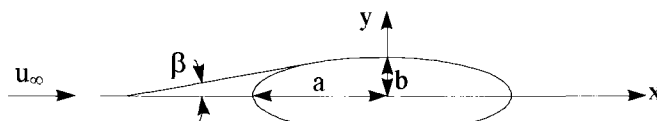


**Fig. 4.14.** Prolate spheroid at  $0^\circ$  incidence.

along its symmetry axis is greater than the diameter of its largest circular cross section. According to inviscid flow theory, for zero angle of attack, the external velocity distribution around the prolate spheroid is given by

$$u_e(s) = u_{\text{ref}} A \cos \beta \quad (4.6.8)$$

Here  $s$  represents the surface distance, and  $\beta$  denotes the angle between the line tangent to the elliptic profile and the positive  $x$ -axis. The parameter  $A$  is a function of the thickness ratio  $t_0 (\equiv b/a)$  of the elliptic profile. It is given by

$$A = \frac{(1 - t_0^2)^{3/2}}{\sqrt{1 - t_0^2} - 1/2t_0^2 \ln \left[ \left( 1 + \sqrt{1 - t_0^2} \right) / \left( 1 - \sqrt{1 - t_0^2} \right) \right]} \quad (4.6.9)$$

The external velocity distribution, the surface distance and body radius needed in BLP2 can be specified as described below.

For clarity of notation we first write Eq. (P3.12.1) as

$$d\bar{s} = \left( \frac{r_0}{L} \right)^{2k} ds \quad (4.6.10)$$

since  $\bar{x}$  and  $x$  in Eq. (P3.12.1) denote the surface distance of the Mangler transformed body and axisymmetric body, respectively. The surface distance  $s$  which is defined by  $(ds)^2 = (dx)^2 + (dr_0)^2$  can be obtained from the equation of a prolate spheroid, centered at  $(a, 0)$ .

$$\frac{(x - a)^2}{a^2} + \frac{r_0^2}{b^2} = 1 \quad (4.6.11)$$

by

$$\frac{ds}{dx} = \frac{ds^*}{d\xi} = \left[ \frac{t_0^2 + (1 - t_0^2)(2\xi - \xi^2)}{2\xi - \xi^2} \right]^{1/2} \quad (4.6.12)$$

where  $\xi = x/a$  and  $s^* = s/a$ . The dimensionless body radius  $r_0^*$  is obtained from Eq. (4.6.11),

$$r_0^* \equiv \frac{r_0}{a} = t_0(2\xi - \xi^2)^{1/2} \quad (4.6.13)$$

The dimensionless Mangler transformed surface distance  $\bar{s}^* = \bar{s}/a$ , with  $L = a$ , follows from Eqs. (4.6.9) to (4.6.11),

$$\bar{s}^* = \int_0^\xi r_0^{*2} ds^* = t_0^2 \int_0^\xi (2\xi - \xi^2)^{1/2} [t_0^2 + (1 - t_0^2)(2\xi - \xi^2)]^{1/2} d\xi \quad (4.6.14)$$

Since  $\cos \beta = dx/ds$ ,

$$\cos \beta = \left[ \frac{2\xi - \xi^2}{t_0^2 + (1 - t_0^2)(2\xi - \xi^2)} \right]^{1/2} \quad (4.6.15)$$

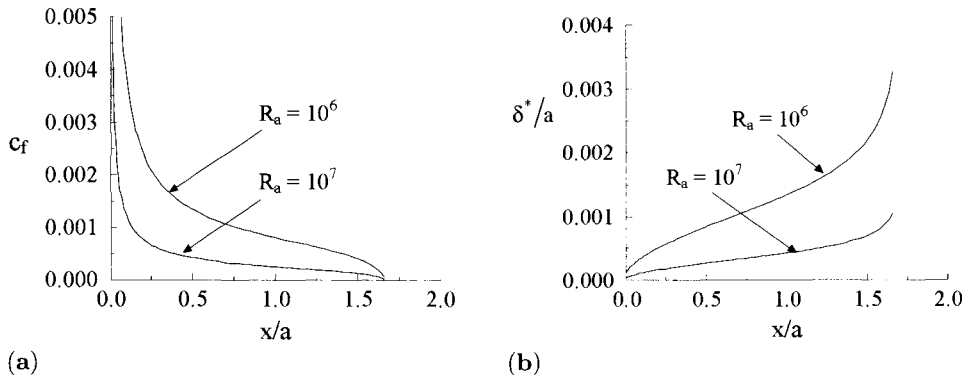


**Fig. 4.15.** Variation of (a) skin friction coefficient and (b) dimensionless displacement thickness,  $\delta^*/a$ , on a prolate spheroid at  $0^\circ$  incidence for  $R_a = 10^6$  and  $R_a = 10^7$ .

Given the axial distance distribution  $\xi = x/a$ , the Mangler transformed surface distance  $\bar{s}^*$  can be computed from Eq. (4.6.14) and the corresponding external velocity is determined from Eqs. (4.6.8), (4.6.9) and (4.6.15). Calculations are performed here for a prolate spheroid with a thickness ratio equal to 0.25 at two Reynolds numbers,  $R_a (\equiv u_\infty a / \nu) = 10^6$  and  $R_a = 10^7$ . The transverse curvature term  $t$  in Eq. (4.6.7b) is negligible for this problem and therefore was not included in the calculations.

Figure 4.15 presents the calculated skin friction coefficient,  $c_f$ , and dimensionless displacement  $\delta^*/a$  thickness distributions,

$$c_f \equiv \frac{2\tau_w}{\rho u_e^2} = ar_0^* \frac{2f_w''}{\sqrt{R_{\bar{s}^*}}}, \quad \frac{\delta^*}{a} = \frac{\bar{s}^*}{a^2 r_0^* \sqrt{R_{\bar{s}^*}}} (\eta_e - f_e)$$

where

$$R_{\bar{s}^*} = u_e \bar{s}^* / \nu$$

As expected and as in two-dimensional flows, for laminar flows, the location of separation is independent of Reynolds numbers occurring at  $x/a = 1.68$  in both cases.

## References

- [1] Hansen, A.G., *Similarity Analysis of Boundary-Value Problems in Engineering*, Englewood Cliffs, NJ, 1964.
- [2] Na, T.Y., *Computational Methods in Engineering Boundary Value Problems*, Academic Press, New York, 1979.
- [3] Falkner, V.G. and Skan, S.W., "Some Approximate Solutions of the Boundary Layer Equations," *ARC R&M 1314*, 1930 (see also *Phil. Mag.*, Vol. 12, p. 865, 1931).
- [4] Hartree, D.R., "On an Equation Occurring in Falkner and Skan's Approximate Treatment of the Equations of the Boundary Layer," *Proc. Cambridge Phil. Soc.*, Vol. 33, p. 223, 1937.

- [5] Stewartson, K., "Further Solutions of the Falkner-Skan Equation," *Phil. Mag.*, Vol. 12, p. 865, 1954.
- [6] Cebeci, T. and Keller, H.B., "Shooting and Parallel Shooting Methods for Solving the Falkner-Skan Boundary-Layer Equation," *J. Comp. Phys.*, Vol. 7, p. 289, 1971.
- [7] Christian, J.W., Hankey, W.L. and Petty, J.S., "Similar Solutions of the Attached and Separated Compressible Laminar Boundary-Layer with Heat Transfer and Pressure Gradient," Aerospace Research Laboratories, 70-0023, 1970.
- [8] Lock, R.C., "Hydrodynamic Stability of the Flow in the Laminar Boundary Layer Between Parallel Streams," *Proc. Cambridge Phil. Soc.*, Vol. 50, p. 105, 1954.
- [9] Crank, J. and Nicholson, P., "A Practical Method for Numerical Evaluation of Solutions of Partial Differential Equations of the Heat-Conduction Type," *Proceedings of the Cambridge Philosophical Society*, Vol. 43, pp. 50-67, January 1947.
- [10] Keller, H.B., "A New Difference Scheme for Parabolic Problems," *Numerical Solution of Partial Differential Equations*, Vol. II, ed. J. Bramble, Academic, New York, 1970.
- [11] Cebeci, T., *Convective Heat Transfer*, Horizons Publ., Long Beach, Calif. and Springer, Heidelberg, 2003.
- [12] Iglisch, R., "Exact Calculation of Laminar Boundary Layer in Longitudinal Flow Over a Flat Plate with Homogeneous Suction," NACA Tech. Memo. 1205, 1949.
- [13] Cebeci, T. and Keller, H.B., "Shooting and Parallel Shooting Methods for Solving the Falkner-Skan Boundary-Layer Equations," *J. Comp. Phys.*, Vol. 7, p. 289, 1971.
- [14] Sparrow, E.M., Quack, H. and Boermer, C.J., "Local Nonsimilarity Boundary Layer Solutions," *AIAA J.*, Vol. 8, p. 1936, 1970.
- [15] Seban, R.A. and Bond, R., "Skin Friction and Heat Transfer Characteristics of a Laminar Boundary layer on a Circular Cylinder in Axial Incompressible Flow," *J. Aero. Sci.*, Vol. 18, p. 671, 1951.
- [16] Kelly, H.R., "A Note on the Laminar Boundary Layer on a Circular Cylinder in Axial Incompressible Flow," *J. Aero. Sci.*, Vol. 21, p. 634, 1954.
- [17] Stewartson, K., "The Asymptotic Boundary Layer on a Circular Cylinder," *Quart. Appl. Math.*, Vol. 13, p. 13, 1955.
- [18] Cebeci, T., "Laminar and Turbulent Incompressible Boundary Layers on Slender Bodies of Revolution in Axial Flow," *J. Basic Eng.*, Vol. 92, p. 545, 1970.
- [19] Schultz-Grunow, F. and Breuer, W., "Laminar Boundary Layers on Cambered Walls," In: *Basic Developments in Fluid Dynamics* (ed. M. Holt), pp. 377-436, Academic Press, NY, 1965.
- [20] Aupoix, B., Brazier, J.Ph., Cousteix, J., "Asymptotic defect boundary-layer theory applied to hypersonic flows," *AIAA J.*, Vol. 30, No. 5, p. 1252, 1992.
- [21] Patel, V.C., "Some Aspects of Thick Three-Dimensional Boundary Layers," Proceedings, 14th Symposium on Novel Hydrodynamics, Ann Arbor, Michigan, 1982.
- [22] Bradshaw, P., "Review Complex Turbulent Flows," *J. Fluids Eng.*, Vol. 971, pp. 146-154, June 1975.

## Problems

**4-1.** By using the transformation

$$\eta = \frac{y}{\sqrt{\nu t}} \quad u = f(\eta, t)$$

express the nonsteady momentum equation

$$\frac{\partial u}{\partial t} = \nu \frac{\partial^2 u}{\partial y^2}$$

in transformed coordinates.

**4-2.** A useful transformation often used in laminar boundary-layer problems is von Mises' transformation, which uses new independent variables  $(x, \psi)$ , where  $\psi$  is the stream function. Show that with this transformation the momentum equation

$$u \frac{\partial u}{\partial x} + v \frac{\partial u}{\partial y} = u_e \frac{du_e}{dx} + \nu \frac{\partial^2 u}{\partial y^2}$$

subject to the boundary conditions

$$y = 0 \quad u = v = 0$$

$$y \rightarrow \infty \quad u \rightarrow u_e$$

can be written as

$$u \frac{\partial u}{\partial x} - u_e \frac{du_e}{dx} = \nu u \frac{\partial}{\partial \psi} \left( u \frac{\partial u}{\partial \psi} \right) \quad (\text{P4.2.1})$$

subject to the new boundary conditions

$$\begin{aligned} \psi = 0 & \quad u = 0 \\ \psi \rightarrow \infty & \quad u \rightarrow u_e \end{aligned} \quad (\text{P4.2.2})$$

Note that when  $u$  is determined from Eqs. (P4.2.1) and (P4.2.2), then  $v$  follows from the continuity equation.

**4-3.** Show that the relation between  $y$  and  $\eta$  for an axisymmetric flow with significant transverse curvature and local surface angle  $\phi$  is

$$y = \frac{r_0}{\cos \phi} \left[ -1 + \sqrt{1 + \frac{2 \cos \phi}{L} \left( \frac{L}{r_0} \right)^2 \sqrt{\frac{\nu \bar{x}}{u_e}} \eta} \right]$$

**4-4.** For a two-dimensional similar laminar flow, what is the value of  $m$  for which the wall shear  $\tau_w$  is proportional to  $x$ ?

**4-5.** For a two-dimensional stagnation point laminar flow with mass transfer, find the variation of wall mass transfer velocity  $v_w$  with  $x$  required for similarity.

**4-6.** Derive Eq. (4.2.5).

**4-7.** Show that for similar flows by differentiating

$$\delta^* = \delta_1^* \sqrt{\frac{\nu x}{u_e}}$$

we get

$$dR_{\delta^*} = \frac{(\delta_1^*)^2}{\delta^*} \frac{m+1}{2} dx$$

Here  $R_{\delta^*} = u_e \delta^* / \nu$ .

**4-8.** Water at 20 °C flows at a velocity of 3 ms<sup>-1</sup> past a flat plate. Plot the velocity profiles,  $u/u_e$  versus  $y$ , at stations 0.5, 1, and 2 m from the leading edge. Also plot the variation of the local skin-friction coefficient over the first 2 m of the plate and determine the average skin-friction drag.

**4-9.** Air at 25 °C and 1 atm pressure flows normal to a 1 cm diameter circular cylinder at a velocity of 10 ms<sup>-1</sup>. According to the inviscid flow theory, the external velocity  $u_e$  along the surface of a circular cylinder is given by

$$u_e = 2u_\infty \sin \xi \quad (\text{P4.9.1})$$

where  $u_\infty$  is the freestream velocity and  $\xi (\equiv x/r_0)$  is measured from the stagnation point.

In the vicinity of the stagnation point, the external velocity can be obtained by expanding Eq. (P4.9.1) by Taylor series and approximating it close to the stagnation point,

$$u_e = \frac{2u_\infty x}{r_0}$$

Calculate the displacement thickness of the boundary-layer at and near the stagnation point. Calculate also the momentum thickness and the wall shear stress. Discuss the significance of the results.

**4-10.** Using the definition of  $\delta_1^*$  and Eq. (4.2.19), show that for the sink flow

$$\begin{aligned}\delta_1^* &= 3\sqrt{2} - 2\sqrt{3} \\ \theta_1 &= \frac{8}{\sqrt{3}} - 3\sqrt{2}\end{aligned}$$

**4-11.** Consider a laminar flow past a flat plate with uniform suction. The boundary conditions follow from Eq. (3.4.1) and can be written as

$$y = 0, \quad u = 0, \quad v = v_w = \text{const.} \quad (\text{P4.11.1a})$$

$$y = \delta, \quad u = u_e = u_\infty \quad (\text{P4.11.1b})$$

At a certain distance from the leading edge, the boundary-layer thickness  $\delta$ , which in general is a function of  $x$ , becomes constant and stays constant with increasing  $x$ . As a result, the streamwise velocity component  $u$  varies only with  $y$ , that is,  $\partial u / \partial x = 0$ . The momentum equation becomes an ordinary differential equation and can be written as

$$v_w \frac{du}{dy} = \nu \frac{d^2 u}{dy^2} \quad (\text{P4.11.2})$$

since from the continuity equation  $v(x, y) = v_w = \text{const.}$

(a) Show that the solution of Eq. (P4.11.2) is

$$\frac{u(y)}{u_\infty} = 1 - \exp\left(\frac{v_w y}{\nu}\right) \quad (\text{P4.11.3})$$

This velocity profile is known as the asymptotic suction profile.

(b) Using Eq. (P4.11.3), show that

$$\delta^* = -\frac{\nu}{v_w}, \quad \theta = -\frac{1}{2} \frac{\nu}{v_w}, \quad \tau(0) = \tau_w = -\rho v_w u_\infty \quad (\text{P4.11.4})$$

**4-12.** Consider a laminar flow on a flat plate with uniform suction, and define the suction drag as the loss of momentum due to mass removed from the boundary-layer. Let the total mass flow rate  $\dot{m}$  removed be

$$\dot{m} = \rho \int_0^L v_w dx \quad (\text{P4.12.1})$$

and assume that there is a streamline  $AB$  (Fig. P4.1) which separates the mass removed from the rest of the flow. If  $A$  denotes the location of the streamline far upstream at a distance  $h$  from the surface, then

$$\dot{m} = \rho h u_\infty \quad (\text{P4.12.2})$$

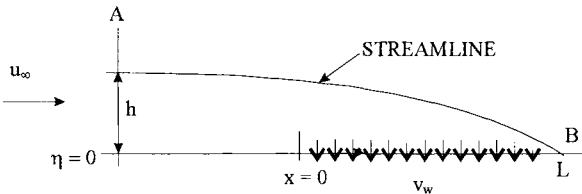


**Fig. P4.1.** Flat-plate flow with uniform suction and a streamline at a distance  $h$  away from the surface.

Assuming that the mass removed occurs normal to the plate, the loss in  $x$ -momentum is

$$\rho u_\infty^2 h$$

show that if  $D$  denotes the force acting on the plate, the suction drag coefficient  $C_{d_q}$  is

$$C_{d_q} = \frac{D}{(\frac{1}{2}) \rho u_\infty^2 L} = 2 \int_0^L \left( \frac{v_w}{u_\infty} \right) \frac{dx}{L} = 2 C_q \quad (\text{P4.12.3})$$

where  $C_q$  is the dimensionless suction volume coefficient

$$C_q = \frac{Q}{A_0 u_\infty} = \frac{(-v_w)}{u_\infty} \quad (\text{P4.12.4})$$

Here  $A_0$  is the surface area sucked and  $Q$  is the rate of volume flow sucked.

**4-13.** The boundary-layer equations for a two-dimensional laminar jet coming out from a slot mixing with the surrounding fluid at rest are

$$\frac{\partial u}{\partial x} + \frac{\partial v}{\partial y} = 0 \quad (\text{P4.13.1})$$

$$u \frac{\partial u}{\partial x} + v \frac{\partial u}{\partial y} = \frac{1}{\rho} \frac{\partial \tau}{\partial y} \quad (\text{P4.13.2})$$

They are subject to the boundary conditions

$$y = 0 \quad u = 0 \quad \frac{\partial u}{\partial y} = 0; \quad y \rightarrow \infty \quad u = 0 \quad (\text{P4.13.3})$$

Here  $\tau$  is given by Eq. (4.3.3) with  $\partial/\partial r = \partial/\partial y$ . As in the circular jet, the total momentum  $J$  in the  $x$ -direction is constant:

$$J = \rho \int_{-\infty}^{\infty} u^2 dy = \text{const.} \quad (\text{P4.13.4})$$

To find the similarity solution for the system of Eqs. (P4.13.1)–(P4.13.4), assume

$$\frac{u(x, y)}{u_c(x)} = f'(\eta), \quad \psi(x, y) = u_c(x)\delta(x)f(\eta)$$

and carry out a procedure similar to the laminar circular jet case. Show that for similarity we must have

$$\frac{\delta^2}{\nu} \frac{du_c}{dx} = \text{const.} = c_1$$

Take  $c_1 = -1$  and show that

$$u_c = M^{2/3}(3\nu x)^{-1/3}$$

$$f(\eta) = \sqrt{2} \tanh \left( \frac{\eta}{\sqrt{2}} \right)$$

$$f'(\eta) = \operatorname{sech}^2 \left( \frac{\eta}{\sqrt{2}} \right)$$

$$u_c = \left( \frac{3}{32} \right)^{1/3} \left( \frac{J}{\rho} \right)^{2/3} (\nu x)^{-1/3} = 0.454 \left( \frac{J}{\rho} \right)^{2/3} (\nu x)^{-1/3}$$

$$\delta = \left( \frac{3}{4\sqrt{2}} \right)^{-1/3} \left( \frac{J}{\rho} \right)^{-1/3} (3\nu x)^{2/3} = 2.57 \left( \frac{J}{\rho} \right)^{-1/3} (\nu x)^{2/3}$$

$$\dot{m} = \rho \frac{3}{2} \left( \frac{32}{3} \right)^{1/3} \left( \frac{J}{\rho} \right)^{1/3} (\nu x)^{1/3} = 3.302 \rho \left( \frac{J}{\rho} \right)^{1/3} (\nu x)^{1/3}$$

**4-14.** With the restriction that the velocity defect in the wake is small, the momentum equation for an axisymmetric wake can be written as

$$-u_\infty \frac{\partial u_1}{\partial x} = \frac{1}{r\rho} \frac{\partial}{\partial r}(r\tau) \quad (\text{P4.14.1})$$

Here  $\tau$  is

$$\tau = -\mu \frac{\partial u_1}{\partial r} - \rho \bar{u}' v' \quad (\text{P4.14.2})$$

The boundary conditions are

$$y = 0 \quad \frac{\partial u_1}{\partial y} = 0; \quad y \rightarrow \infty \quad u_1 = 0 \quad (\text{P4.14.3})$$

The drag of the body subject to Eq. (4.3.23) is

$$F = 2\pi\rho u_\infty \int_0^\infty u_1 r dr = \text{const.} \quad (\text{P4.14.4})$$

To find the similarity solution for the system of Eqs. (P4.14.1)–(P4.14.4), carry out a procedure similar to the two-dimensional laminar wake. For example, use Eqs. (4.3.30) and (4.3.32) and the definition of  $\eta$  given by Eq. (4.3.7) and express Eq. (P4.14.1) in terms of similarity variables  $f$  (negative again) and  $\eta$ . Show that for similarity we must have

$$\frac{u_\infty}{u_c} \frac{du_c}{dx} \frac{\delta^2}{\nu} = \text{const.}, \quad \frac{u_\infty \delta}{\nu} \frac{d\delta}{dx} = \text{const.} = c_1 \quad (\text{P4.14.5})$$

Assume that  $c_1 = 1$  and integrate the second relation in Eq. (P4.14.5) and show that

$$u_c = Ax^{-1} \quad (\text{P4.14.6})$$

where  $A$  is constant. Show that the constant in the first expression in Eq. (P4.14.5) is  $-2$ . This together with  $c_1 = 1$  allows the momentum equation expressed in similarity variables to be written as

$$(\eta f')' + (\eta^2 f)' = 0 \quad (\text{P4.14.7})$$

so that its solution is the same as the velocity profile for a two-dimensional wake, and

$$u = u_\infty - \frac{F}{\rho} \frac{e^{-\eta^2/2}}{4\pi\nu x} \quad (\text{P4.14.8})$$

**4-15.** For laminar mixing of two streams of nearly equal velocity ( $u_1 - u_2 \ll u_1$ ), linearize the momentum equation. Discuss the solution, the velocity profile, the relation of the free shear layer to the external flow, and the shear stress on the dividing streamline. Compare it with Lock's solutions for the cases  $u_2/u_1 = 0$  and  $u_2/u_1 = 0.501$ .

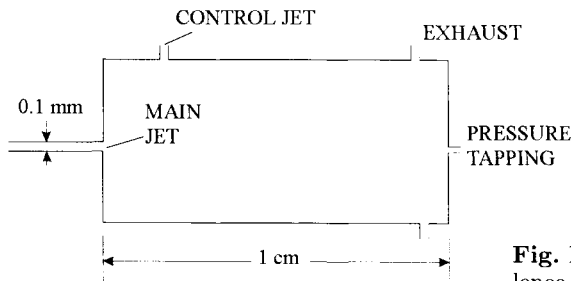


**Fig. P4.2.** Schematic diagram of a turbulence amplifier.

**4-16.** A fluidic device called a *turbulence amplifier* consists of a 0.1 mm diameter jet orifice, fed by a long pipe of the same diameter, in one wall of a chamber, with a pressure tapping on the opposite wall, 1 cm away and on the jet axis.  $1.5 \times 10^{-7} \text{ kgs}^{-1}$  of air is supplied through the pipe. Calculate the difference between the pressure in the chamber (assume atmospheric pressure) and at the pressure tapping.

**4-17.** (a) Assume that the velocity profile for a laminar flow on a flat plate can be approximated by a second-order polynomial given by

$$u = a + by + cy^2$$

Use the momentum integral equation to obtain expressions for the dependence of local boundary-layer thickness and skin-friction coefficient on the local Reynolds number. Compare the results with exact solutions.

(b) Repeat (a) for the velocity profile approximated by

$$u = b \sin ay$$

**4-18.** Repeat Problem 4-17 for a velocity profile approximated by

$$\frac{u}{u_e} = a + b \frac{y}{\delta} + c \left( \frac{y}{\delta} \right)^2 + d \left( \frac{y}{\delta} \right)^3$$

and find the coefficients for a constant-pressure boundary-layer. Show that the value of  $H$  is 2.69 compared with the “exact” value of 2.59. Sketch a typical profile in an *adverse* pressure gradient. What is the sign of  $c$ ?

**4-19.** Assume that the velocity profile for a laminar flow on a flat plate can be approximated by

$$u = a + by \quad (\text{P4.19.1})$$

(a) Using this profile and the continuity equation (3.1.2), show that for the general case of suction and blowing the normal velocity component  $v$  can be written as

$$v = v_w + \left( u_e \frac{d\delta}{dx} - \delta \frac{du_e}{dx} \right) \frac{1}{2} \left( \frac{y}{\delta} \right)^2 \quad (\text{P4.19.2})$$

(b) Using Eqs. (P4.19.1) and (P4.19.2) and the momentum equation (3.1.8) subject to the boundary condition  $\partial u / \partial y = 0$  at  $y = \delta$ , show that for the general case of suction and blowing

$$\begin{aligned} \nu u &= \left( \delta^2 u_e \frac{du_e}{dx} - u_e^2 \delta \frac{d\delta}{dx} \right) \left[ \frac{1}{24} \left( \frac{y}{\delta} \right)^4 - \frac{1}{6} \left( \frac{y}{\delta} \right)^2 \right] \\ &\quad + v_w u_e \delta \left[ \frac{1}{2} \left( \frac{y}{\delta} \right)^2 - \frac{y}{\delta} \right] - \delta^2 u_e \frac{du_e}{dx} \left[ \frac{1}{2} \left( \frac{y}{\delta} \right)^2 - \left( \frac{y}{\delta} \right) \right] \end{aligned} \quad (\text{P4.19.3})$$

(c) Using the boundary condition that  $u = u_e$  at  $y = \delta$ , show that Eq. (P4.19.3) can be written

$$u_e^2 \delta \frac{d\delta}{dx} = -3\delta^2 u_e \frac{du_e}{dx} + 8\nu u_e + 4v_w u_e \delta \quad (\text{P4.19.4})$$

(d) Substituting Eq. (P4.19.4) into Eq. (P4.19.3), show that we get an iterated expression for the  $x$ -component of the velocity profile,

$$\frac{u}{u_e} = \frac{1}{3} \left[ 4 \left( \frac{y}{\delta} \right) - \left( \frac{y}{\delta} \right)^4 \right] + \left( \frac{\delta^2}{\nu} \frac{du_e}{dx} - \frac{u_e \delta}{\nu} \right) \left[ \frac{1}{3} \frac{y}{\delta} - \frac{1}{2} \left( \frac{y}{\delta} \right)^2 + \frac{1}{6} \left( \frac{y}{\delta} \right)^4 \right] \quad (\text{P4.19.5})$$

which is like that of Pohlhausen for  $v_w = 0$ .

(e) Show that after substituting Eq. (P4.19.4) into Eq. (P4.19.2), the variation of normal velocity  $v$  across the boundary-layer is given by

$$\frac{v\delta}{\nu} = 4 \left( \frac{y}{\delta} \right)^2 - 2 \frac{\delta^2}{\nu} \frac{du_e}{dx} \left( \frac{y}{\delta} \right)^2 + \frac{v_w \delta}{\nu} \left[ 1 + 2 \left( \frac{y}{\delta} \right)^2 \right] \quad (\text{P4.19.6})$$

**4-20.** Using the definition of momentum thickness and the results given in Table 4.1, show that for a two-dimensional stagnation point flow a more accurate expression for Eq. (4.4.18) is

$$\left( \frac{\theta}{L} \right)^2 R_L = \frac{0.085}{\left( \frac{du_e^*}{dx} \right)_0}$$

**4-21.** Show that  $(\delta^*/\tau_w)dp/dx$  represents the ratio of net pressure force to wall shear force acting on a two-dimensional boundary-layer. Is it uniquely related to the pressure gradient parameter  $(\theta^2/\nu)du_e/dx$  used in Thwaites' method?

**4-22.** Calculate the nondimensional displacement thickness, momentum thickness, and skin-friction coefficient on a semi-infinite circular cone whose half

angle is  $120^\circ$ . Note that this flow is “inside” the cone and away from the apex. The external velocity varies as

$$u_e \sim s^{2.2}$$

**4-23.** The coordinates of the symmetrical NACA 0012 airfoil shown below (see also Table 5.1) and its external-velocity distribution (in potential flow) for zero angle of attack are given below. Compute the laminar boundary-layer development for a chord Reynolds number of  $R_c \equiv u_\infty c / \nu = 6 \times 10^6$  in the region  $0 \leq x/c \leq 0.20$ . Find

- (a) Displacement thickness distribution.
- (b) Local skin-friction distribution.

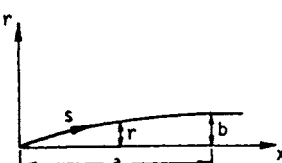
$x, \%c$	$y, \%c$	$u_e/u_\infty$	$x, \%c$	$y, \%c$	$u_e/u_\infty$
0	0	0	25	5.941	1.174
0.5	—	0.800	30	6.002	1.162
1.25	1.894	1.005	40	5.803	1.135
2.5	2.615	1.114	50	5.294	1.108
5.0	3.555	1.174	60	4.563	1.080
7.5	4.200	1.184	70	3.664	1.053
10	4.683	1.188	80	2.623	1.022
15	5.345	1.188	90	1.448	0.978
20	5.737	1.183	95	0.807	0.952
			100	0.126	0.915

**4-24.** Consider a semi-infinite ogival body of revolution as shown in the sketch. The equation of the nose is ( $t \equiv b/a$ ):

$$\left(\frac{x}{a} - 1\right)^2 + \left(\frac{r}{a} + \frac{1-t^2}{2t}\right)^2 = \left(\frac{1+t^2}{2t}\right)^2 \quad 0 \leq \frac{x}{a} \leq 1$$

The inviscid-velocity distribution for this region is given in tabular values. The velocity distribution in the region very close to the nose can be approximated by

$x/a$	$u_e/u_\infty$	$x/a$	$u_e/u_\infty$
0	0	0.5	1.090
0.05	0.485	0.6	1.140
0.1	0.623	0.7	1.168
0.2	0.802	0.8	1.183
0.3	0.930	0.9	1.177
0.4	1.025	1.0	1.130



$$\frac{u_e}{u_\infty} = 1.1135 \left( \frac{s}{a} \right)^{1/3} \quad \text{for } 0 \leq s/a \leq 0.05$$

where  $s$  is the surface distance.

For  $u_\infty = 50 \text{ ms}^{-1}$ ,  $\nu = 1.5 \times 10^{-5} \text{ m}^2\text{s}^{-1}$ ,  $a = 1 \text{ m}$ , and  $b = 0.2 \text{ m}$ , calculate the displacement thickness, momentum thickness, and the local skin-friction coefficient at  $x/a = 0.75$ .

**4-25.** Using Thwaites' method, calculate the laminar boundary-layer parameters  $c_f$ ,  $\theta/L$ , and  $H$  for the following external velocity distributions for  $0 \leq x \leq 0.2$ .

$$(a) \quad u_e = u_\infty \left( 1 - \frac{x}{L} \right)$$

$$(b) \quad u_e = u_\infty \left( 1 + \frac{x}{L} \right)$$

with  $u_\infty = 10 \text{ ms}^{-1}$ ,  $L = 1 \text{ m}$ . The fluid is air at a temperature of  $T = 300 \text{ K}$  and a pressure  $p = 10^5 \text{ Nm}^{-2}$ . Plot and compare the results.

**4-26.** Consider a laminar boundary-layer subject to the external velocity distribution given by Eq. (4.2.10). Using Thwaites' method show that the boundary-layer characteristics can be expressed in the form

$$\frac{R_\theta}{\sqrt{R_x}} = c_1, \quad \frac{R_{\delta^*}}{\sqrt{R_x}} = c_2, \quad c_f \sqrt{R_x} = c_3$$

where  $c_1$ ,  $c_2$ , and  $c_3$  are constants which depend on  $m$ . Compare the results with the exact solutions of the Falkner–Skan equation.

**4-27.** Show that Thwaites' method satisfies the rules of dependency of a laminar boundary-layer as a function of Reynolds number. In other words, show that for a given external velocity distribution with  $u_\infty$  and  $L$  denoting reference quantities

$$\frac{u_e}{u_\infty} = f \left( \frac{x}{L} \right)$$

the boundary-layer characteristics obey the following rules

$$\frac{R_{\delta^*}}{\sqrt{R_L}} = F_1 \left( \frac{x}{L} \right), \quad \frac{R_\theta}{\sqrt{R_L}} = F_2 \left( \frac{x}{L} \right)$$

$$c_f \sqrt{R_L} = F_3 \left( \frac{x}{L} \right), \quad R_L = \frac{u_0 L}{\nu}$$

where  $F_1$ ,  $F_2$  and  $F_3$  are functions which depend on the external velocity distribution.

**4-28.** Consider laminar boundary-layer flow on a flat plate. If for a given external velocity  $u_e$ , the displacement thickness  $\delta^*$  at distance  $x$  from the leading

edge is 2 mm, what is the value of  $\delta^*$  at the same distance  $x$  from the leading edge if the external velocity is  $2u_e$ ?

**4-29.** Using Thwaites' method compute the boundary-layer development of a laminar flow over a circular cylinder of radius  $r_0$  placed normal to the freestream velocity  $u_\infty$ . Take the inviscid velocity distribution given by Eq. (P4.9.1). Plot  $\tau_w/\rho u_\infty^2 (u_\infty r_0/\nu)^{1/2}$  as a function of  $\xi$ . Identify the location of flow separation.

**4-30.** Calculate the drag and drag coefficient of a flat plate for laminar flow for air. Take  $T = 300$  K,  $p = 10^5$  Nm $^{-2}$ ,  $u_\infty = 10$  ms $^{-1}$ ,  $L = 3$  m, width of the plate = 1 m.

**4-31.** An integral method can also be developed for both two-dimensional and axisymmetric flows by using the integral form of the momentum and continuity equations,

$$\frac{d\theta}{dx} + \theta \left( \frac{H+2}{u_e} \frac{du_e}{dx} + \frac{1}{r_0^k} \frac{dr_0^k}{dx} \right) = \frac{c_f}{2} \quad (3.3.15)$$

$$\frac{d}{dx}(\delta - \delta^*) + (\delta - \delta^*) \left( \frac{1}{u_e} \frac{du_e}{dx} + \frac{1}{r_0^k} \frac{dr_0^k}{dx} \right) = C_E \equiv \frac{d\delta}{dx} - \frac{v_e}{u_e}$$

together with the following closure relationships deduced from the solutions of the Falkner–Skan equation

$$\frac{c_f}{2} R_\theta = F_1(H), \quad \frac{C_E R_\theta}{H^*} = F_2(H), \quad H^* \left( \equiv \frac{\delta - \delta^*}{\theta} \right) = F_3(H)$$

where the functions  $F_1(H)$ ,  $F_2(H)$  are

$H$	$F_1$	$F_2$	$H$	$F_1$	$F_2$
2.07979	0.42876	0.00687	2.74409	0.17841	0.25470
2.08950	0.42350	0.01327	2.87177	0.14828	0.27697
2.15541	0.38938	0.05327	3.09067	0.10535	0.30492
2.21623	0.36034	0.08547	4.02923	0	0.34274
2.29694	0.32494	0.12269	6.75200	-0.06561	0.27300
2.36781	0.29649	0.15110	10.05630	-0.06253	0.19135
2.59110	0.22052	0.22052	16.46750	-0.04400	0.11071
2.65639	0.20168	0.23623	35.94357	-0.01955	0.04092

- (a) Examine the solutions of the above integral method for flow near the leading edge of a flat plate. Calculate  $H$  and the development of  $\theta$ ,  $\delta^*$  and  $\tau_w$  and compare them with the Blasius solutions.

- (b) Repeat (a) for flow over the stagnation region of a two-dimensional body ( $u_e = Cx$ ) and compare the calculated boundary layer parameters with those given by the Hiemenz solutions.
- (c) Repeat (b) this time for flow near the stagnation region of an axisymmetric body ( $u_e = Cx$ ,  $r_0 = x$ ).

**4-32.** The idealized flow discussed in Problem 4.11 does not exist close to the leading edge of the plate, even though uniform suction starts at the leading edge. After a certain distance,  $x$  downstream, however, the asymptotic suction will materialize.

The distance  $x$  from the leading edge necessary to have the asymptotic-suction flow has been determined by Iglisch [12] to be

$$-\frac{v_w}{u_\infty} \left( \frac{u_\infty x}{\nu} \right)^{\frac{1}{2}} \sim 2 \quad (\text{P4.32.1})$$

- (a) With appropriate changes use BLP2 and examine the way in which the boundary-layer solutions approach the asymptotic values of

$$H = 2, \quad \frac{\tau_w}{\rho u_\infty^2} = -\frac{v_w}{u_\infty} \quad (\text{P4.32.2})$$

- (b) Compare the calculated wall-shear parameter  $f_w''$  with those given by Iglisch for the region before the asymptotic suction profile is reached at the  $x$ -stations shown in Table P4.1.

**Table P4.1.** Wall-shear parameter  $f_w''$  for a laminar flat-plate with uniform suction.

$x$	Iglisch
0	0.332
0.020	0.422
0.080	0.519
0.180	0.622
0.405	0.787
0.720	0.963
1.280	1.208

*Hint:* Since the boundary-layer equations are being solved in the transformed plane  $(x, \eta)$ , from Eq. (4.5.5a)

$$f_w(x) = -\frac{v_w}{u_\infty} \left( \frac{u_\infty x}{v} \right)^{\frac{1}{2}} \quad (\text{P4.32.3})$$

From Eqs. (P4.32.1) and (P4.32.3), we see that when  $f_w = 2$ , we have the asymptotic suction profile according to Igglisch's expression (P4.32.1).

Figure P4.3 shows the computed values of  $H$  for a flat plate with uniform suction and Table P4.2 shows the computed  $f''_w$  values at the desired  $x$ -stations.

**Table P4.2.** Computed  $f''_w$  values for a laminar flat plate with uniform suction.

$x$	$f''_w$
0	0.332
0.020	0.419
0.080	0.523
0.180	0.626
0.405	0.790
0.720	0.963
1.280	1.208

**4-33.** Repeat Problem 4.29 with BLP2. Take  $h = 0.2$  with 2, 4, 6, 8 degree intervals in  $\xi$ . Plot  $\tau_w/\rho u_\infty^2 (u_\infty r_0/\nu)^{1/2}$  as a function of  $\xi$ .

**4-34.** As discussed in subsection 4.2.3, for positive values of  $m$ , the Falkner–Skan equation has unique solutions but more than one solution exists for each negative value of  $m$  in the range  $-0.0904 < m < 0$ . These “lower-branch” solutions all have the property that  $f''(0) \leq 0$  so that the wall shear  $\tau_w \leq 0$  is less than zero and correspond to flows in a two-dimensional laminar boundary layer beyond separation. Table P4.3 shows solutions obtained by Cebeci and Keller [13] for various values of  $m$ .

The range of negative wall shear parameter  $f''(0)$  is shown in Fig. P4.4 with a typical velocity profile corresponding to  $m = -0.0707$  in Fig. P4.5 together with the Blasius velocity profile,  $m = 0$ .

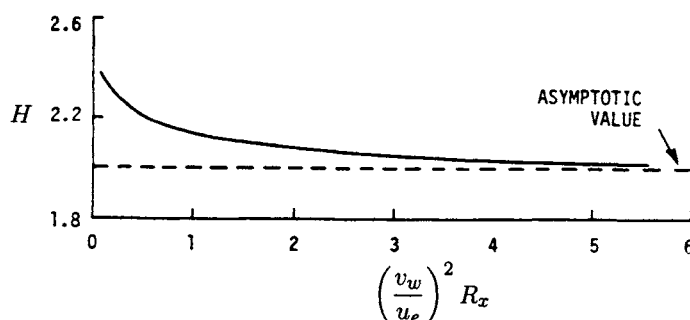


**Fig. P4.3.** Computed values of  $H$  for a flat-plate flow with uniform suction.

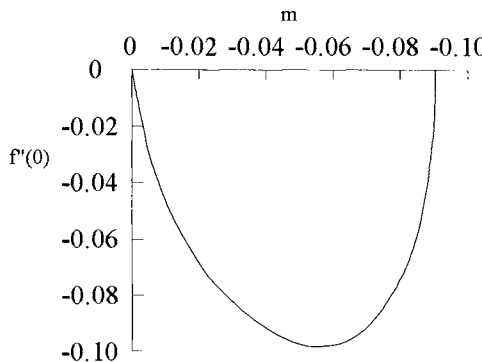


**Fig. P4.4.** Variation of the wall shear parameter  $f''(0)$  with the pressure gradient parameter  $m$ .

Use the shooting method given in the accompanying CD-ROM, Program 1, to verify the lower-branch solutions of Table P4.3 for a value of  $m = -0.07068$  by solving the Falkner–Skan equation subject to the boundary conditions

$$\eta = 0, \quad f = f' = 0, \quad f''(0) = -0.08998; \quad \eta = \eta_e, \quad f' = 1 \quad (\text{P4.34.1})$$

*Suggestion:* Formulate the solution procedure as a nonlinear eigenvalue problem with the nondimensional pressure gradient  $m$  as the unknown parameter. The value of  $f''(0)$  or  $v(0)$  is specified and the appropriate value of  $m$  which satisfies Eq. (1.4), that is,

$$u(\eta_e, m) - 1 \equiv \phi(m) = 0 \quad (\text{P4.34.2})$$

is obtained as an eigenvalue. The successive values of  $m^{\nu+1}$  is computed by using Newton's method,

$$m^{\nu+1} = m^\nu - \frac{\phi(m^\nu)}{d\phi(m^\nu)/dm} = m^\nu - \frac{\partial u(\eta_e, m^\nu)}{\partial m}, \quad \nu = 0, 1, 2, \dots \quad (\text{P4.34.3})$$

$\partial u(\eta_e, m^\nu)/\partial m$  is computed from the variational equations of Eqs. (1.1) and (1.2) obtained by differentiating them with respect to  $m$ . As in the equations

**Table P4.3.** Lower-Branch Solutions of the Falkner–Skan Equation

$m$	$f''(0)$	$\delta_1^*$	$\theta_1$	$H$
-0.09043	0	3.49781	0.86811	4.029
-0.08940	-0.02699	3.83387	0.86293	4.443
-0.08271	-0.06569	4.54159	0.82449	6.508
-0.07068	-0.08998	6.42049	0.74410	7.728
-0.03828	-0.09153	7.92042	0.47814	16.565
-0.02427	-0.07544	9.59482	0.33956	28.257
-0.01975	-0.06791	10.3584	0.29044	36.664
-0.01224	-0.05201	12.1950	0.20202	60.365
-0.00791	-0.04000	14.0049	0.14510	96.519
-0.00456	-0.02822	16.5592	0.09591	172.653

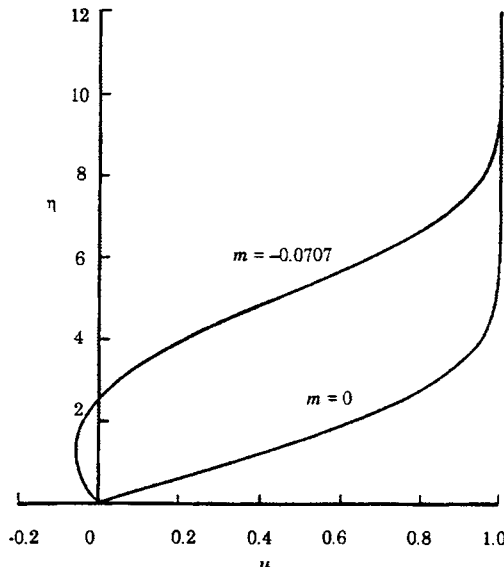


**Fig. P4.5.** Comparison of the reverse velocity profile for  $m = -0.0707$  with the Blasius profile.

leading to Eqs. (4A.6) and (4A.7), the first two equations and boundary conditions are identical to Eqs. (4A.6a,b) and (4A.7) but Eq. (4A.6c) is different,

$$V' = -\frac{1}{2}fv - \frac{m+1}{2}(fV + vF) + u^2 - 1 + 2muU \quad (\text{P4.34.4})$$

where now  $F, U, V$  are

$$F = \frac{\partial f}{\partial m}, \quad U = \frac{\partial u}{\partial m}, \quad V = \frac{\partial v}{\partial m} \quad (\text{P4.34.5})$$

**4-35.** The transformed boundary-layer equation (4.5.4) is a partial differential equation, which with some approximations, can be reduced to a system of ordinary differential equations. If we let

$$g = \frac{\partial f}{\partial x} \quad \text{and} \quad g' = \frac{\partial f'}{\partial x}$$

and consider a laminar flow with no mass transfer, then Eqs. (4.5.4) and (4.5.5) can be written as

$$f''' + \frac{m+1}{2}ff'' + m[1 - (f')^2] = x(f'g' - f''g) \quad (\text{P4.35.1})$$

$$\eta = 0, \quad f = f' = 0, \quad \eta = \eta_e, \quad f' = 1 \quad (\text{P4.35.2})$$

Show that if we differentiate (P4.35.1) and (P4.35.2) with respect to  $x$ , and neglect the terms  $\partial/\partial x(f'g' - f''g)$ , then Eqs. (P4.35.1) and (P4.35.2) can be written as

$$g''' + n \left[ \frac{1}{2} f'' + 1 - (f')^2 \right] + \frac{m+1}{2} (fg'' + gf'') - (2m+1)f'g' + f''g = 0 \quad (\text{P4.35.3})$$

$$\eta = 0, \quad g = g' = 0, \quad \eta = \eta_e, \quad g' = 0 \quad (\text{P4.35.4})$$

Here

$$n = \frac{dm}{dx} \quad (\text{P4.35.5})$$

The system of equations (P4.35.1)–(P4.35.5), sometimes referred to as the *local nonsimilarity equations*, was first proposed by Sparrow et al. [9]. Although their solutions are not as accurate as Eq. (4.5.4), they are quite useful, since they avoid the solution of a partial differential equation and, for flows away from separation, give satisfactory results.

**4-36.** Using the shooting method discussed in the accompanying CD-ROM, Program 1, obtain the solutions of the system of equations given in Problem 4.35 for an external-velocity distribution

$$u_e = u_{\text{ref}}[1 - \frac{1}{8}x]$$

in the region  $0 \leq x \leq 0.3$ . Compare your solutions with those obtained with BLP2D.

**4-37.** Using the Mangler transformation given by Eqs. (P3.12.1) and (P3.12.2) and the Falkner–Skan transformation given by

$$\eta = \left( \frac{u_e}{\nu \bar{x}} \right)^{\frac{1}{2}} \bar{y} \quad (\text{P4.37.1})$$

$$\bar{\psi}(\bar{x}, \bar{y}) = (u_e \nu \bar{x})^{\frac{1}{2}} f(\bar{x}, \eta) \quad (\text{P4.37.2})$$

show that the boundary-layer equations for an axisymmetric flow and their boundary conditions can be written as

$$(bf'')' + \frac{m+1}{2} ff'' + m[1 - (f')^2] = \bar{x} \left( f' \frac{\partial f'}{\partial \bar{x}} - f'' \frac{\partial f}{\partial \bar{x}} \right) \quad (\text{P4.37.3})$$

$$\eta = 0, \quad f' = 0, \quad f(\bar{x}, 0) \equiv f_w = -\frac{1}{(u_e \nu \bar{x})} \int_0^{\bar{x}} \bar{v}_w d\bar{x} \quad (\text{P4.37.4a})$$

$$\eta = \eta_e, \quad f' = 1 \quad (\text{P4.37.4b})$$

where

$$b = (1+t)^{2k}, \quad m = \frac{\bar{x}}{u_e} \frac{du_e}{d\bar{x}}, \quad (\text{P4.37.5a})$$

$$t = -1 + \left[ 1 + \left( \frac{L}{r_0} \right)^2 \frac{2 \cos \phi}{L} \left( \frac{\nu \bar{x}}{u_e} \right)^{\frac{1}{2}} \eta \right]^{\frac{1}{2}} \quad (\text{P4.37.5b})$$

*Hint:* Start with Eqs. (P3.12.4) to (P3.12.6).

**4-38.** Using BLP2, obtain solutions of the following equations

$$f''' + 2ff'' - (f')^2 + (g')^2 = 0 \quad (\text{P4.38.1})$$

$$g''' + 2fg'' - 2f'g' = 0 \quad (\text{P4.38.2})$$

subject to the boundary conditions

$$f(0) = f'(0) = g(0) = 0, \quad g'(0) = 1, \quad f'(\eta_e) = 0, \quad g'(\eta_e) = 0 \quad (\text{P4.38.3})$$

Take  $\eta_e = 8$ ,  $h_1 = 0.2$ , and  $K = 1.0$ .

It would be ideal to solve this system by expressing it as a system of six first-order equations and then solving it by an algorithm similar to SOLV3. However, that procedure will require a new algorithm; at the expense of a less efficient code it is best and sufficient to solve the required system by making use of our already existing SOLV3 algorithm and solve Eqs. (P4.38.1) and (P4.38.2) separately rather than together.

*Hint:* (a) Write Eq. (P4.38.1) in terms of new variables  $u(\equiv f')$ ,  $v(\equiv u')$ , and  $w(\equiv g')$  and Eq. (P4.38.2) in terms of  $t(\equiv w')$ .

(b) Show that  $(s_1)_j$  to  $(s_6)_j$  and  $(r_2)_j$  coefficients of Eq. (P4.38.1) are

$$\begin{aligned} (s_1)_j &= \frac{1}{h_j} + f_j, & (s_2)_j &= -\frac{1}{h_j} + f_{j-1}, & (s_3)_j &= v_j \\ (s_4)_j &= v_{j-1}, & (s_5)_j &= -u_j, & (s_6)_j &= -u_{j-1}, \end{aligned} \quad (\text{P4.38.4})$$

$$(r_2)_j = -(w^2)_{j-\frac{1}{2}} - [h_j^{-1}(v_j - v_{j-1}) + 2(fv)_{j-\frac{1}{2}} - (u^2)_{j-\frac{1}{2}}] \quad (\text{P4.38.5})$$

(c) Since the linearized boundary conditions for Eq. (P4.38.1) are the same as those given by Eq. (4.5.22) no changes are required in SOLV3.

(d) Show that  $(r_1)_j$  to  $(r_3)_j$  and  $(s_1)_j$  to  $(s_6)_j$  coefficients of Eq. (P4.38.2) can be written in the form

$$(r_1)_j = g_{j-1} - g_j + h_j w_{j-\frac{1}{2}} \quad (\text{P4.38.6a})$$

$$(r_2)_j = -[h_j^{-1}(t_j - t_{j-1}) + 2f_{j-\frac{1}{2}}t_{j-\frac{1}{2}} - 2u_{j-\frac{1}{2}}w_{j-\frac{1}{2}}] \quad (\text{P4.38.6b})$$

$$(r_3)_j = w_{j-1} - w_j + h_j t_{j-\frac{1}{2}} \quad (\text{P4.38.6c})$$

$$\begin{aligned} (s_1)_j &= \frac{1}{h_j} + f_{j-\frac{1}{2}}, & (s_2)_j &= -\frac{1}{h_j} + f_{j-\frac{1}{2}} \\ (s_3)_j &= (s_4)_j = 0, & (s_5)_j &= (s_6)_j = -u_{j-\frac{1}{2}} \end{aligned} \quad (\text{P4.38.7})$$

with Eq. (4.5.19c) now expressed as

$$(s_1)_j \delta t_j + (s_2)_j \delta t_{j-1} + (s_3)_j \delta g_j + (s_4)_j \delta g_{j-1} + (s_5)_j \delta w_j + (s_6)_j \delta w_{j-1} = (r_2)_j \quad (\text{P4.38.8})$$

(e) The initial profiles for the system of Eqs. (P4.38.1) and (P4.38.2) can be satisfied by assuming  $u(\eta)$  and  $w(\eta)$  to be

$$u = \frac{\eta}{\eta_e} \left( 1 - \frac{\eta}{\eta_e} \right), \quad w = 1 - \frac{\eta}{\eta_e} \quad (\text{P4.38.9})$$

(f) For this problem, it is necessary to alter five subroutines in BLP2. In subroutine IVPL, use the new initial velocity profiles [Eq. (P4.38.9)] that satisfy the boundary conditions given by Eqs. (P4.38.3). Subroutine COEF3 contains the coefficients of the two momentum equations and their boundary conditions. Programming changes are made to MAIN, SOLV3 and OUTPUT.

**4-39.** Using BLP2, obtain the solutions of equation

$$f''' - 18\eta^2 f'' - 36(\eta f' - f) = -1.8330 \quad (\text{P4.39.1})$$

subject to the boundary conditions

$$f(0) = f'(0) = 0, \quad f''(\eta_e) = 1.0 \quad (\text{P4.39.2})$$

Take  $\eta_e = 8$ ,  $h_1 = 0.2$  and  $K = 1.0$ .

*Hint:* To solve this system, use a new MAIN, COEF3, and SOLV3. Since Eq. (P4.39.1) is a linear equation, the IVPL subroutine is not needed.

(a) Write Eq. (P4.39.1) in terms of new variables  $u(\equiv f')$  and  $v(\equiv u')$ .

(b) Show that  $(s_1)_j$  to  $(s_6)_j$  and  $(r_2)_j$  coefficients of Eq. (P4.39.1) are

$$\begin{aligned} (s_1)_j &= \frac{1}{h_j} - 9\eta_{j-\frac{1}{2}}^2, & (s_2)_j &= -\frac{1}{h_j} - 9\eta_{j-\frac{1}{2}}^2, \\ (s_3)_j &= (s_4)_j = 18, & (s_5)_j &= (s_6)_j = -18\eta_{j-\frac{1}{2}}, \\ (r_2)_j &= -1.833 \end{aligned} \quad (\text{P4.39.3})$$

(c) To account for the different edge boundary conditions, it is necessary to modify SOLV3. This can be done by making changes in the last row of the  $A_J$  matrix [see Eq. (4.5.26b)]. The new  $A_J$  is

$$A_J = \begin{pmatrix} 1 & -h_J/2 & 0 \\ (s_3)_J & (s_5)_J & (s_1)_J \\ 0 & 0 & 1 \end{pmatrix} \quad (\text{P4.39.4})$$

From Eq. (4.5.27c), for  $j = J$ , we write  $\Delta_J$  as

$$\Delta_J = \begin{pmatrix} (\alpha_{11})_J & (\alpha_{12})_J & (\alpha_{13})_J \\ (\alpha_{21})_J & (\alpha_{22})_J & (\alpha_{23})_J \\ 0 & 0 & 1 \end{pmatrix} \quad (\text{P4.39.5})$$

Here the first two rows of  $\Delta_J$  are the same as before. From Eq. (4.5.29a), remembering the definition of  $\vec{\delta}_J$ ,

$$\begin{pmatrix} (\alpha_{11})_J & (\alpha_{12})_J & (\alpha_{13})_J \\ (\alpha_{21})_J & (\alpha_{22})_J & (\alpha_{23})_J \\ 0 & 0 & 1 \end{pmatrix} \begin{pmatrix} f_J \\ u_J \\ v_J \end{pmatrix} = \begin{pmatrix} (w_1)_J \\ (w_2)_J \\ (w_3)_J \end{pmatrix} \quad (\text{P4.39.6})$$

Here  $(w_1)_J$  and  $(w_2)_J$  are the same as before, but  $(w_3)_J = (r_3)_J$  with  $(r_3)_J = 1$ . Solving Eq. (P4.39.6), we get

$$\begin{aligned} v_J &= (w_3)_J \\ u_J &= \frac{e_2(\alpha_{11})_J - e_1(\alpha_{21})_J}{(\alpha_{11})_J(\alpha_{22})_J - (\alpha_{12})_J(\alpha_{21})_J} \\ g_J &= \frac{e_1 - (\alpha_{12})_J u_J}{(\alpha_{11})_J} \\ e_1 &= (w_1)_J - (\alpha_{13})_J v_J \\ e_2 &= (w_2)_J - (\alpha_{23})_J v_J \end{aligned}$$

(d) In summary, we redefine the coefficients  $(s_k)_j$ ,  $(r_2)_j$  and  $(r_3)_j$  in subroutine COEF3 and replace the formulas for the components of  $\vec{\delta}_J$  with the new ones to account for the new boundary conditions at  $\eta = \eta_e$  in subroutine SOLV3. Since we are solving a linear equation, no iteration is required; the solutions in SOLV3 obtained as DELF(J), DELU(J), and DELV(J) are F(J,2), U(J,2), and V(J,2).

**4-40.** The inviscid-velocity distribution of flow past a sphere of radius  $L$  is given by

$$u_e = \frac{3}{2} u_\infty \sin \xi \quad (\text{P4.40.1})$$

where  $\xi = x/L$ . The local cross-sectional radius of the body,  $r_0$ , is

$$r_0 = L \sin \xi \quad (\text{P4.40.2})$$

(a) Show that for this axisymmetric flow, the  $\bar{x}$ -coordinate and the  $m$ -distribution can be obtained from Eqs. (P3.12.1) and (P4.37.5a).

$$\bar{x} = L \left( \frac{\xi}{2} - \frac{1}{4} \sin 2\xi \right), \quad m = \frac{[\xi/2 - (\frac{1}{4}) \sin 2\xi] \cos \xi}{\sin^3 \xi} \quad (\text{P4.40.3})$$

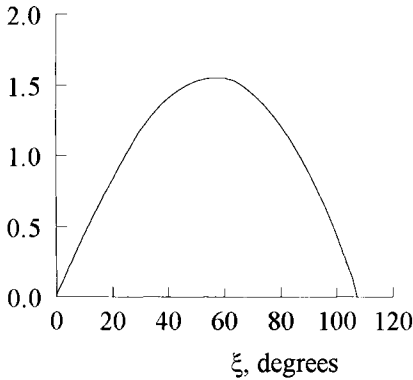


**Fig. P4.6.** Dimensionless wall shear distribution for a laminar flow past a sphere.

- (b) At  $\bar{x} = 0$  the flow starts as a stagnation-point flow for which the value of  $m$  is given by Eq. (P4.40.3b). Show that  $m = 1/3$  at the stagnation point.
- (c) Modify BLP2 for this flow and compare your results with those given in Fig. P4.6. Show that flow separation occurs at  $107.5^\circ$ .

**4-41.** When the radius of a body is of the same order of magnitude as the thickness of the boundary-layer, the transverse-curvature effect, which is of second order, becomes quite important and strongly affects the skin friction and heat transfer. A typical example is axial flow past long circular cylinders.

The transverse-curvature effect on slender circular cylinders has been studied by a number of people. According to Seban and Bond [15] and Kelly [16] the local skin-friction coefficient on slender circular cylinders for large  $R$  values are given by

$$c_f R_x^{1/2} = 0.664 \left( 1 + \frac{1.050}{R^{1/2}} - \frac{0.480}{R} \right) \quad (\text{P4.41.1})$$

where  $R$  is a transverse-curvature parameter,

$$R = \frac{R_x}{4} \left( \frac{r_0}{x} \right)^2 \quad (\text{P4.41.2})$$

The same problem was also studied by Stewartson [17] analytically for values of  $R$  approaching 0. His expression is given by

$$c_f R_x^{1/2} = \frac{2}{R^{1/2}} \left\{ \frac{1}{\ln(1/cR)} - \frac{3.854}{[\ln(1/cR)]^3} + \dots \right\} \quad (\text{P4.41.3})$$

where  $\ln(1/cR) = -\ln R - 0.577$  ( $c$  is Euler's constant).

Numerical solutions of this problem were also obtained by using the numerical method described in Sec. 4.5 [18]. The calculations were performed for  $R$  from zero to infinity. The numerical calculations for this flow differ from the usual laminar boundary-layer calculations in the sense that although for most laminar flows the transformed boundary-layer thickness is almost constant (i.e.,

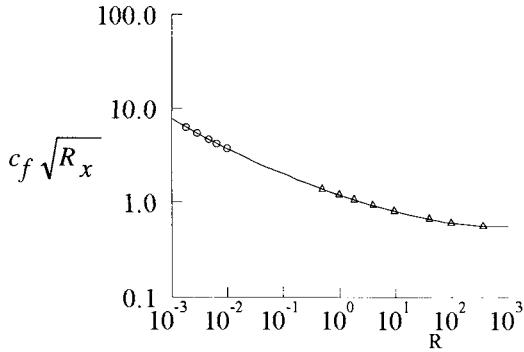


**Fig. P4.7.** Local skin friction coefficient for laminar flows over slender circular cylinders. Circles indicate data from Eq. (P4.41.3). Triangles indicate data from Eq. (P4.41.1). Solid line denotes numerical solutions of [18].

$\eta_e \cong 8$ ), for this flow  $\eta_e$  is a function of  $R$ . For example,  $R \cong 10^{-3}$ ,  $\eta_e \cong 100$ . Furthermore, the wall-shear parameter  $f_w''$  becomes large with decreasing  $R$ . In such cases the laminar-velocity profiles look somewhat like turbulent-velocity profiles. In order to maintain computational accuracy it is necessary to take very small  $\Delta\eta$ -spacing close to the wall. For that reason, the calculations in [18] were made with the variable grid described in Program 3.

- (a) Modify BLP2 for this flow and using a variable grid, obtain solutions for values of  $R$  ranging from 0.001 to 500, compare them with those given by Eqs. (P4.41.1) and (P4.41.3), see Fig. P4.7.
- (b) What is the range of values of  $R$  for which Eqs. (P4.41.1) and (P4.41.3) are valid for?

**4-42.** Solve Problem 4.33 by replacing SOLV3 with the matrix solver in the CD-ROM (Appendix B), Program 5. Take  $h = 0.2$  and compare your solutions with those obtained with the SOLV3 algorithm.

(1) Read in

```
DIMENSION DUMM(3),BB(2,3),YY(3,81),NROW(3,81),GAMJ(2,3,81).
      AA(3,3,81),CC(2,3,81)
DATA IROW,ICOL,ISROW,INP/3,3,3,81
```

Here IROW, ICOL correspond to number of maximum rows and columns respectively. ISROW denotes the number of “wall” boundary conditions and INP the total number of  $j$ -points in the  $\eta$ -direction, and

$$\text{BB} = B_j, \quad \text{YY} = \vec{w}_j, \quad \text{GAMJ} = \Gamma_j, \quad \text{AA} = A_j, \quad \text{CC} = C_j$$

The first and second numbers in the arguments of AA, BB, CC and GAMJ correspond to the number of nonzero rows and columns in  $A_j$  (or  $\Delta_j$ ),  $B_j$ ,  $C_j$  and  $\Gamma_j$  matrices, respectively (see subsection 4.5.2, for example). Note that  $B_j$  and  $\Gamma_j$  have the same structure and the last row of  $B_j$  and the first two rows

of  $C_j$  are all zero. The number 81 in YY, NROW, GAMJ, AA and CC refer to INP.

- (2) Set the elements of all matrices  $A_j$ ,  $B_j$ ,  $C_j$  (and  $\Delta_j$ ) equal to zero.
- (3) Define the matrices  $A_0$  and  $C_0$  by reading in their elements. Note only those nonzero elements in the matrices are read in since in (2) we set all the elements equal to zero.
- (4) Call subroutine GAUSS.
- (5) Read in the elements of  $B_j$  and call subroutine GAMSV to compute  $\Gamma_1$ .
- (6) Define  $A_j$  according to Eq. (4.5.26a), call GAUSS and read in the elements of  $C_j$ .
- (7) Recall the elements of  $B_j$  and call GAMSV to compute  $\Gamma_2$ .
- (8) Repeat (6) and (7) for  $j < J$ .
- (9) At  $j = J$ , read in the last row of  $A_J$  which is also equal to the last row of  $\Delta_J$ .
- (10) Compute  $\vec{w}_0$  according to Eq. (4.5.28a). Here  $\vec{r}_0 = \text{RRR}(1,81)$ .
- (11) Define the right-hand side of Eq. (4.5.28b) and compute  $\vec{w}_j$  according to Eq. (4.5.28b).
- (12) In the backward sweep, with  $\delta_j$  corresponding to UM(I,J), compute  $\vec{\delta}_J$  according to Eq. (4.5.29a) by calling USOLV at INP.
- (13) Define the right-hand side of Eq. (4.5.29b) and solve for  $\delta_j$  by calling USOLV for  $j = J - 1, J - 2, \dots, 0$ .

**4-43.** Equations (3.1.10) and (3.1.11) are based on the assumption that the pressure is constant across the shear layer and stress gradients parallel to the surface are negligible in comparison with those normal to the surface. This assumption, which corresponds to first-order boundary-layer theory has its validity decreased with increasing longitudinal curvature so that, when the curvature effect becomes important, it is necessary to use higher-order boundary-layer theory. Unfortunately, the main body of mathematical work on higher-order boundary-layer theory has been done in laminar flows because the relation between the velocity field and the turbulent stresses remain largely unknown. For a discussion of “second-order” boundary-layer equations for two-dimensional laminar flows, the reader is referred to [19, 20], for three-dimensional laminar flows to Patel [21], and for the basis of the so-called fairly thin-shear-layer approximation in turbulent flow to Bradshaw [22].

The second-order boundary-layer equations for two dimensional laminar flows with longitudinal curvature are:

$$\frac{\partial u}{\partial x} + \frac{\partial}{\partial y}(vh_1) = 0 \quad (\text{P4.43.1})$$

$$\frac{u}{h_1} \frac{\partial u}{\partial x} + v \frac{\partial u}{\partial y} + \frac{\kappa}{h_1} uv = -\frac{1}{h_1 \rho} \frac{\partial p}{\partial x} + \nu \left[ \frac{\partial^2 u}{\partial y^2} + \frac{\kappa}{h_1} \frac{\partial u}{\partial y} - \frac{\kappa^2 u}{h_1^2} \right] \quad (\text{P4.43.2})$$

$$\frac{\kappa u^2}{h_1} = \frac{1}{\rho} \frac{\partial p}{\partial y} \quad (\text{P4.43.3})$$

where the metric coefficient  $h_1$  is given by

$$h_1 = 1 + \kappa y \quad (\text{P4.43.4})$$

with  $\kappa$  denoting the body curvature. With longitudinal curvature the external velocity on the body predicted by inviscid flow theory varies normal to the surface. If we let  $u_e(x)$  denote the edge velocity, which according to first-order boundary layer is  $u_w(x)$ , then the boundary conditions for the velocity field become

$$y = 0, \quad u = 0, \quad v = v_w(x) \quad (\text{P4.43.5a})$$

$$y \rightarrow \infty, \quad u \rightarrow u_e(x, y) \quad (\text{P4.43.5b})$$

We assume the variation of the inviscid velocity  $u_e(x, y)$  away from the wall where its value is  $u_w$ , is of the form

$$u_e(x, y) = \frac{u_w(x)}{h_1} \quad (\text{P4.43.6})$$

The wall curvature  $\kappa$  is calculated from

$$\kappa = -\frac{d\theta}{ds} \quad (\text{P4.43.7a})$$

Here  $s$  denotes the arc length along the surface and  $\theta$  is obtained from the slope of the surface in the plane normal to the leading edge,

$$\theta = \tan^{-1} \frac{d\bar{y}}{d\bar{x}} \quad (\text{P4.43.7b})$$

Here bars denote the Cartesian coordinate that defines the surface. As in the solution of the first-order boundary-layer equations, again for convenience, it is useful to express Eqs. (P4.43.1) to (P4.43.3) in terms of Falkner–Skan variables

$$\eta = \sqrt{\frac{u_w}{\nu x}} y, \quad \psi = \sqrt{u_w x \nu} f(x, \eta) \quad (\text{P4.43.8a})$$

with stream function now defined by

$$u = \frac{\partial \psi}{\partial y}, \quad h_1 v = -\frac{\partial \psi}{\partial x} \quad (\text{P4.43.8b})$$

(a) In terms of transformed variables, show that Eqs. (P4.43.1) to (P4.43.3), with primes denoting differentiation with respect to  $\eta$ , can be written as

$$\begin{aligned} & (1 + B\eta)f''' + \left(\frac{1+m}{2}\right)ff'' + \frac{(1+m)}{2}\frac{B}{1+B\eta}ff' \\ & - \frac{B^2}{1+B\eta}f' + Bf'' - m(f')^2 \\ & = \frac{x}{u_w^2} \frac{\partial p^*}{\partial x} + x \left[ f' \frac{\partial f'}{\partial x} - \frac{\partial f}{\partial x} \left( f'' + \frac{Bf'}{1+B\eta} \right) \right] \end{aligned} \quad (\text{P4.43.9})$$

$$\frac{B}{1+B\eta}(f')^2 = \frac{1}{u_w^2} \frac{\partial p^*}{\partial \eta} = \frac{1}{u_w^2}(p^*)' \quad (\text{P4.43.10})$$

Here with  $L$  denoting a reference length

$$\begin{aligned} p^* &= \frac{p}{\rho}, \quad R_x = \frac{u_w x}{\nu} = \left(\frac{u_w}{u_\infty}\right) \left(\frac{x}{L}\right) R_\infty \\ R_\infty &= \frac{u_\infty L}{\nu}, \quad f' = \frac{u}{u_w}, \\ B &= \left[ \frac{(x/L)}{(u_w/u_\infty)R_\infty} \right]^{1/2} Lk \end{aligned} \quad (\text{P4.43.11})$$

(b) In terms of transformed variables, show that the wall and edge boundary conditions become

$$\eta = 0, \quad f = f' = 0 \quad (\text{P4.43.12a})$$

$$\eta = \eta_e, \quad f' = \frac{1}{h_1} \quad (\text{P4.43.12b})$$

For convenience, the edge boundary condition in Eq. (P4.43.12b) is usually written as

$$f'' + B(f')^2 = 0 \quad (\text{P4.43.12c})$$

by differentiating Eq. (P4.43.12b) with respect to  $\eta$ . Computationally this form is more appropriate.

(c) At the stagnation point where  $u = 0$ , Eq. (P4.43.9) is singular; as in the first-order boundary-layer equations, the singularity can be removed by differentiating Eq. (P4.43.9) once with respect to  $x$  and Eq. (P4.43.10) twice with respect to  $x$ . With  $\eta$  and  $\psi$  now defined by

$$\eta = \sqrt{A/\nu} y, \quad \psi = \sqrt{\nu A} f(\eta) \quad (\text{P4.43.13})$$

and  $A$  and  $f'$  by

$$A = \left( \frac{du_w}{dx} \right)_{x=0}, \quad f' = \left( \frac{\partial u}{\partial x} \right) \frac{1}{A} = \frac{u_x}{A} \quad (\text{P4.43.14})$$

show that Eqs. (P4.43.9), (P4.43.10) and their boundary conditions become

$$(1 + B_0 \eta) f''' + f f'' + \frac{B_0}{1 + B_0 \eta} f f'' - \frac{B_0^2}{1 + B_0 \eta} f' + B_0 f'' - (f')^2 = p_{xx}^* \quad (\text{P4.43.15})$$

$$\frac{B_0}{1 + B_0 \eta} (f')^2 = \frac{1}{2} (p_{xx}^*) \quad (\text{P4.43.16})$$

$$\eta = 0, \quad f = f' = 0; \quad \eta = \eta_e, \quad f'' + B_0 (f')^2 = 0 \quad (\text{P4.43.17})$$

Here

$$p_{xx}^* = \frac{1}{A^2} \frac{\partial^2 p^*}{\partial x^2}, \quad B_0 = \sqrt{\nu/A} k \quad (\text{P4.43.18})$$

# 5 Transition in Two-Dimensional Incompressible Flows

## 5.1 Introduction

At sufficiently high Reynolds numbers, most flows are turbulent rather than laminar, and this transition to turbulence has been the object of many studies utilizing several approaches. One approach discussed, for example, in [1], considers the solutions of the parabolized stability equations (PSE), and another considers the solutions of the unsteady Navier-Stokes equations (called direct numerical simulation, DNS) and another approach considers the solutions of the linear stability equations based on small-disturbance theory. Despite the progress being made with the PSE approach, this method currently is some time away from being used as an engineering tool; it is still under development. The direct numerical simulation (DNS) approach offers exciting possibilities; the excellent review of Kleiser and Zong [2] describes the rapid progress with this approach and shows that the prediction of transition can already be achieved in some simple flows with this method. The computer requirements of DNS, however, are large, and it is unlikely that this approach can be used for transition calculations on complex bodies in the near future. The only engineering calculation method for predicting transition at this time, aside from correlation methods, is the  $e^n$ -method based on small disturbance theory to be discussed in this chapter for two-dimensional flows and in Chapter 8 for three-dimensional flows.

Section 5.2 describes the transition process associated with the growth of disturbances within the boundary-layer. Section 5.3 discusses the linear stability equations based on small-disturbance theory and the properties of the stability equations. Predicting transition by empirical correlations and  $e^n$ -method is addressed in Section 5.4 and the factors that influence transition in Section 5.5. The numerical solution of the stability equation and the eigenvalue procedure associated with the stability equation are described in Section 5.6. A brief description of a computer program for solving the stability equation and calculating the onset of transition is given in Section 5.7.

## 5.2 Transition Process

If the intensity of freestream turbulence (see Eq. 5.5.3) is low, a first step in the transition process is the development of instabilities commonly referred to as Tollmien-Schlichting (TS) waves. Earliest studies on the development of the transition process from the appearance of TS waves to turbulence were conducted by Emmons [3], Schubauer and Skramstad [4], Schubauer and Klebanoff [5]. From observations of the flow on a water table, Emmons formulated the view that turbulence starts in the form of randomly distributed spots of turbulence, each of which expands as it moves downstream. Fully developed turbulent flow begins when these expanding regions of turbulence merge across the whole span. The transition region can therefore be said to start at the streamwise position where the spots first appear and to end where they have merged to form a continuous front.

Figure 5.1 shows the oscillograms of hot-wire response showing fluctuations at various distances behind the leading edge of a flat plate. They were obtained by Schubauer and Skramstad [4] in a low turbulence wind tunnel at the National Bureau of Standards. The oscillations represent fluctuations in the boundary-layer velocity measured at 0.6 mm from the surface. As can be seen, the disturbances grow as the distance from the leading edge increases. At  $x = 1.83$  m, however, some irregularities occur in the TS waves. These are “bursts” of high frequency fluctuations ordinarily associated with turbulent flow. The bursts be-

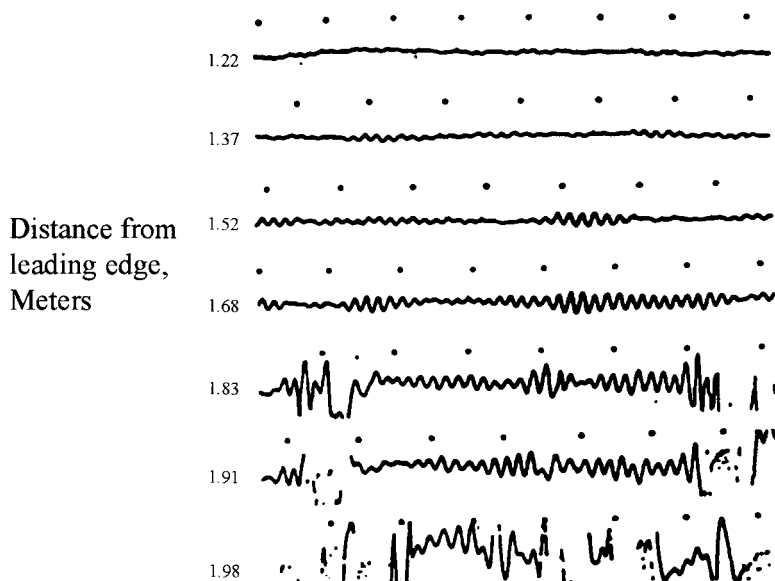


**Fig. 5.1.** Oscillograms of hot-wire response showing fluctuations in the laminar boundary layer on a flat plate [4]. Distance from surface 0.6 mm,  $u_e = 24.4 \text{ ms}^{-1}$ , time interval between dots 0.033 s.

come more frequent and of longer duration with distance; at  $x = 2.44$  m from the leading edge, the entire flow becomes turbulent.

The details of the geometry of the spots and their growth with movement downstream were measured by Schubauer and Klebanoff [5]. A spot was introduced into a laminar boundary layer on a flat plate in a wind tunnel by means of an electrical spark, and the details of its growth were measured as it was carried downstream by the flow. Figure 5.2 shows the spot's development into a roughly triangular region of turbulence. As can be seen, the forward apex moves downstream at close to the mainstream velocity, but its rear records within the growing "triangular" region are much the same as those of fully developed turbulent flow, upstream of this region at any instant the flow is smooth and laminar. Consistent with this, Schubauer and Klebanoff found that the instantaneous velocity profiles in the transition region had the time characteristics of turbulent flow for part of the time, and at other times those of a laminar boundary layer. For a more detailed discussion of the formation of spots and how they arise, the reader is referred to Refs. 5 and 6.

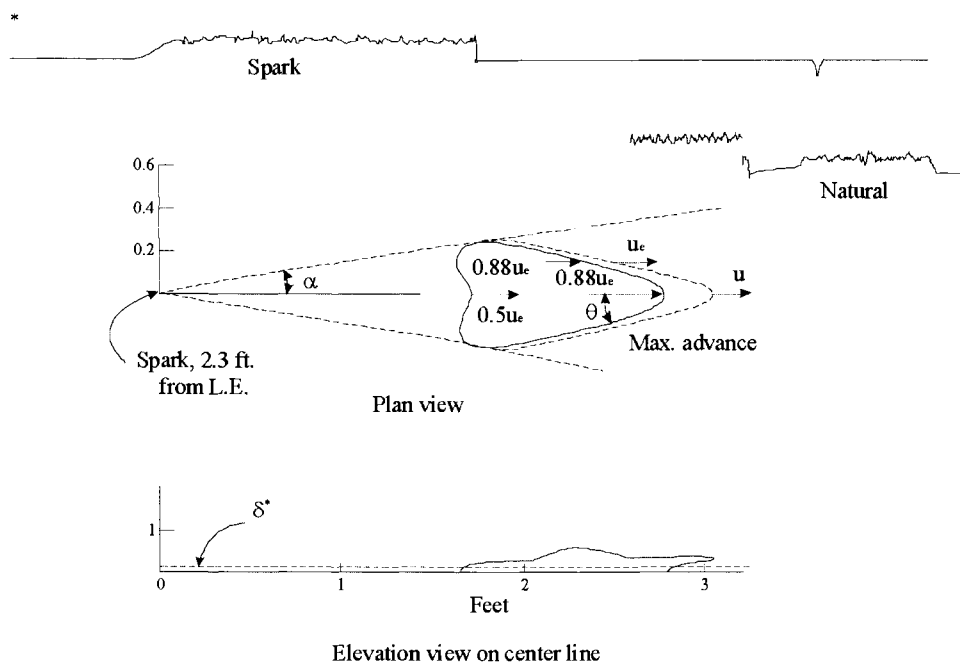


**Fig. 5.2.** Turbulent spot initiated by electric spark between needle electrode and surface. Oscillograms with 1/60 s timing dots shown above, edge is convected downstream at about half that speed 33 ft/s. The spot expands outwards so that its tips define the sides of a wedge of semi-angle  $\alpha \cong 11^\circ$  and apex at the spot origin. Hot-wire time progression from left to right upper showing spark discharge on right and spot passage on left, lower showing natural transition [5].

The fraction of the total time that the flow is turbulent can be quantified at any point in the transition region. This fraction may be defined as the intermittency factor,  $\gamma_{\text{tr}}$  with  $\gamma_{\text{tr}} = 0$  corresponding to the onset of transition, and  $\gamma_{\text{tr}} = 1$  to the stage when the flow is fully turbulent. For a flat plate, it is found that  $\gamma_{\text{tr}}$  can be described as a function of  $\xi$  where, with  $x_{\text{tr}}$  denoting the onset of transition,

$$\xi = \frac{(x - x_{\text{tr}})}{\sigma} \quad (5.2.1)$$

$$\sigma = x_{\gamma_{\text{tr}}=0.75} - x_{\gamma_{\text{tr}}=0.25} \quad (5.2.2)$$

Clearly at small values of  $\gamma_{\text{tr}}$  (less than 0.25), the turbulent spots are small in comparison to the distance between them. As the turbulent spots spread into surrounding nonturbulent fluid,  $\gamma_{\text{tr}}$  rises. When  $\gamma_{\text{tr}}$  is of the order of 0.5, the spots begin to merge with each other, and eventually the whole shear layer becomes turbulent ( $\gamma_{\text{tr}} = 1$ ). According to Dhawan and Narasimha [7], the intermittency factor  $\gamma_{\text{tr}}$  on a flat plate can be described by

$$\gamma_{\text{tr}} = 1 - \exp(-0.412\xi^2) \quad (5.2.3)$$

which correlates well with experimental data.

The process of transition in the presence of a pressure gradient is more complex, and Chen and Tyson [8] proposed the expression

$$\gamma_{\text{tr}} = 1 - \exp \left[ -G(x - x_{\text{tr}}) \int_{x_{\text{tr}}}^x \frac{dx}{u_e} \right] \quad (5.2.4)$$

for incompressible flows with

$$G = \left( \frac{3}{C^2} \right) \left( \frac{u_e^3}{\nu^2} \right) R_{x_{\text{tr}}}^{-1.34} \quad (5.2.5)$$

and  $C = 60$  to represent the intermittency distribution in attached flows where transition takes place naturally. For low Reynolds number flows, the transition is separation induced, and the extent of the transition region can be significantly less than that computed by Eq. (5.2.4). Subsequently, Cebeci [9] devised a formula to represent  $C$  in Eq. (5.2.5) in terms of  $R_{x_{\text{tr}}}$ . This formula is shown in Fig. 5.3 together with the experimental data obtained for several airfoils. The data encompasses a typical low Reynolds number range from  $R_c = 2.4 \times 10^5$  to  $R_c = 2 \times 10^6$ , falls conveniently on a straight line on a semi-log scale and can be represented by the equation

$$C^2 = 213[\log R_{x_{\text{tr}}} - 4.7323] \quad (5.2.6)$$

Care should be taken in the use of this equation outside the range of experiments, particularly at high Reynolds numbers where the separation bubble is likely to be small and a limiting value of  $C = 60$  applies.

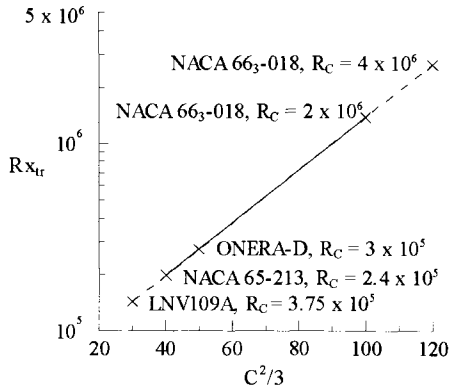


**Fig. 5.3.** Variation of  $C^2/3$  with transition Reynolds number  $R_{x_{tr}}$ .

### 5.3 Linear Stability Theory

The  $e^n$ -method discussed in subsection 5.4.2 is based on small-disturbance theory in which a small sinusoidal disturbance is imposed on a given steady laminar flow to see whether the disturbance will amplify or decay in time. If the disturbance decays, the flow will stay laminar; if the disturbance amplifies sufficiently, the flow must change in some way, probably to become turbulent. The small-disturbance theory does not predict the details of the nonlinear process by which the flow changes from laminar to turbulent. It establishes which shapes of velocity profiles are unstable, identifies those frequencies that amplify fastest, and indicates how the parameters governing the flow can be changed to delay transition.

In this section using the small disturbance theory, we discuss the derivation of the linear stability equations for two-dimensional incompressible mean flows with two-dimensional disturbances. We assume that  $u$ ,  $v$ , and  $p$  in the two-dimensional form of Eqs. (2.2.1) to (2.2.3) represent the instantaneous components of the flow properties, and these components are divided into a mean-flow term and a fluctuating term so that the instantaneous velocity components are  $\bar{u} + u'$  and  $\bar{v} + v'$  and the instantaneous pressure is  $\bar{p} + p'$ . Since  $u'$ ,  $v'$  and  $p'$  are small in Eqs. (2.2.1) to (2.2.3) expressed in terms of mean and fluctuating components, their squares and products can be neglected. Noting that the mean velocity and pressure satisfy the two-dimensional equations of motion, the equations simplify further and can be written as

$$\frac{\partial u'}{\partial x} + \frac{\partial v'}{\partial y} = 0 \quad (5.3.1)$$

$$\frac{\partial u'}{\partial t} + u' \frac{\partial u}{\partial x} + u \frac{\partial u'}{\partial x} + v' \frac{\partial u}{\partial y} + v \frac{\partial u'}{\partial y} = -\frac{1}{\rho} \frac{\partial p'}{\partial x} + \nu \nabla^2 u' \quad (5.3.2)$$

$$\frac{\partial v'}{\partial t} + u' \frac{\partial v}{\partial x} + u \frac{\partial v'}{\partial x} + v' \frac{\partial v}{\partial y} + v \frac{\partial v'}{\partial y} = -\frac{1}{\rho} \frac{\partial p'}{\partial y} + \nu \nabla^2 v' \quad (5.3.3)$$

These equations, with the overbars on  $u$  and  $v$  dropped for convenience, can be simplified further by noting that all velocity fluctuations and their derivatives are of the same order of magnitude and by assuming that the mean flow velocity  $u$  is a function of  $y$  only so that Eq. (3.1.2) gives  $v = 0$ , that is,

$$u = u(y), \quad v = 0 \quad (5.3.4)$$

This assumption is known as the *parallel flow approximation*; which, with the introduction of dimensionless quantities defined by

$$\begin{aligned} u'_* &= \frac{u'}{u_0}, & v'_* &= \frac{v'}{u_0}, & u_* &= \frac{u}{u_0}, & p'_* &= \frac{p'}{pu_0^2}, & t_* &= \frac{tu_0}{L}, \\ x_* &= \frac{x}{L}, & y_* &= \frac{y}{L}, & R &= \frac{u_0 L}{\nu} \end{aligned} \quad (5.3.5)$$

allows Eqs. (5.3.1) to (5.3.3) to be written as

$$\frac{\partial u'}{\partial x} + \frac{\partial v'}{\partial y} = 0 \quad (5.3.6)$$

$$\frac{\partial u'}{\partial t} + u \frac{\partial u'}{\partial x} + v' \frac{\partial u}{\partial y} = -\frac{\partial p'}{\partial x} + \frac{1}{R} \left( \frac{\partial^2 u'}{\partial x^2} + \frac{\partial^2 u'}{\partial y^2} \right) \quad (5.3.7)$$

$$\frac{\partial v'}{\partial t} + u \frac{\partial v'}{\partial x} = -\frac{\partial p'}{\partial y} + \frac{1}{R} \left( \frac{\partial^2 v'}{\partial x^2} + \frac{\partial^2 v'}{\partial y^2} \right) \quad (5.3.8)$$

For convenience, the “star” on the dependent and independent variables has been dropped.

Equations (5.3.6) to (5.3.8) form a set of coupled partial-differential equations with solutions that describe how disturbances originate near the surface  $y = 0$  and spread out through the boundary-layer and beyond as they are convected along the local streamlines. To study the properties of these equations, we apply the standard procedure of stability theory, namely separation of variables. We assume that the small disturbance is a sinusoidal traveling wave and represent a two-dimensional disturbance as

$$q'(x, y, t) = q(y) e^{i(\alpha x - \omega t)} \quad (5.3.9)$$

We seek the solutions of Eqs. (5.3.6) to (5.3.8) in the form of Eq. (5.3.9) since they are linear with respect to  $x$  and  $t$ ; the coefficients of Eqs. (5.3.6) to (5.3.8) depend only on  $y$ . Here  $x, y, t$  are dimensionless quantities defined in Eq. (5.3.5),  $q(y)$  is the amplitude function of a typical flow variable  $q'(x, y, t)$ ,  $\alpha$  is a dimensionless wave number, and  $\omega$  is the radian (circular) frequency of the disturbance. The dimensionless forms of  $\alpha$  and  $\omega$  are defined by

$$\alpha = \frac{2\pi L}{\lambda_x} = \alpha^* L, \quad \omega = \frac{\omega^* L}{u_0} \quad (5.3.10)$$

where  $\lambda_x$  denotes the wavelength in the  $x$ -direction. In general  $q$ ,  $q'$ ,  $\alpha$  and  $\omega$  are complex. With  $q'_r$  and  $q'_i$  denoting the real and imaginary parts of  $q'$ , the magnitude of  $q'$  is  $[(q'_r)^2 + (q'_i)^2]^{1/2}$  and its relative phase angle is  $\tan^{-1}(q'_i/q'_r)$ . The real part of the exponential term represents a growth of disturbance amplitude in  $x$  or  $t$ , while the imaginary part,  $\exp(i\theta)$ , can be rewritten as  $\cos\theta + i\sin\theta$ , which represents the sinusoidal oscillation in  $x$  or  $t$ .

The small-disturbance equations given by Eqs. (5.3.6) to (5.3.8) can also be expressed in other forms. Eliminating pressure and introducing a stream function  $\psi(x, y, t)$  such that

$$u' = \frac{\partial\psi}{\partial y}, \quad v' = -\frac{\partial\psi}{\partial x} \quad (5.3.11)$$

we can express the momentum equations (5.3.7) and (5.3.8) as a fourth-order partial differential equation

$$\frac{\partial}{\partial t}\nabla^2\psi + u\frac{\partial}{\partial x}(\nabla^2\psi) - \frac{\partial\psi}{\partial x}\frac{d^2u}{dy^2} = \frac{1}{R}\nabla^4\psi \quad (5.3.12)$$

Where  $\nabla^4 = \nabla^2\nabla^2$  and  $-\nabla^2\psi$  is the fluctuating  $z$ -component of vorticity,  $\partial v'/\partial x - \partial u'/\partial y$ . Equation (5.3.12) represents the rate of change of fluctuating vorticity following the fluid along a mean streamline.

Taking  $q'$  in Eq. (5.3.9) to represent the disturbance stream function

$$\psi = \phi(y)e^{i(\alpha x - \omega t)}$$

with  $q(y)$  replaced by  $\phi(y)$ , and introducing the resulting expression into Eq. (5.3.12), we obtain the following fourth-order ordinary differential equation for the amplitude  $\phi(y)$

$$\phi'''' - 2\alpha^2\phi'' + \alpha^4\phi = iR(\alpha u - \omega)(\phi'' - \alpha^2\phi) - iR\alpha u''\phi \quad (5.3.13)$$

where a prime denotes differentiation with respect to  $y$ . This equation is known as the *Orr-Sommerfeld equation* and is the fundamental equation for incompressible stability theory.

The solutions of Eq. (5.3.13) correspond to small disturbance waves and are sometimes called Tollmien-Schlichting waves. Despite the major assumptions made to derive this equation, the solutions of Eq. (5.3.13) are encouragingly close to the experimental results. The support to linear stability theory was first provided by the experiments of Schubauer and Skramstad [4] who used a specially designed low turbulence wind tunnel and generated small sinusoidal disturbances in a boundary layer on a flat plate by means of a vibrating ribbon held parallel to the plate and normal to the freestream. The measured neutral stability curve, critical Reynolds number and amplification rates, discussed in [10], were found to agree well with the predictions of the linear stability theory.

The Orr–Sommerfeld equation (5.3.13) can be extended to three-dimensional incompressible flows by using a procedure similar to that used for two-dimensional flows. For a three-dimensional disturbance of  $q'$  of the form

$$q'(x, y, z, t) = q(y)e^{i(\alpha x + \beta z - \omega t)} \quad (5.3.14)$$

the Orr–Sommerfeld equation, with  $\phi$  denoting the amplitude function of the vertical fluctuating velocity  $v'$ , can be written in the same form as Eq. (5.3.13),

$$\begin{aligned} & \phi^{iv} - 2(\alpha^2 + \beta^2)\phi'' + (\alpha^2 + \beta^2)^2\phi \\ &= iR(\alpha u + \beta w - \omega)[\phi'' - (\alpha^2 + \beta^2)\phi] - iR(\alpha u'' + \beta w'')\phi \end{aligned} \quad (5.3.15)$$

or in a compact form

$$\phi^{iv} - \xi_1^2\phi'' - \xi_2^2(\phi'' - \xi_1^2\phi) + \xi_3\phi = 0 \quad (5.3.16)$$

by defining

$$\xi_1^2 = \alpha^2 + \beta^2 \quad (5.3.17a)$$

$$\xi_2^2 = \xi_1^2 + iR(\alpha u + \beta w - \omega) \quad (5.3.17b)$$

$$\xi_3 = iR(\alpha u'' + \beta w'') \quad (5.3.17c)$$

Here  $\beta$  denotes the wave number in the  $z$ -direction and  $w$  the dimensionless velocity profile in the  $z$ -direction.

### 5.3.1 Boundary Conditions

The solution of the Orr–Sommerfeld equation requires conditions to be imposed on the bounding surfaces of the flow. There are many flow configurations to which the stability theory can be applied, but we shall restrict our discussion to boundary-layer flows.

On any rigid boundary surface the perturbation velocities must vanish. Thus, for a two-dimensional flow, we must have  $u' = v' = 0$  at  $y = 0$ , or from Eqs. (5.3.9) and (5.3.11),

$$y = 0, \quad \phi = 0, \quad \phi' = 0 \quad (5.3.18)$$

These boundary conditions also apply to three-dimensional flows.

The boundary conditions away from the surface must be at sufficiently large distances so that the perturbation velocities decay as the edge of the boundary layer is approached. In such cases, the appropriate conditions can be obtained by considering the Orr–Sommerfeld equation in the neighborhood of the edge of the boundary layer,  $y = \delta$ , where Eq. (5.3.16) becomes

$$\phi^{iv} - \xi_1^2\phi'' - \xi_2^2(\phi'' - \xi_1^2\phi) = 0 \quad (5.3.19)$$

with  $u$  and  $w$  in  $\xi_2^2$  evaluated at  $y = \delta$ .

The general solution of this reduced equation is

$$\phi = a_1 e^{-\xi_1 y} + a_2 e^{\xi_1 y} + a_3 e^{-\xi_2 y} + a_4 e^{\xi_2 y}$$

We require that real parts of  $\alpha$ ,  $\xi_1$  and  $\xi_2$  are greater than zero. In order that the boundary-layer disturbances decay near the edge of the boundary-layer, it is necessary that  $a_2 = a_4 = 0$ . This can be assured by imposing the following boundary conditions, with  $D = d/dy$  (see Problem 5.6)

$$y = \delta, \quad (D + \xi_1)(D + \xi_2)\phi = 0, \quad (D + \xi_2)(D^2 - \xi_1^2)\phi = 0 \quad (5.3.20)$$

### 5.3.2 Properties of the Orr–Sommerfeld Equation for Two-Dimensional Flows

Note from the Orr–Sommerfeld equation, given by Eq. (5.3.15) and its boundary conditions given by Eqs. (5.3.18) and (5.3.20) that if a solution to this system can be found with the real parts of  $\xi_1, \xi_2$  strictly positive, then solutions will exist only for certain combinations of Reynolds number  $R$  and the parameters of the disturbance  $\alpha, \beta$  and  $\omega$ , since all the boundary conditions are homogeneous. Thus the problem is an eigenvalue problem in which values of  $R, \alpha, \beta$  and  $\omega$  are the eigenvalues and the corresponding amplitude functions are eigenfunctions. Hence, in general, no nontrivial solution of this system exists. Only if  $\alpha, \beta, \omega, R$  satisfy one or more relations of the form

$$F(\alpha, \beta, \omega, R) = 0 \quad (5.3.21)$$

for three-dimensional flows and

$$F(\alpha, \omega, R) = 0 \quad (5.3.22)$$

for two-dimensional flows can such a solution be found. However, before discussing the solution procedure, it is instructive to review the properties of the Orr–Sommerfeld equation by rewriting Eq. (5.3.13) as

$$\phi^{iv} - 2\alpha^2\phi'' + \alpha^4\phi = i\alpha R(u - c)(\phi'' - \alpha^2\phi) - iR\alpha u''\phi \quad (5.3.23)$$

where  $c$  is the dimensionless complex phase velocity of the disturbance related to its dimensional value  $c^*$  by

$$c = \frac{\omega}{\alpha} = \left( \frac{\omega^*}{\alpha^*} \right) \frac{1}{u_0} = \frac{c^*}{u_0} \quad (5.3.24)$$

The solution of the Orr–Sommerfeld equation and its boundary conditions may be obtained by temporal or spatial amplification theories. The former takes  $\omega$  to be complex ( $\equiv \omega_r + i\omega_i$ ) so that the amplitude of the disturbance varies with time as  $\exp(\omega_i t)$  in contrast to the spatial amplification theory which takes  $\omega$  to be real and  $\alpha$  to be complex, or  $\omega$  to be real and  $c$  to be complex, so that

the amplitude varies with  $x$  as  $\exp(-\alpha_i x)$ . Note that for  $\omega_i = 0$  and given  $\alpha_r$ , a complex value of  $c$  implies values of the real frequency,  $\omega_r$ , and the spatial amplification rate ( $-\alpha_i$ ). Also, if  $\alpha$  and  $\omega$  are both real, then the disturbance propagates through the parallel mean flow with constant amplitude  $|\phi(y)|$ ; if  $\alpha$  and  $\omega$  are complex, the disturbance amplitude will vary in both time and space.

While both procedures have advantages, this discussion favors the solution of the Orr–Sommerfeld equation based on the spatial amplification theory, since the amplitude change of disturbance with distance can be measured in a steady mean flow. The amplitude at a fixed point is independent of time and spatial theory gives the amplitude change in a more direct manner than does the temporal theory.

The eigenvalues of the Orr–Sommerfeld equation for the spatial-amplification case are often presented in  $(\alpha, R)$  and  $(\omega, R)$  diagrams that describe the three states of a disturbance at a given Reynolds number  $R$  as damped, neutral or amplified. For two-dimensional flows the locus  $\alpha_i = 0$ , or  $c_i = 0$ , called the curve of neutral stability, separates the damped (stable) region from the amplified (unstable) region. The point on this curve at which  $R$  has its smallest value is of special interest, because at values of  $R$  less than this value, all disturbances are stable. This smallest Reynolds number is known as the critical Reynolds number,  $R_{cr}$ . The neutral curve is the same in both temporal and spatial amplification theories.

Figure 5.4 shows typical  $(\alpha, R)$  and  $(\omega, R)$  stability diagrams for Blasius flow obtained with the computer program given in the accompanying CD-ROM, Program 5, using the eigenvalue procedure described in subsection 5.6.1. The length scale  $L$  used in Eq. (5.3.5) is chosen to correspond to that used in the definition of the similarity parameter in Eq. (4.2.4a), that is,

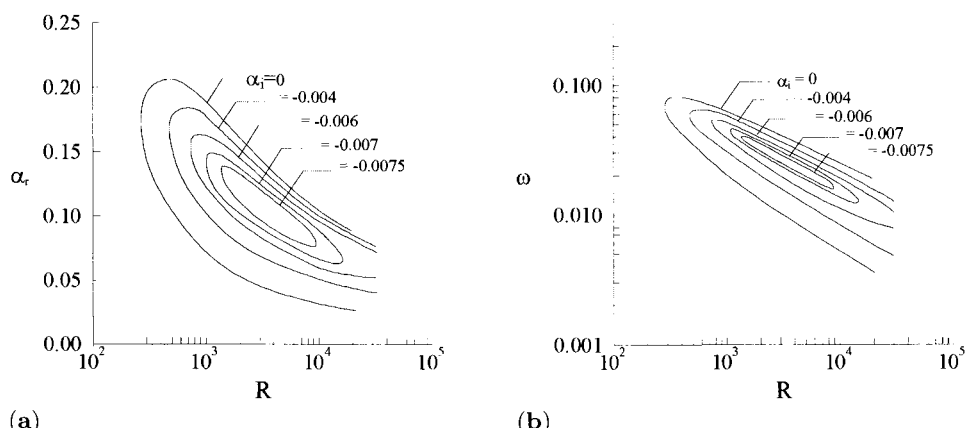


**Fig. 5.4.** Stability diagrams for Blasius flow. (a)  $\alpha_r$  vs  $R$ . (b)  $\omega$  vs  $R$ .

**Table 5.1.** Critical Reynolds number for Falkner–Skan flows [11].

$R_{\delta_{cr}^*}$	$\beta$	$H$
12490	1.0	2.216
10920	0.8	2.240
8890	0.6	2.274
7680	0.5	2.297
6230	0.4	2.325
4550	0.3	2.362
2830	0.2	2.411
1380	0.1	2.481
865	0.05	2.529
520	0.0	2.591
318	-0.05	2.676
199	-0.10	2.801
138	-0.14	2.963
67	-0.1988	4.029

$$L = \sqrt{\frac{\nu x}{u_e}} \quad (5.3.25a)$$

and the velocity scale  $u$  is taken to correspond to the external velocity  $u_e$ .

As a result the Reynolds number in the Orr–Sommerfeld equation is defined by

$$R = \sqrt{\frac{u_e x}{\nu}} = \sqrt{R_x} \quad (5.3.25b)$$

Figure 5.5 and Table 5.1 show the variation of the critical Reynolds number,  $R_{\delta_{cr}^*}$ , with dimensionless pressure gradient parameter  $\beta$  and shape factor  $H$  for Falkner–Skan flows given by Eq. (4.2.5). Note that in this figure the critical Reynolds number is based on displacement thickness  $\delta^*$ , and local velocity  $u_e$ . In terms of Falkner–Skan variables it can be expressed as

$$R_{\delta^*} = \sqrt{R_x} \delta_1^* \quad (5.3.26)$$

with  $\delta_1^*$  denoting a dimensionless displacement thickness parameter expressed in terms of Falkner–Skan variables by

$$\delta_1^* = \int_0^{\eta_e} (1 - f') d\eta = \eta_e - f_e \quad (5.3.27)$$

From Fig. 5.5 it is seen that accelerating flows can tolerate larger Reynolds numbers than decelerating flows and, as a result, have a higher critical Reynolds number. On the other hand, decelerating flows have less tolerance to higher Reynolds numbers, indicating that  $R_{\delta_{cr}^*}$  becomes smaller as  $H$  becomes bigger which corresponds to smaller values of the pressure gradient parameter  $\beta$  in the Falkner–Skan equation.

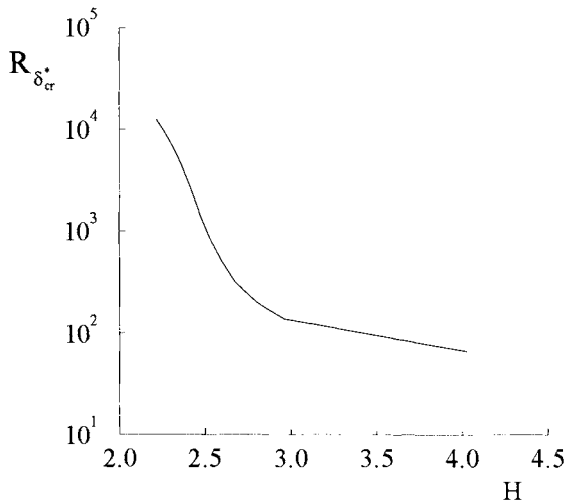


**Fig. 5.5.** Variation of critical Reynolds number,  $R_{\delta_c^*}$ , with  $H$ .

A slightly different kind of stability theory, known as inviscid stability theory, is based on the solution of Eq. (5.3.13) or Eq. (5.3.23) when  $\alpha R \rightarrow \infty$ . In this case the viscous effects on the disturbances are neglected, and the solutions are obtained from

$$(u - c)(\phi'' - \alpha^2 \phi) - u'' \phi = 0 \quad (5.3.28)$$

known as the Rayleigh equation. Since this equation is only of second order, only two boundary conditions are required. For boundary-layer flows

$$y = 0, \quad \phi = 0 \quad (5.3.29a)$$

on the wall and, by an argument similar to that leading to Eq. (5.3.20) and with the real part of  $\alpha$  greater than zero,

$$(D + \alpha)\phi = 0 \quad (5.3.29b)$$

at the edge.

Earlier studies of stability theory solved Eqs. (5.3.28) and (5.3.29) rather than the more complete Orr-Sommerfeld equation, Eq. (5.3.13) or (5.3.23), because of the unavailability of high-speed computers. Although this theory is not applicable exactly to flows at finite Reynolds number, it has led to important theorems concerning the stability of laminar velocity profiles, including those of the following paragraphs.

1. In order to have amplified disturbances, the velocity profile,  $u(y)$ , must have a point of inflection, ( $u'' = 0$ ). This theorem was first proved by Rayleigh. Later Tollmien showed that the existence of a point of inflection is also a *sufficient* condition for the amplification of disturbances. As a result of this theorem, one can conclude that the velocity profiles with a point of inflection are unstable when  $R \rightarrow \infty$ .

2. If  $u'' < 0$ , there is at least one point,  $y = y_c$ , where  $u - c = 0$  for neutral disturbances with  $c_i = 0$ . That is, the phase velocity is equal to the mean velocity at some point inside the flow. The place  $y = y_c$ , where  $u = c$ , is called the *critical layer* of the mean flow.

The second theorem states the fact that any traveling-wave disturbance must move at roughly the speed of the flow if it is to avoid rapid decay. The first theorem implies that profiles with a point of inflection will be unstable at high Reynolds numbers in real life.

## 5.4 Prediction of Transition

### 5.4.1 Empirical Correlations

Current engineering methods for predicting the onset of transition location in two-dimensional incompressible flows are based on empirical correlations and the  $e^n$ -method discussed in the following subsection. Here we present two of these correlations which are useful in the calculation of the complete development of boundary-layers at high Reynolds numbers where the final results are not too severely affected by assumptions about transition. One such useful expression is based on a combination of Michel's method [12] and Smith's  $e^9$  correlation curve [13]. It is given by Cebeci and Smith [14] as a connection between  $R_\theta (\equiv u_e \theta / \nu)$  and  $R_x (\equiv u_e x / \nu)$  at transition (see Fig. 5.6)

$$R_{\theta_{tr}} = 1.174 \left( 1 + \frac{22,400}{R_{x_{tr}}} \right) R_{x_{tr}}^{0.46} \quad (5.4.1)$$

According to this method, the boundary-layer development on the body is calculated for a laminar flow starting at the leading-edge of the flow so that

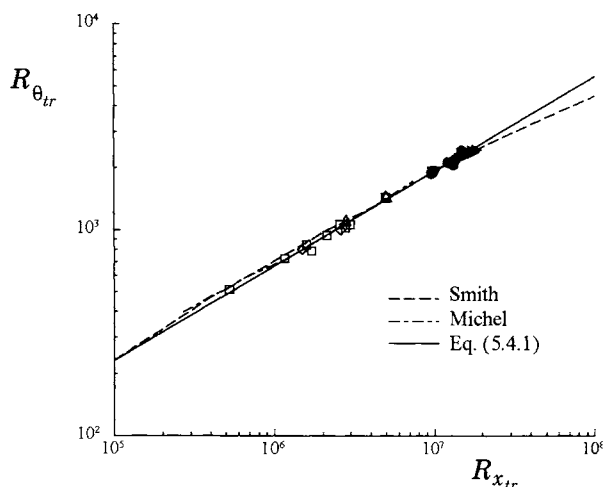


**Fig. 5.6.** Empirical transition correlation curves for two-dimensional incompressible flows. The symbols denote various experimental data taken from Smith [13].

both  $R_\theta$  and  $R_x$  can be determined. Usually, the calculated Reynolds numbers are beneath the curve given by Eq. (5.4.1). The location where the  $(R_\theta, R_x)$  values intersect this curve corresponds to the onset of transition location. In some cases, however, before this happens, flow separation takes place; in those cases, the separation point is assumed to correspond to the onset of transition location.

Another method that can be used to predict transition is due to Granville [15]. This method uses for transition criterion a single curve of  $(R_{\theta_{tr}} - R_{\theta_{cr}})$  as a function of the mean Pohlhausen parameter  $\bar{\lambda}_\theta$  (see Fig. 5.7). The parameter  $\bar{\lambda}_\theta$  is an average  $\lambda_\theta$  [see Eq. (4.4.11)]

$$\bar{\lambda}_\theta = \frac{1}{x - x_{cr}} \int_{x_{cr}}^x \frac{\theta^2}{\nu} \frac{du_e}{dx} dx$$

which is obtained from the laminar boundary-layer solutions by using the expression

$$\bar{\lambda}_\theta = \frac{4}{45} - \frac{1}{5} \left[ \frac{R_\theta^2 - (u_e/u_{e_{cr}})R_{\theta_{cr}}^2}{R_x - (u_e/u_{e_{cr}})R_{x_{cr}}} \right] \quad (5.4.2)$$

where the subscript “cr” denotes the point of instability to TS waves. To predict transition by this method, it is necessary to calculate  $R_{\theta_{tr}}$ . That can be done by means of the curve of Fig. 5.7 which can be expressed by

$$R_\theta - R_{\theta_{cr}} = 375 + e^{6.1+55\bar{\lambda}_\theta} \quad -0.04 \leq \bar{\lambda}_\theta \leq 0.024 \quad (5.4.3)$$

with  $R_{\theta_{cr}}$  given by

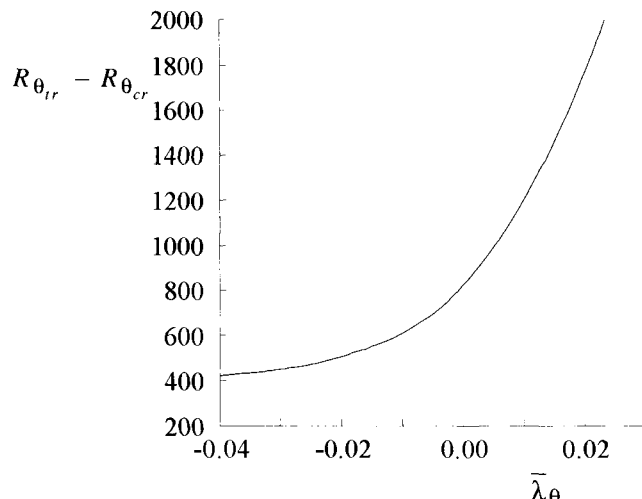


Fig. 5.7. Granville's transition correlation curve for two-dimensional flows.

$$R_{\theta_{cr}} = \begin{cases} \frac{54.2124}{H(H - 2.48)} + \frac{31.6}{H} & H > 2.591 \\ \frac{520}{H} + \frac{2.5 \times 10^6}{H} \left( \frac{1}{H} - \frac{1}{2.591} \right)^{1.95} & H \leq 2.591 \end{cases} \quad (5.4.4)$$

where  $H$  denotes the shape factor at the point of instability. Once  $R_{\theta_{cr}}$  is known, the values of  $(R_\theta - R_{\theta_{cr}})$  and  $\bar{\lambda}$  are calculated from the point of instability,  $R_{x_{cr}}$ , along the body, until they intersect the universal transition curve of Fig. 5.7.

Granville's method has also been extended by Arnal et al. [16] to include the effects of freestream turbulence,  $T_u$  [see Eq. (5.5.1)]

$$R_{\theta_{tr}} - R_{\theta_{cr}} = -206e^{25.7\bar{\lambda}_\theta} [\ln(16.8T_u) - 2.77\bar{\lambda}_\theta] \quad (5.4.5)$$

#### 5.4.2 $e^n$ -Method

The  $e^n$ -method, which utilizes linear stability theory, was first used by Smith [13] and van Ingen [17] and is discussed in some detail in [18]. The basic assumption is that transition starts when a small disturbance is introduced at a critical Reynolds number and is amplified by a factor of  $e^n$  which, for a typical value of  $n$  equal to 9, is about 8000. Either temporal- or spatial-amplification theory can be used, and the latter may be preferred since the amplitude change of disturbance with distance can be measured in a steady mean flow. The amplitude at a fixed point is independent of time, and the spatial theory gives the amplitude change in a more direct manner than does the temporal theory.

The calculation of transition with this procedure is relatively straightforward in two-dimensional (and in axisymmetric) flows, requiring the calculation of the amplification rates ( $-\alpha_i$ ) as a function of  $x$  (or  $R$ ) for a range of dimensional frequencies  $\omega^*$ . The stability calculations are preceded by boundary-layer calculations and, for a given external velocity distribution  $u_e(x)$  and freestream Reynolds number, the laminar boundary-layer equations are solved to obtain the streamwise velocity profile  $u$  and its second derivative  $u''$ . The stability calculations begin at a Reynolds number,  $R_{\delta^*}$ , slightly larger than the critical Reynolds number,  $R_{\delta_{cr}^*}$ , on the lower branch of the neutral stability curve at an  $x$ -location, say  $x = x_1$  (see Fig. 5.8). At this point, since  $u$ ,  $u''$  and  $R$  are known,  $\alpha_r$  and  $\omega$  can be computed by the procedure of subsection 5.6.1 and the dimensional frequency  $\omega^*$  determined from Eq. (5.3.10), that is,

$$\omega^* = \omega \frac{u_0}{L} \quad (5.4.6)$$

and kept constant along line 1 defined by this constant dimensional frequency. At the next  $x$ -location,  $x_2$ , two separate calculations are performed for the newly computed boundary-layer profiles  $u$  and  $u''$  and Reynolds number  $R$ . In one set of calculations (point 2 in Fig. 5.8),  $\alpha_r$  and  $\omega$  are computed on the neutral curve with the procedure used to obtain  $\alpha_r$  and  $\omega$  at point 1 so that a new dimensional

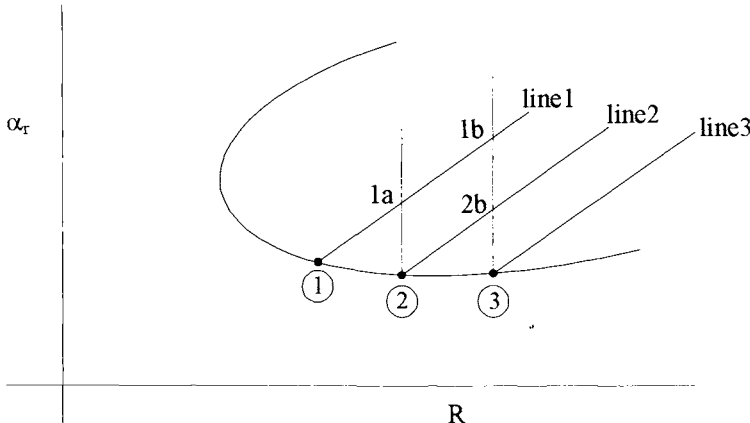


**Fig. 5.8.** Strategy of calculating transition with the  $e^n$ -method.

frequency can be defined on line 2. In the second set of calculations, point 1a, the dimensionless frequency  $\omega$  is first determined from the dimensional frequency  $\omega^*$  on line 1, and its characteristic velocity and length scales at point 2, that is,

$$\omega = \omega^* \frac{L}{u_0} \quad (5.4.7)$$

With  $\omega$  known from Eq. (5.4.7) and  $R$  defined at point 2,  $\alpha$  can be determined by the eigenvalue procedure of subsection 5.6.2. The procedure at point 1a is then repeated at points 2b and 1b, and a dimensional frequency is computed for line 3. For example, at point 1b, values of  $(\alpha_r, \alpha_i)$  are computed with the known dimensional frequency on line 1 and the specified Reynolds number at point 3; at point 2b, they are computed with the known dimensional frequency on line 2 and the specified Reynolds number at point 3. This procedure is repeated for several lines and the variation of the integrated amplification rate, defined by

$$n = - \int_{x_0}^x \alpha_i dx \quad (5.4.8)$$

with  $x_0$  corresponding to each value of  $x$  on the neutral stability curve, is computed for each line. This procedure leads to the curves of constant frequency, Fig. 5.9, and their envelope corresponds to the maximum amplification factors from which transition is computed with a value for  $n$ , commonly assumed between 8 and 9. To cope with the effects of freestream turbulence [see Eq. (5.5.3)], Mack has suggested from the analysis of Dryden's measurements that for freestream turbulence  $T_u > 0.1\%$  [19],

$$n = -8.43 - 2.4 \ln T_u \quad (5.4.9)$$

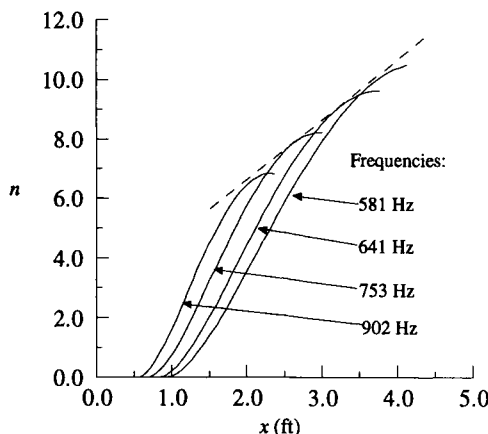


**Fig. 5.9.** Variation of the integrated amplification factors with distance and frequency for Blasius flow.

### 5.4.3 $H-R_x$ Method

A useful shortcut method for predicting transition in a wide class of boundary-layer flows, including the effects of pressure gradient, surface heat transfer and suction, is the  $H-R_x$  method described by Wazzan et al. [20]. Here  $H$  and  $R_x$  are the shape factor ( $\equiv \delta^*/\theta$ ) and the Reynolds number based on surface distance ( $\equiv u_e x / \nu$ ), respectively. This method, which has not been correlated with test data but rather has been justified in terms of TS waves and  $e^n$ -type calculations, is simple to use and a good substitute to the  $e^n$ -method for a class of two-dimensional and axisymmetric flows with pressure gradient, suction and wall heating or cooling with  $n$  factor taken as 9. It is given by

$$\log[R_x(e^9)] = -40.4557 + 64.8066H - 26.7538H^2 + 3.3819H^3 \quad (5.4.10)$$

$2.1 < H < 2.8$

This method differs from the correlation methods discussed in subsection 5.4.1. While Michel's and Granville's methods are strictly for two-dimensional incompressible flows on airfoils and are not applicable to two-dimensional flows with heating and suction and axisymmetric flows, the  $H-R_x$  method is applicable to a wider range of flows. It gives reasonable results so long as the flow does not vary too much from nearby similar flows, i.e., local similarity. Also, it is applicable only so long as the effects of surface roughness and freestream turbulence levels are sufficiently low, just as required in the basic  $e^n$ -method. This method is also restricted to heating rates where the difference between surface temperature and freestream temperature,  $T_w - T_\infty$  does not exceed about 23 °C.

## 5.5 Factors that Influence Transition

There are many factors that influence the onset of transition. These include disturbances in external flow in the form of turbulence and noise, heat transfer, pressure gradient, suction, roughness and surface curvature and are briefly discussed in the following subsections.

### 5.5.1 Effects of Freestream Turbulence and Noise

Depending on the environment, i.e., wind tunnel and flight, disturbances in the external flow can cover wide ranges of frequency, wavelength, velocity of propagation and direction. A comprehensive understanding and prediction of these effects on transition is still very limited. In this section a brief discussion of the effects of freestream turbulence on transition is presented.

The intensity of freestream turbulence  $T_u$  is based on the sum of the Reynolds normal stresses and, with  $u_\infty$  denoting the freestream velocity, may be defined by

$$T_u = \frac{\sqrt{\frac{1}{3}(u'^2 + v'^2 + w'^2)}}{u_\infty} \quad (5.5.1)$$

In general, at a certain distance from the screens or honeycombs, the turbulence in a wind tunnel becomes isotropic which means that

$$\overline{u'^2} = \overline{v'^2} = \overline{w'^2} \quad (5.5.2)$$

In this case, it is customary to base the intensity of the freestream turbulence on the axial normal stress and define  $T_u$  by

$$T_u = \frac{\sqrt{\overline{u'^2}}}{u_\infty} \quad (5.5.3)$$

and use the above definition even in cases where the turbulence is not isotropic.

The influence of freestream turbulence on transition has been studied by several investigators, including Dryden [21], Hall and Hislop [22], Schubauer and Skramstad [4] and Wells [23]. In the latter two studies conducted for flows with zero pressure gradient, the transition Reynolds number was found to increase systematically with decreasing freestream turbulence intensity until a maximum was reached which was not affected by further reductions in turbulence intensity, see Fig. 5.10. As can be seen, the maximum transition Reynolds number found by Wells is 80% greater than that reported by Schubauer and Skramstad, being  $5 \times 10^6$  and  $2.8 \times 10^6$ , respectively, for disturbance intensities less than 0.1% of the free stream.

The turbulence level is not sufficient to characterize the effect on transition in particular at low-turbulence intensities. Freestream perturbations are

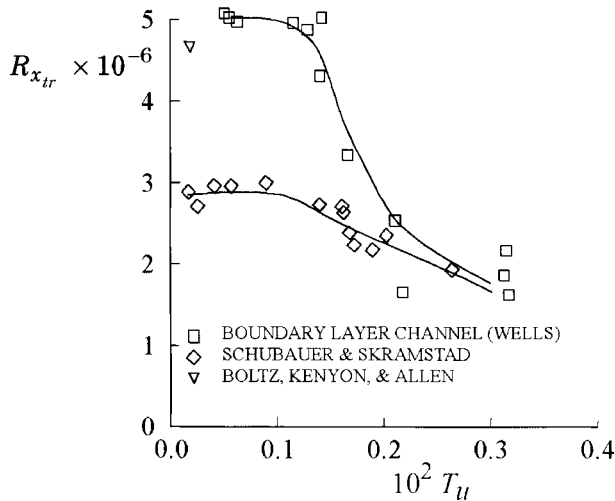


**Fig. 5.10.** The effect of freestream turbulence on boundary-layer transition for low-turbulence intensities.

generally a mixing of turbulence and acoustics. Turbulence is made of three-dimensional velocity fluctuations which are rotational and which span a range of frequencies. Acoustic perturbations are formed of irrotational waves, more or less two-dimensional. A systematic study of the influence of noise frequency on transition shown in Fig. 5.11 has been conducted by Spangler and Wells [24]. If the frequency is in the range of natural unstable TS waves, a significant

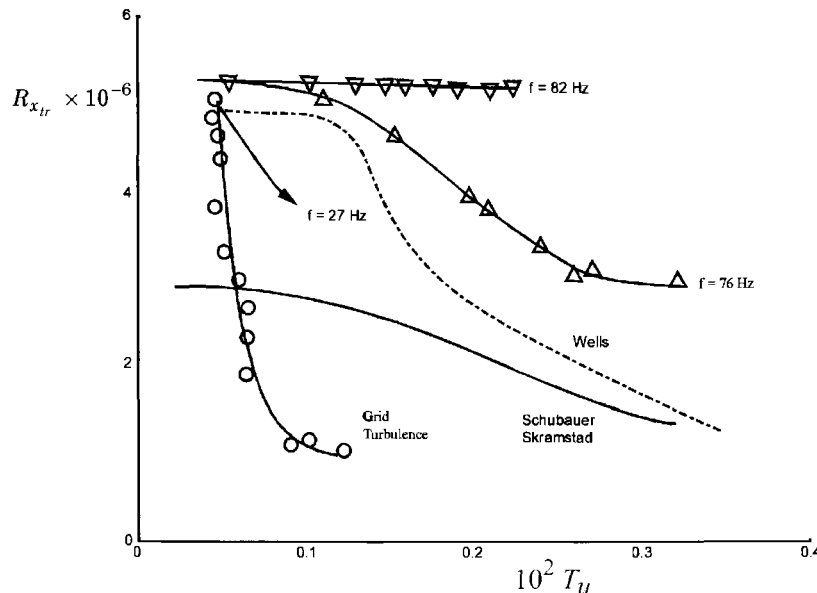


**Fig. 5.11.** Effect of noise frequency on flat plate transition [24].

decrease in transition Reynolds number is recorded. In three-dimensional flows, the effect of noise frequency on transition is not very well known.

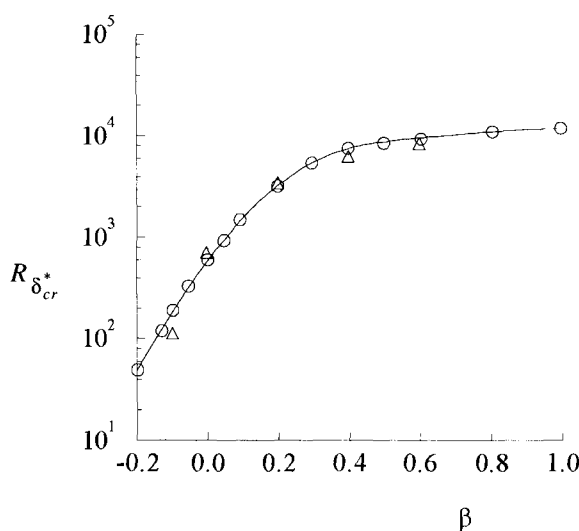
### 5.5.2 Effects of Pressure Gradient

Before we demonstrate the effect of pressure gradient on transition, it is useful to examine the stability diagrams for similar flows which show the effect of pressure gradient on the frequency of unstable disturbances, amplification rates and critical Reynolds number.

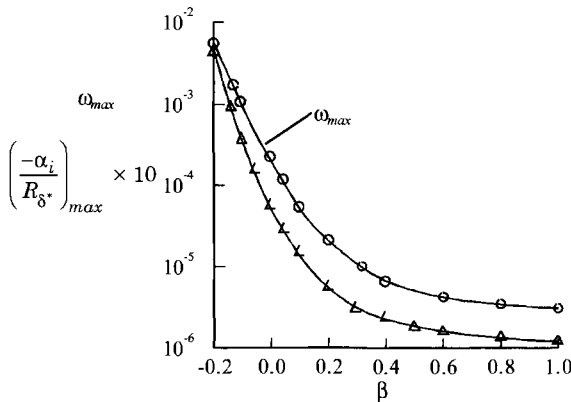
Figure 5.12 shows that an adverse pressure gradient [negative  $\beta (\equiv \frac{2m}{m+1})$ ] decreases the critical Reynolds number based on displacement thickness,  $R_{\delta_{cr}^*}$ . This decrease in  $R_{\delta_{cr}^*}$  causes the range of frequencies to which the boundary layer is unstable to increase. Similarly, a favorable pressure gradient (positive  $\beta$ ) increases the critical Reynolds number and causes the range of frequencies to which the boundary layer is unstable to decrease.

Figure 5.13 shows the variation of the ratio of maximum amplification rate (see Eq. (5.4.8)) and  $R_{\delta_{cr}^*}$  and frequency  $\omega$  (see Eq. (5.4.7)) of unstable disturbances at several values of  $\beta$ . As can be seen, the pressure gradient has a pronounced influence on the amplification rates and frequencies. Positive pressure gradient ( $\beta < 0$ ) increases them and negative pressure gradient ( $\beta > 0$ ) decreases them.

The global effect of a positive pressure gradient is to promote transition at a smaller Reynolds number than with a zero pressure gradient. The location of the beginning of transition is more upstream and the length of the transition region is reduced. If the pressure gradient is strong enough, the boundary-layer



**Fig. 5.12.** The effect of pressure gradient on the critical Reynolds number [11].



**Fig. 5.13.** The effect of pressure gradient on the maximum spatial amplification rate and frequency of unstable disturbances [11].

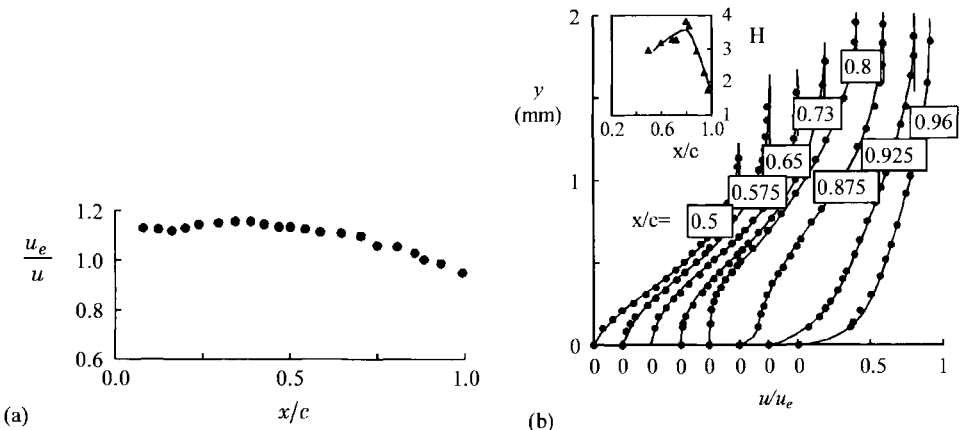


**Fig. 5.14.** Transition on airfoil ONERA D with positive pressure gradient [25]: (a) external velocity distribution and (b) mean velocity profiles in the boundary-layer.

separates. In certain cases, a transition bubble is formed. Transition occurs in the separated boundary-layer and the turbulent boundary-layer can reattach.

Experimental observations show that the first stage of transition is the development of TS waves as in the case of a flat plate boundary-layer. The downstream phenomena seem to depend on the intensity of the pressure gradient. If the pressure gradient is moderate, the phenomena are qualitatively the same as for the flat plate.

In the experimental study concerned with a boundary-layer on an airfoil with positive pressure gradient conducted by Cousteix and Pailhas [25], the development of instabilities looks quite different. The distribution of external velocity is given in Figure 5.14 together with the evolution of mean velocity profiles. Around the location  $x/c = 0.73$ – $0.8$ , a small separation bubble is present.

Downstream, the boundary-layer reattaches and the velocity profile takes on a typical turbulent behavior. The shape parameter  $H$  reflects this evolution.

In order to analyze the characteristics of the laminar-turbulent process, records of the output voltage of anemometer are given in Fig. 5.15 together with the corresponding spectra. A record corresponds to a given station for a fixed distance to the wall ( $y = 0.5$  mm). The voltage fluctuations are directly proportional to the velocity fluctuations, but the records are given without scale: they give only a qualitative information. Upstream of station  $x/c = 0.875$ , the velocity is perturbed by very regular fluctuations which are nearly sinusoidal; the intensity of fluctuations increases downstream. These perturbations have the same characteristics as Tollmien-Schlichting waves in flat plate boundary-layer. The intensity of the waves are however much higher. It seems that this first phase of the transition process is linear because the level of harmonics is low.

At station  $x/c = 0.925$ , nonlinear phenomena develop. The fundamental oscillation is still visible and its frequency is close to the value recorded at station  $x/c = 0.875$ , but the signal is distorted. Each cycle seems to be deformed by similar perturbation. Downstream, the signal becomes richer and richer in harmonics but we still observe a certain regularity in the shape of the sig-

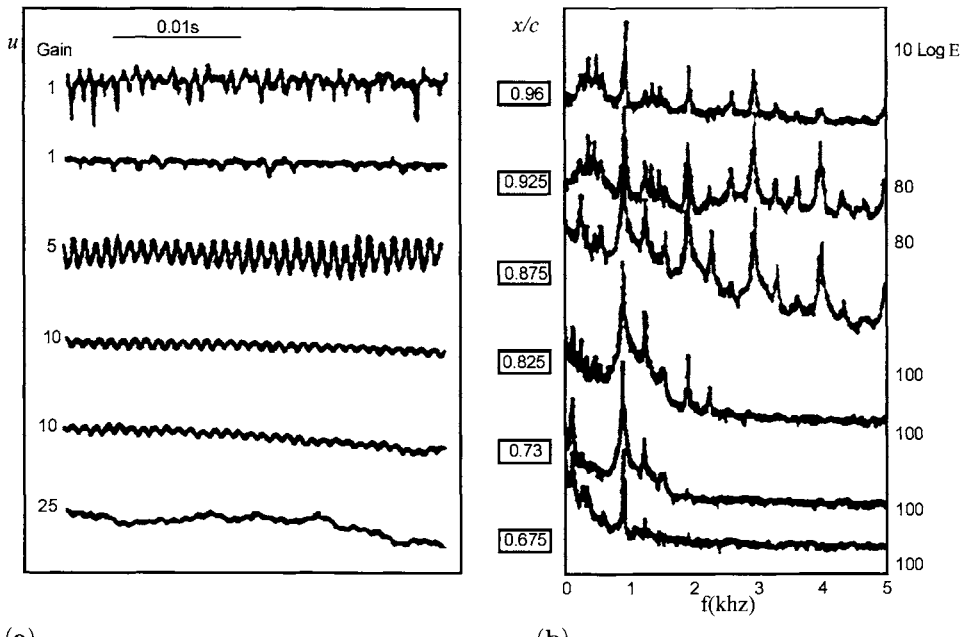


**Fig. 5.15.** Transition on airfoil ONERA D with positive pressure gradient, [25]: (a) records of output voltage of anemometer at  $y = 0.5$  mm and (b) energy spectra of longitudinal velocity  $y = 0.5$  mm.

nal. The spectra exhibit a sharp peak at frequency  $f_1 = 1000$  Hz for stations  $x/c = 0.675, 0.73$  and  $0.825$ . Downstream, we observe harmonics at frequencies  $f_2 = 2000$  Hz,  $f_3 = 3000$  Hz,  $f_4 = 4000$  Hz, etc. ... Other frequencies  $\frac{f}{2}, f, \frac{3}{2}f$  or  $fm/2$  ( $m = 1, 2, 3, \dots$ ) are also observed with symmetrical peaks around these frequencies. This type of transition has very close resemblance with the  $N$ -type of transition studied with controlled disturbances for the flat plate [26]. It is also interesting to note that transition occurs without the formation of turbulent spots.

### 5.5.3 Effects of Heat Transfer

An indication of the qualitative effects of surface temperature, mass transfer and pressure gradient on transition can be obtained from the  $x$ -momentum equation by recalling Rayleigh's theorem which requires that in order to have amplified disturbances, the velocity profile  $u(y)$  must have a point of inflection ( $u'' = 0$ ) within the flow. To show this for the case of heat transfer, we consider the  $x$ -momentum equation for a variable viscosity on a zero pressure gradient, nonporous surface and write it at the wall,

$$0 = \left( \frac{d\mu}{dy} \right)_w \left( \frac{du}{dy} \right)_w + \mu_w \left( \frac{d^2 u}{dy^2} \right)_w \quad (5.5.4)$$

or, with primes denoting differentiation with respect to  $y$ , as

$$\left( \frac{d^2 u}{dy^2} \right)_w \equiv u''_w = - \frac{1}{\mu_w} \left( \frac{d\mu}{dy} \right)_w u'_w \quad (5.5.5)$$

The dynamic viscosity  $\mu$  is a function of temperature, and decreases with increasing temperature for liquids and increases with increasing temperature for gases. It can be seen from Eq. (5.5.5) that if the plate is heated so that  $T_w > T_e$ , then for a liquid  $(dT/dy)_w$  and  $d\mu/dT$  are less than zero and as a result

$$\left( \frac{d\mu}{dy} \right)_w = \left( \frac{d\mu}{dT} \right) \left( \frac{dT}{dy} \right)_w \quad (5.5.6)$$

is positive. Conversely, for a cooled plate,  $(d\mu/dy)_w$  is negative. As both  $\mu_w$  and  $u'_w$  are positive for either case, it follows that for  $T_w > T_e$ ,  $u''_w < 0$  and for  $T_w < T_e$ ,  $u''_w > 0$ . Since the curvature  $u''$  is vanishingly small but negative as  $y \rightarrow \infty$ , it follows that if its value at the wall is positive there must be at least one point of inflexion in the boundary layer (i.e., some point at which  $u'' = 0$ ). Thus for a liquid, we expect that heating stabilizes and cooling destabilizes the laminar boundary layer. Conversely, for gases in which viscosity increases with temperature, heating and cooling destabilizes and stabilizes the flow, respectively.

A similar analysis can be used to show the qualitative effects of suction and injection as well as favorable and adverse pressure gradient on the curvature of the velocity profile and subsequently on transition.

The effect of heat transfer on transition in incompressible flows can be studied with the  $e^n$ -method provided that we modify the Orr–Sommerfeld equation. This can be done by assuming explicit fluid property variations in only the mean dynamic viscosity and no fluctuating temperature field as discussed in [27] or by making use of the energy equation with all fluid properties considered temperature dependent as discussed in [28]. The predictions of both approaches essentially yield similar results and the former approach is considered here.

As discussed in Problem 5.16, the modified Orr–Sommerfeld equation for an incompressible flow with heat transfer is

$$(\alpha u - \omega)(\phi'' - \alpha^2 \phi) - \alpha u'' \phi = -\frac{i}{R} [\mu(\phi^{iv} - 2\alpha^2 \phi'' + \alpha^4 \phi) + 2\mu'(\phi''' - \alpha^2 \phi') + \mu''(\phi'' + \alpha^2 \phi)] \quad (P5.16.9)$$

The variable mean-flow coefficients in this equation can be obtained from the compressible continuity and momentum boundary-layer equations (see [29]),

$$\frac{\partial}{\partial x}(\rho u) + \frac{\partial}{\partial y}(\rho v) = 0 \quad (5.5.7)$$

$$\rho u \frac{\partial u}{\partial x} + \rho v \frac{\partial u}{\partial y} = \rho_e u_e \frac{du_e}{dx} + \frac{\partial}{\partial y} \left( \mu \frac{\partial u}{\partial y} \right) \quad (5.5.8)$$

and from the energy equation, which in terms of total enthalpy  $H$ , can be written as

$$\rho u \frac{\partial H}{\partial x} + \rho v \frac{\partial H}{\partial y} = \frac{\partial}{\partial y} \left[ \frac{\mu}{Pr} \frac{\partial H}{\partial y} + \mu \left( 1 - \frac{1}{Pr} \right) u \frac{\partial u}{\partial y} \right] \quad (5.5.9)$$

subject to

$$y = 0, \quad u = v = 0, \quad H = H_w(x) \quad (5.5.10a)$$

$$y = \delta, \quad u = u_e(x), \quad H = H_e \quad (5.5.10b)$$

All fluid properties are assumed to vary. For example, for water, in terms of SI units, they are given by

$$\mu = 1.79369 \times 10^{-5} / \begin{pmatrix} 35.155539 - 106.9718715T_r + 107.7720376T_r^2 \\ -40.5953074T_r^3 + 5.639148T_r^4 \end{pmatrix} \quad (5.5.11a)$$

$$\rho = 1002.28(0.803928 + 0.4615901T_r - 0.2869774T_r^2 + 0.0234689T_r^3) \quad (5.5.11b)$$

$$c_p = 1301.83(1.4833689 - 0.8072591T_r + 0.328960T_r^2) \quad (5.5.11c)$$

$$Pr = 13.66 / \left( \begin{array}{l} 73.376906 - 208.7474538T_r + 197.7604676T_r^2 \\ - 68.8626188T_r^3 + 7.4779458T_r^4 \end{array} \right) \quad (5.5.11d)$$

Here  $T$  is temperature in Kelvin,  $T_r$  a temperature ratio defined by  $T_r = T/273.16$ .

Before we discuss the results with heat transfer obtained with the  $e^n$ -method, let us consider the unheated case so that the role of heat transfer on transition can be demonstrated. The results presented here were obtained by Lee [30] who used the same numerical procedure described in Section 5.6. Note that with these length and velocity scales,  $u$  and  $u''$  in the Orr-Sommerfeld equation are related to those computed by the boundary-layer program by

$$u = f', \quad u'' = f''' \frac{R_x}{x^2} = f''' \left( \frac{R}{x} \right)^2 \quad (5.5.12)$$

Figure 5.16 shows the variation of  $n$ -factor with  $R_x$  for five dimensional frequencies. For an  $n$ -value of 9, transition occurs at  $R_x = 3.20 \times 10^6$ , a value slightly larger than the experimental value of  $2.84 \times 10^6$ . For  $n = 8.2$ , the calculations agree well with experiment. The small discrepancy is within a scatter of experimental data and within the uncertainties associated with the  $n$ -factor.

Figure 5.17 shows the variation of  $n$ -factor with  $R_x$  for uniformly heated plates on which the difference between the wall and freestream temperature,  $\Delta T$ , is 5 and 30 °F, respectively. As in the results shown in Fig. 5.16, the calculations were again performed for five frequencies. As expected, heat transfer has a significant effect on the location of transition and shifts it downstream, delaying the beginning of turbulent flow.

Figure 5.18 shows the variation of  $R_{x_{tr}}$  as well as  $R_{\delta_{cr}^*}$  with heat transfer for the two cases depicted in Fig. 5.17, including the case for  $\Delta T = 20$  °F. As expected, due to the temperature-viscosity relationship of water, heat transfer increases both the transition and critical Reynolds numbers.

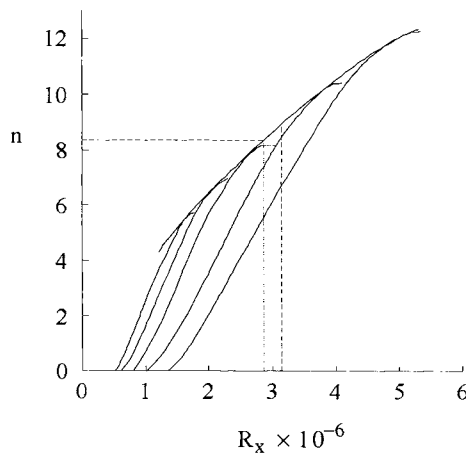
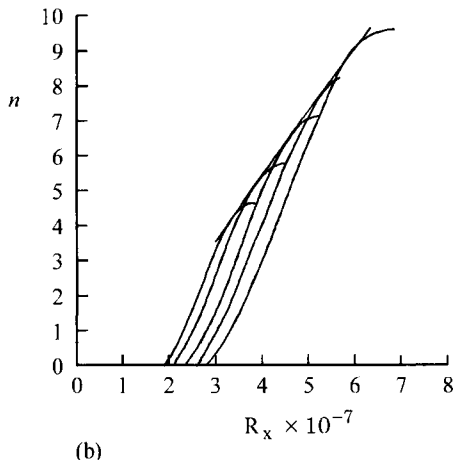
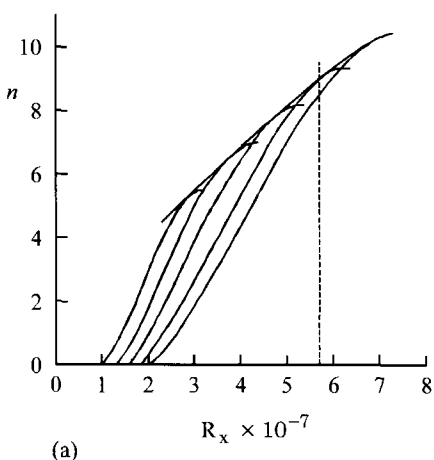
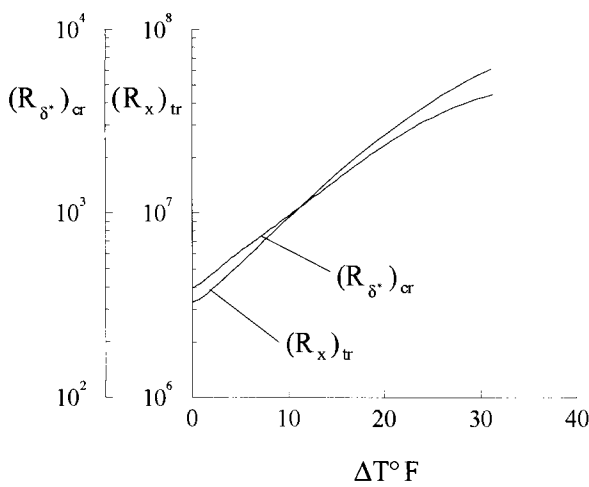


Fig. 5.16. Integrated amplification rates on a flat plate with zero heat transfer [29].



**Fig. 5.17.** Integrated amplification rates – uniformly heated plates with water flow with (a)  $\Delta T = 5^\circ\text{F}$  and (b)  $\Delta T = 30^\circ\text{F}$  [30]. Freestream temperature  $T_\infty$  is  $67^\circ\text{F}$ .



**Fig. 5.18.** Variation of  $R_{x_{\text{tr}}^*}$  and  $R_{\delta_{\text{cr}}^*}$  with heat transfer [30].

Figure 5.19 shows the neutral stability curves in the  $(\alpha_r \delta^*)$  and  $R_{\delta^*}$  plane for flat plates with four different  $\Delta T$  values, namely, 0, 5, 20 and 30. As can be seen, heat transfer strongly influences the stability properties; in addition to increasing the critical Reynolds number, it also reduces the extent of the difference between lower and upper branches of the stability curves as heat transfer rate increases.

#### 5.5.4 Effects of Suction

Suction has a double effect on a boundary-layer. First, the thickness of the boundary-layer is reduced, second, the shape of the velocity profile is modi-

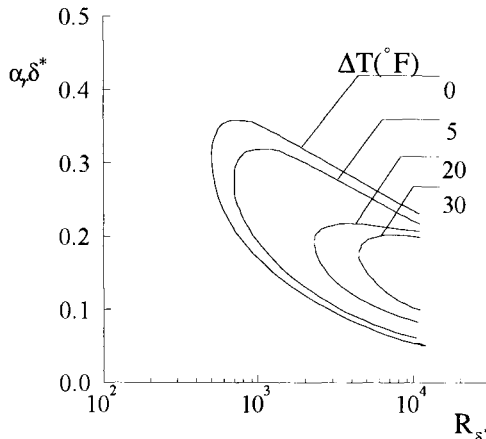


**Fig. 5.19.** Neutral stability curves for heated flat plates [30] for water flow.

fied. These two effects combine to improve the stability properties of laminar boundary-layers. For two-dimensional flows, the second effect can be studied qualitatively from the momentum equation, which at the wall becomes

$$\rho v_w \frac{\partial u}{\partial y} + \frac{dp}{dx} = \mu \frac{\partial^2 u}{\partial y^2}$$

This equation shows that a positive pressure gradient induces a positive value of the second velocity derivative and leads to the presence of an inflection point which is likely to promote instabilities. A wall suction ( $v_w < 0$ ) competes with a positive pressure gradient and can improve the stability of the boundary-layer.

As discussed in detail in [31], it is desirable to have extensive regions of laminar flow on underwater vehicles and aerodynamic bodies in order to reduce the skin-friction drag. Suction is an effective way of accomplishing this objective. To demonstrate this, consider flow over a flat plate with uniform suction and assume that the velocity profile corresponds to the asymptotic suction profile given by Eq. (P4.11.3). The critical Reynolds number based on displacement thickness,  $R_{\delta_{cr}^*}$ , of this profile is about 70,000, as compared with about 500 for a Blasius profile.

The suction drag is defined as loss of momentum due to mass removed from a boundary layer. If the mass removed is assumed to occur normal to the surface, then the force  $D$  acting on a flat plate with length  $L$  is (see problem P4.12)

$$D = \rho u_\infty \int_0^L v_w dx \quad (5.5.13)$$

and the suction drag coefficient  $C_{d_q}$  is defined by Eq. (P4.12.3), that is,

$$C_{d_q} = \frac{D}{(1/2)\rho u_\infty^2 L} = 2 \int_0^L \left( \frac{v_w}{u_\infty} \right) \frac{dx}{L} = 2C_q \quad (P4.12.3)$$

We can estimate the magnitude of the suction coefficient  $C_q$  to ensure stability to small disturbances for the asymptotic suction profile. From the first relation in Eq. (P4.11.4) and Eq. (P4.12.4), we can write

$$C_q = \frac{\nu}{u_e \delta^*} = \frac{1}{R_{\delta^*}} \quad (5.5.14)$$

so that the boundary-layer would be laminar if  $C_q$  had the extremely low value of  $1/70,000 = 1.4 \times 10^{-5}$ .

In an actual case, however, the minimum value of  $C_q$  for a flat plate flow with suction is higher than the value corresponding to the asymptotic suction profile. As discussed in Problem 5.1, this profile develops only at a certain distance from the leading edge. The velocity profiles between that point [see Eq. (P5.1.1)] and the leading edge are of different shapes, changing gradually from the Blasius profile with no suction at short distances behind the leading edge to the asymptotic form. All the profiles in this region have lower limits of stability than the asymptotic one, and it follows that the quantity of fluid to be removed over the initial length must be larger than the value of  $1.4 \times 10^{-5}$ , if laminar flow is to be maintained. According to Schlichting [32], the suction coefficient  $C_q$  must be greater than  $1.18 \times 10^{-4}$ , which is still a relatively small value from a practical point of view as it would pose very modest power requirements with only a small increase of skin friction drag over that of an unsucked laminar boundary layer, as shown in Fig. 5.20. The variation of local skin-friction coefficient  $c_f$  under conditions of *optimum suction* corresponds to  $C_q$  of  $1.18 \times 10^{-4}$ , which is just sufficient to maintain laminar flow. The distance between the curve marked “optimum suction” and that marked “turbulent” corresponds to the saving in drag effected by the application of suction.

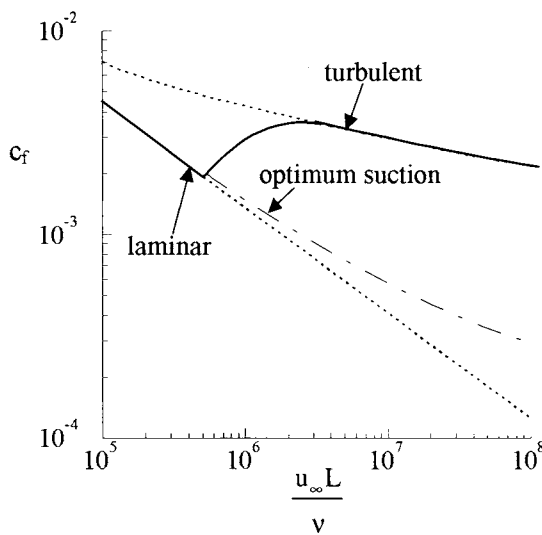


**Fig. 5.20.** Coefficient of local skin friction of a flat plate at zero incidence [31].

The drag associated with boundary-layer flow and mass removed can be conveniently discussed by considering again a flat plate with uniform suction. It follows from the momentum integral equation, Eq. (P3.13.1), that

$$u_e^2 \frac{d\theta}{dx} - v_w u_e = \frac{\tau_w}{\rho} \quad (5.5.15)$$

since the suction velocity is negative. It is clear from this equation that the wall shear ( $\tau_w$ ) represents the total loss and not just viscous loss in the boundary layer.

Integrating Eq. (5.5.15) over the surface length  $L$ , letting T.E. denote the trailing edge of the flat plate and rearranging, we get

$$2 \left( \frac{\theta}{L} \right)_{T.E.} - 2 \int_0^L \frac{v_w}{u_e} \frac{dx}{L} = \int_0^L \frac{\tau_w}{(1/2)\rho u_e^2} \frac{dx}{L} = \int_0^L c_f \frac{dx}{L} \quad (5.5.16)$$

Here  $\theta_{T.E.}$  is obtained from the velocity profile calculated from a flow with blowing. The usual definition of  $\theta$  is used.

The first term on the left-hand side of this equation is the momentum drag associated with the wake,  $c_{d_w}$ . The second term is the suction drag coefficient and the term on the right-hand side is the average skin-friction coefficient,  $c_F$ , which represents the momentum loss in the external viscous flow passing into the wake plus the momentum loss of the fluid taken aboard. The latter loss (suction drag) is analogous to ram drag of air entering an inlet. For this reason, sometimes the momentum drag is also referred to as the ram drag or sink drag, and is considered separately.

There are practical limitations to what can be achieved by suction. Increasing suction rates requires larger ducting system and more power so that at some point, the weight penalty and the higher suction drag will produce diminishing returns. Increased suction also makes the boundary layer thinner, which in turn reduces the critical height of roughness which will cause transition. If suction is applied through discrete holes or slots and is not distributed over the area, increased suction velocities may cause the suction holes or slots to become critical themselves and act as sources for disturbances. It is clear that the suction system must be carefully tailored to the mission at hand if optimum benefits are to be realized. A well-designed pumping system should restore about one  $C_q$  of the loss attributed to the ram drag.

### 5.5.5 Effects of Surface Roughness

It is well known that a dirt particle or similar isolated roughness on the surface in a region of laminar flow may produce immediate transition, a wedge-shaped region of turbulent flow originating at the roughness and extending downstream. It has also been observed that when roughness height or freestream velocity is

reduced, the wedge of turbulence may begin some distance downstream from the roughness element. According to experimental data, see for example, Ref. 29, there is a marked difference between the effects of two-dimensional and isolated roughness on transition.

If we consider an isolated roughness on a body, we find that depending on its shape, the external velocity distribution, location on the body and the fluid viscosity, there is a critical roughness height, often called  $k_{\text{crit}}$ , below which the roughness element has no effect on transition; that is, the location of transition is the same as that on a smooth surface. As the height of the roughness element is increased above this value, however, the location of transition moves upstream until at a second critical value, say  $k^*_{\text{crit}}$ , transition occurs just aft of the roughness element; a wedge-shaped region of turbulent flow then results, trailing downstream from the roughness element at its apex and of semi-angle of the order of  $10^\circ$ . With a two-dimensional roughness element e.g., a transition trip-wire, turbulent flow occurs over a whole span immediately aft of the roughness element for  $k > k^*_{\text{crit}}$ .

These two critical heights are of considerable practical importance:  $k_{\text{crit}}$  defines the stage at which the roughness begins to produce a noticeable effect on drag due to the forward transition movement, while  $k^*_{\text{crit}}$  is a useful guide to the height of a trip required to bring the transition to a specified location. The critical roughness height,  $k^*_{\text{crit}}$ , is often used to help to reduce the uncertainties of scale effect prediction in the use of wind tunnel models to simulate full-scale behavior in flight.

Before closing this brief discussion on the effects of surface roughness on transition, it is useful to mention that the minimum Reynolds number based on momentum thickness  $R_\theta$ , for producing transition at the roughness element is about 320 for full-developed turbulent boundary layers over a flat plate. The minimum height of roughness can therefore be estimated from the equation  $R_\theta + \delta R_\theta = 320$ , where  $R_\theta$  is the Reynolds number on a smooth plate at roughness location and  $\delta R_\theta$  is the increase in  $R_\theta$  associated with the drag of the roughness element. The latter can be expressed in the form

$$\delta R_\theta = \frac{1}{2} C_D \frac{u_e k}{\nu} \left( \frac{u_k}{u_e} \right)^2 \quad (5.5.17)$$

where  $C_D$  is the drag coefficient referred to the velocity  $u_k$  at the height of roughness element and has a value of about 3/4 in the case of circular wire.

In general, surface roughness promotes transition. Sometimes, this effect is favorable. This is indeed the purpose of dimples on golf balls. The advantage is that a turbulent boundary-layer has a better ability to support adverse pressure gradients without separating and the pressure drag of a sphere is reduced if separation occurs further downstream when the boundary-layer is turbulent.

### 5.5.6 Effects of Surface Curvature

Surface curvature can also play an important role in influencing transition. On two-dimensional convex surfaces, transition may occur due to Tollmien-Schlichting (T-S) instability and on three-dimensional convex surfaces due to crossflow instability, or T-S, or a combination of both instabilities. On two- and three-dimensional concave surfaces, transition may also occur due to Görtler instability, also known as Taylor-Görtler instability. While the T-S instability deals with small disturbances superimposed to the flow, the Görtler instability deals with the centrifugal instability caused by the curvature of the concave surface.

There is an essential difference between the T-S waves shown in Fig. 5.1 and the disturbances found by Görtler, shown in Fig. 5.21. The latter type consists of vortices with axis oriented in the streamwise direction and is similar to the disturbances first discovered by G.I. Taylor in 1923 in his investigation of the flow between rotating concentric cylinders. With the outer one at rest and the inner one rotating, the flow close to the surface of the outer one is effectively that over a concave surface. Instability manifests itself in the form of ring-like vortices which appear when the Taylor number  $Ta$  defined by

$$Ta = R_d \sqrt{d/r_i} \quad (5.5.18)$$

is approximately greater than 4.1. Here  $R_d$  is a Reynolds number based on the gap width  $d$  between the cylinders and circumferential velocity  $u_0$  of the inner cylinder of radius  $r_i$ . The regular pattern of laminar vortices arising from the initial instability is found to continue for values of  $Ta$  up to about 4000; at higher values of  $Ta$  the flow becomes turbulent and the vortices lose their regular pattern.

After Taylor's discovery, Görtler analytically showed that an external flow on a concave surface becomes unstable if

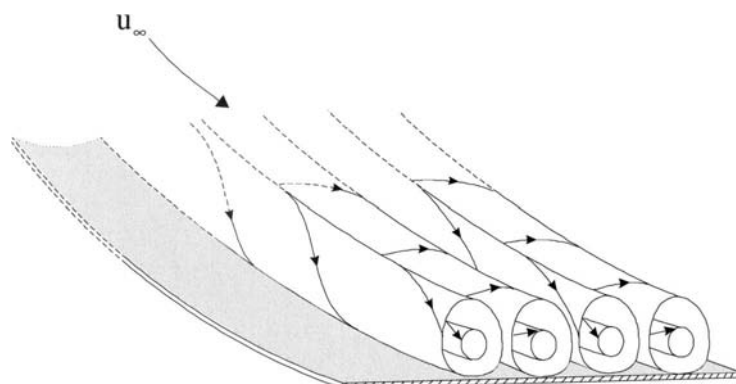


**Fig. 5.21.** Streamline pattern of Görtler disturbances in laminar boundary-layer on a concave surface.

$$Ta = R_\theta \sqrt{\theta/r_0} \quad (5.5.19)$$

is greater than 0.58. Here  $R_\theta$  is the Reynolds number based on the momentum thickness,  $u_e\theta/\nu$ , and  $r_0$  is the radius of curvature. Later, Dryden, based on Liepmann's experiments [33], showed that for transition, the values of  $Ta$ , depending on the freestream turbulence, are between 6 and 9 [34]. Thus, a concave surface induces instabilities in the flow in the form of streamwise vortices to the subsequent development of turbulent flow, but the process of development can be lengthy and complex. Forest [35] proposed a correlation which relates the Taylor number to the freestream turbulence level by

$$Ta = 9e^{-17.3T_u} \quad (5.5.20)$$

Görtler vortices coupled with T-S waves and crossflow instability can trigger early transition to turbulence. They may play an important role in internal flows with concave curvature and on modern supercritical laminar flow control wings which have concave regions near the leading edge and the trailing edges of the lower surface.

There have been extensive studies devoted to the improvement and extension of Görtler's analysis, and a thorough review of these efforts has been reported by Herbert [36] and Saric [37]. There are a number of fundamental differences in these theoretical studies as to the details of the formulation of the problem as well as in the computed results. These are discussed by Floryan [38]. The influence of external disturbances and effects of suction are analyzed by Floryan and Saric [39].

## 5.6 Numerical Solution of the Orr–Sommerfeld Equation

The box scheme described in Chapter 4 to solve the boundary-layer equations for two-dimensional flows is also very appropriate to solve the Orr–Sommerfeld equation as we discuss in this section and the linear stability and boundary-layer equations for three-dimensional flows as we discuss in Chapters 11 and 9, respectively.

To formulate the numerical scheme employing the box method, we consider Eq. (5.3.16) and its boundary conditions given by (5.3.18) and (5.3.20) and reduce them to an equivalent first-order system. We define

$$\phi' = f \quad (5.6.1a)$$

$$f' = s + \xi_1^2 \phi \quad (5.6.1b)$$

$$s' = g \quad (5.6.1c)$$

and write Eq. (5.3.16) as

$$g' = \xi_2^2 s - \xi_3 \phi \quad (5.6.1d)$$

With these variables, the boundary conditions become

$$y = 0, \quad \phi = 0, \quad f = 0 \quad (5.6.2a)$$

$$\begin{aligned} y = \delta; \quad s + (\xi_1 + \xi_2)f + \xi_1(\xi_1 + \xi_2)\phi &= 0; \\ g + \xi_2 s &= 0 \end{aligned} \quad (5.6.2b)$$

where  $\xi_2$ , defined in Eq. (5.3.17b) attains its value at  $y = \delta$ .

We now consider a nonuniform mesh with  $y = 0$  represented by  $y_0$  and  $y = \delta$  by  $y_J$  and approximate the quantities  $(f, s, g, \phi)$  at points  $y_j$  by  $(f_j, s_j, g_j, \phi_j)$ . As in Section 4.5, we write the finite-difference approximations of Eqs. (5.6.1) for the midpoint  $y_{j-\frac{1}{2}}$  using centered-difference derivatives to obtain

$$\phi_j - \phi_{j-1} - c_3(f_j + f_{j-1}) = (r_1)_j = 0 \quad (5.6.3a)$$

$$f_j - f_{j-1} - c_3(s_j + s_{j-1}) - c_1(\phi_j + \phi_{j-1}) = (r_3)_{j-1} = 0 \quad (5.6.3b)$$

$$s_j - s_{j-1} - c_3(g_j + g_{j-1}) = (r_2)_j = 0 \quad (5.6.3c)$$

$$g_j - g_{j-1} - c_4(s_j + s_{j-1}) - c_2(\phi_j + \phi_{j-1}) = (r_4)_{j-1} = 0 \quad (5.6.3d)$$

Here, with  $h_{j-1}$  denoting  $y_j - y_{j-1}$ ,

$$c_3 = \frac{h_{j-1}}{2}, \quad c_1 = \xi_1^2 c_3, \quad c_2 = -(\xi_3)_{j-\frac{1}{2}} c_3, \quad c_4 = (\xi_2^2)_{j-\frac{1}{2}} c_3 \quad (5.6.4)$$

As in the procedure for solving the boundary-layer equations, Eqs. (5.6.3) are again written in a sequence which ensures that the  $A_0$ -matrix in Eq. (4.5.24) is not singular.

Equations (5.6.3) are imposed for  $j = 1, 2, \dots, J$  and additional conditions at  $j = 0$  and  $j = J$  are obtained from the appropriate boundary conditions which, for an external flow, follow from Eqs. (5.6.2) and can be written as

$$\phi_0 = (r_1)_0 = 0, \quad f_0 = (r_2)_0 = 0 \quad (5.6.5a)$$

$$f_J + \tilde{c}_3 s_J + \tilde{c}_1 \phi_J = (r_3)_J = 0, \quad g_J + \tilde{c}_4 s_J = (r_4)_J = 0 \quad (5.6.5b)$$

where now

$$\tilde{c}_3 = \frac{1}{\xi_1 + \xi_2}, \quad \tilde{c}_1 = \xi_1, \quad \tilde{c}_4 = \xi_2 \quad (5.6.6)$$

The difference equations (5.6.3) and (5.6.5) have trivial solutions  $f_j = s_j = \phi_j = g_j = 0$  for all  $j$  and we shall use the iteration procedure described below to find the special parameter values for which nontrivial solutions exist.

Since the Orr–Sommerfeld equation and the boundary conditions are homogenous, the trivial solution  $\phi(y) = 0$  is valid for all values of  $\alpha, \beta, \omega$  and  $R$ . For this reason to compute the eigenvalues and the eigenfunctions we first replace the boundary condition  $\phi'(0) = 0$  (that is  $f_0 = 0$ ) of Eq. (5.6.5) by  $\phi''(0) = 1$ ,

that is  $s_0 = 1$ . Now the difference equations have a non-trivial solution since  $\phi''(0) \neq 0$  and we seek to adjust or to determine parameter values so that the original boundary condition is satisfied. This is achieved by an iteration scheme based on Newton's method. Specifically, we first write the wall boundary conditions

$$\phi_0 = (r_1)_0 = 0, \quad s_0 = (r_2)_0 = 1 \quad (5.6.7)$$

and the edge boundary conditions in Eq. (5.6.5b) and Eq. (5.6.3) in matrix-vector form as in Eq. (4.5.23), that is,

$$A\vec{\delta} = \vec{r} \quad (4.5.23)$$

where

$$\vec{\delta}_j = \begin{vmatrix} \phi_j \\ s_j \\ f_j \\ g_j \end{vmatrix}, \quad \vec{r}_j = \begin{vmatrix} (r_1)_j \\ (r_2)_j \\ (r_3)_j \\ (r_4)_j \end{vmatrix} \quad (5.6.8)$$

and the  $A_j$ ,  $B_j$ ,  $C_j$  denote  $4 \times 4$  matrices given by

$$A_0 \equiv \begin{vmatrix} 1 & 0 & 0 & 0 \\ 0 & 1 & 0 & 0 \\ (c_1)_1 & (c_3)_1 & 1 & 0 \\ (c_2)_1 & (c_4)_1 & 0 & 1 \end{vmatrix}, \quad A_j \equiv \begin{vmatrix} 1 & 0 & -(c_3)_j & 0 \\ 0 & 1 & 0 & -(c_3)_j \\ (c_1)_{j+1} & (c_3)_{j+1} & 1 & 0 \\ (c_2)_{j+1} & (c_4)_{j+1} & 0 & 1 \end{vmatrix}, \quad 1 \leq j \leq J-1$$

$$A_J = \begin{vmatrix} 1 & 0 & -(c_3)_J & 0 \\ 0 & 1 & 0 & -(c_3)_J \\ (\tilde{c}_1) & (\tilde{c}_3) & 1 & 0 \\ 0 & (\tilde{c}_4) & 0 & 1 \end{vmatrix},$$

$$B_j = \begin{vmatrix} -1 & 0 & -(c_3)_j & 0 \\ 0 & -1 & 0 & -(c_3)_j \\ 0 & 0 & 0 & 0 \\ 0 & 0 & 0 & 0 \end{vmatrix} \quad 1 \leq j \leq J$$

$$C_j = \begin{vmatrix} 0 & 0 & 0 & 0 \\ 0 & 0 & 0 & 0 \\ (c_1)_{j+1} & (c_3)_{j+1} & -1 & 0 \\ (c_2)_{j+1} & (c_4)_{j+1} & 0 & -1 \end{vmatrix} \quad 0 \leq j \leq J-1 \quad (5.6.9)$$

We note from the difference equations defined by Eqs. (5.6.3) and (5.6.5) that the solution of Eq. (4.5.23) depends upon the four parameters  $\alpha$ ,  $\beta$ ,  $\omega$  and  $R$  and we can denote this dependence by writing

$$\vec{\delta} = \vec{\delta}(\alpha, \beta, \omega, R) \quad (5.6.10)$$

Recalling that  $\alpha$  and  $\beta$  are complex, and that  $\omega$  is real in spatial-amplification theory, the above relation implies that the solution of Eq. (4.5.23) depends upon six scalars. With any four of these scalars fixed, the remaining scalars can

be computed in such a way that the missing boundary condition  $\phi'(0) = 0$  is satisfied. In our finite-difference notation, this corresponds to the condition

$$f_0(\alpha, \beta, \omega, R) = 0 \quad (5.6.11)$$

The preceding formulation of the numerical method is general but the procedure for computing eigenvalues and eigenfunctions is different for two- and three-dimensional flows. In the following subsections we consider two-dimensional flows and postpone the discussion on three-dimensional flows to Chapters 8 and 14.

### 5.6.1 Eigenvalue Procedure for Two-Dimensional Flows

For a two-dimensional flow, the parameters  $\xi_1$  to  $\xi_3$  in Eqs. (5.6.1) and (5.6.2) are given by

$$\xi_1^2 = \alpha^2, \quad \xi_2^2 = \alpha^2 + iR(\alpha u - \omega), \quad \xi_3 = iR\alpha u'' \quad (5.6.12)$$

and Eq. (5.6.11) can be written as

$$f_0(\alpha, \omega, R) = 0 \quad (5.6.13)$$

To discuss the solution procedure for Eq. (5.6.13), let us consider the computation of  $\alpha_r$ ,  $\omega$  and  $R$  for a specified value of  $\alpha_i$ . In this case since  $\omega$  is real, the solution of Eq. (5.6.13) can be obtained by fixing one parameter and solving for the remaining two. The choice of the fixed parameter depends on the slope of  $d\alpha_r/dR$  so that, for example, it is more convenient to fix  $R$  and solve for  $\alpha_r$  and  $\omega$  away from the critical Reynolds number where  $d\alpha_r/dR$  is small. In the region of critical Reynolds number,  $d\alpha_r/dR$  is large and increases as  $R \rightarrow R_{cr}$  and it is necessary to specify  $\alpha_r$  and solve for  $\omega$  and  $R$ . To explain these points further, consider the *eigenvalue problem corresponding to small  $d\alpha_r/dR$* . Since  $f_0$  is complex,  $\alpha_i$  is given and  $R$  is fixed, Eq. (5.6.13) represents two equations with two unknowns  $(\alpha_r, \omega)$  and the equations can be solved by Newton's method. Specifically, if  $(\alpha^\nu, \omega^\nu)$  are the  $\nu$ -th iterates, the  $(\nu + 1)$ -th iterates are determined by using

$$\alpha_r^{\nu+1} = \alpha_r^\nu + \delta\alpha_r^\nu \quad (5.6.14a)$$

$$\omega^{\nu+1} = \omega^\nu + \delta\omega^\nu \quad (5.6.14b)$$

in Eq. (5.6.13), expanding  $f_0$  about  $\alpha_r^\nu$  and  $\omega^\nu$  and retaining only linear terms in the expansion. This gives the linear system by taking  $f_r^{\nu+1} = 0$  and  $f_i^{\nu+1} = 0$

$$f_r^\nu + \left( \frac{\partial f_r}{\partial \alpha_r} \right)^\nu \delta\alpha_r^\nu + \left( \frac{\partial f_r}{\partial \omega} \right)^\nu \delta\omega^\nu = 0 \quad (5.6.15a)$$

$$f_i^\nu + \left( \frac{\partial f_i}{\partial \alpha_r} \right)^\nu \delta\alpha_r^\nu + \left( \frac{\partial f_i}{\partial \omega} \right)^\nu \delta\omega^\nu = 0 \quad (5.6.15b)$$

Here, for convenience, we have dropped the subscript 0 on  $f$  and used  $r$  and  $i$  to denote the real and imaginary parts of  $f$  at the wall. The solution of Eqs. (5.6.15) is,

$$\delta\alpha_r^\nu = \frac{1}{\Delta_0} \left[ f_i^\nu \left( \frac{\partial f_r}{\partial \omega} \right)^\nu - f_r^\nu \left( \frac{\partial f_i}{\partial \omega} \right)^\nu \right] \quad (5.6.16a)$$

$$\delta\omega^\nu = \frac{1}{\Delta_0} \left[ f_r^\nu \left( \frac{\partial f_i}{\partial \alpha_r} \right)^\nu - f_i^\nu \left( \frac{\partial f_r}{\partial \alpha_r} \right)^\nu \right] \quad (5.6.16b)$$

where

$$\Delta_0 = \left( \frac{\partial f_r}{\partial \alpha_r} \right)^\nu \left( \frac{\partial f_i}{\partial \omega} \right)^\nu - \left( \frac{\partial f_i}{\partial \alpha_r} \right)^\nu \left( \frac{\partial f_r}{\partial \omega} \right)^\nu \quad (5.6.16c)$$

To evaluate the derivatives of  $f_r$  and  $f_i$  with respect to  $\alpha_r$  and  $\omega$ , we need only to differentiate Eq. (4.5.23) and, since the vector  $\vec{r}$  is independent of  $\alpha_r$  and  $\omega$ , we get:

$$A \left( \frac{\partial \vec{\delta}}{\partial \alpha_r} \right)^\nu = - \left( \frac{\partial A}{\partial \alpha_r} \right)^\nu \vec{\delta}^\nu = \vec{r} \quad (5.6.17a)$$

$$A \left( \frac{\partial \vec{\delta}}{\partial \omega} \right)^\nu = - \left( \frac{\partial A}{\partial \omega} \right)^\nu \vec{\delta}^\nu = \vec{r} \quad (5.6.17b)$$

We shall refer to the above equations as *the variational equations of Eq. (4.5.23) with respect to  $\alpha_r$  and  $\omega$* , respectively. Thus, to obtain the required derivatives, we need to solve only two linear systems with the same coefficient matrix  $A$  already computed and factored for Eq. (4.5.23). The vectors on the right-hand side of Eqs. (5.6.17a) are determined from Eqs. (5.6.3), (5.6.5b) and (5.6.7). For Eq. (5.6.17a)  $(r_1)_j = (r_2)_j = 0$  for  $0 \leq j \leq J$ , but  $(r_3)_j$  and  $(r_4)_j$  for  $1 \leq j \leq J$  are given by

$$(r_3)_{j-1} = 2 \left( \frac{\partial c_1}{\partial \alpha_r} \right) \phi_{j-\frac{1}{2}} \quad (5.6.18a)$$

$$(r_4)_{j-1} = 2 \left( \frac{\partial c_4}{\partial \alpha_r} \right) s_{j-\frac{1}{2}} + 2 \left( \frac{\partial c_2}{\partial \alpha_r} \right) \phi_{j-\frac{1}{2}} \quad (5.6.18b)$$

$$(r_3)_J = - \left( \frac{\partial \tilde{c}_3}{\partial \alpha_r} \right)_J s_J - \left( \frac{\partial \tilde{c}_1}{\partial \alpha_r} \right)_J \phi_J \quad (5.6.18c)$$

$$(r_4)_J = - \left( \frac{\partial \tilde{c}_4}{\partial \alpha_r} \right)_J s_J \quad (5.6.18d)$$

For Eq. (5.6.17b), again  $(r_1)_j = (r_2)_j = 0$  for  $0 \leq j \leq J$ , but with  $c_1$ ,  $c_2$  and  $c_3$  being independent of  $\omega$  for  $j \leq J-1$ , the coefficients  $(r_3)_j$  and  $(r_4)_j$  for  $1 \leq j \leq J$  are given by

$$(r_3)_{j-1} = 0 \quad (5.6.19a)$$

$$(r_4)_{j-1} = 2 \left( \frac{\partial c_4}{\partial \omega} \right) s_{j-\frac{1}{2}} \quad (5.6.19b)$$

$$(r_3)_J = - \left( \frac{\partial \tilde{c}_3}{\partial \omega} \right)_J s_J \quad (5.6.19c)$$

$$(r_4)_J = - \left( \frac{\partial \tilde{c}_4}{\partial \omega} \right)_J s_J \quad (5.6.19d)$$

To summarize one part of the iteration process for a fixed value of  $R$  and for assumed values of  $\alpha_r$  and  $\omega$ , we solve Eq. (4.5.23). If the initial estimates of  $\alpha_r$  and  $\omega$  satisfy Eq. (5.6.13) and that  $f_0 = 0$ , then of course there is no need to compute new values of  $\alpha_r$  and  $\omega$ . On the other hand, if  $f_0 \neq 0$ , then new estimates of  $\alpha_r$  and  $\omega$  are obtained by Newton's method. With the right-hand side of Eqs. (5.6.17a,b) given by Eqs. (5.6.18) and (5.6.19), we solve Eqs. (5.6.17a,b) to compute  $\partial f / \partial \alpha_r$  and  $\partial f / \partial \omega$ . Then we compute  $\delta \alpha_r$  and  $\delta \omega$  from Eqs. (5.6.16) and insert them in Eqs. (5.6.14) so that we can solve Eq. (4.5.23) with new estimates of  $\alpha_r$  and  $\omega$  and satisfy Eq. (5.6.13). This process is repeated until the increments  $|\delta \omega|$  and  $|\delta \alpha_r|$  are less than a specified tolerance parameter.

Once a solution to Eq. (5.6.13) is obtained at a specified Reynolds number  $R_0$ , we can determine  $(\partial \alpha_r / \partial R)_0$  and  $(\partial \omega / \partial R)_0$  at  $R = R_0$  and decide whether we are going to solve the eigenvalue problem in which we compute  $(\alpha_r, \omega)$  for a fixed  $R$ , as we did above, or compute  $(R, \omega)$  for a fixed  $\alpha_r$ . For this purpose we take the total derivative of Eq. (5.6.13) with respect to  $R$  and after separating the real and imaginary parts of the resulting expression, we get:

$$\left( \frac{\partial f_r}{\partial \alpha_r} \right)_0 \left( \frac{\partial \alpha_r}{\partial R} \right)_0 + \left( \frac{\partial f_r}{\partial \omega} \right)_0 \left( \frac{\partial \omega}{\partial R} \right)_0 = - \left( \frac{\partial f_r}{\partial R} \right)_0 \quad (5.6.20a)$$

$$\left( \frac{\partial f_i}{\partial \alpha_r} \right)_0 \left( \frac{\partial \alpha_r}{\partial R} \right)_0 + \left( \frac{\partial f_i}{\partial \omega} \right)_0 \left( \frac{\partial \omega}{\partial R} \right)_0 = - \left( \frac{\partial f_i}{\partial R} \right)_0 \quad (5.6.20b)$$

It follows from Eqs. (5.6.20) that

$$\left( \frac{\partial \alpha_r}{\partial R} \right)_0 = \frac{1}{\Delta_0} \left[ \left( \frac{\partial f_i}{\partial R} \right)_0 \left( \frac{\partial f_r}{\partial \omega} \right)_0 - \left( \frac{\partial f_r}{\partial R} \right)_0 \left( \frac{\partial f_i}{\partial \omega} \right)_0 \right] \quad (5.6.21a)$$

$$\left( \frac{\partial \omega}{\partial R} \right)_0 = \frac{1}{\Delta_0} \left[ \left( \frac{\partial f_r}{\partial R} \right)_0 \left( \frac{\partial f_i}{\partial \alpha_r} \right)_0 - \left( \frac{\partial f_i}{\partial R} \right)_0 \left( \frac{\partial f_r}{\partial \alpha_r} \right)_0 \right] \quad (5.6.21b)$$

where

$$\Delta_0 = \left( \frac{\partial f_r}{\partial \alpha_r} \right)_0 \left( \frac{\partial f_i}{\partial \omega} \right)_0 - \left( \frac{\partial f_r}{\partial \omega} \right)_0 \left( \frac{\partial f_i}{\partial \alpha_r} \right)_0 \quad (5.6.21c)$$

To evaluate the derivatives of  $f_r$  and  $f_i$  with respect to  $R$ , this time we differentiate Eq. (4.5.23) to obtain the variational equations with respect to  $R$ ,

$$A \left( \frac{\partial \vec{\delta}}{\partial R} \right)^\nu = - \left( \frac{\partial A}{\partial R} \right)^\nu \vec{\delta}^\nu = \vec{r} \quad (5.6.22)$$

The right hand side vectors of the above equation with  $(r_1)_j = (r_2)_j = 0$  for  $0 \leq j \leq J$ , and with  $(r_3)_j$  and  $(r_4)_j$  for  $1 \leq j \leq J$  are:

$$(r_3)_{j-1} = 0 \quad (5.6.23a)$$

$$(r_4)_{j-1} = 2 \left( \frac{\partial c_4}{\partial R} \right) s_{j-\frac{1}{2}} + 2 \left( \frac{\partial c_2}{\partial R} \right) \phi_{j-\frac{1}{2}} \quad (5.6.23b)$$

$$(r_3)_J = - \left( \frac{\partial \tilde{c}_3}{\partial R} \right)_J s_J \quad (5.6.23c)$$

$$(r_4)_J = - \left( \frac{\partial \tilde{c}_4}{\partial R} \right)_J s_J \quad (5.6.23d)$$

As before, with the coefficient matrix  $A$  already known, we now compute the relations in Eqs. (5.6.23) so that  $\partial f / \partial R$  can be obtained from the solution of Eq. (5.6.22). Since  $\partial f / \partial \alpha_r$  and  $\partial f / \partial \omega$  are already known from the solutions of Eqs. (5.6.17),  $\partial \alpha_r / \partial R$  and  $\partial \omega / \partial R$  can be computed from Eqs. (5.6.21) to decide on the choice of the eigenvalue procedure.

It should be mentioned that the values of  $\partial \alpha_r / \partial R$  and  $\partial \omega / \partial R$  can also be very useful in estimating the initial values of  $\alpha_r$  and  $\omega$  at a different Reynolds number where new sets of  $\alpha_r$  and  $\omega$  are to be obtained. To discuss this point further, we expand  $\alpha_r$  and  $\omega$  by Taylor's series and by retaining only the first term, we write

$$\alpha_r = (\alpha_r)_0 + \left( \frac{\partial \alpha_r}{\partial R} \right)_0 \delta R \quad (5.6.24a)$$

$$\omega = \omega_0 + \left( \frac{\partial \omega}{\partial R} \right)_0 \delta R \quad (5.6.24b)$$

where  $\delta R = R - R_0$  and subscript 0 denotes the values of  $\alpha_r$  and  $\omega$  at  $R = R_0$ .

If the slope  $\partial \alpha_r / \partial R$  is greater than a specified quantity, then the strategy of computing the eigenvalues for the specified value of  $\alpha_i$  needs to be changed. This can be done by incrementing  $\alpha_r$  by small specified values and, for each value,  $\omega$  and  $R$  that satisfies Eq. (5.6.13) are computed. As in the procedure that led to Eqs. (5.6.15), we now expand  $f$  in Eq. (5.6.13) about  $\omega^\nu$  and  $R^\nu$  and retain only linear terms in the expansion,

$$f_r^\nu + \left( \frac{\partial f_r}{\partial \omega} \right)^\nu \delta \omega^\nu + \left( \frac{\partial f_r}{\partial R} \right)^\nu \delta R^\nu = 0 \quad (5.6.25a)$$

$$f_i^\nu + \left( \frac{\partial f_i}{\partial \omega} \right)^\nu \delta \omega^\nu + \left( \frac{\partial f_i}{\partial R} \right)^\nu \delta R^\nu = 0 \quad (5.6.25b)$$

Solving for  $\delta \omega^\nu$  and  $\delta R^\nu$ , we obtain essentially the same equations as those given by Eqs. (5.6.15) if we replace  $\alpha_r$  by  $R$ ,

$$\delta R^\nu = \frac{1}{\Delta_0} \left[ f_i^\nu \left( \frac{\partial f_r}{\partial \omega} \right)^\nu - f_r^\nu \left( \frac{\partial f_i}{\partial \omega} \right)^\nu \right] \quad (5.6.26a)$$

$$\delta \omega^\nu = \frac{1}{\Delta_0} \left[ f_r^\nu \left( \frac{\partial f_i}{\partial R} \right)^\nu - f_i^\nu \left( \frac{\partial f_r}{\partial R} \right)^\nu \right] \quad (5.6.26b)$$

where now

$$\Delta_0 = \left( \frac{\partial f_r}{\partial R} \right)^\nu \left( \frac{\partial f_i}{\partial \omega} \right)^\nu - \left( \frac{\partial f_i}{\partial R} \right)^\nu \left( \frac{\partial f_r}{\partial \omega} \right)^\nu \quad (5.6.26c)$$

To find the eigenvalues at a new chosen value of  $\alpha_r$ , we may again obtain better estimates of  $\omega$  and  $R$  by writing

$$R = R_0 + \left( \frac{\partial R}{\partial \alpha_r} \right)_0 \delta \alpha_r \quad (5.6.27a)$$

$$\omega = \omega_0 + \left( \frac{\partial \omega}{\partial \alpha_r} \right)_0 \delta \alpha_r \quad (5.6.27b)$$

However, the additional work required to compute  $\partial \omega / \partial \alpha_r$  may not justify this advantage since the calculations are being performed near the critical Reynolds number region for small increments in  $\alpha_r$  which make the initial guess and the eigenvalue problem easier.

The calculation of  $\omega$  and  $R$  for a specified value of  $\alpha_r$  is very similar to the one in which  $\omega$  and  $\alpha_r$  are computed for a specified  $R$ . With initial estimates of  $\omega$  and  $R$ , Eq. (4.5.23) can be solved to see whether Eq. (5.6.13) is satisfied. If not, new estimates are computed by using Newton's method. Equations similar to (5.6.17b) and (5.6.22) are solved to get  $\partial f / \partial \omega$  and  $\partial f / \partial R$ , respectively, and then new increments in  $R$  and  $\omega$  are obtained from the solution of Eqs. (5.6.26). The procedure is repeated until convergence, when, for example,  $|\delta \omega|$  and  $|\delta R|$  become less than a specified tolerance parameter.

## 5.6.2 Eigenvalue Procedure for Transition

The eigenvalue procedure for computing  $\alpha$  needed to predict transition with the  $e^n$ -method for specified values of  $\omega$  and  $R$  is analogous to that described in the previous subsection. In this case, Eq. (5.6.13) is expanded with the Taylor series rather than Eqs. (5.6.15), and linear terms are retained to give

$$f_r^\nu + \left( \frac{\partial f_r}{\partial \alpha_r} \right)^\nu \delta \alpha_r^\nu + \left( \frac{\partial f_r}{\partial \alpha_i} \right)^\nu \delta \alpha_i^\nu = 0 \quad (5.6.28a)$$

$$f_i^\nu + \left( \frac{\partial f_i}{\partial \alpha_r} \right)^\nu \delta \alpha_r^\nu + \left( \frac{\partial f_i}{\partial \alpha_i} \right)^\nu \delta \alpha_i^\nu = 0 \quad (5.6.28b)$$

The solution of these equations is similar to those given by Eq. (5.6.16),

$$\delta \alpha_r^\nu = \frac{1}{\Delta_0} \left[ f_i^\nu \left( \frac{\partial f_r}{\partial \alpha_i} \right)^\nu - f_r^\nu \left( \frac{\partial f_i}{\partial \alpha_i} \right)^\nu \right] \quad (5.6.29a)$$

$$\delta \alpha_i^\nu = \frac{1}{\Delta_0} \left[ f_r^\nu \left( \frac{\partial f_i}{\partial \alpha_r} \right)^\nu - f_i^\nu \left( \frac{\partial f_r}{\partial \alpha_r} \right)^\nu \right] \quad (5.6.29b)$$

where

$$\Delta_0 = \left( \frac{\partial f_r}{\partial \alpha_r} \right)^\nu \left( \frac{\partial f_i}{\partial \alpha_i} \right)^\nu - \left( \frac{\partial f_i}{\partial \alpha_r} \right)^\nu \left( \frac{\partial f_r}{\partial \alpha_i} \right)^\nu \quad (5.6.29c)$$

Differentiation of Eq. (4.5.23) with respect to  $\alpha_r$  and  $\alpha_i$  leads to the derivatives of  $f_r$  and  $f_i$  with respect to  $\alpha_r$  and  $\alpha_i$ , and an equation identical to Eq. (5.6.17) with  $\omega$  replaced by  $\alpha_i$  is obtained. Again the vectors on the right-hand side of Eq. (5.6.17) are determined from Eqs. (5.6.3), (5.6.5) and (5.6.7), and  $(r_1)_j = (r_2)_j = 0$  for  $0 \leq j \leq J$ , and  $(r_3)_j$  and  $(r_4)_j$  for  $0 \leq j \leq J$  are given by Eqs. (5.6.18) with  $c_1, c_2, c_3$  and  $c_4$  now differentiated with respect to  $\alpha_r$  and  $\alpha_i$ , respectively.

## 5.7 Applications of STP

In Appendix B, Program 6, we present and describe a stability-transition program (STP) for calculating neutral stability curves and the onset of transition in two-dimensional external flows. Here we discuss its application to a sample of flows. In subsection 5.7.1 we consider the Blasius flow and use STP to calculate the eigenvalues on the lower branch of a neutral stability curve. In subsection 5.7.2 we use STP first to calculate the onset of transition on a flat plate flow and follow it with airfoil, ellipse and prolate spheroid flows.

STP assumes that velocity profiles  $u$  and  $u''$  at each  $x$ -station are calculated as a function of  $\eta$  with the boundary-layer program (BLP2) given also in Appendix B, Program 3. For convenience, the velocity  $u_0$  and length  $l$  in the Orr–Sommerfeld equation are chosen to correspond to the same velocity and length scales used in BLP2,

$$u_0 = u_e, \quad l = \sqrt{\frac{\nu x}{u_e}} = \frac{x}{\sqrt{R_x}} \quad (5.7.1)$$

so that the same grid in BLP2 can be used in STP. This means that  $u$  and  $u''$  in STP are related to the output of BLP2 by

$$u = f', \quad u'' = f''' \quad (5.7.2)$$

and the Reynolds number in the Orr–Sommerfeld equation is given by

$$R = \frac{u_0 l}{\nu} = \sqrt{R_x} \quad (5.7.3)$$

The parameter  $f'''$  can be obtained either by differentiating  $f''$  with respect to  $\eta$  or from the finite-differenced momentum equation, Eq. (4.5.15) which for laminar flow can be written as

$$v'_j \equiv (f'''_j)^n = -\alpha_1(fv)_j^n + \alpha_2(u_j^2)_n - \alpha_n(v_j^{n-1}f_j^n - f_j^{n-1}v_j^n) + R_j^{n-1} \quad (5.7.4)$$

where  $R_j^{n-1}$  is given by Eq. (4.5.16a).

With boundary-layer profiles known at each  $x$ -station, the stability calculations can be started at any  $x$ -station where the critical Reynolds number,  $R_{cr}$  is less than the Reynolds number used in the boundary-layer calculations. For external flows, an estimate of  $R_{\delta^*}$  can be obtained from Fig. 5.5 with  $R_{\delta^*}$  known from the boundary-layer calculations and included in the output subroutine.

The calculations for transition are first performed for a neutral stability curve at the specified  $x$ -location where  $R(\equiv \sqrt{R_x})$  is known. The calculation of  $\omega$  and  $\alpha$  requires initial estimates for the velocity profiles of  $u$  and  $u''$ . A convenient procedure to achieve this is the continuation method discussed in [40] but, to retain a comparatively simple program, this is not part of the present description. The initial estimates of  $\omega$  and  $\alpha$  for a given  $R$  can be obtained for Blasius flow.

To calculate the location of the onset of transition, it is usually sufficient to perform neutral stability calculations at four  $x$ -locations so that four frequencies can be computed and amplification rates determined on four curves with constant dimensional frequencies. While STP is general and can be used for external flows with suction and injection as well as free shear flows such as jets and wakes, changes are required to accommodate boundary conditions and provide better estimates of initial eigenvalues where required. STP can also be used for external flows with heat transfer as discussed in [40].

### 5.7.1 Stability Diagrams for Blasius Flow

The stability diagrams for Falkner–Skan flows, similar to those given in Fig. 5.4, can be constructed by using BLP2 and STP. For a given external velocity distribution (constant for Blasius flow), BLP2 generates the laminar velocity profiles so that  $ETA(J)$ ,  $U(J,2)$  and  $V(J,2)$ ,  $J = 1, \dots, NP$ , can be saved from the MAIN program in a format compatible with the READ statement of subroutine VELPRO.

For the neutral stability diagrams, the calculations can be performed at a sufficiently high Reynolds number by specifying initial estimates of  $\alpha_r$  and  $\omega$ . Once a solution is obtained at one Reynolds number, the calculations for other Reynolds numbers can be obtained with the procedure of subsection 5.6.1. The same procedure can also be used for lower Reynolds numbers provided  $d\alpha_r/dR$  is small. When this is not the case,  $\alpha_r$  is incremented by small specified values and  $\omega$  and  $R$  are computed to satisfy Eq. (5.6.13). STP is written for the case of small  $d\alpha_r/dR$  and needs to be changed when  $d\alpha_r/dR$  becomes large.

To demonstrate the use of STP, we consider the Blasius flow and calculate the eigenvalues  $\alpha_r$  and  $\omega$  at four  $x$ -locations. We take  $u_e = 160$  ft/sec,  $R_L = 5 \times 10^6$ ,  $L = 5$  ft and initiate the calculations at  $x_o = 0.54$  ft for  $\alpha_i = 0$ . This corresponds to a Reynolds number of  $R(\equiv \sqrt{R_x}) = 735$  which is sufficiently high for  $d\alpha_r/dR$  to be small, see Fig. 5.4a. Initial estimates of  $\alpha_r$  and  $\omega$  follow from Fig. 5.4, and

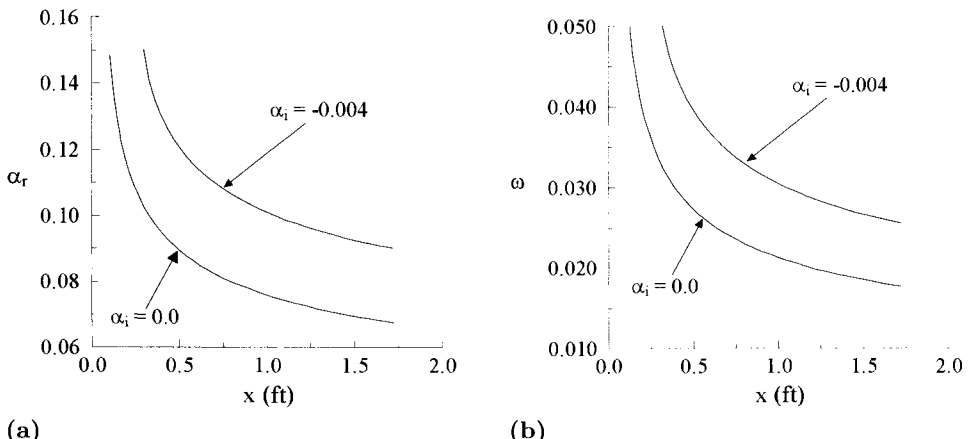


**Fig. 5.22.** Computed eigenvalues for Blasius flow, (a)  $\alpha_r$  and (b)  $\omega_r$ .

are 0.084 and 0.025 respectively, on the lower branch of the neutral stability curve at  $R = 800$ .

Figure 5.22 shows the computed eigenvalues  $\alpha_r$  and  $\omega$  along the surface distance  $x$  for values of  $\alpha_i$  equal to 0 and  $-0.004$ . The calculations for  $\alpha_i = -0.004$  are essentially the same as those for the neutral stability curve,  $\alpha_i = 0$ . The initial estimates of  $\alpha_r$  and  $\omega$  can be obtained from those corresponding to  $\alpha_i = 0$  provided that  $\Delta\alpha_i$  is small. If this is not the case, then it is best to divide the increment in  $\Delta\alpha_i$  to small values and perform the stability calculations for each value of  $\alpha_i$  until the desired value of  $\alpha_i$  is reached.

### 5.7.2 Transition Prediction

To demonstrate the prediction of the onset of transition location with the  $e^n$ -method, we first apply STP to a zero-pressure gradient flow and follow it with the airfoil, ellipse and prolate spheroid flows discussed in Section 4.6.

#### Flat-Plate Flow

The zero-pressure gradient flow is identical to the one in the previous section except that now the stability calculations are performed to compute  $\alpha$ . With dimensional frequencies known at four  $x$ -locations, the amplification rate calculations are performed for frequencies of 902, 753, 641 and 581 Hz, Fig. 5.23a. The  $n$ -values are obtained from Eq. (5.4.8) with  $x_o$  corresponding to each value of  $x$  in the neutral stability curve. Figure 5.23b, which is the same as Fig. 5.9, shows the envelope of the amplification rates (dashed line) and indicates that for a value of  $n = 8$ , the onset of transition takes place at  $x = 2.8$  ft, or at a Reynolds number of  $R_x = 2.8 \times 10^6$ .

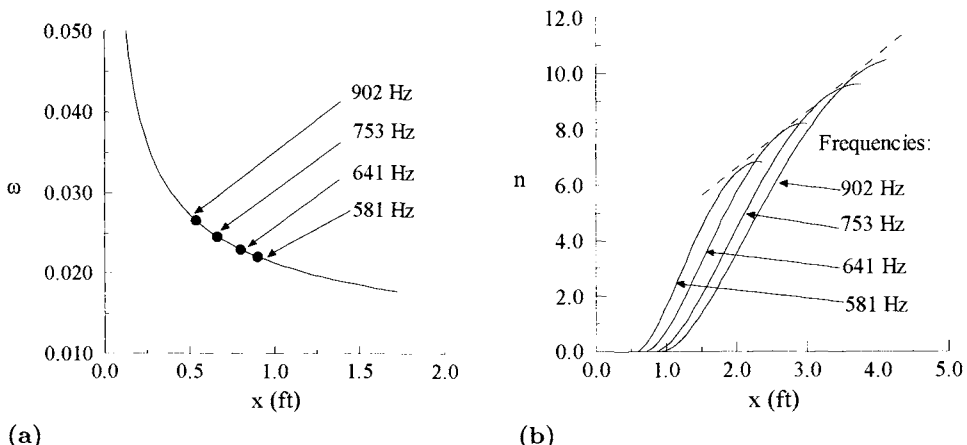


**Fig. 5.23.** Transition calculation for a flat plate flow, (a) origin of the disturbances on neutral curve and (b) integrated amplification rates.

### Airfoil Flow

The procedure for determining the onset of transition location on an airfoil is similar to the procedure used for the flat plate flow discussed above. To demonstrate this, we consider an NACA 0012 airfoil at two chord Reynolds numbers,  $R_c = 10^6$  and  $3 \times 10^6$ . For the external velocity distribution obtained from the HSPM computer program given in the accompanying CD-ROM, Program 4, the laminar velocity profiles are computed with BLP2 for  $\alpha = 0^\circ$ ,  $2^\circ$  and  $4^\circ$ . The neutral stability calculations are then performed for each Reynolds number and angle of attack. These calculations were then followed by amplification rate calculations for each frequency computed on the neutral stability curve. For each calculation, the transition location is determined with respect to the surface distance along the perimeter of the airfoil measured from the stagnation point and the corresponding  $x/c$  location is calculated.

Table 5.2 presents a summary of the calculated transition locations at three angles of attack and two chord Reynolds numbers for  $n = 8$ . The results show that with increasing angle of attack, since the adverse pressure gradient becomes

**Table 5.2.** Onset of transition locations on the upper surface of an NACA 0012 airfoil at two Reynolds numbers and three angles of attack.

$\alpha$	$0^\circ$	$2^\circ$	$4^\circ$
$R_c$	$(s/c)_{tr} - (x/c)_{tr}$	$(s/c)_{tr} - (x/c)_{tr}$	$(s/c)_{tr} - (x/c)_{tr}$
$1 \times 10^6$	0.505–0.49	0.33–0.31	0.16–0.13
$3 \times 10^6$	0.355–0.34	0.21–0.19	0.10–0.075

stronger, the transition location moves upstream. The results also show that with increasing Reynolds number, the transition location moves upstream.

### Ellipse Flow

The determination of the onset of transition location on the ellipse flow discussed in Section 4.6, is similar to the previous two examples discussed above. Again, the laminar boundary-layer calculations are performed for  $R_{2a} = 10^6$  and  $10^7$  using the BLP2 program for the specified external velocity distribution and these are followed by the stability/transition calculations with STP. For  $R_{2a} = 10^6$ , the maximum  $n$ -factor that can be computed before reaching the laminar separation point is less than 8. This suggests that the transition location occurs very close to laminar separation ( $x/2a = 0.85$ ). For  $R_{2a} = 10^7$ , the transition location is computed at  $x/2a = 0.455$  or  $s/2a = 0.49$ .

Figure 5.24 shows the variation of the wall shear  $f_w''$  with axial distance  $x/2a$  for two Reynolds numbers computed with BLP2 for both laminar and turbulent flows.

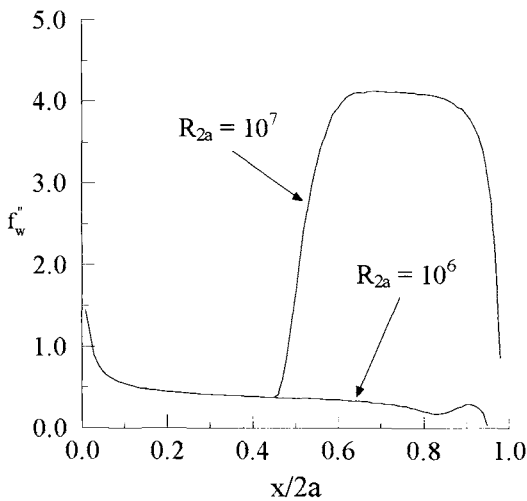


**Fig. 5.24.** Wall shear parameter,  $f_w'' = (c_f/2)\sqrt{R_x}$ , variation on the ellipse with axial distance  $x/2a$ .

### Prolate Spheroid Flow

STP can also be used to determine the transition on a prolate spheroid discussed in Section 4.6. At first the laminar velocity profiles are computed in Falkner–Skan–Mangler variables and are then expressed in Falkner–Skan variables. Assuming that  $r_0 \gg \delta$  so that  $r = r_0$ ,  $f'$  and  $f''$  are written as

$$f'(\eta) = \bar{f}'(\bar{\eta}) \quad (5.7.5)$$

$$f''(\eta) = \sqrt{\frac{\bar{x}}{x}} r_0^* \bar{f}''(\bar{\eta}) \quad (5.7.6)$$

where the quantities without bars are the Falkner–Skan variables used in the stability calculations and the quantities with bars are the Falkner–Skan–Mangler variables used in the boundary layer calculations. The dimensionless  $\eta$  and  $\bar{\eta}$  are related to each other by

$$\eta = \sqrt{\frac{\bar{x}}{x}} \frac{1}{r_0^*} \bar{\eta} \quad (5.7.7)$$

The stability calculations with  $f'$  and  $f''$  given by Eqs. (5.7.5) and the  $\eta$  grid by (5.7.6) are performed for  $R_a = 10^6$  and  $10^7$  and the amplification rates are determined. As in the ellipse flow, for  $R_a = 10^6$ , the maximum  $n$ -factor that can be computed before reaching the laminar separation point is less than 8, suggesting that the transition location occurs very close to laminar separation ( $x/a = 1.68$ ). For  $R_a = 10^7$ , the transition location is computed at  $x/a = 0.49$ ,  $s/a = 0.56$ , or  $\bar{x} = 0.0135$ .

Figure 5.25 shows the variation of the local skin-friction coefficient  $c_f$  and dimensionless displacement thickness  $\delta^*/a$  for two Reynolds numbers computed with modified BLP2.

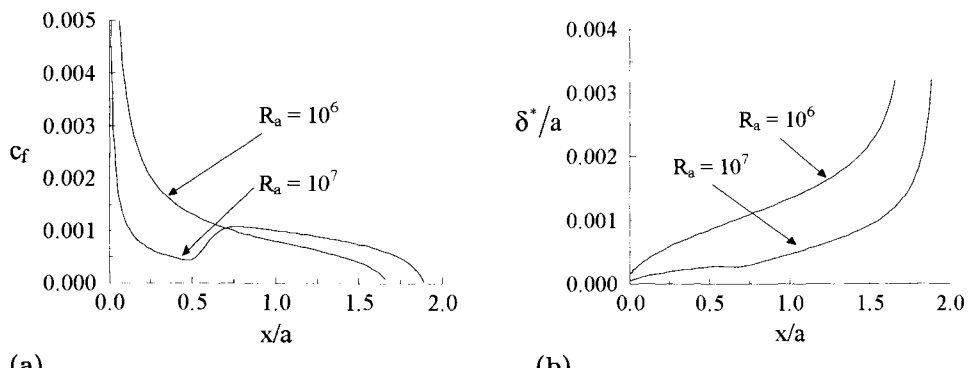


**Fig. 5.25.** Variation of (a) skin friction coefficient and (b) dimensionless displacement thickness,  $\delta^*/a$ , on a prolate spheroid at  $0^\circ$  incidence for  $R_a = 10^6$  and  $R_a = 10^7$ .

## References

- [1] Herbert, T., "Parabolized Stability Equations," Special Course on Progress in Transition Modeling, AGARD Report 793, April 1994.
- [2] Kleiser, L. and Zong, T.A., "Numerical Simulation of Transition in Wall Bounded Shear Flows," *Annual Review of Fluid Mechanics*, Vol. 23, pp. 495–538, 1991.
- [3] Emmons, H.W., "The Laminar-Turbulent Transition in a Boundary Layer, Pt. I.," *J. Aeronaut. Sci.*, Vol. 18, pp. 490–498, 1951.

- [4] Schubauer, G.B. and Skramstad, H., "Laminar Boundary-Layer Oscillations and Transition on a Flat Plate," NACA Rept. 909, 1948.
- [5] Schubauer, G.B. and Klebanoff, P.S., "Contributions on the Mechanics of Transition," NACA TN 3489, 1955.
- [6] Klebanoff, P.S., Tidstrom, K.D. and Sargent, L.R., "The Three-Dimensional Nature of Boundary-Layer Instability," *J. Fluid Mech.*, Vol. 12, p. 1, 1962.
- [7] Dhawan, S. and Narasimha, R., "Some Properties of Boundary-Layer Flow During the Transition from Laminar to Turbulent Motion," *J. Fluid Mech.*, Vol. 3, pp. 418–436, 1958.
- [8] Chen, K.K. and Thyson, N.A., "Extension of Emmons' Spot Theory to Flows on Blunt Bodies," *AIAA J.*, Vol. 9, pp. 821–825, 1971.
- [9] Cebeci, T., "Essential Ingredients of a Method for Low Reynolds-Number Airfoil," *AIAA J.*, Vol. 7, 1989, p. 1680.
- [10] Wazzan, A.R., "Spatial Stability of Tollmien-Schlichting Waves, Progress in Aerospace Sciences," Vol. 16, No. 2, pp. 99–127, Pergamon Press, N.Y., 1975.
- [11] Wazzan, A.R., Okamura, T.T. and Smith, A.M.O., "Spatial and Temporal Stability Charts for the Falkner-Skan Boundary-Layer Profiles," Douglas Aircraft Co. Report DAC-67086, 1968.
- [12] Michel, R., "Etude de la Transition sur les Profils d'Aile, Etablissement d'un Critère de Détermination du Point de Transition et Calcul de la Trainée de Profil Incompressible," ONERA Rept. 1/1578A, 1951.
- [13] Smith, A.M.O., "Transition, Pressure Gradient, and Stability Theory," *Proceedings IX International Congress of Applied Mechanics*, Brussels, Vol. 4, pp. 234–24, 1956.
- [14] Cebeci, T., *Analysis of Turbulent Flows*, Elsevier, London, 2004.
- [15] Granville, P.S., "The Calculation of the Viscous Drag of Bodies of Revolution," David W. Taylor Model Basin Rept. 849, 1953.
- [16] Arnal, D., Habiballah, M., and Coustols, E., "Laminar Instability Theory and Transition Criteria in Two- and Three-Dimensional Flows," La Rech. Aérospace No. 1984-2, 1984.
- [17] Van Ingen, J.L., "A Suggested Semi-empirical Method for the Calculation of the Boundary-Layer Region," Report No. VTH71, VTH74, Delft, Holland, 1956.
- [18] Arnal, D., "Boundary Layer Transition, Predictions Based on Linear Theory," AGARD Rept. No. 793, 1994.
- [19] Mack, L.M., "Transition and Laminar Instability. Jet Propulsion Laboratory Pub.," pp. 77–15, Pasadena, CA, 1977.
- [20] Wazzan, A.R., Gazley, C. Jr. and Smith, A.M.O., "H-R<sub>x</sub> Method for Predicting Transition," *AIAA J.*, Vol. 19, no. 6, pp. 810–812, 1981.
- [21] Dryden, H.L., "Transition from Laminar to Turbulent Flow at Subsonic and Supersonic Speeds," Proceedings of the Conference on High-speed Aeronautics, January 1955.
- [22] Hall, A.A. and Hislop, G.S., "Experiments on the Transition of the Laminar Boundary Layer on a Flat Plate," Brit. Aero. Res. Council Reports and Memoranda, No. 1843, 1938.
- [23] Wells, C.S., "Effect of Free Stream Turbulence on Boundary Layer Transition," *AIAA Journal*, Vol. 5, no. 1, 1967.
- [24] Spangler, J.G. and Wells, C.S., "Effect of Free Stream Disturbances on Boundary Layer Transition," *AIAA Journal*, Vol. 5, no. 1, 1967.
- [25] Cousteix, J. and Pailhas, G., "Etude exploratoire d'un processus de transition laminaire-turbulent au voisinage du décollement d'une couche limite laminaire," La Rech. Aérospace No. 1979-3, 1979.
- [26] Kachanov, Y.S., "Physical Mechanisms of Laminar Boundary-Layer Transition," *Ann. Rev. Fluid Mech.*, Vol. 26, pp. 411–82, 1994.
- [27] Wazzan, A.R., Okamura, T., and Smith, A.M.O., "The Stability of Water Flow Over Heated and Cooled Flat Plate," *J. Heat Transfer*, Vol. 90, pp. 109–114, 1968.
- [28] Lowell, R.L. and Reshotko, E., "Numerical Study of the Stability-Heated Water Boundary Layer," Case Western Reserve University, FTAS TR 73-93, January 1974.

- [29] Cebeci, T., *Convective Heat Transfer*, Horizons Publ., Long Beach, Calif. and Springer, Heidelberg, 2003.
- [30] Lee, D.Q., "Stability and Transition Characteristics of Water Boundary Layers with Heat Transfer," Master's Thesis, Mechanical Eng. Dept., California State University, Long Beach, 1985.
- [31] Bushnell, D.M. and Hefner, J.N., *Viscous Drag Reduction*, AIAA "Progress in Aero-nautics and Astronautics" Series, 1989.
- [32] Schlichting, H., *Boundary-Layer Theory*, McGraw-Hill, New York, 1981.
- [33] Liepmann, H.W., "Investigation of Boundary Layer Transition on Concave Walls," NACA Wartime Report W-87, 1945.
- [34] Dryden, H.L., "Recent Advances in the Mechanics of Boundary Layer Flow," In: *Advances in Appl. Mech. I*, pp. 1–40, ed. R. von Mises and Th. von Kármán, New York, 1948.
- [35] Forest, A.E., "Engineering Predictions of Transitional Boundary-Layers," AGARD CP 224, 1977.
- [36] Herbert, T., "On the Stability of the Boundary Layer along a Concave Wall," *Arch. Mech. Stosowanej*, Vol. 28, 1976.
- [37] Saric, W.S., "Görtler Vortices," *Ann. Rev. Fluid Mech.*, p. 26, 1994.
- [38] Floryan, J., "On the Görtler Instability of Boundary Layers," *Prog. Aerospace Sci.*, Vol. 28, 1991.
- [39] Floryan, J. and Saric, W.S., "Stability of Görtler Vortices in Boundary Layers with Suction," AIAA Paper No. 79-1479, 1979.
- [40] Cebeci, T., *Stability and Transition: Theory and Application*, Horizons Publ., Long Beach, Calif., and Springer, Heidelberg, 2004.

## Problems

**5-1.** In order to illustrate an eigenvalue problem, consider

$$\frac{d^2y}{dx^2} + \alpha^2 y = 0 \quad 0 \leq x \leq 1$$

and its boundary conditions

$$y(0) = 0, \quad y(1) = 0$$

A trivial solution is  $y = 0$ , but non-trivial solutions (eigensolutions) exist for particular values of  $\alpha$  (eigenvalues). Determine the set of eigenvalues and the corresponding eigenfunctions.

**5-2. (a)** Consider a combination of two waves

$$f = A \cos(k_1 x - \omega_1 t) + A \cos(k_2 x - \omega_2 t) \quad (\text{P5.2.1})$$

and show that

$$f = B \cos(kx - \omega t) \quad (\text{P5.2.2})$$

with

$$B = 2A \cos(\Delta k x - \Delta \omega t)$$

$$\omega = \frac{\omega_1 + \omega_2}{2}, \quad k = \frac{k_1 + k_2}{2}$$

$$\Delta\omega = \frac{\omega_2 - \omega_1}{2}, \quad \Delta k = \frac{k_2 - k_1}{2}$$

(b) Assuming that  $\omega_1$  and  $\omega_2$  are close to each other and,  $k_1$  and  $k_2$  are also close to each other, plot qualitatively the function  $f$  in Eq. (P5.2.2) as a function of  $x$  for different values of  $t$ .

(c) Plot the locus of the maximum value of  $B$  in the plane  $(x, t)$  and show that this point travels with velocity  $\Delta\omega/\Delta k$ , called the group velocity.

If we consider a more general combination of waves

$$f = \int_{-\infty}^{+\infty} \hat{f}(k) e^{i(kx - \omega(k)t)} dk \quad (\text{P5.2.3})$$

in which the pulsation and the wave number are related through the dispersion relation  $\omega(k)$ , the group velocity is  $d\omega/dk$ . It can be shown that the energy is transported with the group velocity. The concept of group velocity is as important in wave theory as in studying the stability of laminar boundary-layers (see Section 11.3).

**5-3.** (a) With the definitions in Eq. (5.3.5) and parallel flow approximation, show that Eqs. (5.3.1) to (5.3.3) can be written in the form given by Eqs. (5.3.6) to (5.3.8).

(b) Show that with  $q$  in Eq. (5.3.9) corresponding to  $\hat{u}$ ,  $\hat{v}$ , and  $\hat{p}$ , the continuity and momentum equations given by Eqs. (5.3.6) to (5.3.8) can be written as

$$i\alpha\hat{u} + \frac{d\hat{v}}{dy} = 0 \quad (\text{P5.3.1})$$

$$\frac{d^2\hat{u}}{dy^2} - \alpha^2\hat{u} = iR \left[ (\alpha u - \omega)\hat{u} - i\hat{v}\frac{du}{dy} + \alpha\hat{p} \right] \quad (\text{P5.3.2})$$

$$\frac{d^2\hat{v}}{dy^2} - \alpha^2\hat{v} = iR \left[ (\alpha u - \omega)\hat{v} - i\frac{d\hat{p}}{dy} \right] \quad (\text{P5.3.3})$$

(c) For wall boundary-layer flows, Eqs. (5.3.6) to (5.3.8) or (P5.3.1) to (P5.3.3) are subject to the following boundary conditions at  $y = 0$

$$\hat{u} = \hat{v} = 0 \quad (\text{P5.3.4})$$

Show that  $\hat{u}$ ,  $\hat{v}$ , and  $\hat{p}$  behave exponentially as  $y \rightarrow \infty$  with a typical asymptotic representation

$$\hat{u} \sim A_1 e^{-\xi_1 y} + A_2 e^{-\xi_2 y} \quad (\text{P5.3.5})$$

where  $A_1$  and  $A_2$  are constants and  $\xi_1$  and  $\xi_2$  are defined by

$$\xi_1^2 = \alpha^2 \quad (\text{P5.3.6a})$$

$$\xi_2^2 = \alpha^2 + iR[\alpha u - \omega] \quad (\text{P5.3.6b})$$

with the restriction that their real parts are not negative.

**5-4.** The equations in Problem 5.3 can also be expressed in other forms. Show that if we represent the amplitude functions of the perturbation quantities  $u'$ ,  $v'$  and  $p'$  by  $f$ ,  $\phi$  and  $\Pi$ , respectively, and introduce them into Eqs. (P5.3.1) to (P5.3.3), we get

$$\frac{d\phi}{dy} = -i\alpha f \quad (\text{P5.4.1})$$

$$\alpha f \left[ i(\alpha u - \omega) + \frac{\alpha^2}{R} \right] + \alpha \frac{du}{dy} \phi + i\Pi \alpha^2 - \frac{\alpha}{R} \frac{d^2 f}{dy^2} = 0 \quad (\text{P5.4.2})$$

$$\frac{d\Pi}{dy} = -i(\alpha u - \omega)\phi - \frac{\alpha^2}{R}\phi + \frac{1}{R} \frac{d^2 \phi}{dy^2} \quad (\text{P5.4.3})$$

**5-5.** Show that the equations in Problem 5.3 can also be expressed as a fourth-order differential equation in  $\phi$  in the form given by Eq. (5.3.13).

**5-6.** The boundary conditions for the Orr–Sommerfeld equation follow from the relations given by Eqs. (P5.3.4) and (P5.3.5). At the wall, it follows from Eq. (P5.3.4) that

$$y = 0, \quad \phi = \phi' = 0 \quad (\text{P5.6.1})$$

At the edge of the boundary-layer, Eq. (5.3.13) reduces to

$$\phi^{iv} - (\xi_1^2 + \xi_2^2)\phi'' + \xi_1^2 \xi_2^2 \phi = 0 \quad (\text{P5.6.2})$$

(a) In order that the disturbances in the boundary-layer decay near the edge of the boundary-layer so that  $\phi$  and  $\phi' \rightarrow 0$  as  $y \rightarrow \infty$ , show that the solutions of Eq. (P5.6.2) must be of the form given by Eq. (P5.3.5).

(b) Show that, with  $D \equiv d/dy$ , the “edge” boundary conditions on  $\phi$  can be written as

$$(D + \xi_1)(D + \xi_2)\phi = 0 \quad (\text{P5.6.3a})$$

$$(D + \xi_2)(D^2 - \xi_1^2)\phi = 0 \quad (\text{P5.6.3b})$$

**5-7.** Noting that the characteristic equation for Eq. (P5.6.2) is

$$m^4 - (\xi_1^2 + \xi_2^2)m^2 + \xi_1^2 \xi_2^2 = 0$$

verify Eq. (P5.3.5).

**5-8.** For three-dimensional incompressible flows, the stability equations are given by [16]

$$\frac{d\hat{v}}{dy} + i(\alpha\hat{u} + \beta\hat{w}) = 0 \quad (\text{P5.8.1})$$

$$\frac{d^2\hat{u}}{dy^2} - \xi_2^2\hat{u} = iR \left[ \xi_1\hat{u} - i\hat{v}\frac{du}{dy} + \alpha\hat{p} \right] \quad (\text{P5.8.2})$$

$$\frac{d^2\hat{w}}{dy^2} - \xi_2^2\hat{w} = iR \left[ \xi_1\hat{w} - i\hat{v}\frac{dw}{dy} + \beta\hat{p} \right] \quad (\text{P5.8.3})$$

$$\frac{d^2\hat{v}}{dy^2} - \xi_2^2\hat{v} = iR \left[ \xi_1\hat{v} - i\frac{d\hat{p}}{dy} \right] \quad (\text{P5.8.4})$$

where

$$\xi_1 = \alpha u + \beta w - \omega, \quad \xi_2^2 = \alpha^2 + \beta^2 \quad (\text{P5.8.5})$$

(a) If we represent the amplitude functions of the perturbation quantities  $\hat{u}$ ,  $\hat{v}$ ,  $\hat{w}$  and  $\hat{p}$  by  $f$ ,  $\phi$ ,  $g$  and  $\Pi$ , respectively, and introduce them into Eqs. (P5.8.1) to (P5.8.4), we can also express the stability equations for three-dimensional incompressible flows as

$$\begin{aligned} & (\alpha f + \beta g)(iR\xi_1 + \xi_2^2) + R \left( \alpha \frac{du}{dy} + \beta \frac{dw}{dy} \right) \phi + iR\xi_2^2\Pi \\ & - \left[ \alpha \frac{d^2f}{dy^2} + \beta \frac{d^2g}{dy^2} \right] = 0 \end{aligned} \quad (\text{P5.8.6})$$

$$-iR \left[ \xi_1\phi - i\frac{d\Pi}{dy} \right] - \xi_2^2\phi + \frac{d\phi^2}{dy^2} = 0 \quad (\text{P5.8.7})$$

$$\frac{d\phi}{dy} = -i(\alpha f + \beta g) \quad (\text{P5.8.8})$$

*Hint:* To obtain Eq. (P5.8.6), for example, multiply Eqs. (P5.8.2) and (P5.8.3) by  $\alpha$  and  $\beta$ , respectively, and add them.

(b) Show that Eqs. (P5.8.6) to (P5.8.8) can also be expressed as a fourth-order differential equation in  $\phi$

$$\phi^{iv} - 2\xi_2^2\phi'' + \xi_2^4\phi - iR\xi_1(\phi'' - \xi_2^2\phi) + iR(\alpha u'' + \beta w'')\phi = 0 \quad (\text{P5.8.9})$$

*Hint:* Differentiate Eq. (P5.8.6) with respect to  $y$  and make use of Eqs. (P5.8.7) and (P5.8.8).

(c) In boundary-layer flows,  $u$  and  $w$  tend to constant values as  $y \rightarrow \infty$  which we take to be  $u_e$  and  $w_e$ , respectively. Show that  $\hat{u}$ ,  $\hat{v}$ ,  $\hat{w}$  and  $\hat{p}$  behave exponentially as  $y \rightarrow \infty$  with a typical asymptotic representation,

$$\hat{u} \sim A_1 e^{-\xi_2 y} + A_2 e^{-\xi_3 y} \quad (\text{P5.8.10})$$

where  $A_1$  and  $A_2$  are constants,  $\xi_2$  is defined in Eq. (P5.8.5) and  $\xi_3$  is defined by

$$\xi_3^2 = \xi_2^2 + iR(\alpha u_e + \beta w_e - \omega) \quad (\text{P5.8.11})$$

with the restriction that their real parts again are not negative.

(d) Show that the boundary conditions of Eq. (P5.8.9) can be written as (see Problem 5.6)

$$y = 0, \quad \phi = \phi' = 0 \quad (\text{P5.8.12a})$$

$$y \rightarrow \infty, \quad (D + \xi_2)(D + \xi_3)\phi = 0 \quad (\text{P5.8.12b})$$

$$(D + \xi_3)(D^2 - \xi_2^2)\phi = 0 \quad (\text{P5.8.12c})$$

where with  $Re(\xi_2)$  and  $Re(\xi_3) > 0$ ,  $\xi_1$  and  $\xi_2^2$  are given by Eq. (P5.8.5) and  $\xi_4^2$  is given by

$$\xi_3^2 = \xi_2^2 + iR\xi_1 \quad (\text{P5.8.13})$$

**5-9.** Rayleigh's theorem discussed in subsection 5.3.2 requires that in order to have amplified disturbances, the velocity profile  $u(y)$  must have a point of inflection ( $u'' = 0$ ) within the flow. To show how this can happen with surface temperature, consider a flat-plate flow with a variable viscosity on a nonporous surface and write the  $x$ -momentum equation

$$0 = \left( \frac{d\mu}{dy} \right)_w \left( \frac{du}{dy} \right)_w + \mu_w \left( \frac{d^2u}{dy^2} \right)_w$$

or, with primes denoting differentiation with respect to  $y$ , as

$$\left( \frac{d^2u}{dy^2} \right)_w \equiv u''_w = -\frac{1}{\mu_w} \left( \frac{d\mu}{dy} \right)_w u'_w \quad (\text{P5.9.1})$$

The dynamic viscosity  $\mu$ , which is a function of temperature, decreases with increasing temperature for liquids and increases with increasing temperature for gases. From the energy equation it is seen that if the plate is heated so that  $T_w > T_e$ , then for a liquid  $(dT/dy)_w$  and  $d\mu/dT$  are less than zero, and as a result

$$\left( \frac{d\mu}{dy} \right)_w = \left( \frac{d\mu}{dT} \right) \left( \frac{dT}{dy} \right)_w \quad (\text{P5.9.2})$$

is positive. Conversely, for a cooled plate,  $(du/dy)_w$  is negative. As both  $\mu_w$  and  $u'_w$  are positive for either case, it follows that for  $T_w > T_e$ ,  $u''_w < 0$ , and for  $T_w < T_e$ ,  $u''_w > 0$ . Since the curvature  $u''$  is vanishingly small but negative as  $y \rightarrow \infty$ , it follows that if its value at the wall is positive, there must be at least one point of inflection in the boundary-layer (i.e., some point at which  $u'' = 0$ ). Thus for a liquid, one would expect that heating stabilizes and cooling destabilizes the laminar boundary-layer. Conversely, for gases in which viscosity

increases with temperature, heating and cooling destabilizes and stabilizes the flow, respectively.

Show that a similar analysis can be used to show the qualitative effects of mass transfer (suction and injection) and pressure gradient (favorable and adverse pressure) on the curvature of the velocity profile and subsequently on transition. Note that in this case, Eq. (P5.9.1) becomes,

$$u_w'' = \frac{v_w}{\nu} u_w' + \frac{1}{\mu} \frac{dp}{dx} \quad (\text{P5.9.3})$$

**5-10.** Using Granville's method, calculate the transition location on a flat plate. Compare the result with the one predicted by Michel's method.

**5-11.** Using Granville's method, calculate the location of transition for external velocity distributions given by Eq. (4.2.10) for several values of  $m$ . Plot  $R_{\theta_{tr}}$  as a function of  $R_{x_{tr}}$ .

**5-12.** (a) Using Granville's method, calculate the location of transition for the following two flows

$$(1) \quad u_e = u_\infty$$

$$(2) \quad u_e = \begin{cases} u_\infty \frac{x}{x_c} & x \leq x_c \\ u_\infty & x \geq x_c \end{cases}$$

Take  $u_\infty = 20 \text{ ms}^{-1}$ ,  $x_c = 0.5 \text{ m}$ ,  $\nu = 1.585 \times 10^{-5} \text{ m}^2 \text{s}^{-1}$ .

(b) Explain why transition is delayed in (2). Note that this principle is used on sailplanes, for example, in order to achieve laminar flow on a large part of a wing. The maximum thickness of the wing is moved towards its trailing edge in order to have an accelerated flow in a larger percentage of the wing chord.

**5-13.** Using Eq. (5.4.5), calculate  $R_{x_{tr}}$  as a function of  $T_u$  on a flat plate for values of  $T_u$  between 0.001 and 0.02.

**5-14.** Consider an airflow on a flat plate in a wind tunnel in which the turbulence level is  $T_u = 0.001$ . Take  $u_\infty = 20 \text{ ms}^{-1}$ ,  $T_\infty = 300 \text{ K}$ , and  $p = 10^5 \text{ pa}$ .

(a) Calculate the location of transition from the plate leading edge.

(b) By using turbulence grids in the settling chamber, the turbulence level in the wind tunnel is increased to  $T_u = 0.01$ . Calculate the new transition location.

(c) Determine the freestream velocity required to move the transition at the same location if no turbulence grids are placed.

**5-15.** Roughness is often used in a wind tunnel to trigger transition to simulate the effects of higher Reynolds number. To study the roughness effects consider the freestream conditions in the previous problem and neglect the freestream turbulence effect.

(a) Using Granville's method calculate the location of transition from the plate leading edge and determine the displacement thickness,  $\delta_{tr}^*$ , at this location.

(b) In order to move the transition location towards the leading edge, let us place a wire of circular cross-section with diameter  $d$  at  $x_w = 0.2$  m. Assume that the movement of transition due to the wire is given by

$$\frac{u_e \delta_{tr}^*}{\nu} = \frac{900}{d/\delta_w^*} \quad (\text{P5.15.1})$$

with  $\delta_{tr}^*$  denoting the displacement thickness at transition location. Calculate the displacement thickness  $\delta_w^*$  of the unperturbed boundary-layer at the wire location.

(c) What is the maximum wire diameter,  $d_{min,1}$ , below which transition is not affected by the wire? *Hint:* Transition is not affected if Eq. (P5.15.1) predicts a transition location downstream of the natural transition location.

(d) If the wire diameter is larger than  $d_{min,1}$ , the location of transition will be closer to the wire. Calculate the transition location for  $d = 0.4$  mm.

(e) Calculate the minimum wire diameter  $d_{min,2}$  for which transition occurs at the wire location. Note that if the wire diameter is larger than  $d_{min,2}$ , transition remains at the wire location but the boundary-layer is overthickened by a certain amount which increases with the wire diameter.

**5-16.** The Orr–Sommerfeld equation derived in Section 5.3 can also be extended to include heat transfer effects in incompressible flows. In the approach used by Wazzan et al. [26], the density of the flow is assumed constant but its dynamic viscosity  $\mu$  is a function of temperature. With this restriction, the continuity and the Navier-Stokes equations for  $\rho = \text{const}$  and  $\mu = \mu(T)$  can be written in the following form:

$$\frac{\partial u}{\partial x} + \frac{\partial v}{\partial y} = 0 \quad (\text{P5.16.1})$$

$$\rho \frac{Du}{Dt} = -\frac{\partial p}{\partial x} + \frac{\partial}{\partial x} \left( 2\mu \frac{\partial u}{\partial x} \right) + \frac{\partial}{\partial y} \left[ \mu \left( \frac{\partial u}{\partial y} + \frac{\partial v}{\partial x} \right) \right] \quad (\text{P5.16.2})$$

$$\rho \frac{Dv}{Dt} = -\frac{\partial p}{\partial y} + \frac{\partial}{\partial y} \left( 2\mu \frac{\partial v}{\partial y} \right) + \frac{\partial}{\partial x} \left[ \mu \left( \frac{\partial u}{\partial y} + \frac{\partial v}{\partial x} \right) \right] \quad (\text{P5.16.3})$$

The derivation of the stability equation in this case is identical to that described in Section 5.3 except now the variation of  $\mu$  is obtained from the relation between

viscosity and temperature and from the energy equation, which in terms of total enthalpy  $H$ , can be written as

$$u \frac{\partial H}{\partial x} + v \frac{\partial H}{\partial y} = \frac{\partial}{\partial y} \left[ \frac{\nu}{Pr} \frac{\partial H}{\partial y} + \nu \left( 1 - \frac{1}{Pr} \right) u \frac{\partial u}{\partial y} \right] \quad (\text{P5.16.4})$$

(a) Using the procedure of Section 5.3 and noting again that the mean velocity and pressure satisfy the two-dimensional equations of motion given by Eqs. (P5.16.1) to (P5.16.4), using the parallel-flow approximation, and the dimensionless variables defined by Eq. (5.3.5), show that  $x$ - and  $y$ -momentum equations can be written as

$$\frac{\partial u'}{\partial t} + u \frac{\partial u'}{\partial x} + v' \frac{\partial u}{\partial y} + \frac{\partial p'}{\partial x} = \frac{\mu}{R} \left[ \frac{\partial^2 u'}{\partial x^2} + \frac{\partial^2 u'}{\partial y^2} \right] + \frac{1}{R} \frac{\partial \mu}{\partial y} \left[ \frac{\partial u'}{\partial y} + \frac{\partial v'}{\partial x} \right] \quad (\text{P5.16.5})$$

$$\frac{\partial v'}{\partial t} + u \frac{\partial v'}{\partial x} + \frac{\partial p'}{\partial y} = \frac{\mu}{R} \left[ \frac{\partial^2 v'}{\partial x^2} + \frac{\partial^2 v'}{\partial y^2} \right] + \frac{2}{R} \frac{\partial \mu}{\partial y} \frac{\partial v'}{\partial y} \quad (\text{P5.16.6})$$

where  $\mu$  denotes a dimensionless viscosity ratio defined by  $\mu/\mu_0$  and  $R$  is now defined by  $u_0 \ell / \nu_0$ . It should be noted that Eqs. (P5.16.5) and (P5.16.6) neglect temperature fluctuations.

(b) As in Section 5.3, assuming that the small disturbance is a sinusoidal traveling wave that can be represented by Eq. (5.3.9) where  $q$  is replaced by  $\hat{u}$ ,  $\hat{v}$ , and  $\hat{p}$ ; show that Eqs. (P5.16.5) and (P5.16.6) can be written as

$$\frac{d^2 \hat{u}}{dy^2} - \alpha^2 \hat{u} = \frac{iR}{\mu} \left[ (\alpha u - \omega) \hat{u} - i \hat{v} \frac{du}{dy} + \alpha \hat{p} - \frac{1}{R} \frac{d\mu}{dy} \left( \alpha \hat{v} - i \frac{d\hat{u}}{dy} \right) \right] \quad (\text{P5.16.7})$$

$$\frac{d^2 \hat{v}}{dy^2} - \alpha^2 \hat{v} = \frac{iR}{\mu} \left[ (\alpha u - \omega) \hat{v} - i \frac{d\hat{p}}{dy} + \frac{2i}{R} \frac{d\mu}{dy} \frac{d\hat{v}}{dy} \right] \quad (\text{P5.16.8})$$

(c) Show that, as before, Eqs. (P5.16.7) and (P5.16.8) can also be expressed in the following form for two-dimensional flows

$$\begin{aligned} & [(\alpha u - \omega)(\phi'' - \alpha^2 \phi) - \alpha u'' \phi] iR \\ &= \mu(\phi^{iv} - 2\alpha^2 \phi'' + \alpha^4 \phi) + 2\mu'(\phi''' - \alpha^2 \phi') + \mu''(\phi'' + \alpha^2 \phi) \end{aligned} \quad (\text{P5.16.9})$$

where  $\mu$  is the dynamic viscosity with  $\mu'$  and  $\mu''$  denoting its first and second derivatives with respect to  $y$ , respectively.

**5-17.** Show from Eq. (5.3.9) that if  $A$  is the amplitude of the disturbance stream function  $\psi$  at any time, then

(a) for temporal amplification theory

$$\frac{A}{A_0} = \exp \int_0^t \omega_i dt \quad (\text{P5.17.1})$$

and

(b) for spatial amplification theory,

$$\frac{A}{A_0} = \exp \int_0^x -\alpha_i dx \quad (\text{P5.17.2})$$

Here subscript 0 denotes the initial state where the TS waves are neutrally stable.

**5-18.** For Blasius velocity profiles computed for a uniform grid with  $\Delta\eta = 0.10$  and  $\eta_e = 8$ , calculate the lower and upper branches of the neutral stability curves for  $600 \leq R \leq 3000$  using STP given in the accompanying CD-ROM, Program 5. Take  $u_\infty = 160$  ft/sec,  $\nu = 1.6 \times 10^{-4}$  ft<sup>2</sup>/sec,  $c = 9$  ft.

**5-19.** Repeat Problem 5.18 for two wedge flows for which  $m = -0.01$  and  $-0.05$ .

**5-20.** Calculate the location of transition for  $n = 9$  for the above two problems and discuss the effect of pressure gradient on the results.

**5-21.** Using STP, investigate the effect of suction on the location of transition for Problem 5.18. Let the suction rates vary with  $\xi$  in order to have similarity in velocity profiles. Note that depending on the choice of suction rates, the value of  $c$  may need to be increased.

**5-22.** Using STP, repeat the transition calculations for the

- (a) airfoil flow
- (b) ellipse flow
- (c) prolate spheroid flow

discussed in subsection 5.7.2.

**5-23.** The procedure used to construct the stability diagrams for Blasius flow can be extended to other Falkner–Skan flows. Figure P5.1 shows the stability diagrams for seven values of  $\alpha_i$  and for the value of  $m = -0.0707$  corresponding to the lower-branch solution of the Falkner–Skan equation discussed in Problem 4.34. As can be seen from Fig. P4.5, the velocity profile for  $m = -0.707$  is significantly different from the one for a flat-plate flow ( $m = 0$ ). In this case, initial estimates of  $\alpha_r$  and  $\omega$  to start the stability calculations become very important since Newton's method is being used to compute the subsequent estimates. A convenient procedure, sometimes referred to as the homotopy continuation method [40], can be used for this purpose. This procedure is general and can

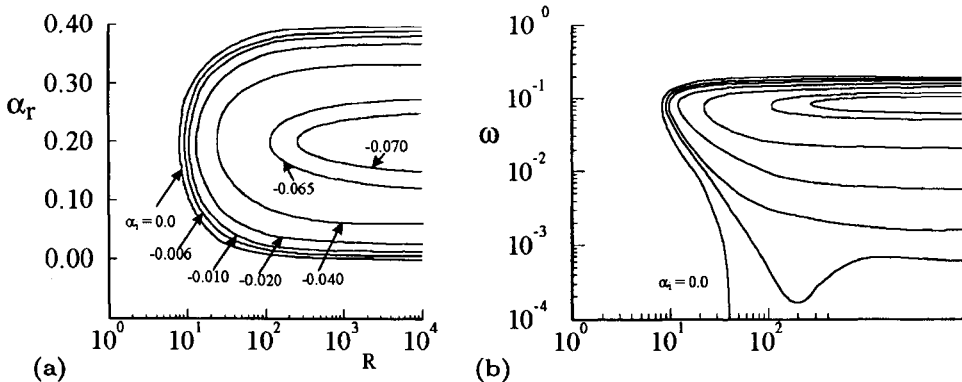


**Fig. P5.1.** Stability diagrams for the lower branch solutions of the Falkner–Skan equation for  $m = -0.0707$ , (a)  $\alpha$  vs.  $R$ , and (b)  $\omega$  vs.  $R$ .

also be used for three-dimensional flows, as well as flows in which the velocity profiles from one  $x$ -station to another change rapidly as discussed in [40].

We define

$$u = u_{\text{ref}} + r(u_f - u_{\text{ref}}) \quad (\text{P5.23.1a})$$

$$u'' = u''_{\text{ref}} + r(u''_f - u''_{\text{ref}}) \quad (\text{P5.23.1b})$$

and

$$R = R_{\text{ref}} + r(R_f - R_{\text{ref}}) \quad (\text{P5.23.1c})$$

Here  $u_f$  corresponds to the velocity profile of the flow under consideration at a given Reynolds number  $R_f$  and  $u_{\text{ref}}$  denotes a reference profile with a Reynolds number  $R_{\text{ref}}$  and with eigenvalues of  $\alpha_0$  and  $\omega_0$ . The parameter  $r$  is a sequence of specified numbers ranging from 0 to 1. Eqs. (P5.23.1) show that the profiles  $u$  and  $u''$  correspond to the reference profiles for  $r = 0$  at  $R = R_{\text{ref}}$ , as well as to those for which eigenvalues  $\alpha$  and  $\omega$  are to be determined at the specified  $R_f$  for  $r = 1$ .

- (a) Obtain the lower branch solutions of the Falkner–Skan equation for  $m = -0.0707$ .
- (b) Compute  $\alpha_r$  and  $\omega$  for the lower branch stability diagrams for  $\alpha_i = 0$ ,  $-0.006$  and  $-0.01$  at  $R = 20$ .

*Hint:* Assume  $\alpha_r = -0.050$ ,  $\omega = 0.00543$  for  $\alpha_i = 0$ . Once a solution is obtained, use the values of  $\alpha_r$  and  $\omega$  from the previous value of  $\alpha_i$  to be initial guesses for the specified  $\alpha_i$ .

**5-24.** Many internal flows are symmetric about some plane  $y = y_1$  and the most unstable disturbance is usually asymmetric. The appropriate boundary conditions on the disturbance at  $y/h = (y_1/h_1) = 0$  are

$$\frac{du'}{dy} = v' = 0 \quad (\text{P5.24.1a})$$

for the symmetric disturbance and

$$u' = \frac{d^2 u'}{dy^2} = 0 \quad (\text{P5.24.1b})$$

for the asymmetric disturbance. Thus, in terms of the perturbation stream function,  $\phi$ , the appropriate centerline boundary conditions, given by Eq. (P5.24.1b) can be written as

$$\phi(0) = \phi'''(0) = 0 . \quad (\text{P5.24.2})$$

The wall boundary conditions at  $y/h = -1$  or  $1$  are the usual ones; that is, the perturbation velocities  $u'$  and  $v'$  are zero. In terms of the disturbance stream function this implies

$$\phi = \phi' = 0 . \quad (\text{P5.24.3})$$

Use STP to compute the neutral stability curve of a plane Poiseuille flow for a Reynolds number range of  $10^4 < R < 5 \times 10^4$  and for a velocity profile given by

$$u = u_{\max}[1 - (y/h)^2] \quad (\text{P5.24.4})$$

with  $u_{\max}$  and  $h$  as reference velocity and length scales. Note that the velocity profile implies wall boundary conditions at  $y/h = -1$  and  $1$  and the centerline at  $y/h = 0$ .

*Hint:* For convenience and for minimum changes in the stability code, use the velocity profile so that  $y/h = 1$  corresponds to the wall boundary conditions and thus requires no changes in the stability/transition computer program. The “edge” conditions are different and the code needs to be changed. This can be done by incorporating the conditions given in Eq. (P5.24.2) into the relations defined by boundary conditions, for

$$\begin{array}{ccccc} \phi & s & f & g \\ c_1 & c_3 & 1 & 0 \\ 0 & c_4 & 0 & 1 \end{array}$$

with  $c_1 = c_3 = c_4 = 0$ .

Take the initial estimates of  $\alpha$  and  $\omega$  as  $\alpha_r = 0.9$ ,  $\omega = 0.02$  for  $R = 6000$ . Note also that the grid is

$$\eta_j = \left(\frac{y}{h}\right)_j = \frac{NP - j}{NP - 1} \quad (\text{P5.24.5})$$

and the velocity profile, is

$$u_j = 1 - \eta_j^2 . \quad (\text{P5.24.6})$$



# 6 Two-Dimensional Incompressible Turbulent Flows

## 6.1 Introduction

Unlike the solution of laminar flows discussed in Chapter 4, the solution of the turbulent boundary-layer equations can not be obtained without a model for the Reynolds shear stress term  $-\rho\overline{u'v'}$ , which introduces an additional unknown to the system given by the continuity and momentum equations. In addition, turbulent boundary-layers do not admit similarity solutions. This means that velocity profiles are not geometrically similar and do not reduce to a single curve if  $u/u_e$  is plotted against a dimensionless  $y$ -coordinate,  $\eta$ . One velocity scale  $u^*$  and one length scale  $l$  ( $u_e$  and  $\sqrt{\nu x/u_e}$ , respectively, for laminar flows) are not sufficient to describe a turbulent boundary-layer velocity profile. Experiments indicate that the behavior of the flow close to the wall is different from the behavior of the flow away from the wall. This leads to a *composite nature* of a turbulent boundary-layer and requires different length scales in each region, as discussed in Section 6.2.

In Section 6.3, we present a brief description of turbulence models of varying complexity. The calculation of turbulent boundary-layers is addressed in Sections 6.4 to 6.6 with Section 6.4 describing the empirical formulas for calculating boundary-layer parameters on smooth and rough surfaces with zero pressure gradient. Section 6.5 describes integral methods and Section 6.6 describes a differential method which extends the differential method of Chapter 5 to turbulent flows with an algebraic eddy-viscosity formulation that places the turbulent boundary-layer equations in a form similar to the laminar boundary-layer equations. Finally, in Section 6.7 we discuss the similarity solutions of turbulent free shear flows which is an extension of Section 4.3 for laminar flows.

## 6.2 Composite Nature of a Turbulent Boundary-Layer

Consider a two-dimensional incompressible flow over a flat plate. For a laminar boundary-layer flow, the velocity profiles are geometrically similar and reduce to

a single curve if  $u/u_e$  is plotted on a dimensionless  $y$ -coordinate,  $\eta = \sqrt{u_e/\nu x} y$ . This is the well-known Blasius profile discussed in Section 4.2. The geometrical similarity is maintained regardless of the Reynolds number of the flow or of the local skin friction. In a turbulent boundary-layer there is no choice of dimensionless  $y$ -coordinate that leads to the collapse of the complete set of velocity profiles into a single curve because the viscous-dependent part of the profile, very close to the surface, and the remaining Reynolds-stress-dependent part of the profile require different length scaling parameters. For that reason it is helpful to treat a turbulent boundary-layer as a composite layer consisting of inner and outer layers.

### 6.2.1 The Inner Layer: Smooth Surface

The thickness of the inner layer of a turbulent boundary-layer is about 10–20% of the entire boundary-layer thickness. It is generally assumed that, if the total (viscous plus turbulent) shear stress varies only slowly with distance from the surface, the mean velocity distribution in this layer is completely determined by the wall shear stress,  $\tau_w$ , density,  $\rho$ , dynamic viscosity,  $\mu$ , and the distance,  $y$ , from the wall. Thus the flow is independent of conditions in the outer part of the boundary-layer and indeed of whether the flow is a boundary-layer or some other type of wall shear layer. Therefore, all the inner-layer formulas derived below are *valid for internal flows as well as boundary-layers* if the explicit restrictions are met by the former. They will not be valid in either case if the flow changes rapidly in the  $x$ -direction, for example, near sudden changes of surface roughness.

Dimensional analysis shows that the mean velocity is given by the “law of the wall”,

$$u^+ \equiv \frac{u}{u_\tau} = \phi_1(y^+) \quad (6.2.1)$$

where  $u_\tau \equiv (\tau_w/\rho)^{1/2}$  is called the “friction velocity”. This velocity provides us with a *turbulence velocity scale* because the experimental data shows that  $-\overline{u'v'}$  is of the same order of  $u_\tau^2$  (Fig. 6.1). In addition, the normal stress terms  $\overline{u'^2}$ ,  $\overline{v'^2}$ , and  $\overline{w'^2}$  are of the same order as  $-\overline{u'v'}$  (Fig. 6.2).

The parameter  $y^+ = u_\tau y / \nu$  is a Reynolds number based on the velocity scale  $u_\tau$  and length scale  $y$  from the wall. When this Reynolds number is large (in practice, more than 30–50; here we shall assume 50), the relation between the Reynolds stress, now equal to  $\tau_w$ , and the mean rate of strain,  $\partial u / \partial y$ , is independent of viscosity. The dimensionally correct relation is

$$\frac{\partial u}{\partial y} = \frac{u_\tau}{\kappa y} \quad (6.2.2)$$

where  $\kappa$  is found experimentally to be about 0.41. This equation indicates that the turbulence time scale is equal to the mean flow time scale. The latter is

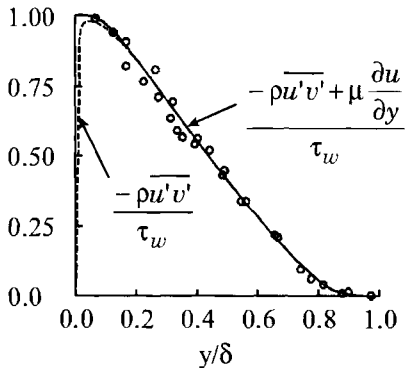


**Fig. 6.1.** Variation of Reynolds shear stress  $-\rho u' v'$  and total shear stress on a flat plate, after Favre and Gaviglio [1].

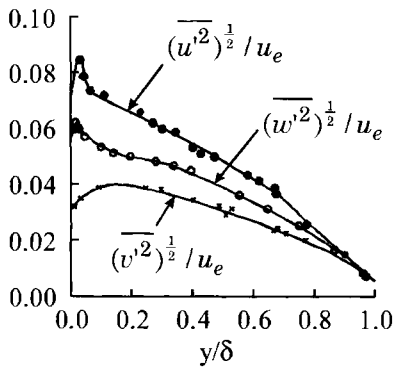


**Fig. 6.2.** Variation of normal stresses on a flat plate, after P.S. Klebanoff [2].

formed with  $\frac{\partial u}{\partial y}$  while the latter assumes that the turbulence velocity scale is  $u_\tau$  and the turbulence length scale is  $y$ , the distance from the wall. Equation (6.2.2) is a special case of Eq. (6.2.1) with  $d\phi_1/dy^+ = 1/\kappa y^+$ , and it follows that for  $50\nu/u_\tau < y < 0.1$  to  $0.2\delta$ ,

$$u^+ = \frac{1}{\kappa} \ln y^+ + c \quad (6.2.3)$$

Here  $c$  is a constant (about 5.0 to 5.2; here we shall assume 5.0) for a smooth surface. This is the famous logarithmic law. It is a universal law in the sense that it does not depend on the Reynolds number or on the pressure gradient provided the boundary-layer is not too close to separation.

For  $y^+ < 50$  (the viscous sublayer), viscous stresses are significant, and the velocity profile departs from Eq. (6.2.3). For  $y^+ < 4$  approximately, the turbulent shear stress  $-\rho u' v'$  is negligible because  $u'$  and  $v'$  are constrained to be zero at the wall, and the velocity profile follows the purely viscous law

$$\tau_w = \mu \frac{\partial u}{\partial y} \quad (6.2.4a)$$

or

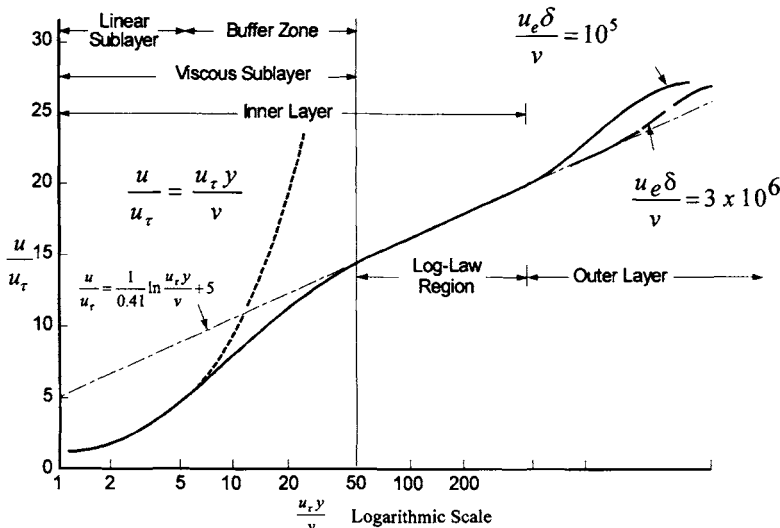


**Fig. 6.3.** Regions of a turbulent boundary-layer. Outer-layer profile shown is for  $u_e = \text{const.}$  Value of  $u_\tau \delta / \nu$  depends on Reynolds number.

$$u^+ = y^+ \quad (6.2.4b)$$

in the present notation. This region is called the linear sublayer and its outer edge will be denoted by  $y = y_s$ . The remainder of the viscous sublayer, in which the velocity profile changes smoothly from Eq. (6.2.4) to Eq. (6.2.3), is the “buffer zone”, sometimes misleadingly called the “transition region”. These regions are shown in Fig. 6.3. It is important to note that the total thickness of the inner layer depends on  $\delta$  and not directly on  $u_\tau / \nu$ .

### 6.2.2 The Inner Layer: Rough Surface

The discussion on the inner layer on a smooth surface can also be extended to a rough surface; surface roughness has a significant effect on a turbulent boundary-layer if the height of the roughness elements corresponds to approximately  $(u_\tau k / \nu) > 5$ . Since in most cases the viscous sublayer is extremely thin, less than one percent of the shear-layer thickness in a boundary-layer with  $(u_e \delta / \nu) > 10^5$ , the roughness elements must be very small if the surface is to be aerodynamically smooth. On a given surface, as the boundary-layer thickness and Reynolds number change, the surface may change from effectively rough to aerodynamically smooth.

According to dimensional analysis, the law-of-the-wall for a surface with uniform roughness of given geometrical shape is

$$u^+ = \phi_2(y^+, k^+) \quad (6.2.5)$$

Here  $k^+$  is a roughness Reynolds number defined by

$$k^+ = \frac{ku_\tau}{\nu} \quad (6.2.6)$$

In the fully turbulent part of the inner region, the turbulence velocity scale is again the friction velocity  $u_\tau$ , and the length scale is the distance from the wall. As for the smooth surface, we again assume the relationship given by Eq. (6.2.2). We also assume that  $\kappa$  is unaffected by sublayer conditions. However, when integrating Eq. (6.2.2), we express the additional constant  $c$  in Eq. (6.2.3) as a function of the roughness Reynolds number,  $k^+$ , and of the roughness geometry,

$$u^+ = \frac{1}{\kappa} \ln y^+ + B_1(k^+) \quad (6.2.7)$$

If we let

$$B_2 = \frac{1}{\kappa} \ln k^+ + B_1(k^+) \quad (6.2.8)$$

we can write Eq. (6.2.7) as

$$u^+ = \frac{1}{\kappa} \ln \frac{y}{k} + B_2 \quad (6.2.9)$$

Here  $B_1$  and  $B_2$  are functions of roughness geometry and density, and in general of  $k^+$ , and must be determined from experiments.

If we let

$$B_3 = c - B_2 \quad (6.2.10)$$

and

$$\Delta u^+ = \frac{\Delta u}{u_\tau} = \frac{1}{\kappa} \ln k^+ + B_3 \quad (6.2.11)$$

then we can write Eq. (6.2.9) as

$$u^+ = \frac{1}{\kappa} \ln y^+ + c - \Delta u^+ \quad (6.2.12)$$

The relation between  $\Delta u^+$  and  $k^+$  has been determined empirically for various types of roughness geometry. Some results are shown in Fig. 6.4.

We see from Eq. (6.2.12) that, since for a given roughness  $\Delta u^+$  is a known function of  $k^+$ , the sole effect of the roughness is to shift the intercept,  $c - \Delta u^+$ , as a function of  $k^+$ . For values of  $k^+$  below approximately 5, the vertical shift  $\Delta u^+$  approaches zero, except for those roughnesses having such a wide distribution of particle sizes that there are some particles large enough to protrude from the sublayer even though the average size is considerably less than the thickness of the sublayer. For large values of  $k^+$  the vertical shift is proportional to  $\ln k^+$ , with the constant of proportionality equal to  $1/\kappa$ , and by comparing Eqs. (6.2.9) and (6.2.12) we can see that this implies that  $B_2$  is independent of  $k^+$ . This means that the drag of the roughness elements is independent of viscosity, a reasonable result for nonstreamlined obstacles at large Reynolds number.

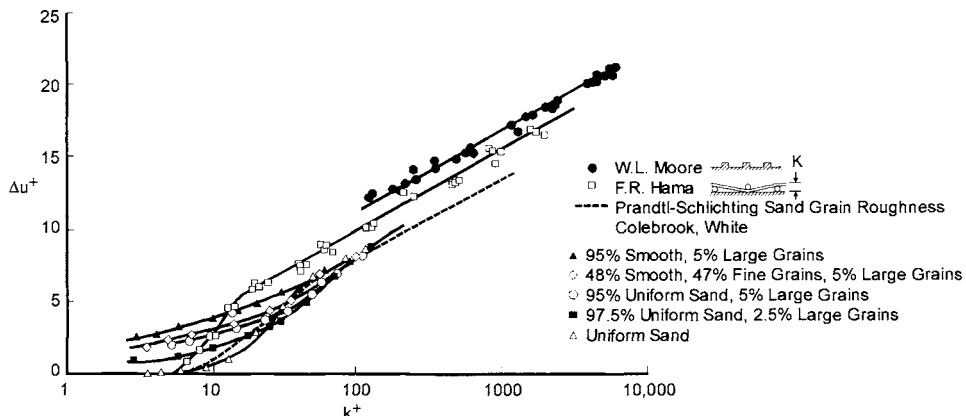


**Fig. 6.4.** Effect of wall roughness on universal velocity profiles, after Clauser [3], who gives the references in full.

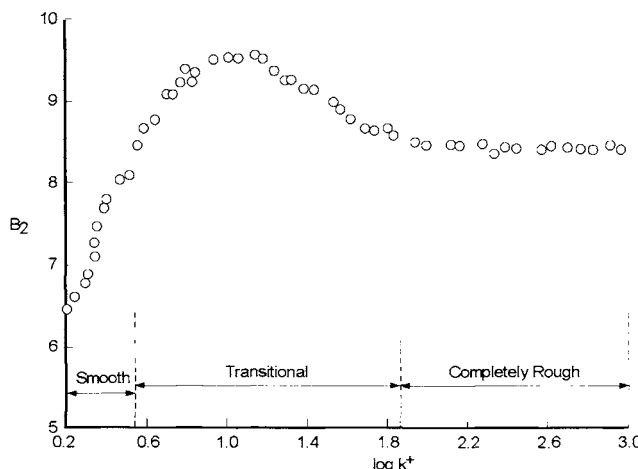


**Fig. 6.5.** Variation of  $B_2$  with  $k^+$  [4].

Figure 6.5 shows the variation of  $B_2$  with  $k^+$  with sand-roughened pipes (Nikuradse, see [4]). Ioselevich and Pilipenko [5] give an analytic fit to the sand-roughness data of Nikuradse: for  $k^+ < 2.25$ ,  $B_1 = c \approx 5.2$  (negligible roughness effect); for  $2.25 < k^+ < 90$ ,  $B_1 = c + [8.5 - c - (1/\kappa) \ln k^+] \sin 0.4258(\ln k^+ - 0.811)$ ; for  $k^+ > 90$ ,  $B_1 = 8.5 - (1/\kappa) \ln k^+$ .

The hydraulically smooth condition exists when roughness heights are so small that the roughness is buried in the viscous sublayer. The fully rough flow condition exists when the roughness elements are so large that the sublayer is completely eliminated and the flow can be considered to be independent of molecular viscosity, that is, the velocity shift is proportional to  $\ln k^+$  and Eq. (6.2.9) holds with  $B_2$  constant. Because molecular viscosity still has some role in the buffer region, the geometry of roughness elements has a relatively large effect

on the velocity shift, as can be seen in Fig. 6.4. The effect of certain types of roughness, notably square-section spanwise grooves with a groove width about half the pitch, scales on the boundary-layer thickness rather than the roughness height. The reason appears to be that the flow would pass smoothly over the grooves if it were not for disturbances caused by outer-layer eddies. For details see Perry et al. [6], who call this “d-type” roughness.

The fact that the shifts in velocity for fully rough flow are linear on the semilogarithmic plot, Fig. 6.4 can be used to express different roughness geometries in terms of a reference roughness. It follows from Eq. (6.2.11) that for the same velocity shift,

$$\frac{k_s}{k} = \exp[\kappa(B_3 - B_{3s})] \quad (6.2.13)$$

where the subscript  $s$  refers to a reference roughness, commonly taken as uniform sand-grain roughness.

### 6.2.3 The Outer Layer

The outer layer of a turbulent boundary-layer contains 80–90% of the boundary-layer thickness (see, Fig. 6.3). Physically, its outer edge is not a regular surface. A smoke visualization (Fig. 6.6) of the flow shows that the boundary-layer edge is a very contorted surface that enhances the mixing between the outer flow and the boundary-layer flow. In the outer region of the boundary-layer, the flow is *intermittently turbulent*. However, for convenience, all the flow characteristics are averaged and the boundary-layer thickness  $\delta$  is the average of the instantaneous location of the boundary-layer edge.

In the outer layer, the velocity scale is  $u_\tau$  because the turbulent shear stress has the same order of magnitude as in the inner layer. The length scale is the boundary-layer thickness  $\delta$ . The mean velocity distribution in this region can

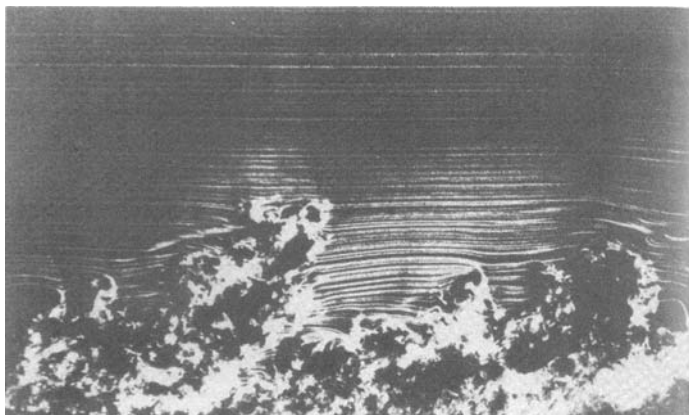


**Fig. 6.6.** Visualization of a turbulent boundary-layer [7].

again be derived by dimensional analysis and for a zero pressure gradient flow it can be expressed in the form

$$\frac{u_e - u}{u_\tau} = f_1 \left( \frac{y}{\delta} \right) \quad (6.2.14)$$

This expression is known as the *velocity-defect law*. If Eq. (6.2.14) is differentiated with respect to  $y$ , and the derivative of  $f_1$  is assumed to be of the order of unity, then the resulting equation, as Eq. (6.2.2), indicates that the turbulence time scale is equal to the mean flow time scale. In the outer region, the mean flow time scale is formed with  $\frac{\partial u}{\partial y}$  while the turbulence time scale is formed with the turbulence velocity scale  $u_\tau$  and length scale  $\delta$ . The effect of moderate wall roughness is negligible (Fig. 6.7) and  $u_\tau \delta / \nu$  has a negligible effect if it exceeds about 2000 ( $u_e \theta / \nu > 5000$ ).

A formula analogous to Eq. (6.2.14) holds for circular pipes if we replace  $\delta$  by the pipe radius,  $r_0$ ;  $f_1$  is rather different from a boundary-layer and the velocity profile follows the logarithmic law [Eq. (6.2.3)] fairly accurately almost to the center of the pipe. In a boundary-layer,  $f_1$  is markedly affected by the history of the pressure gradient and except for specially tailored pressure gradients of which zero is one,  $f_1(y/\delta)$  depends on  $x$ .

The inner and outer layers have a common region called the *overlap layer* in which the logarithmic law, Eq. (6.2.3), and the velocity-defect law, Eq. (6.2.14) are both valid. The velocity-defect law in the overlap layer is given by

$$\frac{u_e - u}{u_\tau} = -\frac{1}{\kappa} \ln \frac{y}{\delta} + c' \quad (6.2.15)$$

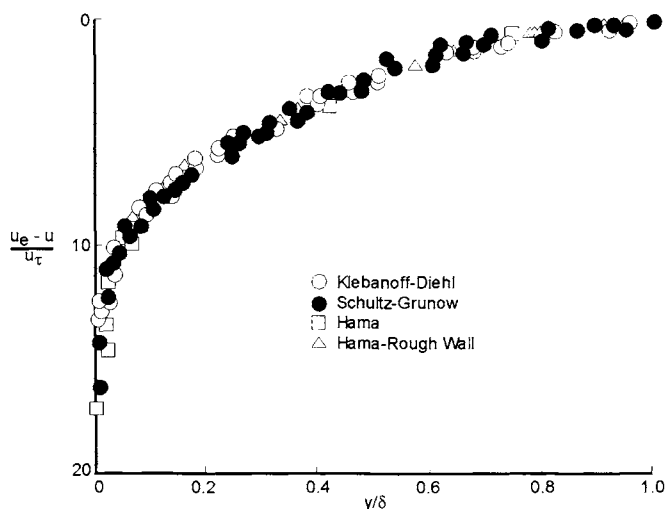


**Fig. 6.7.** Universal plot of turbulent boundary-layer profiles in zero pressure gradient, after Clauser [3]. The symbols denote the experimental data.

where  $c'$  is an absolute constant for  $u_e \theta / \nu > 5000$  for flows with zero-pressure gradient, independent even if there is wall roughness. In contrast to the law-of-the-wall [Eq. (6.2.3)], the velocity-defect law [Eq. (6.2.14)] is of rather restricted application. Of course, Eq. (6.2.15) is always valid for some value of  $c'$ , as long as a logarithmic region exists, but in a general boundary layer,  $c'$ , like  $f_1$ , will be a function of  $x$ .

A class of boundary-layers, in which the external velocity distribution is characterized by the parameter

$$\beta = \frac{\delta^*}{\tau_w} \frac{dp}{dx} = \text{const.} \quad (6.2.16)$$

is known as equilibrium boundary-layer flows. Here  $\beta$  represents the ratio of pressure forces to shear forces in a section of the boundary-layer. These flows are analogous to Falkner Skan flows in laminar layers in that for given flow, the parameter  $\beta$  is constant, but not similar because Eq. (6.2.14) is of the form of Eq. (4.2.3), not Eq. (4.2.2), the form of the Falkner-Skan flows. A flat-plate (zero-pressure gradient) flow is a special case of an equilibrium flow. The function  $f_1$  in Eq. (6.2.14) is different for each value of  $\beta$ . Figure 6.8 shows the velocity-defect profiles for two different experimental pressure distributions corresponding to two equilibrium boundary-layers together with the velocity-defect profile for zero pressure gradient. As can be seen, there is a considerable difference between the velocity profiles with pressure gradient and those with no pressure gradient. Furthermore, the difference increases with increasing pressure gradient parameter  $\beta$ .

#### 6.2.4 Summary

Figure 6.3 summarizes the different regions in a turbulent boundary-layer. The inner layer consists of three regions: the sublayer ( $y^+ < 5$ ), the buffer layer ( $5 < y^+ < 50$ ) and the fully turbulent wall region ( $y^+ > 50$ ). In the sublayer, the viscous stress is larger than the turbulent stress. In the buffer layer, the viscous stress and the turbulent stress have the same order of magnitude. In the fully turbulent region, the viscous stress is negligible. The extent of the fully turbulent wall region depends on the Reynolds number. In the outer region of the boundary-layer, the viscous stress is also negligible. The inner layer and the outer layer have a common part – the overlap layer – in which the velocity profile is logarithmic.

#### 6.2.5 The Whole Layer

There are several empirical formulas for representing the turbulent velocity profile across the whole layer. Two useful formulas are due to Coles [9] and Whitfield [10] and are described below.

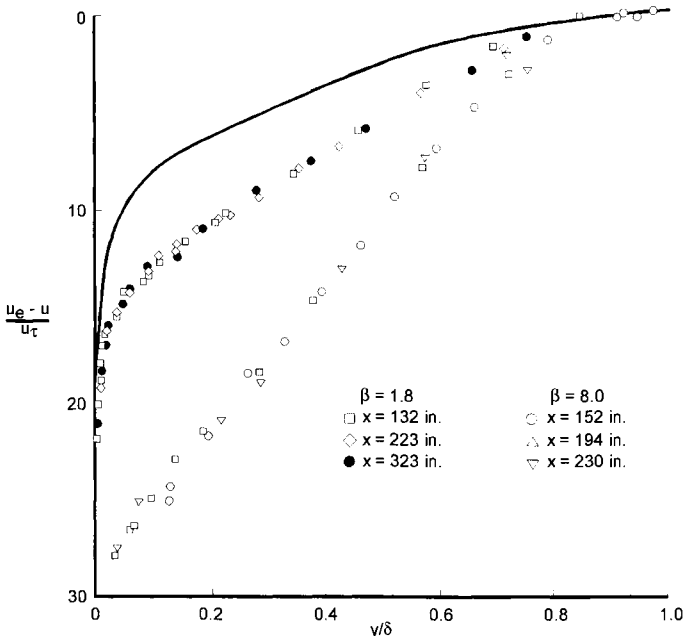


**Fig. 6.8.** Effect of adverse pressure gradient on the velocity-defect profiles. The data for  $\beta = 1.8$  and 8.0 are from Clauser [8].

### Coles Formula

The formula proposed by Coles expresses the velocity profile by

$$u^+ = \phi_1(y^+) + \frac{\Pi(x)}{\kappa} w\left(\frac{y}{\delta}\right) \quad (6.2.17)$$

where  $\phi_1$  is a function appearing in Eq. (6.2.1) and  $w$  is effectively zero in the inner layer.

Equation (6.2.17) is applicable to flows with and without pressure gradient. If the viscous sublayer is excluded, the law of the wall function,  $\phi_1(y^+)$  is given by Eq. (6.2.3).

The quantity  $\Pi$  in Eq. (6.2.17) is a profile parameter that is, in general, a function of  $x$ . The function  $w(y/\delta)$ , representing the deviation of the outer-layer profile from the law of the wall, is called the *law-of-the-wake* function and is of nearly universal character, according to experiments. However, it must be clearly understood that the function  $w(y/\delta)$  is an empirical fit to measured velocity profiles that, to a good approximation, can be represented by the expression

$$w\left(\frac{y}{\delta}\right) = 2 \sin^2 \frac{\pi}{2} \left(\frac{y}{\delta}\right) = 1 - \cos\left(\pi \frac{y}{\delta}\right) \quad (6.2.18)$$

At the edge of the boundary-layer  $w(1)$  becomes 2 and  $w$  denotes a normalized shape function and the  $x$ -wise variation is represented by  $\Pi$ . Note that  $\delta$  is a

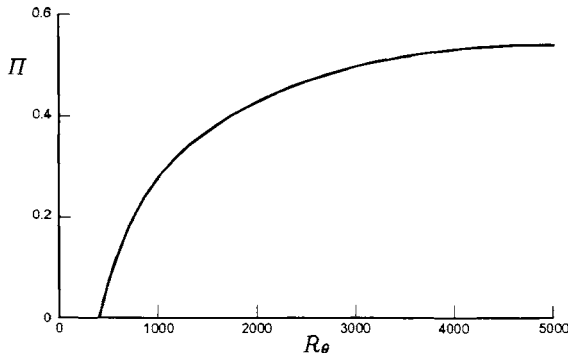


**Fig. 6.9.** Variation of Coles' profile parameter,  $\Pi$ , with momentum-thickness Reynolds number  $R_\theta$ , for zero pressure gradient flow.

freely chosen parameter and is not the same as the choice  $\delta = \delta_{995}$  used elsewhere in this book.

For flows with zero pressure gradient, the profile parameter  $\Pi$  is a constant equal to about 0.55, provided that the momentum-thickness Reynolds number  $R_\theta$  is greater than 5000. For  $R_\theta < 5000$ , the variation of  $\Pi$  with  $R_\theta$  is as shown in Fig. 6.9.

Equation (6.2.17), with  $\phi_1(y^+)$  given by Eq. (6.2.3) and  $w$  by Eq. (6.2.18), gives  $\partial u / \partial y$  nonzero at  $y = \delta$ . To remedy the difficulty, a number of expressions have been proposed for  $w$ . A convenient one proposed by Granville [11] uses a modification of Eq. (6.2.18) written as

$$\frac{u}{u_\tau} = \frac{1}{\kappa} \ln y^+ + c + \frac{1}{\kappa} [\Pi(1 - \cos \pi\eta) + (\eta^2 - \eta^3)] \quad (6.2.19)$$

From Eq. (6.2.19) and from the definitions of  $\delta^*$  and  $\theta$  it can be shown, provided that the logarithmic law is assumed valid to the wall, that

$$\frac{\delta^*}{\delta} = \int_0^1 \frac{u_e - u}{u_\tau} \frac{u_\tau}{u_e} d\eta = \frac{u_\tau}{\kappa u_e} \left( \frac{11}{12} + \Pi \right) \quad (6.2.20a)$$

$$\begin{aligned} \frac{\theta}{\delta} &= \int_0^1 \frac{u}{u_e} \left( 1 - \frac{u}{u_e} \right) d\eta \\ &= \frac{u_\tau}{\kappa u_e} \left( \frac{11}{12} + \Pi \right) - \left( \frac{u_\tau}{\kappa u_e} \right)^2 \\ &\quad \left\{ 2 + 2\Pi \left[ 1 + \frac{1}{\pi} Si(\pi) \right] + 1.5\Pi^2 + \frac{1}{105} - \frac{7}{72} - 0.12925\Pi \right\} \end{aligned} \quad (6.2.20b)$$

where

$$Si(\pi) = \int_0^\pi \left[ \frac{\sin u}{u} \right] du = 1.8519.$$

Equation (6.2.20b) can also be written as

$$\frac{R_\theta}{R_\delta} = \frac{u_\tau}{\kappa u_e} \left( \frac{11}{12} + \Pi \right) - \left( \frac{u_\tau}{\kappa u_e} \right)^2 (1.9123016 + 3.0560\Pi + 1.5\Pi^2) \quad (6.2.20c)$$

Evaluating Eq. (6.2.19) at  $\eta = 1$ , we get

$$\sqrt{\frac{2}{c_f}} \equiv \frac{u_e}{u_\tau} = \frac{1}{\kappa} \left[ \ln \left( \frac{\delta u_e}{\nu} \frac{u_\tau}{u_e} \right) + 2\Pi \right] + c \quad (6.2.21)$$

For given values of  $c_f$  and  $R_\theta$ , Eqs. (6.2.20b) and (6.2.21) can be solved for  $\delta$  and  $\Pi$  so that the streamwise profile  $u$  can be obtained from Eqs. (6.2.19) in the region  $y^+ > 30$ .

The expression (6.2.17) with  $\phi_1(y^+)$  given by Eq. (6.2.3) is applicable for  $y^+ \geq 30$ . It can, however, be extended to include the region  $0 \leq y^+ \leq 30$  by the following formula due to Thompson [12],

$$u^+ = \begin{cases} y^+, & y^+ \leq 4 \\ c_1 + c_2 \ln y^+ + c_3 (\ln y^+)^2 + c_4 (\ln y^+)^3, & 4 < y^+ < 30 \end{cases} \quad (6.2.22)$$

where  $c_1 = 1.0828$ ,  $c_2 = -0.414$ ,  $c_3 = 2.2661$ ,  $c_4 = -0.324$ .

The expression (6.2.17) can also be extended to include the region  $y^+ \leq 50$  by the following formula due to Van Driest [13],

$$u^+ = \int_0^{y^+} \frac{2}{1 + \sqrt{1 + 4a^2}} dy^+ \quad (6.2.23)$$

where

$$a = \kappa y^+ [1 - \exp(y^+/A^+)] \quad (6.2.24)$$

Figure 6.10 shows the resulting profile from Eq. (6.2.23). Note that for large  $y^+$ , it reduces to that given by Eq. (6.2.3). The exponential factor  $A^+$  ( $\equiv 26$ ) is often called the “damping parameter”.

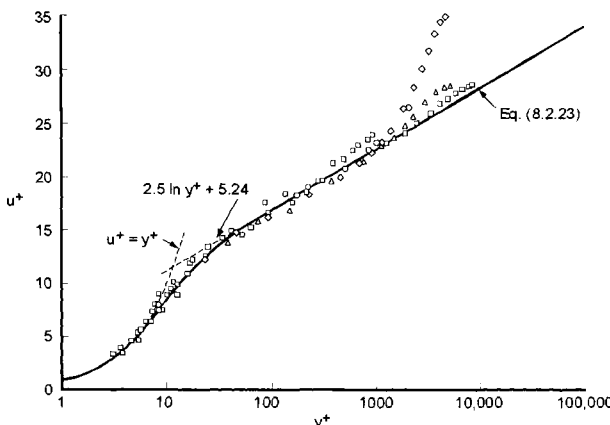


**Fig. 6.10.** Mean-velocity distribution in the inner region as calculated by Eq. (6.2.3) with  $\kappa = 0.4$ ,  $A^+ = 26$ . Symbols denote experimental data.

### Whitfield's Formula

The formula proposed by Whitfield et al. [10] expresses the velocity profile between the wall and the boundary-layer edge in terms of  $y^+$  and  $y/\theta$  by

$$\frac{u}{u_\tau} = \frac{S}{0.09} \tan^{-1}(0.09y^+) + \left( \left| \frac{c_f}{2} \right|^{\frac{1}{2}} - \frac{S\pi}{0.18} \right) \left[ \tanh \left( a \left( \frac{y}{\theta} \right)^b \right) \right]^{\frac{1}{2}} \quad (6.2.25)$$

where  $\theta$  is the momentum thickness and  $u_\tau$  the friction velocity. Absolute values are used because the formulas can also represent separated velocity profiles with negative skin friction. The coefficient  $S$  is equal to 1 for attached boundary-layers and  $S = -1$  for separated boundary layers.

The coefficients  $a$  and  $b$  are given by

$$a = \frac{\tanh^{-1} g^2(2)}{2^b} \quad (6.2.26a)$$

$$b = \frac{\ln \left( \frac{\tanh^{-1} g^2(2)}{\tanh^{-1} g^2(5)} \right)}{\ln \left( \frac{2}{5} \right)} \quad (6.2.26b)$$

The coefficients  $g(2)$  and  $g(5)$  are related to the values of  $u/u_e$  at  $y/\theta = 2$  and  $y/\theta = 5$ ,

$$g(2) = \left[ \frac{u}{u_e}(2) - \frac{S}{0.09} \left( \frac{|c_f|}{2} \right)^{\frac{1}{2}} \tan^{-1} \left( 0.18 \frac{u_e \theta}{\nu} \left( \frac{|c_f|}{2} \right)^{\frac{1}{2}} \right) \right] / \left[ 1 - \frac{S\pi}{0.18} \left( \frac{|c_f|}{2} \right)^{\frac{1}{2}} \right] \quad (6.2.27a)$$

$$g(5) = \left[ \frac{u}{u_e}(5) - \frac{S}{0.09} \left( \frac{|c_f|}{2} \right)^{\frac{1}{2}} \tan^{-1} \left( 0.45 \frac{u_e \theta}{\nu} \left( \frac{|c_f|}{2} \right)^{\frac{1}{2}} \right) \right] / \left[ 1 - \frac{S\pi}{0.18} \left( \frac{|c_f|}{2} \right)^{\frac{1}{2}} \right] \quad (6.2.27b)$$

The values of  $u/u_e$  at  $y/\theta = 2$  and  $y/\theta = 5$  are given as a function of shape parameter  $H$

$$\frac{u}{u_e}(2) = 1.723 \left( 1 + \frac{50}{R_\theta} \right) e^{-0.6H} \quad (6.2.28a)$$

$$\frac{u}{u_e}(5) = 0.87 + 0.08e^{-2.6(H-1.95)^2} \quad (6.2.28b)$$

## 6.3 Turbulence Models

The use of the Reynolds averaging procedure discussed in Section 2.3 introduces additional unknowns to the equations. Further approximations are required to represent the fluctuating quantities known as the Reynolds stresses in order to reduce the number of unknowns to equal the number of equations. This can be

done by using simple turbulence models based on algebraic mixing length and eddy viscosity models, also known as zero-equation models, or advanced turbulence models based on transport equations. Here we present a brief description of zero equation models (subsection 6.3.1) and models based on transport equations (subsection 6.3.2). For a complete discussion of turbulence models, especially advanced turbulence models, the reader is referred to [14, 15].

### 6.3.1 Zero-Equation Models

Zero-equation models used to model the Reynolds shear stress term in the momentum equations employ algebraic eddy viscosity or mixing-length formulations. In the eddy-viscosity ( $\nu_t$ ) approach, the boundary-layer equations for turbulent flow are written in the same form as the equations for laminar flow. For a two-dimensional incompressible flow,  $\nu_t$  is defined by

$$-\rho \overline{u'v'} = \rho \nu_t \frac{\partial u}{\partial y} \quad (6.3.1)$$

In the mixing length ( $l$ ) approach, the Reynolds shear stress is represented by

$$-\rho \overline{u'v'} = \rho l^2 \left( \frac{\partial u}{\partial y} \right)^2 \quad (6.3.2)$$

There are several formulations proposed to specify the variation of eddy viscosity or mixing length distributions in turbulent flows. For wall boundary-layer flows, a popular and widely used algebraic eddy viscosity formulation is due to Cebeci and Smith [14]. This two-layer method assumes that a turbulent boundary-layer can be considered in terms of eddy viscosities for inner and outer layers. The corresponding functions are empirical and based on limited ranges of experimental data; the range of data is, however, extensive so that the full algebraic formulation is the most general available at present.

In the inner region of a boundary-layer on a smooth surface, with or without mass transfer, the eddy viscosity  $\nu_t$  is written as

$$(\nu_t)_i = l^2 \left| \frac{\partial u}{\partial y} \right| \gamma_{tr}, \quad 0 \leq y \leq y_c \quad (6.3.3)$$

Here the mixing length  $l$  is given by

$$l = \kappa y \left[ 1 - \exp \left( -\frac{y}{A} \right) \right] \quad (6.3.4a)$$

where  $\kappa = 0.40$  and  $A$  is a damping-length constant, which may be represented by

$$A = 26 \frac{\nu}{N} u_\tau^{-1}, \quad N = \left\{ \frac{p^+}{v_w^+} [1 - \exp(11.8v_w^+)] + \exp(11.8v_w^+) \right\}^{\frac{1}{2}} \quad (6.3.4b)$$

$$p^+ = \frac{\nu u_e}{u_\tau^3} \frac{du_e}{dx}, \quad v_w^+ = \frac{v_w}{u_\tau} \quad (6.3.4c)$$

For flows with no mass transfer ( $v_w^+ = 0$ ), Eq. (6.3.4b) reduces to

$$N = (1 - 11.8p^+)^{1/2} \quad (6.3.4d)$$

and for a flow with no mass transfer and pressure gradient,  $N = 1$ .

In Eq. (6.3.3)  $\gamma_{\text{tr}}$  is an intermittency factor which represents the streamwise region from the onset of transition to turbulent flow. It is given by Eq. (5.2.4).

In the outer region, the eddy viscosity is given by

$$(\nu_t)_0 = \alpha \int_0^\delta (u_e - u) dy \gamma_{\text{tr}} \gamma = \alpha u_e \delta^* \gamma_{\text{tr}} \gamma, \quad y_c \leq y \leq \delta \quad (6.3.5)$$

Here  $\gamma$  accounts for the intermittency of the outer region and is represented by

$$\gamma = \left[ 1 + 5.5 \left( \frac{y}{\delta} \right)^6 \right]^{-1} \quad (6.3.6)$$

where  $\alpha$  is equal to 0.0168 and  $\delta$  is defined as the  $y$ -location where  $u/u_e = 0.995$ . Continuity of the expressions for the eddy viscosities in the inner and outer regions, Eqs. (6.3.3) and (6.3.5), defines these regions.

For wall boundary-layers on smooth surfaces with no mass transfer, the mixing length in Eq. (6.3.2) can be conveniently calculated from one single expression given by

$$\frac{l}{\delta} = \left[ 1 - \exp \left( -\frac{y}{A} \right) \right] 0.085 \tanh \left( \frac{\kappa}{0.085} \frac{y}{\delta} \right) \quad (6.3.7)$$

with  $\kappa$  equal to 0.41 and  $A = 26\nu/u_\tau$ . This formula, due to Michel et al. [17], is valid for the whole layer.

The mixing length distribution can also be calculated by defining separate expressions for the inner and outer regions of a turbulent boundary-layer. A convenient expression for the inner region is the one given by Eq. (6.3.4a). In the outer region, the mixing length can be represented by

$$l = 0.085\delta \quad (6.3.8)$$

with  $\delta$  defined by  $y$  where  $u/u_e$  is 0.995.

Figure 6.11 represents (a) the mixing-length and (b) eddy viscosity distributions across a flat plate turbulent boundary-layer measured by Klebanoff [2]. It can be seen from the results in Fig. 6.11a that Eq. (6.3.7) is a good representation of the mixing length distribution across a turbulent boundary-layer. Figure 6.11b shows that in the inner region, the eddy viscosity varies linearly with  $y$  and, except for the intermittency effect, stays nearly constant in the outer region.

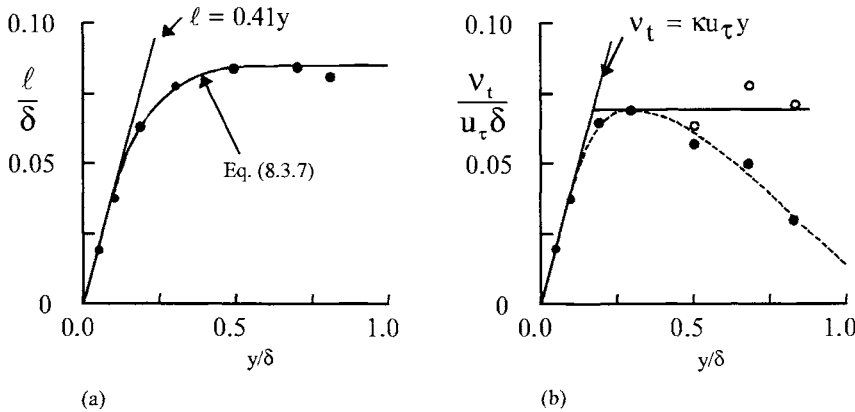


**Fig. 6.11.** Dimensionless (a) mixing-length and (b) eddy viscosity distributions across a turbulent boundary-layer in zero pressure gradient,  $u_e \theta / \nu \cong 8000$ . The symbols denote the experimental data from Klebanoff [2].

Before we conclude this brief discussion on zero-equation models, it is important to point out that neither the eddy viscosity nor the mixing length formulations described here perform well in strong adverse pressure gradient flows and separated flows. Comparison of calculated eddy-viscosity and mixing length distributions with experimental data shows that the parameter  $\alpha$  in Eq. (6.3.5) and the constant (0.085) in Eq. (6.3.8) decrease with increasing adverse pressure gradient. This is expected since the law of the wall region given by Eq. (6.2.3) becomes smaller with strong adverse pressure gradient and flow separation.

So far, two approaches have been pursued to improve the Cebeci-Smith model in strong adverse pressure-gradient flows. In one approach due to Johnson and King [18] and Johnson and Coakley [19], the parameter  $\alpha$  is computed from an ordinary differential equation derived from the turbulence kinetic energy equation. Another approach due to Cebeci and Chang [20, 21] calculates  $\alpha$  not from an ordinary differential equation but from an algebraic formula

$$\alpha = \frac{0.0168}{\left[1 - \beta \left(\frac{\partial u}{\partial x}\right)_m\right]^{1.5}} \quad (6.3.9)$$

where  $m$  corresponds to maximum shear stress. The parameter  $\beta$  is computed from

$$\beta = \begin{cases} \frac{6}{1 + 2R_t(2 - R_t)} & R_t \leq 1.0 \\ \frac{1 + R_t}{R_t} & R_t \geq 1.0 \end{cases} \quad (6.3.10)$$

where  $R_t$  denotes the ratio of wall shear to maximum Reynolds shear stress

$$R_t = \frac{\tau_w}{(-\rho u' v')_m} \quad (6.3.11)$$

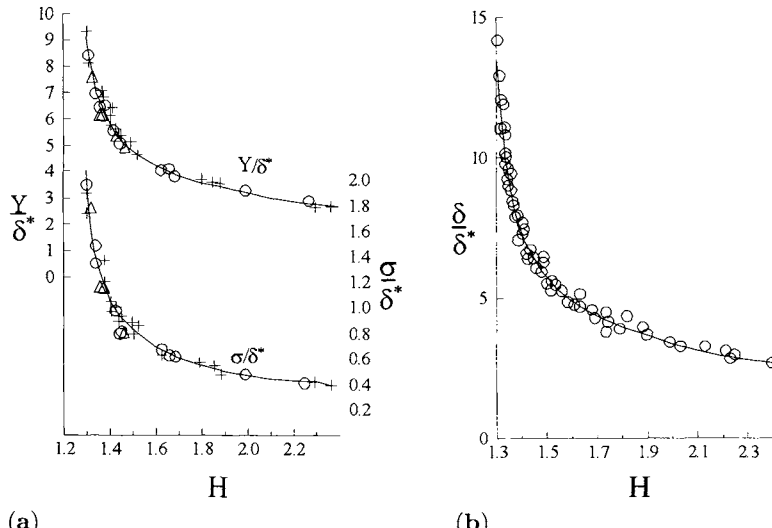


**Fig. 6.12.** Variation of (a)  $Y/\delta^*$  and  $\sigma/\delta^*$  and (b)  $\delta/\delta^*$  with  $H$  according to the data of [22].

Another improvement made by Cebeci and Chang in the CS model is to replace the intermittency parameter  $\gamma$  in Eq. (6.3.6) by another intermittency expression recommended in [22]. According to the experiments conducted by Fiedler and Head, it was found that the pressure gradient has a marked effect on the distribution of intermittency defined as the ratio of time turbulent to total time at any point so that it measures the probability of finding turbulent flow at any instant at the point considered. Their experiments indicated that in the boundary-layer proceeding to separation, the intermittent zone decreases in width and moves further from the surface as shape factor  $H$  increases. The reverse trend is observed with decreasing  $H$  in a favorable pressure gradient.

In the improved CS model the intermittency expression of [22] was written in the form

$$\gamma = \frac{1}{2} \left[ 1 - \operatorname{erf} \frac{[y - Y]}{\sqrt{2}\sigma} \right] \quad (6.3.12)$$

where  $Y$  and  $\sigma$  are general intermittency parameters with  $Y$  denoting value of  $y$  for which  $\gamma = 0.5$  and  $\sigma$ , the standard deviation. The dimensionless intermittency parameters  $Y/\delta^*$  and  $\sigma/\delta^*$  were expressed as functions of  $H$  as shown in Fig. 6.12a. The variation of the ratio of boundary-layer thickness  $\delta$  to  $\delta^*$  with  $H$  is shown in Fig. 6.12b.

### 6.3.2 Turbulence Models Based on Transport Equations

While the zero-equation models are useful and accurate for most wall boundary-layer flows, these models lack generality. For turbulent shear flows other than

wall boundary-layers, they require different expressions for mixing length and eddy viscosities. For example, for a plane jet

$$l = 0.09\delta \quad (6.3.13a)$$

for a round jet

$$l = 0.07\delta \quad (6.3.13b)$$

and for a plane wake

$$l = 0.16\delta \quad (6.3.13c)$$

with  $\delta$  denoting the shear layer thickness.

Turbulence models based on transport equations have less limitations than the zero-equation models for modeling Reynolds stresses. There are several models based on this approach. They are discussed in detail in [14, 15] and briefly here.

### One-Equation Models

Of the several models that fall in this group, we only consider the model due to Spalart and Allmaras (SA), which unlike the Cebeci-Smith model which uses algebraic expressions for eddy viscosity, SA model uses a semi-empirical transport equation for eddy viscosity  $\nu_t$ . Its defining equations are as follows.

$$\begin{aligned} u \frac{\partial \tilde{\nu}_t}{\partial x} + v \frac{\partial \tilde{\nu}_t}{\partial y} &= c_{b1} (1 - f_{t2}) \tilde{S} \tilde{\nu}_t + \frac{1}{\sigma} \left\{ \frac{\partial}{\partial y} \left[ (\nu + \tilde{\nu}_t) \frac{\partial \tilde{\nu}_t}{\partial y} \right] + c_{b2} \left( \frac{\partial \tilde{\nu}_t}{\partial y} \right)^2 \right\} \\ &\quad - \left( c_{w1} f_w - \frac{c_{b1}}{\kappa^2} f_{t2} \right) \left( \frac{\bar{\nu}_t}{d} \right)^2 \end{aligned} \quad (6.3.14)$$

where

$$\nu_t = \tilde{\nu}_t f_{v1} \quad (6.3.15)$$

Here

$$c_{b1} = 0.1355, \quad c_{b2} = 0.622, \quad c_{v1} = 7.1, \quad \sigma = \frac{2}{3} \quad (6.3.16a)$$

$$c_{w1} = \frac{c_{b1}}{\kappa^2} + \frac{(1 + c_{b2})}{\sigma}, \quad c_{w2} = 0.3, \quad c_{w3} = 2, \quad \kappa = 0.41 \quad (6.3.16b)$$

$$f_{\nu_1} = \frac{(\nu_t^+)^3}{(\nu_t^+)^3 + c_{\nu_1}^3}, \quad f_{\nu_2} = 1 - \frac{\nu_t^+}{1 + \nu_t^+ f_{\nu_1}}, \quad f_w = g \left[ \frac{1 + c_{w3}^6}{g^6 + c_{w3}^6} \right]^{1/6} \quad (6.3.16c)$$

$$\nu_t^+ = \frac{\tilde{\nu}_t}{\nu}, \quad g = r + c_{w2}(r^6 - r), \quad r = \frac{\tilde{\nu}_t}{\tilde{S} \kappa^2 d^2} \quad (6.3.16d)$$

$$\tilde{S} = \left| \frac{\partial u}{\partial y} \right| + \frac{\tilde{\nu}_t}{\kappa^2 d^2} f_{\nu_2}, \quad (6.3.16e)$$

$$f_{t2} = c_{t3} e^{-c_{t4}(\nu_t^+)^2}, \quad c_{t3} = 1.1, \quad c_{t4} = 2 \quad (6.3.16f)$$

where  $d$  is the distance to the closest wall.

The boundary conditions are

$$y = 0, \quad \tilde{\nu}_t = 0 \quad (6.3.17a)$$

$$y \rightarrow \infty, \quad \tilde{\nu}_t \rightarrow 0 \quad (6.3.17b)$$

## Two-Equation Models

While one-equation models have found little favor except for the SA model, and where transport of turbulence characteristics is important as in strong adverse gradients or in separated flows, two equations have found extensive use. Various forms of two-equation models have been proposed and details have been given, for example in [14, 15]. Three popular models that are based on this approach are the  $k-\varepsilon$  model of Jones and Launder [23], the  $k-\omega$  model of Wilcox [15], and SST model of Menter [14, 15] which blends the  $k-\varepsilon$  model in the outer region and  $k-\omega$  model in the wall region. Here we consider the  $k-\varepsilon$  model, which is again based on the eddy viscosity concept with  $\nu_t$  given by

$$\nu_t = c_\mu \frac{k^2}{\varepsilon} \quad (6.3.18)$$

where  $c_\mu$  denotes a constant, and  $k$  and  $\varepsilon$  are obtained from differential equations which represent the transport of turbulence energy,  $k$ , and rate of dissipation,  $\varepsilon$ . They are given by [14, 15]

$$u \frac{\partial k}{\partial x} + v \frac{\partial k}{\partial y} = \frac{\partial}{\partial y} \left( \frac{\nu_t}{\sigma_k} \frac{\partial k}{\partial y} \right) + \nu_t \left( \frac{\partial u}{\partial y} \right)^2 - \varepsilon \quad (6.3.19)$$

$$u \frac{\partial \varepsilon}{\partial x} + v \frac{\partial \varepsilon}{\partial y} = \frac{\partial}{\partial y} \left( \frac{\nu_t}{\sigma_\varepsilon} \frac{\partial \varepsilon}{\partial y} \right) + c_{\varepsilon_1} \frac{\varepsilon}{k} \nu_t \left( \frac{\partial u}{\partial y} \right)^2 - c_{\varepsilon_2} \frac{\varepsilon^2}{k} \quad (6.3.20)$$

Here the three terms on the right hand side of Eq. (6.3.19) denote turbulent diffusion, turbulent energy production and viscous dissipation, respectively, and the parameters  $c_\mu$ ,  $c_{\varepsilon_1}$ ,  $c_{\varepsilon_2}$ ,  $\sigma_k$  and  $\sigma_\varepsilon$  are given by

$$c_\mu = 0.09, \quad c_{\varepsilon_1} = 1.44, \quad c_{\varepsilon_2} = 1.92, \quad \sigma_k = 1.0, \quad \sigma_\varepsilon = 1.3 \quad (6.3.21)$$

These equations apply only to free shear flows. For wall boundary-layer flows, they require modifications to account for the presence of the wall.

There are several approaches that can be used to model Eqs. (6.3.19) and (6.3.20) near the wall region. For example, in one approach, wall functions are introduced into Eqs. (6.3.19) and (6.3.20) so that the model equations are applicable throughout the whole layer. Launder and Sharma [24] modify Eq. (6.3.18)

$$\nu_t = c_\mu f_\mu \frac{k^2}{\varepsilon} \quad (6.3.22)$$

and rewrite Eqs. (6.3.19) and (6.3.20) as

$$u \frac{\partial k}{\partial x} + v \frac{\partial k}{\partial y} = \frac{\partial}{\partial y} \left( \frac{\nu_t}{\sigma_k} \frac{\partial k}{\partial y} \right) + \nu_t \left( \frac{\partial u}{\partial y} \right)^2 - \varepsilon - 2\nu \left( \frac{\partial k^{1/2}}{\partial y} \right)^2 \quad (6.3.23)$$

$$u \frac{\partial \varepsilon}{\partial x} + v \frac{\partial \varepsilon}{\partial y} = \frac{\partial}{\partial y} \left( \frac{\nu_t}{\sigma_\varepsilon} \frac{\partial \varepsilon}{\partial y} \right) + c_{\varepsilon_1} \frac{\varepsilon}{k} \nu_t \left( \frac{\partial u}{\partial y} \right)^2 - f_2 c_{\varepsilon_2} \frac{\varepsilon^2}{k} + 2\nu \nu_t \left( \frac{\partial^2 u}{\partial y^2} \right)^2 \quad (6.3.24)$$

where

$$f_\mu = \exp \left[ -\frac{3.4}{(1 + R_t/50)^2} \right], \quad R_t = \frac{k^2}{\nu \varepsilon} \quad (6.3.25a)$$

$$f_2 = 1 - 0.3 \exp(-R_t^2) \quad (6.3.25b)$$

The boundary conditions are

$$y = 0, \quad k = \varepsilon = 0 \quad (6.3.26a)$$

$$y \rightarrow \delta, \quad k \rightarrow k_e, \quad \varepsilon \rightarrow \varepsilon_e \quad (6.3.26b)$$

To avoid numerical problems,  $k_e$  and  $\varepsilon_e$  should not be zero. In addition,  $k_e$  and  $\varepsilon_e$  can not be prescribed arbitrarily because their development is governed by the transport equations (6.3.23) and (6.3.24) written at the boundary-layer edge,

$$u_e \frac{dk_e}{dx} = -\varepsilon_e \quad (6.3.27a)$$

$$u_e \frac{d\varepsilon_e}{dx} = -c_{\varepsilon_2} \frac{\varepsilon_e^2}{k_e} \quad (6.3.27b)$$

The above equations can be integrated with respect to  $x$  with initial conditions corresponding to  $k_{e0}$  and  $\varepsilon_{e0}$  at  $x_0$ . The solution provides the evolutions of  $k(x)$  and  $\varepsilon(x)$  as boundary conditions for the  $k$ - and  $\varepsilon$ -equations.

Another approach, sometimes referred to as the *two-layer method*, employs a simple model near the wall (a mixing length model [25] or a one equation model [26] which is valid only near the wall region and a transport equation model in the outer region of the boundary-layer; the two solutions are matched at a certain point in the boundary-layer as discussed by Arnal et al. [25].

Figure 6.13 shows the results obtained with a  $k$ - $\varepsilon$  model which employed a two-layer method with a mixing-length model. The flow corresponds to an incompressible turbulent adverse pressure-gradient flow in which the turbulence level was not low. The calculations were made in order to assess the ability of the model to predict the effect of higher turbulence levels which improve the mixing between the external flow and the boundary-layer leading to higher skin friction  $c_f$  and lower shape factor  $H$ . The  $k$ - $\varepsilon$  model, contrary to the zero-equation models, allows the freestream turbulence effects to be taken into account by the boundary conditions at the boundary-layer edge (the level of kinetic energy at  $y = \delta$  is specified from experiment). As can be seen, the agreement between calculated results [25] and experimental data is very good.

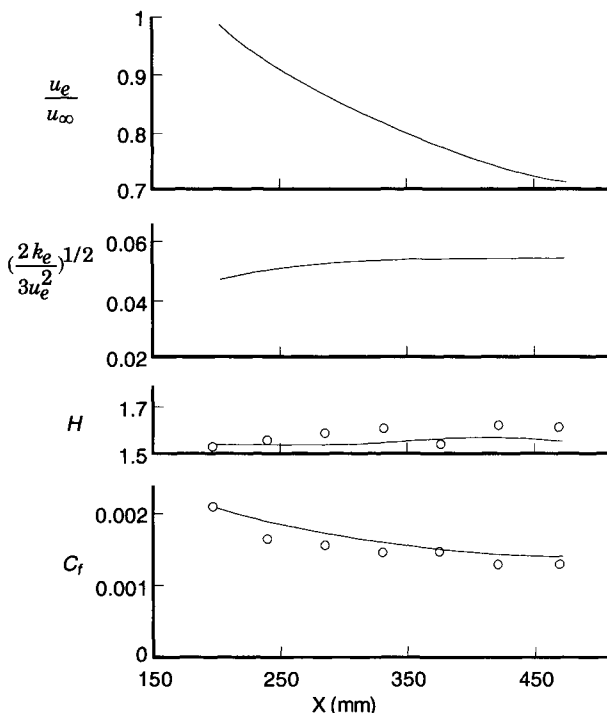


**Fig. 6.13.** Effect of freestream turbulence on the boundary-layer development. Solid lines denote the calculations and symbols denote the experimental data.

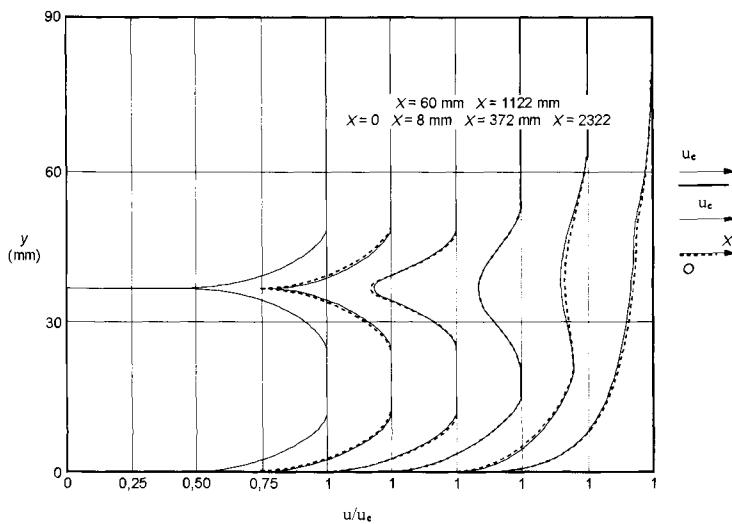


**Fig. 6.14.** Mixing of a boundary-layer and wake. Solid lines denote the calculations and symbols the experimental data.

Figure 6.14 shows another example computed by Cousteix et al. [27], again with a  $k-\varepsilon$  model in order to demonstrate the ability of this model to calculate flows other than wall boundary-layer flows without any modifications to the model. The flow in Fig. 6.14 corresponds to the mixing of a boundary-layer with a wake developing above the boundary-layer. As can be seen, the  $k-\varepsilon$  model produces results which are in very good agreement with the experimental data [28].

### Reynolds Stress Models

The Reynolds shear stress  $-\overline{\rho u' v'}$  appearing in the momentum equation (3.1.10) can also be modelled by using the Reynolds transport equation. In tensor form, this equation can be written as

$$\frac{D(\overline{u'_i u'_j})}{Dt} = P_{ij} - D_{ij} + \Phi_{ij} + \frac{\partial J_{ijl}}{\partial x_l} \quad (6.3.28)$$

$$P_{ij} = -(\overline{u'_i u'_l}) \frac{\partial u_j}{\partial x_l} - (\overline{u'_j u'_l}) \frac{\partial u_i}{\partial x_l} \quad (6.3.29a)$$

$$D_{ij} = 2\nu \frac{\overline{\partial u'_i \partial u'_j}}{\partial x_l \partial x_l} \quad (6.3.29b)$$

$$\Phi_{ij} = \frac{p'}{\rho} \left( \frac{\partial u'_i}{\partial x_j} + \frac{\partial u'_j}{\partial x_i} \right) \quad (6.3.29c)$$

$$J_{ijl} = -\overline{u'_i u'_j u'_l} - \overline{\frac{p'}{\rho}(u'_i \delta_{jl} + u'_j \delta_{il})} + \nu \frac{\partial \overline{u'_i u'_j}}{\partial x_l} \quad (6.3.29d)$$

The meaning of various terms in the above equation are

- $P_{ij}$  is the production term due to the interaction between Reynolds stresses and velocity gradients.
- $D_{ij}$  is the destruction term due to the action of viscosity
- $\Phi_{ij}$  is called the pressure-strain term which distributes kinetic energy  $k$  of turbulence among its components,  $\overline{u'_i}^2$  since  $\Phi_{ii}$  is equal to zero by the continuity equation for the fluctuating velocities.
- $J_{ijl}$  is a diffusion term due to viscosity and the fluctuations of velocity and pressure.

As in the momentum equation, closure assumptions are needed for Eq. (6.3.28) before it can be solved. There are several models developed for this purpose, most of which are applicable to turbulent flows where the effects of viscosity and the presence of the wall are neglected.

A popular model is due to Launder, Reece and Rodi [29]. According to this model, with  $P_{ij}$  given by Eq. (6.3.29c), the terms  $D_{ij}$ ,  $\Phi_{ij}$  and  $J_{ijl}$  are given by

$$D_{ij} = \frac{2}{3} \delta_{ij} \varepsilon \quad (6.3.30a)$$

$$\phi_{ij} + \phi_{ji} = -C_1 \frac{\varepsilon}{k} \left( \overline{u'_i u'_j} - \frac{2}{3} \delta_{ij} k \right) - C'_2 \left( P_{ij} - \frac{2}{3} \delta_{ij} P \right) \quad (6.3.30b)$$

$$k = \frac{\overline{u'_i u'_i}}{2}; \quad P = -\overline{u'_m u'_l} \frac{\partial u_m}{\partial x_l} \quad (6.3.30c)$$

$$J_{ijl} = C'_s \frac{k}{\varepsilon} \overline{u'_l u'_m} \frac{\partial}{\partial x_m} \overline{u'_i u'_j} \quad (6.3.30d)$$

The model is completed by a transport equation for the rate of dissipation  $\varepsilon$ ,

$$\frac{D\varepsilon}{Dt} = -C_{\varepsilon 1} \frac{\varepsilon}{k} \overline{u'_m u'_l} \frac{\partial u_m}{\partial x_l} - C_{\varepsilon 2} \frac{\varepsilon^2}{k} + \frac{\partial}{\partial x_l} \left( C'_\varepsilon \frac{k}{\varepsilon} \overline{u'_m u'_l} \frac{\partial \varepsilon}{\partial x_m} \right) \quad (6.3.31)$$

where

$$\begin{aligned} C_1 &= 1.8, & C'_2 &= 0.6 \\ C_{\varepsilon 1} &= 1.44, & C_{\varepsilon 2} &= 1.92 \\ C'_s &= 0.22, & C'_\varepsilon &= 0.15 \end{aligned} \quad (6.3.32)$$

To include the wall effects in this model, Gibson and Launder [30] modified the pressure-strain term by adding the following terms to Eq. (6.3.30b)

$$\phi_{ij,w} + \phi_{ji,w} = f \left( f_{km} n_k n_m \delta_{ij} - \frac{3}{2} f_{ki} n_k n_j - \frac{3}{2} f_{kj} n_k n_i \right) \quad (6.3.33)$$

where, with  $x_m$  representing distance from the wall and  $n_i$  the components of the unit vector normal to the wall,

$$f = \frac{k^{3/2}}{2.5 \varepsilon x_n}$$

$$f_{\alpha\beta} = C_{1w} \frac{\varepsilon}{k} \overline{u'_\alpha u'_\beta} + C_{2w} (\phi_{\alpha\beta,2} + \phi_{\beta\alpha,2}) \quad (6.3.34)$$

$$C_{1w} = 0.5, \quad C_{2w} = 0.3$$

For a two-dimensional boundary-layer flow, the Reynolds stress model equations discussed above can be written in the following form

$$\frac{D}{Dt} \overline{u'v'} = -A_{12} \overline{v'^2} \frac{\partial u}{\partial y} - B_{12} \frac{\varepsilon}{k} \overline{u'v'} + \frac{\partial}{\partial y} \left( C'_s \frac{k}{\varepsilon} \overline{v'^2} \frac{\partial \overline{u'v'}}{\partial y} \right) \quad (6.3.35)$$

$$\frac{D}{Dt} \overline{u'^2} = -A_{11} \overline{u'v'} \frac{\partial u}{\partial y} - B_{11} \frac{\varepsilon}{k} \overline{u'^2} + C_{11} \varepsilon + D_{11} \frac{\varepsilon}{k} \overline{v'^2} + \frac{\partial}{\partial y} \left( C'_s \frac{k}{\varepsilon} \overline{v'^2} \frac{\partial \overline{u'^2}}{\partial y} \right) \quad (6.3.36)$$

$$\frac{D}{Dt} \overline{v'^2} = -A_{22} \overline{u'v'} \frac{\partial u}{\partial y} - B_{22} \frac{\varepsilon}{k} \overline{v'^2} + C_{22} \varepsilon + \frac{\partial}{\partial y} \left( C'_s \frac{k}{\varepsilon} \overline{v'^2} \frac{\partial \overline{v'^2}}{\partial y} \right) \quad (6.3.37)$$

$$\frac{D}{Dt} \overline{w'^2} = -A_{33} \overline{u'v'} \frac{\partial u}{\partial y} - B_{33} \frac{\varepsilon}{k} \overline{w'^2} + C_{33} \varepsilon + D_{33} \frac{\varepsilon}{k} \overline{v'^2} + \frac{\partial}{\partial y} \left( C'_s \frac{k}{\varepsilon} \overline{v'^2} \frac{\partial \overline{w'^2}}{\partial y} \right) \quad (6.3.38)$$

$$\frac{D\varepsilon}{Dt} = -C_{\varepsilon_1} \frac{\varepsilon}{k} \overline{u'v'} \frac{\partial u}{\partial y} - C_{\varepsilon_2} \frac{\varepsilon^2}{k} + \frac{\partial}{\partial y} \left( C'_\varepsilon \frac{k}{\varepsilon} \overline{v'^2} \frac{\partial \varepsilon}{\partial y} \right) \quad (6.3.39)$$

where with  $f$  given by

$$f = \frac{k^{3/2}}{2.5\varepsilon y} \quad (6.3.40)$$

the various terms in the above equations are

$$\begin{aligned} A_{12} &= 1 - C'_2 + \frac{3}{2} f C'_2 C_{2w}, & B_{12} &= C_1 + \frac{3}{2} f C_{1w} \\ A_{11} &= 2 - \frac{4}{3} C'_2 + \frac{2}{3} f C'_2 C_{2w}, & B_{11} &= C_1 \\ C_{11} &= \frac{2}{3} C_1 - \frac{2}{3}, & D_{11} &= C_{1w} f \\ A_{22} &= \frac{2}{3} C'_2 - \frac{4}{3} f C'_2 C_{2w}, & B_{22} &= C_1 + 2 f C_{1w}, & C_{22} &= \frac{2}{3} C_1 - \frac{2}{3} \\ A_{33} &= \frac{2}{3} C'_2 + \frac{2}{3} f C'_2 C_{2w}, & B_{33} &= C_1, & C_{33} &= \frac{2}{3} C_1 - \frac{2}{3}, & D_{33} &= f C_{1w} \end{aligned} \quad (6.3.41)$$

The presence of the wall is neglected merely by setting  $f = 0$ .

It should be noted that the above model is applicable only to high Reynolds number flows at some distance  $y_0$  away from the wall where the flow is fully turbulent. Modifications are required to extend the model and the calculations all the way to the wall. Several models have been proposed for this purpose [15].

## 6.4 Turbulent Boundary-Layers on Smooth and Rough Surfaces with Zero Pressure Gradient

Once a satisfactory model for Reynolds shear stress is devised, differential methods similar to those discussed in Section 4.5, with  $\nu$  replaced by  $(\nu + \nu_t)$ , can be used to compute the development of external boundary-layers on two-dimensional and axisymmetric bodies with different boundary conditions. One such method based on the extension of the method discussed in Section 4.5 is discussed in Section 6.6. However, all these methods require the use of computers. Sometimes it is useful to have simple methods or formulas that do not require the use of computers and can be used with reasonable accuracy for computing boundary-layers. In this section we discuss such practical formulas, which can be used for turbulent flows over smooth and rough surfaces with zero pressure gradient. In Section 6.5 we discuss integral methods for computing two-dimensional turbulent flows over smooth surfaces with pressure gradient.

### 6.4.1 Smooth Flat Plate

Consider an incompressible flow over a smooth flat plate (zero pressure gradient). If the Reynolds number is sufficiently large, we can identify three different flow regimes on such a surface (Fig. 6.15). Starting from the leading edge, there is first a region ( $0 < R_x < R_{x_{tr}}$ ) in which the flow is laminar, or laminar with small instability oscillations (Chapter 6). Further downstream, there is a region ( $R_{x_{tr}} < R_x < R_{x_t}$ ) in which transition from laminar to turbulent flow takes place, following the first appearance of isolated spots of turbulence at  $x_{tr}$ . In the third region ( $R_x \geq R_{x_t}$ ) the flow is fully turbulent. The transition Reynolds number  $R_{x_{tr}}$  depends partly upon the turbulence in the freestream;  $R_{x_{tr}}$  may be as low as  $5 \times 10^5$ . A typical natural transition Reynolds number on a smooth flat plate is  $3 \times 10^6$ . The dashed line in Fig. 6.15 represents the development of an imaginary turbulent boundary-layer, starting with zero thickness at  $x = x_0$  and matching the thickness of the real boundary-layer at  $x = x_t$ . The point  $x = x_0$  is called the “effective” or “virtual” origin of the turbulent boundary-layer. In practice, it is estimated by upstream extrapolations of the formulas for growth of the real boundary-layer.

For a two-dimensional zero pressure gradient flow, by using the definition of local skin-friction coefficient,  $c_f$ , the momentum integral equation (3.3.10) can be written as

$$\frac{dR_\theta}{dR_x} = \frac{c_f}{2} \quad (6.4.1)$$

where  $R_\theta = u_e \theta / \nu$  and  $R_x = u_e x / \nu$ . Denoting  $(2/c_f)^{1/2}$  by  $z$ , assuming that the transition from laminar to turbulent flow takes place instantaneously, ( $R_{x_{tr}} = R_{x_t}$ ), and using integration by parts, we can express Eq. (6.4.1) in the form

$$R_x = z^2 R_\theta - 2 \int_{z_{tr}}^z R_\theta z dz + \text{const.} \quad (6.4.2)$$

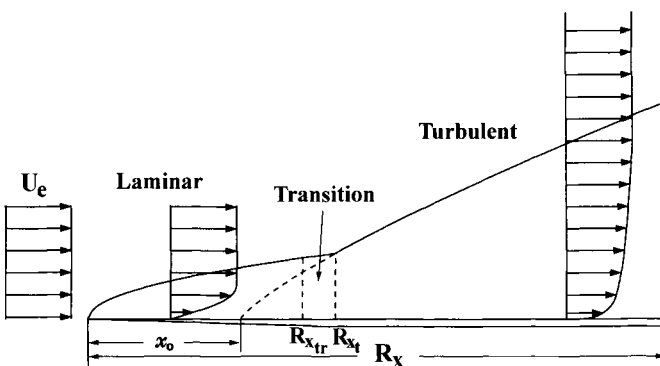


**Fig. 6.15.** Boundary-layer on a smooth flat plate at sufficiently large Reynolds numbers. (The vertical scale is greatly enlarged.)

This equation can be used to obtain a relationship between  $R_x$  and, say,  $c_f$ , if we express  $R_\theta$  as a function of  $z$  and integrate the integral in Eq. (6.4.2). That can be done in a number of ways. Cebeci and Smith [14] describe a procedure that utilizes Coles' expression [Eq. (6.2.17)], together with the integral of the velocity-defect law for a flat plate, and write Eq. (6.4.2) as

$$(R_x - A_2)c_f = 0.324 \exp\left(\frac{0.58}{\sqrt{c_f}}\right) (1 - 8.125\sqrt{c_f} + 22.08c_f) \quad (6.4.3)$$

Here  $A_2$  is an integration constant that depends on where transition occurs. It is given by

$$A_2 = R_{x_{tr}} - \frac{2R_{\theta_{tr}}}{c_{f_{tr}}} + \left( \frac{1.12}{\sqrt{c_{f_{tr}}}} - 7.16 \right) \exp\left(\frac{0.58}{\sqrt{c_{f_{tr}}}}\right) \quad (6.4.4)$$

where  $c_{f_{tr}}$  is the local skin-friction coefficient for turbulent flow calculated at the transition Reynolds number.

Putting  $A_2 = 0$  in Eq. (6.4.3), taking logarithms, and making further approximations leads to formulas like

$$\frac{1}{\sqrt{c_f}} = a + b \log(c_f R_x) \quad (6.4.5a)$$

where  $a$  and  $b$  are constants chosen to get the best agreement with experiment. Such formulas have been derived by many previous workers. Von Karman (see [4]) took  $a = 1.7$  and  $b = 4.15$  and approximated Eq. (6.4.3) as

$$\frac{1}{\sqrt{c_f}} = 1.7 + 4.15 \log(c_f R_x) \quad (6.4.5b)$$

A formula for the streamwise-average skin friction that makes use of Eq. (6.4.5b) was also obtained by Schoenherr [4]

$$\frac{1}{\sqrt{\bar{c}_f}} = 4.13 \log(\bar{c}_f R_x) \quad (6.4.6)$$

where

$$\bar{c}_f = \frac{1}{x} \int_0^x c_f(z) dz$$

Schoenherr also related  $\bar{c}_f$  to  $R_\theta$  and expressed the relationship as

$$\frac{1}{\sqrt{\bar{c}_f}} = 1.24 + 4.13 \log R_\theta \quad (6.4.7)$$

Equation (P6.2.2) with  $H = 0.55$  for a constant pressure boundary-layer, gives

$$H = \frac{1}{1 - 4.67\sqrt{\bar{c}_f}} \quad (6.4.8)$$

which can be used to replace  $R_\theta$  by  $R_{\delta^*} \equiv u_e \delta^* / \nu = H R_\theta$  in the above formulas.

Much simpler, but less accurate, relations between  $\delta$ ,  $c_f$ ,  $\delta^*$ ,  $\theta$  and  $H$  can also be obtained if we use the power-law assumption for the velocity distribution in which we assume

$$\frac{u}{u_e} = \left(\frac{y}{\delta}\right)^{1/n} \quad (6.4.9)$$

Here the exponent  $n$  is about 7 in a constant pressure boundary-layer, increasing slowly with Reynolds number. Using Eq. (6.4.9) and the definitions of  $\delta^*$ ,  $\theta$  and  $H$ , we can show that

$$\begin{aligned} \frac{\delta^*}{\delta} &= \frac{1}{1+n} \\ \frac{\theta}{\delta} &= \frac{n}{(1+n)(2+n)} \\ H &= \frac{2+n}{n} \end{aligned} \quad (6.4.10)$$

Other formulas obtained from power-law assumptions, given by Schlichting [4], are the following:

$$c_f = \frac{0.059}{R_x^{1/5}} \quad (6.4.11)$$

$$\bar{c}_f = \frac{0.074}{R_x^{1/5}} \quad (6.4.12)$$

$$\frac{\delta}{x} = \frac{0.37}{R_x^{1/5}} \quad (6.4.13)$$

$$\frac{\theta}{x} = \frac{0.036}{R_x^{1/5}} \quad (6.4.14)$$

Those equations are valid only for Reynolds numbers,  $R_x$ , between  $5 \times 10^5$  and  $10^7$ . At higher Reynolds numbers the boundary-layer thickness can be calculated more accurately by the following empirical formula given by Granville [31]

$$\frac{\delta}{x} = \frac{0.0598}{\log R_x - 3.170} \quad (6.4.15)$$

This equation was obtained on the assumption that the boundary-layer is turbulent from the leading edge onward, that is, that the effective origin defined above is at  $x = 0$ . If the flow is turbulent but the Reynolds number is moderate, we should consider the portion of the laminar flow that precedes the turbulent flow. There are several empirical formulas for  $\bar{c}_f$  that account for this effect. One is the formula quoted by Schlichting [4]. It is given by

$$\bar{c}_f = \frac{0.455}{(\log R_x)^{2.58}} - \frac{A}{R_x} \quad (6.4.16)$$

and another is

$$\bar{c}_f = \frac{0.074}{R_x^{1/5}} - \frac{A}{R_x}, \quad 5 \times 10^5 < R_x < 10^7 \quad (6.4.17)$$

Here  $A$  is a constant that depends on the transition Reynolds number  $R_{x_t}$ . It is given by

$$A = R_{x_{tr}}(\bar{c}_{f_t} - \bar{c}_{f_l}) \quad (6.4.18)$$

where  $\bar{c}_{f_t}$  and  $\bar{c}_{f_l}$  correspond to the values of average skin friction coefficient for turbulent and laminar flow at  $R_{x_{tr}}$ . We note that while Eq. (6.4.17) is restricted to the indicated  $R_x$  range, Eq. (6.4.16) is valid for a wide range of  $R_x$  and has given good results up to  $R_x = 10^9$ .

#### 6.4.2 Rough Flat Plate

A procedure similar to that used for a smooth flat plate can be used to obtain the boundary-layer parameters for an incompressible turbulent flow over a rough flat plate; see, for example, [14]. The results can be represented in two graphs. Figures 6.16 and 6.17 show the variation of  $c_f$  and  $\bar{c}_f$  with  $R_x$  for sand-roughened flat plates. Also shown in these figures are the lines for constant-roughness Reynolds number,  $R_k = u_e k / \nu$ , and for constant relative roughness,  $x/k$ . As in the case of the smooth flat-plate problem, the origin of the turbulent boundary-layer is assumed to be close to the leading edge of the plate.

In the complete rough regime it is possible to make use of the following interpolation formulas given by Schlichting [4] for the coefficients of skin friction in terms of relative roughness:

$$c_f = \left( 2.87 + 1.58 \log \frac{x}{k_s} \right)^{-2.5} \quad (6.4.19)$$

$$\bar{c}_f = \left( 1.89 + 1.62 \log \frac{x}{k_s} \right)^{-2.5} \quad (6.4.20)$$

which is valid for  $10^2 < x/k_s < 10^6$ .

The values of  $c_f$  and  $\bar{c}_f$  presented in Figs. 6.16 and 6.17 are for sand type of roughness only. Furthermore, the values are for maximum sand density, that is, on the rough plates of Nikuradse the grains of sand are glued to the wall as close as possible to each other. In many practical applications the roughness density is considerably less. Also, the roughness would be of different shapes. As was mentioned in Section 6.2, it is convenient to classify all types of roughness, except the anomalous  $d$ -type, by the “equivalent sand roughness”, where equivalent sand roughness is defined as that value of  $k$  that gives the same skin-friction coefficient as the actual roughness (when it is substituted in the equations for  $c_f$  presented in Figs. 6.16 and 6.17, say). Schlichting [4] and Hoerner [32] report experimentally determined values of equivalent sand roughness for various types of rough surfaces. Some of the values determined for practical physical surfaces

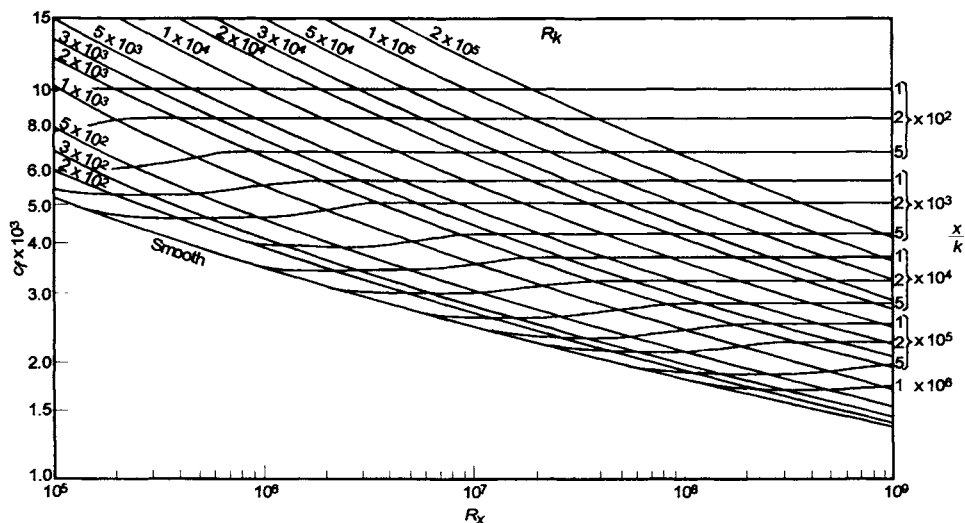


Fig. 6.16. Local skin-friction coefficient on a sand-roughened flat plate.

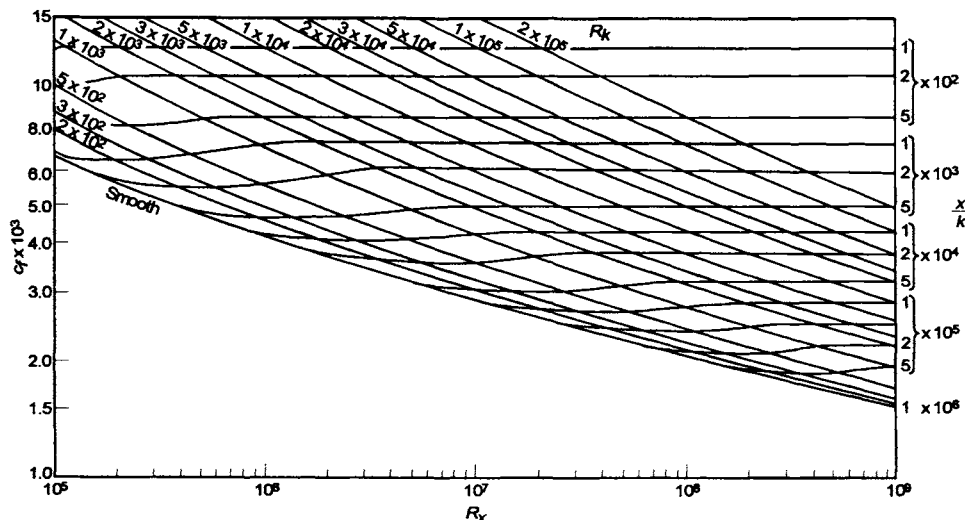


Fig. 6.17. Average skin-friction coefficient on sand-roughened flat plate.

are given in Table 6.1. The  $d$ -type groove roughness, the effects of which do not scale on roughness height, is rare in practice. It should be noted that equivalent sand grain roughness concept only applies to fully rough flow conditions, that is when  $\Delta u_\tau$  shift is independent of  $k^+$ .

**Table 6.1.** Equivalent sand roughness for several types of surfaces.

Type of Surface	$k_s$ , cm
Aerodynamically smooth surface	0
Polished metal or wood	$0.05\text{--}0.2 \times 10^{-3}$
Natural sheet metal	$0.4 \times 10^{-3}$
Smooth matte paint, carefully applied	$0.6 \times 10^{-3}$
Standard camouflage paint, average application	$1 \times 10^{-3}$
Camouflage paint, mass-production spray	$3 \times 10^{-3}$
Dip-galvanized metal surface	$15 \times 10^{-3}$
Natural surface of cast iron	$25 \times 10^{-3}$

## 6.5 Turbulent Boundary-Layers with Pressure Gradient: Integral Methods

There are several integral methods for calculating two-dimensional turbulent boundary-layers in pressure gradient [33], all of which use the momentum-integral equation, a formula relating  $c_f$  to the Reynolds number and a profile shape parameter, and an ordinary differential equation for the rate of change of profile shape parameter with  $x$ . The skin-friction formula can be Eq. (6.2.21) or a wholly empirical data correlation. The shape-parameter equation can be seen to contain all the information about the Reynolds stress within the layer. It is usually a linear relation between  $\theta dH/dx$  and  $(\theta/u_e)du_e/dx$ , the coefficients being in general functions of  $u_e\theta/\nu$  and  $H$ .

### Description of Integral Methods

A good and useful integral method is Head's method [34] which uses the notion that a turbulent boundary-layer flows by a process of "entrainment" of nonturbulent fluid at the outer edge and into the turbulent region. Head assumed that the mean-velocity component normal to the edge of the boundary-layer (which is known as the entrainment velocity, see problem 3.9) depends only on the mean-velocity profile, specifically on  $H$ . It follows from the continuity equation that the dimensionless entrainment velocity  $v_E/u_e$ , is given by

$$\frac{v_E}{u_e} \equiv \frac{1}{u_e} \frac{d}{dx} \int_0^\delta u dy = \frac{1}{u_e} \frac{d}{dx} [u_e(\delta - \delta^*)] = F(H) \quad (6.5.1)$$

If we define

$$H_1 = \frac{\delta - \delta^*}{\theta} \quad (6.5.2)$$

then the right-hand equality in Eq. (6.5.1) can be written as

$$\frac{d}{dx} (u_e \theta H_1) = u_e F \quad (6.5.3)$$

Head also assumed that  $H_1$  is related to the shape factor  $H$  by

$$H_1 = G(H) \quad (6.5.4)$$

The functions  $F$  and  $G$  were determined from experiment, and a best fit to several sets of experimental data showed that they can be approximated by

$$F = 0.0306(H_1 - 3.0)^{-0.6169} \quad (6.5.5)$$

$$G = \begin{cases} 0.8234(H - 1.1)^{-1.287} + 3.3 & H \leq 1.6 \\ 0.5501(H - 0.6778)^{-3.064} + 3.3 & H \geq 1.6 \end{cases} \quad (6.5.6)$$

With  $F$  and  $G$  defined by Eqs. (6.5.5) and (6.5.6), Eq. (6.5.3) provides a relationship between  $\theta$  and  $H$ . Another equation relating  $c_f$  to  $\theta$  and/or  $H$  is needed, and Head used the semi-empirical skin-friction law given by Ludwig and Tillmann [35],

$$c_f = 0.246 \times 10^{-0.678H} R_\theta^{-0.268} \quad (6.5.7)$$

where  $R_\theta = u_e \theta / \nu$ . The system [Eqs. (6.5.1)–(6.5.7)] and Eq. (3.3.10), which includes two ordinary differential equations, can be solved numerically for a specified external velocity distribution to obtain the boundary-layer development on a two-dimensional body with a smooth surface (see subsection 6.5.2). To start the calculations, say at  $x = x_0$ , we note that initial values of two of the three quantities  $\theta$ ,  $H$  and  $c_f$  must be specified, with the third following from Eq. (6.5.7). When turbulent flow calculations follow laminar calculations for a boundary-layer on the same surface, Head's method is often started by assuming continuity of momentum thickness  $\theta$  and taking the initial value of  $H$  to be 1.4, an approximate value corresponding to the flat-plate flow.

This method uses a given value of the shape factor  $H$  as the criterion for separation. [Eq. (6.5.7) predicts  $c_f$  to be zero only if  $H$  tends to infinity.] It is not possible to give an exact value of  $H$  corresponding to separation, and values between the lower and upper limits of  $H$  makes little difference in locating the separation point since the shape factor increases rapidly close to separation. A computer program for this method is given in the accompanying CD-ROM, Program 7.

Michel et al. [17] have also developed an integral method similar to Head's method. They again used the entrainment equation (6.5.1). However, rather than obtaining the closure assumptions from the experimental data and from Eq. (6.5.7), they obtained them from relations that may be regarded as the similar solutions for turbulent boundary-layer equations. Rewriting Eq. (6.5.1) in the form

$$\frac{d}{dx} \left[ \delta^* \left( \frac{\delta}{\delta^*} - 1 \right) \right] = \frac{v_E}{u_e} - \frac{\delta^*}{u_e} \left( \frac{\delta}{\delta^*} - 1 \right) \frac{du_e}{dx} \quad (6.5.8)$$

they expressed  $\delta/\delta^*$ ,  $v_E/u_e$  and the relation between  $\delta^*$  and  $c_f$  by the following expressions

$$\begin{aligned}\frac{\delta}{\delta^*} &= \sqrt{\frac{2}{c_f}} \frac{1}{F_1}, \quad \frac{v_E}{u_e} = \sqrt{\frac{c_f}{2}} P, \quad R_{\delta^*} = \frac{u_e \delta^*}{\nu} \\ \sqrt{\frac{2}{c_f}} &= \frac{1}{\kappa} \ln R_{\delta^*} + D^*, \quad \kappa = 0.41\end{aligned}\quad (6.5.9)$$

The functions  $F_1$ ,  $D^*$  and  $P$  were defined by

$$\begin{aligned}F_1 &= \frac{0.613G - \{3.6 + 76.86(\frac{1}{G} - 0.154)^2\}/G}{1 + 10/G^2} \\ D^* &= 1.4G + \frac{20}{G} - 8.33, \quad P = 0.0558 \frac{G^2}{F_1} - \frac{1.325}{F_1}, \\ G &= \frac{H-1}{H} \sqrt{\frac{2}{c_f}}\end{aligned}\quad (6.5.10)$$

This method has been extended to include the effects of freestream turbulence [25], unsteadiness [36], compressibility [37], wall curvature [38] and three dimensionality [39].

A more refined integral method for computing momentum transfer in turbulent flows is Green's "lag-entrainment" method [40], which is an extension of Head's method in that the momentum integral equation and the entrainment equation are supplemented by an equation for the streamwise rate of change of entrainment coefficient  $F$ . This additional equation allows for more realistic calculations in rapidly changing flows and is a significant improvement over Head's method. In effect, this is an "integral" version of the "differential" method of Bradshaw et al. [41]. It requires the solution of Eqs. (3.3.10) and (6.5.1) as before and also considers the "rate of change of entrainment coefficient" equation given by

$$\begin{aligned}\theta(H_1 + H) \frac{dF}{dx} &= \frac{F(F + 0.02) + 0.2667c_{f0}}{F + 0.01} \\ &\times \left\{ 2.8[(0.32c_{f0} + 0.024F_{eq} + 1.2F_{eq}^2)^{1/2} \right. \\ &\quad \left. - (0.32c_{f0} + 0.024F + 1.2F^2)^{1/2}] \right. \\ &\quad \left. + \left( \frac{\delta}{u_e} \frac{du_e}{dx} \right)_{eq} - \frac{\delta}{u_e} \frac{du_e}{dx} \right\}\end{aligned}\quad (6.5.11)$$

where the numerical coefficients arise from curve fits to experimental data and the empirical functions of Bradshaw et al. [41]. Here  $c_{f0}$  is the flat-plate skin-friction coefficient calculated from the empirical formula

$$c_{f0} = \frac{0.01013}{\log R_\theta - 1.02} - 0.00075 \quad (6.5.12)$$

The subscript “eq” in Eq. (6.5.11) refers to equilibrium flows, which are defined as flows in which the shape of the velocity and shear-stress profiles in the boundary-layer do not vary with  $x$ . The functional forms of the equilibrium values of  $F_{\text{eq}}$ ,  $[(\theta/u_e)(du_e/dx)]_{\text{eq}}$ , and  $[(\delta/u_e)(du_e/dx)]_{\text{eq}}$  are given by

$$F_{\text{eq}} = H_1 \left[ \frac{c_f}{2} - (H + 1) \left( \frac{\theta}{u_e} \frac{du_e}{dx} \right)_{\text{eq}} \right] \quad (6.5.13a)$$

$$\left( \frac{\theta}{u_e} \frac{du_e}{dx} \right)_{\text{eq}} = \frac{1.25}{H} \left[ \frac{c_f}{2} - \left( \frac{H - 1}{6.432H} \right)^2 \right] \quad (6.5.13b)$$

and an obvious consequence of the definitions of  $H$  and  $H_1$ ,

$$\left( \frac{\delta}{u_e} \frac{du_e}{dx} \right)_{\text{eq}} = (H + H_1) \left( \frac{\theta}{u_e} \frac{du_e}{dx} \right)_{\text{eq}} \quad (6.5.13c)$$

The skin-friction formula and the relationship between the shape factors  $H$  and  $H_1$  complete the number of equations needed to solve the system of ordinary differential equations (3.3.10), (6.5.1), and (6.5.11). The skin-friction equation is given by

$$\left( \frac{c_f}{c_{f0}} + 0.5 \right) \left( \frac{H}{H_0} - 0.4 \right) = 0.9 \quad (6.5.14a)$$

where

$$1 - \frac{1}{H_0} = 6.55 \left( \frac{c_{f0}}{2} \right)^{1/2} \quad (6.5.14b)$$

so that Eqs. (6.5.12) and (6.5.14) give  $c_f$  as a function of  $H$  and  $R_\theta$  with values close to Eq. (6.5.7).

The shape-factor relation is

$$H_1 = 3.15 + \frac{1.72}{H - 1} - 0.01(H - 1)^2 \quad (6.5.15)$$

and gives values close to Eq. (6.5.6). Comparisons with experiment show good accuracy in incompressible boundary-layer flows and also in wakes. The method has also been extended to represent compressible flows [40].

## 6.6 Turbulent Boundary-Layers with Pressure Gradient: Differential Methods

Differential methods are based on the solution of the boundary-layer equations in their partial-differential equation form. They vary depending on the numerical method used to solve the equations and the turbulence model employed to model the Reynolds stresses. Unlike integral methods, they are general, accurate depending on the numerical method and turbulence model and can handle

various initial and boundary conditions. The differential methods, which have largely superseded integral methods with the advent of modern computers, however, require more computer time than the integral methods.

An accurate and efficient differential method is the method developed by Cebeci and Smith [14]. It is essentially an extension of the differential method and the computer program BLP2 discussed in Section 4.5 and Appendix B, Program 3, for laminar flows. It uses the Cebeci-Smith algebraic eddy viscosity formulation to model the Reynolds shear stress term in the momentum equation. The boundary-layer equations are solved for both laminar and turbulent flows by specifying the onset of the transition location. The laminar flow calculations are performed up to this location, and the turbulent flow calculations, including the transition region are performed by computing  $\gamma_{tr}$  and eddy viscosity formulas in Program 8 given in Appendix B.

In its present form, BLP2 is for two-dimensional incompressible flows but can be extended to axisymmetric flows by using the Mangler transformation discussed in Problems 3.12 and 4.37. It can also be extended to three-dimensional laminar and turbulent flows as discussed in Chapter 7 and Appendix B, Program 10.

## 6.7 Free Shear Layers

Turbulent free shear layers resemble the corresponding laminar flows more closely than is the case with boundary-layers. It happens that the eddy viscosity in a fully developed jet or wake is roughly constant across the width of the layer except for the extreme edges. It follows that the velocity profile is quite close to the laminar one when it is normalized by the width and maximum-velocity difference. As usual, the eddy viscosity is large in comparison to the molecular viscosity and is proportional to the product for the width and the maximum-velocity difference. Therefore, the growth rates of turbulent free shear layers are large in comparison to the laminar case and vary according to different power laws.

### 6.7.1 Axisymmetric Jet

The discussion of the similarity solutions of free shear layers for turbulent flows considered here for an axisymmetric jet or for a two-dimensional wake in the following subsection is parallel to the discussion in Section 4.3 for laminar flows. In the case of an axisymmetric turbulent jet, we begin with Eq. (4.3.11), that is,

$$\rho u_c^2 \frac{d\delta}{dx} \left[ \frac{(f')^2}{\eta} + f \left( \frac{f'}{\eta} \right)' \right] + (\tau\eta)' = 0 \quad (4.3.11)$$

which applies to both laminar and turbulent jets. For turbulent jets the contribution of the laminar shear stress to  $\tau$  defined by Eq. (4.3.3) is small and can be neglected. Assuming that

$$\frac{\tau}{\rho} = -\overline{u'v'} = u_c^2 g(\eta) \quad (6.7.1)$$

we can write Eq. (4.3.11) as

$$\frac{d\delta}{dx} \left[ \frac{(f')^2}{\eta} + f \left( \frac{f'}{\eta} \right)' \right] + (g\eta)' = 0 \quad (6.7.2)$$

For similarity we must have

$$\frac{d\delta}{dx} = \text{const.} = B$$

or

$$\delta = Bx \quad (6.7.3)$$

Therefore, we can write Eq. (4.3.10) as

$$u_c = \frac{M}{Bx} \quad (6.7.4)$$

We have obtained the power laws for growth rate and centerline velocity decay rate without introducing a turbulence model, but to integrate Eq. (6.7.2), a relation between  $f'$  and  $g'$  is needed. If we use the eddy viscosity concept [see Eq. (6.3.1)] and let

$$\frac{\tau}{\rho} = \nu_t \frac{\partial u}{\partial r} = \frac{\nu_t u_c}{\delta} F' = \frac{\nu_t u_c}{\delta} \left( \frac{f'}{\eta} \right)' \quad (6.7.5)$$

so that  $g = [\nu_t/(u_c \delta)](f'/\eta)'$  with  $\nu_t$  independent of  $y$  – a good approximation in practice – we can write Eq. (6.7.2) as

$$\frac{\nu_t \delta}{\nu_t} \frac{d\delta}{dx} \left[ \frac{(f')^2}{\eta} + f \left( \frac{f'}{\eta} \right)' \right] + \left[ \eta \left( \frac{f'}{\eta} \right)' \right]' = 0 \quad (6.7.6)$$

For similarity we must have

$$\frac{MB}{\nu_t} = \text{const.} = A \quad (6.7.7)$$

If we define

$$\zeta = a\eta, \quad f(\eta) = \beta\phi(\zeta) \quad (6.7.8)$$

then we can express Eq. (6.7.6) in the same form as Eq. (4.3.15) by taking

$$\beta = \frac{1}{A} \quad (6.7.9)$$

and write its solution as

$$\phi(\zeta) = \frac{\frac{1}{2}\zeta^2}{1 + \frac{1}{8}\zeta^2} \quad (6.7.10)$$

$$\frac{\phi'(\zeta)}{\zeta} = \frac{1}{(1 + \frac{1}{8}\zeta^2)^2} \quad (6.7.11)$$

In terms of  $f$  and  $\eta$ , Eq. (6.7.11) can be written as

$$\frac{u}{u_c} = \frac{f'}{\eta} = \frac{1}{(1 + \frac{1}{8}A\eta^2)^2} \quad (6.7.12)$$

Here we have chosen  $a^2\beta = 1$  so that  $u = u_c$  at  $\eta = 0$ , and from Eq. (6.7.9) determined that  $a = \sqrt{A}$ .

To determine the two empirical constants  $A$  and  $B$ , we use experimental data. If we write Eq. (6.7.7) as

$$\nu_t = \frac{B}{A}u_c\delta$$

and define  $\delta$  as the  $y$ -distance where  $u/u_c = 1/2$ , then according to the experimental data of Reichardt (see Schlichting [4]),  $B = 0.0848$  and  $A = 3.31$ . Thus,

$$\delta = 0.0848x \quad (6.7.13)$$

$$\nu_t = 0.0256\delta u_c \quad (6.7.14)$$

Inserting Eq. (6.7.12) into Eq. (4.3.9), we find

$$M = \frac{\sqrt{3}}{2} \sqrt{\frac{J/\rho}{2\pi}} \sqrt{A} \quad (6.7.15)$$

Therefore, from Eq. (6.7.4), with  $A = 3.31$ ,

$$u_c = 7.41 \frac{\sqrt{J/\rho}}{x} \quad (6.7.16)$$

The mass flow rate

$$\dot{m} = 2\pi \int_0^\infty \rho u r dr = 2\pi\rho\delta^2 u_c \int_0^\infty f' d\eta$$

can be obtained using the expression for  $\delta$ ,  $u_c$ , and  $f'$ . It is

$$\dot{m} = 0.404x\sqrt{J\rho} \quad (6.7.17)$$

We note that, in contrast to laminar flow,  $\dot{m}$  depends on  $J$ .

### 6.7.2 Two-Dimensional Wake

Equation (4.3.33) applies to both laminar and turbulent wakes. For turbulent wakes the contribution of the laminar shear stress to  $\tau$  defined by Eq. (4.3.26) is small and can be neglected. Using Eq. (6.7.1), we can write Eq. (4.3.33) as

$$\frac{u_\infty \delta}{u_c^2} \left( f \frac{du_c}{dx} - u_c f' \frac{\eta}{\delta} \frac{d\delta}{dx} \right) - g' = 0 \quad (6.7.18)$$

As in the laminar case this applies only for  $u_c \ll u_\infty$ . For similarity we must have

$$\frac{u_\infty \delta}{u_c^2} \frac{du_c}{dx} = \text{const.}, \quad \frac{u_\infty}{u_c} \frac{d\delta}{dx} = \text{const.} \quad (6.7.19)$$

Since  $u_c \delta = \text{const.}$  [see Eq. (4.3.38)], we can integrate the second relation in Eq. (6.7.19) to get

$$\delta \sim x^{1/2} \quad (6.7.20)$$

Therefore

$$u_c \sim x^{-1/2} \quad (6.7.21)$$

Equations (6.7.20) and (6.7.21) are the power laws for growth rate and wake centerline velocity defect rate, obtained from Eq. (6.7.18) without introducing a turbulence model, as in the previous example concerning the axisymmetric turbulent jet. To integrate (6.7.18), we again use the eddy-viscosity concept and let  $\tau/\rho = \nu_t \partial u / \partial y = \frac{\nu_t}{u_c \delta} f'$  so that  $g = \frac{\nu_t}{u_c \delta} f'$ . With  $\nu_t$  independent of  $y$ , we get

$$-\frac{u_\infty \delta^2}{\nu_t u_c} \left( f \frac{du_c}{dx} - \frac{u_c}{\delta} f' \eta \frac{d\delta}{dx} \right) + f'' = 0 \quad (6.7.22)$$

For similarity we must have

$$\frac{u_\infty \delta^2}{\nu_t u_c} \frac{du_c}{dx} = \text{const.}, \quad \frac{u_\infty \delta}{\nu_t} \frac{d\delta}{dx} = \text{const.} = C_2 \quad (6.7.23)$$

Integration of the second relation in Eq. (6.7.23) gives

$$\delta = \left( \frac{2C_2 \nu_t x}{u_\infty} \right)^{\frac{1}{2}} \quad (6.7.24)$$

Therefore

$$u_c = Ax^{-1/2} \quad (6.7.25)$$

Using Eqs. (6.7.24) and (6.7.25), we find that the constant in the first expression of (6.7.23) is  $-C_2$ . This enables us to write Eq. (6.7.22) as

$$f'' + C_2(\eta f)' = 0 \quad (6.7.26)$$

If we define

$$\zeta = a\eta, \quad f(\eta) = \beta\phi(\zeta) \quad (6.7.27)$$

then we can express Eq. (6.7.26) in the same form as Eq. (4.3.40) by taking  $a = \sqrt{C_2}$  and writing its solution as

$$-\frac{u_1}{u_c} = f(\eta) = Be^{-C_2\eta^2/2} \quad (6.7.28)$$

or

$$u_1 = -ABe^{-C_2\eta^2/2}x^{-1/2} \quad (6.7.29)$$

To evaluate  $AB$ , we use Eqs. (4.3.38). Inserting  $f$  into Eq. (4.3.38) and using the definitions of  $\delta$  and  $u_c$  as given by Eqs. (6.7.24) and (6.7.25), respectively, we get

$$AB = -\frac{F}{\rho b}(2\nu_t u_\infty)^{-1/2}(2\pi)^{-1/2} \quad (6.7.30)$$

We note that Eq. (6.7.30) is the same as Eq. (4.3.42) except that  $\nu_t$  has replaced  $\nu$ .

The expressions Eqs. (6.7.29) and Eq. (6.7.30) give the mean-velocity distribution in the wake of a two-dimensional body provided that  $\nu_t$  and  $C_2$  are determined. According to the measurements conducted behind circular cylinders of diameter  $d$  [4],

$$\delta = \frac{1}{4}(xC_D d)^{1/2} \quad (6.7.31)$$

and

$$\frac{\nu_t}{u_\infty C_D d} = 0.0222 \quad (6.7.32)$$

Here  $C_D$  is the drag coefficient for the cylinder defined by

$$C_D = \frac{F}{\frac{1}{2}\rho u_\infty^2 bd} \quad (6.7.33)$$

Using Eqs. (6.7.31) and (6.7.32), we find from Eq. (6.7.24) that  $C_2 = 1.41$ , so that  $\delta$ , defined as the value of  $y$  at  $u_1 = 0.5u_c$ , can be written as

$$\delta = 1.675 \left( \frac{\nu_t x}{u_\infty} \right)^{\frac{1}{2}} \quad (6.7.34)$$

Solving Eq. (6.7.33) for  $F$  and inserting the resulting expression into Eqs. (6.7.30) and (6.7.29), we can express the mean-velocity distribution behind a circular cylinder as

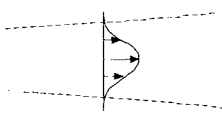
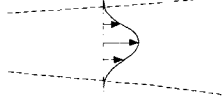
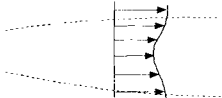
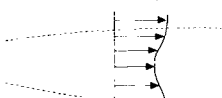
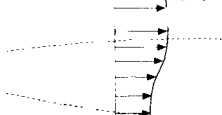
$$\frac{u_1}{u_\infty} = 0.141 \left( \frac{u_\infty C_D d}{\nu_t} \right)^{\frac{1}{2}} \left( \frac{x}{C_D d} \right)^{-\frac{1}{2}} \exp(-0.70\eta^2) \quad (6.7.35)$$

where  $\eta = y/\delta$  and  $\delta$  is given by Eq. (6.7.34).

### 6.7.3 Power Laws for the Width and the Centerline Velocity of Similar Free Shear Layers

Similar to laminar flows (see subsection 4.3.4) the variation of the width,  $\delta$ , and the centerline velocity,  $u_c$  or  $u_1$ , of several turbulent shear layers are summarized in Table 6.2.

**Table 6.2.** Power laws for width and centerline velocity of turbulent similar free shear layers.

Flow	Sketch	Width, $\delta$	Centerline velocity, $u_c(x)$ and $u_1$
Two-dimensional jet		$x$	$x^{-1/2}$
Axisymmetric jet		$x$	$x^{-1}$
Two-dimensional wake		$x^{1/2}$	$x^{-1/2}$
Axisymmetric wake		$x^{1/3}$	$x^{-2/3}$
Two uniform streams		$x$	$x^0$

## References

- [1] Favre, A. and Gaviglio, J., "Turbulence et Perturbations dans la Couche Limite D'une Plaque Plane," AGARD Rep 278, 1960.
- [2] Klebanoff, P.S., "Characteristics of Turbulence in a Boundary Layer with Zero Pressure Gradient," Technical Note TN 3178, NACA, July 1954.
- [3] Clauser, F.H., "The Turbulent Boundary Layer," *Adv. Appl. Mech.*, Vol. 4, p. 1, 1956.
- [4] Schlichting, H., *Boundary Layer Theory*, McGraw-Hill, NY, 1968.
- [5] Ioselevish, V.A. and Pilipenko, V.I., "Logarithmic Velocity Profile for Flow of a Weak Polymer Solution Near a Rough Surface," *Sov. Phys. Dokl.*, Vol. 18, p. 790, 1974.
- [6] Perry, A.E., Schofield, W.H., and Joubert, P.N., "Rough Wall Turbulent Boundary Layers," *J. Fluid Mech.*, Vol. 37, p. 383, 1969.
- [7] Van Dyke, M., "An Album of Fluid Motion," The Parabolic Press, Stanford, Ca, 1982.
- [8] Clauser, F.H., "Turbulent Boundary Layers in Adverse Pressure Gradient," *J. Aero. Sci.*, Vol. 21, no. 91, 1954.
- [9] Coles, D., "The Law of the Wake in the Turbulent Boundary Layer," *J. Fluid Mech.*, Vol. 1, p. 191, 1956.

- [10] Whitfield, D.L., "Analytical Description of the Complete Turbulent Boundary Layer Velocity Profile," *J. AIAA*, Vol. 17, no. 10, pp. 1145–1147, 1979.
- [11] Granville, P.S., "A Modified Law of the Wake for Turbulent Shear Layers," *J. Fluids Engineering*, pp. 578–579, Sept. 1976.
- [12] Thompson, B.G.J., "A Near Two-parameter Family of Mean Velocity Profiles for Incompressible Boundary layers on Smooth Walls," ARC R&M 3463, 1965.
- [13] Van Driest, E.R., "On Turbulent Flow Near a Wall," *J. Aero. Sci.*, Vol. 23, p. 1007, 1956.
- [14] Cebeci, T., *Analysis of Turbulent Flows*, Elsevier, London, 2004.
- [15] Wilcox, D.C., *Turbulence Modeling for CFD*, DCW Industries, Inc., La Cañada, California, 1993.
- [16] Chen, K.K. and Thyson, N.A., "Extension of Emmons' Spot Theory to Flows on Blunt Bodies," *AIAA J.*, Vol. 9, pp. 821–825, 1971.
- [17] Michel, R., Quémard, C., and Durant, R., "Application d'un schéma de longueur de mélange à l'étude des couches limites d'équilibre," ONERA Note Technique No. 154, 1969.
- [18] Johnson, D.A. and King, L.S., "Mathematically Simple Turbulence Closure Model for Attached and Separated Turbulent Boundary Layers," *AIAA J.*, Vol. 23, no. 11, pp. 1684–1692, 1985.
- [19] Johnson, D.A. and Coakley, T.J., "Improvement to a Nonequilibrium Algebraic Turbulence Model," *AIAA J.*, Vol. 28, no. 11, pp. 2000–2003, 1990.
- [20] Cebeci, T., *An Engineering Approach to the Calculation of Aerodynamic Flows*, Horizons Publ., Long Beach, Calif. and Springer, Heidelberg, 1999.
- [21] Cebeci, T. and Chang, K.C., "An Improved Cebeci-Smith Turbulence Model for Boundary-Layer and Navier-Stokes Methods," 20th Congress of the International Council of the Aeronautical Sciences, paper no. ICAS-96-1.7.3, Sorrento, Italy, September 8–13, 1996.
- [22] Fiedler, H. and Head, M.R., "Intermittency Measurements in the Turbulent Boundary Layer," *J. Fluid Mech.*, Vol. 25, Part 4, pp. 719–735, 1986.
- [23] Jones, W.P. and Launder, B.E., "The Prediction of Laminarization with a Two-Equation Model of Turbulence," *Int. J. Heat & Mass Transfer*, Vol. 15, pp. 301–314, 1977.
- [24] Launder, B.E. and Sharma, B.I., "Application of the Energy-Dissipation Model of Turbulence to the Calculation of Flow Near a Spinning Disc," *Letters in Heat and Mass Transfer*, Vol. 1, pp. 131–138, 1974.
- [25] Arnal, D., Cousteix, J., and Michel, R., "Couche limite se développant avec gradient de pression positif dans un écoulement turbulent," *La Rech. Aéosp.*, 1976-1, 1976.
- [26] Norris, L.H. and Reynolds, W.C., "Turbulent Channel Flow with a Moving Wavy Boundary," Report FM-10, Department of Mechanical Engineering, Stanford University, Stanford, California, 1975.
- [27] The 1980-81 AFOSR-HTTM-Stanford Conference on Complex Turbulent Flows: Comparison of Computation and Experiment, Thermosciences Division, Mechanical Engineering Department, Stanford University, Stanford, California, September 3–6, 1980.
- [28] Pot, P.J., Measurements in a Two-Dimensional Wake and in a Two-Dimensional Wake Merging into a Boundary Layer, NLR Data Report 521302, 1979.
- [29] Launder, B.E., Reece, G.J. and Rodi, W., "Progress in the Development of a Reynolds Stress Turbulence Closure," *J. Fluid Mech.*, Vol. 20, p. 3, 1975.
- [30] Gibson, M.M. and Launder, B.E., "Ground Effects on Pressure Fluctuation in the Atmospheric Boundary Layer," *J. Fluid Mech.*, Vol. 86, pp. 491–511, 1978.
- [31] Granville, P.S., "The Determination of the Local Skin Friction and the Thickness of Turbulent Boundary Layers from the Velocity Similarity Laws," David W. Taylor Model Basin Rept. 849, 1953.
- [32] Hoerner, S.F., *Fluid Dynamic Drag*, Hoerner Fluid Dynamics, Brick Town, NJ, 1958.

- [33] Cousteix, J., "Integral Techniques," The 1980–81 AFOSR-HTTM-Stanford Conference on Complex Turbulent Flows: Comparison of Computation and Experiment, Vol. II, Eds. S.J. Kline, B.J. Cantwell, G.M. Lilley, 1982.
- [34] Head, M.R., "Entrainment in the Turbulent Boundary Layers," ARC R&M 3152, 1958.
- [35] Ludwig, H. and Tillmann, W., Investigations of the Wall Shearing Stress in Turbulent Boundary Layers, NACA Rept. TM1285, 1949 (English translation).
- [36] Cousteix, J. and Houdeville, R., Effects of Unsteadiness on Turbulent Boundary Layers. In: *AGARD/FDP/VKI Special Course on Unsteady Aerodynamics*, April 18–22, 1974.
- [37] Cousteix, J., Houdeville, R., and Michel, R, Couches limites turbulentes avec transfert de chaleur, *La Rech. Aérospace*, 1974-4, 1974.
- [38] Cousteix, J. and Houdeville, R., Méthode intégrale de calcul d'une couche limite turbulente sur une paroi courbée longitudinalement, *La Rech. Aérospace*, 1977-1, 1977.
- [39] Cousteix, J., Three-dimensional Boundary Layers – Introduction to Calculation Methods. In: *AGARD/FDP/VKI Special Course: Computation of Three-dimensional Boundary Layers Including Separation - Rep No. 741*, April 18–22, 1974.
- [40] Green, J.E., Weeks, D.J. and Broome, J.W.F., "Prediction of Turbulent Boundary Layers and Wakes in Incompressible Flow by a Lag-Entrainment Method," ARC R&M 3791, 1973.
- [41] Bradshaw, P., Ferriss, D.H. and Atwell, N.P.S., "Calculation of Boundary Layer Development Using the Turbulent Energy Equation," *J. Fluid Mech.*, Vol. 28, p. 593, 1967.
- [42] Hildebrand, F.B. *Advanced Calculus for Applications*. Prentice-Hall, NJ, 1962.

## Problems

**6-1.** Show that the friction velocity  $u_\tau$  can be related to the displacement thickness,  $\delta^*$ , boundary-layer thickness  $\delta$  and profile parameter  $\Pi$  by

$$\kappa \frac{\delta^* u_e}{\delta u_\tau} = 1 + \Pi \quad (\text{P6.1.1})$$

*Hint:* Write the definition of  $\delta^*$  as

$$\delta^* = \int_0^\infty \left( \frac{u_e - u}{u_e} \right) dy = \frac{\delta u_\tau}{u_e} \int_0^1 \left( \frac{u_e}{u_\tau} - \frac{u}{u_\tau} \right) d\left(\frac{y}{\delta}\right)$$

Substitute Eqs. (6.2.17) and (6.2.21) into the above expression and integrate the resulting expression.

**6-2.** Show that  $u_\tau$ ,  $\theta$ , and  $H$  can be related to each other by

$$\kappa^2 \frac{(\delta^* - \theta) u_e^2}{\delta u_\tau^2} = 2 + 2 \left[ 1 + \frac{1}{\pi} Si(\pi) \right] \Pi + \frac{3}{2} \Pi^2 \quad (\text{P6.2.1})$$

$$\frac{H}{H-1} \frac{u_\tau}{\kappa u_e} \equiv \frac{1}{\kappa G} = F(\Pi) \quad (\text{P6.2.2a})$$

$$F(\Pi) = \frac{1 + \Pi}{2 + 2[1 + \frac{1}{\pi} Si(\pi)]\Pi + \frac{3}{2}\Pi^2} \quad (\text{P6.2.2b})$$

**6-3.** Water at 20 °C flows at a velocity of 3 ms<sup>-1</sup> past a flat plate. Use Eq. (5.4.1) to find the transition position, and then use Eq. (6.4.16) and the results in Problem 4.8 to determine the average skin-friction drag of the first 10 m of the plate. Check the contribution of the turbulent portion by Head's method, assuming that  $H = 1.5$  at the end of transition.

**6-4.** By using Eq. (6.3.4a), show that  $\nu_t$  is proportional to  $y^4$  for  $(y/y_l) \ll 1$ . Here  $y_l$  denotes the viscous sublayer thickness.

**6-5.** Show that for equilibrium boundary-layers at high Reynolds numbers, if  $\alpha$  in Eq. (6.3.5) is 0.0168, then  $\alpha_1$  in

$$\nu_t = \alpha_1 u_\tau \delta$$

must be 0.0635 for  $\kappa = 0.41$  for a zero pressure gradient flow.

**6-6.** Express Eq. (6.2.21) in terms of (a)  $u_e \delta^*/\nu$  and (b)  $u_e \theta/\nu$  for a boundary-layer in zero pressure gradient, inserting numerical values where possible.

**6-7.** Compare the prediction of Eq. (6.4.11) for  $c_f$  at  $u_e \theta/\nu = 10^4$  with that obtained in problem 6-6.

**6-8.** Show that Head's assumptions predict that in order to maintain constant  $H$  in a strongly retarded boundary,  $u_e$  must vary as a negative power of  $x$ . Neglect the contribution of the skin-friction coefficient to the momentum integral equation.

**6-9.** The external velocity distribution for the symmetrical NACA 0012 airfoil is given in Problem 4.23. Compute the complete boundary-layer development (laminar and turbulent) on this airfoil for two chord Reynolds numbers,  $R_c = 6 \times 10^6$  and  $9 \times 10^6$  by using Thwaites' and Head's methods. Compute the transition position by Eq. (5.4.1). To start the turbulent flow calculation in Head's method, assume continuity in momentum thickness and take  $H = 1.4$ . Discuss the effect of  $R_c$  on the location of transition.

**6-10.** Determine the equivalent sand-grain height for the wire netting tested by Hama [41] and shown in Fig. 6.4. Assume fully rough conditions.

**6-11.** The solutions of Eq. (3.3.15) can be obtained for laminar and turbulent flows by using relations based on zero-pressure gradient. The  $c_f/2$  relation can be expressed in the form

$$\frac{c_f}{2} = \frac{b}{R_\theta^{m_0}} \quad (\text{P6.11.1})$$

with  $H$  taken as constant equal to 2.591 and 1.4 for laminar and turbulent flows, respectively. The parameters  $b$  and  $m_0$  are

	$m_0$	$b$
laminar	1	0.2205
turbulent	1/5	0.0086

Since the  $c_f$  and  $H$  relations are for flat plate flows, the solutions of this method are restricted to mild pressure gradient flows.

Show that with the above relations, the solution of Eq. (3.3.15) can be written as

$$\underbrace{[\theta r_0^k u_e^{H+2}]^{m_0+1}}_{\text{at station } x_1} = \underbrace{[\theta r_0^k u_e^{H+2}]^{m_0+1}}_{\text{at station } x_0} + (m_0 + 1)b \int_{x_0}^{x_1} \frac{u_e^{(m_0+1)(H+2)} r_0^{k(m_0+1)}}{(u_e/\nu)^{m_0}} dx \quad (\text{P6.11.2})$$

With initial conditions given at station  $x_0$ , the development of  $\theta$  can be obtained from this equation and  $c_f/2$  from Eq. (P6.11.1) and  $\delta^*$  from the definition of  $H$ . Note that  $k = 0$  for a two-dimensional flow and  $k = 1$  for an axisymmetric flow.

**6-12.** Air at a temperature of 300 K and pressure of  $10^5 \text{ N m}^{-2}$  flows at a velocity of  $10 \text{ ms}^{-1}$  past a flat plate with a length of 3 m and width 1 m. Using the integral method of Problem 6.11, and assuming turbulent flow,

- (a) compute the drag of the plate,
- (b) calculate the power needed to maintain the plate at constant speed, and
- (c) repeat the calculations for a laminar flow and compare them with those obtained in (a) and (b).

**6-13.** Using the integral method of Problem 6.11, and assuming that transition occurs instantly at  $\frac{x}{L} = x_{tr}$ , calculate the laminar and turbulent boundary layer development on a flat plate of length  $L$  for  $R_L (\equiv \frac{u_e L}{\nu}) = 10^7$ .

- (a) Calculate  $\frac{\theta}{L}$  and  $c_f$  at  $x = 0, 0.05, 0.1, 0.2, 0.4, 0.6, 0.8, 1$ . Take  $x_{tr} = 0.2$  and assume that the momentum thickness is continuous at the transition location.
- (b) Plot the variation of  $\frac{\theta}{L}$  and  $c_f$  along the plate  $\frac{x}{L}$ .
- (c) Calculate and plot the drag coefficient  $c_d$  of the plate as a function of the momentum thickness at the trailing edge ( $x = 1$ ) for the following locations of the transition point

$$x_{tr} = 0, 0.2, 0.4, 0.6, 0.8, 1$$

*Hint:* Noting that  $u_e = \text{const.}$ , integrate the momentum integral equation, Eq. (3.3.10), with respect to  $x$ .

(d) Plot the variation of  $c_d$  as a function of  $R_{x_{tr}} = \frac{u_c x_{tr}}{\nu}$ .

**6-14.** Derive Eq. (6.2.23).

**6-15.** Write a FORTRAN program to calculate  $u^+(y^+)$  from Eq. (6.2.23). Compare its solutions with Eq. (6.2.4b) at small values of  $y^+$  and with Eq. (6.2.3) at higher values of  $y^+$ . Evaluate  $c$  in Eq. (6.2.3) from the solutions of Eq. (6.2.23).

**6-16.** For a general three-dimensional turbulent flow, the turbulence kinetic energy equation  $k$  and the rate of dissipation equation  $\varepsilon$  can be written as

$$\frac{Dk}{Dt} = -\overline{u'_i u'_j} \frac{\partial u_i}{\partial x_j} - \varepsilon + \frac{\partial}{\partial x_i} \left( c_k \frac{k^2}{\varepsilon} \frac{\partial k}{\partial x_i} \right) \quad (\text{P6.16.1})$$

$$\frac{D\varepsilon}{Dt} = -c_{\varepsilon_1} \frac{\varepsilon}{k} \overline{u'_i u'_j} \frac{\partial u_i}{\partial x_j} - c_{\varepsilon_2} \frac{\varepsilon^2}{k} + \frac{\partial}{\partial x_i} \left( c_\varepsilon \frac{k^2}{\varepsilon} \frac{\partial \varepsilon}{\partial x_i} \right) \quad (\text{P6.16.2})$$

(a) Apply these equations to a two-dimensional boundary layer flow.

(b) Boundary-layer experiments show the existence of a region in which the kinetic energy balance reduces to an equilibrium between the production and dissipation terms such that we can write

$$\frac{-\overline{u'v'}}{k} = 2a_1, \quad a_1 \cong 0, 15$$

Using this relation, calculate  $c_\mu$  in Eq. (6.3.14).

(c) Equations (P6.16.1) and (P6.16.2) can be used to estimate the kinetic energy behind a turbulence grid in a wind tunnel. Taking the mean velocity constant,  $v = 0$ ,  $w = 0$ , and assuming the turbulence to be homogeneous and isotropic, we can neglect the diffusion terms.

Relating the Reynolds stresses to the kinetic energy of turbulence by

$$\overline{u'_i u'_j} = \frac{2}{3} k \delta_{ij}$$

show that the solution of Eqs. (P6.16.1) and (P6.16.2) has the form

$$k = C(x - x_0)^{-m}$$

where, according to experiments,  $m = 1.25$ .

(d) Using the results in (c), calculate the value of  $c_{\varepsilon_2}$ .

**6-17.** (a) Show from Eq. (6.3.15) that in the logarithmic region of a turbulent boundary-layer [Eq. (6.2.3)] where the convection terms and the diffusion term,

$\partial/\partial y[(\nu_t/\sigma_k)(\partial k/\partial y)]$  in Eq. (6.3.15) can be neglected, and where the Reynolds shear stress may be assumed constant and equal to wall shear stress

$$\frac{\partial u}{\partial y} = \frac{u_\tau}{\kappa y}, \quad \varepsilon = \frac{u_\tau^3}{\kappa y}, \quad k = \frac{u_\tau^2}{\sqrt{c_\mu}} \quad (\text{P6.17.1})$$

(b) Eq. (6.3.16) can be simplified by neglecting the convection terms (but not the diffusion terms). Show that

$$c_{\varepsilon_2} - c_{\varepsilon_1} = \kappa^2 \frac{c_\varepsilon}{c_\mu^{3/2}} \quad (\text{P6.17.2})$$

(c) From the assumptions in (a) and the assumption that

$$\varepsilon = c \frac{k^{3/2}}{l} \quad (\text{P6.17.3})$$

show that the Reynolds stress can be expressed by a mixing length model which has the form

$$-\overline{u'v'} \sim l^2 \left( \frac{\partial u}{\partial y} \right)^2 \quad (\text{P6.17.4})$$

**6-18.** Using an eddy viscosity concept, Eq. (6.3.1), Wilcox [15] developed a two-equation model based on the kinetic energy equation  $k$  expressed as

$$\frac{Dk}{Dt} = \nu_t \left( \frac{\partial u}{\partial y} \right)^2 - \beta^* \omega k + \frac{\partial}{\partial y} \left[ (\nu + \sigma^* \nu_t) \frac{\partial k}{\partial y} \right] \quad (\text{P6.18.1})$$

and specific dissipation rate  $\omega$  expressed as

$$\frac{D\omega}{Dt} = \gamma \frac{\omega}{k} \nu_t \left( \frac{\partial u}{\partial y} \right)^2 - \beta \omega^2 + \frac{\partial}{\partial y} \left[ (\nu + \sigma \nu_t) \frac{\partial \omega}{\partial y} \right] \quad (\text{P6.18.2})$$

with  $\nu_t$  given by

$$\nu_t = \frac{k}{\omega} \quad (\text{P6.18.3})$$

The specific dissipation rate  $\omega$  is related to the dissipation rate  $\varepsilon$  by

$$\omega = \frac{1}{c_\mu} \frac{\varepsilon}{k} \quad (\text{P6.18.4})$$

(a) Compare the exact equation for  $k$  with Eq. (P6.18.1) and show that  $\beta^* = c_\mu = 0.09$ .

(b) From Eqs. (P6.18.1) and (P6.18.2) form an equation for the dissipation rate  $\varepsilon$ . Show that this equation is not equivalent to the  $\varepsilon$ -equation used in the  $k$ - $\varepsilon$  model.

(c) Study the behavior of  $k$  and  $\omega$  in the vicinity of the wall, i.e., around  $y = 0$ . Hint: assume that  $k$  and  $\omega$  vary as  $k = by^m$  and  $\omega = a/y^n$  and consider a simplified form of equations (P6.18.1) and (P6.18.2) in which the convection terms, the production terms and the turbulent diffusion terms are neglected. These approximations will be justified a posteriori. It will be shown that  $m = 3.23$ ,  $n = 2$  and  $a = 6\nu/\beta$ .

(d) To study the properties of Wilcox's model equations in the logarithmic region of the boundary-layer, assume that

$$-\overline{u'v'} = u_\tau^2, \quad \frac{\partial u}{\partial y} = \frac{u_\tau}{\kappa y}$$

and with the hypothesis that “*Production = Dissipation*” in the kinetic energy equation, show that

$$-\frac{\overline{u'v'}}{k} = c_\mu^{1/2}$$

(e) Deduce the evolution of  $\omega$  as function of  $y$ . From the  $\omega$ -equation show that the value of  $\kappa$  can be written as

$$\kappa = \frac{(\beta - \gamma c_\mu)^{1/2}}{c_\mu^{1/4} \sigma^{1/2}} = 0.41$$

**6-19.** The jet in the “turbulence amplifier” shown in the sketch in Problem 4.16 is now forced to go turbulent by injecting a small mass flow through the control jet. Using the same figures as those in Problem 4.16, calculate the pressure at the pressure tapping.

**6-20.** In the overlap region, expressions (6.2.3) for the inner layer law and (6.2.15) for the velocity-defect law are simultaneously valid

$$\frac{u}{u_\tau} = \frac{1}{\kappa} \ln \frac{y v_\tau}{\nu} + c$$

$$\frac{u_e - u}{u_\tau} = -\frac{1}{\kappa} \ln \frac{y}{\delta} + c'$$

By adding the two above relations show that

$$\frac{u_e}{u_\tau} = \frac{1}{\kappa} \ln \frac{u_e \delta}{\nu} \frac{u_\tau}{u_e} + c + c'$$

This relationship can be considered as an implicit relation for the reduced friction velocity  $\frac{u_\tau}{u_e}$  (or the skin friction coefficient) as a function of the Reynolds number  $\frac{u_e \delta}{\nu}$ . This relation is also a condition for the existence of the logarithmic overlap region.

# 7

# Three-Dimensional Incompressible Laminar and Turbulent Flows

## 7.1 Introduction

In this chapter and the following chapter we extend the discussion on two-dimensional flows of the previous chapters to three-dimensional flows. Unlike the separate discussion on laminar flows in Chapter 4 and turbulent flows in Chapter 6, this chapter considers both laminar and turbulent flows and begins with a discussion on the origin of crossflow in boundary-layers and presents three-dimensional boundary-layer equations in several coordinate systems. It is followed by Section 7.3 that discusses the initial conditions needed to solve the three-dimensional boundary-layer equations. Section 7.4 addresses the modeling of Reynolds stresses and presents an extension of Section 6.3 to three-dimensional flows. As in two-dimensional flows, it is computationally more convenient and economical to solve the three-dimensional boundary-layer equations in transformed coordinates. This is discussed in Section 7.5, including a discussion of the similarity solutions of the three-dimensional boundary-layer equations. Section 7.6 describes the numerical procedures used to solve the boundary-layer equations for a prescribed external velocity distribution. Unlike two-dimensional flows, the solution of the three-dimensional boundary-layer equations, even in the absence of flow separation, is rather involved due to the possible flow reversals in the spanwise velocity,  $w$ , which can cause numerical instabilities if appropriate numerical schemes are not used. For this reason, in addition to the box scheme discussed in the previous chapters for two-dimensional flows, another version of this scheme is discussed in Section 7.6. In Section 7.7 results obtained with the numerical method of Section 7.6 are presented for turbulent flows to evaluate the turbulence model of Section 7.4 for a range of three-dimensional incompressible flows.

## 7.2 Boundary-Layer Equations for Three-Dimensional Flows

Before we discuss the boundary-layer equations for three-dimensional flows, it is useful to discuss the origin of crossflow in a boundary-layer. In three-dimensional flows, the external velocity vector does not coincide with the pressure gradient vector. As a result, the external streamlines on the surface are curved and this gives rise to crossflow in the boundary-layer. At any point on the external streamline, the pressure gradient has two components, one in the streamwise direction and another normal to it.

As an example, consider an initially two-dimensional boundary-layer and assume that a crosswise component of pressure gradient is applied downstream at a certain point. In Fig. 7.1a we have  $\partial p/\partial z < 0$ . This crosswise pressure gradient is associated with the curvature of the external streamline and the crosswise pressure force is balanced by a centrifugal force

$$\frac{\partial p}{\partial z} = -\frac{\rho u_e^2}{R}$$

where  $R$  is the radius of the curvature of the external streamline.

Close to the wall, if we neglect the viscous and turbulent stresses, we have

$$\frac{\partial p}{\partial z} = -\frac{\rho u^2}{r}$$

where  $r$  is the radius of curvature of the local streamline in the boundary-layer. Since according to the first-order boundary-layer theory, the static pressure remains constant along a normal to the wall,  $\partial p/\partial z$  is also constant along a normal. Since the velocity  $u$  is smaller than its external value, the radius of curvature  $r$  of the boundary-layer streamline is also smaller than the radius of curvature  $R$  of the external streamline. Therefore, the *crosswise pressure gradient generates a crossflow directed towards the center of the external streamline curvature*. Closer to the wall, viscosity ensures a zero crossflow component at the wall. In the vicinity of the wall, pressure forces are balanced by viscous forces

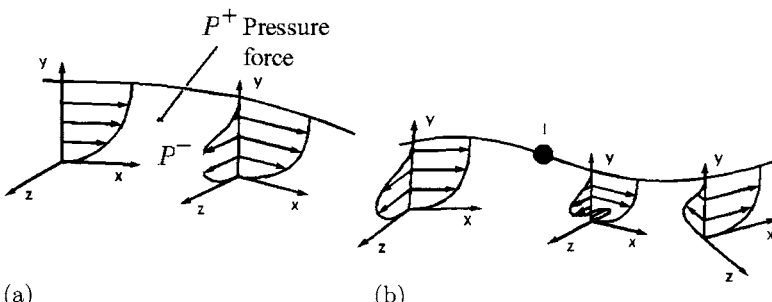
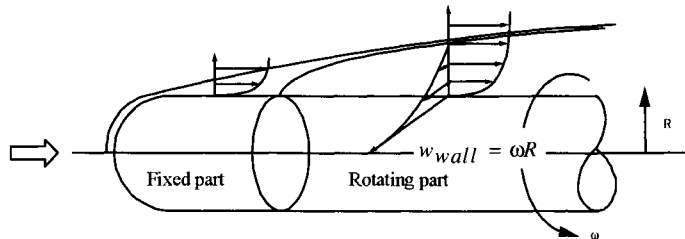


Fig. 7.1. Secondary flow generated by a crosswise component of the pressure gradient.

$$\frac{\partial p}{\partial z} = \frac{\partial \tau_z}{\partial y}$$

When the crosswise pressure gradient changes sign, the external streamlines have an inflection point. In the boundary-layer crossflow changes sign first near the wall because the flow reacts more rapidly near the wall where inertia is smaller (Fig. 7.1b).

The mechanism described above gives rise to *pressure-driven three-dimensional boundary-layers*. A typical example is the flow on a swept wing, but other mechanisms are possible sources for crossflow. For example, crossflow develops in a boundary-layer flowing on a wall moving in the crosswise direction (Fig. 7.2).



**Fig. 7.2.** Three-dimensional boundary-layer generated by wall conditions.

### 7.2.1 Cartesian Coordinate System

The procedure discussed in Section 3.1 for two-dimensional flows can also be applied to the three-dimensional Reynolds-averaged Navier-Stokes equations given by Eqs. (2.2.2) to (2.2.5) in order to obtain the boundary-layer equations for three-dimensional laminar and turbulent flows. The resulting equations, with the  $y$ -momentum equation still given by Eq. (3.1.11), are

$$\frac{\partial u}{\partial x} + \frac{\partial v}{\partial y} + \frac{\partial w}{\partial z} = 0 \quad (7.2.1)$$

$$u \frac{\partial u}{\partial x} + v \frac{\partial u}{\partial y} + w \frac{\partial u}{\partial z} = -\frac{1}{\rho} \frac{\partial p}{\partial x} + \nu \frac{\partial^2 u}{\partial y^2} + \frac{\partial}{\partial y} (-\bar{u}'v') \quad (7.2.2)$$

$$u \frac{\partial w}{\partial x} + v \frac{\partial w}{\partial y} + w \frac{\partial w}{\partial z} = -\frac{1}{\rho} \frac{\partial p}{\partial z} + \nu \frac{\partial^2 w}{\partial y^2} + \frac{\partial}{\partial y} (-\bar{v}'w') \quad (7.2.3)$$

We note that the static pressure  $p$  is now a function of  $x$  and  $z$ , and the freestream velocity has two components  $u_e$  and  $w_e$ , which are also functions of  $x$  and  $z$ ,

The boundary conditions are

$$y = 0, \quad u = w = 0, \quad v = v_w(x, z) \quad (7.2.4a)$$

$$y = \delta, \quad u = u_e, \quad w = w_e \quad (7.2.4b)$$

At the boundary-layer edge, Eqs. (7.2.2) and (7.2.3) reduce to

$$u_e \frac{\partial u_e}{\partial x} + w_e \frac{\partial u_e}{\partial z} = -\frac{1}{\rho} \frac{\partial p}{\partial x} \quad (7.2.5a)$$

$$u_e \frac{\partial w_e}{\partial x} + w_e \frac{\partial w_e}{\partial z} = -\frac{1}{\rho} \frac{\partial p}{\partial z} \quad (7.2.5b)$$

As in two-dimensional flows, under certain conditions the three-dimensional boundary-layer equations also simplify. For flows over yawed cylinders or infinite swept wings (see Fig. 7.3) the flow is independent of the  $z$ -coordinate. The boundary-layer equations become

$$\frac{\partial u}{\partial x} + \frac{\partial v}{\partial y} = 0 \quad (7.2.6a)$$

$$u \frac{\partial u}{\partial x} + v \frac{\partial u}{\partial y} = -\frac{1}{\rho} \frac{dp}{dx} + \nu \frac{\partial^2 u}{\partial y^2} + \frac{\partial}{\partial y} (-\bar{u}'v') \quad (7.2.6b)$$

$$u \frac{\partial w}{\partial x} + v \frac{\partial w}{\partial y} = \nu \frac{\partial^2 w}{\partial y^2} + \frac{\partial}{\partial y} (-\bar{v}'w') \quad (7.2.6c)$$

These equations are referred to as the infinite swept wing equations since a swept wing is also a yawed cylinder. For laminar flows, the solutions of  $u$  and  $v$  are independent of  $w$  and the resulting equations are identical to those for two-dimensional flows. For turbulent flows, however, this is not the case and the  $x$ -momentum and  $z$ -momentum equations are coupled to each other via a turbulence model.

When the external velocity components  $u_e$  and  $w_e$  vary with  $x$  and  $z$  in some specified manner, the three-dimensional boundary-layer equations for laminar flows admit similarity, as in two-dimensional laminar flows, and with appropriate transformations can be reduced to ordinary differential equations. This is discussed in Section 7.5.

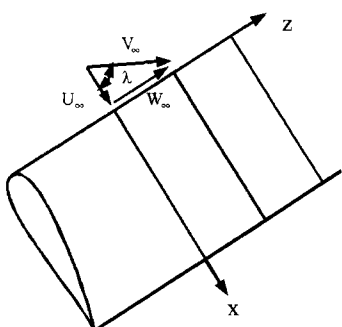


Fig. 7.3. Coordinate system for an infinite swept wing.

### 7.2.2 Streamline Coordinate System

In general, it is desirable and convenient to express the equations of subsection 7.2.1 in more general coordinate systems. Two popular choices for this purpose are the streamline coordinate system discussed in this subsection and the body-oriented coordinate system discussed in the following subsection.

The streamline coordinate system is an orthogonal system formed by the inviscid streamlines and their orthogonal trajectories on the surface. As shown in Fig. 7.4 the projection of the freestream velocity vector on the surface is aligned with the surface coordinate  $x$ . The velocity component along the  $z$ -axis, referred to as the crossflow velocity is zero at the edge of the boundary-layer.

For this coordinate system the continuity and momentum equations and their boundary conditions, for an incompressible laminar and turbulent flow, are

$$\frac{\partial}{\partial x}(uh_2) + \frac{\partial}{\partial z}(wh_1) + \frac{\partial}{\partial y}(vh_1h_2) = 0 \quad (7.2.7)$$

$$\frac{u}{h_1} \frac{\partial u}{\partial x} + \frac{w}{h_2} \frac{\partial u}{\partial z} + v \frac{\partial u}{\partial y} + k_2 w^2 - k_1 uw = -\frac{1}{\rho h_1} \frac{\partial p}{\partial x} + \nu \frac{\partial^2 u}{\partial y^2} + \frac{\partial}{\partial y}(-\bar{u}'v') \quad (7.2.8)$$

$$\frac{u}{h_1} \frac{\partial w}{\partial x} + \frac{w}{h_2} \frac{\partial w}{\partial z} + v \frac{\partial w}{\partial y} + k_1 u^2 - k_2 uw = -\frac{1}{\rho h_2} \frac{\partial p}{\partial z} + \nu \frac{\partial^2 w}{\partial y^2} + \frac{\partial}{\partial y}(-\bar{v}'w') \quad (7.2.9)$$

$$y = 0, \quad u = w = 0, \quad v = v_w(x, z) \quad (7.2.10a)$$

$$y = \delta, \quad u = u_{se}, \quad w = 0 \quad (7.2.10b)$$

where

$$\rho u_{se} \frac{\partial u_{se}}{\partial x} = -\frac{\partial p}{\partial x}, \quad \rho k_1 u_{se}^2 = -\frac{1}{h_2} \frac{\partial p}{\partial z} \quad (7.2.11)$$

Here  $u_{se}$  denotes the inviscid total velocity on the surface, and  $h_1(x, z)$  and  $h_2(x, z)$  denote metric coefficients. The parameters  $k_1$  and  $k_2$  are known as the geodesic curvatures of the curves  $z = \text{constant}$  and  $x = \text{constant}$ , respectively, and are given by

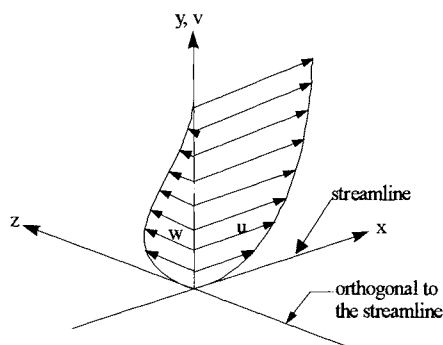


**Fig. 7.4.** Notation for the streamline coordinate system.

$$k_1 = -\frac{1}{h_1 h_2} \frac{\partial h_1}{\partial z}, \quad k_2 = -\frac{1}{h_1 h_2} \frac{\partial h_2}{\partial x} \quad (7.2.12)$$

For an irrotational external flow, the metric coefficients  $h_1$  and  $h_2$  are calculated from the following relations

$$h_1 = \frac{f(x)}{u_{se}}, \quad \frac{1}{h_1} \frac{\partial}{\partial x} [\ln(u_{se} h_2)] = \frac{g(\xi, \eta)}{u_{se}} \quad (7.2.13)$$

Here  $f(x)$  is an integration constant which results from the irrotationality condition  $\frac{\partial(h_1 u_{se})}{\partial z} = 0$  and  $g(\xi, \eta)$  is determined from the expression  $g(\xi, \eta) = -\partial v_e / \partial y$ , with  $\xi$  and  $\eta$  denoting any body-oriented coordinate system. We observe from the relations in Eqs. (7.2.11) to (7.2.13) that  $k_1$  can be calculated either from its definition [Eq. (7.2.12)] or from the second equation in Eq. (7.2.11). The parameter  $k_2$  can be calculated from

$$k_2 = \frac{1}{u_{se}} \left[ \frac{1}{h_1} \frac{\partial}{\partial x} (u_{se}) - g(\xi, \eta) \right] \quad (7.2.14)$$

Although the cross-flow velocity component  $w$  is zero at the edge, it is not so within the boundary-layer. If, on the other hand,  $w$  is also zero, meaning that there is no cross-flow in the layer, it follows from the cross-flow momentum equation that

$$k_1 u^2 = -\frac{1}{\rho h_2} \frac{\partial p}{\partial z} \quad (7.2.15)$$

This equation shows that if the streamline curvature  $k_1$  is small, then the pressure gradient normal to the streamline must be small. In this case, it can be shown that  $w$  and the cross-flow derivatives ( $\partial/\partial z$ ) will be small, allowing the boundary-layer equations to simplify considerably. The resulting equations, known as the small cross-flow equations, are:

$$\frac{\partial}{\partial x} (u h_2) + \frac{\partial}{\partial y} (v h_1 h_2) = 0 \quad (7.2.16)$$

$$\frac{u}{h_1} \frac{\partial u}{\partial x} + v \frac{\partial u}{\partial y} = \frac{u_{se}}{h_1} \frac{\partial u_{se}}{\partial x} + \nu \frac{\partial^2 u}{\partial y^2} + \frac{\partial}{\partial y} (-\overline{u'v'}) \quad (7.2.17)$$

$$\frac{u}{h_1} \frac{\partial w}{\partial x} + v \frac{\partial w}{\partial y} + k_1 u^2 - k_2 uw = k_1 u_{se}^2 + \nu \frac{\partial^2 w}{\partial y^2} + \frac{\partial}{\partial y} (-\overline{v'w'}) \quad (7.2.18)$$

The advantage of this approximation is that for laminar flows the continuity and streamwise momentum equations are independent of the cross-flow velocity  $w$  and that Eqs. (7.2.16) and (7.2.17) can be solved separately from (7.2.18). The computational effort is not too much beyond the effort required to solve the two-dimensional flow equations since Eq. (7.2.18) is a linear equation in terms of  $w$ . It should be noted that they also correspond to the boundary-layer equations on an axisymmetric body at zero incidence (Section 3.2) if we replace

$h_2$  by body radius  $r_0$  and take  $h_1 = 1$  which implies that the  $x$ -coordinate is the distance measured along the streamlines of outer flow and  $k_1 = 0$ . For a turbulent flow, on the other hand, the two momentum equations are, in general, coupled through the turbulence models used for Reynolds stresses.

### 7.2.3 Body-Oriented Coordinate System

Although the streamline coordinate system is very general, its calculation is major undertaking in itself and must be repeated at every change of attitude of the body or Mach number for compressible flows. It is generally more appropriate to use a body-oriented coordinate system which has the advantage that it is independent of the angle of attack and easy to calculate even if the body is not defined analytically. In addition, second-order boundary-layer effects, such as transverse or longitudinal curvature, can be included but requires a special orthogonal coordinate system consisting of lines of principal curvatures of the body and normals. However, in some geometries the choice of the body-oriented coordinate system introduces singularities into the geometric parameters  $h_1$ ,  $h_2$  and geodesic curvatures  $k_1$  and  $k_2$ . Transformations, however, as described in [1, 2] can be used to overcome this problem.

A convenient and useful coordinate system, especially when dealing with geometries like ship hulls, fuselages and wings, is a nonorthogonal coordinate system. Typical examples for a ship hull and a finite wing are shown in Figures 7.5 and 7.6.

For a body-oriented coordinate system, the continuity and momentum equations can be written in the form ( $\csc \theta = 1 / \sin \theta$ )

$$\frac{\partial}{\partial x}(uh_2 \sin \theta) + \frac{\partial}{\partial z}(wh_1 \sin \theta) + \frac{\partial}{\partial y}(vh_1 h_2 \sin \theta) = 0 \quad (7.2.19)$$

$$\begin{aligned} & \frac{u}{h_1} \frac{\partial u}{\partial x} + \frac{w}{h_2} \frac{\partial u}{\partial z} + v \frac{\partial u}{\partial y} - \cot \theta k_1 u^2 + \csc \theta k_2 w^2 + k_{12} uw \\ &= -\frac{\csc^2 \theta}{\rho h_1} \frac{\partial p}{\partial x} + \frac{\cot \theta \csc \theta}{\rho h_2} \frac{\partial p}{\partial z} + \nu \frac{\partial^2 u}{\partial y^2} + \frac{\partial}{\partial y}(-\bar{u}'v') \end{aligned} \quad (7.2.20)$$

$$\begin{aligned} & \frac{u}{h_1} \frac{\partial w}{\partial x} + \frac{w}{h_2} \frac{\partial w}{\partial z} + v \frac{\partial w}{\partial y} - \cot \theta k_2 w^2 + \csc \theta k_1 u^2 + k_{21} uw \\ &= \frac{\cot \theta \csc \theta}{\rho h_1} \frac{\partial p}{\partial x} - \frac{\csc^2 \theta}{\rho h_2} \frac{\partial p}{\partial z} + \nu \frac{\partial^2 w}{\partial y^2} + \frac{\partial}{\partial y}(-\bar{w}'v') \end{aligned} \quad (7.2.21)$$

Here  $\theta$  represents the angle between the coordinate lines;  $\theta = \pi/2$  for an orthogonal system. The geometric curvature parameters  $k_1$  and  $k_2$  are given by

$$k_1 = \frac{1}{h_1 h_2 \sin \theta} \left[ \frac{\partial}{\partial x}(h_2 \cos \theta) - \frac{\partial h_1}{\partial z} \right] \quad (7.2.22a)$$

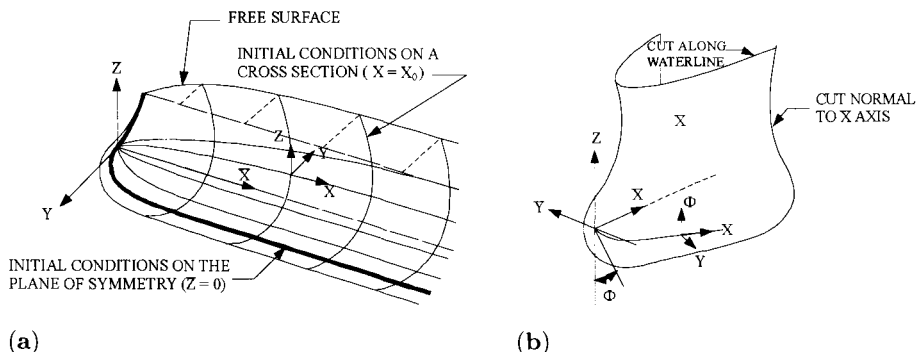


**Fig. 7.5.** The nonorthogonal coordinate system for a ship hull, (a) away from the bow region, and (b) near the bow.

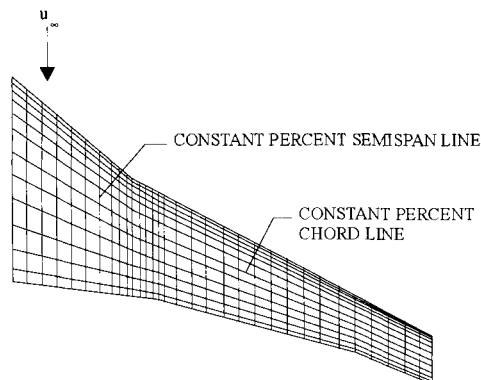


**Fig. 7.6.** The nonorthogonal coordinate system for a finite wing.

$$k_2 = \frac{1}{h_1 h_2 \sin \theta} \left[ \frac{\partial}{\partial z} (h_1 \cos \theta) - \frac{\partial h_2}{\partial x} \right] \quad (7.2.22b)$$

The parameters  $k_{12}$  and  $k_{21}$  are defined by

$$k_{12} = \frac{1}{h_1 h_2 \sin^2 \theta} \left[ (1 + \cos^2 \theta) \frac{\partial h_1}{\partial z} - 2 \cos \theta \frac{\partial h_2}{\partial x} \right] \quad (7.2.23a)$$

$$k_{21} = \frac{1}{h_1 h_2 \sin^2 \theta} \left[ (1 + \cos^2 \theta) \frac{\partial h_2}{\partial x} - 2 \cos \theta \frac{\partial h_1}{\partial z} \right] \quad (7.2.23b)$$

The magnitude of the velocity vector  $u_t$  in the boundary-layer is given by

$$u_t = (u^2 + w^2 + 2uw \cos \theta)^{1/2} \quad (7.2.24)$$

At the boundary-layer edge, Eqs. (7.2.20) and (7.2.21) reduce to

$$\begin{aligned} & \frac{u_e}{h_1} \frac{\partial u_e}{\partial x} + \frac{w_e}{h_2} \frac{\partial u_e}{\partial z} - \cot \theta k_1 u_e^2 + \csc \theta k_2 w_e^2 + k_{12} u_e w_e \\ &= -\frac{\csc^2 \theta}{\rho h_1} \frac{\partial p}{\partial x} + \frac{\cot \theta \csc \theta}{\rho h_2} \frac{\partial p}{\partial z} \end{aligned} \quad (7.2.25a)$$

$$\begin{aligned} \frac{u_e}{h_1} \frac{\partial w_e}{\partial x} + \frac{w_e}{h_2} \frac{\partial w_e}{\partial z} - \cot \theta k_2 w_e^2 + \csc \theta k_1 u_e^2 + k_{21} u_e w_e \\ = \frac{\cot \theta \csc \theta}{\rho h_1} \frac{\partial p}{\partial x} - \frac{\csc^2 \theta}{\rho h_2} \frac{\partial p}{\partial z} \end{aligned} \quad (7.2.25b)$$

The boundary conditions appropriate to Eqs. (7.2.19) to (7.2.21) are

$$y = 0, \quad u, w = 0, \quad v = v_w(x, z) \quad (7.2.26a)$$

$$y = \delta, \quad u = u_e(x, z), \quad w = w_e(x, z) \quad (7.2.26b)$$

### 7.3 Initial Conditions

In the solution of the three-dimensional boundary-layer equations discussed in the previous section, initial and boundary conditions are required along the boundaries where the flow enters the calculation domain. In some problems, depending on the numerical method, it may be sufficient to establish the initial conditions only in one plane as discussed in Program 10 in Appendix B. For some configurations, these conditions can be established with ease, and in others they require careful examination. In the case of a finite wing where it is more convenient to use a body oriented coordinate system, the initial conditions, for example, may correspond to those along the wing leading edge aligned with a  $z$ -coordinate line and often called the attachment line and to those along the wing-fuselage intersection.

A good approximation for calculating the boundary-layers along the attachment line is to assume the flow to correspond to the attachment line of an infinite swept wing. In this case,  $u$  and  $\partial p/\partial x$  are equal to zero and this makes the  $x$ -momentum equation (7.2.20) singular. However, differentiating this equation with respect to  $x$  and taking advantage of the symmetry conditions

$$\frac{\partial w}{\partial x} = \frac{\partial v}{\partial x} = \frac{\partial^2 u}{\partial x^2} = 0$$

and using Eqs. (7.2.25), the attachment line equations with  $\theta = \pi/2$  can be written as

$$h_2 \sin \theta u_x + \frac{\partial}{\partial z} (wh_1 \sin \theta) + \frac{\partial}{\partial y} (vh_1 h_2 \sin \theta) = 0 \quad (7.3.1)$$

$$\begin{aligned} \frac{u_x^2}{h_1} + \frac{w}{h_2} \frac{\partial u_x}{\partial z} + v \frac{\partial u_x}{\partial y} + k_{12} w u_x \\ = \frac{u_{xe}^2}{h_1} + \frac{w_e}{h_2} \frac{\partial u_{xe}}{\partial z} + k_{12} w_e u_{xe} + \nu \frac{\partial^2 u_x}{\partial y^2} + \frac{\partial}{\partial y} (-\overline{u'v'})_x \end{aligned} \quad (7.3.2)$$

$$\begin{aligned} \frac{w}{h_2} \frac{\partial w}{\partial z} + v \frac{\partial w}{\partial y} - \cot \theta k_2 w^2 \\ = \frac{w_e}{h_2} \frac{\partial w_e}{\partial z} - \cot \theta k_2 w_e^2 + \nu \frac{\partial^2 w}{\partial y^2} + \frac{\partial}{\partial y} (-\overline{w'v'}) \end{aligned} \quad (7.3.3)$$

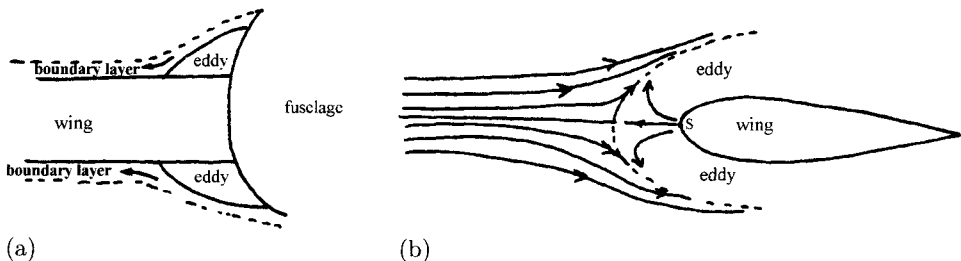


**Fig. 7.7.** (a) Cross-section of wing and fuselage. (b) Surface streamlines on fuselage near junction with wing.

Here  $u_x = \partial u / \partial x$ ,  $u_{xe} = \partial u_e / \partial x$ , and the equations are subject to the following boundary conditions

$$y = 0, \quad u_x = w = 0, \quad v = v_w(z) \quad (7.3.4a)$$

$$y = \delta, \quad u_x = u_{xe}(x, z), \quad w = w_e(x, z) \quad (7.3.4b)$$

The behavior of the flow along the wing-fuselage intersection is very complicated. Unless special care is taken, it is likely to separate ahead of the junction generating an eddy and possibly eddies at the wing-root with a strong horseshoe vortex covering the upper and lower surfaces of the wing. Apart from the consequent loss of lift and drag increase due to the eddy, the boundary-layer on the wing receives an injection of fluid from the fuselage via the eddy boundary with unknown consequences for the flow properties on the wing. The calculation of flow in this region requires the solution of the Navier-Stokes equations. Even then, the prediction of flow along the wing-fuselage intersection accurately is an area that still requires further research.

Figure 7.7a is a sketch of the flowfield at a cross-section of the wing-body region of an airplane. The closed region marked "eddy" are the two components of the horseshoe vortex; the boundary layer of the fuselage flows over them and may spill over into the wing boundary layer. Figure 7.7b shows how the horseshoe vortex starts on the fuselage boundary layer as the wing is approached. The adverse pressure gradient on the fuselage ahead of the wing associated with the stagnation point at  $S$  provokes separation ahead of the wing and sets up an eddying region between the oncoming boundary layer and the wing.

A related problem is the flow over a submarine moving underwater. A projection from the upper surface, known as the sail, is a feature of all submarines and the oncoming flow along the hull interacts with the sail in essentially the same way as at the wing-body junction. The horseshoe eddy generated by the interaction has the additional undesirable feature of having a source of noise which should be reduced as much as possible.

The configuration in Fig. 7.7 is a grossly simplified representation of the wing-body junction region of a modern airplane. Indeed, many of the modifications of this configuration needed to produce a modern junction region were

introduced to reduce the impact of the separation of the fuselage boundary layer. Included in these modifications are the placing of the wing at the lower part of the fuselage, the introduction of fillets between the wing and the fuselage and the fairing of the fuselage ahead of the wing to smooth the geometrical transition between the fuselage and the wing. Most of these changes have been made as a result of wind-tunnel observations and computational fluid dynamics (CFD) has played only a small role in these improvements to the airplane's flight characteristics.

Until a more general and soundly based method for calculating the wing-root flow has been developed, it is necessary to determine corresponding initial conditions with some approximations. A convenient procedure is to solve the boundary-layer equations that simulate quasi-three-dimensional flow conditions discussed in [3]; that is, all derivatives with respect to  $z$  are neglected. This approximation leads to the following equations:

$$\frac{\partial}{\partial x}(uh_2 \sin \theta) + \frac{\partial}{\partial y}(vh_1 h_2 \sin \theta) = 0 \quad (7.3.5)$$

$$\begin{aligned} & \frac{u}{h_1} \frac{\partial u}{\partial x} + v \frac{\partial u}{\partial y} - \cot \theta k_1 u^2 + \csc \theta k_2 w^2 + k_{12} uw \\ &= \frac{u_e}{h_1} \frac{\partial u_e}{\partial x} - \cot \theta k_1 u_e^2 + \csc \theta k_2 w_e^2 + k_{12} u_e w_e + \nu \frac{\partial^2 u}{\partial y^2} + \frac{\partial}{\partial y}(-\bar{u}'v') \end{aligned} \quad (7.3.6)$$

$$\begin{aligned} & \frac{u}{h_1} \frac{\partial w}{\partial x} + v \frac{\partial w}{\partial y} - \cot \theta k_2 w^2 + \csc \theta k_1 u^2 + k_{21} uw \\ &= \frac{u_e}{h_1} \frac{\partial w_e}{\partial x} - \cot \theta k_2 w_e^2 + \csc \theta k_1 u_e^2 + k_{21} u_e w_e + \nu \frac{\partial^2 w}{\partial y^2} + \frac{\partial}{\partial y}(-\bar{w}'v') \end{aligned} \quad (7.3.7)$$

The boundary conditions are the same as those given by Eq. (7.2.26) except that  $u_e$  and  $w_e$  are independent of  $z$ .

## 7.4 Turbulence Models

As in two-dimensional turbulent flows, the solution of the three-dimensional boundary-layer equations for turbulent flows requires a turbulence model for the Reynolds stresses  $-\rho \bar{u}'v'$  and  $-\rho \bar{w}'v'$  appearing in the  $x$ - and  $z$ -momentum equations, respectively. This requirement can be satisfied by using models based on algebraic eddy-viscosity and mixing-length models or two-equation models discussed in Section 6.3.

With the eddy viscosity concept, we write

$$-\rho \bar{u}'v' = \rho \nu_t \frac{\partial u}{\partial y}, \quad -\rho \bar{w}'v' = \rho \nu_t \frac{\partial w}{\partial y} \quad (7.4.1)$$

Here  $-\rho\overline{u'v'}$  denotes the shear stress acting in the  $x$ -direction on a plane parallel to the  $xz$ -plane, and  $-\rho\overline{w'v'}$ , usually written as  $-\rho\overline{v'w'}$ , the shear stress acting in the  $z$ -direction on the same plane. Almost all workers have inferred, from the fact that the choice of direction of the axes in the  $xz$ -plane is arbitrary, that the assumptions made for  $-\rho\overline{v'w'}$  should be closely analogous to those made for  $-\rho\overline{u'v'}$ . Mathematically, they assume that the turbulence model equation for  $-\rho\overline{v'w'}$  should be obtainable from that for  $-\rho\overline{u'v'}$  by cyclic interchange of symbols. However, it is not so obvious that the equations for  $-\rho\overline{u'v'}$  can be simply derived from models used for two-dimensional flow. The argument commonly used is that turbulence, being instantaneously three-dimensional, should not be seriously affected by moderate three-dimensionality of the mean flow. There is, of course, a loss of symmetry, for instance,  $v'w'$  is zero in two-dimensional flow but not in three-dimensional flow, and Rotta [4] has shown that the asymmetry can noticeably affect the modeling of the shear-stress equations.

The law of the wall [Eq (6.2.1)] and the mixing-length formula

$$\frac{\partial u}{\partial y} = \frac{(\tau/\rho)^{1/2}}{\kappa y} \quad (7.4.2)$$

are the foundations of most methods for two-dimensional flow. Clearly, Eq. (6.2.1) requires modification since the velocity now has an extra component. The local equilibrium arguments suggest that it should still be valid in three-dimensional flow if the  $x$ -axis is taken to coincide with the direction of the shear stress at height  $y$ . The assumption of local equilibrium between the magnitudes of  $\tau$  and  $\partial u/\partial y$  that leads to Eq. (7.4.2) implies, when it is taken at face value, that there should be local equilibrium, that is, coincidence between their directions. This leads to

$$\frac{\partial u}{\partial y} = \frac{-\overline{u'v'}}{(\tau/\rho)^{1/2}\kappa y} \quad (7.4.3a)$$

$$\frac{\partial w}{\partial y} = \frac{-\overline{v'w'}}{(\tau/\rho)^{1/2}\kappa y} \quad (7.4.3b)$$

where

$$\tau = \left[ (\rho\overline{u'v'})^2 + (\rho\overline{v'w'})^2 \right]^{1/2}$$

valid only if the  $x$ -axis is orthogonal to the  $z$ -axis. The argument is not, of course, very convincing – the local equilibrium is an approximation whose limits of validity need further investigation by experiment. Experiments in three-dimensional flow, particularly measurements of  $\overline{v'w'}$ , are difficult, and there is evidence both for and against Eq. (7.4.3). A safe position to take is that local equilibrium concepts are not likely to fail catastrophically as soon as the mean flow becomes slightly three-dimensional, and indeed the calculation methods

that use Eq. (7.4.3) seem to agree acceptably with most of the experimental data not too near separation, as we shall see in this section.

An undeniable difficulty in treating three-dimensional wall layers is that the viscous sublayer is not a local-equilibrium region; there is a transfer of turbulent energy toward the wall by the turbulent fluctuations themselves to compensate for viscous dissipation. Therefore, conditions at one value of  $y$  depend on conditions at the other values of  $y$ , and although the directions of velocity gradient and of shear stress coincide at the surface (Reynolds stresses negligible) and, according to Eq. (7.4.3), again coincide outside the sublayer, they may differ within the sublayer. As a result, the direction of the velocity outside the sublayer may differ from that of the shear stress or velocity gradient. In practical terms, the constant of integration in any velocity profile derived from Eq. (7.4.3), or the damping length constant,  $A$  in Eq. (6.3.4), will have two components. The effect will be significant only if the direction of the shear stress changes significantly across the sublayer. Since at the surface,  $\partial\tau_x/\partial y = \partial p/\partial x$  and  $\partial\tau_z/\partial y = \partial p/\partial z$ , this will occur only if there is a significant pressure gradient normal to the wall-stress vector, as for example in a boundary layer flowing into a lateral bend ( $\partial w_e/\partial x \neq 0$ ). Van den Berg [5] has proposed a dimensionally correct empirical correlation taking the  $x$ -axis in the direction of the wall shear stress, the  $z$ -component velocity at the outer edge of the sublayer is  $12u_\tau(\nu/\rho u_\tau^3)\partial p/\partial z$ .

The outer layer, like the sublayer, is not a local equilibrium region, and the direction of the shear stress will lag behind the direction of the velocity gradient if the latter changes with  $x$ . Several experiments have shown that angles between the shear stress and velocity gradient vectors are of the same order as that of the cross-flow (i.e., the angle between the external velocity and the surface shear stress). However, the accuracy of prediction of the boundary-layer thickness and the surface shear-stress vector does not depend critically on the shear-stress direction in the outer layer, and good agreement has been obtained between the available data and an extension of the CS eddy-viscosity formulation of subsection 6.3.1 in which the velocity defect used in Eq. (6.3.5) is just taken as the magnitude of the vector  $(u_{te} - u_t)$  at given  $y$ . The same eddy viscosity is used in Eq. (7.4.2) so that the directions of shear stress and velocity gradient are equated. According to [6], a generalization of the CS eddy-viscosity formulation of subsection 6.3.1 for three-dimensional boundary layers is

$$(\nu_t)_i = l^2 \left[ \left( \frac{\partial u}{\partial y} \right)^2 + \left( \frac{\partial w}{\partial y} \right)^2 + 2 \cos \theta \frac{\partial u}{\partial y} \frac{\partial w}{\partial y} \right]^{\frac{1}{2}} \quad 0 \leq y \leq y_c \quad (7.4.4a)$$

$$(\nu_t)_0 = \alpha \left| \int_0^\delta (u_{te} - u_t) dy \right| \quad y_c \leq y \leq \delta \quad (7.4.4b)$$

with  $\alpha = 0.0168$  for small adverse pressure gradient flows. Its variation with strong pressure gradient flows can again be expressed by a generalization of Eqs. (6.3.9), (6.3.10), and (6.3.12); but this has not been attempted yet.

In Eq. (7.4.4a), for incompressible flows the mixing length  $l$  is given by Eq. (6.3.4a) with  $A$  and  $N$  defined by Eq. (6.3.4b) except that now

$$u_\tau = \left( \frac{\tau_t}{\rho} \right)_{\max}^{\frac{1}{2}}, \quad \left( \frac{\tau_t}{\rho} \right)_{\max} = (\nu + \nu_t) \left[ \left( \frac{\partial u}{\partial y} \right)^2 + \left( \frac{\partial w}{\partial y} \right)^2 + 2 \cos \theta \frac{\partial u}{\partial y} \frac{\partial w}{\partial y} \right]_{\max}^{\frac{1}{2}} \quad (7.4.5)$$

In Eq. (7.4.4b),  $u_{te}$  is the total edge velocity defined by

$$u_{te} = (u_e^2 + w_e^2 + 2u_e w_e \cos \theta)^{1/2} \quad (7.4.6)$$

and  $u_t$  is the total velocity in the boundary layer given by Eq. (7.2.24). The parameter  $\theta$  again denotes the angle between the coordinate lines  $x$  and  $z$  and is equal to  $\pi/2$  for an orthogonal system.

In Section 7.7 we present an evaluation of this turbulence model with experimental data for three-dimensional incompressible flows.

As in two-dimensional flows, mixing-length formulations have also been extended to three-dimensional flows. Cousteix et al. [7] define the mixing-length in Eq. (7.4.4a) with the expression given by Eq. (6.3.7) and apply it for the whole layer. They express the wall shear in the damping parameter  $A$  by

$$\tau_w = \sqrt{\tau_{wx}^2 + \tau_{wz}^2 + 2 \cos \theta \tau_{wx} \tau_{wz}} \quad (7.4.7)$$

The  $k$ - $\varepsilon$  model discussed in subsection 6.3.2 has also been extended to three-dimensional flows, as discussed, for example by Launder and Sharma [8]. The eddy viscosity equation, Eq. (6.3.14), is written as

$$\nu_t = c_\mu f_\mu \frac{k^2}{\tilde{\varepsilon}} \quad (7.4.8)$$

where

$$\tilde{\varepsilon} = \varepsilon - 2\nu \left( \frac{\partial k^{1/2}}{\partial y} \right)^{\frac{1}{2}} \quad (7.4.9)$$

and the transport equations as

$$\frac{Dk}{Dt} = P - \varepsilon + \frac{\partial}{\partial y} \left[ \left( \nu + \frac{\nu_t}{\sigma_k} \right) \frac{\partial k}{\partial y} \right] \quad (7.4.10)$$

$$\frac{D\tilde{\varepsilon}}{Dt} = c_{\varepsilon_1} \frac{\tilde{\varepsilon}}{k} P - f_2 c_{\varepsilon_2} \frac{\tilde{\varepsilon}^2}{k} + 2\nu \nu_t \left[ \left( \frac{\partial^2 u}{\partial y^2} \right)^2 + \left( \frac{\partial^2 w}{\partial y^2} \right)^2 \right] + \frac{\partial}{\partial y} \left[ \left( \nu + \frac{\nu_t}{\sigma_\varepsilon} \right) \frac{\partial \tilde{\varepsilon}}{\partial y} \right] \quad (7.4.11)$$

Here, the constants  $c_\mu$ ,  $c_{\varepsilon_1}$ ,  $c_{\varepsilon_2}$ ,  $\sigma_\varepsilon$  and  $\sigma_k$  are given, and  $f_\mu$  and  $f_2$  by Eqs. (6.3.21) with  $R_t$  now defined by

$$R_t = \frac{k^2}{\nu \tilde{\varepsilon}} \quad (7.4.12)$$

The production term  $P$  for a Cartesian coordinate system is

$$P = -\overline{u'v'} \frac{\partial u}{\partial y} - \overline{w'v'} \frac{\partial w}{\partial y} \quad (7.4.13a)$$

or in terms of eddy viscosity concept

$$P = \nu_t \left[ \left( \frac{\partial u}{\partial y} \right)^2 + \left( \frac{\partial w}{\partial y} \right)^2 \right] \quad (7.4.13b)$$

## 7.5 Transformed Equations

As in two-dimensional flows discussed in Chapters 4 and 6, it is useful and convenient to express the boundary-layer equations in transformed coordinates. There are several transformations that can be used for this purpose. A convenient one, similar to the Falkner-Skan transformation discussed in Section 4.2 is

$$x = x, \quad z = z, \quad \eta = \sqrt{\frac{u_e}{\nu x}} y \quad (7.5.1)$$

For the dependent variables  $u, v, w$ , a two-component vector potential is introduced such that

$$u = \frac{\partial \psi}{\partial y}, \quad w = \frac{\partial \phi}{\partial y}, \quad v = -\left( \frac{\partial \psi}{\partial x} + \frac{\partial \phi}{\partial z} \right) \quad (7.5.2)$$

together with dimensionless parameters  $f$  and  $g$  defined by

$$\psi = (u_e \nu x)^{1/2} f(x, z, \eta) \quad (7.5.3a)$$

$$\phi = \left( \frac{\nu x}{u_e} \right)^{\frac{1}{2}} w_e g(x, z, \eta) \quad (7.5.3b)$$

Using this transformation and the reduced equations at the boundary-layer edge, Eqs. (7.2.1) to (7.2.3) and their boundary conditions, Eqs. (7.2.4), with the definition of eddy viscosity

$$-\overline{u'v'} = \nu_t \frac{\partial u}{\partial y}, \quad -\overline{w'v'} = \nu_t \frac{\partial w}{\partial y} \quad (7.5.4)$$

can be written in the following form

$$\begin{aligned} & (bf'')' + m_1 ff'' + m_2 [1 - (f')^2] + m_5 (1 - f'g') + m_6 gf'' \\ &= x \left[ f' \frac{\partial f'}{\partial x} - f'' \frac{\partial f}{\partial x} + m_7 \left( g' \frac{\partial f'}{\partial z} - f'' \frac{\partial g}{\partial z} \right) \right] \end{aligned} \quad (7.5.5)$$

$$(bg'')' + m_1 fg'' + m_4(1 - f'g') + m_3[1 - (g')^2] + m_6 gg'' = x \left[ f' \frac{\partial g'}{\partial x} - g'' \frac{\partial f}{\partial x} + m_7 \left( g' \frac{\partial g'}{\partial z} - g'' \frac{\partial g}{\partial z} \right) \right] \quad (7.5.6)$$

$$\eta = 0, \quad f = f_w(x, z), \quad g = 0, \quad f' = g' = 0 \quad (7.5.7a)$$

$$\eta = \eta_{e'}, \quad f' = g' = 1 \quad (7.5.7b)$$

Here, primes denote differentiation with respect to  $\eta$ ,  $b$  is defined by Eq. (4.5.6) and the parameters  $m_1$  to  $m_7$  denote dimensionless pressure gradients,

$$\begin{aligned} m_2 &= \frac{x}{u_e} \frac{\partial u_e}{\partial x}, \quad m_1 = \frac{m_2 + 1}{2}, \quad m_3 = \frac{x}{u_e} \frac{\partial w_e}{\partial z} \\ m_4 &= \frac{x}{w_e} \frac{\partial w_e}{\partial x}, \quad m_5 = \frac{w_e}{u_e} \frac{x}{u_e} \frac{\partial u_e}{\partial z}, \quad m_6 = m_3 - \frac{m_5}{2}, \quad m_7 = \frac{w_e}{u_e} \end{aligned} \quad (7.5.8)$$

For external velocity components in the form

$$u_e = Ax^m z^n, \quad w_e = Bx^r z^s \quad (7.5.9)$$

with  $r = m_2 - 1$ ,  $s = n + 1$ , Eqs. (7.5.5) and (7.5.6) become similar for laminar flows ( $b = 1$ ) and can be expressed as ( $m_2 = m$ )

$$f''' + \frac{m+1}{2} f f'' + m[1 - (f')^2] + \frac{B}{A} \left\{ \frac{n+2}{2} g f'' + n(1 - f'g') \right\} = 0 \quad (7.5.10)$$

$$g''' + \frac{m+1}{2} f g'' + (m-1)(1 - f'g') + \frac{B}{A} \left\{ \frac{n+2}{2} g g'' + (n+1)[1 - (g')^2] \right\} = 0 \quad (7.5.11)$$

These equations have been solved by Hansen and Yohner [9] for values of  $B/A = 1$  and 2 and for several combinations of  $m$  and  $n$ . We note that the external inviscid flows represented by Eq. (7.5.9) are rotational and exhibit “overshoots” in some  $f'$ -profiles due to the nonuniformities in total pressure.

Similar solutions of a particularly interesting type also result for arbitrary values of  $m$  for  $r = n = s = 0$ . In this case, the inviscid flow is irrotational and the resulting equations, which sometimes are called Falkner-Skan-Cooke equations, are:

$$f''' + \frac{m+1}{2} f f'' + m[1 - (f')^2] = 0 \quad (7.5.12)$$

$$g''' + \frac{m+1}{2} f g'' = 0 \quad (7.5.13)$$

Analogous to two-dimensional similar flows, these equations correspond to flows over swept wedges of infinite extent. For example  $m = 1$ , they represent the similarity solutions of the attachment-line equations along the leading edge of a wing with  $f' = u_x/u_{xe}$ ,  $g' = w/w_e$ .

For a yawed infinite cylinder, since the spanwise flow is independent of the  $z$ -component, all the coefficients  $m_i$  ( $i = 1$  to 7) defined in Eq. (7.5.8) are independent of  $z$  and as a result, Eqs. (7.5.5) and (7.5.6) reduce to

$$(bf'')' + m_1 ff'' + m_2[1 - (f')^2] = x \left( f' \frac{\partial f'}{\partial x} - f'' \frac{\partial f}{\partial x} \right) \quad (7.5.14)$$

$$(bg'')' + m_1 fg'' = x \left( f' \frac{\partial g'}{\partial x} - g'' \frac{\partial f}{\partial x} \right) \quad (7.5.15)$$

The boundary conditions given by Eq. (7.5.7) apply except that  $f_w$  is only a function of  $x$ .

We note that Eq. (7.5.14) is identical to that in two-dimensional laminar and turbulent flows and in the former case its solutions are independent of the solutions of the  $z$ -momentum equation, Eq. (7.5.15). This is the independence principle which in the case of yawed cylinders, applies only to incompressible laminar flows and is not valid to turbulent flows and to compressible laminar flows. As a result of this independence principle, Eq. (7.5.15) is linear.

## 7.6 Numerical Solution of the Boundary-Layer Equations: Differential Form

Keller's box method discussed in Section 4.5 for two-dimensional flows can also be used to solve the boundary-layer equations for three-dimensional flows. Before we describe the solution procedure in this case, however, it is helpful and important to review briefly the general principles which accurate solutions must obey for three-dimensional flows. These follow from the realization that the momentum equations are diffusive in the direction normal to the body and wave-like in plane parallel to the body, the direction of propagation being along the local stream direction. Since this direction varies across the boundary-layer, it is possible to identify zones of influence and dependence and to obtain solutions to the three-dimensional boundary-layer equations such that their solutions obey these zones. To explain this further, it is useful to consider a grid, as shown in the sketch, Fig. 7.8a, in which the solutions are known at these points indicated by a cross ( $\times$ ) and are required at  $P$ . The wall streamlines and external streamlines have been drawn on the assumption that both  $u$  and  $w$  velocity components are positive.

As was discussed briefly in [10], the domain of dependence of point  $P$  consists of the region denoted by the shaded area and the region of influence of point  $P$  corresponds to the hatched area where the solution is altered when a change occurs in the solution at the point  $P$ . Strictly, the zones of influence (and dependence) are formed by the outermost streamlines crossing the normal to the wall at point  $P$ . Very often these outermost streamlines are the external

streamline and the limiting wall streamline. The information to point  $P$  comes from the domain of dependence. When the  $u$  velocity component is positive across the layer but the  $w$  velocity component is negative near the wall, the wall streamlines cause the domains of dependence and region of influence to change, as shown in Fig. 7.8b. The wall streamlines, which were beneath the external streamlines, move above the external streamlines. The angle between these two streamlines widens further when both velocity components of the wall streamlines become negative (Fig. 7.8c) and information comes from the region where there is none in  $P$ , thus limiting the extent of possible calculations.

The solution of the three-dimensional boundary-layer equations when velocity components  $u$  and  $w$  are positive are routine and can be achieved easily with the Keller or Crank-Nicholson method. These procedures are described in several references, see for example Blottner [11], and Bradshaw et al., [12]. When the spanwise velocity component contains regions of flow reversal, however, the solution of the three-dimensional boundary-layer equations is not so straightforward and requires special procedures to avoid the numerical instabilities which can result from reversal in  $w$ . As discussed in [1], a common procedure is to include the zig-zag formulation of Krause et al. [13]. In common with the often-used Crank-Nicholson method, this scheme is easy to employ, particularly since the orientation of the numerical mesh is chosen *a priori*. This advantage has a corresponding and potentially dangerous drawback in the presence of large reverse flows since the mesh ratio must be related to the velocity field according to the famous Courant, Friedrichs, Lewy (CFL) condition [10] if stability is to be achieved. For a fixed grid chosen *a priori*, this condition may be violated

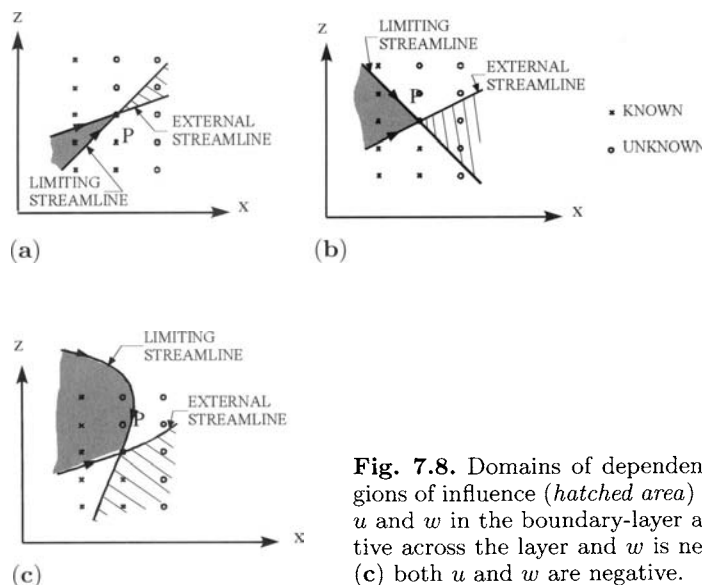


**Fig. 7.8.** Domains of dependence (*shaded area*) and regions of influence (*hatched area*) of point  $P$  when (a) both  $u$  and  $w$  in the boundary-layer are positive, (b)  $u$  is positive across the layer and  $w$  is negative near the wall, and (c) both  $u$  and  $w$  are negative.

as the flow velocities are determined in ever-increasing computational domains. Thus, a natural boundary limiting the domain in which stable computations can be made must also be determined *a priori*.

To date, the most suitable numerical procedure that can be used to avoid the difficulties associated with the reversal  $w$ -profile is the characteristic box scheme, which is based on the solution of the governing equations along local streamlines. This method uses Keller's method and, as we shall discuss later, allows the grid to be determined along with the flow calculations. It has been applied to compute three-dimensional boundary layers on wings, bodies of revolution at incidence and ship hulls with good success [14].

In this section, we consider the numerical solution of the three-dimensional boundary-layer equations for cases which correspond to sketches in Figures 7.8a and 7.8b. For cases in which the streamwise velocity  $u$  becomes negative, Fig. 7.8c, information coming from downstream is needed. For this reason, the solution cannot be obtained from a boundary-layer procedure alone in which the calculations march in the increasing  $x$ -direction.

To describe the solution procedure, we can start with the transformed equations and boundary conditions in the form given by Eqs. (7.5.5) to (7.5.7) or we can start with the same equations expressed in the following form

$$(bf'')' + f''\theta + m_2[1 - (f')^2] + m_5(1 - f'g') = x \left[ f' \frac{\partial f'}{\partial x} + m_7 g' \frac{\partial f'}{\partial z} \right] \quad (7.6.1)$$

$$(bg'')' + g''\theta + m_4(1 - f'g') + m_3[1 - (g')^2] = x \left[ f' \frac{\partial g'}{\partial x} + m_7 g' \frac{\partial g'}{\partial z} \right] \quad (7.6.2)$$

by defining  $\theta'$  as

$$\theta' = m_1 f' + m_6 g' + x \left( \frac{\partial f'}{\partial x} + m_7 \frac{\partial g'}{\partial z} \right) \quad (7.6.3)$$

subject to the boundary conditions

$$\eta = 0, \quad \theta = \theta_w, \quad f' = g' = 0 \quad (7.6.4a)$$

$$\eta = \eta_e, \quad f' = 1, \quad g' = 1 \quad (7.6.4b)$$

The box method described in Section 4.5 can be used for these equations in either form. While each form has its advantages, we shall use the form given by Eqs. (7.6.1) to (7.6.4) since this form is also more convenient for the characteristic box scheme described in subsection 7.6.2.

We again introduce new dependent variables  $u(x, z, \eta)$ ,  $v(x, z, \eta)$ ,  $w(x, z, \eta)$  and  $t(x, z, \eta)$ , so that the two momentum equations and their boundary conditions can be written as

$$u' = v \quad (7.6.5a)$$

$$w' = t \quad (7.6.5b)$$

$$(bv)' + v\theta + m_2(1 - u^2) + m_5(1 - uw) = x \left( u \frac{\partial u}{\partial x} + m_7 w \frac{\partial u}{\partial z} \right) \quad (7.6.5c)$$

$$(bt)' + t\theta + m_4(1 - uw) + m_3(1 - w^2) = x \left( u \frac{\partial w}{\partial x} + m_7 w \frac{\partial w}{\partial z} \right) \quad (7.6.5d)$$

$$\theta' - m_1 u - m_6 w = x \left( \frac{\partial u}{\partial x} + m_7 \frac{\partial w}{\partial z} \right) \quad (7.6.5e)$$

$$\eta = 0, \quad \theta = \theta_w, \quad u = w = 0 \quad (7.6.6a)$$

$$\eta = \eta_e, \quad u = 1, \quad w = 1 \quad (7.6.6b)$$

For given initial conditions in the spanwise and streamwise directions, the solution of the above system of equations can be obtained by the box method at a given streamwise station by “marching” in the spanwise direction. They can also be obtained at a given spanwise station by marching in the streamwise direction. Each procedure has its own advantages and in this section we assume the former procedure and depending on the complexity of the flow, we use two versions of the box scheme. In regions where there is no flow reversal in the  $w$ -profile, we obtain the solutions by the standard box scheme discussed in the following subsection; when there is flow reversal we obtain the solutions by the characteristic box scheme as discussed in subsection 7.6.2.

### 7.6.1 Flows Without Reversal: Standard Box

To solve the system given by Eqs. (7.6.5) and (7.6.6) with the standard box scheme we consider the net cube shown in Fig. 7.8. We denote the net points

$$\begin{aligned} x_0 &= 0, & x_n &= x_{n-1} + k_n, & n &= 1, 2, \dots, N \\ z_0 &= 0, & z_k &= z_{k-1} + r_k, & k &= 1, 2, \dots, K \\ \eta_0 &= 0, & \eta_j &= \eta_{j-1} + h_j, & j &= 1, 2, \dots, J \end{aligned} \quad (7.6.7)$$

We approximate the quantities  $(u, w, v, t, \theta)$  at points  $(x_n, z_k, \eta_j)$  of the net by  $(u_j^{n,k}, w_j^{n,k}, \theta^{n-1/2, k-1/2}, v_j^{n,k}, t_j^{n,k}) = \bar{\Lambda}_j^{n,k}$  which we shall call net functions. We also employ the notation  $u_j^{n,k}$  for points and quantities midway between net points and for any net function.

The difference approximations that are to approximate Eqs. (7.6.5a) and (7.6.5b) are obtained by averaging about the midpoint  $(x^n, z^k, \eta_{j-1/2})$

$$\frac{u_j^{n,k} - u_{j-1}^{n,k}}{h_j} = v_{j-\frac{1}{2}}^{n,k} \quad (7.6.8a)$$

$$\frac{w_j^{n,k} - w_{j-1}^{n,k}}{h_j} = t_{j-\frac{1}{2}}^{n,k} \quad (7.6.8b)$$

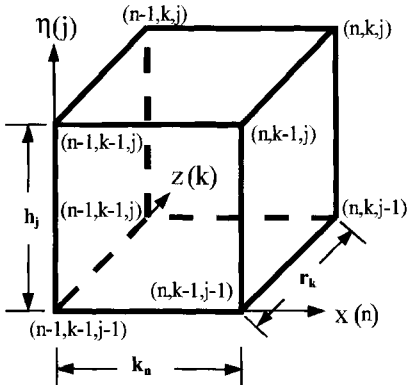


Fig. 7.9. Notation for the net cube.

The difference approximations for Eqs. (7.6.5c) to (7.6.5e) are obtained by centering all quantities at the midpoint of the cube  $(x^{n-1/2}, z^{k-1/2}, \eta_{j-1/2})$  so that the unknown parameters of Eqs. (7.6.5) correspond to  $u_j^{n,k}, v_j^{n,k}, w_j^{n,k}, t_j^{n,k}$  and  $\theta_j^{n-1/2, k-1/2}$ ; when a solution is obtained,  $u, v, w$  and  $t$  are computed at  $(n, k, j)$  and  $\theta$  at  $(n - 1/2, k - 1/2, j)$ . A separate treatment of  $\theta$  from the rest of the unknowns is necessary in order to avoid oscillations due to the use of the continuity equation in the form given by Eq. (7.6.3) rather than the use of the stream function.

We use the following notation for centering the quantities in Eqs. (7.6.5c) to (7.6.5e),

$$\begin{aligned}
 x^{n-\frac{1}{2}} &\equiv \frac{1}{2}(x^n + x^{n-1}), & z^{k-\frac{1}{2}} &\equiv \frac{1}{2}(z^k + z^{k-1}), & \eta_{j-\frac{1}{2}} &\equiv \frac{1}{2}(\eta_j + \eta_{j-1}) \\
 u_j^{n-\frac{1}{2}, k} &\equiv \frac{1}{2}(u_j^{n,k} + u_j^{n-1,k}), & u_j^{n, k-\frac{1}{2}} &\equiv \frac{1}{2}(u_j^{n,k} + u_j^{n,k-1}), & u_{j-\frac{1}{2}}^{n,k} &\equiv \frac{1}{2}(u_j^{n,k} + u_{j-1}^{n,k}) \\
 u_j^{n-\frac{1}{2}, k-\frac{1}{2}} &\equiv \bar{u}_j = \frac{1}{4}(u_j^{n,k} + u_j^{n,k-1} + u_j^{n-1,k-1} + u_j^{n-1,k}) & & & & = \frac{1}{4}(u_j^{n,k} + u_j^{234}) \\
 u_{j-\frac{1}{2}}^{n,k-\frac{1}{2}} &\equiv \bar{u}_n = \frac{1}{2}(u_{j-\frac{1}{2}}^{n,k} + u_{j-\frac{1}{2}}^{n,k-1}), & u_{j-\frac{1}{2}}^{n-\frac{1}{2}, k} &\equiv \bar{u}_k = \frac{1}{2}(u_{j-\frac{1}{2}}^{n,k} + u_{j-\frac{1}{2}}^{n-1,k}), \\
 \theta_{j-\frac{1}{2}}^{n-\frac{1}{2}, k-\frac{1}{2}} &= \frac{1}{2}(\theta_j^{n-\frac{1}{2}, k-\frac{1}{2}} + \theta_{j-1}^{n-\frac{1}{2}, k-\frac{1}{2}})
 \end{aligned} \tag{7.6.9}$$

Here, by  $u_j^{234}$  we mean  $u_j^{234} = u_j^{n,k-1} + u_j^{n-1,k-1} + u_j^{n-1,k}$ , the sum of the values of  $u_j$  at three of the four corners of the face of the box.

The difference approximations that are to approximate Eqs. (7.6.5c) to (7.6.5d) are rather lengthy. To illustrate the difference equations similar to them, we consider the following equation

$$(bv)' + v\theta + m_2(1 - u^2) = x \left( u \frac{\partial u}{\partial x} + m_7 w \frac{\partial u}{\partial z} \right) \tag{7.6.10}$$

The finite-difference approximations for this equation are

$$\begin{aligned} & [(\bar{bv})_j - (\bar{bv})_{j-1}] h_j^{-1} + \bar{v}_{j-\frac{1}{2}} \theta_{j-\frac{1}{2}} + (m_2)_{k-\frac{1}{2}}^{n-\frac{1}{2}} [1 - (\bar{u}^2)_{j-\frac{1}{2}}] \\ & = x^{n-\frac{1}{2}} [\bar{u}_{j-\frac{1}{2}} (\bar{u}_n - \bar{u}_{n-1}) k_n^{-1} + (m_7)_{k-\frac{1}{2}}^{n-\frac{1}{2}} \bar{w}_{j-\frac{1}{2}} (\bar{u}_k - \bar{u}_{k-1}) r_k^{-1}] \end{aligned} \quad (7.6.11)$$

Using the notation in Eqs. (7.6.9), the above equation can also be written as

$$\begin{aligned} & 2[(bv)_j^{n,k} - (bv)_{j-1}^{n,k}] h_j^{-1} + 2(v_{j-\frac{1}{2}}^{n,k} + v_{j-\frac{1}{2}}^{234}) \theta_{j-\frac{1}{2}} - 2(m_2)_{j-\frac{1}{2}}^{n-\frac{1}{2}} (u_{j-\frac{1}{2}}^{n,k})^2 \\ & - \alpha_n [(u_{j-\frac{1}{2}}^{n,k})^2 + \gamma_1 u_{j-\frac{1}{2}}^{n,k}] - \beta_k (u_{j-\frac{1}{2}}^{n,k} w_{j-\frac{1}{2}}^{n,k} + \gamma_2 w_{j-\frac{1}{2}}^{n,k} + \gamma_3 u_{j-\frac{1}{2}}^{n,k}) = \gamma_4 \end{aligned}$$

$$\alpha_n = x^{n-\frac{1}{2}} k_k^{-1}, \quad \beta_k = (m_7)_{k-\frac{1}{2}}^{n-\frac{1}{2}} x^{n-\frac{1}{2}} k_n^{-1} \quad (7.6.12)$$

$$\begin{aligned} \gamma_1 &= u_{j-\frac{1}{2}}^{n,k-1} - 2\bar{u}_{n-1} + u_{j-\frac{1}{2}}^{234}, \\ \gamma_2 &= u_{j-\frac{1}{2}}^{n-1,k} - 2\bar{u}_{k-1}, \quad \gamma_3 = w_{j-\frac{1}{2}}^{234} \\ \gamma_4 &= -2[(bv)_j^{234} - (bv)_{j-1}^{234}] h_j^{-1} - 8(m_2)_{k-\frac{1}{2}}^{n-\frac{1}{2}} + 2(m_2)_{k-\frac{1}{2}}^{n-\frac{1}{2}} (u_{j-\frac{1}{2}}^{234})^2 \\ &+ \alpha_n u_{j-\frac{1}{2}}^{234} (u_{j-\frac{1}{2}}^{n,k-1} - 2\bar{u}_{n-1}) + \beta_k w_{j-\frac{1}{2}}^{234} (u_{j-\frac{1}{2}}^{n-1,k} - 2\bar{u}_{k-1}) \end{aligned} \quad (7.6.13)$$

The finite difference approximations to Eq. (7.6.5e) can be expressed in the following form:

$$\begin{aligned} & h_j^{-1} (\theta_j - \theta_{j-1}) - (m_1)_{k-\frac{1}{2}}^{n-\frac{1}{2}} \bar{u}_{j-\frac{1}{2}} - (m_6)_{k-\frac{1}{2}}^{n-\frac{1}{2}} \bar{w}_{j-\frac{1}{2}} \\ & = x^{n-\frac{1}{2}} k_n^{-1} (\bar{u}_n - \bar{u}_{n-1}) + x^{n-\frac{1}{2}} (m_7)_{k-\frac{1}{2}}^{n-\frac{1}{2}} r_k^{-1} (\bar{w}_k - \bar{w}_{k-1}) \end{aligned} \quad (7.6.14)$$

The boundary conditions given by Eq. (7.6.6) at  $x = x_n$  and  $z = z_k$  become:

$$\theta_0^{n,k} = \theta_w, \quad u_0^{n,k} = w_0^{n,k} = 0 \quad (7.6.15a)$$

$$u_J^{n,k} = 1, \quad w_J^{n,k} = 1 \quad (7.6.15b)$$

Before the difference equations (7.6.8), (7.6.14) and those for Eqs. (7.6.5c,d) can be solved, the net functions  $\bar{\Lambda}_j^{n-1,k-1}$ ,  $\bar{\Lambda}_j^{n,k-1}$  and  $\bar{\Lambda}_j^{n-1,k}$  must be known for all values of  $j$ . Those corresponding to  $\bar{\Lambda}_j^{n-1,k-1}$  and  $\bar{\Lambda}_j^{n-1,k}$  are obtained from the initial conditions specified in the spanwise direction and those to  $\bar{\Lambda}_j^{n,k-1}$  from the initial conditions specified in the chordwise direction. If we assume that they are known, then the difference equations (7.6.8), (7.6.14) and those for Eqs. (7.6.5c,d), together with Eqs. (7.6.15) are a system of  $5J + 5$  equations for the solution of  $5J + 5$  unknowns  $\bar{\Lambda}_j^{n,k}$ ,  $j = 0, 1, \dots, J$ . To solve this nonlinear

system we again use Newton's method discussed in Section 4.5. For simplicity of notation we write the net functions  $\vec{\Lambda}_j^{n,k}$  as  $\vec{\Lambda}_j (\equiv u_j, w_j, \theta_j, v_j, t_j)$ . Then the system given by Eqs. (7.6.8), (7.6.14) and (7.6.5c,d) with superscripts  $i, k$  dropped for convenience can be written in linearized form as

$$(a_1)_j \delta v_j + (a_2)_j \delta v_{j-1} + (a_3)_j \delta u_j + (a_4)_j \delta u_{j-1} + (a_5)_j \delta w_j \\ + (a_6)_j \delta w_{j-1} + (a_7)_j \delta \theta_j + (a_8)_j \delta \theta_{j-1} = (r_1)_j \quad (7.6.16a)$$

$$(b_1)_j \delta t_j + (b_2)_j \delta t_{j-1} + (b_3)_j \delta u_j + (b_4)_j \delta u_{j-1} + (b_5)_j \delta w_j \\ + (b_6)_j \delta w_{j-1} + (b_7)_j \delta \theta_j + (b_8)_j \delta \theta_{j-1} = (r_2)_j \quad (7.6.16b)$$

$$h_j^{-1}(\delta \theta_j - \delta \theta_{j-1}) + (c_1)_j(\delta u_j + \delta u_{j-1}) + (c_2)_j(\delta w_j + \delta w_{j-1}) = (r_3)_j \quad (7.6.16c)$$

$$\delta u_j - \delta u_{j-1} - \frac{1}{2}h_j(\delta v_j + \delta v_{j-1}) = (r_4)_{j-1} \quad (7.6.16d)$$

$$\delta w_j - \delta w_{j-1} - \frac{1}{2}h_j(\delta t_j + \delta t_{j-1}) = (r_5)_{j-1} \quad (7.6.16e)$$

The coefficients  $(a_i)_j$ ,  $(b_i)_j$  ( $i = 1, 2, \dots, 8$ ) and  $(r_i)_j$  ( $i = 1, 2, \dots, 5$ ) are given in Program 10.

Note that in writing the system given by Eqs. (7.6.16), we have used a certain order as in the solution of the boundary-layer equations for two-dimensional flows [see subsection 4.5.2]. The reason for this order is again to ensure that the  $A_0$  matrix in Eq. (4.5.24) is not singular.

Similarly, the boundary conditions given by Eq. (7.6.15) become:

$$\delta \theta_0 = 0, \quad \delta u_0 = 0, \quad \delta w_0 = 0, \quad \delta u_J = 0, \quad \delta w_J = 0 \quad (7.6.17)$$

The linear system given by Eqs. (7.6.16) and (7.6.17) can be written in matrix-vector as [see Eq. (4.5.23)] also,

$$A \delta \vec{\Lambda}_j = \vec{r}_j \quad (7.6.18)$$

and can be solved by the block-elimination method discussed in subsection 4.5.3.

## 7.6.2 Flows with Reversal: Characteristic Box

When there is flow reversal in the spanwise velocity profile, it is necessary to modify the standard box scheme of the previous subsection in order to avoid the numerical instabilities resulting from the integration opposed to the flow direction. As discussed in [3], this objective can be satisfied either with the zig-zag box scheme or the characteristic box scheme. While the numerical mesh is chosen *a priori* in the zig-zag scheme, the characteristic scheme allows the grid to be determined along with the flow calculations. In this scheme, depending upon the magnitude and direction of the velocity field, the grid spacings and orientation can be adjusted to satisfy the CFL condition. The scheme, in a

sense, is intelligent in that it maximizes the domain in which the computations can be carried out for both steady and unsteady flows. It is described below for three-dimensional incompressible steady flows.

To describe the solution procedure for the characteristic box scheme which is based on the solution of the governing equations along the local streamlines, we consider Eqs. (7.6.5) and (7.6.6). Denoting the arc length in the streamline direction by  $\psi$  and the angle it makes with the  $x$ -axis by  $\phi$  (see Fig. 7.9), we write Eqs. (7.6.5c) and (7.6.5d) as

$$(bv)' + v\theta + m_2(1 - u^2) + m_5(1 - uw) = \lambda \frac{\partial u}{\partial \psi} \quad (7.6.19a)$$

$$(bt)' + t\theta + m_4(1 - uw) + m_3(1 - w^2) = \lambda \frac{\partial w}{\partial \psi} \quad (7.6.19b)$$

where

$$\lambda = x[(u)^2 + (m_7w)^2]^{1/2} \quad (7.6.20a)$$

$$\phi = \tan^{-1} \left( \frac{m_7w}{u} \right) \quad (7.6.20b)$$

Note that depending on the sign of, which changes across the shear layer, the direction of the streamlines  $\psi$  may change as discussed in Fig. 7.7.

The difference approximations to Eqs. (7.6.19) are written by centering all quantities except  $\theta$  at point  $B$  shown in Fig. 7.9. For example, the values of each parameter, say  $q$ , are centered between  $(n-1, l, j - \frac{1}{2})$  and  $(n, k, j - \frac{1}{2})$  at  $B$  by

$$q_{j-\frac{1}{2}}^B = \frac{1}{2}(q_{j-\frac{1}{2}}^{n,k} + q_{j-\frac{1}{2}}^{n-1,l}) \quad (7.6.21)$$

The location of  $l$  that intersects the line at  $x_{n-1}$  is obtained by determining the distance from  $k$  and  $l$  from  $\Delta\psi \sin \phi$ . The centering of  $\theta$  is done by writing it as indicated in Eq. (7.6.9).

The finite-difference approximations to Eqs. (7.6.19) are lengthy so we again consider a model equation for them to illustrate the procedure,

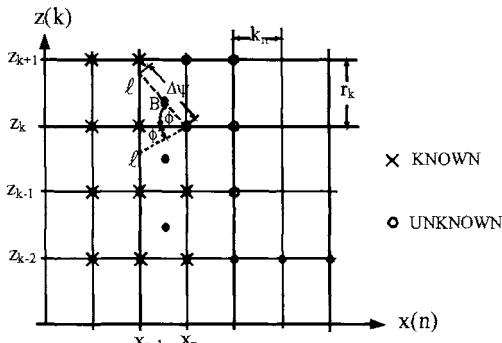


**Fig. 7.10.** Notation for the characteristic scheme.

$$(bv)' + v\theta + m_2 = \lambda \frac{\partial u}{\partial \psi} \quad (7.6.22)$$

For the notation shown in Fig. 7.9, the difference approximations to Eq. (7.6.22) at point  $B$  are

$$\begin{aligned} & \frac{h_j^{-1}}{2} [(bv)_j^{n,k} - (bv)_{j-1}^{n,k}] + \frac{h_j^{-1}}{2} [(bv)_j^{n-1,l} - (bv)_{j-1}^{n-1,l}] \\ & + \frac{1}{2} [v_{j-\frac{1}{2}}^{n,k} + v_{j-\frac{1}{2}}^{n-1,l}] \theta_{j-\frac{1}{2}}^B + \frac{1}{2} [(m_2)_j^{n,k} + (m_2)_{j-1}^{n-1,l}] \\ & = \frac{1}{2} (\lambda_{j-\frac{1}{2}}^{n,k} + \lambda_{j-\frac{1}{2}}^{n-1,l}) \frac{(u_{j-\frac{1}{2}}^{n,k} - u_{j-\frac{1}{2}}^{n-1,l})}{\Delta \psi_{j-\frac{1}{2}}} \end{aligned} \quad (7.6.23)$$

where the relation between  $\theta_j^B$ ,  $\theta_j^{n-1/2,k-1/2}$  and  $\theta^{n-1/2,k-1/2}$  is

$$\theta_j^B = \frac{\theta_j^{n-\frac{1}{2},k-\frac{1}{2}} - \theta_j^{n-\frac{1}{2},k-\frac{3}{2}}}{z^{k-\frac{1}{2}} - z^{k-\frac{3}{2}}} (z^B - z^{k-\frac{1}{2}}) + \theta_j^{n-\frac{1}{2},k-\frac{1}{2}} \quad (7.6.24)$$

As in subsection 7.6.1, this procedure for the model equation is repeated for Eqs. (7.6.19), the resulting equation is linearized, and Eqs. (7.6.19) are written in the same form as given by Eqs. (7.6.16a,e). The coefficients  $(a_i)_j$ ,  $(b_i)_j$  ( $i = 1, 2, \dots, 8$ ) and  $(r_i)_j$  ( $i = 1, 2, \dots, 5$ ) are given in Program 10.

In Appendix B, we discuss the application of the characteristic box to a model problem corresponding to a prolate spheroid at incidence and show how significant loss of numerical accuracy may result from the use of the zig-zag box leading to erroneous conclusions regarding flow separation in three-dimensional flows.

### 7.6.3 Calculation of Geometric Parameters

The geometric parameters such as the metric coefficients and geodesic curvature of the coordinate lines appearing in the three-dimensional boundary-layer equations must be known prior to the boundary-layer calculations for given freestream conditions and inviscid velocity distribution. In Section 13.7 we shall describe an interface program to compute these parameters from the definition of wing geometry together with the nonorthogonal coordinate used in the boundary-layer method.

In general, if the position vector of a surface  $\hat{r}$  is a function of two parameters  $p$  and  $q$ , the surface can be represented by the net of curves  $p = \text{const}$  and  $q = \text{const}$ . It is these lines and the normals to the surface that form the coordinate system for boundary-layer calculations. Assuming that the position vector  $\hat{r}$  is defined in a Cartesian base system  $\bar{x}$ ,  $\bar{y}$ ,  $\bar{z}$  where  $\bar{x}$ ,  $\bar{y}$ , and  $\bar{z}$  are functions of  $p$

and  $q$ , the unit tangent vector along the  $q = \text{const}$ , curve with  $i, j, k$  denoting the unit vectors of the Cartesian base systems, can be written as

$$\hat{t}_p = \frac{\partial \bar{x}}{\partial s_p} i + \frac{\partial \bar{y}}{\partial s_p} j + \frac{\partial \bar{z}}{\partial s_p} k = \left( \frac{\partial \bar{x}}{\partial p} i + \frac{\partial \bar{y}}{\partial p} j + \frac{\partial \bar{z}}{\partial p} k \right) \frac{1}{(\partial s_p / \partial p)} \quad (7.6.25)$$

where  $s_p$  is the arc length along the curve. Since  $\hat{t}_p \cdot \hat{t}_p = 1$  we have

$$h_p = \frac{\partial s_p}{\partial p} = \left[ \left( \frac{\partial \bar{x}}{\partial p} \right)^2 + \left( \frac{\partial \bar{y}}{\partial p} \right)^2 + \left( \frac{\partial \bar{z}}{\partial p} \right)^2 \right]^{\frac{1}{2}} \quad (7.6.26)$$

where  $h_p$  is called the metric coefficient of  $q = \text{const}$  curve and it is a coefficient of proportionality between  $s_p$  and  $p$  in differential form. Similarly, the expansion for the metric coefficient for curve  $p = \text{const}$  is given by

$$h_q = \frac{\partial s_q}{\partial q} = \left[ \left( \frac{\partial \bar{x}}{\partial q} \right)^2 + \left( \frac{\partial \bar{y}}{\partial q} \right)^2 + \left( \frac{\partial \bar{z}}{\partial q} \right)^2 \right]^{\frac{1}{2}} \quad (7.6.27)$$

The angle between the parametric lines on the surface is given by  $\hat{t}_q \cdot \hat{t}_p$ , or

$$\cos \theta = \frac{\left( \frac{\partial \bar{x}}{\partial p} \frac{\partial \bar{x}}{\partial q} + \frac{\partial \bar{y}}{\partial p} \frac{\partial \bar{y}}{\partial q} + \frac{\partial \bar{z}}{\partial p} \frac{\partial \bar{z}}{\partial q} \right)}{h_p h_q} \quad (7.6.28)$$

An arbitrary arc length element on the surface is

$$d\hat{s} = \hat{t}_p ds_p + \hat{t}_q ds_q \quad (7.6.29)$$

and its magnitude is

$$d\hat{s} \cdot d\hat{s} = ds^2 = h_p^2 dp^2 + h_q^2 dq^2 + 2h_p h_q \cos \theta dp dq \quad (7.6.30)$$

The geometric or tangential curvatures  $k_p$  and  $k_q$  of the curves  $q = \text{const}$  and  $p = \text{const}$ , respectively, and the additional parameters  $k_{pq}$  and  $k_{qp}$  can be obtained from the relations discussed above,

$$\frac{d\hat{t}_p}{ds_p} \cdot \hat{t}_q = k_p = \frac{1}{h_p h_q \sin \theta} \left[ \frac{\partial(h_q \cos \theta)}{\partial p} - \frac{\partial h_p}{\partial q} \right] \quad (7.6.31)$$

$$\frac{d\hat{t}_q}{ds_q} \cdot \hat{t}_p = k_q = \frac{1}{h_p h_q \sin \theta} \left[ \frac{\partial(h_p \cos \theta)}{\partial q} - \frac{\partial h_q}{\partial p} \right] \quad (7.6.32)$$

$$k_{pq} = \frac{1}{h_p h_q \sin^2 \theta} \left[ (1 + \cos^2 \theta) \frac{\partial h_p}{\partial q} - 2 \cos \theta \frac{\partial h_q}{\partial p} \right] \quad (7.6.33)$$

$$k_{qp} = \frac{1}{h_p h_q \sin^2 \theta} \left[ (1 + \cos^2 \theta) \frac{\partial h_q}{\partial p} - 2 \cos \theta \frac{\partial h_p}{\partial q} \right] \quad (7.6.34)$$

In the notation used in subsection 7.2.3, the parameters  $p$  and  $q$  correspond to the coordinates  $x$  and  $z$ . It should be remembered that the boundary-layer variables  $x, y, z$  are different from the Cartesian base system  $\bar{x}, \bar{y}, \bar{z}$ . Designation of the geometric parameters associated with the  $x$ - $z$  notation is given by

$$h_p = h_1, \quad h_q = h_2, \quad k_p = k_1, \quad k_q = k_2, \quad k_{pq} = k_{12}, \quad k_{qp} = k_{21}$$

For example, the coordinates for a wing surface is usually taken as  $x$  corresponding to the normalized chordwise surface distance measured from the leading edge and  $z$ -coordinate as the normalized spanwise distance from the plane of symmetry for the section along which  $x$  is determined. It is seen from the definitions of the geometric parameters that first and second order derivatives of  $\bar{x}, \bar{y}, \bar{z}$  with respect to the coordinates  $x$  and  $z$  are required. Since in practice the geometry definition is seldom given analytically, numerical differentiation is required, and unless sufficiently smooth data is available, the problem becomes non-trivial. Oscillations in the coordinate system calculations must be avoided as much as possible because boundary-layer calculations tend to amplify the oscillations and can make the solutions to diverge. To avoid this problem alternate approaches have been considered. Houdeville [15] and Malecki et al. [16] proposed the approach in which the boundary-layer equations are projected into a local Cartesian axis-system. In this local system, the  $(x, z)$ -plane is tangent to the surface and the  $y$ -axis is normal to the surface. As this system is Cartesian orthogonal, it has the advantage of avoiding the calculation of metric and curvature coefficients. The method can be applied even if the coordinate lines are not regular, i.e., the coordinate lines can have slope discontinuities. The extra work involved in this method is that velocities at stations neighboring the calculated station must be expressed in the local axis-system at the calculated station in order to calculate velocity derivatives present in the equations. The second feature of the method is that the equations are written along the local boundary-layer streamlines just as in the characteristic box method described in subsection 7.6.2.

## 7.7 Evaluation of a Turbulence Model for Three-Dimensional Flows

For laminar flows, the accuracy of the solutions of the boundary-layer equations depends on the accuracy of the numerical scheme. In general, for a laminar flow, accurate solutions can be obtained for most engineering problems by taking around 40 points across the boundary-layer. For stability-transition calculations, however, it is necessary to take more than 40 points for higher accuracy.

For a turbulent flow the accuracy of the solutions depends on the accuracy of the turbulence model for the Reynolds stresses. In this section we demonstrate

the accuracy of the turbulence model discussed in Section 7.4 to several three-dimensional flows on infinite swept wings (subsection 7.7.1) and to full three-dimensional flows (subsection 7.7.2)

### 7.7.1 Infinite Swept Wing Flows

The accuracy of the turbulence model of Section 7.4 and other models has been investigated for several infinite swept wing flows, as discussed in [16–19]. Here we present a sample of results taken from those studies and discuss first the results for the data of Bradshaw and Terrell [20] and then for the data of Cumpsty and Head [21] and finally for the NLR data of Van den Berg et al. [22] and Elsenaar and Boelsma [23].

#### Data of Bradshaw and Terrell

This experiment was set up especially to test the outer-layer assumptions made in extending the boundary-layer calculation method of Bradshaw et al. [24] from two dimensions to three [25]. Measurements were made only on the flat rear of the wing in a region of nominally zero pressure gradient and decaying cross flow. See the sketch in Fig. 7.10a. Spanwise and chordwise components of mean velocity and shear stress, and all three components of turbulence intensity, were measured at a number of distances  $x' = 0, 4, 10, 16$  and 20 in. from the start of the flat portion of the wing (Fig. 7.11). The surface shear stress, measured with a Preston tube, was constant along a generator to the start of the flat part of the wing, except for a few inches at each end and except for small undulations of small spanwise wavelength caused by residual nonuniformities in the tunnel flow.

Figure 7.11 shows the calculated results (solid lines) with experimental results (symbols) and those obtained by Bradshaw's method [24] (dashed lines). The cross-flow angle  $\beta$  which represents the departure of the velocity vector within the boundary-layer from the freestream velocity vector was computed from

$$\beta \equiv \tan^{-1} \left( \frac{w}{u} \right) \quad (7.7.1a)$$

The above formula becomes indeterminate at  $y = 0$ ; however, with the use of L'Hopital's rule, it can be written as

$$\beta_w = \tan^{-1} \left( \frac{\partial w}{\partial y} \right)_w \left( \frac{\partial u}{\partial y} \right)_w^{-1} \quad (7.7.1b)$$

The streamwise component of the local skin-friction coefficient  $c_{fs}$  was calculated from

$$c_{fs} = \frac{\tau_{ws}}{\frac{1}{2} \rho U_s^2} \quad (7.7.2)$$

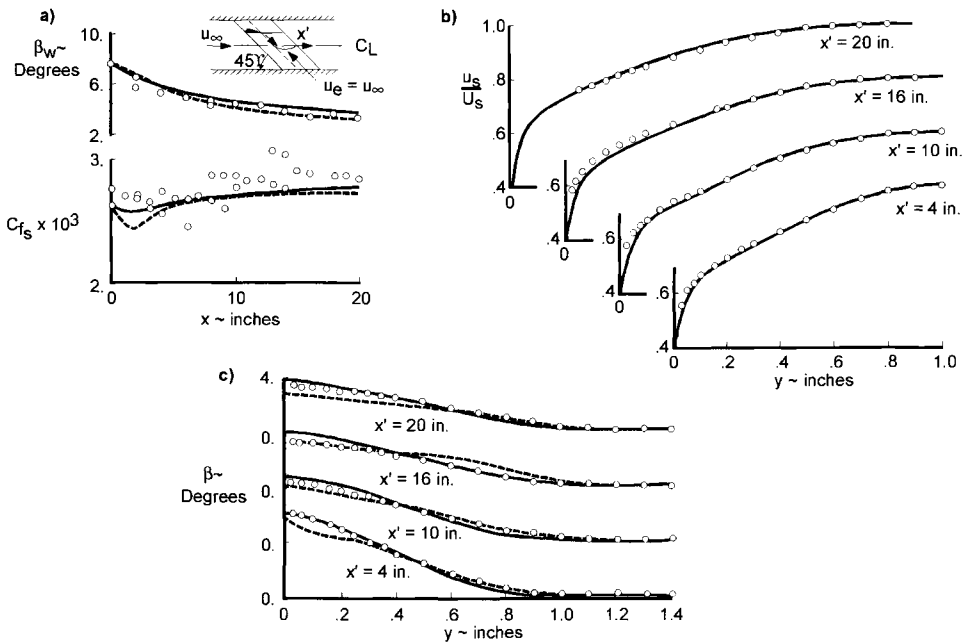


**Fig. 7.11.** Results for the relaxing flow of Bradshaw and Terrell: (a) wall cross-flow angle and local skin friction, (b) velocity profiles, (c) cross-flow angle distributions. The symbols denote the experimental data, the solid line the numerical solutions of Cebeci [17] and the dashed line the numerical solutions of Bradshaw et al. [24].

with  $\tau_{ws}$  and  $U_s$  given by

$$\tau_{ws} = \tau_{wx} \cos \phi + \tau_{wz} \sin \phi \quad (7.7.3a)$$

$$U_s = \frac{u_e}{\cos \phi}, \quad \phi = \tan^{-1} \left( \frac{w_e}{u_e} \right) \quad (7.7.3b)$$

Here  $\tau_{wx}$  and  $\tau_{wz}$  denote the wall shear values in the  $x$ - and  $z$ -directions, respectively, obtained from the solution of the infinite swept wing equations.

### Data of Cumpsty and Head

In this experiment [21] the boundary-layer development was measured on the rear of a wing swept at  $61.1^\circ$ . The boundary-layer separated at about 80% chord. The measured profiles were affected by traverse gear “blockage,” probably because of upstream influence of disturbance caused to the separated flow by the wake of the traverse gear.

Figure 7.12 shows a comparison of calculated and measured streamwise velocity profiles  $u_s/U_s$  and streamwise momentum thickness  $\theta_{11}$  defined by

$$\theta_{11} = \int_0^\delta \frac{u_s}{U_s} \left( 1 - \frac{u_s}{U_s} \right) dy \quad (7.7.4)$$

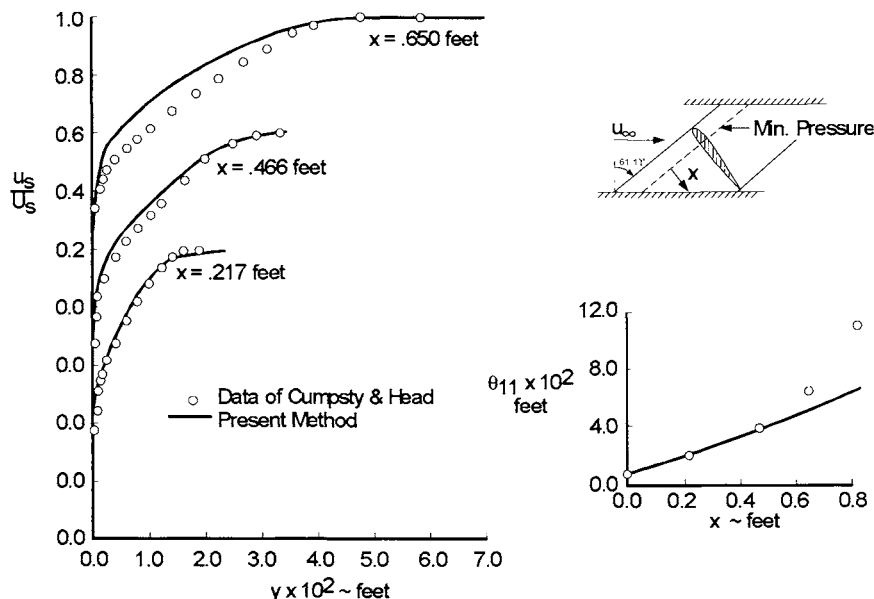


**Fig. 7.12.** Comparison of calculated (solid lines) and experimental (symbols) results for the data of Cumpsty and Head on the rear of a swept infinite wing.

where  $u_s/U_s$  is calculated from

$$\frac{u_s}{U_s} = \frac{u}{u_e} \cos^2 \phi + \frac{w}{w_e} \sin^2 \phi \quad (7.7.5)$$

The results in Fig. 7.12 show good agreement with experiment at two  $x$ -stations. However, with increasing distance they begin to deviate from experimental values and at  $x = 0.650$  ft, the agreement becomes poor.

The above results indicate what was already observed and discussed in relation to the shortcomings of the Cebeci-Smith algebraic eddy-viscosity formulation, that is, it requires improvements for strong adverse pressure gradient flows. As discussed in subsection 6.3.1, the improvements to this formulation were made for two-dimensional flows by allowing  $\alpha$  in the outer eddy-viscosity formula to vary. A similar improvement is needed to the formulation given in Section 7.4.

### NRL Data

The experiments conducted by Van den Berg et al. [22] and Elsenaar and Boelsma [23] are a good illustration of three-dimensional turbulent boundary-layers on a simple configuration. These experiments have been redone and complemented by Bradshaw and Pontikos [26]. The experimental set-up simulates the boundary-layer on an infinite swept wing. The boundary-layer develops on a flat plate the leading edge of which has a sweep angle of 35° with respect

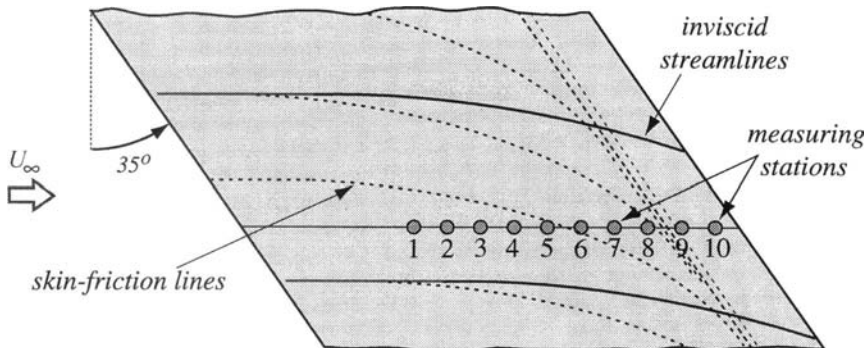


**Fig. 7.13.** NLR experiments: schematic evolution of external streamlines and skin friction lines.

to the freestream. Near the leading edge, the pressure gradient is zero and when the boundary-layer is sufficiently developed, an adverse pressure gradient is imposed with the help of a body placed at a certain distance from the plate. The combination of the pressure gradient and sweep effects gives rise to a three-dimensional boundary-layer. Great care was taken in order to have an invariance of the flow in the spanwise direction, i.e., in a direction parallel to the leading edge of the plate. In this experiment, the pressure gradient was strong enough to induce boundary-layer separation, which for an infinite swept wing, is characterized by a skin friction line parallel to the leading edge (Fig. 7.13). Along the separation line, the total skin friction coefficient is not zero.

From the NLR results, it appears that the mixing length deduced from the experiment decreases as separation is approached. The ratio of the total shear stress to the kinetic energy,  $(\tau_t/\rho)/k$ , also decreases as separation is approached. These results have been complemented by those of Bradshaw and Pontikos [26] who conclude that “turbulent activity decreases as the flow becomes more three-dimensional, leading to reductions in the diffusion (rate of transport, normal to the wall) of momentum, turbulent energy and shear stress”.

A detailed study of several turbulence models for this data was conducted by Malecki [16, 19]. The calculations were performed by using a full three-dimensional boundary-layer code in which the numerical technique employed the method of characteristics. These calculations were carried out in the inverse mode by specifying displacement thickness distributions  $\delta_x^*$  and  $\delta_z^*$  from the experimental data.

The turbulence models used in Malecki's study include the following models.

- *ML*: this is a mixing length model given by Eq. (6.3.7)
- *k- $\varepsilon$* : this is the Launder-Sharma model discussed in Section 7.4.
- *k- $\omega$* : this is an extension of Wilcox's *k- $\omega$*  model (Problem 6.18) to three-dimensional flows.

- *RSM LS*: this is a Reynolds stress model by Launder-Shima [27]. It includes the low Reynolds number effect. The pressure strain term is modelled as a linear function of Reynolds stresses.
- $k/k-\varepsilon$ : this is two-layer model. Near the wall, the Norris-Reynolds one-equation model [28] is used. In the outer part of the boundary-layer, the Launder-Sharma model [8] is used.
- $k/IP-GL$ : this is a two-layer model. Near the wall, the Norris-Reynolds one-equation model [28] is used. In the outer part of the boundary-layer, a Reynolds stress model is used with  $\Phi_{ij}$  given by Eq. (6.3.26b) and with Gibson-Launder correction discussed in subsection 6.3.3.
- $k/LRR-GL$ : this is a two-layer model. Near the wall, the Norris-Reynolds one-equation model [28] is used. In the outer part of the boundary-layer, the Launder-Reece-Rodi model [29] with the Gibson-Launder correction [30] discussed in subsection 6.3.2 is used.
- $k/FLT-GL'$ : this is a two-layer model. Near the wall, the Norris-Reynolds one-equation model [28] is used. In the outer part of the boundary-layer, the Fu-Launder-Tselepidakis model [31] is used. The pressure strain terms are expressed with a cubic model in the Reynolds stresses. The Gibson-Launder correction [30] is included with a modified constant  $c_{1w}$ .

Figures 7.14 and 7.15 show the velocity profiles. At station 8, the comparison of various models with streamwise and crossflow velocity profiles shows the same trend as for the global characteristics: the best results are obtained with the Reynolds stress model *RSM LS* and with the  $k-\omega$  model. It is noted, however, that the intensity of crossflow is slightly underestimated. The evolution of the total velocity profiles shows that the shape of these profiles is not well reproduced by the mixing length model; a slight improvement is obtained with the  $k-\varepsilon$  model and the Reynolds stress model *RSM LS* gives the best results.

It is useful to point out that the calculated total velocities with mixing length and  $k-\varepsilon$  models do not agree with measured values at the boundary-layer edge (Fig. 7.15). The reason for the disagreement is that the edge velocities  $u_e$  and  $w_e$  are not input but computed with the inverse method. However, the results computed with the *RSM LS* model are in very good agreement with the measured values of  $u_{te}$ . This confirms the good behavior of the *RSM LS* model.

The above results for velocity profiles are consistent with the behavior of the Reynolds shear stresses. As expected, the poor predictions of separation are associated with too high levels of the Reynolds stresses. The *RSM LS* model produces the right level.

Another interesting result is the direction of the turbulent shear stress. The experimental results (Fig. 7.16) show a lag in shear stress direction,  $\beta_\tau$ , defined by

$$\beta_\tau = \tan^{-1} \left( \frac{-\overline{v'w'}}{-\overline{u'v'}} \right) \quad (7.7.6)$$

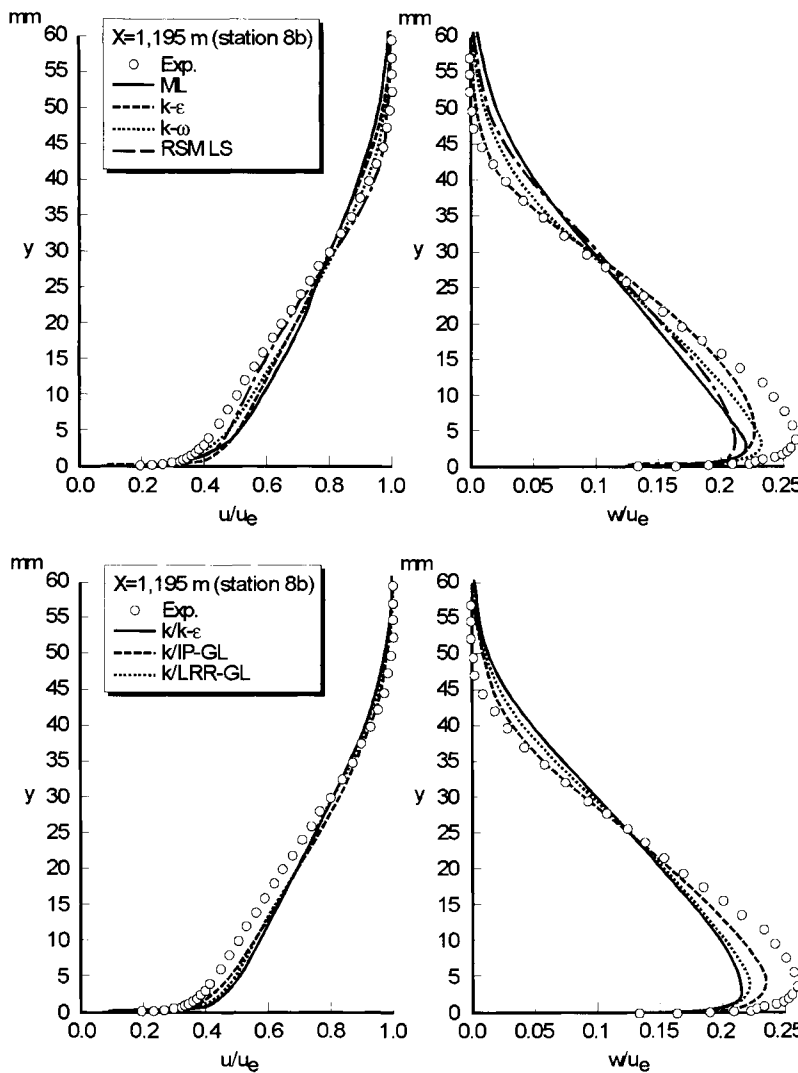


**Fig. 7.14.** NLR experiment: streamwise and crossflow velocity profiles.

behind the direction of the velocity gradient,  $\beta_g$ , defined by

$$\beta_g = \tan^{-1} \left( \frac{\partial w}{\partial y} \right) \left( \frac{\partial u}{\partial y} \right)^{-1} \quad (7.7.7)$$

A possible interpretation of these results is that the turbulent structures associated with the turbulent shear stress are tilted when the initially two-dimensional boundary-layer enters the region of crossflow. However, these structures do not respond immediately to the crossflow gradient so that this lag effect creates a lag in the direction of the shear stress behind the direction of the velocity gradient.

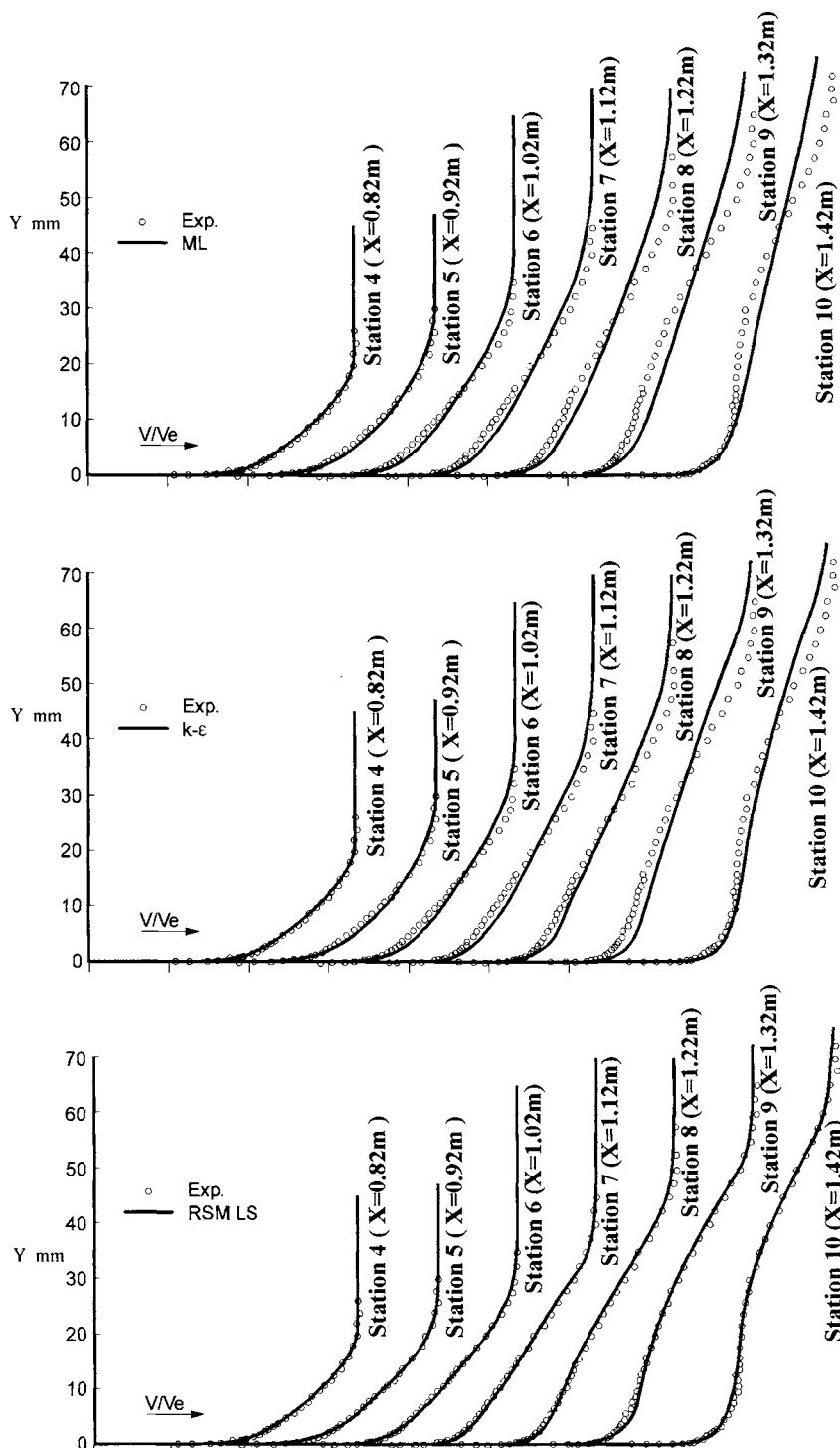


Fig. 7.15. NLR experiment: comparison of calculated and measured total velocity profiles.

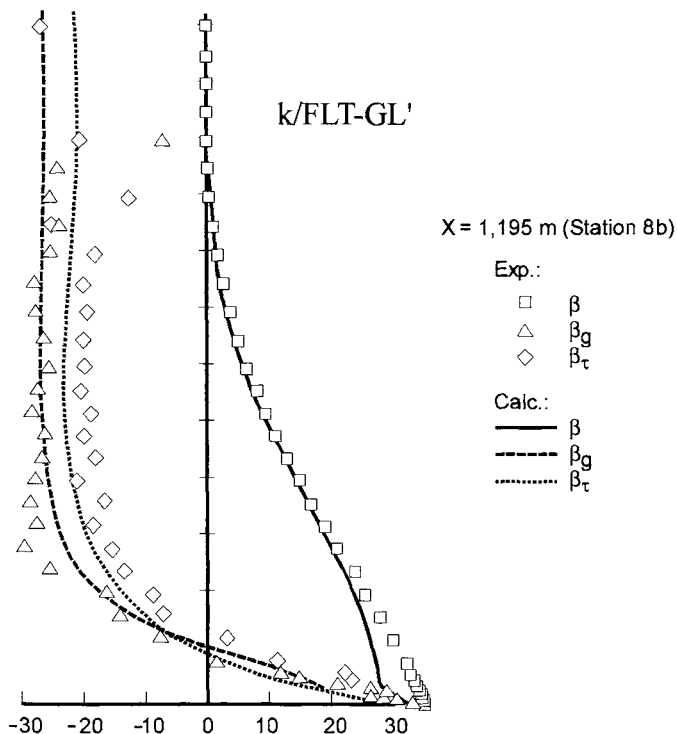


Fig. 7.16. NLR experiment: direction of velocity, velocity gradient and shear stress.

Detailed comparisons provided in [16, 19] indicate that none of the turbulence models, except the  $k/FLT-GL'$  model is able to reproduce the lag of shear stress direction. As can be seen in Fig. 7.16, the  $k/FLT-GL'$  model predicts a slight shear stress lag.

### 7.7.2 Full Three-Dimensional Flows

To illustrate the evaluation of the Cebeci-Smith-algebraic eddy-viscosity formulation of Section 7.4 for full three-dimensional flows, we consider two flows corresponding to an external flow formed by placing an obstruction in a thick two-dimensional boundary-layer (data of East and Hoxey [32]) and an external flow on a prolate spheroid at an incidence angle of  $10^\circ$  (data of Meier and Kreplin [33]).

#### Data of East and Hoxey

Figure 7.17 shows a schematic drawing of East and Hoxey's test setup in which a wing is placed in a thick two-dimensional boundary layer [32]. The strong pressure gradients produced by the obstruction caused the boundary layer to become

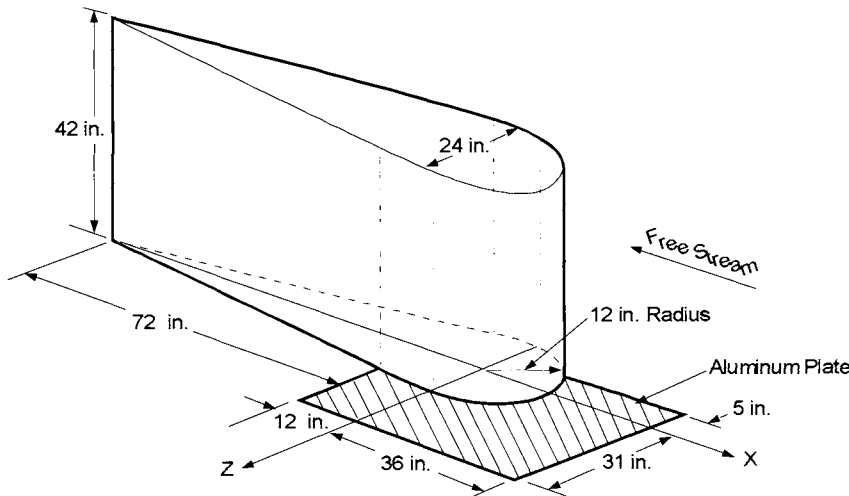


Fig. 7.17. Schematic drawing of East and Hoxey's test setup.

three-dimensional and to separate. The measurements were made in the three-dimensional boundary layer upstream of and including the three-dimensional separation.

The plane of symmetry calculations for this flow, shown in Fig. 7.18, were made for the external inviscid velocity distribution given by

$$u_e = u_\infty \left( 1 + a^2 \frac{\Delta_2}{\Delta_1^2} \right), \quad w_e = 2u_\infty a^2 \left( \frac{\Delta_3}{\Delta_1^2} \right) \quad (7.7.8)$$

where

$$\Delta_1 = (x - x_0)^2 + z^2, \quad \Delta_2 = -(x - x_0)^2 + z^2, \quad \Delta_3 = (x - x_0)z$$

Here  $u_\infty$  is a reference velocity,  $a$  is the cylinder nose radius (taken to be 12 in.) and  $x_0$  denotes the distance of cylinder axis from the leading edge,  $x = 0$ . Initial velocity profiles were specified at  $x = 6.5$  ft, which corresponded to  $x = 30$  in. in the experimental data.

Figure 7.19 shows a comparison between calculated and measured velocity profiles off the line of symmetry. These calculations were made by using the experimental external velocity distribution. In general, the agreement with experiment is satisfactory.

### Data of Meier and Kreplin

We now consider laminar, transitional and turbulent flows on a prolate spheroid with a thickness ratio of 6 for a Reynolds number of  $6.6 \times 10^6$  and compare the calculated results with the data of Meier and Kreplin [33–35] for freestream

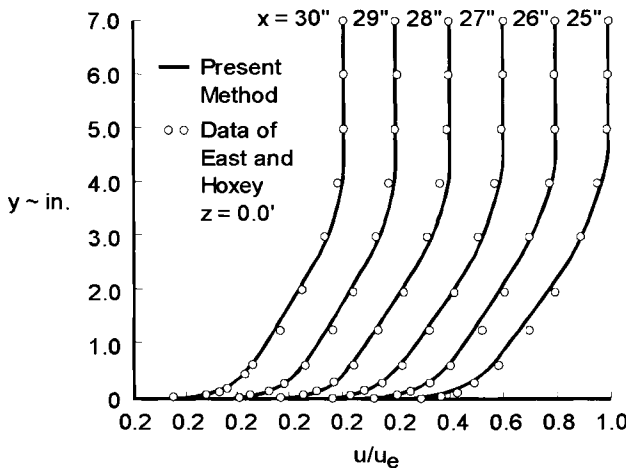


**Fig. 7.18.** Comparison of calculated (*solid lines*) and measured (*symbols*) velocity profiles for the attachment-line ( $z = 0$ ) flow of East and Hoxey.

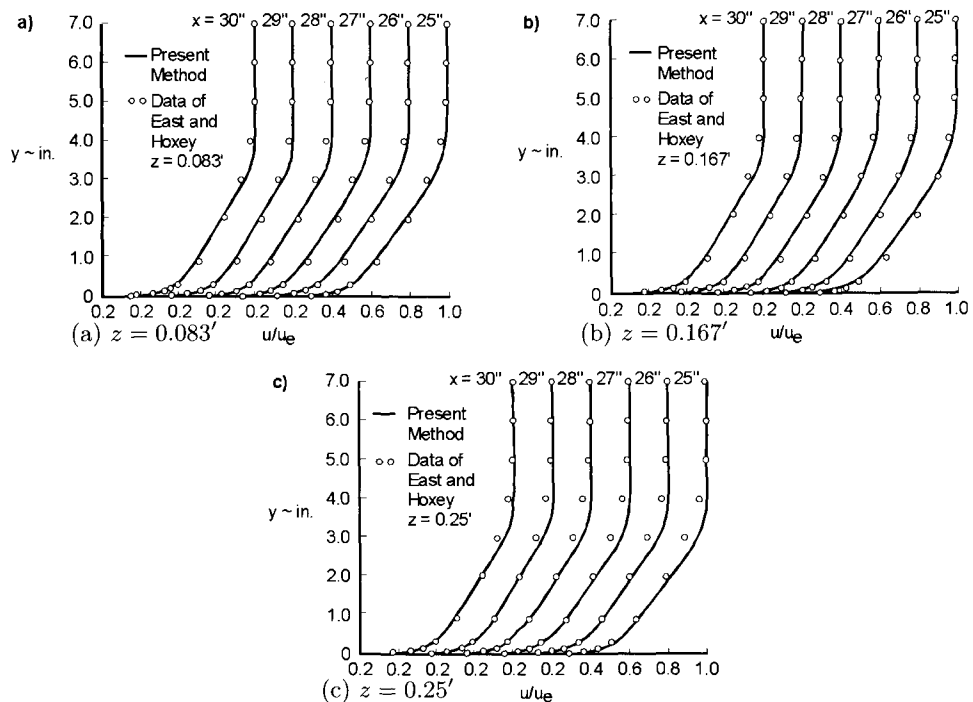


**Fig. 7.19.** Comparison of calculated (*solid lines*) and measured (*symbols*) velocity profiles off the line of symmetry of the East and Hoxey flow.

velocities of 45 and 55 m/s corresponding to natural and imposed transition. To account for the transitional region between laminar and turbulent flow, the right-hand sides of Eqs. (7.4.4) are multiplied by the intermittency factor  $\gamma_{tr}$  defined by Eqs. (6.3.3) and (6.2.4). Since detailed and corresponding correlation formulas for three-dimensional transitional flows are lacking, the same expression was used for three-dimensional flows by using the local similarity assumption with  $u_e$  in Eqs. (6.3.3) and (6.2.4) replaced by the total velocity.

The experimental data of Meier and Kreplin consists of surface shear stress magnitude and direction vectors and velocity profiles over a range of angles of attack. Figure 7.20 shows a comparison of calculated surface shear stress vectors in laminar flow at  $\alpha = 10^\circ$  [36]. The magnitude of the shear stress vector is proportional to the shear intensity. The agreement between the calculation and measurements on the windward side is generally good, although there are some differences that are partly due to the use of inviscid potential flow in the calculations, whereas the measured pressure distribution shows viscous-inviscid interaction effects. It is clear that the laminar flow is separated on the leeward side of the body at some distance aft of the nose. The origin or nature of the high shear intensities leeward of the separation line cannot be determined from calculations because calculations based on external flow that is purely inviscid is not expected to account for strong interactions.

Figure 7.21 shows wall shear vectors for laminar, transitional and turbulent flow with natural transition. In general, the calculated and measured results are in agreement with discrepancies (which are small) confined to the region close to the specified transition [36]. More quantitative comparison with the imposed transition experiment of Meier et al. [33–35] is afforded by Fig. 7.22,

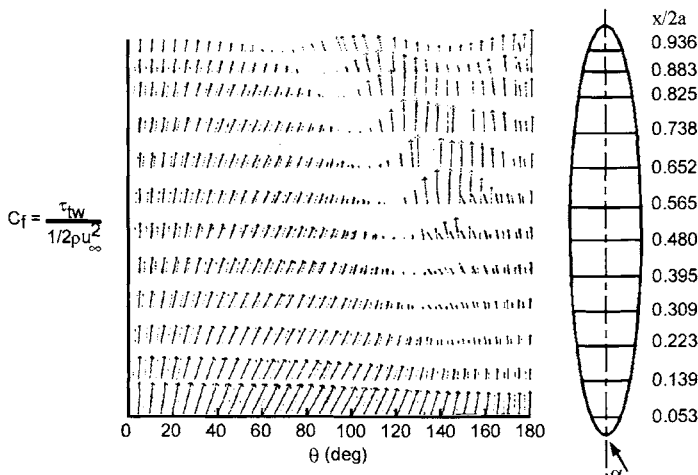


**Fig. 7.20.** Measured (dashed line) and calculated (solid line) distributions of wall shear stress vectors on the prolate spheroid at  $\alpha = 10^\circ$  for laminar flow.

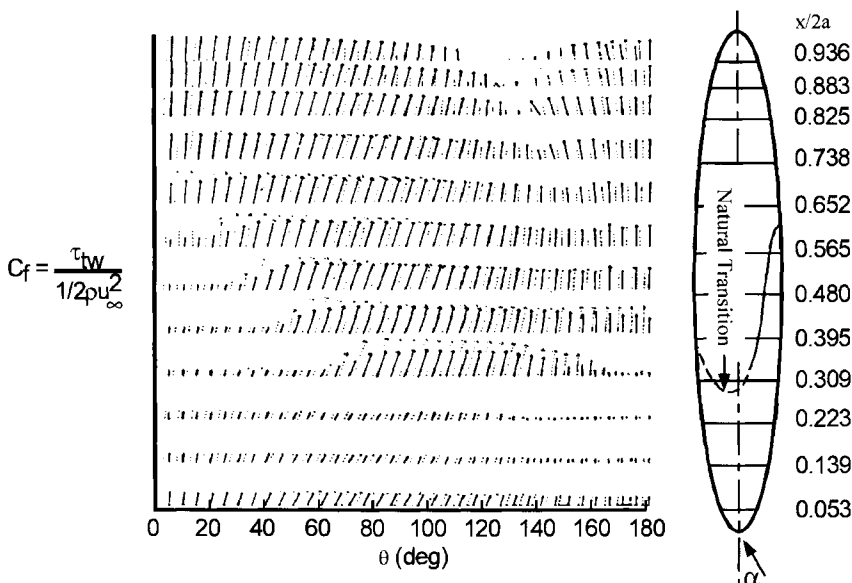


**Fig. 7.21.** Measured (dashed line) and calculated (solid line) resultant wall shear stress values on the prolate spheroid at  $\alpha = 10^\circ$ .

which displays circumferential distributions of wall shear stress at four axial locations. The calculated results display the correct trends and are within 15% of the measured values with discrepancies tending to diminish with downstream distance. The flow angles of Fig. 7.23 show even better agreement except, perhaps, in the downstream region where the boundary condition obtained from the inviscid flow calculation is in error. A sample of the velocity profiles is shown in Fig. 7.24 and corresponds to  $x/2a$  of 0.48 and 0.73, and again the agreement is within or very close to the error bounds of the measurements, except in the regions where the inviscid velocity distribution differed from the measured one. The same conclusion can be drawn from the calculated and experimental values of displacement thickness of Fig. 7.24.

## 7.8 Boundary-Layer Program for Three-Dimensional Flows

In Appendix B, Program 10, we present and describe the extension of the boundary-layer program BLP2, Program 3, to three-dimensional flows. This program which we shall refer to as BLP3 has a structure similar to its counterpart in two-dimensional flows. It employs the numerical method of the previous chapter and can be used to compute three-dimensional flows with and without flow reversal in the spanwise direction. In the absence of flow reversal in the  $w$ -profile, the numerical method employs the standard box scheme and where is one, the numerical method employs the characteristic box scheme. As

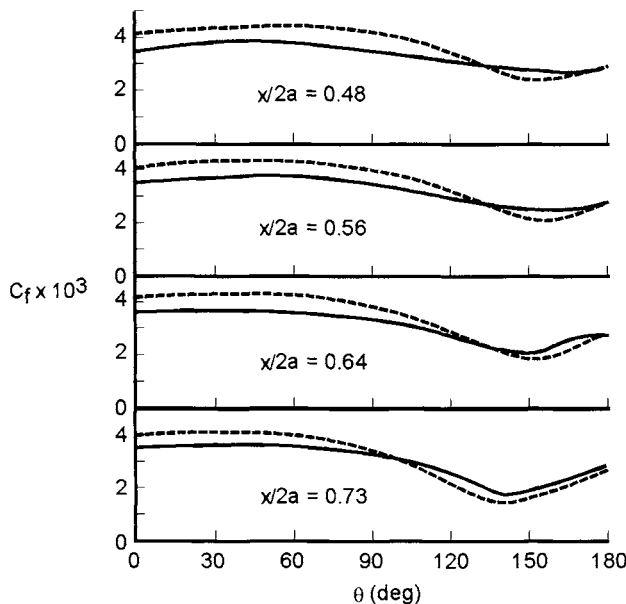


**Fig. 7.22.** Measured (dashed line) and calculated (solid line) resultant wall shear stress values on the prolate spheroid at  $\alpha = 10^\circ$ .

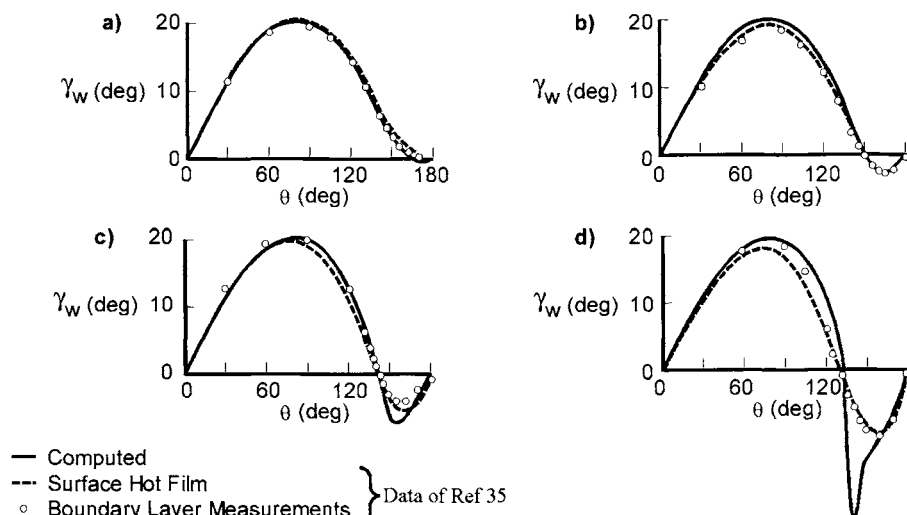


**Fig. 7.23.** Comparison of calculated (solid lines) and measured (symbols) wall crossflow angle  $\beta_w$ .

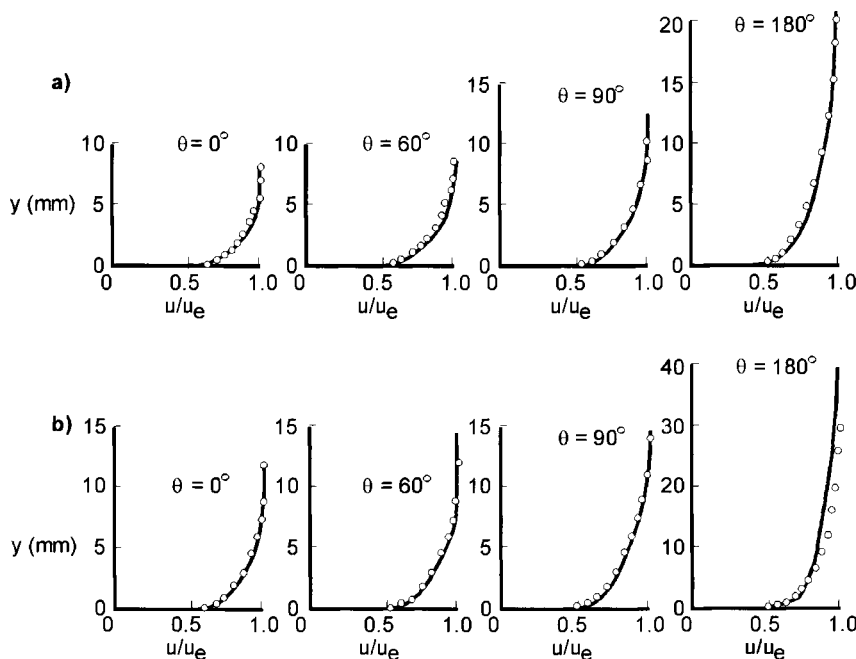


Fig. 7.24. Comparison of calculated (solid lines) and measured (symbols) streamwise  $u_s/U_s$  and crossflow  $u_c/U_s$  velocity profiles at (a)  $x/2a = 0.48$  and (b)  $x/2a = 0.73$ .

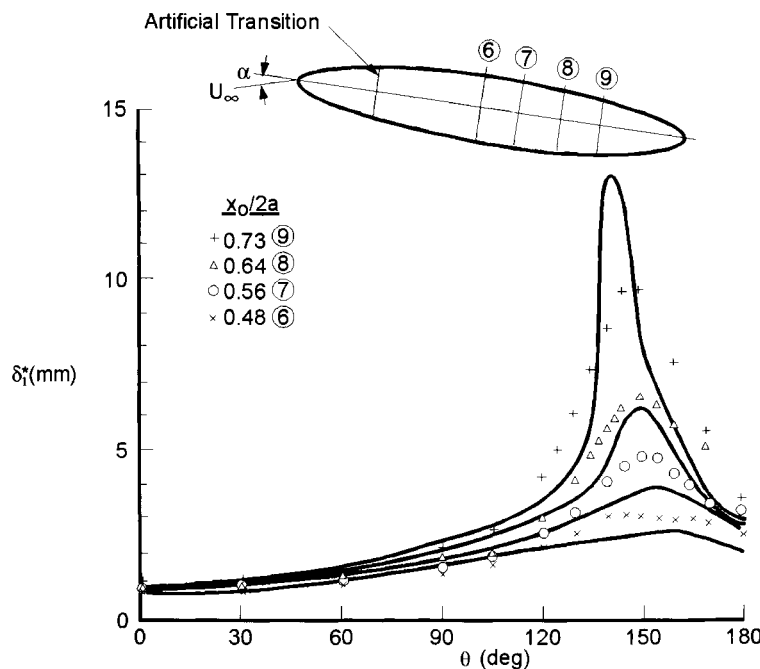


Fig. 7.25. Comparison of calculated (solid lines) and experimental (symbols) values of displacement thickness  $\delta_1^*$ .

in two-dimensional flows, when the streamwise shear stress vanishes, then the calculations are terminated due to the breakdown of the solutions.

As discussed in Section 7.3, the solution of the three-dimensional boundary layer equations requires initial conditions. The generation of these conditions can vary depending on the flow problem under consideration. For the sample flow problem discussed in Program 10, the initial conditions in the  $(x, y)$  plane are generated by solving the attachment line equations, Eqs. (10.71) through (10.73), and their boundary conditions, Eq. (10.74), given in Program 10. The initial conditions in the  $(z, y)$  plane are generated by solving the Blasius equations, Eqs. (10.57) through (10.59), subject to the boundary conditions given by Eq. (10.60).

The boundary-layer equations require the specification of external velocities  $u_e$  and  $w_e$  as a function of  $x$  and  $z$  so that the dimensionless pressure gradient parameters defined in transformed boundary-layer equations can be calculated by the Lagrange interpolation formulas given by Eqs. (3.4) to (3.7) in Program 3. In most problems, these velocities are specified in tabular form and not in analytical form. In the sample problem discussed in Program 10, however, the external velocity distributions are given analytically and the dimensionless pressure gradient parameters are obtained analytically rather than by Lagrange interpolation formulas as in BLP2.

Even though the sample problem discussed in Program 10 is for a laminar flow, BLP3 is constructed for both laminar and turbulent flows as BLP2. Again the eddy viscosity concept [see Eq. (7.4.1)] is used to model the Reynolds shear stress terms in the  $x$ - and  $z$ -momentum equations.

As in two-dimensional flows, a variable grid is used in the  $\eta$ -direction. It is generated by specifying the variable grid parameters  $K$  and  $h_1$ ; the spacings in the  $x$ - and  $z$ -directions are arbitrary and must be input as discussed in Program 10.

## References

- [1] Cebeci, T., Khattab, A.A., and Stewartson, K., "On Nose Separation," *J. Fluid Mech.*, Vol. 97, pp. 435–454, 1980.
- [2] Cebeci, T., Chen, H.H., and Kaups, K., "A Method for Removing the Coordinate Singularity on Bodies with Blunt Rounded Noses at Incidence," *Computers and Fluids*, Vol. 28, No. 4, pp. 369–389.
- [3] Cebeci, T., "Problems and Opportunities with Three-Dimensional Boundary-Layers," AGARD Rept. No. 719 – Three-Dimensional Boundary-Layers.
- [4] Rotta, J.C., "A Family of Turbulence Models for Three-Dimensional Thin Shear Layers," DFVLR-AVA Göttingen IB251-76A25, 1977.
- [5] Van den Berg, B., "A Three-Dimensional Law of the Wall for Turbulent Shear Flows," *J. Fluid Mech.*, Vol. 70, p. 149, 1975.
- [6] Cebeci, T., "Calculation of Three-Dimensional Boundary Layers, Part 1, Swept Infinite Cylinders and Small Cross Flow," *AIAA J.*, Vol. 12, p. 779, 1974.

- [7] Cousteix, J., Quémard, C., and Michel, R., "Application d'un schéma amélioré de longueur de mélange à l'étude des couches limites turbulentes tridimensionnelles," AGARD CP No. 93 – Turbulent Shear Flow, 1971.
- [8] Launder, B.E. and Sharma, B.I., "Application of the Energy-Dissipation Model of Turbulence to the Calculation of Flow near a Spinning Disc," *Letters in Heat and Mass Transfer*, Vol. 1, pp. 131–138, 1974.
- [9] Hansen, A.G. and Yohner, P.L., "Some Numerical Solutions of Similarity Equations for Three-Dimensional, Laminar Incompressible Boundary-Layer Flows," NACA TN 4370, 1958.
- [10] Isaacson, E. and Keller, H.B., *Analysis of Numerical Method*, John Wiley, New York, 1966.
- [11] Blottner, F.G., "Computational Techniques for Boundary Layers," Computational Methods for Inviscid and Viscous Two- and Three-Dimensional Flowfields. AGARD LS73, von Karman Institute, Brussels, Belgium, Feb 1975.
- [12] Bradshaw, P., Cebeci, T., and Whitelaw, J.H., *Engineering Calculation Methods for Turbulent Flows*, Academic Press, N.Y., 1981.
- [13] Krause, E., Hirschel, E.H. and Bothmann, Th., Die numerische Integration der Bewegungsgleichungen dreidimensionaler laminarer kompressibler Grenzschichten. Fachtagung Aerodynamik, Verling, 1968, DGLR-Fachzeitschrift, Band 3.
- [14] Cebeci, T., *An Engineering Approach to the Calculation of Aerodynamic Flows*, Horizons Publ., Long Beach, Calif. and Springer, Heidelberg, 1999.
- [15] Houdeville, R., "Three-Dimensional Boundary-Layer Calculation by a Characteristic Method," Fifth Symposium on Numerical and Physical Aspects of Aerodynamic Flows, Long Beach, California, ed. T. Cebeci, 1992.
- [16] Malecki, P., Cousteix, J., and Houdeville, R., "Three-Dimensional Boundary-Layer Calculations with Two-layer Turbulence Models," In: *5th International Symposium on Refined Flow Modeling and Turbulence Measurements – PARIS*, September 7–10, 1993.
- [17] Cebeci, T., "Calculation of Three-Dimensional Boundary Layers, Part 2, Three-Dimensional Flows in Cartesian Coordinates," *AIAA J.*, Vol. 13, p. 1056, 1975.
- [18] Cebeci, T., Kaups, K., and Moser, A., "Calculation of Three-Dimensional Boundary Layers, Part 3, Three-Dimensional Incompressible Flows in Curvilinear Orthogonal Coordinates," *AIAA J.*, Vol. 14, p. 1090, 1976.
- [19] Malecki, P., "Etude de modèles de turbulence pour les couches limites tridimensionnelles," Thèse de l'ENSAE, 1994.
- [20] Bradshaw, P. and Terrell, M.G., "The Response of a Turbulent Boundary Layer on an "Infinite" Swept Wing to the Sudden Removal of Pressure Gradient," *NPL Aero. Rept.* 1305, ARC 31514, 1969.
- [21] Cumpsty, N.A. and Head, M.R., "The Calculation of Three-Dimensional Turbulent Boundary-Layers, Part IV: Comparison of Measurements with Calculations on the Rear of a Swept Wing," C.P. 1077, Aero Research Council, London, England, 1970.
- [22] Van den Berg, B., Elsenaar, A., Lindhout, J.P.L. and Wessling, P., "Measurements in an Incompressible Three-Dimensional Turbulent Boundary Layer under Infinite Swept Wing Conditions and Comparisons with Theory," *J. Fluid Mech.*, Vol. 70; pp. 127–149, 1975.
- [23] Elsenaar, A. and Boelsma, S.H., "Measurements of the Reynolds Stress Tensor in a Three-Dimensional Turbulent Boundary-Layer under Infinite Swept Wing Conditions," NLR TR 74095 U, 1974.
- [24] Bradshaw, P., Ferriss, D.H., and Atwell, N.P., "Calculation of Boundary-Layer Development Using the Turbulent Energy Equation," *J. Fluid Mech.*, Vol. 23, p. 593, 1967.
- [25] Bradshaw, P., Mizner, G., and Unsworth, K., "Calculation of Compressible Turbulent Boundary Layers on Straight-Tapered Swept Wings," *AIAA J.*, Vol. 14, p. 399, 1976.
- [26] Bradshaw, P. and Pontikos, N.S., "Measurements in the Turbulent Boundary-Layer on an "Infinite Swept" Wing," *J. Fluid Mech.*, Vol. 159; pp. 105–130, 1985.

- [27] Launder, B.E. and Shima, N., "Second-Moment Closure for the Near-Wall Sublayer: Development and Application," *AIAA Journal*, Vol. 27, No. 10, pp. 1319–1325, 1989.
- [28] Norris, L.H., and Reynolds, W.C., "Turbulent Channel Flow with a Moving Wavy Boundary," Report FM-10, Department of Mechanical Engineering, Stanford University, Stanford, California, 1975.
- [29] Launder, B.E., Reece, G.J. and Rodi, W., "Progress in the Development of a Reynolds-Stress Turbulence Closure," *J. Fluid Mech.*, Vol. 68, No. 2, pp. 537–566, 1975.
- [30] Gibson, M.M. and Launder, B.E., "Ground Effects on Pressure Fluctuations in the Atmospheric Boundary Layer," *J. Fluid Mech.*, Vol. 86, No. 3, pp. 491–511, 1978.
- [31] Fu, S., Launder, B.E. and Tselepidakis, D.P., "Accommodating the Effects of High Strain Rates in Modelling the Pressure-Strain Correlation," University of Manchester Institute of Science and Technology, Mech. Engr. Report TFD/87/5, 1987.
- [32] East, L.F. and Hoxey, R.P., "Low-Speed Three-Dimensional Turbulent Boundary-Layer Data," Pt. I, TR 69041, Royal Aircraft Establishment, Farnborough, England, 1969.
- [33] Meier, H.U., and Kreplin, H.P., "Experimental Investigation of the Boundary Layer Transition and Separation on a Body of Revolution," *Zeitschrift für Flugwissenschaften und Weltraumforschung*, Vol. 4, pp. 65–71, March–April 1980.
- [34] Meier, H.U., Kreplin, H.P., Landhäuser, A., and Baumgarten, D., "Mean Velocity Distributions in Three-Dimensional Boundary Layers, Developing on a 1:6 Prolate Spheroid with Natural Transition ( $\alpha = 10^\circ$ ,  $U_\infty = 45$  m/s, Cross Sections  $x_0/2a = 0.56; 0.64$  and  $0.73$ )," German Aerospace Research Establishment, Rept. IB 222-84 A 10, Göttingen, Germany, March 1984.
- [35] Meier, H.U., Kreplin, H.P., Landhäuser, A., and Baumgarten, D., "Mean Velocity Distributions in Three-Dimensional Boundary Layers, Developing on 1:6 Prolate Spheroid with Natural Transition ( $\alpha = 10^\circ$ ,  $U_\infty = 55$  m/s, Cross Sections  $x_0/2a = 0.48; 0.56; 0.64$  and  $0.73$ )," German Aerospace Research Establishment, Rept. IB 222-84 A 11, Göttingen, Germany, March 1984.
- [36] Cebeci, T. and Meier, H.U., "Turbulent Boundary Layers on a Prolate Spheroid," AIAA Paper 87-1299, June 1987.

## Problems

**7-1.** (a) Show that for an infinite swept wing, the spanwise component of the external velocity is constant on the wing and that

$$w_e = V_\infty \sin \phi$$

where  $V_\infty$  is the freestream velocity and  $\phi$  is the sweep angle.

(b) If for an infinite swept wing flow the chordwise pressure gradient,  $dp/dx = 0$ , show that the external streamlines are straight lines.

(c) Show that for a laminar flow, the boundary-layer is collateral, i.e., the solution is such that

$$w = u \frac{w_e}{u_e}$$

(d) Show that this solution is the same as the solution of flow over a two-dimensional flat plate.

(e) Is this solution also valid for turbulent flow?

**7-2.** (a) Derive the laminar boundary-layer equations for an attachment line on an infinite swept wing.

(b) Show that the solutions for  $u$  and  $v$  are the same as for a two-dimensional stagnation point.

**7-3.** The attachment-line equations for an infinite swept wing are given by Eqs. (7.5.12) and (7.5.13) for  $m = 1$ .

$$f''' + ff'' + 1 - f'^2 = 0 \quad (\text{P7.3.1})$$

$$g''' + fg'' = 0 \quad (\text{P7.3.2})$$

(a) Integrate Eq. (P7.3.2) analytically for  $g'$  as a function of  $f$ .

(b) Use Program 1 in the accompanying CD-ROM to obtain the solutions of Eq. (P7.3.1) subject to the boundary conditions

$$\eta = 0, \quad f = 0, \quad f' = g' = 0 \quad (\text{P7.3.3a})$$

$$\eta = \eta_e, \quad f' = 1, \quad g' = 1 \quad (\text{P7.3.3b})$$

(c) With  $f(\eta)$  known from (b), compute  $g'(\eta)$ .

(d) Calculate the following integrals.

$$\begin{aligned} \int_0^\infty (1 - f') d\eta, \quad & \int_0^\infty f'(1 - f') d\eta, \quad \int_0^\infty (1 - g') d\eta, \\ \int_0^\infty g'(1 - f') d\eta, \quad & \int_0^\infty f'(1 - g') d\eta, \quad \int_0^\infty g'(1 - g') d\eta \end{aligned} \quad (\text{P7.3.4})$$

(e) From Eq. (P7.3.2) show that

$$g''(0) = \int_0^\infty f'(1 - g') d\eta \quad (\text{P7.3.5})$$

(f) Write the equation of the external streamlines.

(g) Write the equation of the skin-friction lines.

(h) Plot schematically the external streamlines and skin-friction lines.

**7-4.** Show that, for a polar coordinate system,  $\theta = \frac{\pi}{2}$ , in which the coordinates  $x$  and  $z$  are denoted by  $\xi$  ( $\equiv x/a$ ) and  $\phi$ , respectively, Eqs. (7.2.19) to (7.2.21) can be written as

$$\frac{\partial}{\partial \xi}(uh_2) + \frac{\partial}{\partial \phi}(wh_1) + \frac{\partial}{\partial y}(vh_1h_2) = 0 \quad (\text{P7.4.1})$$

$$\frac{u}{h_1} \frac{\partial u}{\partial \xi} + \frac{w}{h_2} \frac{\partial u}{\partial \phi} + v \frac{\partial u}{\partial y} + k_2 w^2 = -\frac{1}{\rho h_1} \frac{\partial p}{\partial \xi} + \frac{\partial}{\partial y} \left( \nu \frac{\partial u}{\partial y} - \overline{u'v'} \right) \quad (\text{P7.4.2})$$

$$\frac{u}{h_1} \frac{\partial u}{\partial \xi} + \frac{w}{h_2} \frac{\partial w}{\partial \phi} + v \frac{\partial w}{\partial y} + k_2 uw = -\frac{1}{\rho h_2} \frac{\partial p}{\partial \phi} + \frac{\partial}{\partial y} \left( \nu \frac{\partial w}{\partial y} - \overline{v'w'} \right) \quad (\text{P7.4.3})$$

**7-5.** To discuss the initial conditions on a body of revolution, let us choose a prolate spheroid at incidence. At zero angle of incidence, the stagnation point is at the nose and there is no problem in solving the boundary-layer equations for an axisymmetric flow as was discussed in Sections 3.2 and 4.6.3. With incidence and using a body-oriented coordinate system, the stagnation point moves away from the nose. To generate the initial conditions for this case, it is necessary to obtain solutions of the three-dimensional boundary-layer equations at the stagnation point on the plane of symmetry and continue them on the windward and leeward sides. The equations on the plane of symmetry can be obtained by taking advantage of the symmetry conditions.

Noting that the circumferential velocity,  $w$ , in the boundary layer and the circumferential pressure gradient,  $\partial p / \partial \phi$ , are identically zero on the line of symmetry, use a procedure similar to that used to obtain the attachment-line equations along the wing leading edge and show that Eqs. (P7.4.1) to (P7.4.3) can be written as

$$\frac{\partial}{\partial \xi} (uh_2) + h_1 w_\phi + \frac{\partial}{\partial y} (vh_1 h_2) = 0 \quad (\text{P7.5.1})$$

$$\frac{u}{h_1} \frac{\partial u}{\partial \xi} + v \frac{\partial u}{\partial y} = -\frac{1}{\rho h_1} \frac{\partial p}{\partial \xi} + \frac{\partial}{\partial y} \left( \nu \frac{\partial u}{\partial y} - \overline{u'v'} \right) \quad (\text{P7.5.2})$$

$$\frac{u}{h_1} \frac{\partial w_\phi}{\partial \xi} + \frac{w_\phi^2}{h_2} + v \frac{\partial w_\phi}{\partial y} - uw_\phi k_2 = -\frac{1}{\rho h_2} \frac{\partial^2 p}{\partial \phi^2} + \frac{\partial}{\partial y} \left[ \nu \frac{\partial w_\phi}{\partial y} - (\overline{u'w'})_\phi \right] \quad (\text{P7.5.3})$$

where  $w_\phi = \partial w / \partial \phi$ .

**7-6.** The equation of a prolate spheroid at incidence can be written as

$$F(\bar{x}, \bar{y}, \bar{z}) = \left( \frac{\bar{x}}{a} \right)^2 + \left( \frac{\bar{y}}{b} \right)^2 + \left( \frac{\bar{z}}{b} \right)^2 - 1 = 0$$

(a) Show that the relations between the coordinates that define the body  $(\bar{x}, \bar{y}, \bar{z})$  and those for boundary-layer equations are (see Fig. P7.1)

$$\bar{x} = a\xi \quad (\text{P7.6.1a})$$

$$\bar{y} = -r \cos \phi = -b \sqrt{1 - \xi^2} \cos \phi \quad (\text{P7.6.1b})$$

$$\bar{z} = r \sin \phi = b \sqrt{1 - \xi^2} \sin \phi \quad (\text{P7.6.1c})$$

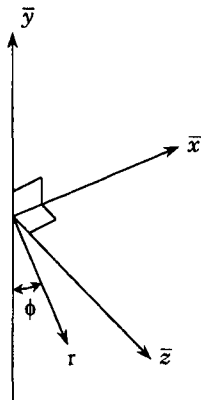


Fig. P7.1.

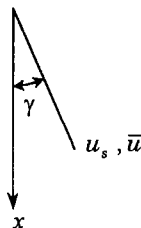


Fig. P7.2.

- (b) Show that the metric coefficients in Eqs. (P7.4.1) to (P7.4.3) can be written as

$$h_1 = a \left[ 1 + \frac{t_0^2 \xi^2}{1 - \xi^2} \right]^{1/2} \quad (\text{P7.6.2a})$$

$$h_2 = at_0[1 - \xi^2]^{1/2} = r \quad (\text{P7.6.2b})$$

where  $t_0 = b/a$ .

- 7-7.** Show that the metric coefficients  $h_1$  and  $h_2$  in a streamline coordinate system are given by Eq. (7.2.13).

- 7-8.** Derive the small cross-flow equations given by Eqs. (7.2.16) to (7.2.18) and discuss the approximations used to reduce them from those given by Eqs. (7.2.7) to (7.2.9).

- 7-9.** In some problems it is desirable to express the solutions of the boundary-layer equations obtained in one coordinate system in terms of another coordinate system. For example, suppose that we know the velocity profiles  $\bar{u}$ ,  $\bar{w}$  in the streamline coordinate system  $(\bar{x}, \bar{z})$  and need to know the corresponding velocity profiles  $u$  and  $w$  in a body-oriented coordinate system  $(x, z)$ . Assume that the system  $(x, z)$  is orthogonal.

- (a) If  $\gamma$  denotes the angle that the external streamline makes with the  $x$ -coordinate direction (see Fig. P7.2), show that

$$u = \bar{u} \cos \gamma - \bar{w} \sin \gamma$$

$$w = \bar{u} \sin \gamma + \bar{w} \cos \gamma$$

where

$$\gamma = \tan^{-1}(w_e/u_e)$$

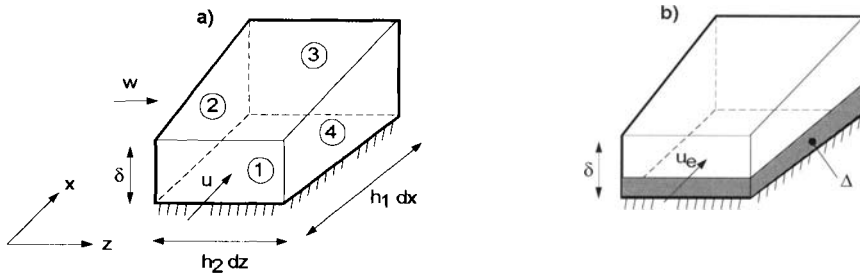


**Fig. P7.3.** Control volume for (a) real flow and (b) equivalent fictitious inviscid flow.

(b) On the attachment line where the coordinate directions coincide so that the  $u = \bar{u}$ ,  $\bar{u}_e = u_s$  and  $w = \bar{w} = 0$ , show that

$$w_z = \frac{\bar{u}}{u_{se}} \frac{\partial w_e}{\partial z} + \frac{\partial \bar{w}}{\partial \bar{z}} \frac{h_2}{h_2}$$

**7-10.** An equation for displacement thickness in three-dimensional flows can be obtained by constructing a fictitious inviscid flow (Fig. P7.3b) which has the same mass flow as the real flow (Fig. P7.3a) through faces 1, 2, 3, 4 of the control volume shown in Fig. P7.3b. The fictitious flow has constant properties along a normal to the wall below the line  $y = \delta$ .

(a) Using an orthogonal coordinate system and with  $h_1$  and  $h_2$  denoting the metric coefficients, show that the sum of mass flows of the real flow  $\dot{m}_{\text{real}}$  through faces 1, 2, 3, 4 is

$$\dot{m}_{\text{real}} = dx \frac{\partial}{\partial x} \left[ h_2 dz \int_0^\delta \rho u dy \right] + dz \frac{\partial}{\partial z} \left[ h_1 dx \int_0^\delta \rho w dy \right] \quad (\text{P7.10.1})$$

and the sum of mass flows of the fictitious flow  $\dot{m}_{\text{fictitious}}$  through faces 1, 2, 3, 4 is

$$\dot{m}_{\text{fictitious}} = dx \frac{\partial}{\partial x} \left[ h_2 dz \int_\Delta^\delta \rho u_e dy \right] + dz \frac{\partial}{\partial z} \left[ h_1 dx \int_\Delta^\delta \rho w_e dy \right] \quad (\text{P7.10.2})$$

where  $\Delta$  is the displacement thickness.

(b) Write the equality of the two mass flows in (a) and show that the displacement thickness is given by the following partial differential equation

$$\frac{\partial}{\partial x} [h_2 u_e \Delta] + \frac{\partial}{\partial z} [h_1 w_e \Delta] = \frac{\partial}{\partial x} [h_2 u_e \delta_x^*] + \frac{\partial}{\partial z} [h_1 w_e \delta_z^*] \quad (\text{P7.10.3})$$

with

$$\delta_x^* = \int_0^\delta \left( 1 - \frac{u}{u_e} \right) dy, \quad \delta_z^* = \int_0^\delta -\frac{w}{u_e} dy \quad (\text{P7.10.4})$$

**7-11.** For the general nonorthogonal body-oriented coordinate system discussed in subsection 7.2.3, extend the discussion in Problem 7-10 to derive the following equation for the displacement surface  $\Delta$ ,

$$\frac{\partial}{\partial x} [u_e h_2 \sin \theta (\Delta - \delta_x^*)] + \frac{\partial}{\partial z} [w_e h_1 \sin \theta (\Delta - \delta_z^*)] = 0 \quad (\text{P7.11.1})$$

where  $\delta_x^*$  and  $\delta_z^*$  are given by Eq. (P7.15.5d).

**7-12.** The  $k$ - $\varepsilon$  model discussed in subsection 6.3.2 for two-dimensional flows and for three-dimensional low Reynolds numbers in Section 7.4, takes the following form at high Reynolds numbers,

$$\frac{Dk}{Dt} = P - \varepsilon + \frac{\partial}{\partial y} \left( \frac{c_\mu}{\sigma_k} \frac{k^2}{\varepsilon} \frac{\partial k}{\partial y} \right) \quad (\text{P7.12.1})$$

$$\frac{D\varepsilon}{Dt} = c_{\varepsilon 1} \frac{\varepsilon}{k} P - c_{\varepsilon 2} \frac{\varepsilon^2}{k} + \frac{\partial}{\partial y} \left( \frac{c_\mu}{\sigma_\varepsilon} \frac{k^2}{\varepsilon} \frac{\partial \varepsilon}{\partial y} \right) \quad (\text{P7.12.2})$$

The production term is given by Eq. (7.4.13).

A simplified form of these equations can be obtained by neglecting the convection and diffusion terms in the  $k$ -equation and by neglecting the convection term in the  $\varepsilon$ -equation

$$P = \varepsilon \quad (\text{P7.12.3})$$

$$c_{\varepsilon 1} \frac{\varepsilon}{k} P - c_{\varepsilon 2} \frac{\varepsilon^2}{k} + \frac{\partial}{\partial y} \left( \frac{c_\mu}{\sigma_\varepsilon} \frac{k^2}{\varepsilon} \frac{\partial \varepsilon}{\partial y} \right) = 0 \quad (\text{P7.12.4})$$

(a) Assuming that the dissipation rate is given by

$$\varepsilon = c \frac{k^{3/2}}{y} \quad (\text{P7.12.5})$$

demonstrate the following relations

$$-\overline{u'v'} = \frac{c_\mu}{c} k^{1/2} y \frac{\partial u}{\partial y} \quad (\text{P7.12.6a})$$

$$-\overline{w'v'} = \frac{c_\mu}{c} k^{1/2} y \frac{\partial w}{\partial y} \quad (\text{P7.12.6b})$$

$$\frac{\tau_t}{\rho k} = c_\mu^{1/2} \quad (\text{P7.12.6c})$$

$$\tau_t = \rho \frac{c_\mu^{3/2}}{c^2} y^2 \left[ \left( \frac{\partial u}{\partial y} \right)^2 + \left( \frac{\partial w}{\partial y} \right)^2 + 2 \frac{\partial u}{\partial y} \frac{\partial w}{\partial y} \cos \theta \right]^{1/2} \quad (\text{P7.12.6d})$$

with

$$\tau_t = \rho (\overline{u'v'}^2 + \overline{w'v'}^2 + 2 \overline{u'v'w'v'} \cos \theta)^{1/2} \quad (\text{P7.12.6e})$$

(b) Neglecting the variation of  $k$  with  $y$ , show that a relation between  $c$ ,  $c_\mu$ ,  $c_{\varepsilon 1}$ ,  $c_{\varepsilon 2}$ , and  $\sigma_\varepsilon$  is

$$(c_{\varepsilon 1} - c_{\varepsilon 2})c^2 + \frac{c_\mu}{\sigma_\varepsilon} = 0 \quad (\text{P7.12.7})$$

**7-13.** Consider the following partial differential equation

$$u \frac{\partial f}{\partial x} + w \frac{\partial f}{\partial z} = a^2 \frac{\partial^2 f}{\partial y^2} \quad (\text{P7.13.1})$$

where  $u$ ,  $w$  and  $a$  are constants. Introducing new variables  $X$  and  $Z$ ,

$$X = \frac{u}{u^2 + w^2}x + \frac{w}{u^2 + w^2}z \quad (\text{P7.13.2a})$$

$$Z = -\frac{w}{u^2 + w^2}x + \frac{u}{u^2 + w^2}z \quad (\text{P7.13.2b})$$

show that Eq. (P7.13.1) can be written as

$$\frac{\partial f}{\partial X} = a^2 \frac{\partial^2 f}{\partial y^2} \quad (\text{P7.13.3})$$

(b) Show that

$$f = \frac{1}{2a\sqrt{\pi X}} e^{-\eta^2} \quad (\text{P7.13.4})$$

with

$$\eta = \frac{y}{2a\sqrt{X}}$$

is a solution of Eq. (P7.13.3).

(c) Eq. (P7.13.3) represents the response to a perturbation introduced at point  $P$  ( $y = 0$ ,  $X = 0$ ). Study this solution and deduce how a perturbation propagates in the original  $x, y, z$  domain.

**7-14.** Consider a quasi-linear system of first order partial differential equations

$$A_i \frac{\partial F}{\partial x_i} = B, \quad i = 1, m \quad (\text{P7.14.1})$$

The number of  $x_i$ -coordinates is  $m$ ,  $F$  is a column vector with  $n$  elements (the unknowns),  $A_i$  are  $(n \times n)$  square matrices and  $B$  is a column vector with  $n$  elements. The elements of  $A_i$  and  $B$  may depend on  $x_i$  and  $F$ .

The mathematical nature of three-dimensional boundary-layer equations expressed in the form of Eq. (P7.14.1) can be studied from the characteristic determinant

$$\det(A_i \lambda_i) = 0 \quad (\text{P7.14.2})$$

where  $\lambda_i$  are the components of a vector normal to the characteristic surfaces.

- (a) Consider a laminar boundary-layer developing on a flat surface and express the boundary-layer equations by a system of first-order partial differential equations by introducing new functions

$$\hat{u} = \frac{\partial u}{\partial y}, \quad \hat{w} = \frac{\partial w}{\partial y}$$

The unknowns are  $u$ ,  $v$ ,  $w$ ,  $\hat{u}$ , and  $\hat{w}$ . Show that the characteristic determinant is

$$\nu^2 \lambda_y^5 = 0 \quad (\text{P7.14.3})$$

As the characteristic roots are real and identical, the system is parabolic (the properties are the same as for the heat conduction equation). The characteristic surfaces are normal to the wall.

- (b) In order to study the role of convection terms, it is not necessary to consider the second-order terms (i.e., the viscous terms) in the boundary-layer equations. In this way, subcharacteristics are determined. Show that the characteristic determinant is

$$\lambda_y(u\lambda_x + v\lambda_y + w\lambda_z)^2 = 0 \quad (\text{P7.14.4})$$

- (c) Deduce that surfaces normal to the wall and stream surfaces are characteristic surfaces. If a perturbation is introduced at a point  $P$ , the perturbation will propagate along the normal passing through  $P$  and along the streamline passing through  $P$ . Deduce the domain of influence and of dependence of a point  $P$  located in the boundary-layer.

- 7-15.** (a) For the body-oriented coordinate system discussed in subsection 7.2.3, derive the integral equation of continuity (see problem 3.9) with  $\Delta$  corresponding to the displacement surface height.

$$\begin{aligned} \frac{v_E}{u_{te}} &= \left( \frac{u_e}{u_{te}} \right) \frac{1}{h_1} \frac{\partial \delta}{\partial x} + \left( \frac{w_e}{u_{te}} \right) \frac{1}{h_2} \frac{\partial \delta}{\partial z} - \frac{v_e}{u_{te}} \\ &= \frac{1}{u_{te} h_1 h_2 \sin \theta} \left[ \frac{\partial}{\partial x} \{u_e h_2 \sin \theta (\delta - \Delta)\} + \frac{\partial}{\partial z} \{w_e h_1 \sin \theta (\delta - \Delta)\} \right] \end{aligned} \quad (\text{P7.15.1})$$

where  $u_{te}$  is total edge-velocity defined by

$$u_{te} = \sqrt{u_e^2 + w_e^2 + 2u_e w_e \cos \theta} \quad (\text{P7.15.2})$$

See also Eq. (6.5.1) for two-dimensional flows.

(b) Show that the integral equations for the  $x$ -momentum

$$\begin{aligned} \frac{c_{fx}}{2} = & \frac{1}{u_{te}^2 h_1 h_2 \sin \theta} \left[ \frac{\partial}{\partial x} (h_2 \sin \theta u_{te}^2 \theta_{11}) + \frac{\partial}{\partial z} (h_1 \sin \theta u_{te}^2 \theta_{12}) \right] \\ & + \frac{\delta_x^*}{u_{te} h_1} \frac{\partial u_e}{\partial x} + \frac{\delta_z^*}{u_{te} h_2} \frac{\partial u_e}{\partial z} - k_1 \cot \theta \left( \frac{u_e}{u_{te}} \delta_x^* + \theta_{11} \right) \\ & + \frac{k_2}{\sin \theta} \left( \frac{w_e}{u_{te}} \delta_z^* + \theta_{22} \right) + k_{12} \left( \frac{u_e}{u_{te}} \delta_z^* + \theta_{12} \right) \end{aligned} \quad (\text{P7.15.3})$$

and  $z$ -momentum for the body-oriented coordinate system can be written as

$$\begin{aligned} \frac{c_{fz}}{2} = & \frac{1}{u_{te}^2 h_1 h_2 \sin \theta} \left[ \frac{\partial}{\partial x} (h_2 \sin \theta u_{te}^2 \theta_{21}) + \frac{\partial}{\partial z} (h_1 \sin \theta u_{te}^2 \theta_{22}) \right] \\ & + \frac{\delta_x^*}{u_{te} h_1} \frac{\partial w_e}{\partial x} + \frac{\delta_z^*}{u_{te} h_2} \frac{\partial w_e}{\partial z} - k_2 \cot \theta \left( \frac{w_e}{u_{te}} \delta_z^* + \theta_{22} \right) \\ & + \frac{k_1}{\sin \theta} \left( \frac{u_e}{u_{te}} \delta_x^* + \theta_{11} \right) + k_{21} \left( \frac{w_e}{u_{te}} \delta_x^* + \theta_{21} \right) \end{aligned} \quad (\text{P7.15.4})$$

Here

$$\frac{c_{fx}}{2} = \frac{\tau_{wx}}{\rho u_{te}^2}, \quad \frac{c_{fz}}{2} = \frac{\tau_{wz}}{\rho u_{te}^2} \quad (\text{P7.15.5a})$$

$$\theta_{11} = \left( \frac{u_e}{u_{te}} \right)^2 \int_0^\delta \frac{u}{u_e} \left( 1 - \frac{u}{u_e} \right) dy, \quad \theta_{12} = \frac{u_e w_e}{u_{te}^2} \int_0^\delta \frac{w}{w_e} \left( 1 - \frac{u}{u_e} \right) dy \quad (\text{P7.15.5b})$$

$$\theta_{22} = \frac{w_e^2}{u_{te}^2} \int_0^\delta \frac{w}{w_e} \left( 1 - \frac{w}{w_e} \right) dy, \quad \theta_{21} = \frac{u_e w_e}{u_{te}^2} \int_0^\delta \frac{u}{u_e} \left( 1 - \frac{w}{w_e} \right) dy \quad (\text{P7.15.5c})$$

$$\delta_x^* = \frac{u_e}{u_{te}} \int_0^\delta \left( 1 - \frac{u}{u_e} \right) dy, \quad \delta_z^* = \frac{w_e}{u_{te}} \int_0^\delta \left( 1 - \frac{w}{w_e} \right) dy \quad (\text{P7.15.5d})$$

**7-16.** Use Program 10 given in Appendix B to solve Eqs. (7.5.12) and (7.5.13) for  $m = 1$  subject to the boundary-conditions given by Eq. (7.5.7). Take  $k = 1$ ,  $\eta_e = 8$ ,  $h_1 = 0.2$ .

**7-17.** Repeat Problem 7-16 for Eqs. (7.5.14) and (7.5.15) for a yawed circular cylinder at zero incidence for a yaw angle of  $\lambda = 30^\circ$  and for a freestream velocity  $V_\infty$  of 160 ft/sec.

$$u_e = 2V_\infty \cos \lambda \sin x$$

$$w_e = V_\infty \sin \lambda$$

**7-18.** Repeat Problem 7-17 for a yawed ellipse for a yaw-angle of  $\lambda = 30^\circ$  and for a freestream velocity of 160 ft/sec.

*Hint:* See Eq. (4.6.2).

# 8

# Transition in Three-Dimensional Incompressible Flows

## 8.1 Introduction

As discussed in Chapter 5, transition in two-dimensional flows usually occurs in zero-pressure gradient or decelerating flows due to the growth of the Tollmien–Schlichting (TS) waves. Transition can also occur in accelerating flows if the Reynolds number is very high.

Transition on swept wings may occur by three separate mechanisms. It may occur along the leading edge of a wing as a result of the turbulent boundary layer developing on the fuselage and wing-fuselage intersection. Under certain conditions discussed in Section 8.2, the fuselage flow can contaminate the leading edge of the wing, causing it to become turbulent.

The second mechanism on a swept wing which may cause transition is due to the streamwise instability of the flow. This usually occurs at some distance away from the leading edge, especially at lower angles of attack and is related to the properties of the streamwise velocity profile  $u$ . Essentially it is similar to the transition process in two-dimensional flows except that now it is necessary to include the effect of the spanwise velocity profile when making a stability analysis of the velocity profiles. As we shall see, the eigenvalue procedure is now much more difficult than the procedure used in two-dimensional flows.

The third mechanism which may cause transition is due to the crossflow instability of the flow. This usually occurs near the leading edge of the wing where the external velocity in the streamwise direction is undergoing a rapid acceleration. However, the crossflow profile may exhibit the behavior similar to profiles with inflexional instability by virtue of Rayleigh's criterion and can cause transition to occur even in this region of favorable pressure gradient.

The second and third mechanisms are two aspects of transition due to instabilities and are effectively observed on swept wings, for example. More complex phenomena involve nonlinear interactions between instabilities and require nonlinear stability theory.

The prediction of transition in three-dimensional flows can also be achieved by using empirical correlations and the  $e^n$ -method as in two-dimensional flows [1, 2]. The correlation formulas, however, unlike those for two-dimensional flows, are not as accurate and useful for wing flows as those discussed in subsection 6.4.1 for airfoil flows. The above mentioned three mechanisms that may cause transition, make the development of accurate correlation formulas difficult. For this reason, the only reliable engineering tool for predicting transition in three-dimensional flows, as in two-dimensional flows, is the  $e^n$ -method discussed in Section 8.3. This method is again based on the solution of the linear stability equations discussed in Section 5.3 for incompressible flows as well as compressible flows discussed in [3]. The stability equations are solved for an assigned dimensional frequency and amplification rates are computed in order to determine the  $n$ -factor in the  $e^n$ -method. The eigenvalue procedure used for three-dimensional flows, however, is not as straight forward as the one in two-dimensional flows. There are two main reasons for this difficulty with the first one involving the eigenvalue formulation used to solve the linear stability equations as discussed in subsection 8.3.1. The second one involves the procedure used to specify the dimensional frequencies needed in the calculation of the amplification rates as discussed in subsection 8.3.2.

The Section 8.4 of this chapter deals with the numerical solution of the Orr–Sommerfeld equation for three-dimensional incompressible flows and the following section discusses the applications of the calculation method of Section 8.4 to several three-dimensional flows and in order to demonstrate the flow conditions in which transition may occur on a swept wing as a result of the second or the third mechanisms that may cause transition.

## 8.2 Mechanisms of Transition

### 8.2.1 Tollmien–Schlichting and Crossflow Instabilities

The transition mechanisms are described in three steps [4]. In the first step, called the receptivity which describes the means by which forced disturbances such as freestream noise, freestream turbulence, small roughnesses, ... enter the laminar boundary-layer and excite the eigenmodes. In the second step, the eigenmodes are damped or amplified. As far as the amplitude of these eigenmodes is small, the linear stability theory can be applied. Finally, in the third step nonlinear interactions occur when the amplitude of the instabilities is large enough and turbulence develops.

The evolution of the pressure gradient and of the three-dimensionality in the boundary-layer are key parameters in the transition process. Typically, on the upper surface of a swept wing, the flow decelerates over a large extent downstream of a region, near the leading edge where the flow accelerates. In this

latter region, the streamwise velocity profile in the boundary-layer is generally very stable unless the Reynolds number is very large. On the contrary, the crossflow is highly unstable even if the intensity of the crosswise velocity is only a few percent of the external velocity. As the sweep angle increases, the crossflow instabilities are more likely to occur (Problem 8-2). On the rear part of the wing, where the flow decelerates, the streamwise velocity profile becomes very unstable just like a two-dimensional boundary-layer developing with a positive pressure gradient.

The receptivity phase is also very important because it represents the triggering phenomenon of instabilities. In a complete theory, the receptivity should determine the initial amplitude of instabilities along the neutral curve. It is now accepted that the receptivity process is very different for Tollmien and Schlichting, TS, and Crossflow, CF, instabilities. TS instabilities are very sensitive to freestream disturbances, such as noise of freestream turbulence. In the application of the  $e^n$ -method, this is more or less accounted for with the dependence of the  $n$ -factor with respect of the turbulence level  $Tu$ . A higher turbulence level implies a lower value of the  $n$ -factor. Whereas the TS waves are travelling waves with non-zero frequencies, the CF waves are amplified over a very large range of frequencies and the zero frequency waves play an important role when the turbulence level is low. These waves involve vortices roughly aligned with the external velocity which deform the streamwise velocity profile leading to an inflexional velocity profile. Experiments have shown that the source of the CF vortices is associated with micron-sized roughnesses located along the neutral curve path [5, 6]. On a swept wing, this location is typically between 1 and 5% chord, depending on the Reynolds number, the sweep angle and the leading edge radius. The improvement of the surface polishing of the leading edge area should decrease the initial amplitude of the vortices. Until now, the roughness effect on CF transition is not accounted for in the transition criteria. With the  $e^n$ -method, a possibility would be to introduce an  $n$ -factor different for the TS and CF transitions and to make the CF value of  $n$  dependent on roughness characteristics [4]. The effect of roughness has been used to manipulate the CF transition on a swept wing [7, 8]. The idea is to promote an artificial array of stationary vortices by a row of micron-sized roughnesses placed parallel to the leading edge of the wing along the path of the neutral curve. With a careful choice of the spacing between the roughnesses and of the pressure gradient, a nonlinear interaction of the artificial vortices and of the natural vortices occur in such a way that transition is delayed.

### 8.2.2 Leading Edge Contamination

A useful parameter in discussing the leading edge contamination on a swept wing is the spanwise Reynolds number based on momentum thickness,  $R_{\theta_z}$ , defined by

$$R_{\theta_z} = \frac{w_e \theta_z}{\nu} \quad (8.2.1)$$

where

$$\theta_z = \int_0^\delta \frac{w}{w_e} \left(1 - \frac{w}{w_e}\right) dy \quad (8.2.2)$$

According to experiments, for  $R_{\theta_z}$  less than about 100, all disturbances, large or small damp out, for  $R_{\theta_z}$  less than about 230 only small disturbances are damped out and for  $R_{\theta_z}$  greater than 240, natural laminar flow is unattainable [9, 10].

The  $R_{\theta_z}$ -criterion can also be expressed as a function of another Reynolds number defined by

$$R = \frac{w_e}{\nu} \left[ \frac{\nu}{(du_e/dx)_{x=0}} \right]^{\frac{1}{2}} \quad (8.2.3)$$

where  $x$  denotes the coordinate along the direction normal to the leading edge with  $x = 0$  corresponding to the location where the external velocity  $u_e$  along  $x$  is zero.

On the leading edge of the wing where the boundary-layers are similar, we can write

$$\frac{w_e \theta_z}{\nu} = 0.404 R \quad (8.2.4)$$

According to the leading edge contamination criterion, the flow is laminar if  $R < 250$ . For cylinders of elliptic section at zero angle of attack, it can be shown that

$$R = \left[ \frac{V_\infty r_0 \sin \phi \tan \phi}{\nu} \frac{1 + \frac{t}{c}}{1 + \frac{t}{c}} \right]^{\frac{1}{2}} \quad (8.2.5)$$

where  $V_\infty$  is the freestream velocity,  $r_0$  is the leading edge radius and  $t/c$  is the thickness ratio which is equal to 1 for a swept circular cylinder.

Equation (8.2.5) shows that the flow becomes turbulent if the leading edge radius or the sweep angle are too large. This phenomenon is called the leading edge contamination.

To delay the leading edge contamination two approaches can be employed. One possible approach is to use the Gaster bump [11] which is a small bump placed on the wing leading edge at a certain distance from the fuselage (well outside the fuselage boundary-layer). This bump diverts the flow from the fuselage and creates a stagnation point from which a fresh boundary-layer develops. This device can delay the onset of leading edge contamination up to values of  $R$  around 350 to 400.

Another approach to delay the leading edge contamination is to apply suction in the wing leading edge region. Figure 8.1 shows the influence of suction parameter  $K$ ,

$$K = \frac{v_w}{V_\infty \sin \phi} R$$

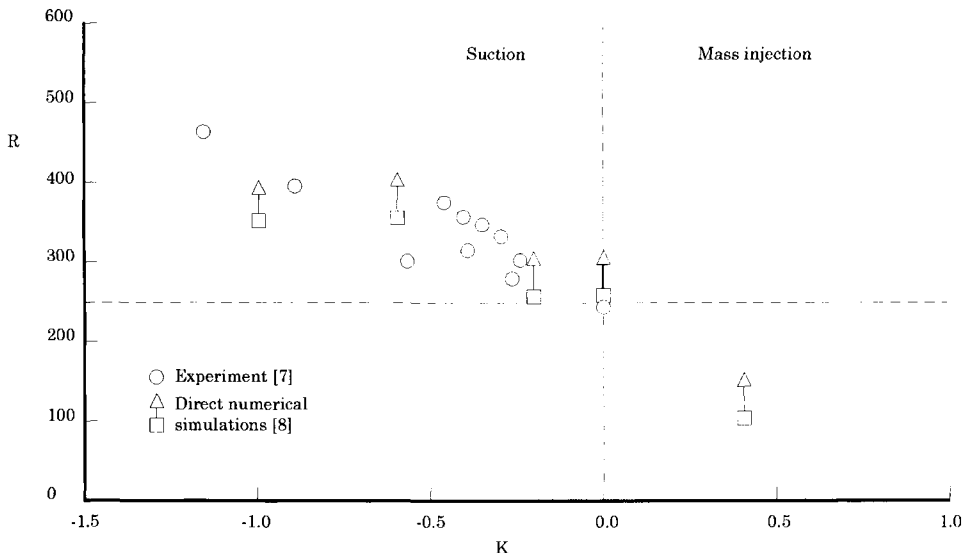


**Fig. 8.1.** Influence of suction on leading edge contamination.

on the leading edge contamination Reynolds number  $R$ , indicating that  $R$  can be as high as 450. These experiments were conducted by Juillen and Arnal [12] for a swept cylinder which is circular in front and triangular in the rear. The nose radius was 6 cm and the model span was 1.5 m. Suction was applied through perforated wall, the holes having a diameter of 0.06 mm and a pitch-to-diameter ratio of around 5. This experimental setup did not allow the use of higher suction rates for higher Reynolds numbers. For example, for a sweep angle of  $30^\circ$  and  $R = 500$ ,  $v_w/V_\infty$  was of the order of  $1.5 \times 10^{-3}$ , which is indeed a small number. Figure 8.1 also shows that the measurements are in good agreement with results obtained from direct numerical simulation (DNS) as discussed in [13].

## 8.3 $e^n$ -Method for Three-Dimensional Flows

### 8.3.1 Eigenvalue Formulations

In the solution of three-dimensional linear stability equation, Eq. (5.3.15), the eigenvalue formulation requires an assumption or a relationship between the two wave numbers  $\alpha$  and  $\beta$ . The formulation of this relationship or the assumption plays a crucial role in the eigenvalue problem since the onset of transition depends on the direction, magnitude and rate of the growth of the disturbances which propagate through the boundary layer, and this information is represented by  $\alpha$  and  $\beta$  which form a wave number vector,  $\vec{k}$ , at an angle  $\phi$  to the flow direction.

There are several formulations developed to provide this relationship or the assumption. In the temporal amplification approach used by Malik [14], the wave numbers  $\alpha$  and  $\beta$  are related by the disturbance angle  $\phi$  through

$$\phi = \tan^{-1} \left( \frac{\beta}{\alpha} \right) \quad (8.3.1)$$

with  $\phi$  assumed and the dimensional frequency  $\omega_r^*/2\pi$  are specified, and  $\alpha$  and  $\beta$  represent one unknown from Eq. (8.3.1); with  $R$  known, the second unknown is the growth rate of the disturbance  $\omega_i$ . The stability equations are solved for initial estimates of  $\alpha$  and  $\omega_i$  for a given  $\omega_r$ ,  $\phi$  and specified  $R$ . After convergence,  $\alpha$  and  $\omega_i$  were computed for different values of  $\phi$  in order to find the maximum value of  $\omega_i/|V_g|$ , where  $V_g$  is the group velocity with components

$$V_g = \left[ \left( \frac{\partial \omega}{\partial \alpha} \right)_{\beta, R}, \left( \frac{\partial \omega}{\partial \beta} \right)_{\alpha, R} \right] \quad (8.3.2)$$

Once the maximum value of  $\omega_i/|V_g|$  is computed, the onset of transition is obtained from

$$n = \int_{x_0}^x \frac{\omega_i}{|V_g|} dx \quad (8.3.3)$$

Here  $x_0$  corresponds to the  $x$ -location where the amplification rate is zero.

Mack [15] uses spatial amplification theory and a different eigenvalue procedure that is restricted to infinite swept wings. In this formulation, he assumes the spanwise wave number  $\beta$  is real, thus allowing the wave to grow only in the chordwise direction. The value of  $\beta$  is obtained from the irrotationality condition applied to the complex wave number vector which, for an infinite swept wing, requires that the dimensional spanwise wave number  $\beta^*$  remains constant as the wave moves downstream. With these assumptions, the problem reduces to the calculation of the complex chordwise wave number  $\alpha$  at each chordwise position for the specified dimensional values of  $\beta$  and  $\omega$ . Arnal et al. [16] have improved this procedure by maximizing the amplification rate  $\alpha_i$  with respect to  $\beta_r$ . More specifically, they solved the stability equations for initial estimates of  $\alpha_r$ ,  $\alpha_i$  for a given  $\beta_r$  and specified  $\omega^*/2\pi$  and  $R$ . After convergence,  $\alpha_r$  and  $\alpha_i$  are computed for different values of  $\beta_r$  in order to find the maximum value of  $\alpha_i$  so that the onset of transition can be calculated from Eq. (5.4.8).

The eigenvalue formulation of Cebeci and Stewartson [17] is also based on the spatial amplification theory but differs from the approaches of Mack [15] and Arnal et al. [16] in that the relationship between the two wave numbers  $\alpha$  and  $\beta$  is not assumed but is computed by making use of concepts based on group velocity using the saddle-point discussed by Cebeci and Stewartson [17] and Nayfeh [18]. We assume the disturbance to be of the form given by Eq. (5.3.14), that is,

$$q'(x, y, z, t) = q(y) e^{i(\alpha x + \beta z - \omega t)} \quad (5.3.14)$$

We use spatial amplification theory and consider a wave packet made of disturbances of all possible waves of given frequency. The wave packet disturbance is

$$Q = \int_c q(y) e^{i(\alpha x + \beta z - \omega t)} d\beta \quad (8.3.4)$$

where  $c$  is a contour in the complex volume of  $\beta$ , extending to  $\infty$  in either direction. Noting that at a given spatial location and for a given frequency

$$\alpha = \alpha(\beta)$$

we can write Eq. (8.3.4) as

$$Q = \int q(y) e^{ix[\alpha(\beta) + \beta \frac{z}{x} - \frac{\omega}{x} t]} d\beta$$

For large values of  $x$  (assuming that  $z/x$  is given), the saddle point method (or the stationary phase method) requires that the leading contribution to  $Q$  is obtained when the phase of the exponential term is stationary. This means that the derivative of the phase with respect to  $\beta$  is zero, that is,

$$\left( \frac{\partial \alpha}{\partial \beta} \right)_{\omega, R} + \frac{z}{x} = 0$$

or

$$\left( \frac{\partial \alpha}{\partial \beta} \right)_{\omega, R} = -\frac{z}{x} \quad (8.3.5)$$

Since  $x$  and  $z$  are real, the imaginary part of  $(\partial \alpha / \partial \beta)_{\omega, R}$  must be zero to satisfy Eq. (8.3.5). According to the saddle point method, the real part of  $(\partial \alpha / \partial \beta)_{\omega, R}$  is related to the disturbance angle  $\phi$

$$\left( \frac{\partial \alpha}{\partial \beta} \right)_{\omega, R} = -\tan \phi \quad (8.3.6)$$

The above relation provides the wave orientation and growth direction of the disturbance. This can be used to relate the two wave numbers  $\alpha$  and  $\beta$  to each other as needed in the eigenvalue problem. The angle  $\phi$  in Eq. (8.3.6) is also the direction of the group velocity  $\vec{V}_g$ , since

$$\left( \frac{\partial \alpha}{\partial \beta} \right)_{\omega, R} = -\frac{\left( \frac{\partial \omega}{\partial \beta} \right)_{\alpha, R}}{\left( \frac{\partial \omega}{\partial \alpha} \right)_{\beta, R}} \quad (8.3.7)$$

We observe that with  $\alpha$  and  $\beta$  defined by Eq. (8.3.6), the magnitude of the disturbance at  $(x, z)$  (see Eq. (5.3.14)) is dominated by the exponential factor

$$\exp[-(\alpha_i x + \beta_i z)]$$

and, the disturbances are damped with increasing  $x$  if the amplification rate  $\Gamma$  defined by

$$\Gamma \equiv \alpha_i - \beta_i \left( \frac{\partial \alpha}{\partial \beta} \right)_{\omega, R} \quad (8.3.8)$$

is  $> 0$ , neutral if  $\Gamma = 0$ , and amplified when  $\Gamma < 0$ . In the eigenvalue procedure of Cebeci and Stewartson [17], once  $\alpha$  and  $\beta$  are computed subject to the requirements of Eq. (8.3.6), additional calculations are then made for different values of  $\partial \alpha / \partial \beta$  to determine the maximum amplification rate,  $\Gamma$ . In accordance with the  $e^n$ -method, the values of  $\Gamma(x)$  are then integrated to find the value of  $n$  for the specified frequency. As in two-dimensional flows, this process is repeated for different dimensional frequencies to find the critical frequency that leads to the highest integrated amplification rate. In their use of this eigenvalue procedure for a rotating disk, Cebeci and Stewartson [17] fixed the direction of the disturbance angle  $\phi$  as computed on the three-dimensional neutral stability curve called *zarf* discussed below and did not maximize it during the calculations. However, as discussed in Section 8.5,  $\Gamma$  can vary considerably with  $\phi$  and must be maximized.

### 8.3.2 The Zarf

As discussed in subsection 5.4.2, the  $e^n$ -method calculations for two-dimensional flow begin on the lower branch of the neutral stability curve where at first a dimensional frequency is obtained to perform the amplification rate calculations. It is plausible to assume that the  $e^n$ -method calculations for three-dimensional flows should also begin on a neutral curve and be used to compute the dimensional frequencies needed in the calculation of amplification rates as in two-dimensional flows. The precise definition or extension of a neutral stability curve for three-dimensional flows has not, however, been formally discussed and used in the literature except in the work of Cebeci and Stewartson [17]. It may be expected that a neutral stability curve for three-dimensional flows can be found for any chosen value of, say,  $\beta/\alpha$  as a curve in the three-dimensional space of  $\alpha, \omega, R$  but, as discussed by Cebeci and Stewartson [17], it will not penetrate to values of  $R$  as low as the critical Reynolds number  $R_{cr}$ . Only for one value of  $\beta/\alpha$  will this lower bound be achieved. The plethora of neutral curves can cause some complication and it is convenient to isolate a special curve which in some sense mimics their principal properties. An obvious choice is the envelope of the neutral curves, which we may think of as the *absolute neutral curve* in that it is independent of  $\beta/\alpha$ , or to give it a short evocative name we shall name it to be the *zarf* (lit. envelope, Turk.). This curve, first introduced by Cebeci and Stewartson [17], passes through the critical point in  $\alpha, \beta, \omega, R$  space at which  $R = R_{cr}$  and is of significant importance in the calculation of transition, as we shall see later. It also has a number of interesting properties. The first and most important of these is that along the *zarf*.

$$\alpha, \beta, \text{ and } \frac{\partial \alpha}{\partial \beta} \text{ are all real} \quad (8.3.9)$$

In order to see this, let us consider the Orr–Sommerfeld equation and its boundary conditions for three-dimensional incompressible flows, Eqs. (5.3.16), (5.3.18) and (5.3.20), and represent the solution as

$$\omega = F(\alpha, \lambda, R), \quad \lambda = \beta/\alpha \quad (8.3.10)$$

and the real and imaginary parts of  $F$  by  $F_r$  and  $F_i$ .

For a point on the neutral curve at fixed  $\lambda$ ,  $F_i(\alpha, \lambda, R) = 0$ . Let us make small changes  $d\alpha$ ,  $d\lambda$ ,  $dR$  in  $\alpha, \lambda, R$  at a point of the zarf. We have for the change in  $d\omega$

$$d\omega = F_{r\alpha}d\alpha + F_{r\lambda}d\lambda + F_{rR}dR \quad (8.3.11)$$

where the subscripts  $\alpha$ ,  $\lambda$  and  $R$  denote differentiation with respect to the variable. Also  $d\alpha$ ,  $d\lambda$ ,  $dR$  are connected by

$$0 = F_{i\alpha}d\alpha + F_{i\lambda}d\lambda + F_{iR}dR \quad (8.3.12)$$

since  $F_i = 0$ . Thus eliminating  $d\alpha$

$$d\omega = \left( F_{r\lambda} - \frac{F_{r\alpha}F_{i\lambda}}{F_{i\alpha}} \right) d\lambda + \left( F_{rR} - \frac{F_{r\alpha}F_{iR}}{F_{i\alpha}} \right) dR \quad (8.3.13)$$

But  $d\omega$  does not depend on  $d\lambda$  on an envelope since adjacent neutral curves touch, so

$$F_{r\lambda}F_{i\alpha} = F_{r\alpha}F_{i\lambda} \quad (8.3.14)$$

on the zarf.

For general values of  $\alpha$ ,  $\lambda$ ,  $R$ , Eq. (8.3.10) can be regarded as defining  $\alpha$  as a function of  $\lambda$  for fixed  $R$  and  $\omega$ , and then it can be shown that Eq. (8.3.14) is equivalent to requiring  $\partial\alpha/\partial\lambda$  to be real. Since  $\beta = \alpha\lambda$ , this condition is equivalent in turn to requiring

$$\left( \frac{\partial \alpha}{\partial \beta} \right)_{\omega, R} = \text{a real number} \quad (8.3.15)$$

Some interesting properties of the zarf have been computed by Cebeci and Stewartson for yawed stagnation and Blasius flows [19, 20]. Figure 8.2 shows the projections of the zarf  $(\alpha_r, R)$ ,  $(\beta_r, R)$  and  $(\omega, R)$  planes based on the solution of Eq. (5.3.16) together with the neutral curves for Blasius flow based on the solution of Eq. (5.3.13). We note that the upper branch of the zarf coincides with that of the neutral curve for two-dimensional flows, but on the lower branch of the zarf bifurcation from the neutral curve occurs at  $R = 703$  where  $\alpha = 0.2132$  and  $\omega = 0.0438$ . As discussed in [20], on the lower branch of the zarf,  $R\alpha$ ,  $R\omega$  and  $|\beta|$  approach a finite limit of 149.1, 53.0 and 0.212, respectively, as  $R \rightarrow \infty$ .

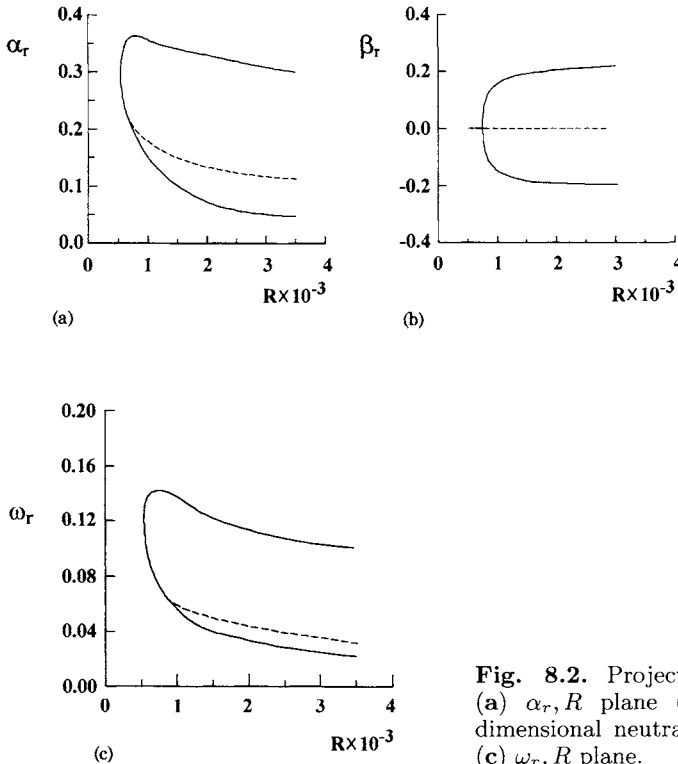


**Fig. 8.2.** Projection of the zarf on the (a)  $\alpha_r, R$  plane (dashed line is the two-dimensional neutral curve), (b)  $\beta_r, R$  plane, (c)  $\omega_r, R$  plane.

In incompressible flows, near the leading edge of the wing where  $u_e = Ax$ , the boundary-layer equations are given by the Falkner–Skan–Cooke equations, Eqs. (7.5.12) and (7.5.13), for  $m = 1$ , that is,

$$f''' + f f'' - (f')^2 + 1 = 0 \quad (8.3.16a)$$

$$g''' + f g'' = 0 \quad (8.3.16b)$$

and their boundary conditions given by

$$\eta = 0, \quad f = f' = g = g' = 0, \quad \eta \rightarrow \eta_e, \quad f' \rightarrow 1, \quad g' \rightarrow 1 \quad (8.3.16c)$$

Figure 8.3 shows the zarfs for the attachment line flow. In the stability calculations, the length scale in Eq. (5.3.5) with  $u_e = Ax$  was chosen to correspond to  $\sqrt{\nu/A}$  and the characteristic velocity to be  $w_e$  with  $R$  then defined as

$$R = \sqrt{R_x}/b, \quad R_x = u_e x/\nu, \quad b = \frac{u_e}{w_e} \quad (8.3.17)$$

We note from Fig. 8.3a that  $\alpha_r$  is zero for all values of  $R$  less than 795 and that bifurcation for  $\beta_r$ , Fig. 8.3b, occurs at this Reynolds number and differs from its two-dimensional form as shown by the dashed line. As discussed in [21],  $\beta R$ ,  $\omega R$  and  $|\alpha|$  approach a finite limit of 161.0 and 55.81 and 0.2025 as

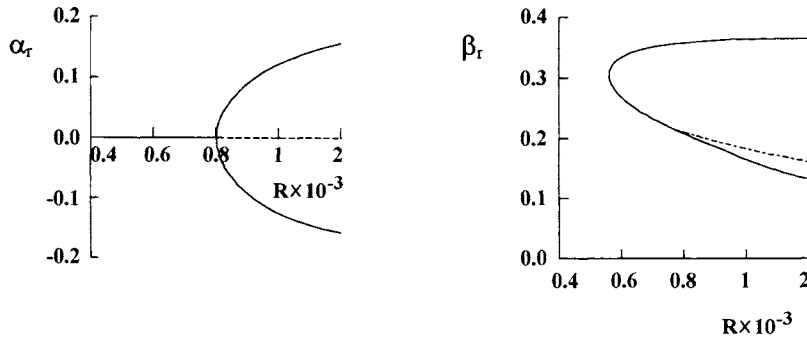


**Fig. 8.3.** Zarf plots for the attachment-line flow. Dashed lines denote two-dimensional flow.

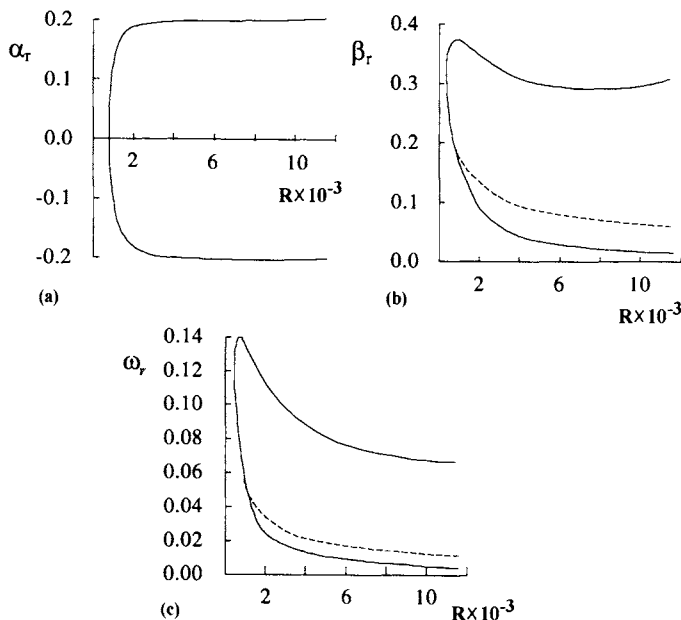


**Fig. 8.4.** Behavior of the zarf for the attachment-line flow at high Reynolds number.

$R \rightarrow \infty$ . Figure 8.4 shows the variation of  $\alpha_r$ ,  $\beta_r$  and  $\omega$  at higher values of  $R$  and indicates good agreement between the calculations and those predicted by asymptotic analysis.

## 8.4 Numerical Solution of the Orr–Sommerfeld Equation for Three-Dimensional Flows

As discussed in [22], the numerical solution of Eqs. (5.3.15), (5.3.18) and (5.3.20) is similar to the solution of Eqs. (5.3.13), (5.3.18) and (5.3.20). The finite-

difference approximations, Eqs. (5.6.3), boundary conditions, Eqs. (5.6.5b) and (5.6.7), remain the same, and the linear system can be expressed in the same form as Eq. (4.5.23) with relations given by Eqs. (5.6.8) and (5.6.9) remaining the same. The solution of Eq. (4.5.23) can again be obtained with the same block-elimination method, with the solution now depending on four parameters  $\alpha$ ,  $\beta$ ,  $\omega$  and  $R$  rather than three parameters  $\alpha$ ,  $\omega$  and  $R$  in two-dimensional flows as indicated by Eq. (5.6.13).

Recalling that  $\alpha$  and  $\beta$  are complex and that  $\omega$  is real in spatial amplification theory, the solution of Eq. (4.5.23) depends upon six scalars  $(\alpha_r, \alpha_i, \beta_r, \beta_i, \omega, R)$ . With any four of these scalars fixed, the remaining two scalars can be computed in such a way that the missing boundary condition

$$f_0(\alpha, \beta, \omega, R) = 0 \quad (5.6.11)$$

is satisfied. Similarly, for temporal amplification theory, the solution of Eq. (4.5.23) depends upon five scalars  $(\alpha, \beta, \omega_r, \omega_i, R)$ . In either case, a relationship or an assumption between the two complex wave numbers  $\alpha_r$  and  $\beta_r$  is needed if  $\omega$  and  $R$  are fixed as discussed in subsection 8.4.1 for the zarf and in subsection 8.4.2 for predicting transition.

#### 8.4.1 Eigenvalue Procedure for Zarf

In the Cebeci–Stewartson eigenvalue formulation, the relationship between the two complex wave numbers  $\alpha$  and  $\beta$  is obtained from the saddle-point method, and, for the zarf, it is given by Eq. (8.3.9). Since  $\alpha_i$  and  $\beta_i$  are zero on the zarf, Eq. (5.6.11) contains three unknowns  $(\alpha_r, \beta_r, \omega)$  for a given  $R$ , and an additional equation is needed. This equation can be obtained by first expanding Eq. (5.6.11) with  $\omega$  constant. Neglecting the subscript  $o$  of  $f$  for convenience, we write

$$df = \left( \frac{\partial f}{\partial \alpha} \right)_\beta d\alpha + \left( \frac{\partial f}{\partial \beta} \right)_\alpha d\beta = 0 \quad (8.4.1)$$

Solving Eq. (8.4.1) for  $d\alpha/d\beta$ , we get

$$\left( \frac{d\alpha}{d\beta} \right)_\omega = -\frac{\partial f / \partial \beta}{\partial f / \partial \alpha} = e \quad (8.4.2)$$

Expanding Eq. (5.6.11) about  $\alpha^\nu$ ,  $\beta^\nu$  and  $\omega^\nu$  and retaining only the linear terms in the expansion, and after separating the real and imaginary parts of the resulting expression, we get

$$f_r^\nu + \left( \frac{\partial f}{\partial \alpha} \right)_r^\nu \delta\alpha + \left( \frac{\partial f}{\partial \beta} \right)_r^\nu \delta\beta + \left( \frac{\partial f}{\partial \omega} \right)_r^\nu \delta\omega = 0 \quad (8.4.3a)$$

$$f_i^\nu + \left( \frac{\partial f}{\partial \alpha} \right)_i^\nu \delta\alpha + \left( \frac{\partial f}{\partial \beta} \right)_i^\nu \delta\beta + \left( \frac{\partial f}{\partial \omega} \right)_i^\nu \delta\omega = 0 \quad (8.4.3b)$$

Similar to Eq. (5.6.11), we now expand Eq. (8.4.2) to obtain

$$e^\nu + \left( \frac{\partial e}{\partial \alpha} \right)^\nu \delta \alpha + \left( \frac{\partial e}{\partial \beta} \right)^\nu \delta \beta + \left( \frac{\partial e}{\partial \omega} \right)^\nu \delta \omega = 0 \quad (8.4.4)$$

valid only for the imaginary part. Since we are interested in the values of  $\alpha$ ,  $\beta$  and  $\omega$  for which the imaginary part of  $(d\alpha/d\beta)$  or  $e_i$  is zero, from Eq. (8.4.4) we can write

$$e_i^\nu + \left( \frac{\partial e_i}{\partial \alpha} \right)^\nu \delta \alpha + \left( \frac{\partial e_i}{\partial \beta} \right)^\nu \delta \beta + \left( \frac{\partial e_i}{\partial \omega} \right)^\nu \delta \omega = 0 \quad (8.4.5)$$

Solving Eqs. (8.4.3) and (8.4.5), we write  $\delta\alpha$ ,  $\delta\beta$ , and  $\delta\omega$  as:

$$\delta\alpha = \frac{1}{\Delta_1} [-f^r(f_\beta^i e_\omega^i - f_\omega^i e_\beta^i) + f^i(f_\beta^r e_\omega^i - e_\beta^i f_\omega^r) - e^r(f_\beta^r f_\omega^i - f_\omega^r f_\beta^i)] \quad (8.4.6a)$$

$$\delta\beta = \frac{1}{\Delta_1} [f_\alpha^r(-f^i e_\omega^i + e^i f_\omega^i) - f_\alpha^i(-f^r e_\omega^i + e^i f_\omega^r) + e_\alpha^i(-f^r f_\omega^i + f^i f_\omega^r)] \quad (8.4.6b)$$

$$\delta\omega = \frac{1}{\Delta_1} [f_\alpha^r(-f_\beta^i e^i + f^i e_\beta^i) - f_\alpha^i(-f_\beta^r e^i + f^r e_\beta^i) + e_\alpha^i(-f_\beta^r f^i + f^r f_\beta^i)] \quad (8.4.6c)$$

$$\Delta_1 = e_\alpha^i(f_\beta^r f_\omega^i - f_\beta^i f_\omega^r) - e_\beta^i(f_\alpha^r f_\omega^i - f_\alpha^i f_\omega^r) + e_\omega^i(f_\alpha^r f_\beta^i - f_\alpha^i f_\beta^r) \quad (8.4.7)$$

For simplicity we have dropped the superscripts  $\nu$  and  $\nu + 1$ , and denoted the real and imaginary parts of  $f$ ,  $f_\alpha (\equiv \partial f / \partial \alpha)$ ,  $f_\beta (\equiv \partial f / \partial \beta)$ ,  $f_\omega (\equiv \partial f / \partial \omega)$ ,  $e_\alpha (\equiv \partial e / \partial \alpha)$ ,  $e_\beta (\equiv \partial e / \partial \beta)$ ,  $e_\omega (\equiv \partial e / \partial \omega)$  by superscripts  $r$  and  $i$ . We note from Eq. (8.4.5) that if  $\delta\alpha$ ,  $\delta\beta$  and  $\delta\omega$  are all zero, then  $e_i$  is zero and  $e$  is real.

To calculate the derivative of  $e$  with respect to  $\alpha$ ,  $\beta$  and  $\omega$ , we make use of Eq. (8.4.2), rewritten as

$$e = -\frac{f_\beta}{f_\alpha} \quad (8.4.8)$$

Differentiating with respect to  $\beta$ , we get

$$e_\beta = -\frac{f_{\beta\beta}}{f_\alpha} + \frac{f_\beta}{f_\alpha^2} f_{\alpha\beta} \quad (8.4.9a)$$

Similarly,

$$e_\alpha = -\frac{f_{\beta\alpha}}{f_\alpha} + \frac{f_\beta}{f_\alpha^2} f_{\alpha\alpha} \quad (8.4.9b)$$

$$e_\omega = -\frac{f_{\beta\omega}}{f_\alpha} + \frac{f_\beta}{f_\alpha^2} f_{\alpha\omega} \quad (8.4.9c)$$

Note from Eqs. (8.4.6) and (8.4.9) that the calculations of  $\delta\alpha$ ,  $\delta\beta$  and  $\delta\omega$  require the calculations of  $f_{\alpha\beta}$ ,  $f_{\alpha\alpha}$ ,  $f_{\beta\omega}$ ,  $f_{\beta\beta}$  and  $f_{\alpha\omega}$ , which can be obtained by differentiating Eq. (4.5.23) with respect to appropriate eigenvalues. For example, to find the eigenfunction  $f_{\alpha\beta}$ , we differentiate Eq. (4.5.23) first with respect to  $\alpha$ , then with respect to  $\beta$ .

$$A \left( \frac{\partial^2 \vec{\delta}}{\partial \alpha \partial \beta} \right)^\nu = - \frac{\partial A}{\partial \beta} \left( \frac{\partial \vec{\delta}}{\partial \alpha} \right)^\nu - \frac{\partial A}{\partial \alpha} \left( \frac{\partial \vec{\delta}}{\partial \beta} \right)^\nu - \frac{\partial^2 A}{\partial \alpha \partial \beta} \vec{\delta}^\nu \quad (8.4.10)$$

The above equation is the variational form of Eq. (4.5.23) with respect to  $\alpha$  and  $\beta$ . Thus, to obtain the required derivative  $f_{\alpha\beta}$ , Eq. (8.4.10) must be solved with the same coefficient matrix  $A$  already computed and factored for Eq. (4.5.23). The vectors on the right-hand side of Eq. (8.4.10) are determined from Eqs. (5.6.3), (5.6.7) and (5.6.5b). The eigenfunctions  $f_\alpha$  and  $f_\beta$  are obtained from the solutions of the variational equations with respect to  $\alpha$  and  $\beta$ , that is,

$$A \left( \frac{\partial \vec{\delta}}{\partial \alpha} \right)^\nu = - \left( \frac{\partial A}{\partial \alpha} \right) \vec{\delta}^\nu, \quad A \left( \frac{\partial \vec{\delta}}{\partial \beta} \right)^\nu = - \left( \frac{\partial A}{\partial \beta} \right) \vec{\delta}^\nu \quad (8.4.11)$$

To find the variational equations with respect to  $\alpha\alpha$ ,  $\beta\beta$ ,  $\alpha\omega$  and  $\beta\omega$ , a similar procedure is followed. For example, to find those for  $\alpha\alpha$ , Eq. (4.5.23) is differentiated twice with respect to  $\alpha$

$$A \left( \frac{\partial^2 \vec{\delta}}{\partial \alpha^2} \right)^\nu = -2 \frac{\partial A}{\partial \alpha} \left( \frac{\partial \vec{\delta}}{\partial \alpha} \right)^\nu - \frac{\partial^2 A}{\partial \alpha^2} \vec{\delta}^\nu \quad (8.4.12)$$

To summarize one step of the calculation of the eigenvalues of the zarf, we first solve Eq. (4.5.23) for initial estimates of  $\alpha$ ,  $\beta$  and  $\omega$ . If the computed value of  $f_0$  does not satisfy Eq. (5.6.11), then appropriate variational equations are solved in order to calculate the increments in  $\alpha$ ,  $\beta$  and  $\omega$  from Eqs. (8.4.6) so that new estimates of  $\alpha$ ,  $\beta$  and  $\omega$  can be obtained that will satisfy Eq. (5.6.11) and make  $e$  real. This procedure is repeated until convergence is achieved. Since the eigenvalue formulation is based on Newton's method, the calculations usually indicate quadratic convergence provided that initial guesses are good estimates.

#### 8.4.2 Eigenvalue Procedure for Transition

With  $\omega$  known from the specified dimensional frequency and  $R$  given, and with  $e_r$  fixed (equal to its value at zarf, say at  $R_1$ ), we solve Eq. (4.5.23) for initial estimates of  $\alpha$  and  $\beta$  to get a solution at  $R = R_2$ . To obtain the next values of  $\alpha$  and  $\beta$ , we use Newton's method in which we expand  $f$  and  $e$  in Eqs. (5.6.11) and (8.4.2).

$$f_0 + \left( \frac{\partial f}{\partial \alpha} \right)_0 \delta \alpha + \left( \frac{\partial f}{\partial \beta} \right)_0 \delta \beta = 0 \quad (8.4.13a)$$

$$e_0 + \left( \frac{\partial e}{\partial \alpha} \right)_0 \delta \alpha + \left( \frac{\partial e}{\partial \beta} \right)_0 \delta \beta = e = \text{given} \quad (8.4.13b)$$

Solving for  $\delta\alpha$  and  $\delta\beta$ , we get

$$\delta\alpha = -\frac{1}{\Delta_0} [f_0 e_\beta + f_\beta (e - e_0)] \quad (8.4.14a)$$

$$\delta\beta = \frac{1}{\Delta_0} [f_\alpha (e - e_0) + f_0 e_\alpha] \quad (8.4.14b)$$

where

$$\Delta_0 = f_\alpha e_\beta - f_\beta e_\alpha \quad (8.4.15)$$

As before,  $f_\alpha$ ,  $f_\beta$ ,  $e_\alpha$  and  $e_\beta$  are determined by solving the variational equations with respect to  $\alpha$ ,  $\beta$ ,  $\alpha\alpha$ ,  $\alpha\beta$  and  $\beta\beta$ . This procedure is repeated until  $\delta\alpha$  and  $\delta\beta$  are less than a specified tolerance parameter. Upon convergence, the amplification parameter  $\Gamma$  is computed from Eq. (8.3.8). Since the calculation of  $\Gamma$  assumes that the value of  $e$  on the right-hand side of Eq. (8.3.6) is fixed by the value it takes on the zarp, we compute a new value of  $e$  and subsequently a new  $\phi$  for which  $\Gamma$  is minimum, and this is achieved by assigning a new value of  $e$ . After convergence, we again compute  $\Gamma$  from Eq. (8.3.8) and test to see whether  $\Gamma$  is increasing or decreasing. Since a positive  $\Gamma$  implies that disturbances are damped, we can increment  $e$  until a minimum value of  $\Gamma$  is computed.

## 8.5 Application of the $e^n$ -Method with Saddle-Point Eigenvalue Formulation

The  $e^n$ -method with various eigenvalue formulations discussed in subsection 8.3.1 has been applied to three-dimensional flows in order to explore its accuracy. The studies conducted for limited data discussed in this chapter show that, in general, the  $e^n$ -method employing the saddle-point eigenvalue formulation of Cebeci and Stewartson predicts the onset of transition with an accuracy that is sufficient for most engineering problems of interest. In this section we demonstrate the accuracy of this method for the infinite swept wing data of Arnal and Juillen [23] in subsection 8.5.1 and for the prolate spheroid data of Meier and Kreplin [24] in subsection 8.5.2.

### 8.5.1 Infinite Swept Wing Data of Arnal and Juillen

The measurements for the infinite swept wing data of Arnal and Juillen were obtained in the F2 wind tunnel at Le Fauga-Mauzac Center. The model had an ONERA D airfoil section, symmetric between  $x/c = 0.20$  and  $x/c = 1$  and equipped with a cambered leading edge (Fig. 8.5a), so that the pressure distributions differed from those observed on the classical ONERA D profile. The chord normal to the leading edge was 300 mm and the span 900 mm. The wing and the half-fuselage were mounted on a turntable. The experimental arrangement is sketched in Fig. 8.5b. Three kinds of experiments were performed so that pressure distribution measurements, flow visualizations by sublimation

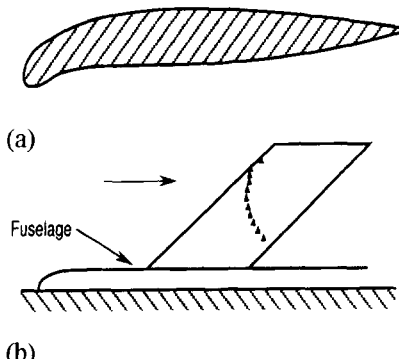


**Fig. 8.5.** ONERA-D airfoil with a cambered leading-edge: experimental setup.

technique, and hot-film measurements were obtained. Ten hot-films were glued on the model, from 2.5 to 86 percent of chord, and recorded simultaneously for more than one hundred combinations of the wind tunnel speed, angle of sweep, and angle of attack. The positions of the hot-films are indicated on Fig. 8.5b and were chosen to avoid interactions between probes. These results were verified by comparing the transition positions obtained by the hot-film records and by the flow visualization (in the absence of hot-films): the results were similar. Three angles of sweep ( $\lambda = 49^\circ, 55^\circ$  and  $61^\circ$ ) and four angles of attack ( $\alpha = 0^\circ, -2^\circ, -4^\circ$  and  $-6^\circ$ ) were studied, and typical freestream velocity distributions are plotted in Fig. 8.6; due to the presence of the cambered leading edge, the curves exhibit a complex evolution in the negative pressure gradient region.

The stability-transition calculations start with the solution of the boundary-layer equations for an incompressible laminar flow over an infinite swept wing. The equations in transformed form are given by Eqs. (7.5.14) and (7.5.15) with  $b = 1$ .

For a given external velocity distribution and freestream conditions, the computer program of Chapter 4 or 7 can be used to obtain the solution of the above equations subject to

$$\eta = 0, \quad f = f' = g = g' = 0 \quad (8.5.1a)$$

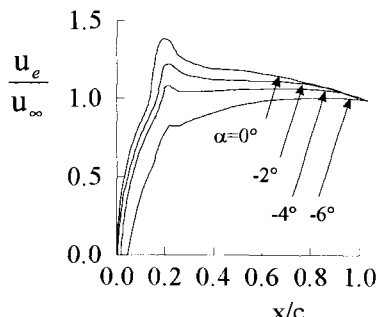


**Fig. 8.6.** Typical measured velocity distributions (suction side).

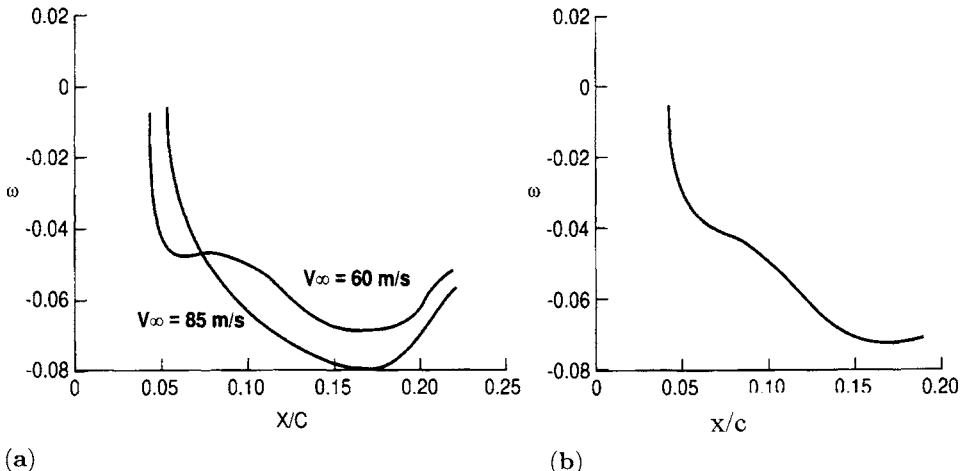


**Fig. 8.7.** Variation of  $\omega$  on zarf near the leading edge: (a)  $\lambda = 49^\circ$ ,  $V_\infty = 60 \text{ ms}^{-1}$ ,  $85 \text{ ms}^{-1}$ ,  $\alpha = 0^\circ$ ; and (b)  $\lambda = 49^\circ$ ,  $V_\infty = 60 \text{ ms}^{-1}$ ,  $\alpha = -2^\circ$ .

$$\eta = \eta_e, \quad f' = 1, \quad g' = 1 \quad (8.5.1b)$$

With velocity profiles known, the stability/transition calculations then begin on the zarf where the eigenvalue problem is solved subject to the requirements given in Eq. (8.3.9). Once the eigenvalues of the zarf are computed at a specified  $R$ , the calculation of the eigenvalues of the zarf at the next Reynolds number are computed as described in [25].

Figure 8.7a shows the variation of zarf  $\omega$  near the leading edge of the wing for  $\lambda = 49^\circ$ ,  $V_\infty = 60 \text{ ms}^{-1}$  and  $85 \text{ ms}^{-1}$  at  $\alpha = 0^\circ$ , and in Fig. 8.7b its variation is shown for  $\lambda = 49^\circ$ ,  $V_\infty = 60 \text{ ms}^{-1}$ , at  $\alpha = -2^\circ$ . As can be seen, the lower branch of the  $\omega$ -zarf is negative with relatively flat values of  $\omega$  away from the leading edge, whereas  $\omega$  undergoes a very rapid variation near  $x/c = 0.04$  and  $0.05$ . Figures 8.8a and 8.8b show that  $\omega$  becomes positive and increases rapidly around  $x/c = 0.04$  for  $\alpha = 0^\circ$ ,  $V_\infty = 60 \text{ ms}^{-1}$ , and around  $x/c = 0.05$  for  $\alpha = -2^\circ$ ,  $V_\infty = 85 \text{ ms}^{-1}$ . This behavior of  $\omega$  near the leading edge is very important since the  $e^n$ -method requires the calculation of the frequency that leads to the greatest amplification rate  $\Gamma$ . An accurate calculation of this frequency and its location is crucial to the accuracy of calculating the transition location.

Once the eigenvalues of the zarf are computed at a specified  $x/c$ -location, we proceed to the next  $x/c$ -station to solve the eigenvalue problem of subsection 8.4.2 for a specified dimensional  $\omega$  determined on the zarf with the assumption that  $\partial\alpha/\partial\beta$  is given by its value at the previous  $x/c$ -location, which amounts to specifying the disturbance angle  $\phi$ . The amplification rate  $\Gamma$  is computed according to Eq. (8.3.8), and then for different values of the eigenvalue procedure for  $\alpha$  and  $\beta$  is repeated to find the value of  $\phi$  for which  $\Gamma$  is minimum. Once it

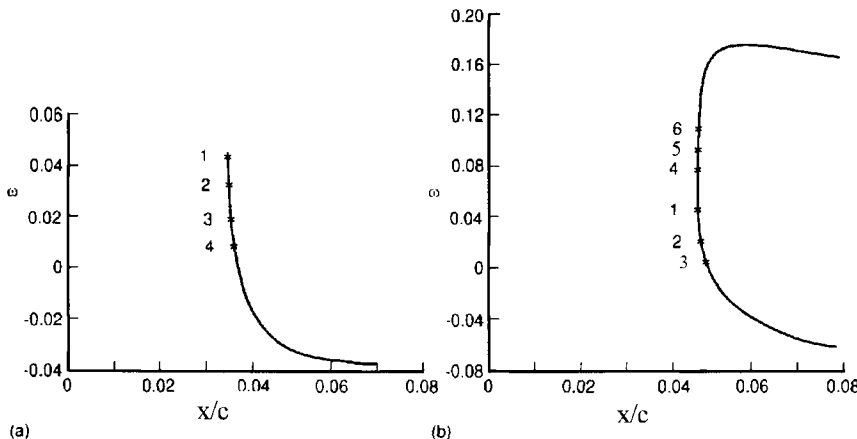


**Fig. 8.8.** Variation of  $\omega$  on zarf very close to the leading edge for (a)  $\alpha = 0^\circ$ ,  $V_\infty = 60 \text{ ms}^{-1}$ ; and (b)  $\alpha = -2^\circ$ ,  $V_\infty = 85 \text{ ms}^{-1}$ .

is determined, we proceed to the next  $x/c$ -station and compute new values of  $\alpha$ ,  $\beta$  to determine  $\Gamma$  and repeat the procedure to obtain its minimum value.

The above procedure is for one value of frequency  $\omega$  chosen at a certain  $x/c$ -location. As in two-dimensional flows, it is repeated for different values of  $\omega$  computed for a zarf at different  $x/c$ -locations. Since the frequency near the leading edge of the wing varies drastically, it is important to choose these  $x/c$ -locations carefully. Figures 8.8a and 8.9a show the computed frequencies and the resulting integrated amplification rates  $n$  for four different frequencies for  $\lambda = 49^\circ$ ,  $\alpha = 0^\circ$ ,  $V_\infty = 60 \text{ ms}^{-1}$ . As can be seen, the computed amplification rates originate at nearly the same  $x/c$ -location and amplify differently depending on the choice of the frequency and may give different predictions of transition. Figures 8.8b and 8.9b show a similar behavior for  $\lambda = 49^\circ$ ,  $\alpha = -2^\circ$ ,  $V_\infty = 85 \text{ ms}^{-1}$  and indicate clearly that the amplification rates computed with frequencies denoted by 1 and 4 lead to results which are substantially different from those computed with others.

In [25], the accuracy of the above procedure for computing transition was investigated for thirteen cases of which, seven were for a sweep angle  $\lambda = 49^\circ$ , three were for  $\lambda = 55^\circ$ , and three were for  $\lambda = 61^\circ$ . Calculated and experimental results shown in Fig. 8.10 indicate that the predictions of the  $e^n$ -method with  $n = 8$  are generally in good agreement with the experimental data.

### 8.5.2 Prolate Spheroid Data of Meier and Kreplin

The measurements for the prolate spheroid data of Meier and Kreplin [24] were obtained for a thickness ratio of one to six at an incidence angle of  $10^\circ$ . The application of the  $e^n$ -method to this configuration is considerably more difficult than the infinite swept configuration discussed in the previous subsection.

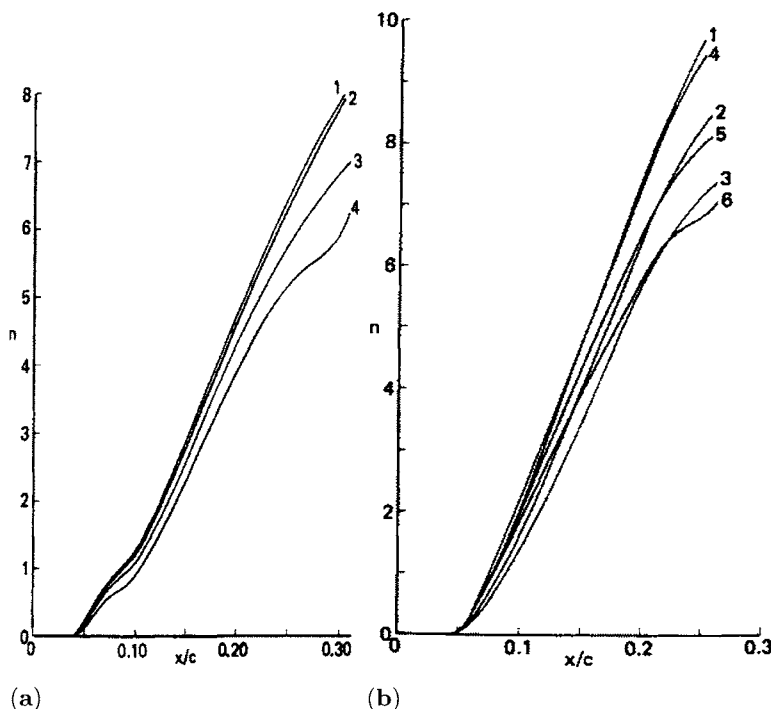


**Fig. 8.9.** Variation of the amplification factors for the frequencies of (a) Fig. 8.8a and (b) Fig. 8.8b.

The boundary-layer calculations are fully three-dimensional for this flow and the spanwise similarity assumption used for the infinite swept wing does not apply. In addition, on this body there are regions where both streamwise and circumferential velocity profiles ( $u$  and  $w$ ), respectively, are positive, regions where  $u$  is positive but  $w$  is negative and regions where both  $u$  and  $w$  are negative. Fortunately, for this flow the onset of transition occurs before flow separation and as a result it is sufficient to perform the boundary-layer calculations with a standard boundary-layer method rather than an inverse boundary-layer method. The standard method, on the other hand, should be able to handle negative circumferential velocities with accuracy since the accuracy of the stability calculations depend not only on the eigenvalue formulation but also on the accuracy of the velocity profiles provided by the boundary-layer method.

In the study reported in [26], the boundary-layer calculations were performed with the numerical method described in Section 7.6 for a grid with nonuniform step lengths in the circumferential ( $\theta$ ) and streamwise ( $x$ ) directions. The step lengths in both directions were chosen to ensure the accuracy of the velocity profiles in the streamwise and circumferential directions to be used in the solution of the Orr–Sommerfeld equation as discussed below.

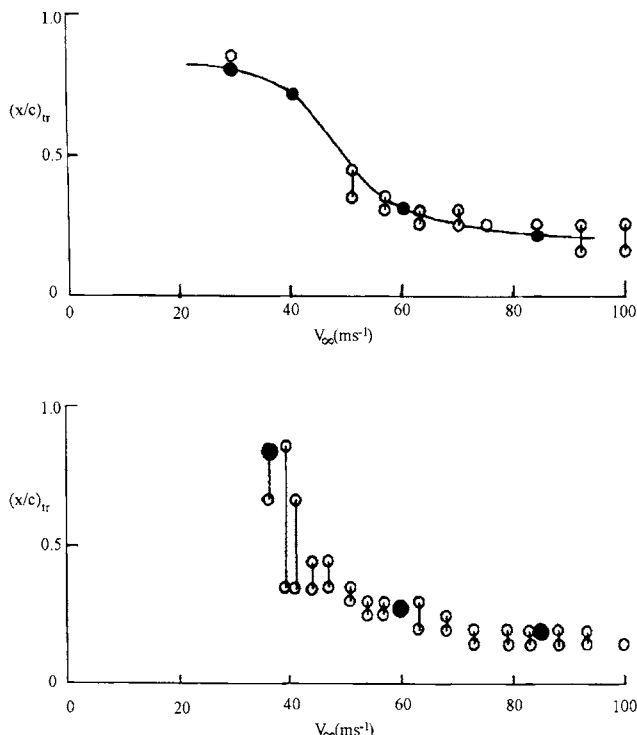


**Fig. 8.10.** Experimental (open symbols) and calculated (closed symbols) transition locations for (a)  $\lambda = 49^\circ$ ,  $\alpha = -2^\circ$  and (b)  $\lambda = 55^\circ$ ,  $\alpha = -2^\circ$ .

### Line of Symmetry

The stability-transition calculations for the windward and leeward lines of symmetry where  $\theta = 0^\circ$  and  $180^\circ$ , respectively, are somewhat similar to the calculation of transition in two-dimensional flows. The stability-transition calculations for off-the-line of symmetry, however, require the calculation of the amplification rates  $\Gamma$  in which  $\alpha_i$  and  $\beta_i$  are determined as a function of  $\xi$  ( $\equiv x/a$ ),  $\theta$  as the disturbance moves from  $(\xi_1, \theta_1)$  corresponding to the zarp to  $(\xi, \theta)$ . Thus, at each point of the path,  $\alpha_i$  and  $\beta_i$  are computed as a function  $(\xi, \theta)$ . In addition, the value of  $\Gamma$  is computed for different disturbance angles in order to find the maximum amplification rate. As in the case of wing flows, a search is also made for the critical frequency that leads to the greatest integrated amplification rate.

On both lines of symmetry where the circumferential velocity component  $w$  is zero, stability calculations can be performed by solving the eigenvalue problem for  $\alpha$ ,  $\omega$  and  $R$  or for  $\alpha$ ,  $\beta$ ,  $\omega$  and  $R$ . The second choice leads to bifurcation on the leeward line of symmetry where the flow is decelerating but not on the windward line of symmetry where the flow is accelerating and bifurcation of such flows requires relatively high Reynolds numbers. The assumption made in both cases is that transition is caused by disturbances that originate on the

line of symmetry. It is possible, however, that transition can also be caused by disturbances that originate off-the-line of symmetry. If they are amplified with negligible crossflow, their properties will be similar to those on the line of symmetry. In that event, it is necessary to determine which disturbance causes transition first. If the cross-flow effect is not negligible, then the disturbances will have properties found in three-dimensional flows and, even if they manage to reach either line of symmetry, the transition may be triggered by those originating on the line of symmetry since the three-dimensional disturbances are more stable than two-dimensional.

Figures 8.11 and 8.12 present the results for the leeward line of symmetry and Fig. 8.13 those for the windward line. Figure 8.11a shows the lower branch of the neutral stability curves (solid lines,  $\beta = 0$ ) and zarfs (dashed lines,  $\beta \neq 0$ ) with bifurcation taking place at  $\xi = -0.9175$ . Figure 8.11b shows the variation of  $\beta$  with  $\xi$  and indicates that, as in the case of Blasius and Hiemenz' flows and attachment-line flow, bifurcation takes place symmetrically.

According to Squire's theorem [27], the two-dimensional disturbances are more unstable than three-dimensional disturbances so that the stability calculations for transition should be made without bifurcation. As a result, at a location  $\xi = \xi_0$ , the eigenvalues  $\alpha, \omega$  on the lower branch of the neutral stability curve were determined so that a dimensional frequency  $\omega^*/2\pi$  can be specified at subsequent  $\xi$ -locations and used in the calculation of the eigenvalues  $\alpha_r, \alpha_i$

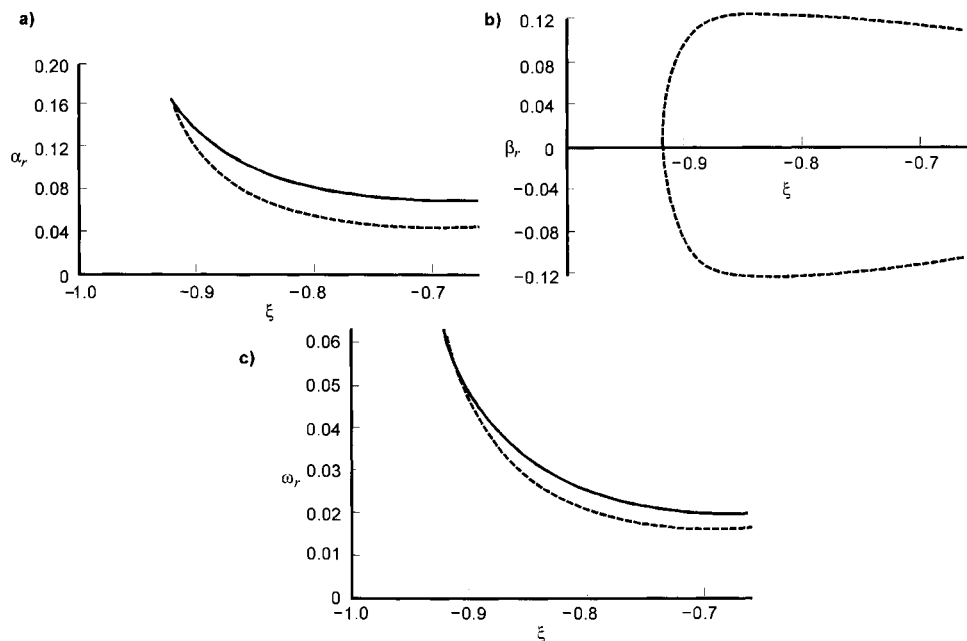


**Fig. 8.11.** Neutral stability curves (solid lines) and zarfs (dashed lines) for the leeward line of symmetry.

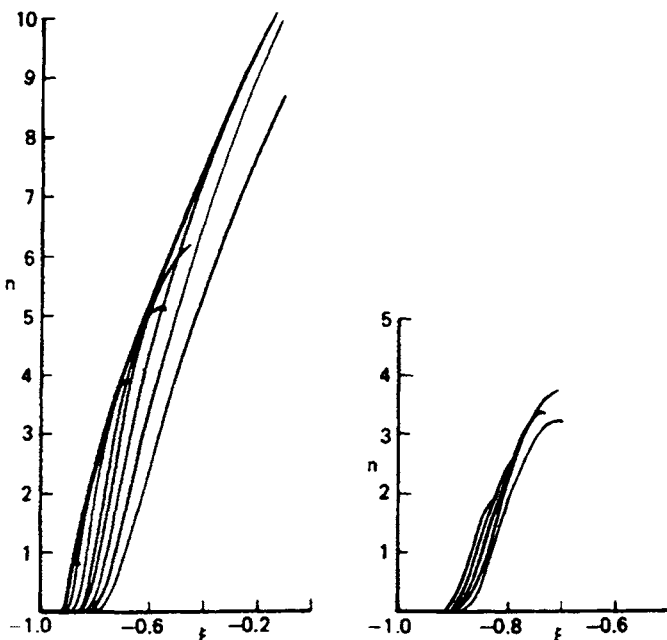


**Fig. 8.12.** Amplification factors for (a) two-dimensional disturbances ( $\beta = 0$ ), and (b) three-dimensional disturbances ( $\beta \neq 0$ ) on the leeward line of symmetry.

as a function of Reynolds number or as  $\xi$  in order to determine the value of  $n$  from Eq. (6.4.8). This procedure led to one of the amplification curves of Fig. 8.12a and was repeated for other dimensional frequencies computed at different  $\xi$ -locations in order to determine the first most amplified wave whose amplification reached the specified value of  $n$ . The results in Fig. 8.12a indicate that transition takes place at  $\xi = -0.15$ , which agrees well with the experimental value of  $-0.18$ .

The results of Fig. 8.12b present amplification rates computed by the above procedure for three-dimensional disturbances. In this case, the calculations were initiated on the lower branch of the zarf by computing the eigenvalues  $\alpha$ ,  $\beta$  and  $\omega$  at  $\xi = \xi_0$  so that the eigenvalues  $\alpha$  and  $\beta$  can be computed for a specified dimensional frequency at subsequent  $\xi$ -locations and transition can be computed from the integrated values of  $\Gamma$ . As can be seen, the results obtained with this procedure are considerably more stable than their counterparts in Fig. 8.12a and do not indicate transition.

Figure 8.13 shows the amplification rates on the windward line of symmetry obtained with the same procedure used to compute those shown in Fig. 8.12a. The envelope of the resulting curves indicates a value of  $n = 10$  after  $\xi = 0.30$ , which does not agree well with the experimental data indicating that transition occurs at  $\xi = 0.13$ . We note from the results in Figs. 8.12a and 8.13 that the amplification rates form an envelope as in two-dimensional flows and suggest

that the disturbances that cause the growth of instability, and subsequently transition can be interpreted as Tollmien–Schlichting waves.

Figure 8.14 shows the amplification rates originated off the line of symmetry, at  $\theta = 10^\circ$ , determined with the procedure discussed under “Off-The-Line-Of-Symmetry.” In this case, the disturbances with five frequencies resulting from the zarf and with their wave propagation trajectories varying as shown in the two inserts of Fig. 8.14 lead to five amplification rates. Of these, the frequencies denoted by 4 and 5 correspond to the critical values, and the wave with a frequency of 5 causes transition in the line of symmetry at  $\xi = 0.20$ , ahead of the wave that originated on the line of symmetry and caused transition to occur after  $\xi = 0.30$ . The disturbance with frequency 4 also causes transition. However, in this case it takes place off the line of symmetry at  $\xi = 0.18$ . This indicates that in three-dimensional flows there can be more than one critical frequency emerging at a fixed  $\theta$ -location and leading to transition.

### Off-the-Line-of-Symmetry

Off-the-line of symmetry, the flow is three dimensional and, in general the circumferential wave number  $\beta$  is not equal to zero. In addition, unlike the flow over the infinite swept wings discussed in the previous subsection, the flow cannot be assumed sectionally similar in either streamwise or circumferential direction. As a result, as the eigenvalues  $\alpha$  and  $\beta$  are being computed to obtain the amplification rates for a specified dimensional frequency, wave angle,  $\phi$  and  $\xi$ -location, the variation of the velocity profiles  $u$  and  $w$  in the circumferential direction must also be accounted for. To discuss this point further and describe the computational strategy off-the-line of symmetry, let us consider Fig. 8.15 in which  $C_0$  represents the fundamental stability curve of the flow in the sense that to the left of it all disturbances decay, while to the right some – but not necessarily all – of the disturbances grow as  $\xi$  increases. We assume that at point  $(\xi_1, \theta_1)$  within a domain lying to the right of  $C_0$ , there passes a zarf and the appropriate value of  $\omega$  on this zarf is  $\omega_1$  at this point. The curve  $C_1$  passing through  $(\xi_1, \theta_1)$  is the curve on which the growth factor is a maximum at the dimensional frequency  $\omega_1^*/2\pi$ , and this growth factor reaches a value of  $n$  at a point  $(\xi_n, \theta_n)$ . Similar curves originating at different  $\xi$ -locations but the same  $\theta$  location with dimensional frequencies  $\omega^*/2\pi$  will lead to curves similar to  $C_1$  with end points denoted by circles, except that the location and the value of  $n$  at the end of the integration process will be different. According to the philosophy of the  $e^n$ -method, the first such wave to increase in amplitude by a factor of  $e^n$  as  $\xi$  increases is said to be a critical transition-wave, and the corresponding value of  $\xi_T(\theta)$  is a good approximation to the onset portion of transition. Thus, by varying  $\theta$ , and computing amplification rates corresponding to zarf frequencies at different  $\xi$ -locations, an estimate of the transition curve on the body of revolution under consideration is obtained.

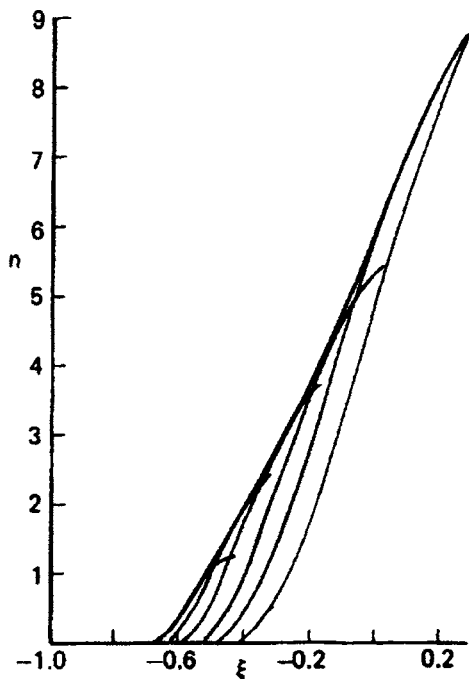


Fig. 8.13. Amplification factors for the windward line of symmetry ( $\beta = 0$ ).

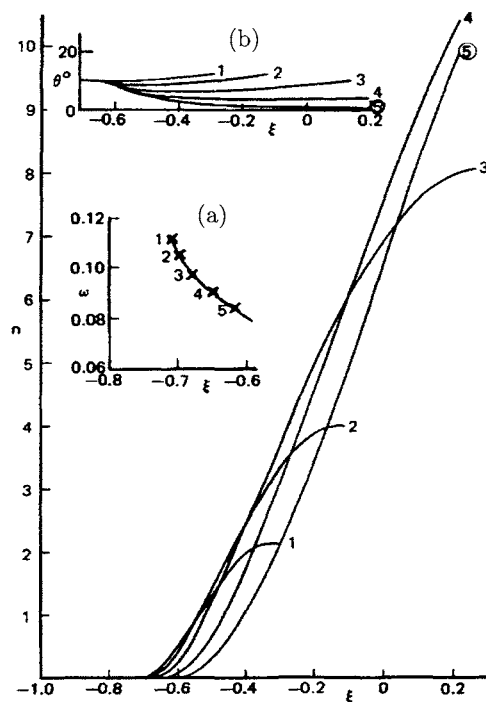


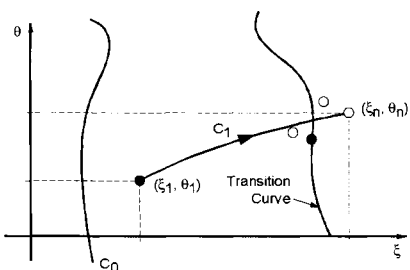
Fig. 8.14. Amplification factors computed with disturbances originating at  $\theta = 10^\circ$  with five frequencies determined on the zarf (insert a) and with different wave propagation trajectories (insert b).

Figure 8.16a shows the integrated amplification rates with disturbances originating at  $\theta = 20^\circ$  for five frequencies determined on the zarf. We note that those denoted by 1 and 5 do not lead to amplified waves, but those designated by 2, 3 and 4 on the lower branch do. Of these three frequencies, the one designated by 4 corresponds to the critical frequency that causes transition.

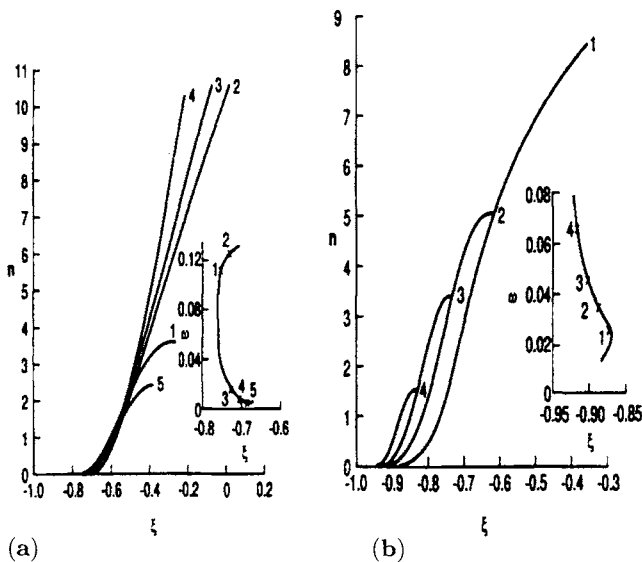
Figure 8.16b shows the results for  $\theta = 150^\circ$ . The shape of the zarf in this case is different from the shape of all the other zarfs computed for  $\theta = 20^\circ, 40^\circ, 80^\circ$  and  $120^\circ$  as discussed in [26]. Except for the frequency designated by 1, none of the other frequencies leads to high amplification rates. It appears that as the value of  $\theta$  increases from its value on the windward line of symmetry, the critical frequencies that were on the lower branch of the zarf, shift to the upper branch; with further increase in  $\theta$ , as the leeward line is approached this trend reverses and the critical frequencies begin to migrate toward the inflection point of the zarf.

Figure 8.17 shows the trajectories of the wave propagation computed with different frequencies originated at specified values of  $e$  corresponding to  $10^\circ, 20^\circ, 40^\circ, 80^\circ$  (Fig. 8.17a) and  $120^\circ, 150^\circ$  (Fig. 8.17b). We note from those for  $\theta = 10^\circ$  that the trajectories of the waves with frequencies 1 and 2 have small angles, which suggests that their behavior is similar to those already discussed for the line of symmetry, the behavior of the disturbances, especially those corresponding to frequencies 4 and 5, are more two-dimensional than three-dimensional. For  $\theta = 20^\circ$  the trajectories with frequencies 3, 4, 5 have angles comparable to others originating at values of  $\theta$  greater than  $20^\circ$ . It is interesting to note that the results for  $\theta = 40^\circ$ , the disturbance angle corresponding to the most amplified wave is not the largest, since in this case the disturbance with frequency of 1 leads to transition.

As the leeward line of symmetry is approached, however, a behavior similar to that found near the windward line of symmetry for some frequencies is observed. For example, for the disturbances that originate at  $\theta = 150^\circ$ , those with frequencies of 1, 2, 3 have initially very small angles which remain relatively constant over a portion of the body before they increase. This behavior again suggests that the disturbances with these frequencies are nearly two dimensional but become three dimensional later, unlike the behavior of nearly two-



**Fig. 8.15.** Computational strategy.



**Fig. 8.16.** Amplification factors with disturbances originating at (a)  $\theta = 20^\circ$  for five frequencies determined on the zarf (insert) and (b)  $\theta = 150^\circ$  for four frequencies determined on the zarf (insert).

dimensional disturbances near the windward line of symmetry. The reason for this behavior is due to the difference in the crossflow velocity profiles [26]. The disturbance that originated at  $\theta = 150^\circ$  with a frequency of 4 is three dimensional, and as expected, is more stable than those with frequencies of 1, 2 and 3.

Figure 8.18 presents a summary of the stability/transition and boundary-layer calculations for the data of Meier and Kreplin. The first curve on the left-hand-side corresponds to the location of the critical frequencies on the zarf. We note from this curve that its behavior approaching the leeward line of symmetry begins to exhibit a difference for  $\theta \geq 160^\circ$  from  $\theta < 160^\circ$ . This difference is due to the effect of the cross-flow velocity profiles which, as in the case for  $\theta = 150^\circ$ , begin to exhibit significant changes with  $\xi$  as the calculations progress downstream of the zarf. To the right of this curve is the dashed line which corresponds to the locus of transition location computed with the present method for  $n = 10$ . The experimental values are denoted by the solid line to the right of this computed transition curve.

## 8.6 Transition Prediction by Parabolized Stability Equations

In the previous sections we have discussed the prediction of transition with the  $e^n$ -method based on the linear stability theory where we assume that the mean flow changes more slowly in the streamwise direction than in the wall-normal direction. As a result, we have assumed that in the vicinity of a given location,

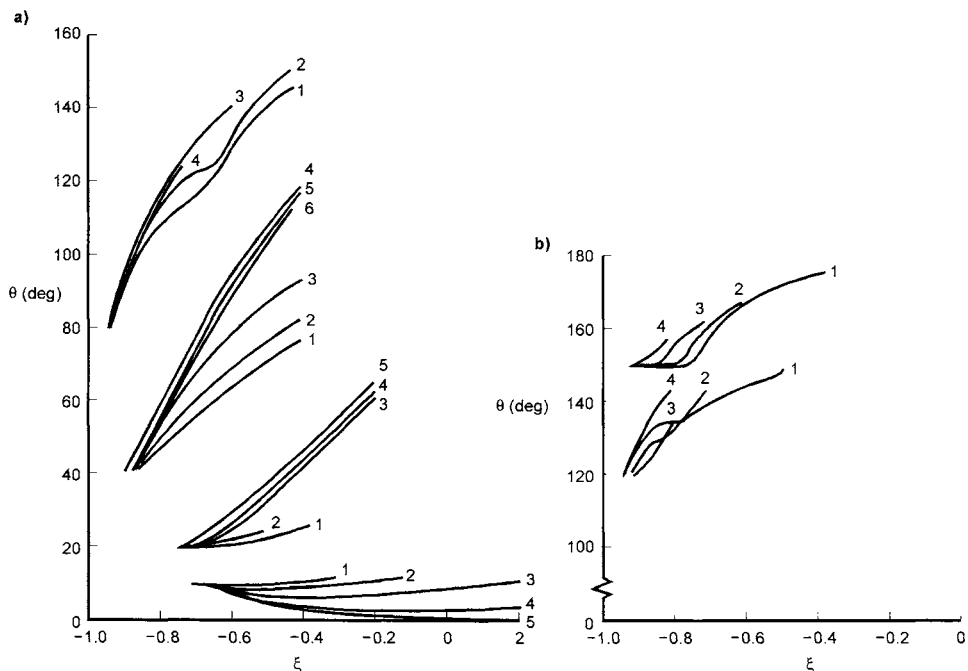


**Fig. 8.17.** The trajectories of the wave originating at specified values of  $\theta$  with different frequencies. (a)  $\theta$  from  $10^\circ$  to  $80^\circ$ ; and (b)  $\theta$  for  $120^\circ$  and  $150^\circ$ .

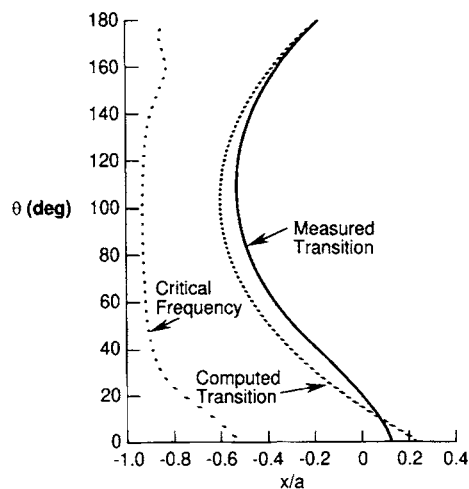


**Fig. 8.18.** Calculated and experimental transition locations on the prolate spheroid at  $\alpha = 10^\circ$ .

the mean flow is quasi-parallel, that is, the mean flow variation in the streamwise direction is negligible.

The approach for predicting transition based on the linear parabolized stability equations (PSE) to be discussed in this section does account for the non-parallel effects neglected in the linear stability theory [27–29]. It is no longer

assumed that the mean flow, amplitude functions and wave number  $\alpha$  are independent of  $x$ . It is assumed instead that these quantities exhibit a weak dependence on  $x$  and the form of the disturbance is, with  $x_0$  denoting the arbitrary point where the calculations begin, written as

$$q'(x, y, t) = \hat{q}(x, y) e^{i \int_{x_0}^x \alpha(\xi) d\xi + \beta z - \omega t} \quad (8.6.1)$$

in contrast to the form given by Eq. (5.3.14),

$$q'(x, y, t) = q(y) e^{i(\alpha x + \beta z - \omega t)}$$

for linear stability theory.

The PSE theory retains the independence of  $z$  of the mean flow and amplitude functions; its strict validity is therefore limited to infinite swept wings. Rather than an eigenvalue problem, the linearized Navier–Stokes equations, Eqs. (P8.4.5)–(P8.4.8), now lead to an  $x$ -variation problem. Reference 30 describes the numerical method based on the box method to solve the parabolized stability equations and also contains a computer program called the PSE code, that has two parts. The first one generates the initial conditions which involve the solution of the boundary-layer equations and the Orr–Sommerfeld equation. The second one solves the parabolized stability equations for given initial conditions.

In this PSE code part one is provided with the boundary-layer and stability-transition codes discussed in [30]. With profiles obtained from the boundary layer code and eigenvalues from the stability-transition code, stability-transitions calculations are performed with the PSE code. The initial values of eigenvalues obtained from the stability-transition code correspond to values on *zarf*, namely  $\alpha_r$ ,  $\omega$ , and  $\beta_r$ . In the stability calculations with the PSE code,  $\beta_r$  is kept constant.

Before we present sample calculations with this computer program (subsection 8.6.3), we first discuss the  $n$ -factor calculations with the PSE code (subsection 8.6.1) and the initial conditions (subsection 8.6.2).

### 8.6.1 $n$ -Factor Calculations

This is done by noting that the wave decomposition in Eq. (8.6.1) is non-unique because we can place the wave part in either  $\hat{q}$  or  $\alpha$ . Ideally we should place as much oscillatory wave in the  $\alpha$  as possible and thus the shape function  $\hat{q}$  variation in  $x$  is minimal. For this reason we assume that a disturbance quantity  $\hat{q}_n$  is selected to “normalize” the decomposition and obtain a wave number  $\alpha_n$ . Then the “effective” wave number  $\alpha_e$  should include the part from the normalized wave number  $\alpha_n$  and the variation of the shape function

$$\alpha_e = \alpha_n - i \frac{1}{\hat{q}_n} \frac{\partial \hat{q}_n}{\partial x} \quad (8.6.2)$$

The real part of  $\alpha_e$  represents the phase of the disturbance and the imaginary part gives the growth rate, both corresponding to the variable  $\hat{q}_n$  chosen. For a given location  $x$ , Eq. (8.6.2) may be applied repeatedly to the selected  $\hat{q}_n$  until the change in  $\alpha_e$  is small. Thus most of the oscillatory motion is contained in  $\alpha$  for the variable  $\hat{q}_n$ . The solution then marches to the next  $x$ -location.

Various different flow variables  $\hat{q}_n$  can be used to normalize the wave decomposition. According to [31], the PSE results were found to be insensitive to the variables selected. In the PSE code of [29], the kinetic energy integral

$$\hat{q}_{KE} = \int^{y_{\max}} (\hat{u}^* \hat{u} + \hat{v}^* \hat{v} + \hat{w}^* \hat{w}) dy$$

is used to normalize  $\alpha$  via the following normalization

$$\alpha_e = \alpha_n - \frac{1}{\hat{q}_{KE}} \int^{y_{\max}} \left( \hat{u}^* \frac{\partial \hat{u}}{\partial x} + \hat{v}^* \frac{\partial \hat{v}}{\partial x} + \hat{w}^* \frac{\partial \hat{w}}{\partial x} \right) dy \quad (8.6.3)$$

In the above two equations, the superscript \* represents the complex conjugate. The parameters  $\hat{u}$ ,  $\hat{v}$ , and  $\hat{w}$  are related to  $z_1$  to  $z_6$  by the following relations

$$\hat{u} = f = (\alpha z_1 - \beta z_5) / \xi_2^2 \quad (8.6.4a)$$

$$\hat{v} = \phi = z_3 \quad (8.6.4b)$$

$$\hat{w} = g = (\alpha z_5 + \beta z_1) / \xi_2^2 \quad (8.6.4c)$$

## 8.6.2 Initial Conditions

The initial conditions for a PSE code can be very important as stated by Langlois et al. [31], “The most important difficulty for the PSE, and maybe the only serious one, lies in the choice of initialisation location, when Orr–Sommerfeld (OS) results are used for initialisation. As explained herein, there is an  $x$ -region upstream of the OS neutral curve in which the results are independent of this location. However, for practical use of this approach, a large number of spanwise wave numbers and frequencies must be considered. The difficulty is then to divide these  $\beta^*$  and  $f$  into different groups and to find the proper initialisation location for each group. The problem could be partly alleviated by using results from a non-parallel local method (such as the multiple-scale analysis) to initialise the PSE.”

In the study reported in [32], Cebeci et al. investigated the possibility of using the zarf concept in the saddle-point method to generate the initial conditions. Noting the drastic variation of  $\omega$  and other eigenvalues in the region where transition calculations start, see for example, Fig. 8.8, they investigated the existence of a “critical” Reynolds number that can be used to specify the initial conditions at this Reynolds number for cross-flow dominated flows. Once that number is known, then the stability calculations can be started in a highly refined grid

centering around the  $x/c$ -location corresponding to the critical Reynolds number. Studies conducted in [32] indicate that there is a critical Reynolds number for cross-flow dominated flows. This number can be obtained from a relationship between  $R_s$ ,  $R_\theta$  and  $H^*$  shown in Fig. 8.19. Here  $R_\theta$  and  $H^*$  are based on the streamwise velocity profile  $u_s/u_{se}$  and are defined by

$$R_\theta = \frac{u_{se}}{\nu} \int_0^\infty \frac{u_s}{u_{se}} \left( 1 - \frac{u_s}{u_{se}} \right) dy \quad (8.6.5a)$$

$$H^* = \int_0^\infty \left( 1 - \frac{u_s}{u_{se}} \right) dy / \int_0^\infty \frac{u_s}{u_{se}} \left( 1 - \frac{u_s}{u_{se}} \right) dy \quad (8.6.5b)$$

In [30] the results leading to these relations were obtained by using the zarf of the saddle point method. Calculations were performed for three values of  $R_L$  ( $\equiv V_\infty L/\nu$ ) corresponding to 5, 10, 17.3 million, three values of  $\lambda = 20^\circ, 30^\circ$  and  $40^\circ$  and two values of  $\alpha = 0^\circ$  and  $2^\circ$  leading to eighteen flows. For a given sweep angle  $\lambda$ , angle of attack  $\alpha$ , and freestream Reynolds number  $R_L$ , an approximate value of a critical Reynolds number  $(R_s)_{cr}$  was determined. This number corresponds to the minimum Reynolds number for which the eigenvalues  $\alpha_r$ ,  $\beta_r$  and  $\omega$  can be obtained with zarf. This critical Reynolds number is approximate because, as was discussed before, in cross-flow dominated flows the critical frequencies that lead to the highest amplification rates vary significantly in a very small region around this Reynolds number. For this reason from this Reynolds number, an approximate  $x/c$ -location needs to be determined to define a very fine  $x$ -grid to perform zarf calculations so that a set of new frequencies can be determined for amplification rate calculations. One of these frequencies corresponds to a critical frequency. It appears from the results shown in Fig. 8.20 that the critical eigenvalues  $(\alpha_r, \beta_r, \omega)$  correlate well with Reynolds number in cross-flow dominated flows.

In Fig. 8.19 the variation of  $R_\theta$  and  $H$  with  $R_s$  can be represented by ( $x = R_s \times 10^{-3}$ )

$$R_\theta = 336 - 0.035x + 1.18 \times 10^{-6}x^2 \quad (8.6.6a)$$

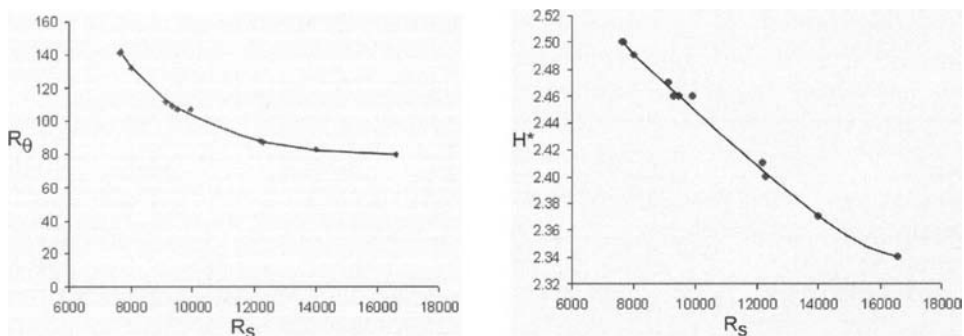
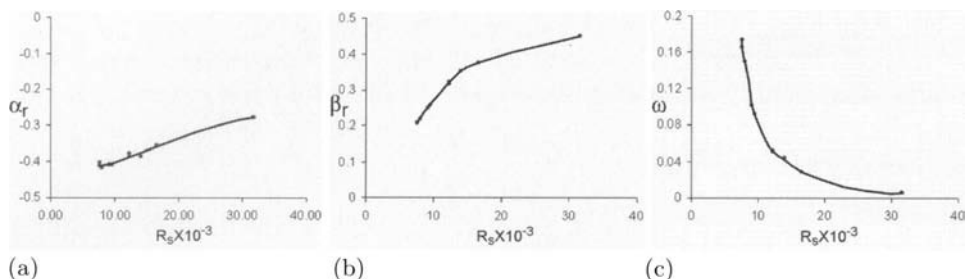


Fig. 8.19. Variation of  $R_\theta$  and  $H^*$  with  $R_s$  for flows with strong cross-flow instability



**Fig. 8.20.** Variation of the eigenvalues determined at the critical Reynolds with  $R_s$

$$H = 2.71 - 0.32 \times 10^{-5}x^2 \quad (8.6.6b)$$

Similarly in Fig. 8.20c the variation of  $\omega$  with  $R_s$  can be represented by

$$\omega = \begin{cases} 0.944 - 0.148x + 0.006x^2 & x < 12.2423 \\ 0.1522 - 0.0105x + 0.00018x^2 & x \geq 12.2423 \end{cases} \quad (8.6.7)$$

### 8.6.3 Sample Calculations

Of the eighteen flows corresponding to the chosen combination of  $\lambda$ ,  $\alpha$  and  $R_L$ , the saddle-point method (SPM) produced ten transition locations and the PSE produced six. A comparison between the predictions of both methods for  $n = 9$  at different values of  $\lambda$ ,  $\alpha$  and  $R_L$  for ten flows is shown in Table 8.1 and for two flows in Fig. 8.21. Six transition locations, all near the leading edge, predicted by both methods agree well with each other. Those four that are predicted by SPM but not by PSE correspond to transition locations away from the leading edge. Clearly those six that are predicted by both methods correspond to flows where the cross-flow is dominant. The other four, as will be discussed later, also correspond to transition locations in a cross-flow dominated flow.

**Table 8.1.** Comparison of transition locations computed with SPM and PSE for cross-flow dominated flows

$\alpha$	$\lambda$	$R_L \times 10^{-6}$	$(s/c)_{tr}$	
			SPM	PSE
0	20	17.3	0.172	—
0	30	17.3	0.035	0.030
0	30	10.0	0.134	—
0	40	17.3	0.019	0.023
0	40	10.0	0.050	0.035
0	40	5.0	0.158	—
2	30	17.3	0.040	0.040
2	40	17.3	0.019	0.035
2	40	10.0	0.060	0.040
2	40	5.0	0.159	—

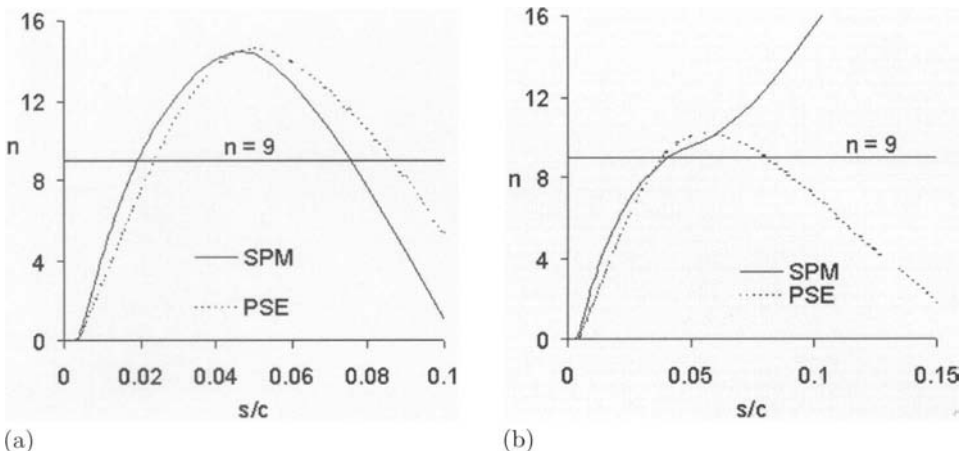


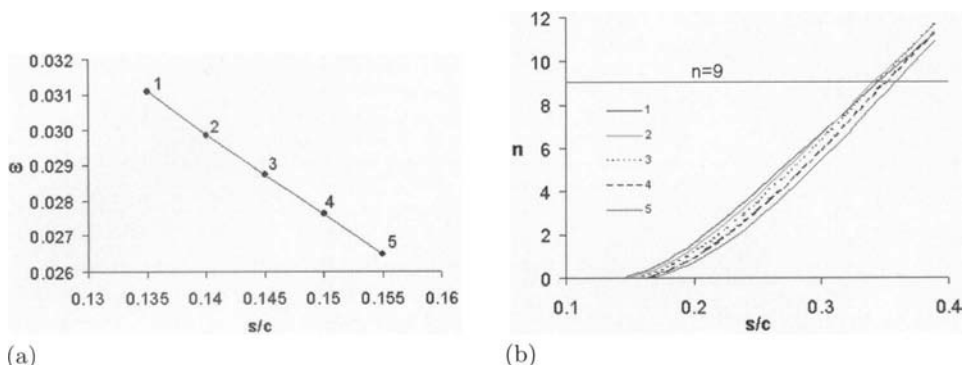
**Fig. 8.21.** Comparisons of SPM and PSE results for  $R_L = 17.3 \times 10^6$ , (a)  $\alpha = 0^\circ, \lambda = 40^\circ$ ; (b)  $\alpha = 2^\circ, \lambda = 30^\circ$

To predict transition location in other flows in which transition does not occur near the leading edge, additional calculations were performed with both methods [32]. This time zarf calculations were initiated away from the leading edge where the cross-flow effects are relatively weak and flow instability is caused by Tollmien–Schlichting (T-S) waves.

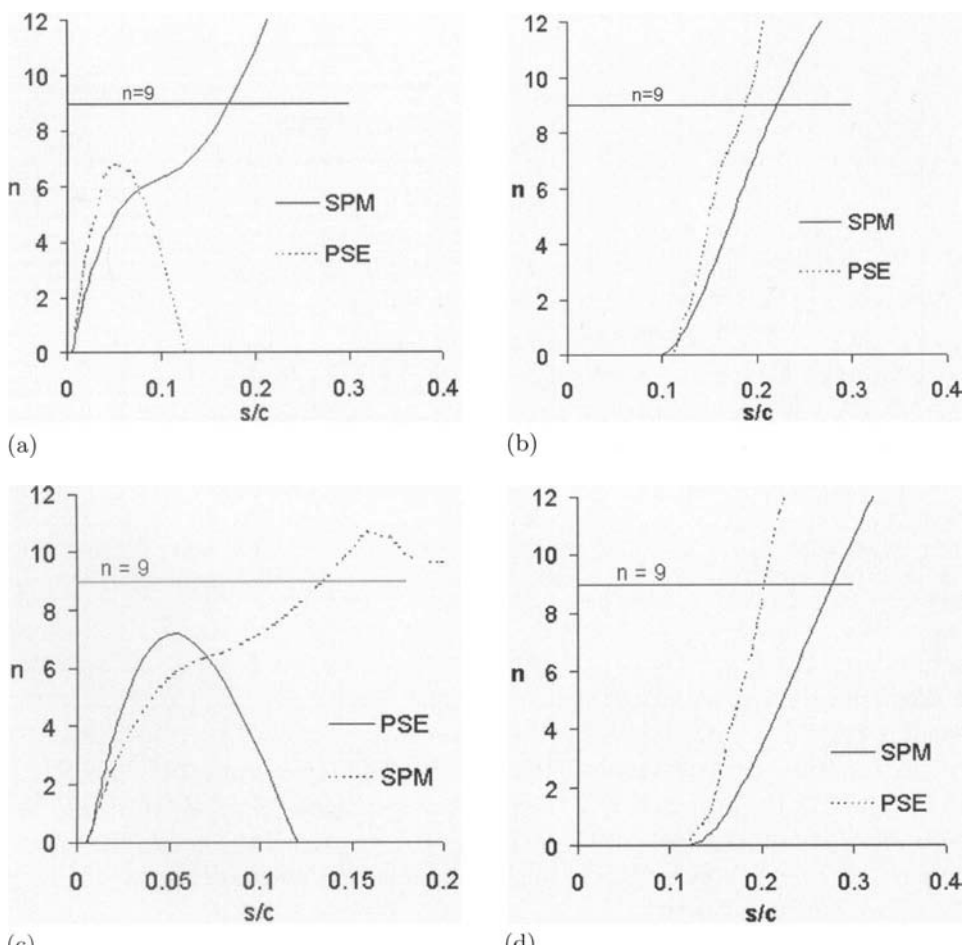
Figure 8.22 shows the variation of  $\omega$  and the integrated amplification rates with  $s/c$  for  $\alpha = 0^\circ, \lambda = 20^\circ, R_L = 5 \times 10^6$ . The variation of frequencies with  $s/c$  is significantly different than those in cross-flow dominated flows. Whereas integrated amplification rates are strongly influenced by the choice of frequencies, this is not the case for flows in which T-S instability dominates.

Table 8.2 shows two sets of results obtained by both methods with initial zarf calculations performed away from the leading edge. The results of set 1 correspond to eight flows that SPM and PSE did not predict transition at the leading edge. The results of set 2 correspond to those flows that PSE did not predict transition but SPM did with frequencies originating at the leading edge.

Results in set 1 are good in agreement with each other. Also we see a similar good agreement in set 2 except for  $\alpha = 0^\circ, \lambda = 30^\circ$  and  $R_L = 10 \times 10^6$ . For this flow SPM predicts transition at  $s/c = 0.28$  and PSE predicts at  $s/c = 0.21$ . It is interesting that the results in set 2 obtained by SPM with frequencies originated away from the leading edge are quite different from those with frequencies originating at the leading edge. Figure 8.23 shows a comparison for two cross-flow dominated flows (Table 8.1) and two flows in which T-S waves dominate (Table 8.2). We see from the results in Tables 8.1 and 8.2 that four flows in Table 8.1 that PSE did not predict transition but SPM did, correspond to cross-flow dominated flows. The results for the corresponding flows in Table 8.2 are erroneous since transition has already occurred. This indicates that according to



**Fig. 8.22.** SPM Results for  $\alpha = 0^\circ$ ,  $\lambda = 20^\circ$ ,  $R_L = 5 \times 10^6$  (a) variation of  $\omega$  with  $s/c$  and (b) resulting integrated amplification rates



**Fig. 8.23.** Comparison of results for flows with cross-flow (a, c) and T-S instability (b, d). (a) and (b) are for  $\alpha = 0^\circ$ ,  $\lambda = 20^\circ$ ,  $R_L = 17.3 \times 10^6$  and (c) and (d) for  $\alpha = 0^\circ$ ,  $\lambda = 30^\circ$  and  $R_L = 10 \times 10^6$

**Table 8.2.** Comparison of transition locations computed with SPM and PSE for flows where T-S waves dominate

$\alpha$	$\lambda$	$R_L \times 10^{-6}$	$(s/c)_{tr}$	
			SPM	PSE
0	20	17.3	0.200	0.190
0	20	10	0.266	0.260
0	20	5	0.342	0.330
0	30	10	0.280	0.210
0	30	5	0.350	0.340
0	40	5	0.360	0.340
2	20	17.3	0.118	0.110
2	20	10	0.146	0.146
2	20	5	0.196	0.185
2	30	10	0.151	0.146
2	30	5	0.200	0.199
2	40	5.0	0.213	0.199

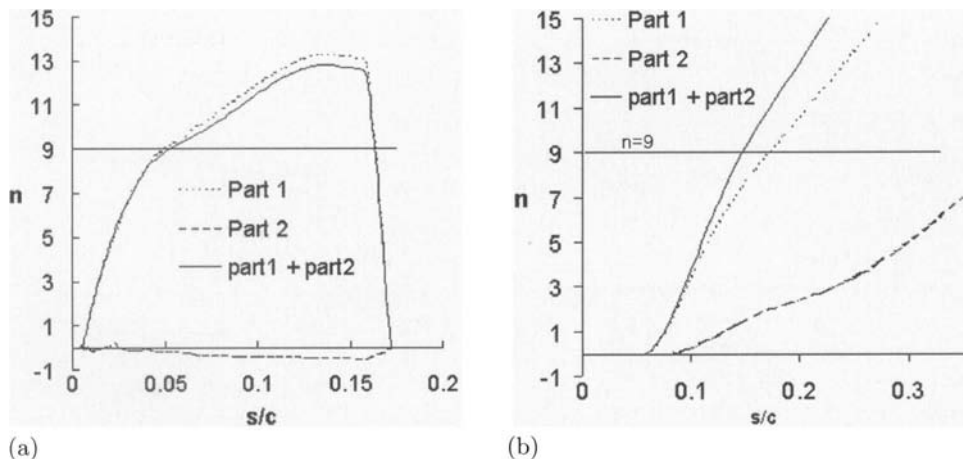
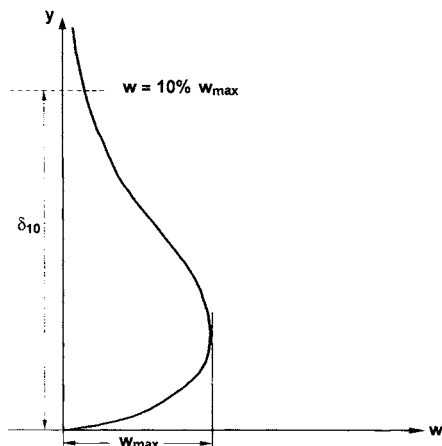


**Fig. 8.24.** Variation of integrated amplification rate  $\Gamma$  and its components for flows with (a) cross-flow instability,  $\alpha = 0^\circ$ ,  $\lambda = 40^\circ$ ,  $R_L = 10 \times 10^6$ , and (b) T-S instability,  $\alpha = 2^\circ$ ,  $\lambda = 20^\circ$ ,  $R_L = 10 \times 10^6$ , all calculated with SPM

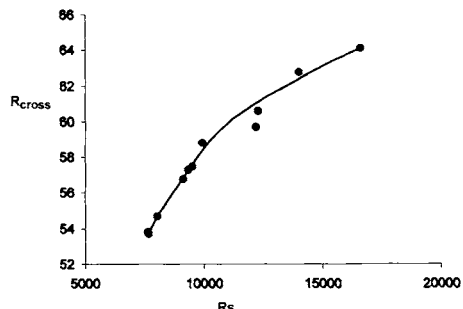
SPM, transition takes place earlier with the frequencies originating near the leading edge.

Figure 8.24 shows  $n$ -factors for flows in which cross-flow dominates (Fig. 8.24a) and those in which T-S waves dominate (Fig. 8.24b), both computed with SPM. Here part 1 refers to the integrated  $\alpha_i$ , part 2 to  $-\beta_i(\partial\alpha/\partial\beta)_{\omega,R}$  of integrated  $\Gamma$ . It is interesting to note that contribution of each part of  $\Gamma$  is a function of flow instability.

In current transition methods based on stability theory, it is not clear where the stability calculations should be started. A common procedure for cross-flow dominated flows is to start them at a location where the cross-flow Reynolds



**Fig. 8.25.** Cross-flow velocity profile



**Fig. 8.26.** Variation of  $R_{\text{cross}}$  with  $R_s$  for cross-flow dominated flows

number,  $R_{\text{cross}}$ , is around 80. This number (see Fig. 8.25) is defined by

$$R_{\text{cross}} = \frac{|w_{\max}| \delta_{10}}{\nu}$$

where

$w_{\max}$  = maximum of the cross-flow profile across the boundary layer

$\delta_{10}$  = value of  $y$  where cross-flow velocity  $w$  is 10% of  $w_{\max}$ , measured from the boundary layer edge

Once the eigenvalues and eigenfunctions are calculated at that location, additional calculations are performed *upstream* of that location until one is not able to obtain solutions to the stability equations. We believe that this location corresponds to the critical Reynolds number location discussed previously.

Figure 8.26 shows the cross-flow Reynolds number computed for the ten flows in Table 8.1. These values are consistent with the procedure for searching for the location to initiate the stability-transition calculations.

## References

- [1] Arnal, D.: "Boundary Layer Transition: Prediction, Application to Drag Reduction," AGARD Report 786, 1992.
- [2] Arnal, D.: "Boundary Layer Transition: Predictions Based on Linear Theory," AGARD Report 793, 1994.
- [3] Cebeci, T.: *Stability and Transition*. Horizons Publ., Long Beach, Calif., and Springer, Heidelberg, 2004.
- [4] Arnal, D.: Laminarity and laminar-turbulent transition control. 39ème Colloque d'Aérodynamique Appliquée, Paris, 22–24 March 2004.
- [5] Radetsky, R. H., Reibert, M. S., Saric, W. S. and Takagi, S.. Effect of micron-sized roughness on transition in swept wing flows. AIAA Paper 93-0076, 1993.

- [6] Louis, F.: *Étude de la transition laminaire-turbulent en écoulement supersonique*. PhD thesis, SUPAERO, Toulouse, April 2004.
- [7] Arnal, D., Séraudie, A. and Archambaud, J. P.: Influence of surface roughness and suction on the receptivity of a swept wing boundary-layer. In H.F. Fasel and W.S. Saric, editors, *Laminar-turbulent transition*. Springer, 2000.
- [8] Pupator, P. and Saric, W.S.: Control of random disturbances in a boundary-layer. AIAA Paper 89-1007, 1989.
- [9] Pfenninger, W., "Flow Phenomena at the Leading Edge of Swept Wings," *Recent Developments in Boundary Layer Research, Part IV*, AGARDograph 97, May 1965.
- [10] Poll, D.I.A.: "Some Aspects of the Flow Near a Swept Attachment Line with Particular Reference to Boundary-Layer Transition," College of Aeronautics Report 7805, August 1978.
- [11] Gaster, M.: "On the Flow Along Leading Edges," *The Aeron. Quarterly*, Vol. XVIII, Part 2, May 1967.
- [12] Juillen, J.C. and Arnal, D.: "Experimental Study of Boundary Layer Suction Effects on Leading Edge Contamination Along the Attachment Line of a Swept Wing," IUTAM Symposium on Laminar-Turbulent Transition, Sendai, Japan, September 1994.
- [13] Spalart, P.R.: "Direct Numerical Study of Leading Edge Contamination," AGARD CP No. 438, 1988.
- [14] Malik, M.R.: "COSAL - A Black Box Compressible Stability Analysis Code for Transition Prediction in Three-Dimensional Boundary Layers," NASA CR 165 925, 1982.
- [15] Mack, L.M.: "Stability of Three-Dimensional Boundary Layers on Swept Wings at Transonic Speeds," IUTAM Symposium, Transsonicum III, Göttingen, May 1988.
- [16] Arnal, D., Casalis, G. and Juillen, J.C.: "Experimental and Theoretical Analysis of Natural Transition on Infinite Swept Wing," IUTAM Symposium, Toulouse, France, 1989, *Laminar-Turbulent Transition* (eds. D. Arnal, R. Michel) Springer, pp. 311–326, 1989.
- [17] Cebeci, T. and Stewartson, K.: "Stability and Transition in Three-Dimensional Flows," *AIAA J.*, Vol. 18, pp. 398–405, 1980.
- [18] Nayfeh, A.H.: "Stability of Three-Dimensional Boundary Layers," *AIAA J.*, Vol. 18, pp. 406–416, 1980.
- [19] Cebeci, T. and Stewartson, K.S.: "On the Prediction of Transition in Three-Dimensional Flows," Proceedings of the IUTAM Symposium: *Laminar Turbulent Transition* (Ed. R. Eppeler and H. Fasel), Springer, N.Y., pp. 243–252, 1980.
- [20] Cebeci, T. and Stewartson, K.: "Asymptotic Properties of the Zarf," *AIAA J.*, Vol. 19, pp. 806–807, 1981.
- [21] Cebeci, T. and Chen, H.H.: "Prediction of Transition on Airfoils with Separation Bubbles, Swept Wings and Bodies of Revolution at Incidence," Numerical and Physical Aspects of Aerodynamic Flows IV (Ed. T. Cebeci), Springer, N.Y., 1990.
- [22] Cebeci, T., Chen, H.H.: "Numerical Method for Predicting Transition in Three-Dimensional Flows by Spatial Amplification Theory," *AIAA J.*, Vol. 30, No. 8, pp. 1972–1979, 1992.
- [23] Arnal, D. and Juillen, J.C.: "Three-Dimensional Transition Studies at ONERA/CERT," AIAA Paper No. 87-1335, 1987.
- [24] Meier, H.U. and Kreplin, H.P.: "Experimental Investigation of the Boundary-Layer Transition on a Body of Revolution," *Zeitschrift f. Flugwiss. Weltraumforsch.*, Vol. 4, p. 65, 1981.
- [25] Cebeci, T., Chen, H.H. and Arnal, D.: "A Three-Dimensional Linear Stability Approach to Transition on Wings at Incidence," AGARD Symposium on Fluid Dynamics of Three-Dimensional Turbulent Shear Flows and Transition, Cesme, Turkey, 3–6 October 1988.
- [26] Cebeci, T., Chen, H.H., Arnal, D. and Huang, T.T.: "Three-Dimensional Linear Stability Approach to Transition on Wings and Bodies of Revolution at Incidence," *AIAA J.*, Vol. 29, No. 12, pp. 2077–2085, 1991.

- [27] Li, F., Malik, M. R.: "Mathematical Nature of Parabolized Stability Equations," in *Laminar Turbulent Transition*, ed. R. Kobayashi, pp. 205–212, New York, Springer, 1994.
- [28] Herbert, T.: "Parabolized Stability Equations," AGARD R-793 Draft (Handout) Special Courses on "Progress in Transition Modelling," Madrid, Spain and Brussels, Belgium, 1993.
- [29] Herbert, T. and Bertolotti, F. P.: "Stability Analysis of Nonparallel Boundary Layers," *Bull. Am. Phys. Soc.* Vol. 32, 1987.
- [30] Cebeci, T.: *Stability and Transition: Theory and Application*. Horizons Publ., Long Beach, CA, and Springer, Heidelberg, 2004.
- [31] Langlois, M., Casalis, G. and Arnal, D.: "On the Practical Application of the PSE Approach to Linear Stability Analysis," Aerospace, Science and Technology, 1997.
- [32] Cebeci, T., Chen, H., Chang, K. C. and Shao, J. P.: "Prediction of Transition in Three-Dimensional Incompressible and Compressible Flows," Proceedings of the 9th Aerodynamics Symposium, Montréal, Québec, April 28–30, 2003.

## Problems

**8-1.** Derive Eq. (8.2.5)

**8-2.** Another criterion that can be used to predict transition due to crossflow instability near the leading edge of a swept wing ( $x$ -axis is orthogonal to the leading edge and  $z$ -axis is parallel to the leading edge) is to use a Reynolds number defined in terms of external streamline velocity  $u_{se}$  and  $\delta_z^*$  given by Eq. (P7.10.4)

$$R_{\delta_z^*} = \frac{u_{se}\delta_z^*}{\nu} \quad (\text{P8.2.1})$$

According to this criterion, transition occurs when

$$R_{\delta_z^*} = 150 \quad (\text{P8.2.2})$$

(a) Show that for a circular swept cylinder Eq. (P8.2.1) can also be written as

$$R_{\delta_z^*} = 0.2677 \sqrt{\frac{V_\infty r_0}{\nu}} \sqrt{\sin \phi \tan \phi} \frac{x/r_0}{\sqrt{\frac{\tan^2 \phi}{4} + \left(\frac{x}{r_0}\right)^2}} \quad (\text{P8.2.3})$$

where  $\phi$  is the sweep angle of the wing and  $r_0$  is the leading edge radius of the cylinder.

(b) According to the criterion given by Eq. (8.2.1) the boundary-layer remains laminar if  $R_{\theta_z} < 100$ . Show that  $R_{\theta_z}$  can be expressed as a function of  $V_\infty r_0 / \nu$  and  $\phi$  by

$$R_{\theta_z} = 0.286 \sqrt{\frac{V_\infty r_0}{\nu}} \sqrt{\sin \phi \tan \phi} \quad (\text{P8.2.4})$$

(c) Show that if the boundary-layer remains laminar according to criterion given by Eq. (8.2.1), then the boundary-layer remains necessarily laminar according to the criterion given by Eq. (P8.2.2).

- (d) Plot  $R_{\theta_z}$  as a function of sweep angle  $\phi$  for values of  $R_c (\equiv \frac{V_\infty c}{\nu})$  15  $\times 10^6$ , 25  $\times 10^6$  and 35  $\times 10^6$ .
- (e) Deduce the value of the maximum sweep angle for maintaining a laminar boundary-layer along the leading edge for the three values of Reynolds number in (d).

**8-3.** Extend STP, with some modifications, to compute the onset of transition on an infinite swept wing with the Mack/Arnal eigenvalue formulation discussed in Section 8.3. Assume that the velocity profiles  $u$ ,  $u''$ ,  $w$  and  $w''$  are available. Use the procedure described below.

With  $\beta_i = 0$ ,  $\omega^*/2\pi$  specified,  $R$  given and  $\beta_r$  assumed, Eq. (5.6.11) represents two equations with two unknowns  $(\alpha_r, \alpha_i)$ , and the equations can be solved by Newton's method. Specifically, if  $(\alpha_r^\nu, \alpha_i^\nu)$  are the  $\nu$ -th iterates, the  $(\nu + 1)$ -th iterates are determined inserting

$$\alpha_r^{\nu+1} = \alpha_r^\nu + \delta\alpha_r^{\nu+1} \quad (\text{P8.3.1a})$$

$$\alpha_i^{\nu+1} = \alpha_i^\nu + \delta\alpha_i^{\nu+1} \quad (\text{P8.3.1b})$$

in Eq. (5.6.11), expanding it around  $\alpha_r^\nu$  and  $\alpha_i^\nu$  by the Taylor series and retaining only linear terms in the expansion. This results in the linear system

$$f_r^\nu + \left( \frac{\partial f}{\partial \alpha_r} \right)_r^\nu \delta\alpha_r^\nu + \left( \frac{\partial f}{\partial \alpha_i} \right)_r^\nu \delta\alpha_i^\nu = 0 \quad (\text{P8.3.2a})$$

$$f_i^\nu + \left( \frac{\partial f}{\partial \alpha_r} \right)_i^\nu \delta\alpha_r^\nu + \left( \frac{\partial f}{\partial \alpha_i} \right)_i^\nu \delta\alpha_i^\nu = 0 \quad (\text{P8.3.2b})$$

Here, for convenience, the subscript 0 on  $f$  has been omitted, and  $r$  and  $i$  denote the real and imaginary parts of  $f$  at the wall. The solution of Eq. (P8.3.2) is,

$$\delta\alpha_r^\nu = \frac{1}{\Delta_0} \left[ f_i^\nu \left( \frac{\partial f}{\partial \alpha_i} \right)_r^\nu - f_r^\nu \left( \frac{\partial f}{\partial \alpha_i} \right)_i^\nu \right] \quad (\text{P8.3.3a})$$

$$\delta\omega_r^\nu = \frac{1}{\Delta_0} \left[ f_r^\nu \left( \frac{\partial f}{\partial \alpha_r} \right)_i^\nu - f_i^\nu \left( \frac{\partial f}{\partial \alpha_r} \right)_r^\nu \right] \quad (\text{P8.3.3b})$$

where

$$\Delta_0 = \left( \frac{\partial f}{\partial \alpha_r} \right)_r^\nu \left( \frac{\partial f}{\partial \alpha_i} \right)_i^\nu - \left( \frac{\partial f}{\partial \alpha_r} \right)_i^\nu \left( \frac{\partial f}{\partial \alpha_i} \right)_r^\nu \quad (\text{P8.3.3c})$$

To evaluate the derivatives of  $f_r$  and  $f_i$  with respect to  $\alpha_r$  and  $\alpha_i$ , we differentiate Eq. (4.5.23) with respect to  $\alpha_r$  and  $\alpha_i$ , since the vector  $\vec{r}$  is independent of  $\alpha_r$  and  $\alpha_i$ ,

$$A \left( \frac{\partial \vec{\delta}}{\partial \alpha_r} \right)^\nu = - \left( \frac{\partial A}{\partial \alpha_r} \right)^\nu \vec{\delta}^\nu \quad (\text{P8.3.4a})$$

$$A \left( \frac{\partial \vec{\delta}}{\partial \alpha_i} \right)^\nu = - \left( \frac{\partial A}{\partial \alpha_i} \right)^\nu \vec{\delta}^\nu \quad (\text{P8.3.4b})$$

The above equations are the variational equations of Eq. (4.5.23) with respect to  $\alpha_r$  and  $\alpha_i$ , respectively. Thus, to obtain the required derivatives, two linear systems are solved with the same coefficient matrix  $A$  (given by Eq. (6.6.9)) already computed and factored for Eq. (4.5.23). The vectors on the right-hand side of Eqs. (P8.3.4a) are determined from Eqs. (6.6.3), (6.6.5b) and (6.6.7). For example, for Eq. (P8.3.4a),  $(r_1)_j = (r_2)_j = 0$  for  $0 \leq j \leq J$ , but  $(r_3)_j$  and  $(r_4)_j$  for  $0 \leq j \leq J$  are given by

$$(r_3)_{j-1} = 2 \left( \frac{\partial c_1}{\partial \alpha_r} \right) (\phi)_{j-\frac{1}{2}} \quad (\text{P8.3.5a})$$

$$(r_4)_{j-1} = 2 \left( \frac{\partial c_4}{\partial \alpha_r} \right) (s)_{j-\frac{1}{2}} + 2 \left( \frac{\partial c_2}{\partial \alpha_r} \right) (\phi)_{j-\frac{1}{2}} \quad (\text{P8.3.5b})$$

$$(r_3)_J = - \left( \frac{\partial c_3}{\partial \alpha_r} \right)_J s_J - \left( \frac{\partial c_1}{\partial \alpha_r} \right)_J (\phi)_J \quad (\text{P8.3.5c})$$

$$(r_4)_J = - \left( \frac{\partial c_4}{\partial \alpha_r} \right)_J (s)_J \quad (\text{P8.3.5d})$$

To summarize one part of the iteration process for a fixed value of  $R$ ,  $w^*/2\pi$  and the assumed value of  $\beta_r$ , we solve Eq. (4.5.23) for assumed values of  $\alpha_r$  and  $\alpha_i$ . If the initial estimates of  $\alpha_r$  and  $\alpha_i$  satisfy Eq. (5.6.11) and  $f_0 = 0$ , there is no need to compute new values of  $\alpha_r$  and  $\alpha_i$ . On the other hand, if  $f_0 \neq 0$ , new estimates of  $\alpha_r$  and  $\alpha_i$  are obtained by Newton's method by first solving Eqs. (P8.3.4) to compute  $\partial f / \partial \alpha_r$  and  $\partial f / \partial \alpha_i$ . Then we compute  $\delta \alpha_r$  and  $\delta \alpha_i$  from Eqs. (P8.3.3) and insert them in Eqs. (P8.3.1) so that Eq. (4.5.23) can be solved with new estimates of  $\alpha_r$  and  $\alpha_i$  to satisfy Eq. (5.6.11). This process is repeated until the increments  $|\delta \alpha_r|$  and  $|\delta \alpha_i|$  are less than a specified tolerance parameter.

Once a solution of Eq. (5.6.11) is obtained, the calculations are repeated for other values of  $\beta_r$  to determine the value of  $\beta_r$  for which the amplification rate  $\alpha_i$  is maximum. The procedure is repeated at each specified value of  $R$  in order to determine the maximum amplification rates as a function of  $x$  (or  $R$ ) so that the value of  $n$  can be computed from Eq. (5.4.8).

**8-4.** The procedure for deriving the parabolized stability equations (PSE) is similar to the procedure for deriving the linear stability equations. We start with the three-dimensional version of the linearized perturbation equations, Eqs. (5.3.1) to (5.3.3) except that we retain the mean flow derivatives with respect to the surface coordinates  $x$  and  $z$  and also do not set the vertical mean velocity  $v$  equal to zero as we did with parallel flow approximation.

(a) For example, for a three-dimensional incompressible flow the linearized perturbation equation for the  $x$ -component can be written as

$$\frac{\partial u'}{\partial t} + u \frac{\partial u'}{\partial x} + u' \frac{\partial u}{\partial x} + v \frac{\partial u'}{\partial y} + v' \frac{\partial u}{\partial y} + w \frac{\partial u'}{\partial z} + w' \frac{\partial u}{\partial z} = -\frac{1}{\rho} \frac{\partial p'}{\partial x} + \nu \nabla^2 u' \quad (\text{P8.4.1})$$

Write similar equations for the  $y$ - and  $z$ -components of the perturbation momentum equation.

(b) Since the mean flow variation in the  $x$ - and  $z$ -directions is retained, it is necessary that the amplitude of the disturbance function  $q(y)$  and the wave numbers  $\alpha$  and  $\beta$  in Eq. (5.3.14) become functions of  $x$  and  $z$ . For the simplified case of no mean flow variation in the  $z$ -direction, the three-dimensional disturbance of  $q'$  can be written in the form

$$q'_j(x, z, y, t) = q_j(x, y) \exp \left\{ i \left[ \int_{x_0}^x \alpha(x) dx + \beta z - \omega t \right] \right\} = q_j e^m \quad (\text{P8.4.2})$$

where

$$q'_j = \begin{pmatrix} u' \\ v' \\ w' \\ p' \end{pmatrix} = \begin{pmatrix} f \\ \phi \\ g \\ \Pi \end{pmatrix} e^m \quad (\text{P8.4.3})$$

Show that the differentials of the  $u'$ -disturbance function are

$$\begin{aligned} \frac{\partial u'}{\partial x} (\equiv u'_x) &= (f_x + i\alpha f) e^m \\ \frac{\partial^2 u'}{\partial x^2} (\equiv u'_{xx}) &= (-\alpha^2 f + \alpha f_x + i\alpha_x f + f_{xx}) e^m \quad (\text{P8.4.4}) \\ \frac{\partial u'}{\partial y} &= f_y e^m \\ \frac{\partial^2 u'}{\partial y^2} &= f_{yy} e^m \\ \frac{\partial u'}{\partial z} &= i\beta f e^m \\ \frac{\partial^2 u'}{\partial z^2} &= -\beta^2 f e^m \end{aligned}$$

(c) Show that by substituting the differentials of the disturbance functions  $q'_j$  into the linearized perturbation equations in (a) and by setting all  $q_{xx}$  to zero (since they contribute very little), we obtain the following system of linear differential equations.

$$i\alpha f + \phi' + i\beta g = -\frac{\partial f}{\partial x} \quad (\text{P8.4.5})$$

$$\begin{aligned} & i\xi_1 f + u' \phi + i\alpha \Pi + \frac{1}{R} (\xi_2^2 f - f'') \\ = & -\frac{\partial u}{\partial x} f - v f' - u \frac{\partial f}{\partial x} - \frac{\partial \Pi}{\partial x} + \frac{2i\alpha}{R} \frac{\partial f}{\partial x} + \frac{i}{R} \frac{d\alpha}{dx} f \end{aligned} \quad (\text{P8.4.6})$$

$$\begin{aligned} & i\xi_1 \phi + \Pi' + \frac{1}{R} (\xi_2^2 \phi - \phi'') \\ = & -\frac{\partial v}{\partial x} f - v \phi' - v' \phi - u \frac{\partial \phi}{\partial x} + \frac{2i}{R} \alpha \frac{\partial \phi}{\partial x} + \frac{i}{R} \frac{d\alpha}{dx} \phi \end{aligned} \quad (\text{P8.4.7})$$

$$\begin{aligned} & i\xi_1 g + w' \phi + i\beta \Pi + \frac{1}{R} (\xi_2^2 g - g'') \\ = & -\frac{\partial w}{\partial x} f - v g' - u \frac{\partial g}{\partial x} + \frac{2i\alpha}{R} \frac{\partial g}{\partial x} + \frac{i}{R} \frac{d\alpha}{dx} g \end{aligned} \quad (\text{P8.4.8})$$

where  $\xi_1$  and  $\xi_2^2$  are defined by Eq. (P5.8.5), that is,

$$\xi_1 = \alpha u + \beta w - \omega, \quad \xi_2^2 = \alpha^2 + \beta^2 \quad (\text{P5.8.5})$$

Here a prime denotes differentiation with respect to  $y$ .

The above equations are the linear PSE for three-dimensional incompressible flows. Their left-hand sides are identical to the linear stability equations given by Eqs. (P5.8.1) to (P5.8.4) obtained with the parallel flow approximation. For two-dimensional flows Eqs. (P8.4.5) to (P8.4.7) reduce to those given by Eqs. (P5.4.1) to (P5.4.3).

The usual boundary conditions for PSE are

$$q_j(x, 0) = 0, \quad q_i(x, \infty) = 0 \quad (\text{P8.4.9})$$

**8-5.** Show that by introducing the definitions

$$z_1 = \alpha f + \beta g \quad (\text{P8.5.1a})$$

$$z_2 = \alpha f' + \beta g' \quad (\text{P8.5.1b})$$

$$z_3 = \phi \quad (\text{P8.5.1c})$$

$$z_4 = \Pi \quad (\text{P8.5.1d})$$

$$z_5 = \alpha g - \beta f \quad (\text{P8.5.1e})$$

$$z_6 = \alpha g' - \beta f' \quad (\text{P8.5.1f})$$

Equations (P8.4.5) to (P8.4.9) can be written as

$$z'_1 = z_2 \quad (\text{P8.5.2a})$$

$$\begin{aligned}
z'_2 = & \left[ \xi_2^2 + i\xi_1 R - i \frac{d\alpha}{dx} + \frac{\alpha R}{\xi_2^2} + \left( \alpha \frac{\partial u}{\partial x} + \beta \frac{\partial w}{\partial x} \right) - \frac{\alpha}{\xi_2^2} \frac{d\alpha}{dx} (Ru - 2i\alpha) \right] z_1 \\
& + Rvz_2 + R \left( \alpha \frac{\partial u}{\partial y} + \beta \frac{\partial w}{\partial x} \right) z_3 + i\xi_2^2 Rz_4 \\
& + \left[ \frac{d\alpha}{dx} \frac{\beta}{\xi_2^2} (Ru - 2i\alpha) - \frac{\beta R}{\xi_2^2} \left( \alpha \frac{\partial u}{\partial x} + \beta \frac{\partial w}{\partial x} \right) \right] z_5 \\
& + (Ru - 2i\alpha) \frac{\partial z_1}{\partial x} + \alpha R \frac{\partial z_4}{\partial x} \tag{P8.5.2b}
\end{aligned}$$

$$z'_3 = \left[ -i - \frac{1}{\xi_2^2} \frac{d\alpha}{dx} + \frac{2\alpha^2}{\xi_2^4} \frac{d\alpha}{dx} \right] z_1 - \frac{2\alpha\beta}{\xi_2^4} \frac{d\alpha}{dx} z_5 - \frac{\alpha}{\xi_2^2} \frac{\partial z_1}{\partial x} + \frac{\beta}{\xi_2^2} \frac{\partial z_5}{\partial x} \tag{P8.5.2c}$$

$$\begin{aligned}
z'_4 = & \left[ iv + \frac{v}{\xi_2^2} \frac{d\alpha}{dx} - \frac{\alpha}{\xi_2^2} \frac{dv}{dx} - \frac{2v}{\xi_2^4} \alpha^2 \frac{d\alpha}{dx} \right] z_1 \\
& + \frac{1}{R} \left[ -i - \frac{1}{\xi_2^2} \frac{d\alpha}{dx} + \frac{2\alpha^2}{\xi_2^4} \frac{d\alpha}{dx} \right] z_2 + \left[ \frac{i}{R} \frac{d\alpha}{dx} \right. \\
& \left. - \frac{1}{R} (\xi_2^2 + i\xi_1 R) - \frac{\partial v}{\partial y} \right] z_3 + \left( \frac{2\alpha\beta v}{\xi_2^4} \frac{d\alpha}{dx} + \frac{\beta}{\xi_2^2} \frac{\partial v}{\partial x} \right) z_5 \\
& - \frac{2\alpha\beta}{R\xi_2^4} \frac{d\alpha}{dx} z_6 + \frac{\alpha v}{\xi_2^2} \frac{\partial z_1}{\partial x} - \frac{\alpha}{R\xi_2^2} \frac{\partial z_2}{\partial x} + \left( \frac{2i\alpha}{R} - u \right) \frac{\partial z_3}{\partial x} \\
& - \frac{\beta v}{\xi_2^2} \frac{\partial z_5}{\partial x} + \frac{\beta}{R\xi_2^2} \frac{\partial z_6}{\partial x} \tag{P8.5.2d}
\end{aligned}$$

$$z'_5 = z_6 \tag{P8.5.2e}$$

$$\begin{aligned}
z'_6 = & \left[ R \left( \alpha \frac{\partial w}{\partial x} - \beta \frac{\partial u}{\partial x} \right) \frac{\alpha}{\xi_2^2} - \frac{\beta}{\xi_2^2} (Ru - 2i\alpha) \frac{d\alpha}{dx} \right] z_1 \\
& + R \left( \alpha \frac{\partial w}{\partial y} - \beta \frac{\partial u}{\partial y} \right) z_3 + \left[ \xi_2^2 + i\xi_1 R - i \frac{d\alpha}{dx} \right. \\
& \left. - \frac{R\beta}{\xi_2^2} \left( \alpha \frac{\partial w}{\partial x} - \beta \frac{\partial u}{\partial x} \right) - \frac{\alpha}{\xi_2^2} \frac{d\alpha}{dx} (Ru - 2i\alpha) \right] z_5 \\
& + Rvz_6 - \beta R \frac{\partial z_4}{\partial x} + (Ru - 2i\alpha) \frac{\partial z_5}{\partial x} \tag{P8.5.2f}
\end{aligned}$$

Boundary conditions

$$\begin{aligned}
z_1(x, 0) &= 0 & z_1(x, \infty) &= 0 \\
z_3(x, 0) &= 0 & z_3(x, \infty) &= 0 \\
z_5(x, 0) &= 0 & z_5(x, \infty) &= 0 \tag{P8.5.3}
\end{aligned}$$

**8-6.** Show that Eqs. (P8.5.2a) to (P8.5.2f) can be written in matrix-vector form as

$$\bar{z}' = A\bar{z} + B \frac{\partial \bar{z}}{\partial x} \quad (\text{P8.6.1})$$

where

$$\bar{z} = \begin{pmatrix} z_1 \\ z_2 \\ \vdots \\ z_6 \end{pmatrix} \quad (\text{P8.6.2})$$

and  $A$  and  $B$  are  $6 \times 6$  matrices whose elements are zero except for those given below

$$\begin{aligned} a_{12} &= 1 \\ a_{21} &= \left[ \xi_2^2 + i\xi_1 R - i \frac{d\alpha}{dx} + \frac{\alpha R}{\xi_2^2} \left( \alpha \frac{\partial u}{\partial x} + \beta \frac{\partial w}{\partial x} \right) - \frac{\alpha}{\xi_2^2} \frac{d\alpha}{dx} (Ru - 2i\alpha) \right. \\ a_{22} &= Rv, \quad a_{23} = R \left( \alpha \frac{\partial u}{\partial y} + \beta \frac{\partial w}{\partial y} \right), \quad a_{24} = i\xi_2^2 R \\ a_{25} &= \frac{\beta}{\xi_2^2} \frac{d\alpha}{dx} (Ru - 2i\alpha) - \frac{\beta R}{\xi_2^2} \left( \alpha \frac{\partial u}{\partial x} + \beta \frac{\partial w}{\partial x} \right) \\ b_{21} &= Ru - 2i\alpha, \quad b_{24} = \alpha R \\ a_{31} &= -i - \frac{1}{\xi_2^2} \frac{d\alpha}{dx} + \frac{2\alpha^2}{\xi_2^4} \frac{d\alpha}{dx}, \quad a_{35} = -2 \frac{\alpha\beta}{\xi_2^4} \frac{d\alpha}{dx} \\ b_{31} &= -\frac{\alpha}{\xi_2^2}, \quad b_{35} = \frac{\beta}{\xi_2^2} \\ a_{41} &= iv + \frac{v}{\xi_2^2} \frac{d\alpha}{dx} - \frac{2\alpha^2 v}{\xi_2^4} \frac{d\alpha}{dx} - \frac{\alpha}{\xi_2^2} \frac{\partial v}{\partial x} \\ a_{42} &= \frac{1}{R} \left( -i - \frac{1}{\xi_2^2} \frac{d\alpha}{dx} + \frac{2\alpha^2}{\xi_2^4} \frac{d\alpha}{dx} \right) \\ a_{43} &= \frac{i}{R} \frac{d\alpha}{dx} - \frac{1}{R} (\xi_2^2 + i\xi_1 R) - \frac{\partial v}{\partial y} \\ a_{45} &= \frac{2\alpha\beta v}{\xi_2^4} \frac{d\alpha}{dx} + \frac{\beta}{\xi_2^2} \frac{\partial v}{\partial x}, \quad a_{46} = -\frac{2\alpha\beta}{R\xi_2^4} \frac{d\alpha}{dx}, \quad b_{41} = \frac{\alpha v}{\xi_2^2} \\ b_{42} &= -\frac{\alpha}{R\xi_2^2}, \quad b_{43} = \frac{2i\alpha}{R} - u, \quad b_{45} = -\frac{\beta v}{\xi_2^2}, \quad b_{46} = \frac{\beta}{R\xi_2^2} \\ a_{56} &= 1 \\ a_{61} &= R \left( \alpha \frac{\partial w}{\partial x} - \beta \frac{\partial u}{\partial x} \right) \frac{\alpha}{\xi_2^2} - (Ru - 2i\alpha) \frac{\beta}{\xi_2^2} \frac{d\alpha}{dx} \\ a_{63} &= R \left( \alpha \frac{\partial w}{\partial y} - \beta \frac{\partial u}{\partial y} \right) \end{aligned}$$

$$a_{65} = \xi_2^2 + i\xi_1 R - i \frac{d\alpha}{dx} - \frac{R\beta}{\xi_2^2} \left( \alpha \frac{\partial w}{\partial x} - \beta \frac{\partial u}{\partial x} \right) - \frac{\alpha}{\xi_2^2} \frac{d\alpha}{dx} (Ru - 2i\alpha)$$

$$a_{66} = Rv$$

$$b_{64} = -\beta R, \quad b_{65} = Ru - 2i\alpha$$

**8-7.** Since parabolized stability equations are solved by a marching procedure, they require initial conditions of the form

$$q_i(x_0, y) = h_j(y) \quad (\text{P8.7.1})$$

and are obtained by a local approximation to the system of equations (P8.4.5) to (P8.4.8) and by solving the eigenvalue problem.

It has been shown that the above system of equations is ill-posed as an initial value problem, but stable marching solutions can be derived if one of the following restrictions are observed [27, 28].

$$\frac{\partial H}{\partial x} = 0 \quad (\text{P8.7.2})$$

$$\Delta x > \frac{1}{|\alpha_r|} \quad (\text{P8.7.3})$$

The first condition implies a limitation of the allowable number of steps per wave length, and the second condition addresses the basic reason for the ill-posedness, which is the possibility of upstream propagation of pressure waves.

Using the box method and with streamwise derivatives expressed by two-point backward differences, show that Eqs. (P8.6.1) and (P8.5.3) can be written in matrix-vector form given by Eq. (4.5.23) where the  $6 \times 6$  matrices  $A_j$ ,  $B_j$ ,  $C_j$  in the coefficient matrix  $A$  and compound vector  $r$  are defined by where

$$A_0 = \begin{pmatrix} 1 & 0 & 0 & 0 & 0 & 0 \\ 0 & 0 & 1 & 0 & 0 & 0 \\ 0 & 0 & 0 & 0 & 1 & 0 \\ 0 & 0 & 0 & 0 & -1 & -a_1 a_{56} \\ e_2 & 0 & e_4 & e_6 & e_8 & e_{10} \\ d_2 & d_4 & d_6 & d_8 & d_{10} & d_{12} \end{pmatrix} \quad C_0 = \begin{pmatrix} & & & & & \\ & & & & & \\ & & & & & \\ & & & & & \\ 0 & 0 & 0 & 0 & -1 & -a_1 a_{56} \\ e_1 & 0 & e_3 & e_5 & e_7 & e_9 \\ d_1 & d_3 & d_5 & d_7 & d_9 & d_{11} \end{pmatrix}$$
  

$$B_j = \begin{pmatrix} b_2 & b_4 & b_6 & b_8 & b_{10} & 0 \\ c_2 & 0 & c_4 & 0 & c_6 & 0 \\ -1 & -a_j a_{12} & 0 & 0 & 0 & 0 \end{pmatrix} \quad A_j = \begin{pmatrix} b_1 & b_3 & b_5 & b_7 & b_9 & 0 \\ c_1 & 0 & c_3 & 0 & c_5 & 0 \\ 1 & -a_j a_{12} & 0 & 0 & 0 & 0 \\ 0 & 0 & 0 & 0 & -1 & -a_{j+1} a_{56} \\ e_2 & 0 & e_4 & e_6 & e_8 & e_{10} \\ d_2 & d_4 & d_6 & d_8 & d_{10} & d_{12} \end{pmatrix}$$

$$C_j = \begin{pmatrix} & & & & & \\ & 0 & 0 & 0 & 0 & 1 & -a_{j+1}a_{56} \\ & e_1 & 0 & e_3 & e_5 & e_7 & e_9 \\ & d_1 & d_3 & d_5 & d_7 & d_9 & d_{11} \end{pmatrix}$$

$$B_J = \begin{pmatrix} b_2 & b_4 & b_6 & b_8 & b_{10} & 0 \\ c_2 & 0 & c_4 & 0 & c_6 & 0 \\ -1 & -a_J a_{12} & 0 & 0 & 0 & 0 \end{pmatrix} \quad A_J = \begin{pmatrix} b_1 & b_3 & b_5 & b_7 & b_9 & 0 \\ c_1 & 0 & c_3 & 0 & c_5 & 0 \\ 1 & -a_J a_{12} & 0 & 0 & 0 & 0 \\ 1 & 0 & 0 & 0 & 0 & 0 \\ 0 & 0 & 1 & 0 & 0 & 0 \\ 0 & 0 & 0 & 0 & 1 & 0 \end{pmatrix}$$

where

$$(b_1)_j = -\frac{1}{2}(a_{21} + b_{21}k_i^{-1}), \quad (b_2)_j = (b_1)_j, \quad (b_3)_j = h_{j-1}^{-1} - \frac{a_{22}}{2}$$

$$(b_4)_j = -h_{j-1}^{-1} - \frac{a_{22}}{2}, \quad (b_5)_j = -\frac{a_{23}}{2}, \quad (b_6)_j = (b_5)_j,$$

$$(b_7)_j = -\frac{1}{2}(a_{24} + k_i^{-1}b_{24}), \quad (b_8)_j = (b_7)_j, \quad (b_9)_j = -\frac{a_{25}}{2}, \quad (b_{10})_j = (b_9)_j$$

$$(r_1)_j = -b_{21}k_i^{-1}z_{1,j-1/2}^{i-1} - b_{24}k_i^{-1}z_{4,j-1/2}^{i-1}$$

$$(c_1)_j = (c_2)_j = -\frac{1}{2}(a_{31} + b_{31}k_i^{-1}), \quad (c_3)_j = h_{j-1}^{-1}, \quad (c_4)_j = -(c_3)_j$$

$$(c_5)_j = (c_6)_j = -\frac{1}{2}(a_{33} + b_{35}k_i^{-1})$$

$$(r_2)_{j-1} = -b_{31}k_i^{-1}z_{1,j-1/2}^{i-1} - b_{35}k_i^{-1}z_{5,j-1/2}^{i-1}$$

$$(e_1)_j = (e_2)_j = -\frac{1}{2}a_{61}, \quad (e_3)_j = (e_4)_j = -\frac{1}{2}a_{63}$$

$$(e_5)_j = (e_6)_j = -\frac{1}{2}b_{64}k_i^{-1}, \quad (e_7)_j = (e_8)_j = -\frac{1}{2}(a_{63} + b_{65}k_i^{-1})$$

$$(e_9)_j = -\frac{1}{2}a_{66} + h_{j-1}^{-1}, \quad (e_{10})_j = -\frac{1}{2}a_{66} - h_{j-1}^{-1}$$

$$(r_5)_{j-1} = -b_{64}k_i^{-1}z_{4,j-1/2}^{i-1} - b_{65}k_i^{-1}z_{5,j-1/2}^{i-1}$$

$$(d_1)_j = (d_2)_j = -\frac{1}{2}(a_{41} + b_{41}k_i^{-1}), \quad (d_3)_j = (d_4)_j = -\frac{1}{2}(a_{42} + b_{42}k_i^{-1})$$

$$(d_5)_j = (d_6)_j = -\frac{1}{2}(a_{43} + b_{43}k_i^{-1}), \quad (d_7)_j = h_{j-1}^{-1}, \quad (d_8)_j = -(d_7)_j$$

$$(d_9)_j = (d_{10})_j = -\frac{1}{2}(a_{43} + b_{45}k_i^{-1}), \quad (d_{11})_j = (d_{12})_j = -\frac{1}{2}(a_{46} + b_{46}k_i^{-1})$$

$$(r_6)_{j-1} = -k_i^{j-1}(b_{41}z_{1,j-1/2}^{i-1} + b_{42}z_{2,j-1/2}^{i-1} + b_{43}z_{3,j-1/2}^{i-1} + b_{45}z_{5,j-1/2}^{i-1} + b_{46}z_{6,j-1/2}^{i-1})$$

$$(r_3)_j = (r_4)_{j-1} = 0$$

Note: For second order accuracy in  $\Delta x$ , the streamwise derivatives should be expressed by three-point backward differences.

- 8-8.** (a) Solve the system of the finite difference PSE equations in the form expressed by Eq. (4.5.23). Use the matrix solver algorithm, Program 5 in the accompanying CD-ROM. Solve the infinite swept wing boundary layer equations to obtain the velocity profiles including the normal velocity  $v$  and its derivative. Generate the initial conditions by solving the linear stability equations with the eigenvalue formulation discussed in problem 8-3. Assume the infinite swept wing has a NACA 0012 cross section.
- (b) Calculate the onset of transition location with the above program for a chord Reynolds number of  $R_c = (\equiv \frac{u_\infty c}{\nu}) = 20 \times 10^6$  and sweep angle of  $\lambda = 30^\circ$ .
- (c) Compare the solutions of (b) with those obtained with the computer program discussed in problem 8-3.

# 9

# Interactive Boundary-Layer Theory

## 9.1 Introduction

Throughout this book we have discussed the solution of the boundary-layer equations for external flows with prescribed external velocity distribution. This approach to boundary-layer theory, sometimes referred to as the *standard problem* or *direct problem*, allows viscous flow solutions provided that boundary-layer separation, which corresponds to vanishing wall shear in two-dimensional steady flows, does not occur. If the wall shear vanishes at some  $x$ -location, the solutions breakdown and convergence cannot be obtained. This is referred to as the singular behavior of the boundary-layer equations at separation. For laminar flows, the behavior of the wall shear  $\tau_w$  close to the separation point  $x_s$ , has been shown to be of the form

$$\left( \frac{\partial u}{\partial y} \right) \sim (x_s - x)^{1/2} \quad (9.1.1)$$

by Goldstein [1] who considered a uniformly retarded flow past a semi-infinite plate and showed that, with the relation given above, there is no real solution downstream of separation; the normal velocity component  $v$  becomes infinite at  $x_s$  (see Problem 9.6). Goldstein also pointed out that the pressure distribution around the separation point cannot be taken arbitrarily and must satisfy conditions associated with the existence of reverse flow downstream of separation.

The inviscid-pressure distribution for flow past a circular cylinder leads to a velocity maximum at  $90^\circ$  and separation at about  $105^\circ$  from the front stagnation point, whereas viscous flow in the subcritical range of Reynolds number leads to a velocity maximum at  $70^\circ$  and separation at  $83^\circ$ . As can be seen from Fig. 9.1, viscosity modifies the inviscid flow, which cannot serve even as a first approximation to the actual flow. In the case of streamlined bodies, where separation takes place close to the rear stagnation point, the solution of the inviscid flow equations can serve as a good approximation to real flow, as we shall discuss briefly in this chapter and as discussed in detail in [2, 3].

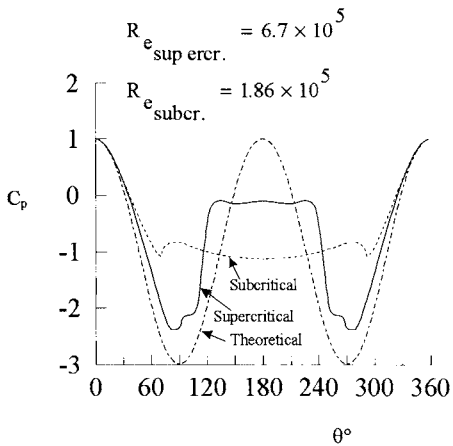


**Fig. 9.1.** Pressure distribution around a circular cylinder in the subcritical and supercritical range of Reynolds numbers  $q_\infty = 1/2\rho V_\infty^2$ .

The boundary-layer equations are not singular at separation when the external velocity or pressure is computed as part of the solution. Catherall and Mangler [4] were the first to show that in two-dimensional steady laminar flows, the modification of the external velocity distribution near the region of flow separation leads to solutions free of numerical difficulties. Prescribing the displacement thickness as a boundary condition at the boundary-layer edge, that is,

$$y = \delta, \quad \delta^*(x) = \text{given} \quad (9.1.2)$$

in addition to those given by Eq. (3.4.1a) with no mass transfer, they were able to integrate the boundary-layer equations through the separation location and into a region of reverse flow without any evidence of singularity at the separation point. This procedure for solving the boundary-layer equations for a prescribed displacement thickness distribution, with the external velocity or pressure computed as part of the solution is known as the *inverse problem*. This observation of Catherall and Mangler has led to other studies by various investigators of inverse solutions of the boundary-layer equations; these are obtained by prescribing distributions of displacement thickness or wall shear. Furthermore, it has been demonstrated in [5, 6] that for flows with separation bubbles, these solutions are in good agreement with the solutions of the Navier-Stokes equations.

A problem associated with the use of these inverse techniques for external flows is the lack of a priori knowledge of the required displacement thickness or wall shear. The appropriate value must be obtained as part of the overall problem from interaction between the boundary layer and the inviscid flow. In the case of internal flows, the problem is somewhat easier because the conservation of mass in integral form can be used to relate pressure  $p(x)$  to velocity  $u(x, y)$  in terms of mass balance in the duct.

For two-dimensional external flows, two procedures have been developed to couple the solutions of the inviscid and viscous equations for airfoil flows. In the first procedure, developed by Le Balleur [7] and Carter [8], the solution of the boundary-layer equations is obtained by the standard method, and a displacement-thickness,  $\delta^{*0}(x)$ , distribution is determined. If this initial calculation encounters separation,  $\delta^{*0}(x)$  is extrapolated to the trailing edge of the airfoil. For the given  $\delta^{*0}(x)$  distribution, the boundary-layer equations are then solved in the inverse mode to obtain an external velocity  $u_{ev}(x)$ . An updated inviscid velocity distribution,  $u_{ei}(x)$ , is then obtained from the inviscid flow method with the added displacement thickness. A relaxation formula is introduced to define an updated displacement-thickness distribution,

$$\delta^*(x) = \delta^{*0}(x) \left\{ 1 + \omega \left[ \frac{u_{ev}(x)}{u_{ei}(x)} - 1 \right] \right\} \quad (9.1.3)$$

where  $\omega$  is a relaxation parameter, and the procedure is repeated with this updated mass flux.

In the second approach, developed by Veldman [9], the external velocity  $u_e(x)$  and the displacement thickness  $\delta^*(x)$  are treated as unknown quantities, and the equations are solved in the inverse mode simultaneously in successive sweeps over the airfoil surface. For each sweep, the external boundary condition for the boundary-layer equation dimensionless form, with  $u_e(x)$  normalized with  $u_\infty$ , is written as

$$u_e(x) = u_e^0(x) + \delta u_e(x) \quad (9.1.4a)$$

Here  $u_e^0(x)$  denotes the inviscid velocity and  $\delta u_e$  the perturbation due to the displacement thickness, which is calculated from the Hilbert integral

$$\delta u_e = \frac{1}{\pi} \int_{x_a}^{x_b} \frac{d}{d\sigma} (u_e \delta^*) \frac{d\sigma}{x - \sigma} \quad (9.1.4b)$$

The term  $\frac{d}{d\sigma} (u_e \delta^*)$  in the above equation denotes the blowing velocity used to simulate the boundary-layer in the region  $(x_a, x_b)$ . This approach is more general and should be used in all the external flow problems requiring interaction.

Veldman was inspired to develop his interaction law by the results of the triple deck theory described in Sections 11.7, 11.8 and 12.7, but the justification of the interactive boundary layer (IBL) theory was lacking. A rational basis of the IBL theory is discussed in Sections 9.2 and 9.3, and the interaction law developed by Veldman is used in the solution of the equations for two-dimensional, steady, incompressible flows, including separation. This interaction law is also used in the solution of three-dimensional and compressible steady flows in [2] and in Chapter 13, and its extension to unsteady airfoil flows is described in [3]. A sample of results obtained with this method is presented in Sections 9.4 to 9.6.

## 9.2 Rational Basis of the Interactive Boundary-Layer Theory

The Interactive Boundary-Layer (IBL) theory, in the sense of strong coupling between the inviscid flow and boundary-layer equations, was used successfully [2, 7, 8, 9] for some time, but a sound justification has not been given until recently, as noted by Sychev et al. [10] with their comment that: “No rational mathematical arguments (based, say, on asymptotic analysis of the Navier-Stokes equations) have been given to support the model approach”.

The problem can be studied with a method called the Successive Complementary Expansions Method (SCEM) [11]. It is convenient to describe the SCEM briefly by considering a singular perturbation problem where the function  $\Phi(x, \varepsilon)$  is defined in a domain  $D$  with  $\varepsilon$  representing a small parameter. It is assumed that two significant domains are identified, an outer domain where the relevant variable is  $x$  and an inner domain where the boundary-layer variable is  $X$  (for example  $X = x/\varepsilon$ ). According to the SCEM, the starting point requires for a uniformly valid generalized approximation

$$\Phi_a = \sum_{i=1}^n \delta_i(\varepsilon) [\varphi_i(x, \varepsilon) + \psi_i(X, \varepsilon)] \quad (9.2.1)$$

where the functions  $\delta_i$  are order functions such that  $\delta_{i+1}/\delta_i \rightarrow 0$  when  $\varepsilon \rightarrow 0$ . This approximation is constructed step by step without requiring any matching principles. The boundary conditions are sufficient for calculating the successive approximations. When the functions  $\varphi_i$  depend on  $x$  only and when the functions  $\psi_i$  depend on  $X$  only, the approximation is said to be *regular*; the standard Method of Matched Asymptotic Expansion provides such an approximation. If the functions  $\varphi_i$  and  $\psi_i$  depend on  $\varepsilon$ , the approximation is said to be *generalized*.

### 9.2.1 IBL Model

The Navier–Stokes equations, Eqs. (2.2.1) to (2.2.3) with  $\sigma_{ij}$  given by Eq. (2.2.7), can be written in dimensionless form for a laminar incompressible two-dimensional steady flow as

$$\frac{\partial U}{\partial x} + \frac{\partial V}{\partial y} = 0 \quad (9.2.2a)$$

$$U \frac{\partial U}{\partial x} + V \frac{\partial U}{\partial y} = - \frac{\partial P}{\partial x} + \varepsilon^2 \left( \frac{\partial^2 U}{\partial x^2} + \frac{\partial^2 U}{\partial y^2} \right) \quad (9.2.2b)$$

$$U \frac{\partial V}{\partial x} + V \frac{\partial V}{\partial y} = - \frac{\partial P}{\partial y} + \varepsilon^2 \left( \frac{\partial^2 V}{\partial x^2} + \frac{\partial^2 V}{\partial y^2} \right) \quad (9.2.2c)$$

where  $\varepsilon$  is a small parameter which implies that Reynolds number is high, that is

$$\varepsilon^2 = \frac{1}{Re} = \frac{\nu}{VL} \quad (9.2.3)$$

with  $V$  and  $L$  denoting reference quantities. The coordinate normal to the wall is  $y$  and the coordinate along the wall is  $x$ ; the  $x$ - and  $y$ -velocity components are  $\mathcal{U} (\equiv u/V)$  and  $\mathcal{V} (\equiv v/V)$ ; the pressure is  $\mathcal{P} (\equiv p/\rho V^2)$ .

We first look for an outer generalized approximation beginning with the terms

$$\mathcal{U} = u_1(x, y, \varepsilon) + \dots; \quad \mathcal{V} = v_1(x, y, \varepsilon) + \dots; \quad \mathcal{P} = p_1(x, y, \varepsilon) + \dots \quad (9.2.4)$$

Neglecting terms of order  $O(\varepsilon^2)$ , Eqs. (9.2.2) reduce to the Euler equations discussed in Section 2.4,

$$\frac{\partial u_1}{\partial x} + \frac{\partial v_1}{\partial y} = 0 \quad (9.2.5a)$$

$$u_1 \frac{\partial u_1}{\partial x} + v_1 \frac{\partial u_1}{\partial y} = - \frac{\partial p_1}{\partial x} \quad (9.2.5b)$$

$$u_1 \frac{\partial v_1}{\partial x} + v_1 \frac{\partial v_1}{\partial y} = - \frac{\partial p_1}{\partial y} \quad (9.2.5c)$$

Uniform flow at infinity provides the usual boundary conditions for the above equations and, since the no-slip conditions cannot be used for the Euler equations, the approximation in Eq. (9.2.4) needs refinement to determine the missing wall boundary condition. We define (see Fig. 9.2)

$$\mathcal{U} = u_1(x, y, \varepsilon) + U_1(x, Y, \varepsilon) + \dots \quad (9.2.6a)$$

$$\mathcal{V} = v_1(x, y, \varepsilon) + \varepsilon V_1(x, Y, \varepsilon) + \dots \quad (9.2.6b)$$

$$\mathcal{P} = p_1(x, y, \varepsilon) + \varepsilon^2 P_1(x, Y, \varepsilon) + \dots \quad (9.2.6c)$$

where  $Y$  is the boundary layer variable  $Y = y/\varepsilon$ . The  $\mathcal{V}$ -expansion comes from the continuity equation which must be non-trivial, and the  $\mathcal{P}$ -expansion comes from the analysis of the  $y$ -momentum equation (see Problem 9-7).

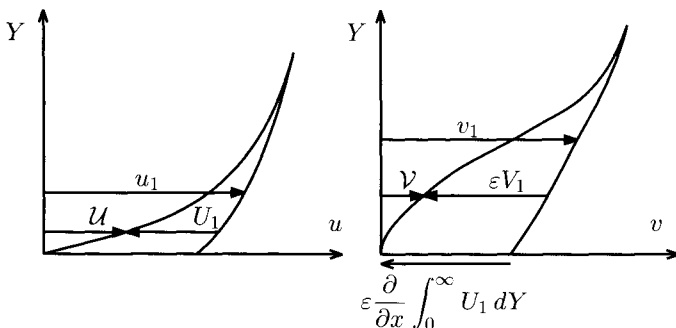


**Fig. 9.2.** Sketch of the velocity components in the boundary layer.

The Navier–Stokes equations are rewritten with expansions (9.2.6a)–(9.2.6c). A first-order IBL model is obtained by neglecting terms of order  $O(\varepsilon)$  in the  $x$ -momentum equation and a second-order IBL model is obtained by neglecting terms of order  $O(\varepsilon^2)$ . By using the definitions

$$u = u_1 + U_1 \quad ; \quad v = v_1 + \varepsilon V_1 \quad (9.2.7)$$

the second-order model leads to the following generalized boundary-layer equations (see Problem 9-8)

$$\left. \begin{aligned} \frac{\partial u}{\partial x} + \frac{\partial v}{\partial y} &= 0 \\ u \frac{\partial u}{\partial x} + v \frac{\partial u}{\partial y} &= u_1 \frac{\partial u_1}{\partial x} + v_1 \frac{\partial u_1}{\partial y} + \frac{1}{Re} \frac{\partial^2 (u - u_1)}{\partial y^2} \end{aligned} \right\} \quad (9.2.8)$$

which must be solved together with the Euler equations for  $u_1$ ,  $v_1$  and  $p_1$ . The solution for  $u$  and  $v$  applies over the whole domain and not only in the boundary layer, thereby providing a *uniformly valid approximation*. Indeed, Eqs. (9.2.8) are valid in the whole field and not only in the boundary-layer; the solution of these equations outside the boundary-layer gives  $u \rightarrow u_1$  and  $v \rightarrow v_1$ , which implies that we recover the solution of the Euler equations.

The boundary conditions are

$$\begin{aligned} U_1(x, 0, \varepsilon) &= -u_1(x, 0, \varepsilon) ; \varepsilon V_1(x, 0, \varepsilon) = -v_1(x, 0, \varepsilon) \\ U_1(x, \infty, \varepsilon) &= 0 \quad ; \quad V_1(x, \infty, \varepsilon) = 0 \end{aligned} \quad (9.2.9)$$

or, equivalently

$$\begin{aligned} y = 0 : u &= 0 \quad ; \quad v = 0 \\ y \rightarrow \infty : u - u_1 &\rightarrow 0 \quad ; \quad v - v_1 \rightarrow 0 \end{aligned} \quad (9.2.10)$$

In addition, boundary conditions at infinity are prescribed for the Euler equations.

The condition  $v - v_1 \rightarrow 0$  when  $y \rightarrow \infty$  implies that the system of generalized boundary layer Eqs. (9.2.8) and the Euler Eqs. (9.2.5a)–(9.2.5c) must be solved together. It is not possible to solve the Euler equations independently from the boundary layer equations; *the two sets of equations interact*. The IBL theory has been proposed earlier heuristically or on the basis of the triple deck theory [8, 2, 7, 9] and is fully justified here thanks to the use of *generalized expansions*. In effect, with regular expansions, all the terms are strictly classified by orders of magnitude and the boundary conditions, Eqs. (9.2.9), would give the wall boundary condition for the inviscid flow  $v_1 = 0$ . Then, the standard uncoupling between the inviscid flow equations and the boundary layer equations is obtained and the first order inviscid flow equations can be solved without knowing that the boundary-layer exists.

It is important to note that the generalized boundary layer equations account for possible pressure variations normal to the wall.

### 9.2.2 Reduced Model for an Outer Irrotational Flow

When the outer flow is irrotational, as is often the case in aerodynamics, and if the validity of Eqs. (9.2.8) is restricted to the boundary-layer, it can be shown that Eqs. (9.2.8) reduce to the standard boundary layer equations

$$\begin{aligned}\frac{\partial u}{\partial x} + \frac{\partial v}{\partial y} &= 0 \\ u \frac{\partial u}{\partial x} + v \frac{\partial u}{\partial y} &= u_1(x, 0) \frac{\partial u_1(x, 0)}{\partial x} + \frac{1}{Re} \frac{\partial^2 u}{\partial y^2}\end{aligned}\quad (9.2.11)$$

subject to the boundary conditions

$$u(x, 0, \varepsilon) = 0 \quad (9.2.12a)$$

$$v(x, 0, \varepsilon) = 0 \quad (9.2.12b)$$

$$\lim_{y \rightarrow \infty} u = u_1(x, 0, \varepsilon) \quad (9.2.12c)$$

$$\lim_{y \rightarrow \infty} \left[ v + y \frac{\partial u_1(x, 0, \varepsilon)}{\partial x} \right] = \frac{v_1(x, 0, \varepsilon)}{\varepsilon} \quad (9.2.12d)$$

The last equation can be expressed in terms of the displacement thickness and can be written as (see Problem 9-9)

$$v_1(x, 0, \varepsilon) = \frac{d}{dx} \left[ \int_0^\infty (u_1(x, 0, \varepsilon) - u) dy \right] \quad (9.2.13)$$

This reduced model is usually used in interactive boundary-layer calculations but it should be noted that the boundary-layer and inviscid-flow equations are strongly coupled by Eq. (9.2.12d). There is no hierarchy between the boundary-layer and inviscid-flow equations; the two sets of equations interact.

It is also interesting to note that the first order triple deck theory (see Sections 11.7, 11.8 and 12.7) can be deduced from the IBL theory [11]. This completes the link with the interaction law proposed by Veldman.

### 9.2.3 Applications

The above discussion justifies the IBL theory and provides a solid foundation for its applications to many engineering problems as we shall discuss in this chapter for two-dimensional flows and in Chapter 13 for three-dimensional flows.

## 9.3 Interaction Problem

Predicting the flowfield by solutions based on inviscid-flow theory is usually adequate as long as the viscous effects are negligible. A boundary layer that forms on the surface causes the irrotational flow outside it to be on a surface

displaced into the fluid by a distance equal to the displacement thickness  $\delta^*$ , which represents the deficiency of mass within the boundary layer. Thus, a new boundary for the inviscid flow, taking the boundary-layer effects into consideration, can be formed by adding  $\delta^*$  to the body surface. The new surface is called the displacement surface and, if its deviation from the original surface is not negligible, the inviscid flow solutions can be improved by incorporating viscous effects into the inviscid flow equations [2, 12, 13].

A convenient and popular approach described in detail in [2] for aerodynamic flows and justified in Section 9.2, is based on the concept that the displacement surface can also be formed by distributing a blowing or suction velocity on the body surface. The strength of the blowing or suction velocity  $v_b$  is determined from the boundary-layer solutions according to

$$v_b = \frac{d}{dx}(u_e \delta^*) \quad (9.3.1)$$

where  $x$  is the surface distance of the body, and the variation of  $v_b$  on the body surface simulates the viscous effects in the potential flow solution. This approach, which can be used for both incompressible and compressible flows [2], is used in this section to address the interaction problem for an airfoil in subsonic flows.

For a given airfoil geometry and freestream flow conditions, we first obtain the inviscid velocity distribution with a panel method such as the one given in the accompanying CD-ROM, Program 4, then we solve the boundary-layer equations in the inverse mode as described in Section 9.4. The blowing velocity distribution,  $v_b(x)$ , is computed from Eq. (9.3.1) and the displacement thickness distribution  $\delta^*(x)$  on the airfoil and in the wake are then used in the panel method to obtain an improved inviscid velocity distribution with viscous effects as described in detail in [2]. The  $\delta_{te}^*$  is used to satisfy the Kutta condition in the panel method at a distance equal to  $\delta_{te}^*$ ; this is known as the off-body Kutta condition (Fig. 9.3). In the first iteration between the inviscid and the inverse boundary-layer methods,  $v_b(x)$  is used to replace the zero blowing velocity at the surface. At the next and following iterations, a new value of  $v_b(x)$  in each

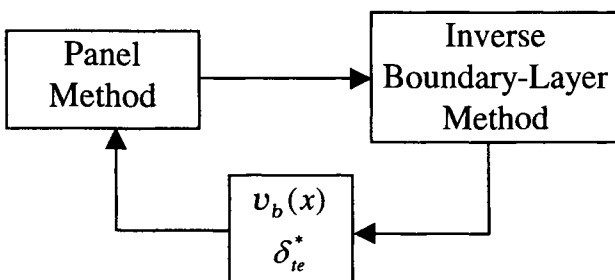


**Fig. 9.3.** Interactive boundary-layer scheme.

iteration is used as a boundary condition in the panel method. This procedure is repeated for several cycles until convergence is obtained, which is usually based on the lift and total drag coefficients of the airfoil. Studies discussed in [2] show that with three boundary-layer sweeps for one cycle, convergence is obtained in less than 10 cycles.

## 9.4 Inverse Boundary-Layer Method

The solution procedure discussed in Chapter 4 for two-dimensional boundary layer equations for a prescribed external velocity distribution (standard problem) can easily be extended to include the solution of the inverse problems arising in internal and external flows. In an internal flow, the choice is easier because the conservation of mass in integral form can be used to relate the pressure  $p(x)$  to the velocity  $u(x, y)$  in terms of mass balance in the duct. For external flows, the extension can be achieved, for example, by prescribing the displacement thickness or the wall shear. In the former case, two different procedures, as discussed in Section 9.1 can be used to establish a relationship between the external velocity and displacement thickness so that the external velocity is computed as part of the solution. The procedure of Veldman has substantial advantages over that based on the relaxation formula, Eq. (9.1.3), and is discussed here and in detail in [2]. In both cases, however, modifications are needed to the solution procedure of the standard problem.

We consider an external flow over a nonporous wall in which the viscous effects on the edge boundary condition are to be accounted for by Veldman's procedure. In this case, the boundary conditions for a flow with no mass transfer, can be rewritten as

$$y = 0, \quad u = 0, \quad v = 0 \quad (9.4.1a)$$

$$y = \delta, \quad u = u_e, \quad u_e = u_e^0 + \delta u_e(x), \quad \xi = \frac{x}{L} \quad (9.4.1b)$$

with  $\delta u_e(x)$  given by Eq. (9.1.4b) and  $u_e^0$  is calculated with the panel method. As in the case of the standard problem, it is convenient and prudent to use transformed variables, but since  $u_e(x)$  is also an unknown in the inverse problem, slight changes are made in the Falkner-Skan transformation given by Eqs. (4.2.4a) and (4.5.3), replacing  $u_e(x)$  by  $u_\infty$  and redefining new variables  $Y$  and  $F$  by

$$Y = \sqrt{u_\infty/\nu x} y, \quad \psi = \sqrt{u_\infty \nu x} F(\xi, Y) \quad (9.4.2)$$

so that Eqs. (3.1.2) and (3.1.10), with a prime now denoting differentiation with respect to  $Y$ , can be written in a form analogous to that given by Eq. (4.5.4),

$$(bF'')' + \frac{1}{2}FF'' = \xi \left( F' \frac{\partial F'}{\partial \xi} - F'' \frac{\partial F}{\partial \xi} \right) - \xi w \frac{dw}{d\xi} \quad (9.4.3)$$

where  $w = u_e/u_\infty$ . The boundary conditions, except for the second one in Eq. (9.4.1b), can be written as

$$Y = 0, \quad F' = 0, \quad F_w = -\frac{\sqrt{R_L}}{\sqrt{\xi}} \int_{x_0}^x \frac{v_w}{u_\infty} d\xi \quad (9.4.4a)$$

$$Y = Y_e, \quad F'_e = w(\xi) \quad (9.4.4b)$$

The boundary condition corresponding to the second equation (9.4.1b) is obtained by applying a discretization approximation to the Hilbert integral

$$u_e(x_i) = u_e^0(x_i) + C_{ii}D_i + \sum_{j=1}^{i-1} C_{ij}D_j + \sum_{j=i+1}^N C_{ij}D_j \quad (9.4.5)$$

where the subscript  $i$  denotes the  $\xi$ -station where the inverse calculations are to be performed,  $C_{ij}$  is a matrix of interaction coefficients obtained by the procedure described in [2], and  $D$  is given by  $D = u_e\delta^*$ . In terms of transformed variables, the parameter  $D$  becomes

$$\bar{D} = \frac{D}{Lu_\infty} = \sqrt{\frac{\xi}{R_L}} (Y_e w - F_e) \quad (9.4.6)$$

and the relationship between the dimensionless external velocity  $w$  and displacement thickness  $\delta^*$  provided by the Hilbert integral can then be written in dimensionless form as

$$Y = Y_e, \quad F'_e(\xi^i) - \lambda[Y_e F'_e(\xi) - F_e(\xi^i)] = g_i \quad (9.4.7)$$

where

$$\lambda = C_{ii} \sqrt{\frac{\xi^i}{R_L}}, \quad R_L = \frac{u_\infty L}{\nu} \quad (9.4.8a)$$

$$g_i = \bar{u}_e^0(\xi^i) + \sum_{j=1}^{i-1} C_{ij} \bar{D}_j + \sum_{j=i+1}^N C_{ij} \bar{D}_j \quad (9.4.8b)$$

In an inverse method which makes use of the Hilbert integral formulation, the boundary-layer calculations must be repeated on the body. Each boundary-layer calculation, starting at  $\xi = \xi^0$  and ending at  $\xi = \xi^N$ , is called a sweep. In sweeping through the boundary-layer, the right-hand side of Eq. (9.4.5) uses the values of  $\delta^*$  from the previous sweep when  $j > i$  and the values from the current sweep when  $j < i$ . Thus, at each  $\xi$ -station the right-hand side of Eq. (9.4.5) provides a prescribed value for the linear combination of  $u_e(\xi^i)$  and  $\delta^*(\xi^i)$ . After convergence of the Newton iterations at each station, the summations of Eq. (9.4.5) are updated for the next  $\xi$ -station. Note that the Hilbert integral coefficients  $C_{ij}$  discussed in [2] have been computed and stored at the start of the boundary-layer calculations.

### 9.4.1 Transformed Equations: General Form

It is convenient to write the transformed equations for standard and inverse modes in one general form so that the numerical method described in Section 4.5 can be used for both cases. For this purpose, we write Eqs. (4.5.4) and (9.4.3) in the following form

$$\begin{aligned} (bf'')' + \lambda_1 \left\{ \frac{m}{2} ff'' + m[1 - (f')^2] \right\} + \frac{1}{2} ff'' \\ = \xi \left\{ \frac{\partial}{\partial \xi} \left[ \frac{(f')^2}{2} \right] - f'' \frac{\partial f}{\partial \xi} - \lambda_2 \frac{d}{d\xi} \left( \frac{w^2}{2} \right) \right\} \end{aligned} \quad (9.4.9)$$

where for  $\lambda_1 = 1$  and  $\lambda_2 = 0$  we recover Eq. (4.5.4) which is subject to the boundary conditions given by Eqs. (4.5.5). For  $\lambda_1 = 0$  and  $\lambda_2 = 1$ , we recover Eq. (9.4.3) provided that we note that  $F$  now corresponds to  $f$ , primes denote differentiation with respect to  $Y$  and not  $\eta$ . For consistency, we also rewrite Eqs. (9.4.4) and (9.4.7) in the adopted notation of Eq. (9.4.9),

$$\eta = 0; \quad f' = 0, \quad f_w = -\frac{\sqrt{R_L}}{\sqrt{\xi}} \int_{\xi_0}^{\xi} \frac{v_w}{u_\infty} d\xi \quad (9.4.10a)$$

$$\eta = \eta_e; \quad f' - \lambda(\eta_e f' - f) = g_i \quad (9.4.10b)$$

The switch from the standard problem to the inverse problem is specified. This is usually done after two or three  $\xi$ -stations from the stagnation point.

### 9.4.2 Numerical Method

The numerical formulation of Eq. (9.4.9) is similar to one described for Eq. (4.5.4). Again we introduce new dependent variables  $u(\xi, \eta)$ ,  $v(\xi, \eta)$  and express Eq. (9.4.9) as a first-order given by Eqs. (4.5.8a), (4.5.8b) and

$$(bv)' + \lambda_1 m \left[ \frac{1}{2} fv + (1 - u^2) \right] + \frac{1}{2} fv = \xi \left[ \frac{\partial}{\partial \xi} \left( \frac{u^2}{2} \right) - v \frac{\partial f}{\partial \xi} - \lambda_2 \frac{d}{d\xi} \left( \frac{w^2}{2} \right) \right] \quad (9.4.11)$$

The boundary conditions for the standard mode are identical to those given by Eq. (4.5.9); for the inverse mode they become

$$\eta = 0; \quad u = 0, \quad f = f_w \quad (9.4.12a)$$

$$\eta = \eta_e; \quad \lambda f + (1 - \lambda \eta_e) w = g_i \quad (9.4.12b)$$

The difference approximations to Eqs. (4.5.8a) and (4.5.8b) are given by Eqs. (4.5.11a) and (4.5.11b). For Eq. (9.4.11) they are given by

$$\begin{aligned}
& \frac{1}{2} \left[ \frac{(bv)_j^n - (bv)_{j-1}^n}{h_j} + \frac{(bv)_j^{n-1} - (bv)_{j-1}^{n-1}}{h_j} \right] \\
& + \frac{\lambda_1}{2} \left[ \frac{m^{n-1/2}}{2} \left\{ (fv)_{j-1/2}^n + (fv)_{j-1/2}^{n-1} \right\} \right. \\
& \left. + 2m^{n-1/2} \left\{ 1 - \frac{(u^2)_{j-1/2}^n + (u^2)_{j-1/2}^{n-1}}{2} \right\} \right] \\
& + \frac{1}{2} [(fv)_{j-1/2}^n + (fv)_{j-1/2}^{n-1}] \\
= & \xi^{n-1/2} \left[ FLARE \frac{(u^2)_{j-1/2}^n - (u^2)_{j-1/2}^{n-1}}{2k_n} \right. \\
& \left. - \left( \frac{v_{j-1/2}^n + v_{j-1/2}^{n-1}}{2} \right) \left( \frac{f_{j-1/2}^n - f_{j-1/2}^{n-1}}{k_n} \right) - \lambda_2 \left\{ \frac{(u_J^2)^n - (u_J^2)^{n-1}}{k_n} \right\} \right]
\end{aligned}$$

In the above equation, the parameter *FLARE* refers to the Flügge–Lotz–Reyhner approximation [14] used to set  $u \partial u / \partial x$  equal to zero in the momentum equation wherever  $u < 0$ . As a result, the numerical instabilities that plague attempts to integrate the boundary-layer equations against the local direction of flow are avoided. In regions of positive streamwise velocity ( $u_j > 0$ ), it is taken as unity and as zero in regions of negative streamwise velocity ( $u_j \leq 0$ ).

After some algebra and rearranging, the above expression can be written as

$$\begin{aligned}
& h_j^{-1} [(bv)_j^n - (bv)_{j-1}^n] + \alpha_1 (fv)_{j-1/2}^n - \alpha_2 (u^2)_{j-1/2}^n \\
& + \alpha^n [v_{j-1/2}^{n-1} f_{j-1/2}^n - f_{j-1/2}^{n-1} v_{j-1/2}^n + \lambda_2 (u_J^2)^n] = R_{j-1/2}^{n-1}
\end{aligned} \tag{9.4.13}$$

where

$$\alpha^n = \frac{\xi^{n-1/2}}{k_n}, \quad \alpha_1 = 1 + \frac{\lambda_1}{2} m^{n-1/2} + \alpha^n, \quad \alpha_2 = \lambda_1 m^{n-1/2} + \alpha^n FLARE \tag{9.4.14a}$$

$$R_{j-1/2}^{n-1} = -L_{j-1/2}^{n-1} + \alpha^n \left[ -FLARE (u^2)_{j-1/2}^{n-1} + f_{j-1/2}^{n-1} v_{j-1/2}^{n-1} + \lambda_2 (u_J^2)^{n-1} \right] \tag{9.4.14b}$$

$$\begin{aligned}
L_{j-1/2}^{n-1} = & h_j^{-1} [(bv)_j^{n-1} - (bv)_{j-1}^{n-1}] + \left( 1 + \frac{\lambda_1}{2} m^{n-1/2} \right) (fv)_{j-1/2}^{n-1} \\
& + 2\lambda_1 m^{n-1/2} \left[ 1 - \frac{(u^2)_{j-1/2}^{n-1}}{2} \right]
\end{aligned} \tag{9.4.14c}$$

Equations (4.5.11a), (4.5.11b) and (9.4.13) are imposed for  $j = 1, 2, \dots, J$  at a given  $\xi^n$ . They are accompanied with the boundary conditions given by Eqs. (4.5.17) for the standard mode, and by Eqs. (9.4.12) for the inverse mode

$$f_0^n = f_w^n, \quad u_0^n = 0, \quad \lambda f_J^n + (1 - \lambda \eta_J) u_J^n = g_i \tag{9.4.15}$$

The solution of the algebraic equations represented by Eqs. (4.5.11a,b), (9.4.13) and (4.5.17) is similar to the procedure described in subsection 4.5.2. They are linearized with Newton's method and written in the matrix-vector form given by Eq. (4.5.23).

The linear system for Eqs. (4.5.11a,b) is given by Eqs. (4.5.19a,b) and (4.5.20a,b) and for Eq. (9.4.13) by

$$(s_1)_j \delta v_j + (s_2)_j \delta v_{j-1} + (s_3)_j \delta f_j + (s_4)_j \delta f_{j-1} \\ + (s_5)_j \delta u_j + (s_6)_j \delta u_{j-1} + (s_7)_J \delta u_J = (r_2)_j \quad (9.4.16)$$

where

$$(s_1)_j = h_j^{-1} b_j^{(\nu)} + \frac{\alpha_1}{2} f_j^{(\nu)} - \frac{\alpha^n}{2} f_{j-1/2}^{n-1} \quad (9.4.17a)$$

$$(s_2)_j = -h_j^{-1} b_{j-1}^{(\nu)} + \frac{\alpha_1}{2} f_{j-1}^{(\nu)} - \frac{\alpha^n}{2} f_{j-1/2}^{n-1} \quad (9.4.17b)$$

$$(s_3)_j = \frac{\alpha_1}{2} v_j^{(\nu)} + \frac{\alpha^n}{2} v_{j-1/2}^{n-1} \quad (9.4.17c)$$

$$(s_4)_j = \frac{\alpha_1}{2} v_{j-1}^{(\nu)} + \frac{\alpha^n}{2} v_{j-1/2}^{n-1} \quad (9.4.17d)$$

$$(s_5)_j = -\alpha_2 u_j^{(\nu)} \quad (9.4.17e)$$

$$(s_6)_j = -\alpha_2 u_{j-1}^{(\nu)} \quad (9.4.17f)$$

$$(s_7)_J = 2\alpha^n \lambda_2 u_J^{(\nu)} \quad (9.4.17g)$$

$$(r_2)_j = R_{j-1/2}^{n-1} - \left[ h_j^{-1} (b_j^{(\nu)} v_j^{(\nu)} - b_{j-1}^{(\nu)} v_{j-1}^{(\nu)}) + \alpha_1 (f v)_{j-1/2}^{(\nu)} \right. \\ \left. - \alpha_2 (u^2)_{j-1/2}^{(\nu)} + \alpha^n (v_{j-1/2}^{n-1} f_{j-1/2}^{(\nu)} - f_{j-1/2}^{n-1} v_{j-1/2}^{(\nu)}) + \lambda_2 (u_J^{(\nu)})^2 \right] \quad (9.4.18)$$

The boundary conditions for the standard mode are given by Eq. (4.5.22) and for the inverse mode by

$$\delta f_0 = (r_1)_0 = 0, \quad \delta u_0 = (r_2)_0 = 0, \quad (9.4.19a)$$

$$\lambda \delta f_J + (1 - \lambda \eta_J) \delta u_J = (r_3)_J = g_i - [\lambda f_J + (1 - \lambda \eta_J) u_J] \quad (9.4.19b)$$

The linear system for the standard mode ( $\lambda_2 = 0$ ) has the same block tridiagonal structure as before; it can be expressed in matrix-vector form given by Eq. (4.5.23) and solved by the block-elimination method discussed in subsection 4.5.3.

The linear system for the inverse mode ( $\lambda_2 = 1$ ) can also be written in matrix-vector form as

$$G \vec{\delta} = \vec{r} \quad (9.4.20)$$

where  $\vec{\delta}$  and  $\vec{r}$  are identical to those defined by Eq. (4.5.25), and

$$G = \begin{vmatrix} A & D \\ E^T & A_J \end{vmatrix} \quad (9.4.21)$$

The coefficient matrix  $A$  is identical to that defined in Eq., (4.5.24) except that the index of  $A_j$ ,  $B_j$  and  $C_j$  matrices run up to  $j = J - 1$ , that is, the last row of  $A$  is now  $B_{J-1}, A_{J-1}$ . This causes complications to the block-elimination method. A convenient and efficient way to overcome this complication is to use Keller's bordering algorithm [15] discussed in detail in [2].

### 9.4.3 Computer Program

The computer program for the standard problem (BLP2) can be extended to the inverse boundary layer problem with some modifications to its subroutines, adding new subroutines and replacing SOLV3 algorithm with the bordering algorithm. Reference [2] describes such a computer program, including the solution of interactive boundary-layer problems with inviscid flows.

## 9.5 Applications of the Inverse Boundary-Layer Method: Trailing Edge Flow of a Flat Plate

The main purpose of an inverse boundary-layer method for external flows is to calculate flows with separation which can cause solutions to become singular and which require that the external velocity be treated as an unknown. Two popular approaches for accomplishing this objective were outlined in Section 9.1. Inverse formulations are, however, required in some external-flow problems without separation, and one such problem corresponding to the trailing-edge flow of a flat plate is presented in this section.

The nature of the flow near the trailing edge of an airfoil has long been a subject of both theoretical and practical interest. The problem exhibits a singularity intriguing to the theoretician, and the question of finite Reynolds number effects on aerodynamic forces is of significant practical importance. The problem was first treated within the framework of boundary-layer theory by Goldstein [16], who showed that continuation of the flat-plate solution beyond the trailing edge required introduction of a thin sublayer along the wake centerline, with thickness of order  $x^{1/3}$ , where  $x$  is the distance from the trailing edge. At the point of origin of this sublayer ( $x = 0$ ), the transverse velocity  $v$  is singular, much as it is at the leading edge of the plate. In a higher-order theory, this large magnitude of  $v$  would produce a similarly large pressure gradient in the external inviscid flow, which in turn would produce a significant change in the skin friction near the trailing edge. A number of studies have been made to construct such a higher-order theory for this region, as discussed by Van Dyke [17]. However, none of these older theories properly account for the Goldstein

singularity, and more accurate solutions than those provided by simple perturbation series are required. One alternative to the solution of this problem is to solve the Navier–Stokes equations, as followed by Dennis and Chang [18] and Dennis and Dunwoody [19] and Cousteix et al. [20]. A second alternative is to use the triple-deck theory developed by Stewartson [21] and Messiter [22], and a third alternative is to use interactive boundary-layer theory such as the one discussed here and a fourth one is to solve the reduced forms of the Navier–Stokes equations, such as the one due to Rubin and his coworkers [23, 24], which emulates boundary-layer/triple-deck methodology in viscous regions and potential flow theory in inviscid regions. A useful review of these approaches is given by Khosla et al. [24].

Very accurate solutions have been obtained for a laminar flow over a wide range of Reynolds numbers by procedures based on the triple-deck theory of Stewartson. This approach, which may be regarded as a form of interactive boundary-layer theory, combines solutions of inviscid and viscous flow equations by procedures that address the physics of the flow and the numerical accuracy of the solutions. Solutions employing the triple-deck theory may be regarded as a means of calibrating solutions of the Navier–Stokes equations so that more complicated problems involving turbulent flows in two and three dimensions can be tackled by more general methods.

Before reviewing the application of the inverse method of the previous section to the trailing-edge flow of a flat plate, it is useful to discuss the mathematical problem used in the triple-deck theory which essentially couples a system of equations corresponding to boundary-layer and inviscid flow equations. See also the discussion in Section 11.7. Figure 9.4 is a schematic of the triple-deck region which intervenes between the region of validity of the Blasius solution and that of the Goldstein [16] wake solutions. The function of the triple deck is to remove the discontinuity in the transverse velocity (or slope of the displacement thickness) at the trailing edge. The main deck corresponds to Goldstein’s outer wake, which to first order is the inviscid continuation of the Blasius boundary-layer solution. The lower deck corresponds to Goldstein’s inner viscous wake, which is produced by the altered boundary condition at the trailing edge. The classical boundary-layer equations (for a prescribed external velocity distribution) apply in the lower deck. The additional upper deck is required because of the displacement effect of the wake, which has not been accounted for properly in earlier theories. The upstream influence is felt because of the strong coupling between the upper deck and the lower deck. Thus, the downstream wake affects the boundary layer on the plate via viscous interaction with the potential-flow upper deck.

The notation used in Fig. 9.4 is that of Stewartson [25] with the exception that the plate length  $L$  here replaces its lower-case script version. The parameter  $\varepsilon$  denotes  $Re^{1/8}$ . As indicated in Fig. 9.4, the streamwise extent of the triple

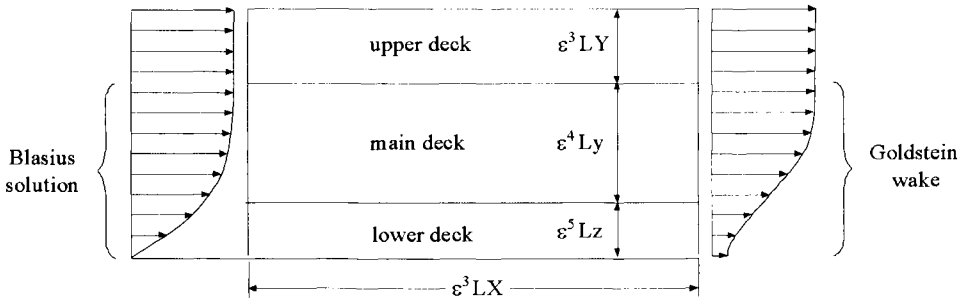


**Fig. 9.4.** The triple-deck flow structure.

deck is of order  $\varepsilon^3$ , wherein the lower, main and upper decks have thicknesses of order  $\varepsilon^5$ ,  $\varepsilon^4$  and  $\varepsilon^3$ , respectively. Further details, including the solution of the appropriate equations in each deck are given in [26].

The calculations employing the inverse method of Section 9.4 were performed for a plate length of  $L$  and for a transformed boundary-layer thickness height  $\eta_e$  of 9 with several step sizes in  $\xi$  and  $\eta$  directions. Since the modified BLP2D computes the flow only on the plate, modifications are made to the inverse boundary-layer method in order to extend the calculations into the wake from the trailing edge. This is done by changing the wall boundary conditions from

$$u = 0, \quad v = 0 \quad (9.5.1a)$$

to the wake centerline boundary conditions,

$$\frac{\partial u}{\partial y} = 0, \quad v = 0 \quad (9.5.1b)$$

by setting  $f''(0)$  and  $f(0)$  equal to zero rather than  $f(0)$  and  $f'(0)$  equal to zero. These changes at the trailing edge, however, can introduce numerical problems in wake calculation since the velocity profile at the trailing edge, which satisfies the boundary conditions in Eq. (9.5.1a), does not satisfy the boundary conditions in Eq. (9.5.1b). Furthermore, near the trailing edge the streamwise centerline velocity  $u_c$  changes rather rapidly and care is needed in prescribing the distribution of  $x$ -stations in this region. The problem associated with boundary conditions can, however, be easily avoided by making the initial guess for the first  $\xi$ -station in the wake to come not from the profiles at the trailing edge but from those that satisfy the centerline conditions in Eq. (9.5.1b).

The problem associated with the grid distribution near the trailing edge requires some care. In the calculations performed here, the near-wake centerline velocity,  $u_c$ , given by Stewartson [25], namely,

$$u_c = 0.8991 \lambda_1^{2/3} X^{1/3} \quad (9.5.2)$$

is used with  $\lambda_1 = 1.343$  and with  $\lambda = 0.3321$  and  $\varepsilon = Re^{1/8}$ ,

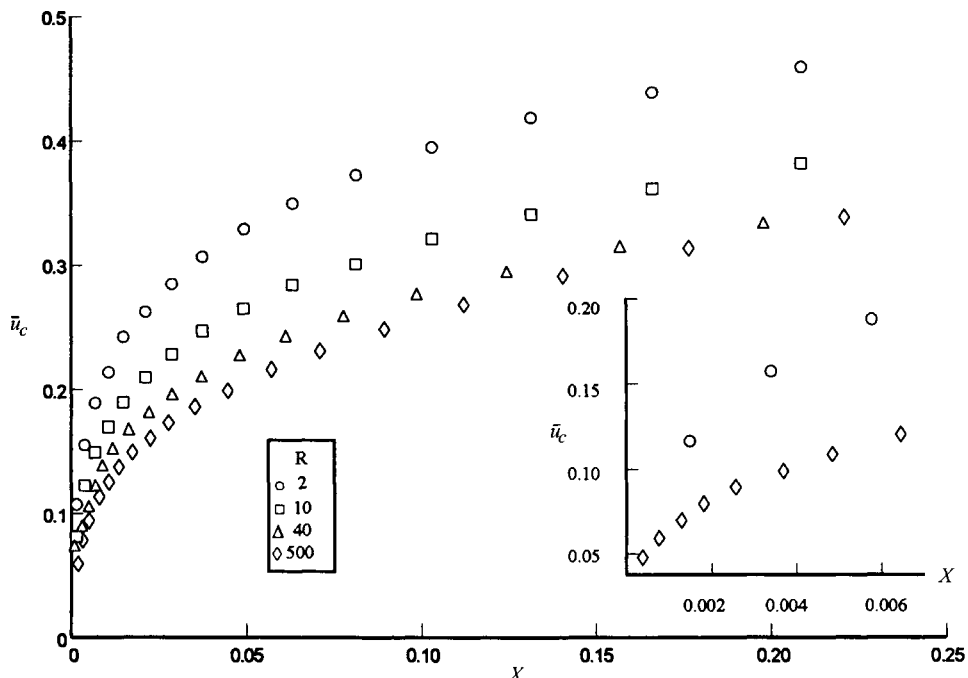


**Fig. 9.5.** Grid distribution and centerline velocity at different Reynolds numbers near the trailing edge.

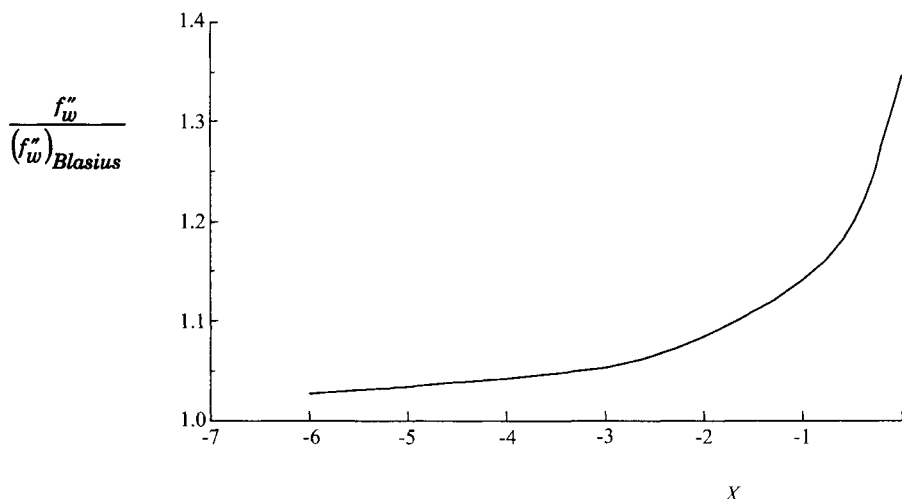


**Fig. 9.6.** Ratio of  $f_x'' / (f_w'')_{\text{Blasius}}$  near the trailing edge.

**Table 9.1.** Comparison of calculated drag coefficients with those computed by (a) Jobe, (b) Dennis, (c) Dennis and Chang, and (d) Dennis and Dunwoody.

<i>R</i>	$C_d$	(a) $C_d$	(b) $C_d$	(c) $C_d$	(d) $C_d$
1	3.60	4.022	3.708	3.64	3.79
2	2.22	2.408	—	2.20	—
4	1.38	1.465	—	1.36	—
10	0.756	0.779	0.7535	0.748	0.773
15	0.590	0.595	—	0.581	—
20	0.485	0.493	0.4862	0.483	0.504
40	0.318	0.317	0.3144	0.316	0.323
100	0.186	0.181	0.1826	0.188	0.187
200	0.123	0.120	0.1220	—	0.123
500	0.0723	0.0711	—	0.0731	—
1,000	0.0489	0.0484	—	0.0502	—
2,000	0.0335	0.0332	—	0.0341	—
5,000	0.02048	0.0203	—	0.0206	—
10,000	0.0142	0.0141	—	0.0141	—

**Table 9.2.** Comparison of calculated drag coefficients with experimental data [28].

<i>R</i>	$C_d$ (Experimental)	$C_d$ (Computed)	<i>R</i>	$C_d$ (Experimental)	$C_d$ (Computed)
11.93	0.668	0.681	640.0	0.0620	0.0653
20.00	0.500	0.485	993.0	0.0460	0.0491
34.9	0.364	0.360	1050.0	0.0458	0.0470
40.08	0.300	0.316	1143.0	0.0450	0.0442
60.3	0.243	0.239	1336.0	0.0417	0.0391
102.5	0.177	0.187	1542.0	0.0391	0.0356
219.1	0.1073	0.113	2133.0	0.0313	0.0316
340.0	0.0872	0.0912	2335.0	0.0304	0.0297
483.0	0.0702	0.0725			

$$X = \lambda^{5/4} \varepsilon^3 \left( \frac{x}{L} \right) \quad (9.5.3)$$

The grid in  $x/L$  is chosen in such a way that  $u_c$  changes very slowly from its zero value at the trailing edge of the flat plate with length  $L$ .

Figure 9.5 shows the variation of the centerline velocity in the wake close to the trailing edge at several Reynolds numbers. The symbols that denote the grid distribution used in the wake region for each Reynolds number indicate that step sizes in the streamwise direction are rather small, and they become even smaller with increasing Reynolds number.

Figure 9.6 shows the variation of the ratio of the computed  $f_w''$  to the Blasius  $f_w''$  value of 0.332 as this ratio increases smoothly from unity to its value at the trailing edge. These computed values are in excellent agreement with those reported by Jobe [26].

Table 9.1 shows a comparison between the drag coefficients computed with the present computer program and those given by Dennis [27], Dennis and Chang [18] and Dennis and Dunwoody [19], as well as those predicted by the following equation

$$C_d = \frac{1.328}{R^{1/2}} + \frac{1.694}{R^{7/8}} \quad (9.5.4)$$

given by Jobe [26] for Reynolds numbers ranging from  $R = 1$  to 10,000. The drag coefficients with the computer program were obtained from twice the momentum thickness of the far wake velocity profile. As can be seen, the agreement is remarkably good.

## 9.6 Applications of the Interactive Boundary-Layer Method: Airfoils

In [2], an extensive evaluation of the interaction procedure described in Section 9.3 was conducted for aerodynamic flows. With a combination of inviscid and inverse boundary-layer methods and methods for predicting the onset of transition, calculations were performed for single and multi-element airfoil flows, wing and multiwing flows, all with and without compressibility effects, for a wide range of Reynolds numbers and angles of attack, including stall and post stall. Comparison of the calculated results indicated good agreement with experimental data and showed that this interactive procedure is an accurate and efficient approach for calculating aerodynamic flows.

In this section, we first present a brief description of the solution procedure used in the interactive method for incompressible flow over airfoils before we present results for a sample of single airfoil flows at high (subsection 9.6.1) and at low (subsection 9.6.2) Reynolds numbers and multielement airfoils (subsection 9.6.3) obtained with this method [2].

The calculation method described in Chapters 2 to 4 of [2] for two-dimensional incompressible flows uses the Hess-Smith panel, Program 4, to obtain the external velocity distribution for the specified airfoil geometry and to identify the airfoil stagnation point.

The inverse boundary-layer method obtains solutions on the upper and lower surfaces from the stagnation point. If the onset of the transition location is not specified, the laminar flow solutions are used to calculate the transition location by using either Michel's formula, Eq. (5.4.1), or the  $e^n$ -method described in subsection 5.4.2. As discussed in Section 5.4, when the Reynolds number is high and the angles of attack are low to moderate, the onset of transition occurs before the flow separation point, and the extent of the transition region is confined to a relatively small region. In this case, it is satisfactory to determine the onset of transition from Eq. (5.4.1) by calculating local Reynolds numbers based on momentum thickness,  $R_\theta$ , and surface distance from the leading edge,

$R_x$ , at each chordwise station. Initially the computed Reynolds numbers in the coordinates of  $R_\theta$  and  $R_x$  are always beneath the transition curve, and if transition occurs, then the calculated  $R_\theta$  and  $R_x$  values will be over this curve. The onset of transition is then determined by interpolating the last values of  $R_\theta$  and  $R_x$  and the first high values of  $R_\theta$  and  $R_x$  which intersect the transition curve. Sometimes, however, especially at higher angles of attack, before transition location can be computed with this procedure, laminar separation takes place. In that case, the separation location may be assumed to correspond to the onset of transition.

When the Reynolds number is low and the angles of attack are low to moderate, it is necessary to use the  $e^n$ -method. Of course, this method can also be used when the Reynolds number is high. In either case, the computed laminar velocity profiles are analyzed with the linear stability method and growth rates are determined for different physical frequencies as described in Chapter 5. Transition is assumed to take place when the integrated amplification factor reaches to an  $n$ -value between 8 and 10. At higher angles of attack, as in the case of high Reynolds number flows, the prediction of the onset of transition with the  $e^n$ -method must be replaced with the assumption that the onset of transition corresponds to the separation location.

Once the onset of transition location is known, the viscous flow solutions are obtained for both laminar and turbulent flows on the airfoil and in the wake, with calculations taking place separately on the upper and lower surfaces of the airfoil and wake. For a given external velocity distribution, these calculations are repeated. Each boundary-layer calculation, starting at the stagnation point and ending at some specified  $\xi$ -location in the wake is called a sweep. In sweeping through the boundary-layer, the right-hand side of Eq. (9.4.5) uses the values of  $\delta^*$  from the previous sweep when  $j > i$  and the values from the current sweep when  $j < i$ . Thus, at each  $\xi$ -station the right-hand side of Eq. (9.4.5) provides a prescribed value for the linear combination of  $u_e(\xi^i)$  and  $\delta^*(\xi^i)$ . After convergence of the Newton iterations at each station, the summations of Eq. (9.4.5) are updated for the next  $\xi$ -station. Note that the Hilbert integral coefficients  $C_{ij}$  discussed in Section 9.4 have been computed and stored at the start of the boundary-layer calculations.

At the completion of the boundary-layer sweeps on the airfoil and in the wake, boundary-layer solutions are available on the airfoil and in the wake. The blowing velocity on the airfoil  $v_b$  is computed from Eq. (9.3.1) and a jump in the normal velocity component  $\Delta v_i$  in the wake is computed from

$$\Delta v_i = \frac{d}{dx}(u_e \delta_u^*) + \frac{d}{dx}(u_e \delta_l^*) \quad (9.6.1)$$

and they are used to obtain a new distribution of external velocity  $u_e^0(x)$  from the inviscid method. As before, the onset of transition location is determined

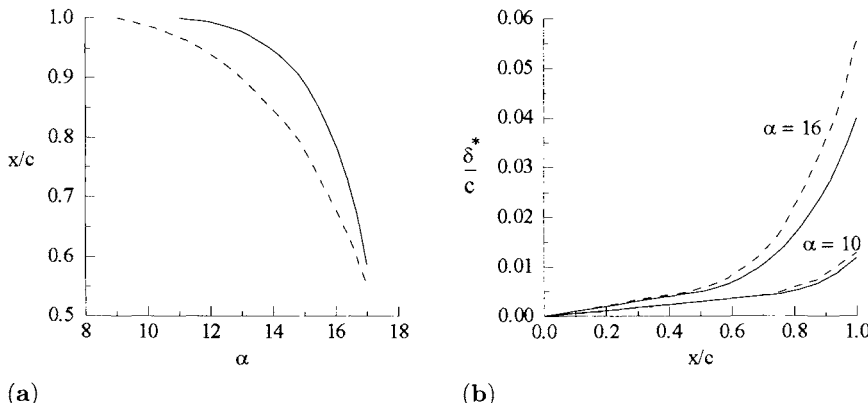


**Fig. 9.7.** Wake effect on (a) flow separation and (b) displacement thickness – NACA 0012 airfoil. —, with wake; - - -, without wake.

from the laminar flow solutions and the boundary-layer calculations are performed on the upper and lower surfaces of the airfoil and in the wake by making several specified sweeps. This sequence of calculations is repeated for the whole flowfield until convergence is achieved.

### 9.6.1 Airfoils at High Reynolds Numbers

In performing calculations for airfoils, either at high or low Reynolds numbers, it is usually sufficient to neglect the wake effect and perform the calculations on the airfoil, provided that there is no or little flow separation on the airfoil. With flow separation, the relative importance of including the wake effect in the calculations depends on the flow separation as shown in Fig. 9.7. Figure 9.7a shows the computed separation locations on a NACA 0012 airfoil at a chord Reynolds number,  $R_c$  of  $6 \times 10^6$ . When the wake effect is included, separation is encountered for angles of attack greater than  $10^\circ$ , and attempts to obtain results without consideration of the wake effect lead to erroneously large regions of recirculation that increases with angle of attack, as discussed in [2].

Figure 9.7b shows that the difference in displacement thickness at the trailing edge is negligible for  $\alpha = 10^\circ$  but more than 30% for  $\alpha = 16^\circ$ . Since the viscous effects are introduced into the panel method through the blowing velocity and off-body Kutta condition, both of which involve  $\delta^*$ , the accuracy of the inviscid flow depends on the accuracy of determining  $\delta^*$  everywhere in the flowfield, especially at the airfoil trailing edge and in the wake.

Results for the NACA 0012 airfoil, with calculations including the wake effects, are shown in Figs. 9.8 to 9.10 with Figs. 9.8 and 9.9 corresponding to a chord Reynolds number of  $3 \times 10^6$  and Fig. 9.10 to Reynolds numbers of  $6 \times 10^6$  and  $9 \times 10^6$ . Figure 9.8 shows the variation of the lift and drag coefficients of the NACA 0012 airfoil for a chord Reynolds number of  $3 \times 10^6$ . As can be seen

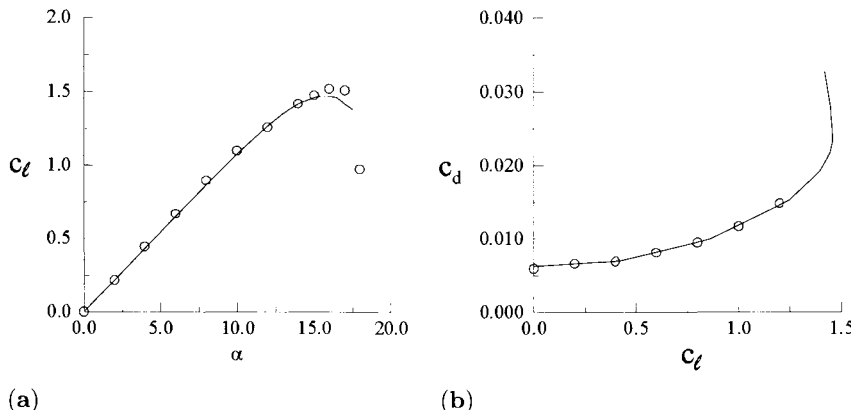


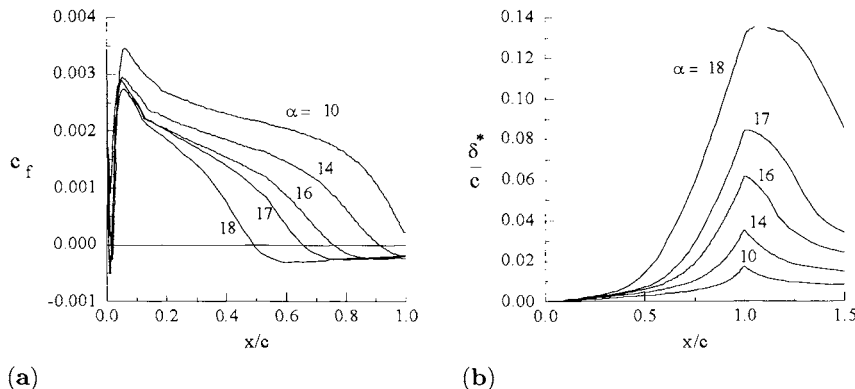
**Fig. 9.8.** Comparison between calculated (solid lines) and experimental values (symbols) of: (a)  $C_l$  vs  $\alpha$ , and (b)  $C_d$  vs  $C_l$ . NACA 0012 airfoil at  $R_c = 3 \times 10^6$ .

from Fig. 9.8a, viscous effects have a considerable effect in reducing the  $(C_l)_{\max}$  of the airfoil, which occurs at a stall angle of around  $16^\circ$ , and the calculated results agree well with measurements [2].

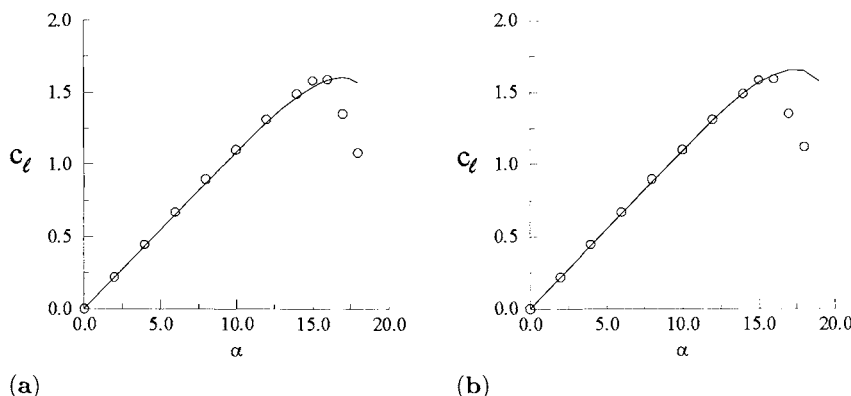
Figure 9.8b shows the variation of the drag coefficient with lift coefficient. As can be seen, the measurements of drag coefficients do not extend beyond an angle of attack of 12 degrees and at smaller angles agree well with the calculations. The nature of the lift-drag curve is interesting at higher angles of attack with the expected increase in drag coefficient and reduction in lift coefficient for post-stall angles.

Figure 9.9 shows the variation of the local skin-friction coefficient  $c_f$  and dimensionless displacement thickness  $\delta^*/c$  distribution, for the same airfoil at the same Reynolds number. As can be seen from Fig. 9.9a, flow separation occurs around  $\alpha = 10^\circ$  and its extent increases with increasing angle of attack. At an angle of attack  $\alpha = 18^\circ$ , the flow separation on the airfoils is 60% of the chord length.

The variation of dimensionless displacement thickness along the airfoil and wake of the airfoil shown in Fig. 9.9b indicates that, as expected, displacement thickness increases along the airfoil, becoming maximum at the trailing edge, and decreases in the wake. For  $\alpha = 10^\circ$ ,  $\delta^*$  at the trailing edge is around 2% of the chord, becoming 4% at  $\alpha = 14^\circ$  and 6% at  $\alpha = 16^\circ$ . With increase in angle of attack, the trailing-edge displacement thickness increases significantly, becoming 8% of the chord at  $\alpha = 17^\circ$  and 14% at  $\alpha = 18^\circ$ . However, what is quite interesting, aside from this rather sharp increase in displacement thickness, is the behavior of the maximum value of the displacement thickness. While for angles of attack up to and including stall angle,  $\alpha = 16^\circ$ , its maximum value is at the trailing edge, at higher angles of attack corresponding to post-stall, its maximum is after the trailing edge.



**Fig. 9.9.** Variation of (a) local skin-friction coefficient and (b) dimensionless displacement thickness distribution. NACA 0012 airfoil at  $R_c = 3 \times 10^6$ .



**Fig. 9.10.** Effect of Reynolds number on the lift coefficient. NACA 0012 airfoil at (a)  $R_c = 6 \times 10^6$ , and (b)  $R_c = 9 \times 10^6$ .

Figure 9.10, together with Fig. 9.8, shows the effect of the Reynolds number on the lift coefficient. In accord with the measurements, the calculation method satisfactorily accounts for the effects of Reynolds number. The results show that the maximum lift coefficient,  $(C_\ell)_{\max}$  increases with increase in Reynolds number in agreement with measurements.

### 9.6.2 Airfoils at Low Reynolds Numbers

The behavior of airfoils at low Reynolds numbers differs from those at high Reynolds numbers in that rather large separation bubbles can occur some way downstream of the leading edge with transition taking place within the bubble prior to reattachment. The length of the bubble increases with a decreasing Reynolds number and strongly influences the performance characteristics of the airfoils.

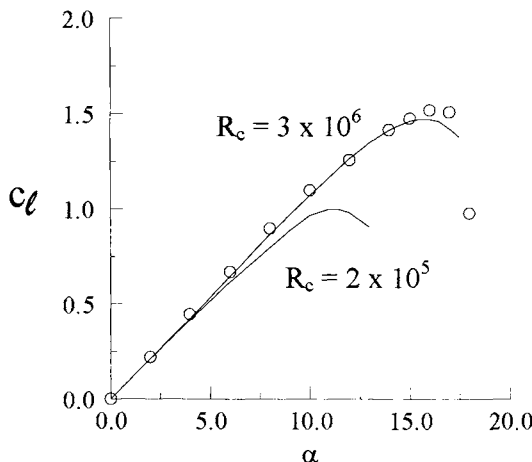


**Fig. 9.11.** Variation of lift coefficient of the NACA 0012 airfoil at two Reynolds numbers.

The calculation method described in the previous subsection can also be applied to low Reynolds numbers airfoils with the onset of the transition location computed with the  $e^n$ -method since Eq. (5.4.1) is not applicable to flows with separation. The  $e^n$ -method, however, is used only for low to moderate angles of attack since, as in high Reynolds number flows where the transition location is very close to the leading edge, it is not possible to calculate the onset of transition with the  $e^n$ -method. For this reason, the onset of transition is assumed to correspond to the location of laminar flow separation.

Figure 9.11 shows the variation of the lift coefficient of the NACA 0012 airfoil for a chord Reynolds number of  $2 \times 10^5$  together with the results obtained at  $R_c = 3 \times 10^6$ . As can be seen, the Reynolds number has a significant effect, not only on the value of the maximum lift coefficient but also on the stall angle. With this change in Reynolds number, the  $(C_l)_{\max}$  is reduced from a value of 1.5 to a value slightly over 1. The corresponding reductions in angle of attack are from  $16^\circ$  to around  $11^\circ$ .

Figures 9.12 and 9.13 show a comparison between calculated and measured results for the Eppler airfoil which is a low-drag airfoil. In the experimental data [2], the measured turbulence level was 0.06% for a total pressure  $P_t = 15$  psi, which according to Eq. (5.4.6), corresponds to a value of  $n = 9.4$  and was used in all the calculations presented below.

Figure 9.12 presents a comparison between measured and calculated distributions, pressure coefficients and local skin-friction coefficients for angles of attack of  $0^\circ$ ,  $4^\circ$  and  $8^\circ$ . As can be seen, at lower angles of attack, the separation bubble is long and located away from the leading edge, and becomes smaller with increasing angle of attack as the separation bubble moves towards the leading edge.

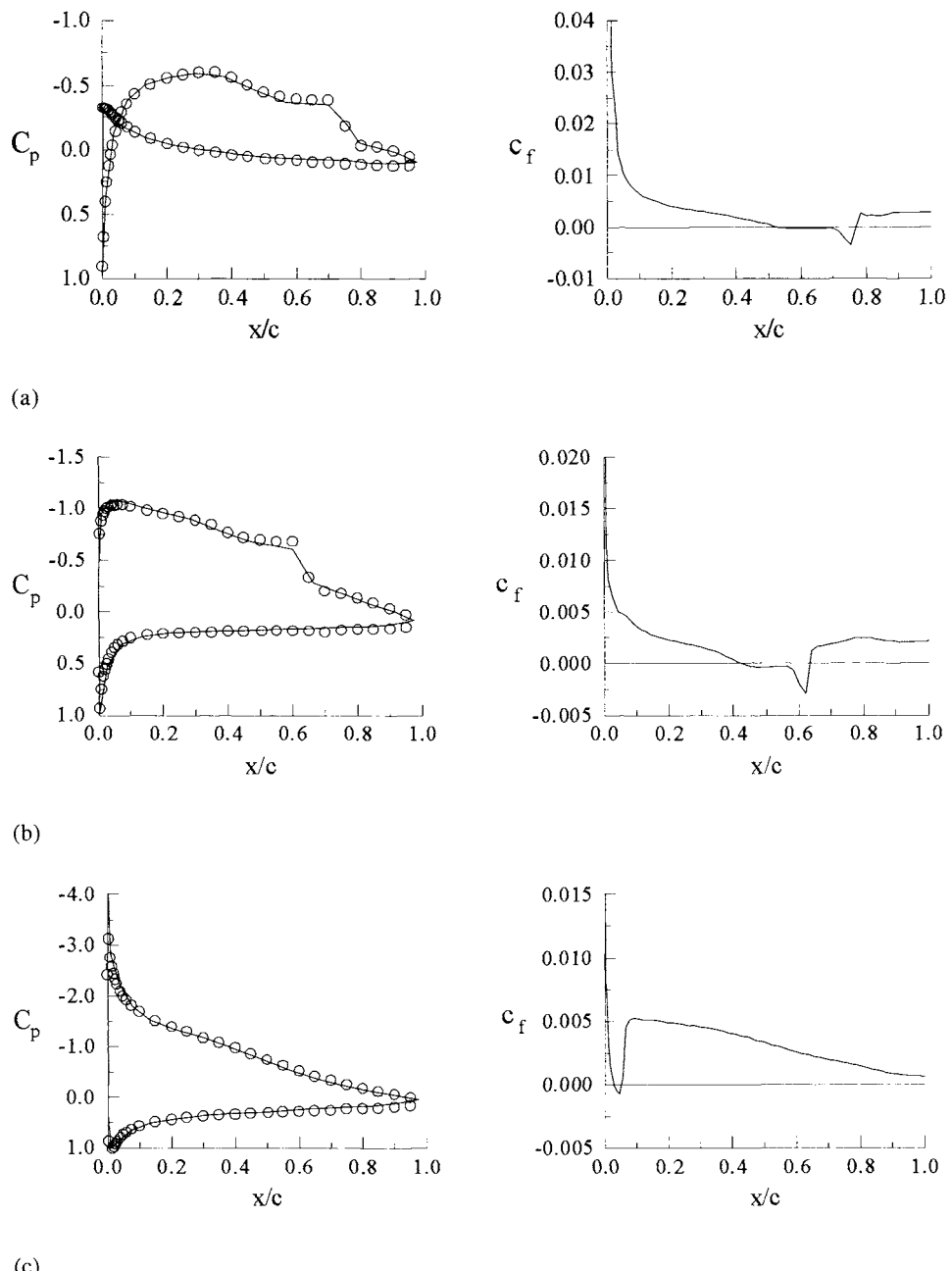


**Fig. 9.12.** Comparison of calculated (solid lines) and measured (symbols) pressure-coefficient and local skin-friction-coefficient distributions for the Eppler airfoil at (a)  $\alpha = 0^\circ$ , (b)  $\alpha = 4^\circ$ , and (c)  $\alpha = 8^\circ$  for  $R_c = 2 \times 10^5$ .

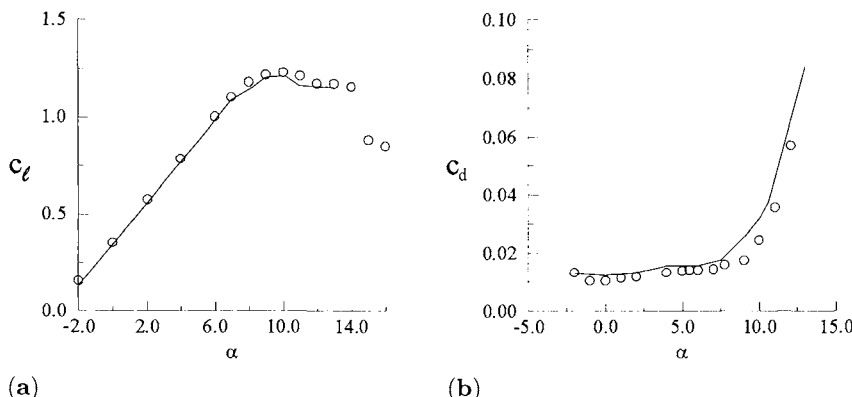


**Fig. 9.13.** Comparison of calculated (solid lines) and measured (symbols) (a) lift, and (b) drag coefficients for the Eppler airfoil at  $R_c = 2 \times 10^5$ .

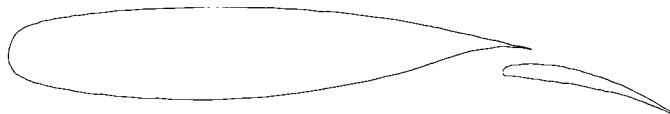


**Fig. 9.14.** NLR 7301 airfoil with flap.

Figure 9.13 shows a similar comparison for the lift and drag coefficients up to the stall angle. In general, the calculated results agree remarkably well with the measured ones.

Further details of the results shown in Figs. 9.12 and 9.13 are presented in Table 9.3. The calculated values of the chordwise location of laminar separation (LS), turbulent reattachment (TR), and the onset of transition are given for several angles of attack.

The experimental results of this table are subject to some uncertainty because of difficulties associated with the surface visualization technique. With this proviso, comparison between measured and calculated values must be con-

**Table 9.3.** Experimental and calculated chordwise laminar separation (LS), and turbulent reattachment (TR), and transition locations on the upper surface of the Eppler airfoil for  $R_c = 2 \times 10^5$ .

$\alpha$	Calculated			Experiment	
	LS	$(x/c)_{tr}$	TR	LS	TR
-2	0.56	0.748	0.835	0.53	0.80
0	0.51	0.688	0.785	0.48	0.74
2	0.46	0.624	0.716	0.43	0.67
4	0.415	0.564	0.65	0.40	0.62
5	0.40	0.526	0.60	0.38	0.59
6	0.39	0.467	0.52	0.37	0.55

sidered outstanding. It should be noted that when there is a separation bubble, the transition location obtained from the  $e^n$ -method occurs within the bubble in all cases, and, in accord with experimental observation, leads to reattachment some distance downstream.

## 9.7 Applications of the Interactive Boundary-Layer Method: Multielement Airfoils

The calculation method of the previous two subsections has also been applied to high-lift flows, this time by computing the inviscid flow with a multielement panel method and accounting for the viscous effects with a procedure similar to that used for single airfoils. A detailed description of the calculation method is given in [2].

Figures 9.15 and 9.16 show a comparison of calculated and experimental results for the airfoil/flap configuration of Van den Berg and Oskam (Fig. 9.15) which corresponds to a supercritical main airfoil (NLR 7301) with a flap of 32% of the main chord at a deflection angle of 20 degrees and with a gap of 2.6% chord [29]. Measurements of surface pressure and velocity profiles were obtained at a chord Reynolds number of  $2.51 \times 10^6$  and for angles of attack of 6 and 13.1 degrees, the latter recognized as the highest angle which corresponded to fully attached flow. Lift coefficients were deduced for five angles of attack.

Figures 9.15a and 9.15b show a comparison between measured and computed pressure distributions at  $\alpha = 6^\circ$  and  $13.1^\circ$ , respectively. The results for  $\alpha = 13.1^\circ$  confirm the absence of separation and the calculated lift coefficients of Fig. 9.16 show very good agreement with measurements at low angles of attack. While some discrepancies exist at higher angles of attack, the stall is predicted accurately. It is believed that these discrepancies are due to the merging of the

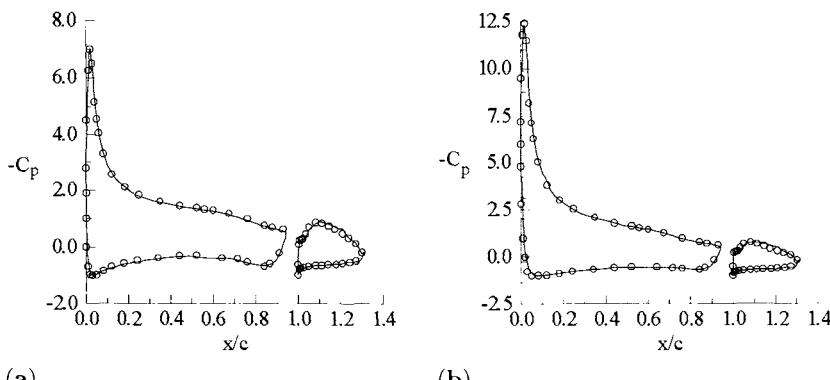


**Fig. 9.15.** Calculated and measured pressure distributions for the NLR 7301 airfoil with flap (a)  $\alpha = 6^\circ$ , (b)  $\alpha = 13.1^\circ$ .

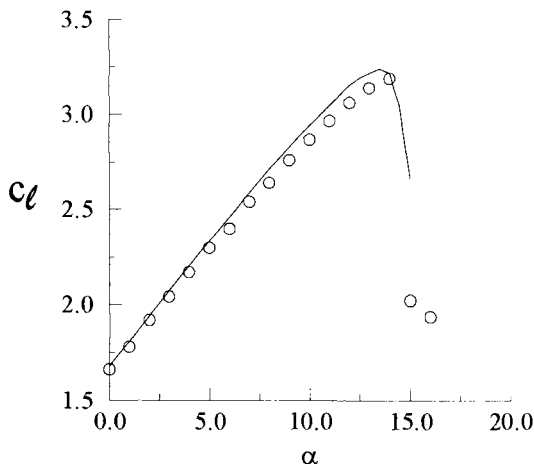


**Fig. 9.16.** Calculated and measured lift coefficients for the NLR 7301 airfoil with flap.

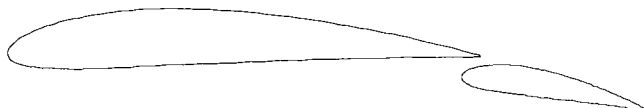
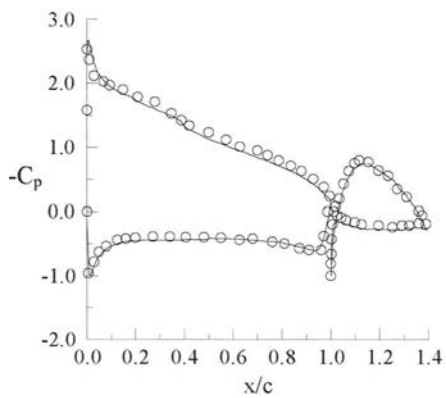
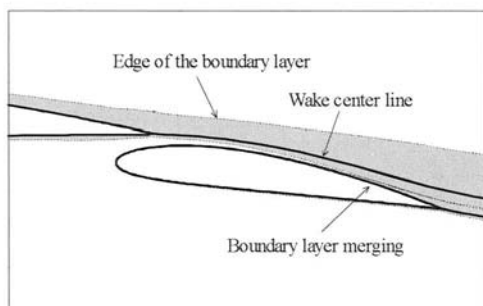


**Fig. 9.17.** NACA 4412/4415 airfoil/flap configuration.



(a)



(b)

**Fig. 9.18.** Results for the NACA 4412/4415 airfoil/flap configuration at  $\alpha = 2.2^\circ$ . (a) calculated and measured pressure distributions, and (b) boundary-layer growth.

airfoil shear layer with the boundary-layer on the upper surface of the flap which was not considered in the calculation method.

Figure 9.18 shows the results for a two-element airfoil with an NACA 4412 profile for the main element and an NACA 4415 flap profile deflected by 10 degrees which Olson and Orloff tested at NASA Ames [30] (Fig. 9.17). The freestream Mach number was 0.06 and the chord Reynolds number  $1.3 \times 10^6$ .

**Table 9.4.** Measured and computed lift coefficients for the NACA 4412/4415 configuration.

	Main element	Flap	Total
Calculated	1.6979	0.2417	1.9396
Measured	1.69	0.22	1.91

The pressure distribution was obtained at  $\alpha = 2.2^\circ$ . Figure 9.18a indicates a reasonably good agreement between the computed and measured pressure distributions. The transition location on the upper surface of the main element was computed at  $x/c = .186$  and on the upper surface of the flap at  $x/c = .63$ . Table 9.4 shows a comparison of the measured and computed lift coefficients for each element. The lift coefficient for the main airfoil is computed accurately. However, there exists some discrepancy on the flap, which suggests that the merging of the shear layers, shown in Fig. 9.18b and not modeled in the calculation of [2], has an influence on the flow field computation. Overall, however, the calculated results agree well with the measurements.

## References

- [1] Goldstein, S.: “On Laminar Boundary Layer Flow near a Point of Separation,” *Quart. J. Mech. & Appl. Math.*, Vol. 1, pp. 43–69, 1948.
- [2] Cebeci, T.: *An Engineering Approach to the Calculation of Aerodynamic Flows*, Horizons Publ., Long Beach, Calif. and Springer, Heidelberg, 1999.
- [3] Cebeci, T., Platzer, M., Chen, H., Chang, K.-C. and Shao, J. P.: *Analysis of Low Speed Unsteady Airfoil Flows*. Horizons Publ., Long Beach, Calif. and Springer, Heidelberg, 2005.
- [4] Catherall, D. and Mangler, K. W.: “The Interpretation of Two-Dimensional Laminar Boundary Layer Equations Past the Point of Vanishing Skin Friction,” *J. Fluid Mech.*, Vol. 26, p. 163, 1966.
- [5] Briley, W. R.: “A Numerical Study of Laminar Separation Bubbles Using the Navier-Stokes Equations,” *J. Fluid Mech.*, Vol. 47, no. 4, pp. 713–736, 1971.
- [6] McDonald, H. and Briley, W. R.: “A Survey of Recent Work on Interacted Boundary-Layer Theory for Flows with Separation,” In: *Numerical and Physical Aspects of Aerodynamic Flows II*, ed. T. Cebeci, 1983.
- [7] LeBalleur, J. C.: “Couplage visqueux–non visqueux: analyse du problème incluant décollements et ondes de choc.” *La Recherche Aérospatiale* **6**, 349–358, 1977.
- [8] Carter, J. E.: A new boundary layer inviscid iteration technique for separated flow. AIAA Paper 79-1450, 4th Computational fluid dynamics conf., Williamsburg, 1979.
- [9] Veldman, A. E. P.: New, quasi-simultaneous method to calculate interacting boundary layers. *AIAA J.* **19**, 79–85, 1981.
- [10] Sychev, V. V., Ruban, A. I., Sychev, Vic. V. and Korolev, G. L.: *Asymptotic theory of separated flows*. Cambridge University Press, Cambridge, U.K., 1998.
- [11] Cousteix, J. and Mauss, J.: “Approximations of the Navier-Stokes equations for high Reynolds number flows past a solid wall.” *J. Comp. and Appl. Math.* **166**, 101–122, 2004.
- [12] Gleyzes, C., Cousteix, J., and Bonnet, J. L.: “A Calculation Method of Leading-Edge Separation Bubbles,” *Numerical and Physical Aspects of Aerodynamic Flow, II*, ed. T. Cebeci, Springer, 1984.

- [13] LeBalleur, J. C.: "New Possibilities of Viscous-Inviscid Numerical Techniques for Solving Viscous Flow Equations with Massive Separation," In: *Numerical and Physical Aspects of Aerodynamic Flows, IV*, ed. T. Cebeci, Springer, Heidelberg, 1990.
- [14] Reyner, T. A. and Flügge-Lotz, I.: "The Interaction of Shock Wave with a Laminar Boundary Layer," *Int. J. Non-Linear Mech.*, Vol. 3, no. 2, p. 173, 1968.
- [15] Keller, H. B.: "The Bordering Algorithm and Path Following Near Singular Points of Higher Nullity," *SIAM J. on Scientific and Statistical Computing*, Vol. 4, No. 4, pp. 573–582, 1983.
- [16] Goldstein, S.: "Concerning Some Solutions of the Boundary Layer Equations in Hydrodynamics," *Proc. Cambridge Phil. Soc.*, Vol. 26, pp. 1–30, 1930.
- [17] Van Dyke, M.: *Perturbation Methods in Fluid Mechanics*, Academic Press, New York, 1964.
- [18] Dennis, S. C. R. and Chang, G-A.: "Numerical Integration of the Navier-Stokes Equations for Steady Two-dimensional Flow," *Phys. Fluids Suppl.*, Vol. II, pp. 88–93, 1969.
- [19] Dennis, S. C. R. and Dunwoody, J.: "The Steady Flow of a Viscous Fluid Past a Flat Plate," *J. Fluid Mech.*, Vol. 24, pp. 577–595, 1966.
- [20] Cousteix, J., de Saint-Victor, X., and Houdeville, R.: "x-Marching Methods to Solve the Navier-Stokes Equations in Two- and Three-dimensional Flows," Third Symposium on Numerical and Physical Aspects of Aerodynamic Flows, Long Beach, California, ed. T. Cebeci, 1985.
- [21] Stewartson, K.: "On the Flow Near the Trailing Edge of a Flat Plate II," *Mathematika*, Vol. 16, pp. 106–121, 1969.
- [22] Messiter, A. F.: "Boundary-layer flow near the trailing edge of a flat plate," *SIAM J. Appl. Math.*, Vol. 18, pp. 241–257, 1970.
- [23] Rubin, S. G. and Srinivasan, K.: "A multigrid domain decomposition strategy for viscous flow computations, ASME Symposium, Anaheim, CA, AMD Vol. 157, pp. 249–274, 1992.
- [24] Khosla, P. K., Pordal, H. and Rubin, S. G.: "A 3D pressure flux-split formulation for subsonic and supersonic flow in inlets, AIAA 24th Fluid Dyn. Conf., Orlando, FL, AIAA 93-3063, 1993.
- [25] Stewartson, K.: *Multi-Structural Boundary Layers on Flat Plates and Related Bodies*, 1924.
- [26] Jobe, C. E.: "The numerical solution of the asymptotic equations of trailing edge flow, Ph.D. dissertation, The Ohio State University, 1973.
- [27] Dennis, S. C. R.: private communication, 1973.
- [28] Janour, Z.: "Resistance of a Plate in Parallel Flow at Low Reynolds Numbers," NACA TM 1316, 1924.
- [29] Van Den Berg, B. and Oskam, B.: "Boundary Layer Measurements on a Two-Dimensional Wing with Flaps and Comparison with Calculations," AGARD CP-271, Sept. 1979.
- [30] Olson, L. E. and Orloff, K. L.: "On the Structure of Turbulent Wakes and Merging Shear Layers of Multielement Airfoils," AIAA Paper No. 81-1238, June 1981.

## Problems

**9-1.** To discuss the concept of displacement thickness used to account for the viscous effects in inviscid flow methods, let us refer to Fig. P9.1 which defines the real flow (with viscous effects) and an equivalent fictitious inviscid flow defined as a continuation of the inviscid flow in the boundary-layer. Assume that for  $y > \delta$ , both flows are the same. In particular, along the line  $y = \delta$ , assume that the values of  $v_e$  and  $u_e$  are same in both flows. Assume also that the inviscid

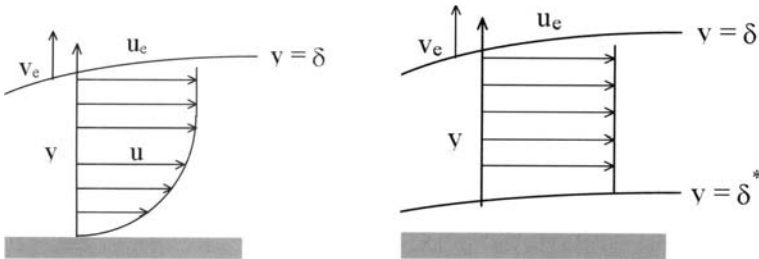


**Fig. P9.1.** (a) Real and (b) equivalent inviscid fictitious flows.

fictitious flow is on a surface  $y = \delta^*$  and the flow is such that  $u_e$  is constant along a normal to the wall between  $y = \delta^*$  and  $y \leq \delta$

- (a) Using the continuity equation for the real flow, show that the velocity  $v_e$  at the edge of the boundary-layer is

$$\begin{aligned} v_e &= - \int_0^\delta \frac{\partial u}{\partial x} dy \\ &= \frac{d}{dx} \left[ \int_0^\delta (u_e - u) dy \right] - \delta \frac{du_e}{dx} \end{aligned} \quad (\text{P9.1.1})$$

- (b) Using the continuity equation for the equivalent inviscid fictitious flow, show that the velocity  $v_e$  along the line  $y = \delta$  is

$$v_e = \frac{d}{dx} (u_e \delta^*) - \delta \frac{du_e}{dx} \quad (\text{P9.1.2})$$

*Hint:* Note that the  $y$ -component velocity along the line  $y = \delta^*$  is  $u_e \frac{d\delta^*}{dx}$ .

- (c) Deduce that  $\delta^*$  is defined as

$$\delta^* = \int_0^\delta \left( 1 - \frac{u}{u_e} \right) dy$$

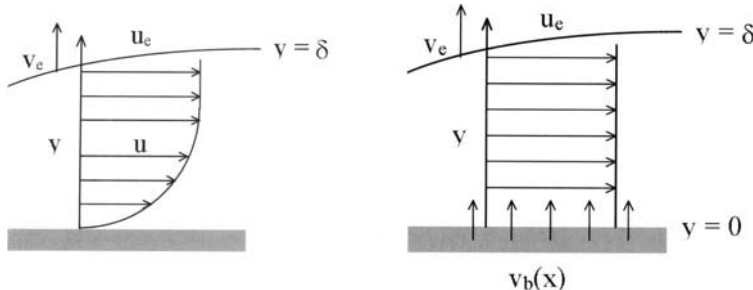


**Fig. P9.2.** (a) Real and (b) equivalent inviscid fictitious flows.

**9-2.** To discuss the concept of blowing velocity which is applied to inviscid flow methods in order to account for the viscous effects, let us consider Fig. P9.2 which is similar to Fig. P9.1. This time we assume that the fictitious flow is such that  $u_e$  is constant along a normal to the wall between  $y = 0$  and  $y = \delta$ .

(a) Using the continuity equation for the equivalent inviscid fictitious flow, show that the velocity  $v_e$  along the line  $y = \delta$  is

$$v_e = v_b - \delta \frac{du_e}{dx}$$

(b) With  $v_e$  given by (P9.1.2) deduce that  $v_b(x)$  is given by Eq. (9.3.1).

**9-3.** The concept of blowing velocity for two-dimensional flows can also be extended to three-dimensional flows by the following expression for an incompressible steady flow

$$v_b = \frac{1}{h_1 h_2 \sin \theta} \left[ \frac{\partial}{\partial x} (h_2 u_e \sin \theta \delta_x^*) + \frac{\partial}{\partial z} (h_1 w_e \sin \theta \delta_z^*) \right] \quad (\text{P9.3.1})$$

To derive this equation consider again a fictitious flow defined as a continuation of the inviscid flow in the boundary-layer. Denote the velocity components of the fictitious flow by  $u^*$ ,  $v^*$  and  $w^*$  where  $u^*$  and  $w^*$  are equal to  $u_e$  and  $w_e$ . The normal velocity component  $v^*$  is given by the continuity equation, Eq. (7.2.19), for the fictitious flow

$$\frac{1}{h_1 h_2 \sin \theta} \frac{\partial}{\partial x} (u^* h_2 \sin \theta) + \frac{1}{h_1 h_2 \sin \theta} \frac{\partial}{\partial z} (w^* h_1 \sin \theta) + \frac{\partial v^*}{\partial y} = 0 \quad (\text{P9.3.2})$$

(a) Integrating the above equation with respect to  $y$  from  $y = \delta$  and noting that  $u^* = u_e$  and  $w^* = w_e$ , show that

$$v^*(y) = v_e^* - \frac{(y - \delta)}{h_1 h_2 \sin \theta} \left[ \frac{\partial}{\partial x} (u_e h_2 \sin \theta) + \frac{\partial}{\partial z} (w_e h_1 \sin \theta) \right] \quad (\text{P9.3.3})$$

where  $v_e^*$  is the value of  $v^*$  at  $y = \delta$ .

(b) The matching condition between the external flow and boundary-layer is

$$v_e^* = v_e$$

where  $v_e$  is calculated from the continuity equation, Eq. (7.2.19). Assuming that the boundary-layer develops on an impermeable wall ( $v_w = 0$ ), integrate Eq. (7.2.19) and show that

$$\begin{aligned} \frac{v^*(y)}{u_e} &= \frac{1}{u_e h_1 h_2 \sin \theta} \left[ \frac{\partial}{\partial x} (u_e h_2 \sin \theta \delta_x^*) + \frac{\partial}{\partial z} (w_e h_1 \sin \theta \delta_z^*) \right] \\ &\quad - \frac{y}{u_e h_1 h_2 \sin \theta} \left[ \frac{\partial}{\partial x} (u_e h_2 \sin \theta) + \frac{\partial}{\partial z} (w_e h_1 \sin \theta) \right] \end{aligned} \quad (\text{P9.3.4})$$

The value of  $v^*(y)$  in the above equation is the boundary condition that must be applied to the fictitious inviscid flow at a distance  $y$  from the wall in order to account for the boundary-layer effects on inviscid flow.

(c) Using the definition of the displacement surface  $\Delta$ , Eq. (P7.11.1), and taking  $y = \Delta$  in Eq. (P9.3.4), show that

$$\frac{v^*(\Delta)}{u_e} = \frac{1}{h_1} \frac{\partial \Delta}{\partial x} + \frac{w_e}{u_e} \frac{1}{h_2} \frac{\partial \Delta}{\partial z}$$

This equation shows that the surface  $y = \Delta$  is a stream surface of the fictitious inviscid flow. In other words, the boundary-layer effects are accounted for if the fictitious inviscid flow is calculated around a body obtained by displacing the real body surface over a distance  $\Delta$ .

(d) If the boundary condition is applied to the fictitious inviscid flow at the wall, show that  $v^*(0)[\equiv v_b]$  is given by Eq. (P9.3.1).

**9-4.** To study the properties of an integral method (for two-dimensional incompressible steady turbulent flows) based on the solutions of the global continuity [Eq. (P3.9.1)] and momentum [Eq. (3.3.10)] equations, let us assume that the entrainment coefficient  $c_E(\equiv v_E/u_e)$  and local skin-friction coefficient  $c_f$  are known functions of  $H$  and  $R_\theta$ . Let us also assume that  $H^*[\equiv (\delta - \delta^*)/\theta]$  is a function of  $H$  given by

$$H^* = \frac{\alpha H^2 + H}{H - 1}, \quad \alpha = 0.631 \quad (\text{P9.4.1})$$

(a) Express Eqs. (P3.9.1) and (3.3.10) as a system  $S$  of two equations where the derivatives are  $d\delta^*/dx$ ,  $d\theta/dx$  and  $du_e/dx$ .

*Hint:* Differentiate

$$\delta - \delta^* = \theta H^* \quad (\text{P9.4.2})$$

and write it in the form

$$\frac{d}{dx}(\delta - \delta^*) = H^* \frac{d\theta}{dx} + \theta H^{*\prime} \frac{d}{dx} \left( \frac{\delta^*}{\theta} \right), \quad H^{*\prime} = \frac{dH^*}{dH} \quad (\text{P9.4.3})$$

and

$$\frac{d}{dx}(\delta - \delta^*) = (H^* - HH^{*\prime}) \frac{d\theta}{dx} + H^{*\prime} \frac{d\delta^*}{dx} \quad (\text{P9.4.4})$$

(b) Assume that  $u_e(x)$  is known. System  $S$  is a system for  $d\delta^*/dx$  and  $d\theta/dx$ . Analyze the determinant  $\Delta$  of this system as a function of  $H$ .

(c) Write an equation for  $dH^*/dx$  from Eqs. (P3.9.1) and (3.3.10). Show that if there exists a point  $x = x_s$  for which  $\Delta = 0$ , the derivative  $dH^*/dx$  at this point is not zero in general. Deduce that it is not possible to integrate Eqs. (P3.9.1)

and (3.3.10) beyond  $x = x_s$ , where  $x_s$  represents the  $x$ -location corresponding to boundary-layer separation.

(d) Assume  $\delta^*$  is known. System  $S$  is a system for  $d\theta/dx$  and  $du_e/dx$ . Analyze the determinant  $\Delta'$  of this system as a function of  $H$  and show that  $\Delta'$  is never null. This way of solving the boundary-layer equations is called the inverse approach.

**9-5.** An integral method based on the solutions of Eqs. (P3.9.1) and (3.3.10) can be used to calculate flow in a plane diffuser, assuming that the core of the flow is an inviscid one-dimensional flow.

(a) Assuming that the entrainment coefficient  $c_E$  and local skin-friction coefficient  $c_f$  are known functions of  $H$  and  $R_\theta$ , and  $H^*$  is related to  $H$  by Eq. (P9.4.1), show that Eqs. (P3.9.1) and (3.3.10) can be written as

$$(H^* - HH^{*\prime}) \frac{d\theta}{dx} + H^{*\prime} \frac{d\delta^*}{dx} + \frac{\delta - \delta^*}{u_e} \frac{du_e}{dx} = c_E \quad (\text{P9.5.1})$$

$$\frac{d\theta}{dx} + \theta \frac{H + 2}{u_e} \frac{du_e}{dx} = \frac{c_f}{2} \quad (\text{P9.5.2})$$

where

$$H^{*\prime} = \frac{dH^*}{dH} = \frac{\alpha H^2 - 2\alpha H - 1}{(H - 1)^2} \quad (\text{P9.5.3})$$

(b) With  $2h$  denoting the total height of the diffuser and the function  $h(x)$  known, assume that the velocity in the inviscid core  $u_e$  is constant in a cross-section of the diffuser. Show that the conservation of mass flow in the diffuser

$$u_e(h - \delta^*) = cst \quad (\text{P9.5.4})$$

can be written as

$$-u_e \frac{d\delta^*}{dx} + (h - \delta^*) \frac{du_e}{dx} + u_e \frac{dh}{dx} = 0 \quad (\text{P9.5.5})$$

(c) The calculation of flow in a diffuser with this integral method consists of solving the following system of differential equations

$$(H^* - HH^{*\prime}) \frac{d\theta}{dx} + H^{*\prime} \frac{d\delta^*}{dx} + \frac{\delta - \delta^*}{u_e} \frac{du_e}{dx} = c_E \quad (\text{P9.5.6})$$

$$\frac{d\theta}{dx} + \theta \frac{H + 2}{u_e} \frac{du_e}{dx} = \frac{c_f}{2} \quad (\text{P9.5.7})$$

$$-u_e \frac{d\delta^*}{dx} + (h - \delta^*) \frac{du_e}{dx} = -u_e \frac{dh}{dx} \quad (\text{P9.5.8})$$

In the above system, the unknowns are  $d\delta^*/dx$ ,  $d\theta/dx$  and  $du_e/dx$ . Show that the determinant of this system is zero when

$$\frac{h}{\theta} = f(H)$$

with

$$f(H) = \frac{(H^* - HH^{*\prime})(H + 1)}{H^{*\prime}}$$

(d) Study the function  $f(H)$  and deduce that the system is non-singular if  $h/\theta < 28.9$ .

(e) In Problem 9.4 the boundary-layer separation occurs at a location where  $H'^* = 0$ . In the present problem this location is not singular (if  $h/\theta < 28.9$ ). The reason is that the coupling between the boundary-layer and the inviscid flow is taken into account. Note that the restriction  $h/\theta < 28.9$  is partly due to the assumed shape of the function  $H^*(H)$  and also to the hypothesis that the inviscid core velocity is constant in a cross-section. When the height of the diffuser is too large compared to the boundary-layer, the coupling between the inviscid flow and the boundary-layer is no longer effective to avoid the singular behavior of boundary-layer equations at separation.

**9-6.** As discussed in Section 9.1, Goldstein studied the structure of the solutions of the boundary-layer equations downstream of a point  $x_0$  where the velocity profile is known.

In his study, all the quantities are dimensionless. Reference quantities are  $\ell$ ,  $u_0$ ,  $\rho$ ,  $\nu$ . The Reynolds number is  $R = u_0\ell/\nu$ . The quantities  $x$ ,  $y$ ,  $u$ ,  $v$ , and  $p$  are nondimensional quantities, the reference quantities being respectively  $\ell$ ,  $\ell/R^{1/2}$ ,  $u_0$ ,  $R^{1/2}$ ,  $\rho u_0^2$ .

(a) Show that the boundary-layer equations can be written as

$$\frac{\partial u}{\partial x} + \frac{\partial v}{\partial y} = 0 \quad (\text{P9.6.1})$$

$$u \frac{\partial u}{\partial x} + v \frac{\partial v}{\partial y} = -\frac{dp}{dx} + \frac{\partial^2 u}{\partial y^2} \quad (\text{P9.6.2})$$

(b) Assume that the velocity profile at point  $x_0$  can be written in the form

$$u = a_1 y + a_2 y^2 + a_3 y^3 + \dots \quad (\text{P9.6.3})$$

and satisfies the boundary condition  $u = 0$  at  $y = 0$ . Also assume that the pressure gradient can be written in the form

$$-\frac{dp}{dx} = p_0 + p_1(x - x_0) + p_2(x - x_0)^2 + \dots \quad (\text{P9.6.4})$$

By introducing the above relations into Eqs. (P9.6.1) and (P9.6.2) show that

$$\begin{aligned} 2a_2 + p_0 &= 0, \quad a_3 = 0, \quad a_1 \frac{da_1}{dx} - 24a_4 = 0, \\ \frac{2}{3}a_1 \frac{da_2}{dx} - 20a_5 &= 0 \end{aligned} \quad (\text{P9.6.5})$$

(c) By differentiating the boundary-layer equations with respect to  $x$ , show that

$$2 \frac{da_2}{dx} + p_1 = 0, \quad \frac{da_3}{dx} = 0 \quad (\text{P9.6.6})$$

(d) Show that

$$2a_2 + p_0 = 0, \quad a_3 = 0, \quad 5!a_5 + 2a_1p_1 = 0 \quad (\text{P9.6.7})$$

the coefficients  $a_1, a_4, \dots$  are free. Notice that the pressure gradient and therefore the coefficients  $p_i$  are prescribed.

Conditions given by Eq. (P9.6.7) are called compatibility conditions. If these conditions are not satisfied, singularities occur if we want to obtain the solutions of boundary-layer equations for  $x > x_0$ . The relations given by Eq. (P9.6.7) introduce severe constraints. Goldstein studied the behavior of the solutions if these compatibility conditions are not satisfied. A particular case arises if  $a_1 = 0$ ; it corresponds to the boundary-layer separation. Show that the compatibility conditions in this case are

$$\begin{aligned} 2a_2 + p_0 &= 0, \quad a_3 = 0, \quad a_4 = 0, \quad a_5 = 0, \\ 6!a_6 &= 2p_0p_1, \quad a_7 = 0, \quad a_9 = 0 \end{aligned} \quad (\text{P9.6.8})$$

The coefficients  $a_8, a_{12}, a_{16}, a_{20}, \dots$  are free.

In general, all these compatibility conditions are not satisfied. Goldstein assumed that the condition  $2a_2 + p_0 = 0$  is satisfied but the other conditions did not. Show that

$$a_1 = \sqrt{48a_4(x - x_0)} \quad (\text{P9.6.9})$$

and deduce that  $da_1/dx$  is infinite at  $x = x_0$ . If the solution exists upstream of  $x_0$ , coefficient  $a_4$  is negative. Then the solution is not possible downstream of  $x_0$ . This behavior is known as Goldstein's singularity. Goldstein confirmed this conclusion by studying in great details the structure of the solution in the neighborhood of separation. The fundamental reason for this behavior is that the pressure gradient is prescribed. To overcome the singularity, Catherall and Mangler proposed the inverse boundary-layer methods.

**9-7.** The behavior of the flow past a solid wall at high Reynolds numbers can be studied by applying the SCEM to Eqs. (9.2.2a) to (9.2.2c). The expansion

for the outer flow is given by Eq. (9.2.4) and Euler equations are given by Eqs. (9.2.5). To account for the presence of the wall, it is assumed that

$$\mathcal{U} = u_1(x, y, \varepsilon) + U_1(x, Y, \varepsilon) + \dots \quad (\text{P9.7.1a})$$

$$\mathcal{V} = v_1(x, y, \varepsilon) + \delta(\varepsilon)V_1(x, Y, \varepsilon) + \dots \quad (\text{P9.7.1b})$$

where the order function  $\delta(\varepsilon)$  is not known.

- (a) Using the expansion given by Eqs. (P9.1) derive the continuity equation and show that this equation is not trivial if  $\delta = \varepsilon$ .
- (b) With the pressure expanded in the form

$$\mathcal{P} = p_1(x, y, \varepsilon) + \Delta(\varepsilon)P_1(x, Y, \varepsilon) \quad (\text{P9.7.2})$$

derive the  $y$ -momentum equation and show that the best choice for  $\Delta$  is  $\Delta = \varepsilon^2$  (Examine three possibilities i)  $\Delta$  much larger than  $\varepsilon^2$ , ii)  $\Delta$  much smaller than  $\varepsilon^2$ , iii)  $\Delta = \varepsilon^2$ ).

**9-8.** Apply a uniformly valid approximation given by Eqs. (9.2.6a)–(9.2.6c) to Eqs. (9.2.2a)–(9.2.2b) and write

- (a) the continuity and the  $x$ -momentum equations for  $U_1$  and  $V_1$  by neglecting terms of order  $\varepsilon^2$  in the momentum equation.
- (b) Let

$$u = u_1 + U_1$$

$$v = v_1 + \varepsilon V_1$$

and write the continuity and  $x$ -momentum equations obtained above in terms of  $u$ ,  $u_1$ ,  $v$ ,  $v_1$ .

**9-9.** From Eqs. (9.2.10), it can be shown that one boundary condition in the IBL theory is

$$\lim_{y \rightarrow \infty} (v - v_1) = 0 \quad (\text{P9.9.1})$$

Write the continuity equation for  $v$  and  $v_1$  and show that this condition requires

$$v_{10} = \frac{d}{dx} \left[ \int_0^\infty (u_1 - u) dy \right] \quad (\text{P9.9.2})$$

where  $v_{10}$  is the value of  $v_1$  at the wall ( $y = 0$ ). Interpret the result.



# 10

# Conservation Equations for Mass, Momentum and Energy

## 10.1 Introduction

In Chapters 2 and 3, we discussed the continuity and momentum equations for incompressible flows. Here, we extend the discussion to compressible flows. If the typical temperature difference in a gas flow is an appreciable fraction of the absolute temperature, the typical density difference will be an appreciable fraction of the absolute density, and the density appearing in the velocity field equations discussed in the previous chapters can no longer be taken as constant. Instead, the conservation equations for momentum and energy must be solved simultaneously since they are coupled, i.e., density appears in the momentum equations and is linked through an equation of state to the dependent variable of the energy equation.

In this chapter we briefly discuss the conservation equations for mass, momentum and energy equations (Sections 10.2 and 10.3) before we discuss the inviscid flow equations (Section 10.4) and boundary-layer equations in differential (Section 10.5) and integral (Section 10.6) forms.

## 10.2 Navier–Stokes Equations

For compressible flows, the Navier–Stokes equations are similar to those given by Eqs. (2.2.1) and (2.2.2) for incompressible flows. Since the fluid properties now also vary with temperature, the continuity and momentum equations are coupled to the energy equation, and the solution of the energy equation provides the temperature distribution in the flow field. These equations are discussed in some detail in several references, see for example [1], and are summarized below for an unsteady compressible three-dimensional flow in a Newtonian fluid.

The continuity equation is

$$\frac{\partial \rho}{\partial t} + \nabla \cdot \rho \vec{V} = 0 \quad (10.2.1a)$$

or

$$\frac{D\rho}{Dt} + \rho \nabla \cdot \vec{V} = 0 \quad (10.2.1b)$$

For a Cartesian coordinate system, it becomes

$$\frac{\partial \rho}{\partial t} + \frac{\partial \rho u}{\partial x} + \frac{\partial \rho v}{\partial y} + \frac{\partial \rho w}{\partial z} = 0 \quad (10.2.2a)$$

or in tensor notation

$$\frac{\partial \rho}{\partial t} + \frac{\partial \rho u_i}{\partial x_i} = 0 \quad (10.2.2b)$$

The momentum equations are

$$\rho \frac{D\vec{V}}{Dt} = -\nabla p + \nabla \cdot \sigma + \rho \vec{f} \quad (10.2.3)$$

For a Cartesian coordinate system, in tensor notation, the momentum equations can be written as

$$\rho \frac{\partial u_i}{\partial t} + \rho u_j \frac{\partial u_i}{\partial x_j} = -\frac{\partial p}{\partial x_i} + \frac{\partial \sigma_{ij}}{\partial x_j} + \rho f_i \quad (10.2.4a)$$

or, using the continuity equation

$$\frac{\partial \rho u_i}{\partial t} + \frac{\partial \rho u_j u_i}{\partial x_j} = -\frac{\partial p}{\partial x_i} + \frac{\partial \sigma_{ij}}{\partial x_j} + \rho f_i \quad (10.2.4b)$$

Eq. (10.2.4a) is identical to Eq. (2.2.5) provided that, with  $\delta_{ij}$  denoting the Kronecker delta function ( $\delta_{ij} = 1$  if  $i = j$  and  $\delta_{ij} = 0$  if  $i \neq j$ ), the viscous stress tensor  $\sigma_{ij}$  is written as

$$\sigma_{ij} = \mu \left[ \left( \frac{\partial u_i}{\partial x_j} + \frac{\partial u_j}{\partial x_i} \right) - \frac{2}{3} \delta_{ij} \frac{\partial u_k}{\partial x_k} \right] \quad (i, j, k = 1, 2, 3) \quad (10.2.5)$$

The components of the viscous stress tensor  $\sigma_{ij}$  follow from Eq. (10.2.5)

$$\begin{aligned}
\sigma_{xx} &= \frac{2}{3}\mu \left( 2\frac{\partial u}{\partial x} - \frac{\partial v}{\partial y} - \frac{\partial w}{\partial z} \right) \\
\sigma_{yy} &= \frac{2}{3}\mu \left( 2\frac{\partial v}{\partial y} - \frac{\partial u}{\partial x} - \frac{\partial w}{\partial z} \right) \\
\sigma_{zz} &= \frac{2}{3}\mu \left( 2\frac{\partial w}{\partial z} - \frac{\partial u}{\partial x} - \frac{\partial v}{\partial y} \right) \\
\sigma_{xy} &= \mu \left( \frac{\partial u}{\partial y} + \frac{\partial v}{\partial x} \right) \\
\sigma_{xz} &= \mu \left( \frac{\partial w}{\partial x} + \frac{\partial u}{\partial z} \right) \\
\sigma_{yz} &= \mu \left( \frac{\partial v}{\partial z} + \frac{\partial w}{\partial y} \right) \\
\sigma_{xy} &= \sigma_{yx} \\
\sigma_{xz} &= \sigma_{zx} \\
\sigma_{yz} &= \sigma_{zy}
\end{aligned} \tag{10.2.6}$$

The energy equation can be written in terms of specific enthalpy  $h$  ( $\equiv e+p/\rho$ )

$$\rho \frac{Dh}{Dt} = -\nabla \cdot \vec{q} + \frac{Dp}{Dt} + \Phi \tag{10.2.7}$$

or in terms of total enthalpy  $H \equiv h + \frac{\|\vec{V}\|^2}{2}$  as

$$\rho \frac{DH}{Dt} = \rho \vec{f} \cdot \vec{V} + \frac{\partial p}{\partial t} + \nabla \cdot [(\bar{\sigma} - p\bar{I}) \cdot \vec{V} - \vec{q}] \tag{10.2.8}$$

It can also be written in terms of internal energy  $e$ ,

$$\rho \frac{D}{Dt} \left( e + \frac{\|\vec{V}\|^2}{2} \right) = \rho \vec{f} \cdot \vec{V} + \nabla \cdot [(\bar{\sigma} - p\bar{I}) \cdot \vec{V} - \vec{q}] \tag{10.2.9}$$

In Eq. (10.2.7),  $\Phi$  represents the dissipation function given by

$$\Phi = \bar{\sigma} : \nabla \vec{V} \tag{10.2.10a}$$

or using Cartesian coordinates

$$\Phi = \sigma_{ij} \frac{\partial u_i}{\partial x_j} \tag{10.2.10b}$$

The heat flux  $\vec{q}$  is given by the Fourier law

$$\vec{q} = -k \nabla T \tag{10.2.11}$$

where  $k$  is the coefficient of heat conductivity.

Equation (10.2.10b), when expanded, becomes

$$\Phi = \mu \left[ \left( \frac{\partial u}{\partial y} + \frac{\partial v}{\partial x} \right)^2 + \left( \frac{\partial v}{\partial z} + \frac{\partial w}{\partial y} \right)^2 + \left( \frac{\partial w}{\partial x} + \frac{\partial u}{\partial z} \right)^2 \right] \\ + \frac{2}{3} \mu \left[ \left( \frac{\partial u}{\partial x} - \frac{\partial v}{\partial y} \right)^2 + \left( \frac{\partial v}{\partial y} - \frac{\partial w}{\partial z} \right)^2 + \left( \frac{\partial w}{\partial z} - \frac{\partial u}{\partial x} \right)^2 \right] \quad (10.2.12)$$

This expression shows that  $\Phi \geq 0$ , i.e. it corresponds to an increase of enthalpy.

With Cartesian coordinates, in terms of tensor notation, the three forms of the energy equation are

$$\rho \frac{D}{Dt} \left( e + \frac{\|\vec{V}\|^2}{2} \right) = \rho f_j u_j + \frac{\partial}{\partial x_j} [u_i \sigma_{ij} - p u_j - \dot{q}_j] \quad (10.2.13a)$$

$$\rho \frac{Dh}{Dt} = - \frac{\partial \dot{q}_j}{\partial x_j} + \frac{Dp}{Dt} + \Phi \quad (10.2.13b)$$

$$\rho \frac{DH}{Dt} = \rho f_j u_j + \frac{\partial p}{\partial t} + \frac{\partial}{\partial x_j} (u_i \sigma_{ij} - \dot{q}_j) \quad (10.2.13c)$$

It is useful to write the kinetic energy equation obtained by multiplying the momentum equations with  $\vec{V}$

$$\rho \frac{D}{Dt} \left( \frac{\|\vec{V}\|^2}{2} \right) = \rho \vec{f} \cdot \vec{V} + \vec{V} \cdot [\nabla \cdot (\bar{\sigma} - p \bar{I})] \quad (10.2.14)$$

which, in terms of Cartesian coordinates, can be written as

$$\rho \frac{D}{Dt} \left( \frac{\|\vec{V}\|^2}{2} \right) = \rho f_j u_j + u_i \frac{\partial \sigma_{ij}}{\partial x_j} - u_j \frac{\partial p}{\partial x_j} \quad (10.2.15)$$

Finally, we need an equation of state for the fluid to relate  $p$ ,  $\rho$  and  $e$ . The commonest example is the perfect gas law

$$\frac{p}{\rho} = \frac{\mathcal{R}}{\mathcal{M}} T \quad (10.2.16)$$

where  $\mathcal{R}$  is the universal perfect gas constant ( $\mathcal{R} = 8.3145 \text{ J} \cdot \text{mol}^{-1} \cdot \text{K}^{-1}$ ) and  $\mathcal{M}$  is the molar mass of the gas; for air,  $\mathcal{M} = 0.02896 \text{ kg} \cdot \text{mol}^{-1}$  and  $\mathcal{R}/\mathcal{M} = 287.1 \text{ J} \cdot \text{kg}^{-1} \cdot \text{K}^{-1}$ .

Fluid properties that appear in the above equations are density  $\rho$ , viscosity  $\mu$ , specific heat at constant pressure  $c_p$  and thermal conductivity  $k$ . The latter appears in the energy equation through the laminar Prandtl number  $\text{Pr}$  defined as

$$\text{Pr} = \frac{\mu c_p}{k} \quad (10.2.17)$$

For a perfect gas, the fluid property  $\mu$  is function of temperature  $T$  only. The viscosity  $\mu$  is usually obtained from Sutherland's law expressed as

$$\mu = \mu_0 \sqrt{\frac{T}{T_0}} \frac{1 + S/T}{1 + S/T_0} \quad (10.2.18)$$

where

$$T_0 = 273 \text{ K}, \quad S = 110,4 \text{ K}, \quad \mu_0 = 1.711 \times 10^{-5} \text{ N} \cdot \text{m}^{-2}$$

The density is given by the equation of state, Eq. (10.2.16). The specific heat at constant pressure  $c_p$  is assumed to be constant equal to  $1005 \text{ J} \cdot \text{kg}^{-1} \cdot \text{K}^{-1}$ . The Prandtl number is a function of temperature assumed to be a constant evaluated at a given wall temperature; generally, the Prandtl number is taken equal to 0.72.

### 10.3 Reynolds-Averaged Navier–Stokes Equations

The equations given in the previous section for the conservation of mass, momentum and energy apply to turbulent flows as in incompressible flows provided the values of fluid properties and dependent variables are replaced by their instantaneous values. As before, we express  $u$ ,  $v$ ,  $w$ ,  $p$  by the sum of their mean  $\bar{u}$ ,  $\bar{v}$ ,  $\bar{w}$ ,  $\bar{p}$  and fluctuating parts  $u'$ ,  $v'$ ,  $w'$  and  $p'$ , Eq. (2.3.1), and the fluid properties  $\mu$  and  $\rho$  by

$$\mu = \bar{\mu} + \mu', \quad \rho = \bar{\rho} + \rho' \quad (10.3.1)$$

Introducing these relations into the continuity, momentum and energy equations, after averaging, we obtain the Reynolds averaged Navier–Stokes equations (RANS) equations for three-dimensional compressible unsteady flows,

$$\frac{\partial \rho}{\partial t} + \frac{\partial}{\partial x_i} (\rho u_i + \overline{\rho' u'_i}) = 0 \quad (10.3.2)$$

$$\begin{aligned} \frac{\partial}{\partial t} (\rho u_i + \overline{\rho' u'_i}) + \frac{\partial}{\partial x_j} \left[ (\rho u_j + \overline{\rho' u'_j}) u_i \right] &= -\frac{\partial p}{\partial x_i} + \frac{\partial \sigma_{ij}}{\partial x_j} + \rho f_i + \overline{\rho' f'_i} \\ &+ \left\{ \frac{\partial}{\partial x_j} \left[ -(\rho \overline{u'_i u'_j} + \overline{\rho' u'_i u'_j} + \overline{\rho' u'_i u_j}) \right] \right\} \end{aligned} \quad (10.3.3)$$

$$\begin{aligned} \frac{\partial}{\partial t} (\rho h + \overline{\rho' h'}) + \frac{\partial}{\partial x_j} \left[ (\rho u_j + \overline{\rho' u'_j}) h \right] &= \\ \frac{\partial}{\partial x_j} \left( k \frac{\partial T}{\partial x_j} \right) + \left\{ \frac{\partial}{\partial x_j} \left[ -(\rho \overline{u'_j h'} + \overline{\rho' u'_j h'} + \overline{\rho' h' u_j}) \right] \right\} & \\ + \frac{\partial p}{\partial t} + u_j \frac{\partial p}{\partial x_j} + \Phi + \rho \varepsilon & \end{aligned} \quad (10.3.4)$$

where

$$\sigma_{ij} = 2\mu \left[ S_{ij} - \frac{1}{3} \frac{\partial u_\ell}{\partial x_\ell} \delta_{ij} \right], \quad S_{ij} = \frac{1}{2} \left( \frac{\partial u_i}{\partial x_j} + \frac{\partial u_j}{\partial x_i} \right) \quad (10.3.5)$$

$$\Phi = \sigma_{ij} \frac{\partial u_i}{\partial x_j} \quad (10.3.6)$$

$$\rho \varepsilon = \sigma'_{ij} \frac{\partial u'_i}{\partial x_j} \quad (10.3.7)$$

$$\sigma'_{ij} = 2\mu \left[ \frac{1}{2} \left( \frac{\partial u'_i}{\partial x_j} + \frac{\partial u'_j}{\partial x_i} \right) - \frac{1}{3} \frac{\partial u'_\ell}{\partial x_\ell} \delta_{ij} \right] \quad (10.3.8)$$

If the flow is steady and two-dimensional, i.e. if the *mean flow* is steady and two-dimensional, the equations become

$$\frac{\partial}{\partial x} (\rho u + \overline{\rho' u'}) + \frac{\partial}{\partial y} (\rho v + \overline{\rho' v'}) = 0 \quad (10.3.9)$$

$$\begin{aligned} (\rho u + \overline{\rho' u'}) \frac{\partial u}{\partial x} + (\rho v + \overline{\rho' v'}) \frac{\partial u}{\partial y} &= -\frac{\partial p}{\partial x} + \frac{\partial \sigma_{xx}}{\partial x} + \frac{\partial \sigma_{xy}}{\partial y} + \rho f_x + \overline{\rho' f'_x} \\ &+ \left\{ \frac{\partial}{\partial x} \left[ -(\rho \overline{u'^2} + \overline{\rho' u'^2} + \overline{\rho' u' u}) \right] \right\} \\ &+ \left\{ \frac{\partial}{\partial y} \left[ -(\rho \overline{u' v'} + \overline{\rho' u' v'} + \overline{\rho' u' v}) \right] \right\} \end{aligned} \quad (10.3.10)$$

$$\begin{aligned} (\rho u + \overline{\rho' u'}) \frac{\partial v}{\partial x} + (\rho v + \overline{\rho' v'}) \frac{\partial v}{\partial y} &= -\frac{\partial p}{\partial y} + \frac{\partial \sigma_{yx}}{\partial x} + \frac{\partial \sigma_{yy}}{\partial y} + \rho f_y + \overline{\rho' f'_y} \\ &+ \left\{ \frac{\partial}{\partial x} \left[ -(\rho \overline{u' v'} + \overline{\rho' u' v'} + \overline{\rho' v' u}) \right] \right\} \\ &+ \left\{ \frac{\partial}{\partial y} \left[ -(\rho \overline{v'^2} + \overline{\rho' v'^2} + \overline{\rho' v' v}) \right] \right\} \end{aligned} \quad (10.3.11)$$

$$\begin{aligned} (\rho u + \overline{\rho' u'}) \frac{\partial h}{\partial x} + (\rho v + \overline{\rho' v'}) \frac{\partial h}{\partial y} &= \frac{\partial}{\partial x} \left( k \frac{\partial T}{\partial x} \right) + \frac{\partial}{\partial y} \left( k \frac{\partial T}{\partial y} \right) \\ &+ \left\{ \frac{\partial}{\partial x} \left[ -(\rho \overline{u' h'} + \overline{\rho' u' h'} + \overline{\rho' h' u}) \right] \right\} + \left\{ \frac{\partial}{\partial y} \left[ -(\rho \overline{v' h'} + \overline{\rho' v' h'} + \overline{\rho' h' v}) \right] \right\} \\ &+ u \frac{\partial p}{\partial x} + v \frac{\partial p}{\partial y} + \Phi + \rho \varepsilon \end{aligned} \quad (10.3.12)$$

We note from the energy equation that, as in the momentum equations, additional terms appear on its right-hand side. These terms in curly brackets, which are the thermal analogs of the Reynolds-stress terms in momentum equations are the divergence of the so-called *turbulent heat flux vector*.

## 10.4 Inviscid Flow Equations

As in Section 2.4, the inviscid flow equations are again obtained from the Navier-Stokes equations by neglecting the viscous terms. We have

$$\frac{\partial \rho}{\partial t} + \nabla \cdot \rho \vec{V} = 0 \quad (10.4.1)$$

$$\rho \frac{D \vec{V}}{Dt} = \rho \vec{f} - \nabla p \quad (10.4.2)$$

$$\rho \frac{DH}{Dt} = \rho \vec{f} \cdot \vec{V} + \frac{\partial p}{\partial t} \quad (10.4.3)$$

The equation of state, Eq. (10.2.16), remains unchanged. The energy equation can also be written in terms of internal energy or enthalpy,

$$\rho \frac{D}{Dt} \left( e + \frac{\|\vec{V}\|^2}{2} \right) = \rho \vec{f} \cdot \vec{V} - \nabla \cdot (p \vec{V}) \quad (10.4.4a)$$

$$\rho \frac{Dh}{Dt} = \frac{Dp}{Dt} \quad (10.4.4b)$$

## 10.5 Boundary-Layer Equations

As in Chapter 3, the Navier–Stokes equations for compressible flows can be reduced to the boundary-layer equations. The resulting equations for two-dimensional axisymmetric and three-dimensional flows are given in the following three subsections. The equation of state, Eq. (10.2.16), remains unchanged.

### 10.5.1 Two-Dimensional Flows

For a two-dimensional steady, laminar or turbulent flow, the boundary-layer equations and their boundary conditions are

$$\frac{\partial \rho u}{\partial x} + \frac{\partial \rho v}{\partial y} = 0 \quad (10.5.1a)$$

$$\rho u \frac{\partial u}{\partial x} + \overline{\rho v} \frac{\partial u}{\partial y} = - \frac{dp}{dx} + \frac{\partial \tau}{\partial y} + \rho f_x + \overline{\rho' f'_x} \quad (10.5.1b)$$

$$\rho u \frac{\partial H}{\partial x} + \overline{\rho v} \frac{\partial H}{\partial y} = \frac{\partial}{\partial y} [u \tau - \dot{q}] \quad (10.5.1c)$$

$$y = 0, \quad u = 0 \quad , \quad v = 0, \quad H = H_w \quad (10.5.1d)$$

$$y = \delta, \quad u = u_e(x), \quad H = H_e \quad (10.5.1e)$$

where

$$\overline{\rho v} = \rho v + \overline{\rho' v'} \quad (10.5.2a)$$

$$\tau = \mu \frac{\partial u}{\partial y} - \rho \overline{u' v'} \quad (10.5.2b)$$

$$\dot{q} = -k \frac{\partial T}{\partial y} + \rho \overline{v' h'} \quad (10.5.2c)$$

### 10.5.2 Axisymmetric Flows

For an axisymmetric and two-dimensional, steady, laminar or turbulent flow, the boundary-layer equations are

$$\frac{\partial r^k \rho u}{\partial x} + \frac{\partial r^k \bar{p}v}{\partial y} = 0 \quad (10.5.3a)$$

$$\rho u \frac{\partial u}{\partial x} + \bar{p}v \frac{\partial u}{\partial y} = -\frac{dp}{dx} + \frac{1}{r^k} \frac{\partial r^k \tau}{\partial y} + \rho f_x + \bar{\rho}' f'_x \quad (10.5.3b)$$

$$\rho u \frac{\partial H}{\partial x} + \bar{p}v \frac{\partial H}{\partial y} = \frac{1}{r^k} \frac{\partial}{\partial y} \left[ r^k (u\tau - \dot{q}) \right] \quad (10.5.3c)$$

where  $k$  denotes the flow index being unity for an axisymmetric flow and zero for a two-dimensional flow. The definitions in Eqs. (10.5.2a–10.5.2c) and the boundary conditions in Eqs. (10.5.1d)–(10.5.1e) remain the same.

Again, the distance  $r$  from a point to the axis of symmetry is related to the radius  $r_0$  of the surface  $y = 0$  by Eq. (3.2.3). If the body radius is quite large in relation to the boundary-layer thickness, the variations of  $r$  with  $y$  can be neglected and we can take  $r = r_0$ ; the boundary-layer equations then become

$$\frac{1}{r_0^k} \frac{\partial r_0^k \rho u}{\partial x} + \frac{\partial \bar{p}v}{\partial y} = 0 \quad (10.5.4a)$$

$$\rho u \frac{\partial u}{\partial x} + \bar{p}v \frac{\partial u}{\partial y} = -\frac{dp}{dx} + \frac{\partial \tau}{\partial y} + \rho f_x + \bar{\rho}' f'_x \quad (10.5.4b)$$

$$\rho u \frac{\partial H}{\partial x} + \bar{p}v \frac{\partial H}{\partial y} = \frac{\partial}{\partial y} [u\tau - \dot{q}] \quad (10.5.4c)$$

### 10.5.3 Three-Dimensional Flows

For a body-oriented coordinate system (see subsection 7.2.3), the boundary-layer equations for a steady, three-dimensional, laminar or turbulent compressible flow are

$$\frac{\partial}{\partial x} (\rho u h_2 \sin \theta) + \frac{\partial}{\partial z} (\rho w h_1 \sin \theta) + \frac{\partial}{\partial y} (\bar{p}v h_1 h_2 \sin \theta) = 0 \quad (10.5.5)$$

$$\begin{aligned} \rho \frac{u}{h_1} \frac{\partial u}{\partial x} + \rho \frac{w}{h_2} \frac{\partial u}{\partial z} + \bar{p}v \frac{\partial u}{\partial y} - \rho \cot \theta k_1 u^2 + \rho \csc \theta k_2 w^2 + \rho k_{12} uw \\ = -\frac{\csc^2 \theta}{h_1} \frac{\partial p}{\partial x} + \frac{\cot \theta \csc \theta}{h_2} \frac{\partial p}{\partial z} + \frac{\partial \tau_x}{\partial y} \end{aligned} \quad (10.5.6)$$

$$\begin{aligned} \rho \frac{u}{h_1} \frac{\partial w}{\partial x} + \rho \frac{w}{h_2} \frac{\partial w}{\partial z} + \bar{p}v \frac{\partial w}{\partial y} - \rho \cot \theta k_2 w^2 + \rho \csc \theta k_1 u^2 + \rho k_{21} uw \\ = \frac{\cot \theta \csc \theta}{h_1} \frac{\partial p}{\partial x} - \frac{\csc^2 \theta}{h_2} \frac{\partial p}{\partial z} + \frac{\partial \tau_z}{\partial y} \end{aligned} \quad (10.5.7)$$

$$\begin{aligned} & \rho \frac{u}{h_1} \frac{\partial H}{\partial x} + \rho \frac{w}{h_2} \frac{\partial H}{\partial z} + \overline{\rho v} \frac{\partial H}{\partial y} \\ &= \frac{\partial}{\partial y} [u\tau_x + w\tau_z + w\tau_x \cos \theta + u\tau_z \cos \theta - \dot{q}] \end{aligned} \quad (10.5.8)$$

where the parameters  $k_1$ ,  $k_2$ ,  $k_{12}$  and  $k_{21}$  are given by Eqs. (7.2.22) and (7.2.23) and

$$\overline{\rho v} = \rho v + \overline{\rho' v'} \quad (10.5.9)$$

$$\tau_x = \mu \frac{\partial u}{\partial y} - \rho \overline{u' v'} \quad (10.5.10)$$

$$\tau_z = \mu \frac{\partial w}{\partial y} - \rho \overline{w' v'} \quad (10.5.11)$$

$$\dot{q} = -k \frac{\partial T}{\partial y} + \rho \overline{v' h'} \quad (10.5.12)$$

The boundary conditions are

$$y = 0 : u = w = 0, \quad v = v_w(x, z),$$

$$H = H_w(x, z) \text{ or } \left( \frac{\partial H}{\partial y} \right)_w = -\frac{c_{pw}}{k_x} \dot{q}_w \quad (10.5.13a)$$

$$y = \delta : u = u_e(x, z), \quad w = w_e(x, z), \quad H = H_e \quad (10.5.13b)$$

## 10.6 Integral Equations

The integral equations for a steady two-dimensional or an axisymmetric flow with negligible body forces are given below.

### 10.6.1 Continuity Equation

For an axisymmetric flow, the integral continuity equation is

$$\frac{d}{dx} [\rho_e u_e (\delta_r - \delta^*)] = \rho_e u_e r_e \left[ \frac{d\delta}{dx} - \frac{v_e}{u_e} \right] \quad (10.6.1)$$

where

$$\delta_r = \int_0^\delta r dy \quad (10.6.2)$$

$$\delta^* = \int_0^\delta r \left( 1 - \frac{\rho u}{\rho_e u_e} \right) dy \quad (10.6.3)$$

If the boundary-layer thickness is much smaller than the body radius, Eq. (10.6.1) can be written as

$$\frac{d}{dx}(\delta - \delta^*) + (\delta - \delta^*) \left[ \frac{1}{u_e} \frac{du_e}{dx} + \frac{1}{\rho_e} \frac{d\rho_e}{dx} + \frac{1}{r_0^k} \frac{dr_0^k}{dx} \right] = \frac{d\delta}{dx} - \frac{v_e}{u_e} \quad (10.6.4)$$

with

$$\delta^* = \int_0^\infty \left( 1 - \frac{\rho u}{\rho_e u_e} \right) dy \quad (10.6.5)$$

and  $r_0$  is the distance of the body surface to the axis of symmetry.

Using the flow index  $k$ , Eq. (10.6.4) applies to both axisymmetric ( $k = 1$ ) or two-dimensional ( $k = 0$ ) flow.

When the outer flow is isentropic, we have

$$\frac{1}{\rho_e} \frac{d\rho_e}{dx} = - \frac{M_e^2}{u_e} \frac{du_e}{dx} \quad (10.6.6)$$

### 10.6.2 Momentum Equation

For an axisymmetric flow, the integral momentum equation is

$$\frac{d\theta}{dx} + \theta \left[ \frac{H+2}{u_e} \frac{du_e}{dx} + \frac{1}{\rho_e} \frac{d\rho_e}{dx} \right] = r_0 \frac{c_f}{2} \quad (10.6.7)$$

where

$$\theta = \int_0^\infty r \frac{\rho u}{\rho_e u_e} \left( 1 - \frac{u}{u_e} \right) dy \quad (10.6.8)$$

$$\frac{c_f}{2} = \frac{\tau_w}{\rho_e u_e^2} \quad (10.6.9)$$

$$H = \frac{\delta^*}{\theta} \quad (10.6.10)$$

with  $\delta^*$  defined by Eq. (10.6.5).

If the boundary-layer thickness is much smaller than the body radius, Eq. (10.6.7) becomes

$$\frac{d\theta}{dx} + \theta \left[ \frac{H+2}{u_e} \frac{du_e}{dx} + \frac{1}{\rho_e} \frac{d\rho_e}{dx} + \frac{1}{r_0^k} \frac{dr_0^k}{dx} \right] = \frac{c_f}{2} \quad (10.6.11)$$

where

$$\theta = \int_0^\infty \frac{\rho u}{\rho_e u_e} \left( 1 - \frac{u}{u_e} \right) dy \quad (10.6.12)$$

with  $\delta^*$  defined by Eq. (10.6.5).

With the flow index  $k$ , Eq. (10.6.11) applies to both axisymmetric ( $k = 1$ ) or two-dimensional ( $k = 0$ ) flow.

### 10.6.3 Energy Equation

For an axisymmetric flow, the integral energy equation is

$$\frac{d}{dx} [\rho_e u_e H_e \Delta_H] = r_0 \dot{q}_w \quad (10.6.13)$$

where

$$\Delta_H = \int_0^\infty r \frac{\rho u}{\rho_e u_e} \left( \frac{H}{H_e} - 1 \right) dy \quad (10.6.14)$$

If the boundary-layer thickness is much smaller than the body radius, Eq. (10.6.13) becomes

$$\frac{d\Delta_H}{dx} + \Delta_H \left[ \frac{1}{u_e} \frac{du_e}{dx} + \frac{1}{\rho_e} \frac{d\rho_e}{dx} + \frac{1}{r_0^k} \frac{dr_0^k}{dx} \right] = \frac{\dot{q}_w}{\rho_e u_e H_e} \quad (10.6.15)$$

where

$$\Delta_H = \int_0^\infty \frac{\rho u}{\rho_e u_e} \left( \frac{H}{H_e} - 1 \right) dy \quad (10.6.16)$$

With the flow index  $k$ , Eq. (10.6.15) applies to both axisymmetric ( $k = 1$ ) or two-dimensional ( $k = 0$ ) flow.

## References

- [1] Cebeci, T.: *Convective Heat Transfer*. Horizons Pub., Long Beach, Calif. and Springer, Heidelberg, 2002.
- [2] Van Driest, E. R.: Turbulent boundary layer in compressible fluids. *J. Aeronaut. Sci.* **18**, 145, 1951.
- [3] Favre, A., Kovasznay, L. S. G., Dumas, R., Gaviglio, J. and Coantic, M.: *La turbulence en mécanique des fluides*. Gauthier Villars, 1976.
- [4] Cebeci, T.: *Analysis of Turbulent Flows*. Elsevier, London, 2004.

## Problem

**10-1.** Another procedure for obtaining the conservation equations for turbulent flows is to use the *mass-weighted-averaging* procedure used by Van Driest [2] and Favre [3] as described in [4]. This procedure eliminates the mean-mass term  $\bar{\rho}' \bar{u}'_j$  and some of the momentum transport terms such as  $\bar{u}_i \bar{\rho}' \bar{u}'_j$  and  $\bar{\rho}' \bar{u}'_i \bar{u}'_j$  across mean streamlines. We define a mass-weighted velocity

$$\tilde{u}_i = \frac{\bar{\rho} \bar{u}_i}{\bar{\rho}},$$

where the bar denotes conventional time averaging and the tilde denotes mass-weighted averaging.

1. Show that

$$\overline{\rho u'_i} = 0 \quad (\text{P10.1.1})$$

and similarly that

$$\overline{\rho h'} = 0 \quad (\text{P10.1.2a})$$

$$\overline{\rho H'} = 0 \quad (\text{P10.1.2b})$$

2. Show that

$$\overline{\rho u_i u_j} = \bar{\rho} \tilde{u}_i \tilde{u}_j + \overline{\rho u'_i u'_j} \quad (\text{P10.1.3a})$$

$$\overline{\rho u_i H} = \bar{\rho} \tilde{u}_i \tilde{H} + \overline{\rho u'_i H'} \quad (\text{P10.1.3b})$$

3. Show that

$$\tilde{H} = \tilde{h} + \frac{\tilde{u}_i \tilde{u}_i}{2} + \frac{\overline{\rho u'_i u'_i}}{2\bar{\rho}} \quad (\text{P10.1.4})$$

and that

$$\overline{\rho u'_j H'} = \overline{\rho u'_j h'} + \tilde{u}_i \overline{\rho u'_i u'_j} + \frac{\overline{\rho u'_j u'_i u'_i}}{2} \quad (\text{P10.1.5})$$

4. Show that, if the body forces are negligible, the ensemble averages of the continuity equation, momentum equation, energy equation and of the equation of state are

$$\frac{\partial \bar{\rho}}{\partial t} + \frac{\partial}{\partial x_j} (\bar{\rho} \tilde{u}_j) = 0 \quad (\text{P10.1.6a})$$

$$\frac{\partial \bar{\rho} \tilde{u}_i}{\partial t} + \frac{\partial \bar{\rho} \tilde{u}_i \tilde{u}_j}{\partial x_j} = - \frac{\partial \bar{p}}{\partial x_i} + \frac{\partial}{\partial x_j} [\bar{\sigma}_{ij} - \overline{\rho u'_i u'_j}] \quad (\text{P10.1.6b})$$

$$\frac{\partial \bar{\rho} \tilde{H}}{\partial t} + \frac{\partial \bar{\rho} \tilde{u}_j \tilde{H}}{\partial x_j} = \frac{\partial \bar{p}}{\partial t}$$

$$+ \frac{\partial}{\partial x_j} \left[ \bar{u}_i \bar{\sigma}_{ij} - \bar{q}_j - \tilde{u}_i \overline{\rho u'_i u'_j} - \overline{\rho u'_j h'} - \frac{\overline{\rho u'_j u'_i u'_i}}{2} \right] \quad (\text{P10.1.6c})$$

$$\bar{p} = \bar{\rho} \frac{\mathcal{R}}{\mathcal{M}} \tilde{T} \quad (\text{P10.1.6d})$$

# 11

# Two-Dimensional Compressible Laminar Flows

## 11.1 Introduction

In the discussion of incompressible laminar boundary layers in Chapter 4, it was assumed that the typical temperature difference in gas flow was a small fraction of the absolute temperature so that fluid properties such as density and dynamic viscosity were assumed to be constant. When this is not the case, it is necessary to solve the momentum and energy equations simultaneously together with the continuity equation.

The discussion in Chapter 4 is extended to compressible flows and two useful transformations are considered in Section 11.2. The first is the compressible version of the Falkner–Skan transformation discussed in subsection 11.2.1 for incompressible flows and the second a transformation that eliminates the dependence of the equations on compressibility effects. Similar flows for compressible flows and the relation between compressible and incompressible laminar flows are addressed in Sections 11.3 and 11.4, respectively and are followed by non-similar flows in Section 11.5.

Sections 11.6 to 11.8 are devoted to boundary-layer flows with separation. Sections 11.6 and 11.7 discuss the effects of a shock wave in a shear layer, and Section 11.8 discusses a prescription for computing interactive flows with shocks.

## 11.2 Transformations for Compressible Flows

Again, as in incompressible flows, it is useful and desirable to express the governing equations in transformed variables before they are solved. In this section we discuss two totally different types of transformation for this purpose. The first, used in simpler form in constant-property flow (subsection 11.2.1), is the Falkner–Skan transformation and is intended to *reduce* (but not usually

eliminate) the dependence of the equations on  $x$ . The second transformation (subsection 11.2.2), due to Illingworth [2] and Stewartson [3], is intended to eliminate the dependence of the equations on the Mach number, the ratio of wall temperature to freestream temperature, or other variable-property parameters. In fact, the effect of variable properties can be eliminated in only a few special laminar-flow cases, but both in laminar flow and in turbulent flow, a *reduction* of variable-property effect makes the remaining effects easier to calculate. However, calculations can be done in primitive untransformed variables, although less efficiently.

### 11.2.1 Falkner–Skan Transformation

We define the compressible version of the Falkner–Skan transformation by

$$d\eta = \left( \frac{u_e}{\nu_e x} \right)^{1/2} \frac{\rho}{\rho_e} dy, \quad \psi(x, y) = (\rho_e \mu_e u_e x)^{1/2} f(x, \eta) \quad (11.2.1)$$

With the usual definitions of stream function

$$\rho u = \frac{\partial \psi}{\partial y}, \quad \rho v = -\frac{\partial \psi}{\partial x} \quad (11.2.2)$$

we use a procedure similar to that described in Sect. 4.2 and replacing  $-\frac{dp}{dx}$  term with  $\rho_e u_e \frac{du_e}{dx}$  and omitting turbulence and body-force terms, we write the momentum and energy equations for a laminar flow as

$$(bf'')' + m_1 ff'' + m_2[c - (f')^2] = x \left( f' \frac{\partial f'}{\partial x} - f'' \frac{\partial f}{\partial x} \right), \quad (11.2.3)$$

$$(eS' + df' f'')' + m_1 f S' = x \left( f' \frac{\partial S}{\partial x} - S' \frac{\partial f}{\partial x} \right). \quad (11.2.4)$$

In the absence of mass transfer, the boundary conditions are

$$y = 0, \quad v = 0, \quad u = 0, \quad H = H_w(x) \text{ or } \left( \frac{\partial H}{\partial y} \right)_w = -\frac{c_{p_w}}{k_w} \dot{q}_w,$$

$$y = \delta, \quad u = u_e(x), \quad H = H_e.$$

In terms of transformed variables these boundary conditions become

$$\eta = 0, \quad f = 0, \quad f' = 0, \quad S = S_w(x) \text{ or } S'_w = -\frac{c_{p_w}}{k_w} x \frac{c_w x \dot{q}_w}{H_e \sqrt{R_x}}, \quad (11.2.5a)$$

$$\eta = \eta_e, \quad f' = 1, \quad S \equiv H/H_e = 1. \quad (11.2.5b)$$

As before, in Eqs. (11.2.3), (11.2.4), and (11.2.5) the primes denote differentiation with respect to  $\eta$ , and  $f'$  and  $S$  denote the dimensionless velocity and

total-enthalpy ratios,  $u/u_e$  and  $H/H_e$ , respectively. The other parameters  $b$ ,  $C$ ,  $c$ ,  $e$ ,  $d$ ,  $m_1$ ,  $m_2$ , and  $R_x$  are defined by

$$b = C, \quad C \equiv \frac{\rho\mu}{\rho_e\mu_e}, \quad c = \frac{\rho_e}{\rho}, \quad d = \frac{Cu_e^2}{H_e} \left(1 - \frac{1}{\text{Pr}}\right), \quad e = \frac{b}{\text{Pr}}, \quad (11.2.6a)$$

$$m_1 = \frac{1}{2} \left[ 1 + m_2 + \frac{x}{\rho_e\mu_e} \frac{d}{dx}(\rho_e\mu_e) \right], \quad m_2 = \frac{x}{u_e} \frac{du_e}{dx}, \quad R_x = \frac{u_ex}{\nu_e}. \quad (11.2.6b)$$

### 11.2.2 Illingworth–Stewartson Transformation

Because the Prandtl number of the fluid may assume a wide range of values, and because the viscosity-temperature relationship may vary greatly from one fluid to another, it is useful to consider a model fluid, for which  $\text{Pr} = 1$  and for which there is a simple relationship between  $\mu$  and  $T$ . The Illingworth–Stewartson transformation used with these simplifications for the fluid properties, simplifies the form of the governing equations and allows us to study the solutions of compressible laminar boundary layers with and without heat transfer through the surface. Further, if the heat transfer through the surface is zero (adiabatic flow), the equations reduce to their incompressible form.

We define the Illingworth–Stewartson transformation by

$$dX = \frac{a_e}{a_\infty} \frac{p_e}{p_\infty} dx, \quad (11.2.7a)$$

$$dY = \frac{a_e}{a_\infty} \frac{\rho}{\rho_\infty} dy, \quad (11.2.7b)$$

where  $a$  is the speed of sound and subscript  $\infty$  denotes again conditions at freestream. We also relate the dimensional stream function  $\psi$  to an incompressible stream function  $F(X, Y)$  by

$$\psi = \rho_\infty F. \quad (11.2.8)$$

Then, using the definition of stream function given by Eq. (11.2.2) and the relations given by Eqs. (11.2.7) and (11.2.8), and employing the usual chain rule for differentiation, we can write the momentum equation, Eq. (10.5.1b) for laminar flow without body forces, with primes denoting differentiation with respect to  $Y$ , as

$$\begin{aligned} F' \frac{\partial F'}{\partial X} - F'' \frac{\partial F}{\partial X} \\ = \frac{a_\infty}{a_e} \left[ -(F')^2 \frac{d}{dX} \left( \frac{a_e}{a_\infty} \right) + \frac{\rho_e}{\rho} \frac{a_\infty}{a_e} u_e \frac{du_e}{dX} \right] + \frac{T_\infty}{T_e} \frac{\mu_e}{\mu_\infty} \nu_\infty (CF'').' \end{aligned} \quad (11.2.9)$$

Here  $C$  denotes the density-viscosity parameter defined in Eq. (11.2.6a). In general, it is a function of  $x$  and  $y$ , but in the model fluid we assume that  $C$

is only a function of  $x$ . This assumption leads to useful simplifications in the solution of boundary-layer equations by approximate methods. Since viscous effects are most important near the wall, we may approximate  $C$  with good accuracy as

$$C(x) = \frac{\rho_w \mu_w}{\rho_e \mu_e} = \frac{\mu_w T_e}{T_w \mu_e} \quad (11.2.10)$$

by virtue of the perfect-gas assumption and the  $y$  independence of pressure. This empirical relationship is known as the *Chapman-Rubesin viscosity law*. Note that Eq. (11.2.10) would be exact, with  $C = 1$ , if  $\mu$  were proportional to  $T$ ; actually, for air at temperatures near atmospheric,  $\mu$  is approximately proportional to  $T^{0.76}$ .

Let us consider the first expression in Eq. (11.2.2) and write it as

$$\rho u = \frac{\partial \psi}{\partial y} = \rho_\infty \frac{\partial F}{\partial Y} \frac{\partial Y}{\partial y} = \rho \frac{a_e}{a_\infty} F'. \quad (11.2.11)$$

If  $\bar{u}$  denotes the incompressible velocity ( $\equiv F'$ ), then it follows from Eq. (11.2.11) that the relationship between compressible and incompressible  $u$  velocities is

$$u = \frac{a_e}{a_\infty} \bar{u}. \quad (11.2.12)$$

(The speed of sound in the incompressible flow is simply assumed to be very large compared with  $u$ ; the type of fluid need not be specified.) From the definition of speed of sound for an isentropic flow we can write

$$a_e^2 = \gamma R T_e = \frac{\gamma R}{c_p} c_p T_e = \frac{\gamma R}{c_p} \left[ H_e - \frac{u_e^2}{2} \right]. \quad (11.2.13)$$

Differentiating this expression with respect to  $X$ , we get

$$2a_e \frac{da_e}{dX} = -\frac{\gamma R}{c_p} u_e \frac{du_e}{dX}. \quad (11.2.14)$$

The first term on the right-hand side of Eq. (11.2.9) is the pressure-gradient term. Noting that  $\partial F/\partial Y = \bar{u} = a_\infty/a_e u$  and that  $H = c_p T + u^2/2$ , we can write this pressure-gradient term as

$$\frac{1}{c_p T_e} \left( \frac{a_\infty}{a_e} \right)^2 H u_e \frac{du_e}{dX}. \quad (11.2.15)$$

Further, after writing  $u_e = a_e/a_\infty \bar{u}_e$ , we can show, by making use of Eq. (11.2.14), that

$$\frac{du_e}{dX} = \frac{c_p T_e}{H_e} \frac{a_e}{a_\infty} \frac{d\bar{u}_e}{dX}. \quad (11.2.16)$$

If we now substitute  $du_e/dX$  into Eq. (11.2.14) and again note the relationship between  $u_e$  and  $\bar{u}_e$ , we may write Eq. (11.2.14) as

$$S\bar{u}_e \frac{d\bar{u}_e}{dX}, \quad (11.2.17)$$

where  $S = H/H_e$ . Also for a perfect gas and with  $C = 1$ , the transformed momentum equation (11.2.9) in Illingworth–Stewartson variables can be written as

$$\nu_\infty F''' + S\bar{u}_e \frac{d\bar{u}_e}{dX} = F' \frac{\partial F'}{\partial X} - F'' \frac{\partial F}{\partial X}, \quad (11.2.18)$$

where the primes now denote differentiation with respect to  $Y$ . If the somewhat more general Chapman–Rubesin formula (11.2.10) is used for  $C$ , Eq. (11.2.18) is still valid, provided  $X$  is replaced by  $\hat{x}$ , where

$$d\hat{x} = C(X)dX = \frac{a_e p_e}{a_\infty p_\infty} C(x)dx. \quad (11.2.19)$$

In order to express the energy equation in terms of Illingworth–Stewartson variables, we assume the Prandtl number to be unity. Then by using the relations given by Eqs. (11.2.2), (11.2.7), and (11.2.8) and by a procedure similar to that used for the momentum equation, the energy equation, Eq. (10.5.1c), can be written as

$$\nu_\infty S'' = F' \frac{\partial S}{\partial X} - S' \frac{\partial F}{\partial X} \quad (11.2.20)$$

with primes now denoting differentiation with respect to  $Y$ .

Similarly, in the absence of mass transfer the boundary conditions given by Eqs. (10.5.4) become

$$Y = 0, \quad F = F' = 0, \quad S' = 0 \text{ (adiabatic flow)} \quad (11.2.21a)$$

or  $S = S_w(x)$  (prescribed wall temperature),

$$Y \rightarrow \infty, \quad F' \rightarrow \bar{u}_e, \quad S \rightarrow 1.0. \quad (11.2.21b)$$

It is easy to see that the energy equation for  $\text{Pr} = 1$ , Eq. (10.5.1c) for laminar flow, has the solution  $H = H_e$ , (that is,  $S = 1$ ), which of course corresponds to an adiabatic laminar flow. We can therefore see that  $S = 1$  must also be a solution of Eq. (11.2.20), which then reduces Eq. (11.2.18) exactly to the standard form for an incompressible flow. We should remember, however, that when this equation is solved subject to the boundary conditions given by Eq. (11.2.21), the  $x$  and  $y$  coordinates are distorted according to Eq. (11.2.7), and the external velocity distribution of the incompressible flow ( $\bar{u}_e$ ) is distorted according to  $u_e(x) = \{[a_e(x)]/a_\infty(x)\}\bar{u}_e(X)$ .

The adiabatic-wall solution  $H = H_e$  of the energy equation is called the *Crocco integral*. Note that since (1) the velocity  $u$  in a zero-pressure-gradient flow satisfies the same equation as Eq. (10.5.1c) for laminar flow but with  $H$  replaced by  $u$ , and (2) if  $H$  is a solution of Eq. (10.5.1c), so is  $H = H_w$ , it follows that Eq. (10.5.1c) for laminar flow has a solution  $H = H_w + (\text{const})u$ .

The constant is evaluated by requiring  $H = H_e$ , when  $u = u_e$  (external-flow conditions), giving

$$H = H_w - (H_w - H_e) \frac{u}{u_e}, \quad (11.2.22a)$$

$$T = T_w - \frac{1}{c_p} (H_w - H_e) \frac{u}{u_e} - \frac{u^2}{2c_p} \quad (11.2.22b)$$

for arbitrary wall temperature  $T_w \equiv H_w/c_p$  and  $\text{Pr} = 1$ .

### 11.3 Similar Flows

For similar flows the dimensionless stream function  $f$  and dimensionless total-enthalpy ratio  $S$  in the compressible version of the Falkner–Skan transformation are functions of  $\eta$  only, by definition, and as a result, Eqs. (11.2.3) to (11.2.5) reduce to

$$(bf'')' + m_1 f f'' + m_2 [c - (f')^2] = 0, \quad (11.3.1)$$

$$(eS' + df' f'')' + m_1 f S' = 0, \quad (11.3.2)$$

$$\eta = 0, \quad f = 0, \quad f' = 0, \quad S = S_w, \text{ or } S' = S'_w \quad (11.3.3a)$$

$$\eta = \eta_e, \quad f' = 1, \quad S = 1, \quad (11.3.3b)$$

and for similarity all the parameters  $b$ ,  $e$ ,  $d$ ,  $c$ ,  $m_1$ , and  $m_2$  defined by Eqs. (11.2.6) as well as the boundary conditions are independent of  $x$ .

To obtain the similarity solutions of the momentum and energy equations expressed in Illingworth–Stewartson transformed variables, we use the Falkner–Skan transformation for incompressible flows discussed in Sect. 4.2, namely,

$$\eta = \left( \frac{\bar{u}_e}{\nu_\infty X} \right)^{1/2}, \quad F(X, Y) = (\bar{u}_e \nu_\infty X)^{1/2} \phi(\eta). \quad (11.3.4)$$

Using this transformation, we can write Eqs. (11.2.18) and (11.2.20) as

$$\phi''' + \frac{m+1}{2} \phi \phi'' + m[S - (\phi')^2] = 0, \quad (11.3.5)$$

$$S'' + \frac{m+1}{2} \phi S' = 0, \quad (11.3.6)$$

where in Eq. (11.3.4) we have changed the notation used for the stream function from  $f(\eta)$  to  $\phi(\eta)$  in order to distinguish it from the definition used in Eq. (4.2.5). In Eqs. (11.3.5) and (11.3.6),  $m$  is the usual definition of the dimensionless pressure-gradient parameter

$$m = \frac{X}{\bar{u}_e} \frac{d\bar{u}_e}{dX}. \quad (11.3.7)$$

The same equations are obtained when the Chapman–Rubesin approximation is used except that  $X$  is replaced by  $\hat{x}$ .

Similarly the boundary conditions given by Eqs. (11.2.21) can be written as

$$\eta = 0, \quad \phi = \phi' = 0, \quad S = S_w \text{ or } S' = 0, \quad (11.3.8a)$$

$$\eta = \eta_e, \quad \phi' = 1, \quad S = 1. \quad (11.3.8b)$$

Again, the solutions of Eqs. (11.3.5) and (11.3.6) are independent of  $X$  provided that the above boundary conditions are independent of  $X$ . These requirements are satisfied if  $S_w$  and  $m$  are constants.

The requirement that  $S_w$  is constant leads to uniform wall temperature, since  $H_e$  is constant in an isentropic external stream, and the requirement that  $m$  is constant, as in incompressible flows, leads to

$$\bar{u}_e = cX^m, \quad (11.3.9)$$

where  $C$  is a constant. Thus, we get similarity solutions in compressible laminar boundary layers on impermeable walls only when the distorted external velocity  $\bar{u}_e$  varies with the distorted surface distance  $X$  as prescribed by Eq. (11.3.9) and when the surface temperature is constant. As in incompressible laminar flows, the importance of similar flows is quite evident; we solve two ordinary differential equations, rather than two partial differential equations. However, as in incompressible flows, values of  $m$  other than 0 or 1, corresponding to flat-plate flow and stagnation-point flow, respectively, are rare in practice.

## 11.4 Relation Between Compressible and Incompressible Boundary-Layer Parameters

As in incompressible similar flows, the boundary-layer parameters such as  $\delta^*$ ,  $\theta$ , and  $c_f$  can be written in simplified forms by using either the compressible version of the Falkner–Skan transformation or the Illingworth–Stewartson transformation. Formulas that connect compressible boundary-layer parameters to the solutions of Eqs. (1.3.5) and (11.3.6), subject to Eq. (11.3.8) with constant  $S_w$ , can also be derived. For an *adiabatic* flow their solutions reduce to incompressible flow solutions; in this case Table 4.1 can be used.

As an example, let us consider a flow with zero pressure gradient, governed by the incompressible version of the compressible-flow equations given by Eqs. (11.3.5) and (11.3.6). Regardless of heat transfer, the latter can be written as

$$\phi''' + \frac{1}{2}\phi\phi'' = 0, \quad (11.4.1)$$

$$S'' + \frac{1}{2}\phi S' = 0. \quad (11.4.2)$$

Solving Eqs. (11.4.1) and (11.4.2) for  $\phi$  and equating the two expressions, we get

$$\frac{S''}{S'} = \frac{\phi'''}{\phi''}. \quad (11.4.3)$$

Integrating this expression twice and using the boundary conditions given by Eq. (11.3.8), with  $S_w$  now being constant for similarity, we get

$$S = S_w - (S_w - 1)\phi', \quad (11.4.4)$$

which is the same as Eq. (11.2.22) when that equation is written in terms of  $S$ . From Eq. (11.4.4) we see that the static-temperature distribution across the boundary layer is

$$\frac{T}{T_e} = -\frac{\bar{u}_e^2}{2c_p T_e}(\phi')^2 + \left(1 + \frac{\bar{u}_e^2}{2c_p T_e}\right)[\phi' + S_w(1 - \phi')]. \quad (11.4.5)$$

By definition, the displacement thickness for a compressible flow is

$$\delta_c^* = \int_0^\infty \left(1 - \frac{\rho u}{\rho_e u_e}\right) dy, \quad (11.4.6a)$$

which in terms of Illingworth–Stewartson variables can be written as

$$\delta_c^* = \frac{a_\infty \rho_\infty}{a_e \rho_e} \left[ \int_0^\infty \left( \frac{\rho_e}{\rho} - \frac{\bar{u}}{\bar{u}_e} \right) dY \right]. \quad (11.4.6b)$$

For a perfect gas, the above expression becomes

$$\delta_c^* = \frac{a_\infty \rho_\infty}{a_e \rho_e} \left[ \int_0^\infty \left( \frac{T}{T_e} - \frac{\bar{u}}{\bar{u}_e} \right) dY \right]. \quad (11.4.6c)$$

The temperature distribution for an adiabatic flow ( $S \equiv 1$ ) can be obtained by recalling the definition of total enthalpy, which can be written as

$$H = c_p T + \frac{u^2}{2} = c_p T_e + \frac{u_e^2}{2},$$

or in terms of Illingworth–Stewartson variables

$$\frac{T}{T_e} = 1 + \frac{\gamma - 1}{2} M_\infty^2 \left[ 1 - \left( \frac{\bar{u}}{\bar{u}_e} \right)^2 \right]. \quad (11.4.7)$$

Inserting Eq. (11.4.7) into (11.4.6c) arranging, and recalling that for a constant-pressure flow  $a_\infty \rho_\infty / a_e \rho_e = 1$ , we can write  $\delta_c^*$  as

$$\delta_c^* = \int_0^\infty \left( 1 - \frac{\bar{u}}{\bar{u}_e} \right) dY + \frac{\gamma - 1}{2} M_\infty^2 \int_0^\infty \left[ 1 - \left( \frac{\bar{u}}{\bar{u}_e} \right)^2 \right] dY. \quad (11.4.8)$$

Noting that for any variable  $z$ ,

$$\int_0^\infty (1 - z^2) dY = \int_0^\infty z(1 - z) dY + \int_0^\infty (1 - z) dY,$$

we can write Eq. (11.4.8) as

$$\delta_c^* = \delta_i^* + \sigma(\delta_i^* + \theta_i), \quad (11.4.9)$$

where  $\delta_i^*$  and  $\theta_i$  are dimensionless incompressible displacement and momentum-thickness parameters, respectively (see Table 4.1), and  $\sigma$  is a Mach-number parameter defined by

$$\sigma = \frac{\gamma - 1}{2} M_\infty^2. \quad (11.4.10)$$

By following a procedure similar to that described for displacement thickness, we can also derive relations between compressible and incompressible values of momentum thickness and local skin-friction coefficients. For an adiabatic flat-plate flow they are

$$\theta_c = \theta_i, \quad c_{f_c} = \frac{\rho_w}{\rho_\infty} \frac{\mu_w}{\mu_\infty} c_{f_i}. \quad (11.4.11)$$

Here  $c_{f_i}$  denotes the incompressible value of the local skin-friction coefficient at the same value of  $u_c \theta / \nu_c$ .

Since  $\theta_c = \theta_i$ , we can rewrite Eq. (11.4.9) as

$$H_c = H_i + \sigma(H_i + 1), \quad (11.4.12)$$

where  $H$  is the shape parameter  $\delta^*/\theta$  and not the total enthalpy. This shows that the shape parameter  $H_c$  of a compressible laminar boundary layer increases with Mach number. The physical reason is that viscous dissipation of kinetic energy into heat increases  $T$  and reduces  $\rho$  near the surface so that the integrand  $\rho u / \rho_e u_e (1 - u/u_e)$  in the definition of  $\theta$  is a smaller fraction of the integrand  $1 - \rho u / \rho_e u_e$  in the definition  $\delta^*$  than if  $\rho/\rho_e$  were equal to unity.

If we assume that  $\mu \sim T$ , then it follows from the second relation in Eq. (11.4.11) that for an adiabatic flat plate, the compressible local skin-friction coefficient is the same as in the transformed (incompressible) flow since  $T_e = T_\infty$ .

### Solution with Heat Transfer

For an adiabatic flow,  $S \equiv 1$ , and the solution of the momentum equation (11.3.5) is independent of the energy equation (11.3.6). This means that we can now use the incompressible flow solutions of Eq. (11.3.5) for compressible adiabatic flows. For a flow with heat transfer,  $S_w \neq 1$ , the solutions of the momentum and energy equations are coupled. In this case it is necessary to solve Eqs. (11.3.5) and (11.3.6) simultaneously for specified values of  $S_w$  and  $m$ . Note that for each value of the dimensionless pressure gradient  $m$ , we can get different solutions corresponding to different values of  $S_w \neq 1$ .

Figure 11.1 shows the variation of the wall shear parameter  $\phi_w''$ , with pressure-gradient parameter  $m$  and with heat-transfer parameter  $S_w$ . We note

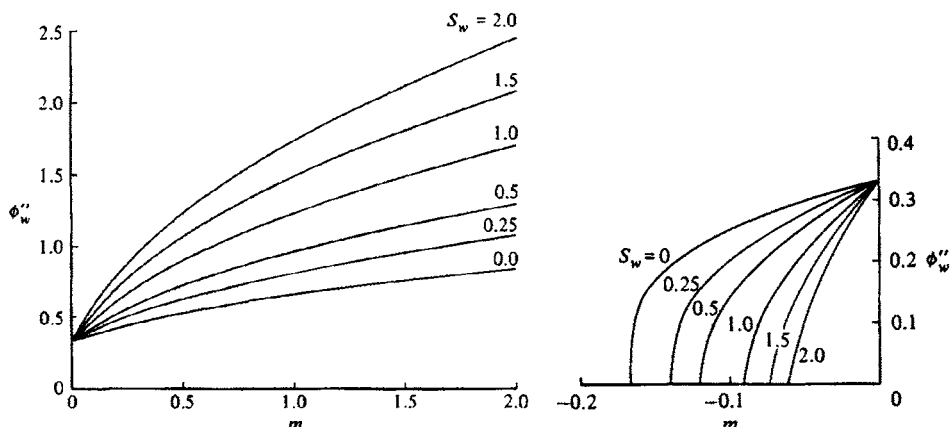


**Fig. 11.1.** Variation of the wall shear parameter  $\phi_w''$  with pressure gradient parameter  $m$  and heat transfer parameter  $S_w$  for compressible similar flows: Note different scales for  $m > 0$  or  $m < 0$ .

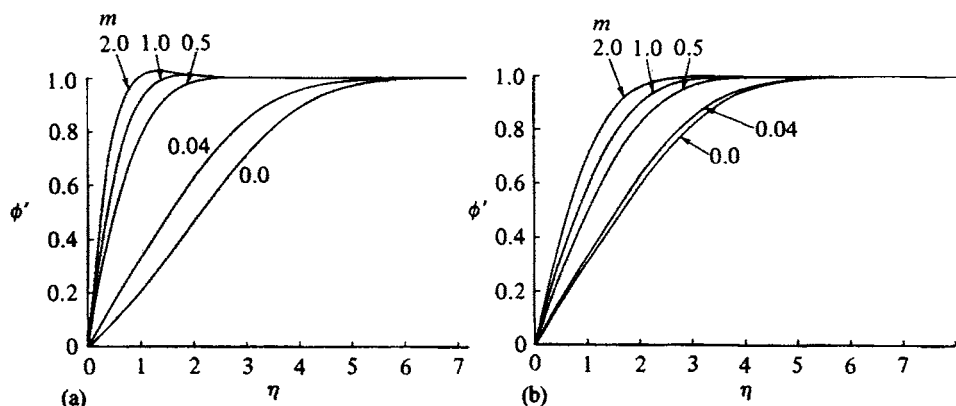


**Fig. 11.2.** The dimensionless velocity,  $f'$  as a function of  $\eta$  for various values of  $m$  (a)  $S_w = 2.0$ . (b)  $S_w = 0$ .

that although in zero pressure gradient ( $m = 0$ ) the Illingworth-Stewartson transformation makes the solution of the momentum equation in transformed variables independent of  $S_w$  [see Eq. (11.4.1)], heat transfer has a large effect on the solution in pressure-gradient flows. From Fig. 11.1 we see that for a given pressure gradient, heating the wall ( $S_w > 1$ ) increases the value of  $\phi_w''$  and cooling the wall ( $S_w < 1$ ) decreases the value of  $\phi_w''$ .

Figures 11.2 and 11.3 show the velocity profiles and enthalpy profiles across the boundary layer for various values of  $S_w$  and  $m$ . From Fig. 10.2a we see that, with heating, the velocity in the boundary layer can exceed the external velocity ( $\phi' > 1$ ) when the pressure gradient is *favorable*. This feature occurs at all positive values of  $m$ ,  $0 < m < \infty$ , if the wall is heated, but it is less marked as  $m$  becomes smaller. Physically the reason is that when  $m > 0$ , the favorable

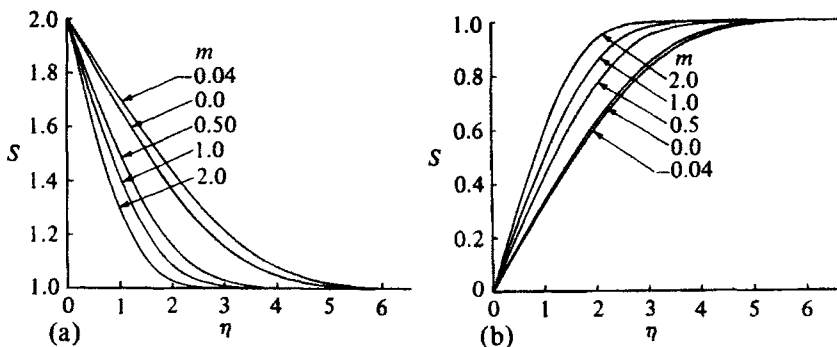


**Fig. 11.3.** The dimensionless enthalpy,  $S$ , as a function of  $\eta$  for various values of  $m$  (a)  $S_w = 2.0$ . (b)  $S_w = 0$ .

**Table 11.1.** Solutions of Eqs. (11.3.5) and (11.3.6) for  $m = 1$ .

$S_w$	$\phi''_w$	$\delta_1^* = \int_0^\infty (S - \phi') d\eta$	$\theta_1 = \int_0^\infty \phi' (1 - \phi') d\eta$	$H$	$S'_w$
2	1.7361	1.3855	0.1753	7.904	-0.6154
1.5	1.4911	1.0235	0.2338	4.378	-0.2972
1.0	1.2326	0.6479	0.2919	2.216	0
0.5	0.9545	0.2567	0.3489	0.736	0.2710
0.25	0.8060	0.0529	0.3766	0.141	0.3041
0	0.6487	-0.1577	0.4032	-0.391	0.5066

pressure gradient tends to accelerate the fluid: heating the wall diminishes  $\rho$ , from the equation of state, and so augments the effect of the pressure gradient on the acceleration of the fluid, increasing  $\phi'$  and, as remarked above,  $\phi''_w$ . Also, an inflexion appears even in the zero-pressure-gradient profile ( $m = 0$ ) because  $\mu$  varies with  $y$ .

From Fig. 11.3 we see that the effect of the pressure gradient on the enthalpy profiles is not as marked as its effect on the velocity profiles, as already demonstrated for incompressible flows in Fig. 4.4.

Table 11.1 shows the solutions of Eqs. (11.3.5) and (11.3.6) for several values of  $S_w$  when  $m = 1$ . We see that the dimensionless momentum thickness decreases with increasing heating, and in extreme cases (if  $\phi' > 1$ ) it may be negative. On the other hand, *cooling* the wall decreases the dimensionless displacement thickness and can even cause it to be negative, as shown in Table 11.1.

## 11.5 Nonsimilar Flows

As mentioned at the beginning of this chapter, the prediction of momentum and heat transfer in compressible nonsimilar laminar flows is slightly different

from the procedure for incompressible nonsimilar flows. The main reason is that the continuity and momentum equations contain fluid properties such as  $\rho$  and  $\mu$  that depend on the temperature field, and so the solution of these equations, unlike those for incompressible flows, depends on the energy equation. Of course, the solution of the energy equation still depends on the solution of the continuity and momentum equations, as in incompressible flows, and so an iteration procedure is needed.

As an example of a two-dimensional compressible nonsimilar laminar flow, we consider Howarth's flow (see Problem 4.25), whose external velocity distribution varies linearly with  $x$ , that is,

$$u_e = u_\infty \left(1 - \frac{x}{8}\right). \quad (11.5.1)$$

This flow can be started with a flat-plate profile of negligible thickness (at  $x = 0$ ), but the pressure gradient is adverse, and separation eventually occurs. For an incompressible flow with no heat transfer, calculations (Problem 4.25) indicate separation at  $x = 0.96$ .

To show the effect of heat transfer on separation point, we first consider the momentum and energy equations expressed in Illingworth–Stewartson variables, namely, Eqs. (11.2.18), (11.2.20), and (11.2.21). Using the Falkner–Skan transformation given by Eq. (11.3.4) and allowing the dimensionless stream function  $\phi$  to vary with  $X$  as well, we can write Eqs. (11.2.18), (11.2.20), and (11.2.21) as

$$\phi''' + \frac{m+1}{2} \phi \phi'' + m[S - (\phi')^2] = X \left( \phi' \frac{\partial \phi'}{\partial X} - \phi'' \frac{\partial \phi}{\partial X} \right), \quad (11.5.2)$$

$$S'' + \frac{m+1}{2} \phi S' = X \left( \phi' \frac{\partial S}{\partial X} - S' \frac{\partial \phi}{\partial X} \right), \quad (11.5.3)$$

$$\eta = 0, \quad \phi = \phi' = 0, \quad S = S_w(x) \text{ or } S' = 0, \quad (11.5.4a)$$

$$\eta = \eta_e, \quad \phi' = 1, \quad S = 1. \quad (11.5.4b)$$

We solve the above equations by using the numerical method discussed in Section 12.8 and the computer program given in the accompanying CD-ROM for values of  $S_w$  ( $\equiv H_w/H_e$ ) equal to 2, 1, 0.25, and 0, thus covering the case in which the wall is heated ( $S_w = 2$ ), cooled ( $S_w = 0.25$ ), or cooled to effectively zero enthalpy ( $S_w = 0$ ) and the case in which there is no heat transfer ( $S_w = 1$ ). In the latter case, we expect the solutions of the momentum equation to indicate the flow separation to be at  $X = 0.96$ , as in incompressible flow.

Figures 11.4 and 11.5 show the variation of dimensionless wall shear and heat-transfer parameters  $\phi_w''$  and  $S_w'$  with  $X$  for four different values of  $S_w$ . As anticipated, for  $S_w = 1$ , we find flow separation at  $X = 0.96$  (Fig. 11.4). With heating, the flow separation moves forward to  $X = 0.6$  if  $S_w = 2$ . On the other hand, cooling stabilizes the boundary layer and delays the separation. The calculations indicate separation at  $X = 1.86$  for  $S_w = 0.25$  and at  $X = 2.74$  for

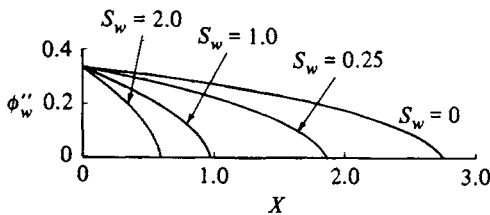


**Fig. 11.4.** Variation of the wall shear parameter  $\phi_w''$  for a compressible Howarth flow with dimensionless wall temperature.

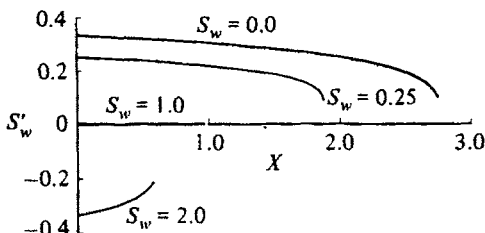


**Fig. 11.5.** Variation of the wall heat transfer parameter  $S'_w$  for a compressible Howarth flow with dimensionless wall temperature.

$S_w = 0$ . We also note from Fig. 11.5 that at separation, the wall heat-transfer parameter  $S'_w$  is finite, indicating that the Reynolds analogy is not realistic near separation.

Figures 11.6 and 11.7 show the effect of Mach number on the solutions of momentum and energy equations. These calculations are made for the same external velocity distribution, Howarth's flow, by solving the momentum and energy equations given by Eqs. (11.2.3) and (11.2.4) for values of  $S_w$  equal to 2.0 and 0.25. The results in Figs. 11.6 and 11.7 are for a Prandtl number of 0.72 and for freestream Mach numbers of 0.05, 1.0, and 2.0. Shown in these figures are the incompressible results obtained by the solution of Eqs. (11.5.2) and (11.5.3).

The results in Fig. 11.6 show that with either heating or cooling, the Mach number has a considerable influence on the separation point. In the case of heating ( $S_w = 2$ ), the separation point moves from  $X = 0.61$  for  $M_\infty = 0.05$  to  $X = 0.55$  for  $M_\infty = 1.0$  and to  $X = 0.425$  for  $M_\infty = 2.0$ . In the case of cooling ( $S_w = 0.25$ ), the separation point moves from  $X = 1.9$  for  $M_\infty = 0.05$  to  $X = 1.86$  for  $M_\infty = 1.0$  and to  $X = 1.7$  for  $M_\infty = 2.0$ . We see that for a given  $S_w$ , the effect of Mach number on the location of separation point is similar to the effect of heating for a given  $M_\infty$ ; that is, the separation point moves forward with increase of  $M_\infty$  or  $S_w$ . In Figs. 11.6 and 11.7 we also observe that the wall shear parameter  $\phi_w''$  and the location of separation are affected little by compressibility if  $M_\infty$  is less than about 1.0. We also observe that the Mach

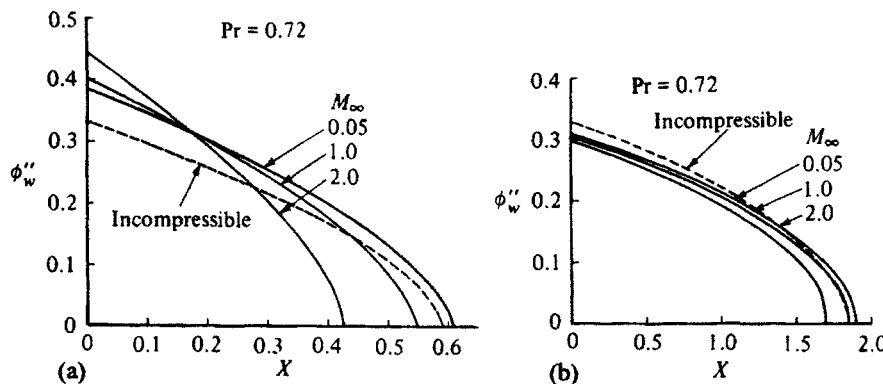


**Fig. 11.6.** Effect of Mach number on the wall shear parameter  $\phi_w''$  (a)  $S_w = 2.0$ . (b)  $S_w = 0.25$ .

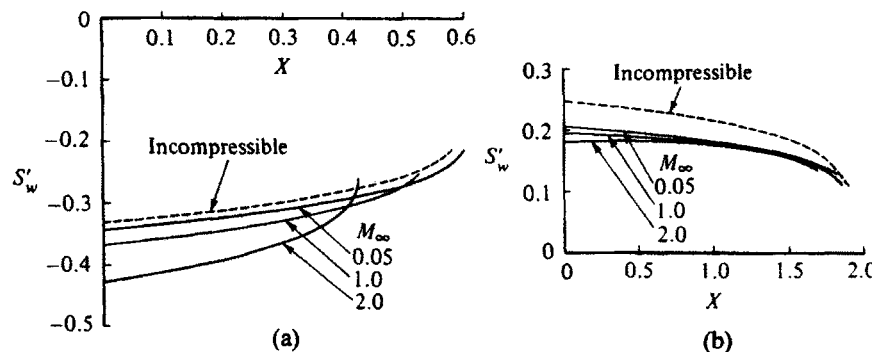


**Fig. 11.7.** Effect of Mach number on the wall heat transfer parameter  $S'_w$  (a)  $S_w = 2.0$ . (b)  $S_w = 0.25$ .

number has a smaller effect on the heat-transfer parameter  $S'_w$  when the surface is cooled than when it is heated.

## 11.6 Shock-Wave/Shear-Layer Interaction

A shock wave is a sudden increase of pressure and density across a very thin “wave” front in supersonic flow. It is, of course, governed by the equations of conservation of mass, momentum, and energy outlined above, but it results in a sudden decrease in total pressure and increase in entropy; the dissipation is effected by viscosity (as modified by the fact that the thickness of the shock wave is only a few times the mean free path between gas molecule collisions), but the details of total-pressure loss, etc., do not depend on viscosity. The increase in entropy implies that a concentrated “rarefaction wave” cannot exist because entropy would decrease. The simplest kind of compression wave is a

“normal” shock, i.e., normal to the flow direction (see Fig. 11.8a), for which the fractional pressure rise is a unique function of the upstream Mach number. If the upstream Mach number is 1.3, the pressure increases by a factor of 1.80 (if the ratio of specific heats is 1.4, as in air), and the total pressure decreases to 0.98 of its initial value. The downstream Mach number, always less than unity, is 0.79 in this case. The pressure rise and total-pressure loss increase as the upstream Mach number increases and the downstream Mach number decreases. A normal shock wave with an upstream Mach number of 1.3 is just about sufficient to cause separation of a *turbulent* boundary layer from a surface on which the shock wave abuts. *Oblique* shock waves (Fig. 11.8b,c) are simply normal shock waves with a component of velocity parallel to the shock; this component remains unchanged as the flow passes through the shock, the pressure rise being determined mainly by the normal component of Mach number. For further details of shock waves and the formulas for pressure rise, see, e.g., Liepmann and Roshko [3].

In this section we consider the effect of a shock wave on a shear layer. The two main cases are that in which the shock wave is imposed from outside (an “incident” shock) and that in which the shock springs from a solid surface carrying a boundary layer; note that in the latter case a shock system of some sort would be present even in the absence of a boundary layer. Figure 11.9a shows the pattern of shock waves and expansion fans that occurs in a jet exhausting into a still atmosphere at a speed greater than that of sound when the atmospheric pressure is greater than that in the jet nozzle; an example is the lift-off of a launch vehicle whose rocket nozzle is optimized for flight in the upper atmosphere. Figure 11.9b shows the case of an underexpanded jet, where the atmospheric pressure is less than that in the nozzle. The obvious difference between the two cases is that the overexpanded flow starts with a shock wave, through which the pressure rises so that the pressure in the downstream part of the jet boundary is equal to atmospheric pressure, whereas the underexpanded flow starts with an expansion fan, through which the pressure *falls* to the atmospheric value. The expansion takes place over a finite distance because the speed of sound decreases through the expansion and the Mach number  $M$  increases, so that the angle of a weak-disturbance wave to the flow direction,  $\sin^{-1}(1/M)$ , increases.

In a compression, on the other hand, the Mach number decreases downstream, the inclination of a weak-disturbance wave is greater than upstream of the shock, and all the weak-compression waves merge into a shock wave. Where a shock wave intersects a constant-pressure boundary, such as the atmospheric boundary at point  $A$  in Fig. 11.9a, it has to reflect as an expansion (crudely speaking, the pressure rise caused by the shock has to be followed immediately by a fall in pressure through an expansion starting at the boundary, to keep the pressure constant). Conversely, an expansion fan reflects from a constant-

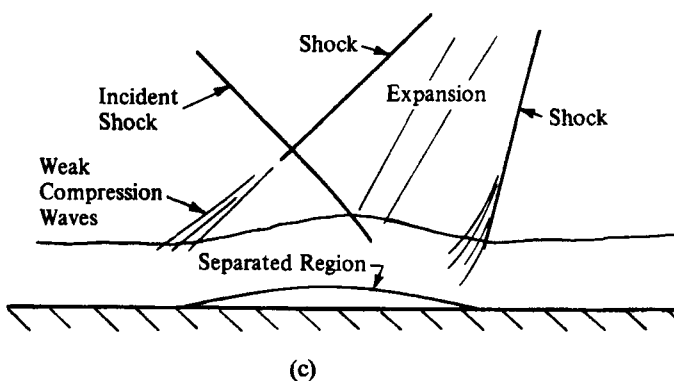
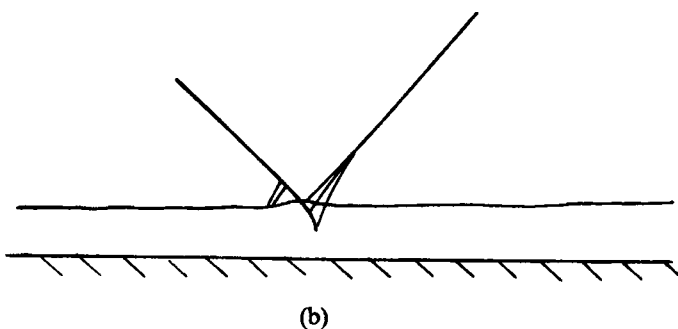
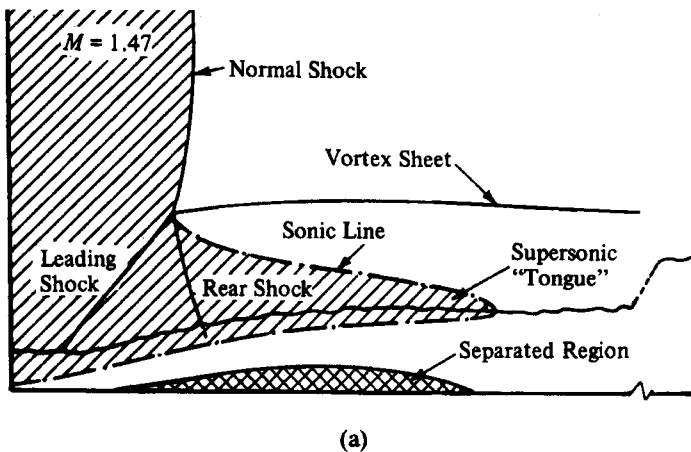


**Fig. 11.8.** (a) Interaction between normal shock wave and turbulent boundary layer (after [4]). (b) Weak incident oblique shock. (c) Strong oblique shock (the reflected shocks and expansion merge to form one shock).

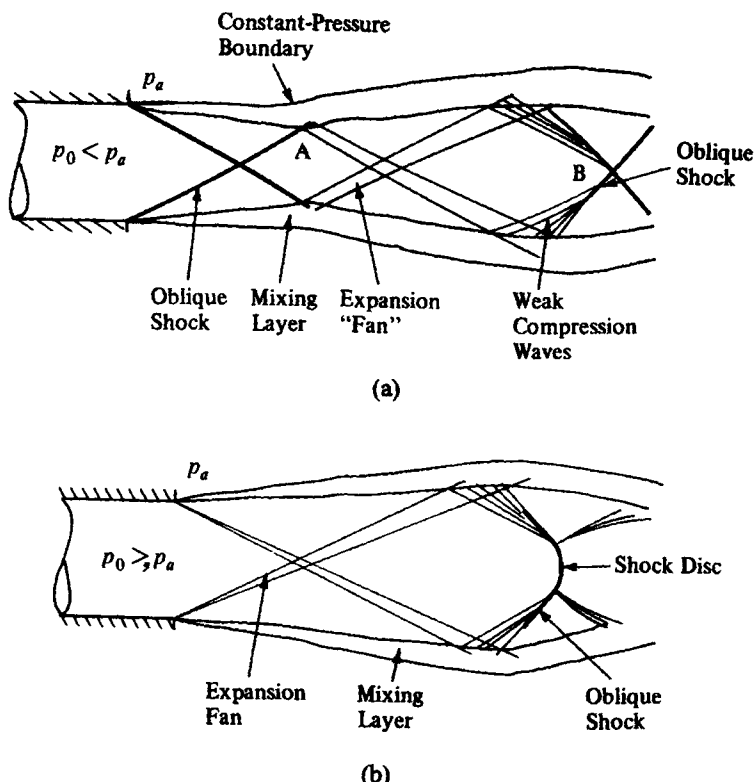


**Fig. 11.9.** Interactions between shock or expansion waves and a jet mixing layer. (a) “Over-expanded” jet: exit pressure below ambient. (b) “Under-expanded” jet: exit pressure above ambient.

pressure boundary as a series of weak compressions that then merge into a shock, so that the shock wave that forms near point B in Fig. 11.9a is at first sight the same strength as the original nozzle lip shock. In fact a loss in total pressure occurs through a shock wave, so that successive shocks and expansions are not quite identical. As seen in Fig. 11.9a, the shock angle changes at an intersection, and if the intersecting waves are strong enough, they will merge into a normal shock near the intersection as shown in Fig. 11.9b. As shock waves can occur only in supersonic flow, the shock at point A weakens into a continuous compression by the time it reaches the subsonic, outer part of the jet mixing layer, and the subsonic flow arranges itself so that the compression disappears at the outer “still air” edge of the shear layer. Note that the flow direction changes through an inclined (oblique) shock wave or expansion fan irrespective of the presence or absence of a shear layer.

Another type or interaction between a shock or expansion and a shear layer occurs in the wake of a transonic “cascade” (axial-flow turbomachine blade row) where waves shed from one blade – say, at the trailing edge – intersect the wake

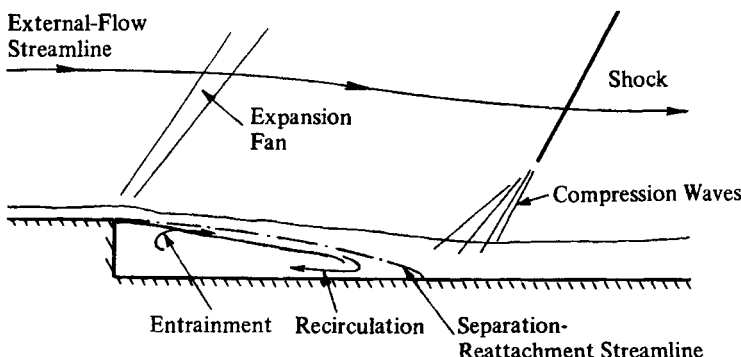


**Fig. 11.10.** Supersonic flow down a backward-facing step.

of another blade. Here the wave passes right through the wake, and only if the speed near the wake centerline is subsonic will there be a large spread of the pressure disturbance upstream and downstream of the intersection point.

Figure 11.8b shows the interaction of a shock wave, generated somewhere upstream, with a boundary layer. At a solid surface the boundary condition is one of constant flow direction rather than constant pressure, so that the incoming shock, which deflects the flow downward, is followed by an outgoing shock – not an expansion – which deflects the external flow upward to something near its original direction. As in the case of the jet mixing layer, the shock cannot penetrate into the subsonic part of the flow, near the wall, so that a distributed pressure rise occurs upstream and downstream of the shock intersection position.

Whether the shock wave is an incident (usually oblique) shock or a shock wave generated at the surface – and therefore necessarily normal to the surface so that the flow remains nominally parallel to the surface – a large positive (“adverse”) pressure gradient is imposed on the boundary layer so that the flow is retarded, especially near the surface. If the shock is strong enough, the boundary layer may separate, as shown in Fig. 11.8a. The separated region is often fairly short because of the effects of upstream influence. As can be seen in Fig. 11.8c, the retardation of the flow at the front of the interaction region causes the streamlines to move away from the surface, generating compression waves in the supersonic part of the flow that then merge into an outgoing shock. The first and second outgoing shocks and the expansion fan from the point of intersection of the incoming shock merge further out in the flow into a shock wave of the right strength to cancel the incoming shock’s deflection of the flow. If the incident shock is strong enough, a nearly normal shock may extend outward from the shear layer to the intersection of the normal and reflected shocks, as in the shock intersection near the centerline of a jet (Fig. 11.9). Similar behavior can occur, less spectacularly, even if the flow does not separate, because the slow-moving fluid near the wall tends to simulate a constant-pressure boundary whether it is moving downstream or upstream.

Other forms of shock-wave shear-layer interaction include the flow over a backward-facing step, the prototype of many more complicated flows that reattach to a solid surface after an extended separation region (shock induced or otherwise). As seen in Fig. 11.10, an expansion occurs at the edge of the step, and since the pressure in the separated region behind the step is nearly constant, the external flow is also nearly straight, according to the usual rules of supersonic flow in which flow angle and pressure are simply connected. Thus, a well-behaved free-mixing layer develops, and unless the initial boundary-layer thickness is a large fraction of the step height, the mixing layer is nearly independent of the initial conditions. Fluid is entrained into the underside of the mixing layer, as shown by the streamlines in Fig. 11.10 and is supplied by the upstream deflection of fluid near the reattachment point – indeed without this entrainment the flow would not reattach. The pressure gradient near reattachment is large because the downstream-going flow has to be turned to follow the surface again, and the distributed pressure rise near the surface leads to the formation of a shock wave in the outer part of the flow, nominally canceling the expansion at the edge of the step. That is, the shock wave is caused by the shear layer rather than being imposed on it from outside.

## 11.7 Free Interaction and Upstream Influence

A striking feature of the interaction between shock waves and (especially laminar) boundary layers is that when the shock is of moderate strength, typically with pressure rises of 20 percent or more, the boundary layer is disturbed by the shock at considerable distances ahead of it. At first sight this phenomenon is surprising since the inviscid flow above the boundary layer is supersonic and cannot permit disturbances to travel upstream, moreover the boundary-layer equations for a given pressure distribution are parabolic, and so, unless separation occurs, disturbances can only travel downstream. It would seem that upstream disturbances are simulated only if an inviscid/viscous interaction (inviscid flow and boundary-layer equations and an intersection law, Section 9.3) or the full Navier–Stokes equations are used since these are elliptic and permit upstream disturbances. However, the expected distance upstream that disturbances within the shear layer would be propagated in this way is only one or two boundary-layer thicknesses and much smaller than the extent actually observed in laminar flow.

The explanation for this dramatic phenomenon was provided by Oswatitsch and Wieghardt [5]. They pointed out that the interaction between the boundary layer and the external supersonic inviscid stream is of such a character as to permit the “spontaneous” evolution of the flow at any position  $x = x_0$ , as follows. Suppose the pressure in the external stream at  $x_0$  increased by a small amount. Then the boundary layer for  $x < x_0$  would be under the influence of

an adverse pressure gradient and would be expected to thicken, leading to an increase in the displacement thickness and an increase in the equivalent blowing velocity  $v_w = (1/\rho_e) d(\rho_e u_e \delta^*)/dx$  which is the compressible version of Eq. (9.3.1). Once this happens, the external stream starts to turn away from the wall, and then Ackeret's formula [3]

$$\Delta p = \frac{u_e \rho_e v_w}{\sqrt{M_e^2 - 1}} \quad (11.7.1)$$

implies that the pressure also increases. Hence the boundary layer will continue to develop until something happens to change the mutual interaction. It turns out that if the development carries on far enough, separation occurs, and thereafter an increase in the boundary-layer thickness is associated with a decrease in the pressure gradient. Eventually the pressure reaches a constant value, the so-called plateau pressure, while the separated boundary layer continues to grow. Part of the reason for the decrease in the adverse pressure gradient in separated flows is that the reverse flow at the bottom of the boundary layer is moving very slowly and needs only a weak pressure gradient to sustain it.

In a similar way the assumption of a small pressure *fall* leads to a boundary-layer change that encourages a further fall in the pressure so that the process is amplified. Now, however, an acceptable ultimate form of the interaction is not possible, and the development continues until the assumptions underlying the division of the flow field into inviscid and boundary-layer flows is no longer tenable. These two ways in which the interaction can evolve are commonly referred to in the literature as *compressive free interaction* and *expansive free interactions*, respectively, the first being relevant to shock-wave interactions and concave corners, while the second is relevant to the flows just upstream of convex corners.

If the external flow was subsonic, this boundary-layer behavior would be impossible since perturbations in the boundary layer and the external stream would tend to act in opposition to each other. For example, a small pressure *increment* thickens the boundary layer and induces a positive normal velocity  $v_w$ , but positive values of  $v_w$  induce small pressure *decrements*.

The principal reason why the growth of free interactions in boundary layers is limited is that the pressure changes with  $x$  and hence must be compensated for by a geometrical or physical feature of the flow field. Otherwise, there will be an imbalance with the pressure at large distances from the body.

The scaling laws of the evolutionary part of the free interaction were given by Lighthill [6]. As might be expected, the length scale along the body over which it occurs is short, being formally  $O(\delta^* R^{1/8})$ , where  $\delta^*$  is the displacement thickness of the boundary layer and  $R$  is the Reynolds number equal to  $(u_{ex_0})/\nu_w$ , and amounts in practice to only a few boundary-layer thicknesses. The distinguishing feature of compressible free interactions that gives them special importance in practical calculations is that the final state of the evolution is self preserving. As

already explained, it consists of a wedge-shaped separation region over which the oncoming boundary layer and inviscid stream are deflected. This flow deflection leads to a pressure increment that for adiabatic walls is

$$\frac{1}{2} \frac{c C^{1/4} \lambda_0^{1/2} \rho_e u_e^2}{R^{1/4} (M_e^2 - 1)^{1/4}}. \quad (11.7.2)$$

where  $\lambda_0$  is Chapman's constant equal to  $(T_e \mu_e / T_w \mu_w)$  and  $c$  is a quantity that appears to take an almost constant value of about 1.6. Below this forward-moving fluid, there is a slowly recirculating region of "back-flow".

Since the occurrence of the free interaction is surprising at first sight, it is worthwhile describing at length the arguments that lead to Lighthill's scaling laws so that the reader may appreciate in detail how they arise.

The starting point for our analysis is a remarkable and simple result originally due to Prandtl, known as the *transposition theorem*. This states that if  $u(x, y), v(x, y), T(x, y)$  is any solution of the boundary-layer equations of steady flow, then so is  $U(x, Y), V(x, Y), \theta(x, Y)$ , where

$$Y = y + A(x), \quad U(x, Y) = u(x, y), \quad V = v - A'(x)u, \quad \theta = T \quad (11.7.3)$$

and  $A(x)$  is an arbitrary function of  $x$ . The proof is by direct substitution into the boundary-layer equations and is immediate. It is an exact theorem there being no restriction on  $A$ , and in particular we shall be able to allow  $A'(x) = O(R^{-1/4})$ , where  $R$  is the Reynolds number of the flow,  $u_e x_0 / \nu_w$ . Then the contribution to  $V$  from  $A'(x)u$  is much larger than that from  $v$ , which is only  $O(R^{-1/2}u)$ . Hence we may neglect  $v$  in Eq. (11.7.3).

For simplicity we consider a boundary layer on a flat plate under a uniform external stream. Let the free interaction be centered at a station  $x_0$  of the boundary layer, and let the distance over which it evolves be small compared with  $x_0$  but large compared with  $\delta^* = O(R^{-1/2}x_0)$ . Further let it be described by a displacement of the streamlines and characterized by the function  $A(x)$ , which we have to determine. To a first approximation, therefore, we are assuming that any induced pressure gradient does not modify the flow properties of the majority of the boundary layer in the interaction region. It follows from Eq. (11.7.3) that the normal component of the velocity just outside the boundary layer is given by

$$v_e(x) = v(x_0, \infty) - A'(x)u_e(x_0), \quad (11.7.4)$$

and, as pointed out earlier, we shall neglect  $v(x_0, \infty)$  in Eq. (11.7.4). Notice that  $x - x_0$  is assumed to be small so that in the *unperturbed* boundary layer the flow properties do not change to first order. The induced pressure is then given by

$$\Delta p = - \frac{u_e^2(x_0) \rho_e A'(x)}{(M_e^2 - 1)^{1/2}} \quad (11.7.5)$$

from Eq. (11.7.1).

Although this pressure rise is not significant over most of the boundary layer, it does become important near the plate because the fluid is moving slowly there. In addition to this induced pressure, the simple solution given by Eq. (11.7.3) must itself be modified near the plate because  $U \neq 0$  when  $y = 0$ . A velocity sub-boundary layer must be introduced near  $y = 0$ , which is driven by the pressure  $\Delta p$  and matches the solution given by Eq. (11.7.5), i.e., has the property

$$u = \lambda[y + A(x)], \quad (11.7.6)$$

where  $\lambda$  is the value of the undisturbed velocity gradient at  $y = 0$ , when  $y$  is small on the scale of the main boundary layer and large on the scale of the sub-boundary layer. A similar sub-boundary layer is needed in general to adjust the thermal properties of the fluid, but this does not affect the velocity sub-boundary layer.

The governing equations for the sub-boundary layer are essentially the same as those for the main boundary layer except that the density and kinematic viscosity may be assigned their wall values. They are given by

$$\frac{\partial u}{\partial x} + \frac{\partial v}{\partial y} = 0, \quad (11.7.7)$$

$$u \frac{\partial u}{\partial x} + v \frac{\partial u}{\partial y} = -\frac{1}{\rho_w} \frac{\partial p}{\partial x} + \nu_w \frac{\partial^2 u}{\partial y^2}, \quad (11.7.8)$$

where we note that the scale of  $y$  is now much smaller than in the main boundary layer. Indeed we shall see that the scale of  $y$  here is  $O(R^{-5/8})$ , whereas in the main boundary layer the scale of  $y$  is  $O(R^{-1/2})$ . The boundary conditions are

$$u = v = 0 \quad \text{at } y = 0, \quad (11.7.9a)$$

$$u \rightarrow \lambda y \quad \text{upstream of the disturbance,} \quad (11.7.9b)$$

$$u \rightarrow \lambda[y + A(x)] \quad \text{as } y \rightarrow \infty \quad (11.7.9c)$$

as the sub-boundary layer merges with the main boundary layer. Here  $\rho_w$  and  $\nu_w$  are the undisturbed density and kinematic viscosity of the fluid at the plate. The boundary condition given by Eq. (11.7.9b) reflects the fact that the interaction is spontaneous; i.e., there is no external agency forcing it in the neighborhood of  $x = x_0$ . Finally Eq. (11.7.9c) is necessary since  $u$  takes this form near the base of the main boundary layer. Recall that  $\lambda = O(R^{1/2})$  and  $\nu_w = O(R^{-1})$ , and bear in mind that we shall have to assume  $y$  and  $A(x)$  are of the same size in the sub-boundary layer – otherwise a contradiction is obtained.

The set of equations given by Eqs. (11.7.7) and (11.7.8) is sufficient to determine  $A$  as a function of  $x$ , although it is clear that a considerable numerical effort is required. It is straightforward to determine the scaling laws of the free interaction, however. We write, in the sub-boundary layer,

$$\begin{aligned}
y &= \lambda^{-5/4} \alpha z, \quad x = x_0 + \frac{\lambda^{-3/4} \alpha^3 X}{\nu_w \lambda^2}, \\
u &= \lambda^{-1/4} \alpha \bar{u}(X, z), \quad v = \lambda^{-3/4} \alpha^{-1} \bar{v}(X, z) (\nu_w \lambda^2), \\
A(x) &= \lambda^{-5/4} \alpha \bar{A}(X), \quad p = p_e(x_0) + \frac{\lambda^{-1/2} \rho_e u_e^2 \alpha^{-2} P(X) (\nu_w \lambda^2)}{(M_e^2 - 1)^{1/2}} \quad (11.7.10)
\end{aligned}$$

where

$$\alpha = \left( \frac{\rho_e u_e^2 \nu_w \lambda^2}{\rho_w (M_e^2 - 1)^{1/2}} \right)^{1/4}, \quad (11.7.11)$$

and note that since  $\lambda^2 \nu_w$  is independent of the Reynolds number, so is  $\alpha$ . The governing equations to determine  $A(x)$  now reduce to

$$\frac{\partial \bar{u}}{\partial X} + \frac{\partial \bar{v}}{\partial z} = 0, \quad (11.7.12)$$

$$\bar{u} \frac{\partial \bar{u}}{\partial X} + \bar{v} \frac{\partial \bar{u}}{\partial z} = \frac{d^2 \bar{A}}{dX^2} + \frac{\partial^2 \bar{u}}{\partial z^2} \quad (11.7.13)$$

with boundary conditions

$$\bar{u} = \bar{v} = 0 \quad \text{at } z = 0, \quad (11.7.14a)$$

$$\bar{u} \rightarrow z \quad \text{as } X \rightarrow -\infty, \quad (11.7.14b)$$

$$\bar{u} \rightarrow z + A(x) \quad \text{as } z \rightarrow \infty. \quad (11.7.14c)$$

It now follows, from the fact that  $\lambda = O(R^{1/2})$ , that the pressure rise in the compressible free interaction is  $O(R^{-1/4})$ , as indicated in Eq. (11.7.2), and that the longitudinal extent of the interaction is  $O(R^{-3/8}) = O(R^{1/8} \delta^*)$ . Further discussion of the scaling laws depends on the nature of the fluid, but if, for example, the fluid satisfies the Chapman–Rubesin relation,

$$\lambda = 0.332 \frac{\rho_w u_e}{\rho_e x_0} R^{1/2} C^{-1/2},$$

then Eq. (11.7.2) follows at once.

We now demonstrate that a solution to a linearized form of Eq. (11.7.13) can be found when  $A$  is small and  $X$  is large and negative. Assume that

$$\begin{aligned}
\bar{A} &= a_1 e^{\kappa X}, \quad \bar{u} = z + a_1 e^{\kappa X} f'(z), \\
v &= -a_1 \kappa e^{\kappa X} f(z), \quad (11.7.15)
\end{aligned}$$

where  $\kappa$  is a positive constant to be found and  $e^{2\kappa X}$  is neglected. The constant  $a_1$  is chosen to be equal to  $-1$  for a compressive free interaction and  $+1$  for an expansive free interaction. Then from Eq. (11.7.15) we have at once

$$\kappa z f' - \kappa f = \kappa^2 + f'' \quad (11.7.16)$$

with

$$f'(0) = f(0) = 0, \quad f'(\infty) = 1. \quad (11.7.17)$$

The solution of the differential equation is

$$f(z) = \frac{-\kappa^{5/3} \text{Ai}(z\kappa^{1/3})}{\text{Ai}'(0)}, \quad (11.7.18)$$

where  $\text{Ai}(t)$  is Airy's function, satisfying  $w'' - tw = 0$  and tending to zero as  $t \rightarrow \infty$ . The boundary conditions (11.7.17) are also satisfied if

$$-\kappa^{4/3} \int_0^\infty \frac{\text{Ai}(t)dt}{\text{Ai}'(0)} = 1, \quad \text{that is, } \kappa = 0.8272. \quad (11.7.19)$$

This solution, due to Lighthill, shows that the boundary layer can spontaneously change from the conventional kind to one in which interaction effects are important. For expansive interactions the pressure is decreasing, and for compressive interactions the pressure is increasing. In both cases the change in the fluid velocity is small, but the change in the skin friction is important, since it is represented by  $\partial u / \partial z$ . Indeed in compressive flows, the skin friction changes sign, and thereafter the boundary layer separates from the plate as explained earlier. In expansive flows the skin friction increases without limit, and eventually the velocity changes do become significant. The solution given by Eq. (11.7.18) can be made the basis of a series expansion in powers of  $e^{\kappa X}$ , but it is more usual to solve the equations numerically.

This account of free interactions forms the basis of the triple-deck theory of interactive flows, which has been reviewed by Stewartson [7] and by Smith [8]. Further details are given in these references.

## 11.8 A Prescription for Computing Interactive Flows with Shocks

Formally the flow configuration described in the last section can persist indefinitely along the body and in fact is brought to an end by the feature provoking the interaction. If it is a shock wave, it strikes the boundary layer (see Fig. 11.11), which by now is behaving in essence like a mixing layer, is reflected as a rarefaction fan, and deflects the mixing layer back to the body. Now, however, the backflow in the boundary layer moves under quite a strong favorable pressure gradient and must also disappear at the reattachment point  $R_0$  (Fig. 11.11). Thus if we consider the behavior of this back-flow starting from  $R_0$  and following it to the separation point  $S$ , we see that to begin with it acquires a significant momentum between  $R_0$  and the shock interaction that it must lose by entrainment to the mixing layer between the shock interactions and  $S$ . Since entrainment is a rather weak method of losing momentum, it is not surprising

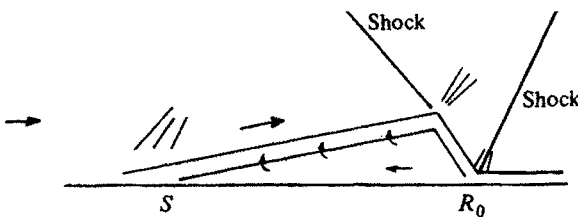


**Fig. 11.11.** Representative sketch (not to scale) of the interaction between a shock wave and laminar boundary layer.  $S$  denotes location of separation and  $R_0$  reattachment.

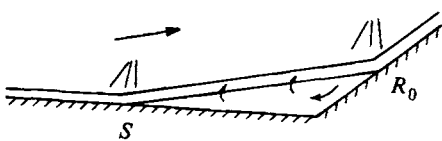


**Fig. 11.12.** Representative sketch (not to scale) of the interaction between a shock wave and the laminar boundary layer on a ramp.

that separation often occurs at considerable distances ahead of the shock. In practice this argument needs modification because a separated boundary layer is very prone to instability, and transition to turbulence occurs between  $S$  and the shock if it is at all strong. A turbulent boundary layer entrains fluid at a much greater rate than a laminar boundary layer and consequently the pressure plateau between separation and the shock interaction is reduced, although still of importance.

If the feature provoking the free interaction is a concave corner or ramp (see Fig. 11.12), the mixing layer continues unchanged in character past the corner, but now instead of it slightly diverging from the wall, the two are coming together rather quickly, and when they meet at reattachment, the mixing layer is turned sharply to move parallel to the wall, inducing a rapid rise in pressure. This compression fan merges into a shock outside the boundary layer and also serves to turn around some of the fluid in the mixing layer to initiate the boundary-layer back-flow. It was argued by Chapman et al. [9] that the length of the separated region can be determined by computing the velocity just upstream of reattachment on the streamline that bifurcates from the wall at separation. This velocity must be reduced to zero at reattachment to preserve continuity, and this is affected by the inviscid forces associated with the pressure rise there.

At first sight one might think that a boundary-layer approach to strong interaction problems is ruled out because a basic assumption of that theory, namely that the variation of the velocity across the boundary layer is much larger than that along it, is contradicted in the shock structure. Indeed the length scale in the shock is  $O(R^{-1})$  and much smaller than for the boundary layer, which is  $O(R^{-1/2})$ . Nevertheless there are a number of arguments that

suggest that a boundary-layer approach is worth considering. The obvious alternative, the Navier–Stokes equations, even if taken in their steady form, require large computers.

However, if we restrict attention to a boundary-layer approach, we must recognize that it has its limitations. For example, if the separated region is thick enough, then the basic assumptions must be called into question. At the present time it is not possible to put a frame around the external conditions outside which the theory gives unacceptable errors, but we may note that in the case of wholly laminar flow, calculations at  $M_\infty = 4$  are in quite good agreement with observation and solution of the Navier–Stokes equations [10–12].

The first problem to be faced in the computation is the determination of the point where the pressure begins to rise. We have already explained that this is fixed in some way by the strength of the incident shock, but it can only be found by trial and error. It will in fact be necessary to make a number of sweeps of the boundary layer in the downstream direction and to develop an iterative sequence that converges as discussed in the IBL method of Chapter 9. The interaction law by which the boundary layer influences the inviscid stream given in Eq. (9.3.1) for incompressible flows, may be written down as

$$v_b = \frac{1}{\rho_e} \frac{d}{dx} \int_0^\infty (\rho_e u_e - \rho u) dy, \quad (11.8.1)$$

for compressible flows. Here  $\rho$  and  $u$  are computed from the boundary-layer solution and  $v_w$  is the blowing velocity. The contribution to the inviscid pressure from  $v_w$  in simple cases is then given by Eq. (11.7.1), but in general it may be more appropriate to use Eq. (11.7.2) as a replacement for the boundary condition  $v = 0$  on the body in the general inviscid program. Such a procedure is particularly appropriate when the external flow is transonic, when Eq. (11.7.1) is not correct. A further complication should be mentioned at this stage. Should the flow downstream of the main shock be subsonic, which is always a possibility in a transonic situation and must be the case if the incident shock arises from a Mach reflection, then the computation of the external flow is even more complicated. Upstream influences, in addition to fixing the initial pressure rise of the interaction, make the iterative process more difficult to treat.

A first guess is made of the position of the critical pressure rise, and this is introduced into the flow field. Typically this is of relative order  $10^{-3}$  or  $10^{-4}$ . The evolution of the boundary layer is then self-sustaining, and separation soon occurs. If the oncoming boundary layer is turbulent, the turbulence model may need modification, and if it is laminar, a numerical scheme must be devised to carry the integration against the direction of motion of the fluid in the backflow. There are various ways in which this might be done, but among the more popular ones is the so-called FLARE approach discussed in Chap. 9.

One point should be born in mind when endeavoring to continue the integration through separation: whether the boundary layer is laminar or turbulent,

the solution of the equations must become singular if the external velocity is prescribed. In order to avoid its occurrence, and there is no reason to expect the final converged solution to have such a singularity, the external velocity must be related to the displacement thickness in some way as discussed in Chap. 9. Thus, in each sweep along the wall solving the boundary-layer equation, the external velocity must in some sense be regarded as unknown. There are many ways in which this can be done, and well-known examples include the use of Ackeret's formula, Eq. (11.7.1), to relate the external velocity and  $v_w$  for supersonic flow, Veldman's use of the Hilbert integral in subsonic flow, Eq. (9.1.4), and the relaxation formula suggested for displacement thickness by Le Balleur, Eq. (9.1.3).

## References

- [1] Illingworth, C. R., Steady flow in the laminar boundary layer of a gas. *Proc. Roy. Soc. A* **199**, 533, 1949.
- [2] Stewartson, K., Correlated compressible and incompressible boundary layers. *Proc. Roy. Soc. A* **200**, 84, 1949.
- [3] Liepmann, H. W. and Roshko, A., *Elements of Gas Dynamics*. Wiley, New York, 1957.
- [4] Seddon, S., The flow produced by interaction of a turbulent boundary layer with a normal shock wave of sufficient strength to cause separation. Aero Res. Council R&M 3502 (London), 1960.
- [5] Oswatitsch, K. and Wieghardt, K., Theoretical investigations on steady potential flows and boundary layers at high speed. Aero Res. Council Rep. 10356, London, 1946.
- [6] Lighthill, M. J., On boundary layers and upstream influence. II. Supersonic flows without separation. *Proc. Roy. Soc. A* **217**, 478, 1953.
- [7] Stewartson, K., Multistructured boundary layers on flat plates and related bodies. *Adv. Appl. Mech.* **14**, 145, 1974.
- [8] Smith, F. T., On the high Reynolds number theory of laminar flows. *IMA J. Appl. Math.* **28**, 207, 1982.
- [9] Chapman, D. R., Kuehn, D. M., and Larson H. K., Investigation of separated flows in supersonic and subsonic streams with emphasis on the effect of transition. NACA Rep. 1356, 1958.
- [10] Carter, J. E., Numerical solution of the Navier-Stokes equations for the supersonic laminar flow over a two-dimensional compression corner. NASA Rep. TR-R-385, 1972.
- [11] Werle, M. J. and Vatsa, V. N., A new method for supersonic boundary-layer separation. *AIAA J.* **12**, 1491, 1974.
- [12] Lewis, J. E., Kubota, T., and Lees, L., Experimental investigation of supersonic laminar two-dimensional boundary-layer separation in a compression corner with and without cooling. *AIAA J.* **6**, 7–14, 1968.
- [13] Rott, N. J., Compressible laminar boundary layer on a heat-insulated body. *J. Aero. Sci.* **20**, 67, 1953.
- [14] Stewartson, K., On supersonic laminar boundary layers near convex corners. *Proc. Roy. Soc. A* **319**, 289, 1970.

## Problems

- 11-1.** For an adiabatic flow the static temperature distribution across the boundary layer is given by Eq. (11.4.7).

(a) Show that for a nonadiabatic flow the static temperature  $t_s$  given by

$$\frac{T}{T_e} = S + \frac{\gamma - 1}{2} M_\infty^2 \left( S - \frac{\bar{u}^2}{\bar{u}_e^2} \right). \quad (\text{P11.1})$$

(b) Using the above expression and Eq. (11.4.4), show that an equivalent relation for Eq. (11.4.9) for a flow with heat transfer is

$$\delta_e^* = S_w \delta_i^* + \sigma(S_w \delta_i^* + \theta_i). \quad (\text{P11.2})$$

Here  $S_w \delta_i^*$  with  $\delta_i^*$  corresponding to the incompressible value of displacement thickness, is given by

$$S_w \delta_i^* = \int_0^\infty \left( S - \frac{\bar{u}}{\bar{u}_e} \right) d\bar{Y}. \quad (\text{P11.3})$$

(c) Show that for a flow with heat transfer, the relations given by Eq. (11.4.11) remain unchanged.

(d) Show that the heat transfer at the wall can be calculated from the following expression

$$\dot{q}_w = \frac{\rho_\infty u_\infty H_\infty}{\sqrt{R_x}} \left( \frac{\mu_w}{\mu_\infty} \right) S_w f_w'' \quad (\text{P11.4})$$

or from

$$\dot{q}_w = \frac{\rho_w u_\infty H_\infty}{\sqrt{R_x}} \left( \frac{\mu_w}{\mu_\infty} \right) S'_w \quad (\text{P11.5})$$

$$R_x = \frac{\rho_\infty u_\infty x}{\mu_\infty}.$$

**11-2.** Consider a cooled flat plate with  $S_w = 0.5$  at  $M_\infty = 3.0$  at 2300 m altitude. Assume standard atmosphere. Calculate the displacement thickness, shape factor, the local skin-friction coefficient, and the heat transfer rate per unit width at 3 m from the leading edge. Use Sutherland's viscosity law and take  $\gamma = 1.4$ .

**11-3.** Calculate the Chapman–Rubesin factor at the wall for laminar boundary layers in air of total temperature 300 K, at  $M_e = 1, 2, 5$  and 10. Take recovery factor as 0.9.

**11-4.** Show that the shape factor  $H = \delta^*/\theta$  is always greater than unity in constant density flows but may be less than unity in boundary layers on highly-cooled walls, even at low speeds.

**11-5.** Show that in the similar flows for a model fluid on either a heated or a cooled wall,  $S$  takes extreme values at the wall and at infinity.

*Note:* If  $m < 0$ , the solutions of Eqs. (11.3.5) and (11.3.6) are not unique unless an extra condition is applied, namely that  $1 - \phi'$  is exponentially small when  $\eta$  is large. Without this condition velocity overshoot is possible whether the wall is heated or not.

**11-6.** For Prandtl numbers  $\text{Pr}$  not too different from unity, a reasonably good approximation to the temperature in a boundary layer near an adiabatic wall is

$$T = T_e \left[ 1 + \frac{\gamma - 1}{2} \text{Pr}^{1/2} M_e^2 \left( 1 - \frac{u^2}{u_e^2} \right) \right]$$

Show that the Illingworth-Stewartson transformation may be generalized to

$$dX = \left( \frac{a_e}{a_\infty} \right)^{\text{Pr}^{1/2}} \frac{p_e}{p_\infty} dx; \quad dY = \left( \frac{a_e}{a_\infty} \right)^{\text{Pr}^{1/2}} \frac{\rho_e}{\rho_\infty} dy$$

for such flows, and determine the equivalent external velocity of the incompressible flow. For details see Rott [13].

**11-7.** A model fluid flows past an adiabatic flat plate at Mach number  $M_\infty$ . If the momentum thickness of the boundary layer at distance  $x$  from the leading edge is  $\theta$ , show that

$$\theta_e = \theta_i + \frac{\gamma - 1}{2} M_\infty^2 \theta_{1i}$$

where  $\theta_i$  is the momentum thickness and

$$\theta_{1i} = \int_0^\infty \frac{\bar{u}}{\bar{u}_e} \left( 1 - \frac{\bar{u}^2}{\bar{u}_e^2} \right) dY$$

for the equivalent incompressible flow. Obtain an approximation to  $\theta_e$ , in the following way. Write down the momentum integral for the equivalent incompressible flow and, assuming that

$$\bar{u} = \bar{u}_e \sin \left( \frac{\pi Y}{2\delta(x)} \right) \quad Y < \bar{\delta}$$

$$= \bar{u}_e \quad Y > \bar{\delta}$$

show that

$$\delta^2 = \frac{2x\nu_\infty}{(4 - \pi)u_e}$$

Hence deduce that

$$\theta_c = \frac{2}{\pi} \left( \frac{2x\nu_\infty}{u_e} \right)^{1/2} \left[ 0.463 + \frac{\gamma - 1}{6} M_\infty^2 \right]$$

**11-8.** Obtain the results corresponding to Problem 11.7 when the temperature of the wall is maintained at a constant value  $T_w$ . Hint: Make use of Eq. (11.4.4).

**11-9.** Instead of Eq. (11.7.10), assume that

$$\begin{aligned}y &= \beta_1 z & x &= x_0 + \beta_2 X \\u &= \beta_3 \bar{u} & v &= \beta_4 \bar{v} \\A &= \beta_5 \bar{A} & p &= p_e(x_0) + \beta_6 P\end{aligned}$$

where  $\beta_1 \dots \beta_6$  are constants. Show that the only choice of  $\beta$ 's which reduces Eqs. (11.7.5)–(11.7.9) to (11.7.12)–(11.7.14) is given by Eqs. (11.7.10) and (11.7.11).

**11-10.** In Eqs. (11.7.12)–(11.7.14), assume that

$$\bar{u} = \frac{1}{X_s - X} F(\eta), \quad \eta = \frac{z}{X_s - X}$$

where  $X_s$  is a constant,  $X < X_s$  and  $F$  is a function of  $\eta$  only, to be found. Obtain the corresponding form for  $\bar{v}$  by the use of Eq. (11.7.12). Verify that these forms satisfy Eqs. (11.7.13) and (11.7.14) in the limit  $X \rightarrow X_s$  provided

$$F = 3 \tanh^2(\eta + \beta) - 2, \quad \tanh^2 \beta = \frac{2}{3}$$

and write down the corresponding form of the pressure. For details, see Stewartson [14].

# 12

# Two-Dimensional Compressible Turbulent Flows

## 12.1 Introduction

As in Chapter 6, we begin with the statement that the main difference between laminar flows and turbulent flows is that the effective diffusivities in turbulent flow are unknown. In Chapter 6 the temperature differences were small enough not to affect the mean velocity field, and it was assumed without explicit comment that the *fluctuating* velocity field, which controls the turbulent transport of momentum, heat, or mass, was also unaffected.

In most practical cases, the effect of density fluctuations on the fluctuating velocity field is quite small, except in buoyant flow, because density fluctuations are usually only a small fraction of the mean density. The effect of *mean*-density gradients on turbulence, however, may be significant in some cases. For many purposes the turbulence models developed for incompressible flows may be adequate for variable-density flows of the same general type, provided that the local mean density is inserted in differential equations or algebraic formulas relating turbulent stresses and enthalpy-flux rates to the mean velocity and temperature fields. Of course, the local mean density must also be inserted in the time-average momentum and energy equations just as in the laminar flows discussed in the previous chapter.

Like the corresponding material in Chapter 11, the preceding part of this introduction, and most of the analysis below, applies both to low-speed flows (in which large density changes are introduced by high heat-transfer rates or by the mixing of dissimilar fluids) and to high-speed flows (in which large temperature changes result from viscous dissipation of kinetic energy into thermal energy or from pressure changes that are large fractions of the absolute pressure). Of course, the configurations, and the engineering hardware, are likely to be rather different in low-speed and high-speed flows, and comparatively little work has been done on low-speed compressible flows; this means that since current

turbulence models are empirical and are all based on data for limited ranges of flows, the formulas or differential equations developed for turbulent transfer rates may have slightly different coefficients in the two cases.

In Section 12.2 we extend the discussion of turbulence models for incompressible flows (Section 6.3) to compressible flows. For simplicity the discussion is carried through for gas flows. Liquid flows with large fractional variations in density are rare, so that coupling arises mainly via the dependence of viscosity on temperature, which is a fairly minor complication in turbulent flow.

In Section 12.3 we discuss inner-layer similarity ideas in compressible flows, corresponding to the discussion in subsection 6.2.1.

Section 12.4 is a brief review of attempts to find a mathematical transformation of coordinates and variables to convert a compressible turbulent flow into an observable (or calculable) low-speed flow. These transformations do not have the rigorous justification of the laminar-flow transformations discussed in Chapter 11; they are just as arbitrary as turbulence models and rather less easy to check against experimental data. The exception is that the transformation used in the inner-layer analysis for compressible turbulent flows is useful for *correlating data* for velocity profiles and skin friction coefficients.

In Section 12.5 we discuss the calculation of compressible flows in zero pressure gradient flows. In general, it is best to obtain solutions of compressible turbulent boundary layers, as in incompressible flows, by differential methods. For a given two-dimensional or axisymmetric body, which implies that the external velocity distribution can be determined and that the surface boundary condition is known, the momentum- and heat-transfer properties of the flow can be obtained by solution of the momentum and energy equations with accuracy sufficient for most engineering purposes.

In Section 12.6 we discuss the numerical method which is similar to the one discussed in Section 4.5. It again uses the eddy-viscosity formulation of Cebeci and Smith. A general computer program based on the Box scheme and CS model is given in Appendix B (Program 11) together with results for a wide range of compressible turbulent flows.

Finally Section 12.7 extends the discussion on shock-wave / shear layer interaction for laminar flows in Section 11.5 to turbulent flows.

## 12.2 Turbulence Models

The use of the Reynolds averaging procedure discussed in Section 10.3 introduces additional unknowns to the equations. Further approximations are required to represent the effects of turbulence on the mean flow, i.e. the Reynolds stresses and the turbulent heat fluxes; these approximations should reduce the number of unknowns to equal the number of equations. As in incompressible flow, this can be done by using simple turbulence models based on algebraic

mixing length and eddy viscosity models or advanced turbulence models based on transport equations.

The simplest turbulence models are based on the idea that the turbulence time scale is of the same order as the time scale of the mean flow. For two-dimensional thin shear layers the turbulence time scale is obtained from a velocity scale the order of magnitude of which is given by the Reynolds stress  $-\overline{u'v'}$ ; the order of the mean flow time scale is the inverse of the shear  $\frac{\partial u}{\partial y}$ . This leads to the definition of an eddy viscosity  $\nu_t (\equiv \mu_t/\rho)$  given by Eq. (6.3.1), that is

$$-\rho\overline{u'v'} = \mu_t \frac{\partial u}{\partial y} \quad (6.3.1)$$

Analogous quantities can be defined for turbulent heat-transfer rates. Just as  $-\rho\overline{u'v'}$  is the most important of the six independent Reynolds stresses in a thin shear layer, being the rate of turbulent transfer of  $x$ -component momentum in the  $y$ -direction (normal to the surface in the case of a boundary-layer),  $\rho c_p \overline{v'T'}$  is the most important of the three turbulent heat-flux rates, being the rate of turbulent transport of enthalpy in the  $y$ -direction. This does not mean that the other Reynolds stresses or turbulent heat fluxes are negligible. In fact, the important quantities are the variations of  $-\rho\overline{u'v'}$  and  $\rho c_p \overline{v'T'}$  in the  $y$ -direction and in this direction the length scale is very short. By analogy with the eddy viscosity, we define the eddy diffusivity of heat and the turbulent heat flux is expressed as

$$\rho c_p \overline{v'T'} = -k_t \frac{\partial T}{\partial y} \quad (12.2.1)$$

Note that a minus sign still appears; in heat transfer, as in momentum transfer, we expect transport *down* the gradient of the quantity in question. In other words, the effect of the turbulent heat transfer is expected to smooth the variations of mean temperature in the flow, just as the effect of the Reynolds stress is expected to smooth the variations of mean velocity  $u$  in the flow.

Very often an analogy between the transport of momentum and the transport of heat is advocated to introduce a *turbulent Prandtl number*  $\text{Pr}_t \equiv \mu_t c_p / k_t$  defined by

$$\text{Pr}_t = \frac{\mu_t c_p}{k_t} = \frac{\overline{u'v'}/\frac{\partial u}{\partial y}}{\overline{v'T'}/\frac{\partial T}{\partial y}} \quad (12.2.2)$$

and is assumed to be a constant. This assumption is very attractive from a computational point of view and leads to good results if the value of the Prandtl number is adapted to the flow considered. In boundary-layers and wall flows, a value around 0.9 is adequate although it can be affected by the pressure gradient. For a jet, the value of the Prandtl number is around 0.7 and for a low-speed mixing-layer the value would be 0.5. The value of the Prandtl number is

flow dependent. In addition, the Prandtl number is not really constant within a given shear layer. In boundary-layers, models have been proposed to reproduce the variations observed experimentally [1].

For standard boundary-layers, the assumption of a turbulent Prandtl number is convenient and the comparisons with experimental data of the wall heat-flux for example justify such an approach. For more complex flows, this assumption is not sufficient and more elaborated models are needed. This implies to consider the transport equations for the turbulent heat-fluxes and to model them.

### 12.2.1 Zero-Equation Models

The extension of the mixing length approach to compressible flows used in [2] is

$$-\rho \overline{u'v'} = \rho F_d^2 \ell^2 \left( \frac{\partial u}{\partial y} \right)^2 \quad (12.2.3)$$

$$\rho c_p \overline{v'T'} = -\frac{\rho c_p}{Pr_t} F_d^2 \ell^2 \frac{\partial u}{\partial y} \frac{\partial T}{\partial y} \quad (12.2.4)$$

The mixing-length is expressed by the same formula as in incompressible flow

$$\frac{\ell}{\delta} = 0.085 \tanh \left( \frac{\kappa}{0.085} \frac{y}{\delta} \right), \quad \kappa = 0.41 \quad (12.2.5)$$

and the damping function is

$$F_d = 1 - \exp \left[ -\frac{1}{26\mu} (\tau \rho)^{1/2} \right] \quad (12.2.6)$$

where  $\tau$  is given by Eq. (10.5.2b), that is

$$\tau = \mu \frac{\partial u}{\partial y} - \rho \overline{u'v'} \quad (10.5.2b)$$

The turbulent Prandtl number is taken as  $Pr_t = 0.89$ .

The CS model for compressible flows uses the same expression for inner eddy viscosity formula, Eq. (6.3.3),

$$(\mu_t)_i = \rho \ell^2 \left| \frac{\partial u}{\partial y} \right| \gamma_{tr}, \quad 0 \leq y \leq y_c \quad (6.3.3)$$

and outer eddy viscosity formula, Eq. (6.3.5) used for incompressible flows

$$(\mu_t)_o = \alpha \left| \int_0^\delta (u_e - u) dy \right| \gamma_{tr} \gamma, \quad y_c \leq y \leq \delta \quad (6.3.5)$$

The mixing-length in Eq. (6.3.3) is now given by

$$\ell = \kappa y \left[ 1 - \exp \left( -\frac{y}{A} \right) \right], \quad \kappa = 0.4 \quad (12.2.7)$$

and the damping-length constant  $A$  is represented by

$$A = 26 \frac{\nu}{N} u_{\tau}^{-1} \left( \frac{\rho}{\rho_w} \right)^{1/2}, \quad u_{\tau} = \left( \frac{\tau_w}{\rho_w} \right)^{1/2}$$

$$p^+ = \frac{\nu_e u_e}{u_{\tau}^3} \frac{du_e}{dx}, \quad v_w^+ = \frac{v_w}{u_{\tau}} \quad (12.2.8a)$$

$$N = \left\{ \frac{\mu}{\mu_e} \left( \frac{\rho_e}{\rho_w} \right)^2 \left( \frac{p^+}{v_w^+} \right) \left[ 1 - \exp \left( 11.8 \frac{\mu_w}{\mu} v_w^+ \right) \right] + \exp \left( 11.8 \frac{\mu_w}{\mu} v_w^+ \right) \right\}^{1/2} \quad (12.2.8b)$$

For flows with no mass transfer through the surface,  $N$  is

$$N = \left[ 1 - 11.8 \left( \frac{\mu_w}{\mu_e} \right) \left( \frac{\rho_e}{\rho_w} \right)^2 p^+ \right]^{1/2} \quad (12.2.8c)$$

In Eq. (6.3.3),  $\gamma_{tr}$  is an intermittency factor which represents the region of transition from laminar to turbulent flow. The expression (6.2.4) obtained for incompressible flows is also useful for compressible adiabatic flows with Mach numbers less than 5; it is not applicable to nonadiabatic compressible flows since appreciable differences between the wall and freestream temperatures can strongly influence the length of the transition region.

In Eq. (6.3.5)  $\gamma$  again represents the intermittency and is given by the same formula as in incompressible flows, Eq. (6.3.6).

In the CS model, the turbulent Prandtl number is expressed as

$$\text{Pr}_t = \frac{\kappa}{\kappa_h} \frac{1 - \exp(-y/A)}{1 - \exp(-y/B)} \quad (12.2.9)$$

where  $\kappa_h = 0.44$ . The parameter  $B$  is a function of the Prandtl number  $\text{Pr}$  given by a series

$$B = \frac{B^+ \nu}{u_{\tau}}, \quad B^+ = \frac{1}{\text{Pr}^{1/2}} \sum_{i=1}^5 C_i (\log_{10} \text{Pr})^{i-1} \quad (12.2.10)$$

where  $C_1 = 34.96$ ,  $C_2 = 28.79$ ,  $C_3 = 33.95$ ,  $C_4 = 6.3$  and  $C_5 = -1.186$ .

## 12.2.2 Turbulence Models Based on Transport Equations

As in incompressible flows, there are several turbulence models based on transport equations extended from incompressible to compressible flows by taking into account the variation of density  $\rho$  across the shear layers. These models,

as in subsection 6.3.2, include one-equation, two-equation and Reynolds stress models. The SA model given by Eqs. (6.3.14) to (6.3.17) can be used for compressible flows by taking into account the variation of  $\rho$  in their model. The  $k-\varepsilon$  model requires some changes as discussed below. The extension of the Reynolds stress models to compressible flows is not discussed here since they are less popular than the one- and two-equation models.

The standard extension to compressible flow of the  $k-\varepsilon$  model given in section 6.3.2 for an incompressible flow is

$$\rho u \frac{\partial k}{\partial x} + \bar{\rho} v \frac{\partial k}{\partial y} = -\bar{\rho} u' v' \frac{\partial u}{\partial y} - \rho \varepsilon + \frac{\partial}{\partial y} \left[ \frac{\mu_t}{\sigma_k} \frac{\partial k}{\partial y} \right] \quad (12.2.11a)$$

$$\rho u \frac{\partial \varepsilon}{\partial x} + \bar{\rho} v \frac{\partial \varepsilon}{\partial y} = \left( -c_{\varepsilon_1} \bar{\rho} u' v' \frac{\partial u}{\partial y} - c_{\varepsilon_2} \rho \varepsilon \right) \frac{\varepsilon}{k} + \frac{\partial}{\partial y} \left[ \frac{\mu_t}{\sigma_\varepsilon} \frac{\partial \varepsilon}{\partial y} \right] \quad (12.2.11b)$$

where  $\mu_t$  is given by Eq. (6.3.14)

$$\mu_t = \rho c_\mu \frac{k^2}{\varepsilon} \quad (6.3.14)$$

These equations apply only to free shear flows. For wall boundary-layer flows, as in incompressible flows, they require modifications to account for the presence of the wall. In the inner region, the model is corrected by near wall damping functions. When a local Reynolds number is used to express these damping functions, the same form as in incompressible flow is kept. In the extension of the Launder-Sharma model (subsection 6.3.2), Eqs. (6.3.23) and (6.3.24) are written as

$$\begin{aligned} \rho u \frac{\partial k}{\partial x} + \bar{\rho} v \frac{\partial k}{\partial y} &= -\bar{\rho} u' v' \frac{\partial u}{\partial y} - \rho \varepsilon - 2\mu \left( \frac{\partial \sqrt{k}}{\partial y} \right)^2 \\ &\quad + \frac{\partial}{\partial y} \left[ \mu \frac{\partial k}{\partial y} + \frac{\mu_t}{\sigma_k} \frac{\partial k}{\partial y} \right] \end{aligned} \quad (12.2.12a)$$

$$\begin{aligned} \rho u \frac{\partial \varepsilon}{\partial x} + \bar{\rho} v \frac{\partial \varepsilon}{\partial y} &= \left( -c_{\varepsilon_1} \bar{\rho} u' v' \frac{\partial u}{\partial y} - c_{\varepsilon_2} f_2 \rho \varepsilon \right) \frac{\varepsilon}{k} \\ &\quad + 2 \frac{\mu \mu_t}{\rho} \left( \frac{\partial^2 u}{\partial y^2} \right)^2 + \frac{\partial}{\partial y} \left[ \mu \frac{\partial \varepsilon}{\partial y} + \frac{\mu_t}{\sigma_\varepsilon} \frac{\partial \varepsilon}{\partial y} \right] \end{aligned} \quad (12.2.12b)$$

with the damping functions given by Eq. (6.3.25).

Often, the damping functions are expressed as functions of a wall variable  $y^+$ . According to the study conducted by Aupoix and Viala [3], the appropriate definition of  $y^+$  is

$$y^+ = \frac{y \sqrt{\tau_w \rho}}{\mu} \quad (12.2.13)$$

The systematic study performed by Aupoix and Viala confirmed the analysis of van Driest [4] who proposed the same variable. It is interesting to note that the CS model also uses the same wall variable.

A desirable feature of turbulence models is that they should be able to retrieve the logarithmic law of the wall. For compressible flows, this law is [see Eq. (12.3.2b)]

$$u^{*+} = \frac{1}{\kappa} \ln \frac{y \sqrt{\tau_w \rho_w}}{\mu_w} + c \quad (12.2.14)$$

where  $\kappa$  and  $c$  have the same values as in incompressible flow and  $u^{*+}$  is the van Driest transformed velocity

$$u^{*+} = \sqrt{\frac{\rho_w}{\tau_w}} \int_0^u \sqrt{\frac{\rho}{\rho_w}} du \quad (12.2.15)$$

A straightforward extension of two-equation models, such as given above does not produce the law of the wall, Eq. (12.2.14). Modifications of different two-equation models have been proposed by Catris–Aupoix [5]. For the  $k$ - $\varepsilon$  model, the equations are (see Problem 12-1)

$$\rho u \frac{\partial k}{\partial x} + \rho v \frac{\partial k}{\partial y} = -\rho \bar{u}' v' \frac{\partial u}{\partial y} - \rho \varepsilon + \frac{\partial}{\partial y} \left[ \frac{\mu_t}{\rho \sigma_k} \frac{\partial \rho k}{\partial y} \right] \quad (12.2.16)$$

$$\begin{aligned} \rho u \frac{\partial \rho \varepsilon}{\partial x} + \rho v \frac{\partial \rho \varepsilon}{\partial y} &= \left( -c_{\varepsilon_1} \rho \bar{u}' v' \frac{\partial u}{\partial y} - c_{\varepsilon_2} \rho \varepsilon \right) \frac{\rho \varepsilon}{k} \\ &\quad + \frac{\partial}{\partial y} \left[ \frac{\mu_t}{\rho^{1/2} \sigma_\varepsilon} \frac{\partial \rho^{3/2} \varepsilon}{\partial y} \right] \end{aligned} \quad (12.2.17)$$

Near the wall, the same modifications as in the standard  $k$ - $\varepsilon$  model apply [6].

## 12.3 Inner-Layer Similarity Analysis for Velocity and Temperature Profiles

In compressible turbulent flows, the velocity and temperature profiles in the inner layer depend on all the quantities that affect the velocity or temperature profile in incompressible flows, and in addition the absolute temperature (at the wall, say) must be included since, by definition, the temperature differences in compressible flows are a significant fraction of the absolute temperature. Also, if the Mach number of the flow is not small compared with unity, the speed of sound,  $a$ , and the ratio of specific heats,  $\gamma$ , will appear; in a perfect gas  $a = \sqrt{\gamma R T} = \sqrt{(\gamma - 1)c_p T}$ , so that either  $a$  or  $T$  or both may be used as a variable. With these additions to the variables, according to the Rotta's analysis [6] which is an extension of that of Van Driest [4], the law of the wall for compressible turbulent flows may be written in the form

$$\frac{u}{u_e} = \frac{\sqrt{c_1}}{R} \sin \left( R \frac{u^*}{u_\tau} \right) - H \left[ 1 - \cos \left( R \frac{u^*}{u_\tau} \right) \right]. \quad (12.3.1)$$

Here with  $w$  denoting wall,  $c_1$  is a constant fairly close to the unity,  $u_\tau = \sqrt{\tau_w/\rho_w}$ , and

$$R = \frac{u_\tau}{a_w} \left[ \frac{(\gamma - 1)\Pr_t}{2} \right]^{1/2}, \quad H = \frac{\dot{q}_w}{\tau_w u_\tau} \equiv \frac{1}{(\gamma - 1)} \frac{\dot{q}_w}{\rho_w c_p u_\tau T_w} \left( \frac{a_w}{u_\tau} \right)^2, \quad (12.3.2a)$$

$$\frac{u^*}{u_\tau} = \frac{1}{\kappa} \ln \frac{u_\tau y}{\nu_w} + c. \quad (12.3.2b)$$

If  $\dot{q}_w = 0$  and  $u_\tau/a_w \rightarrow 0$ , then  $H = 0$ ,  $R \rightarrow 0$ , and

$$\frac{u}{u_\tau} = \sqrt{c_1} \frac{u^*}{u_\tau}. \quad (12.3.3)$$

It can be shown that if  $u_\tau/a_w$  is small, then  $c_1 = 1 - O(\dot{q}_w)$  and  $u = u^*$  for small  $\dot{q}_w$ ; thus the constant  $c$  in Eq. (12.3.2b) can be identified with the additive constant  $c$  in the logarithmic law for constant property wall layers, Eq. (8.2.3). In general  $c$ , like  $c_1$ , is a function of the friction Mach number  $M_\tau$  ( $\equiv \frac{u_\tau}{a_w}$ ) and of  $B_q$  defined

$$B_q = \frac{\dot{q}_w}{\rho_w c_p u_\tau T_w}. \quad (12.3.4)$$

Similarly the temperature profile is given by

$$T = c_1 T_w - \frac{(\Pr_t) \dot{q}_w u}{c_p \tau_w} - \frac{(\Pr_t) u^2}{2 c_p} \quad (12.3.5)$$

Simpler versions of Eqs (12.3.1) and (12.3.5) have been proposed by many authors. Van Driest [4], assuming  $c_1 = 1$  and  $\Pr_t = 1$ , presented the inverse of Eq. (12.3.1), giving  $u^*$  in terms of  $u$ . In one more general notation this is

$$\frac{u^*}{u_\tau} = \frac{1}{R} \left( \sin^{-1} \frac{R(u/u_\tau + H)}{(c_1 + R^2 H^2)^{1/2}} - \sin^{-1} \frac{RH}{(c_1 + R^2 H^2)^{1/2}} \right). \quad (12.3.6)$$

This formula is called the Van Driest transformation; it can be regarded as transforming the inner-layer part of the compressible boundary-layer profile  $u(y)$  to an equivalent incompressible flow  $u^*(y)$  that obeys the logarithmic formula, Eq. (12.3.2b). However, it is simpler to regard Eq. (12.3.1), with Eq. (12.3.2), as the direct prediction of inner-layer similarity theory for the incompressible boundary layer.

If there is no heat transfer through the surface,  $H$  is zero, the second term on the right of Eq. (12.3.1) disappears, and Eq. (12.3.6) reduces to

$$\frac{u^*}{u_\tau} = \frac{1}{R} \sin^{-1} \left( \frac{R}{\sqrt{c_1}} \frac{u}{u_\tau} \right), \quad (12.3.7)$$

which is easy to identify as the inverse of Eq. (12.3.5) without the second term on the right and of course reduces to  $u^* = u$  as  $R \rightarrow 0$  and  $c_1 \rightarrow 1$ .

If we replace  $H$  by the expressions given Eqs. (12.3.2) and (12.3.5), use the definition of Mach number,  $M_e = u_e/a_e$ , take  $c_1 = 1$  and  $\text{Pr}_t = 1$  following Van Driest [4], and note that  $\rho_w/\rho_e = T_e/T_w$ , then Eq. (12.3.6) can be written as

$$\frac{u^*}{u_\tau} = \frac{1}{A\sqrt{(c_f/2)(T_w/T_e)}} \left( \sin^{-1} \frac{A\sqrt{(c_f/2)(T_w/T_e)}(u/u_\tau) + B/2A}{\sqrt{1 + (B/2A)^2}} - \sin^{-1} \frac{B/2A}{\sqrt{1 + (B/2A)^2}} \right) \quad (12.3.8)$$

or as

$$u^* = \frac{u_e}{A} \left( \sin^{-1} \frac{2A^2(u/u_e) - B}{(B^2 + 4A^2)^{1/2}} + \sin^{-1} \frac{B}{(B^2 + 4A^2)^{1/2}} \right). \quad (12.3.9)$$

where

$$A^2 = \frac{\gamma - 1}{2} \frac{M_e^2}{T_w/T_e}, \quad B = \frac{1 + (\gamma - 1)/2M_e^2}{T_w/T_e} - 1. \quad (12.3.10)$$

Note that the above relations assume that the recovery factor  $r$  defined by

$$r = \frac{T_{aw} - T_e}{T_{oe} - T_e} \quad (12.3.11)$$

is 1. In the above equation,  $T_{aw}$  is the recovery temperature reached by an insulated (adiabatic) surface and  $T_{oe}$  is the told temperature. To account for the fact that  $r$  is less than unity (about 0.89), we rewrite Eqs. (12.3.10) as

$$A^2 = \frac{[(\gamma - 1)/2]M_e^2 r}{T_w/T_e}, \quad B = \frac{1 + [(\gamma - 1)/2]M_e^2 r}{T_w/T_e} - 1. \quad (12.3.12)$$

## 12.4 Transformations for Compressible Turbulent Flows

The Van Driest transformation, Eq. (12.3.6), applied to the fully turbulent part of the inner (constant-stress) layer of a compressible boundary layer produces the logarithmic profile, Eq. (12.3.2c). Applying the transformation to the outer layer of a constant-pressure compressible boundary layer, we obtain a profile that looks qualitatively like that of a constant-pressure constant-density boundary layer. In particular, the transformed profile  $u^*(y)$  can be described, more or less as accurately as an incompressible profile, by the wall-plus-wake formula given by Eqs. (6.2.17) and (6.2.18),

$$\frac{u^*}{u_\tau} = \frac{1}{\kappa} \ln \frac{u_\tau y}{\nu_w} + c + \frac{\Pi}{\kappa} \left( 1 - \cos \pi \frac{y}{\delta} \right). \quad (12.4.1)$$

However, this convenient data correlation is a consequence of the strong constraint on the wake profile, which has to have zero slope and zero intercept at

$y = 0$ , whereas the profile as a whole has zero slope at  $y = \delta$  [although the crude wake formula in Eq. (12.4.1) does not]; also, the “wake parameter”  $\Pi$  and the boundary-layer thickness  $\delta$  are constants that can be adjusted to optimize the fit of Eq. (12.4.1) to any real or transformed profile.

As was discussed in subsection 6.2.5,  $\Pi$  is constant in incompressible constant-pressure flows at high Reynolds number and equal to about 0.55. The value of  $\Pi$  that best fits a transformed profile is expected to be a function of the friction Mach number  $M_\tau$  ( $\equiv u_\tau/a_w$ ) and of the heat-transfer parameter  $B_q$  ( $\equiv \dot{q}_w/\rho_w c_p u_\tau T_w$ ). Evaluation of this function from experimental data is hampered by the low Reynolds number of most of the compressible-flow data and uncertainty about the definition of Reynolds number that should be used in correlating low-Reynolds-number effects on the velocity-defect profile. According to the studies conducted by Fernholz [7] the Reynolds number  $\rho_e u_e \theta / \mu_w$  gives excellent correlations of data over a wide range of Mach numbers and Reynolds numbers.

The Van Driest transformation can be regarded as a *solution* of the compressible-flow problem only if the coefficients  $c$ ,  $c_1$ , and  $\Pi$  were independent of Mach number and heat-transfer parameter. However, we can use the transformation, plus *compressible-flow* data for  $c_1$  and  $\Pi$ , to correlate the mean properties of constant-pressure compressible boundary layers. In pressure gradients, the transformed boundary-layer profile still fits Eq. (12.4.1) as does its true low-speed equivalent, but, as at low speeds, there is no simple formula to relate the shape parameter  $\Pi$  to the local pressure gradient. Moreover, the variation of  $u_\tau$ ,  $\Pi$ , and  $\delta$  with  $x$  will not generally correspond to any realizable low-speed boundary layer; that is, it may not be possible to choose a pressure distribution  $p(x)$  for a low-speed flow that will reproduce, at each  $x$ , the same velocity profile as in the compressible flow. The spirit of Van Driest’s transformation, although not its details, would be retained if compressible boundary layers were calculated using the mixing-length formula to predict the shear stress and the assumption of constant turbulent Prandtl number to predict the heat transfer. We consider such calculation methods in Section 12.6.

## 12.5 Two-Dimensional Boundary Layers with Zero Pressure Gradient

### 12.5.1 Skin-Friction Formulas on Smooth Surfaces

A number of empirical formulas for varying degrees of accuracy have been developed for calculating compressible turbulent boundary layers on flat plates. Those developed by Van Driest [4] and by Spalding and Chi [8] have higher accuracy than the rest (see Hopkins and Keener [9] and Cary and Bertram [10]) and cover a wide range of Mach number and ratio of wall temperature to

total temperature. These two methods have similar accuracy, although the approaches followed to obtain the formulas are somewhat different. Both methods define compressibility factors by the following relation between the compressible and incompressible values:

$$c_{f_i} = F_c c_f, \quad (12.5.1a)$$

$$R_{\theta_i} = F_{R_\theta} R_\theta, \quad (12.5.1b)$$

$$R_{x_i} = \int_0^{R_x} \frac{F_{R_\theta}}{F_c} dR_x = F_{R_x} R_x, \quad (12.5.1c)$$

Here the subscript  $i$  denotes the incompressible values, and the factors  $F_c$ ,  $F_{R_\theta}$ , and  $F_{R_x}$  ( $\equiv F_{R_\theta}/F_c$ ) defined by Eq. (12.5.1) are functions of Mach number, ratio of wall temperature to total temperature, and recovery factor. Spalding and Chi's method is based on the postulate that a unique relation exists between  $c_f F_c$  and  $F_{R_x} R_x$ . The quantity  $F_c$  is obtained by means of mixing-length theory and  $F_R$  is obtained semiempirically. According to Spalding and Chi,

$$F_c = \frac{T_{aw}/T_e - 1}{(\sin^{-1} \alpha + \sin^{-1} \beta)^2}, \quad F_{R_\theta} = \left( \frac{T_{aw}}{T_e} \right)^{0.772} \left( \frac{T_w}{T_e} \right)^{-1.474}. \quad (12.5.2)$$

where

$$\alpha = \frac{T_{aw}/T_e + T_w/T_e - 2}{[(T_{aw}/T_e + T_w/T_e)^2 - 4(T_w/T_e)]^{1/2}}, \quad (12.5.3a)$$

$$\beta = \frac{T_{aw}/T_e - T_w/T_e}{[(T_{aw}/T_e + T_w/T_e)^2 - 4(T_w/T_e)]^{1/2}},$$

$$\frac{T_{aw}}{T_e} = 1 + \frac{r}{2}(\gamma - 1)M_e^2. \quad (12.5.3b)$$

According to Van Driest's method, which is based entirely on the mixing-length theory,  $F_c$  is again given by the expression defined in Eqs. (12.5.2) and (12.5.3). However, the parameter  $F_{R_\theta}$  is now given by

$$F_{R_\theta} = \frac{\mu_e}{\mu_w}. \quad (12.5.4)$$

The development of Van Driest's formula for skin friction is analogous to the solution steps discussed for incompressible flows (see Section 6.4) except that the derivation is more tedious. The solution requires the expansion of the integral into a series by means of integration by parts and a simple expression is again obtained when higher-order terms are neglected. With this procedure and with the power-law temperature-viscosity relation

$$\mu \propto T^\omega,$$

which implies  $F_{R_\theta} = (T_e/T_w)^\omega$ , the following relation for  $c_f$  and  $R_x$  is obtained for compressible turbulent boundary layers with and without heat transfer, with  $x$  measured from the effective origin of the turbulent flow:

$$\frac{0.242(\sin^{-1}\alpha + \sin^{-1}\beta)}{A\sqrt{c_f(T_w/T_e)}} = 0.41 + \log R_x c_f - \left(\frac{1}{2} + \omega\right) \log \frac{T_w}{T_e}, \quad (12.5.5)$$

where  $A$  is defined by Eq. (12.3.10). This formula is based on Prandtl's mixing-length formula  $l = \kappa y$ . If the procedure leading to this equation is repeated with the mixing-length expression given by von Karman's similarity law

$$l = \kappa \left| \frac{\partial u / \partial y}{\partial^2 u / \partial y^2} \right|,$$

a formula similar to that given by Eq. (12.5.5) is obtained except that  $\frac{1}{2} + \omega$  in Eq. (12.5.5) is replaced by  $\omega$ . This formula is known as Van Driest II, in order to distinguish it from Eq. (12.5.5), which is known as Van Driest I, and may be written as

$$\frac{0.242(\sin^{-1}\alpha + \sin^{-1}\beta)}{A\sqrt{c_f(T_w/T_e)}} = 0.41 + \log R_x c_f - \omega \log \frac{T_w}{T_e}. \quad (12.5.6)$$

The predictions of Eq. (12.5.6) are in better agreement with experiment than those of Eq. (12.5.5) and Van Driest II should therefore be used in preference to Van Driest I.

Equations (12.5.5) and (12.5.6) constitute a compressible form of the von Karman equation discussed in Section 6.4 [see Eq. (6.4.5a)]. For an incompressible flow, they reduce to Eq. (6.4.5a). For an incompressible adiabatic flow,  $T_w/T_e \rightarrow 1$  and  $B = 0$ , so that with Eq. (12.5.3a), we can write Eq. (12.5.6) as

$$\frac{0.242 \sin^{-1} A}{A\sqrt{c_f}} = 0.41 + \log R_x c_f.$$

In addition,  $A$  is of the order of  $M_e$ , and since it is small,  $\sin^{-1} A = A$ . The resulting equation is then identical to Eq. (6.4.5a).

According to Van Driest II, the average skin-friction coefficient  $\bar{c}_f$  is obtained from the expression

$$\frac{0.242(\sin^{-1}\alpha + \sin^{-1}\beta)}{A\sqrt{\bar{c}_f(T_w/T_e)}} = \log R_x \bar{c}_f - \omega \log \frac{T_w}{T_e}. \quad (12.5.7)$$

Figures 12.1 and 12.2 show the variation of local and average skin-friction coefficients calculated from Eqs. (12.5.6) and (12.5.7), respectively, on an adiabatic flat plate for various Mach numbers. The recovery factor was assumed to be 0.88.

Figure 12.3 shows the effect of compressibility on the local and average skin-friction coefficients. Here, the skin-friction formulas were solved at a specified Reynolds number ( $R_x = 10^7$ ) as functions of Mach number for fixed values of  $T_w/T_e$ . In the results shown in Fig. 12.1, the local skin-friction values for

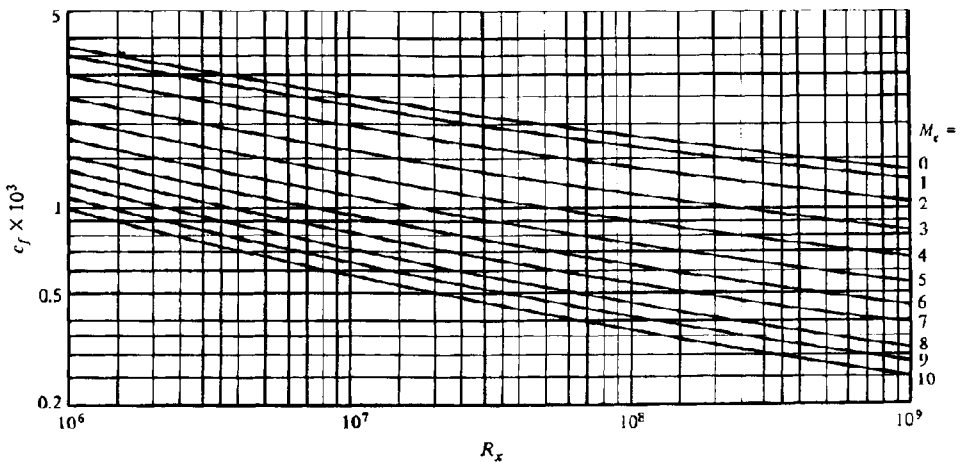


**Fig. 12.1.** Local skin-friction coefficient on a smooth adiabatic flat plate, according to Van Driest II.

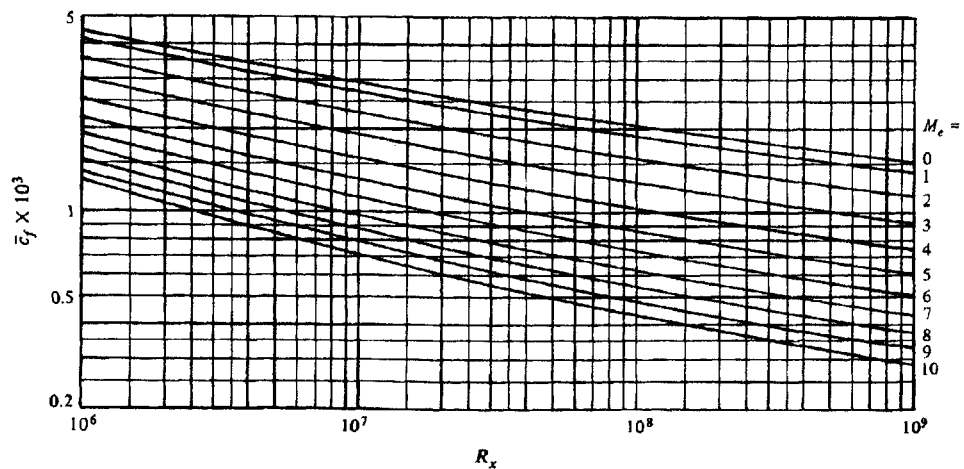


**Fig. 12.2.** Average skin-friction coefficient on a smooth adiabatic flat plate, according to Van Driest II.

incompressible flows with heat transfer were obtained from the limiting form of Eq. (12.5.6). We note that as  $M_e \rightarrow 0$  and when  $T_w/T_e = 1$ ,  $A \rightarrow 0$ ,  $\alpha \rightarrow -1$ , and  $\beta \rightarrow 1$ . It follows that the term

$$\frac{\sin^{-1} \alpha + \sin^{-1} \beta}{A}$$

is indeterminate. Using L'Hospital's rule and recalling that  $B = T_e/T_w - 1$ , we can write Eq. (12.5.6) for an incompressible turbulent flow with heat transfer, after some algebraic manipulation, as

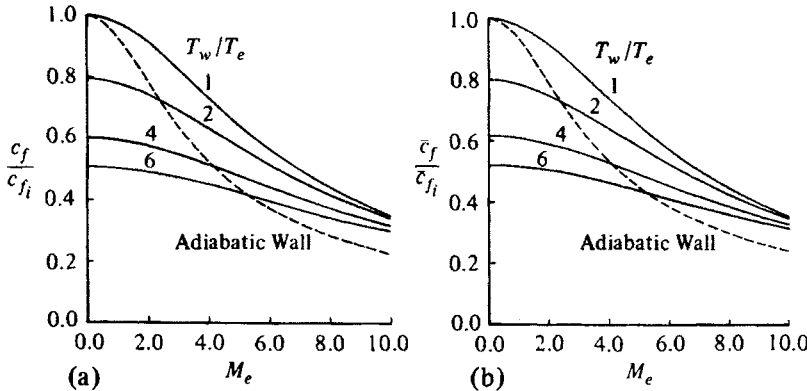


**Fig. 12.3.** Effect of compressibility on (a) local skin-friction coefficient and (b) average skin-friction coefficient on a smooth adiabatic flat plate, according to Van Driest II.

$$\frac{2}{\sqrt{T_w/T_e + 1}} \frac{0.242}{\sqrt{c_f}} = 0.41 + \log R_x c_f - \omega \log \frac{T_w}{T_e}. \quad (12.5.8)$$

The average skin-friction formula, Eq. (12.5.7), can also be written for an incompressible flow by a similar procedure, yielding

$$\frac{2}{\sqrt{T_w/T_e + 1}} \frac{0.242}{\sqrt{\bar{c}_f}} = \log R_x \bar{c}_f - \omega \log \frac{T_w}{T_e}. \quad (12.5.9)$$

### 12.5.2 Reynolds Analogy Factor

According to the studies conducted by Spalding and Chi [8] and Cary [11] it appears that for Mach numbers less than approximately 5 and near-adiabatic wall conditions, a Reynolds analogy factor of

$$\frac{St}{c_f/2} = 1.16 \quad (12.5.10)$$

adequately represents the available experimental data for zero-pressure gradient flows. However, for turbulent flow with significant wall cooling and for Mach numbers greater than 5 at any ratio of wall temperature to total temperature, the Reynolds analogy factor is ill-defined. Experimental data [10] indicate that for local Mach numbers greater than 6 and  $T_w/T_0$  less than approximately 0.3, the Reynolds analogy factor scatters around a value of 1.0. A sample of the results is presented in Fig. 12.4 for a Mach number of 11.3 and indicates that the Reynolds measured analogy factor is scattered from around 0.8 to 1.4 with no discernible trend for  $T_w/T_0$ .

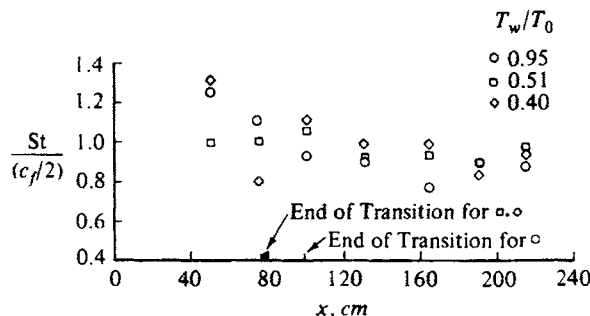


Fig. 12.4. Reynolds analogy factors at  $M_e = 11.3$ ,  $R_c/m = 54 \times 10^6$  [11].

### 12.5.3 Skin-Friction Formulas on Rough Surfaces

The skin-friction formulas for a smooth flat plate, Eqs. (12.5.7) and (12.5.8), can also be used to obtain formulas for sand-grain-roughened flat plates by assuming a relation between the compressible and incompressible values such as that given by Eq. (12.5.1a). According to the experiments of Goddard [12] on adiabatic fully rough flat plates,

$$F_e = \frac{T_{aw}}{T_e}, \quad (12.5.11)$$

and the experimental values of  $c_f$  verified the relation (12.5.11) for his chosen turbulent recovery factor,  $r = 0.86$ . It should be emphasized that this equation is for fully rough flow in which the flow on top of the roughness elements remains subsonic. It is consistent with the observation originally noted by Nikuradse for incompressible flow, namely, that the skin-friction drag for fully rough flow is the sum of the form drags of the individual roughnesses.

Fenter [13] also presented a theory for the effect of compressibility on the turbulent skin friction of rough plates with heat transfer. This gave results that agree with those of relation (12.5.11) only at Mach numbers close to unity and only for zero heat transfer. For  $T_w = T_e$ , the value of  $c_f$  given by this theory is 14 percent less than that given by Goddard's relation at  $M_e = 2.0$  and 45 percent less at  $M_e = 4.0$ . Fenter presented experimental data for  $M_e = 1.0$  and 2.0 that agreed well with this theory for the case of zero heat transfer. The difference in the experimental values of  $c_f$  of the two reports is probably within the accuracy to which the roughness heights were measured. The theory of Fenter is based on assumptions whose validity is questionable at high Mach numbers, and these assumptions may account for the difference in  $c_f$  predicted by Fenter and by Goddard for the case of  $T_w = T_e$ .

Figures 12.5 and 12.6 show the average skin-friction distribution for a sand-roughened adiabatic plate, and Figs. 12.7 and 12.8 show the results for a sand-roughened plate with a wall temperature equal to the freestream temperature,

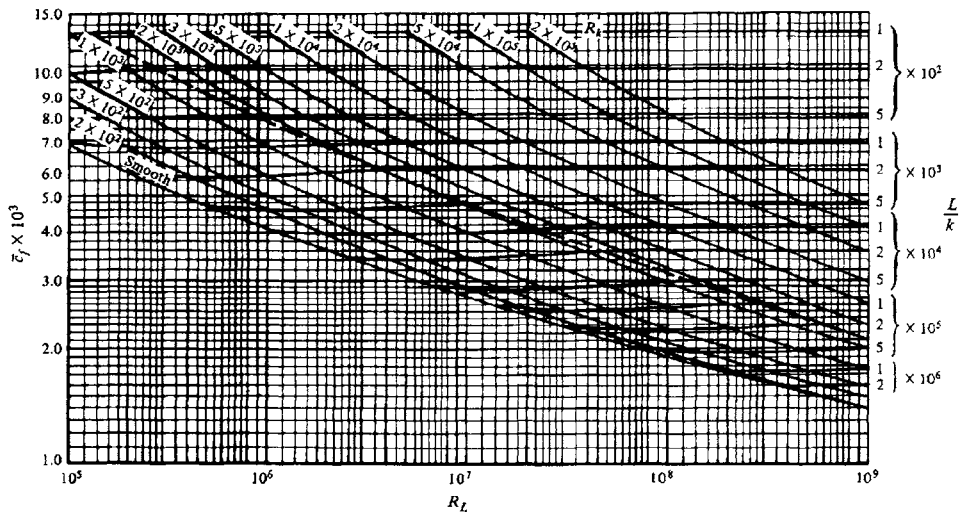


**Fig. 12.5.** Average skin-friction coefficient for a sand-roughened adiabatic flat plate at  $M_e = 1$ .

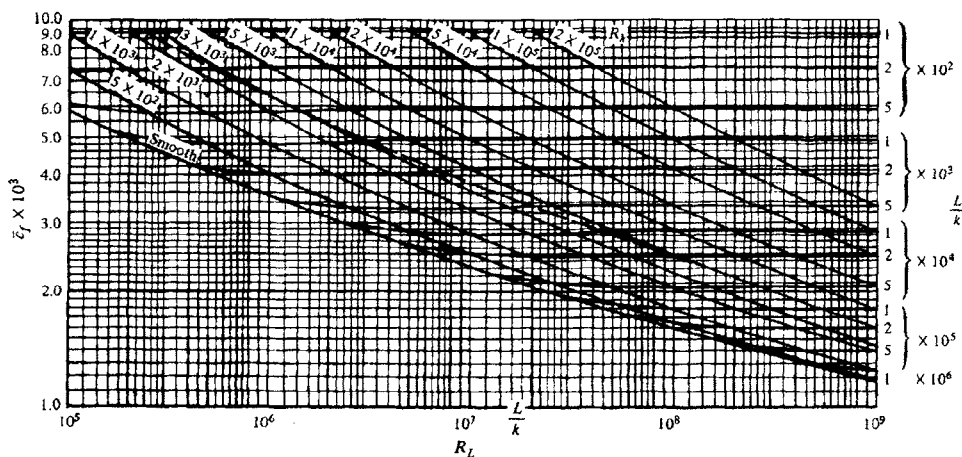


**Fig. 12.6.** Average skin-friction coefficient for a sand-roughened adiabatic flat plate at  $M_e = 2$ .

all at  $M_e = 1$  and 2. In all these figures, transition was assumed to take place at the leading edge.

Figure 12.9 shows the variation of the ratio of the compressible to incompressible values of skin-friction coefficient with Mach number for the various types of flow on an adiabatic plate. The variation is much larger for turbulent flow than for laminar flow and increases as the Reynolds number increases, being largest for a fully rough wall where viscous effects are negligible. The reason is that the effect of viscosity is felt mainly near the wall (in the viscous sub-layer), and so the relevant Reynolds number for correlating skin friction is that

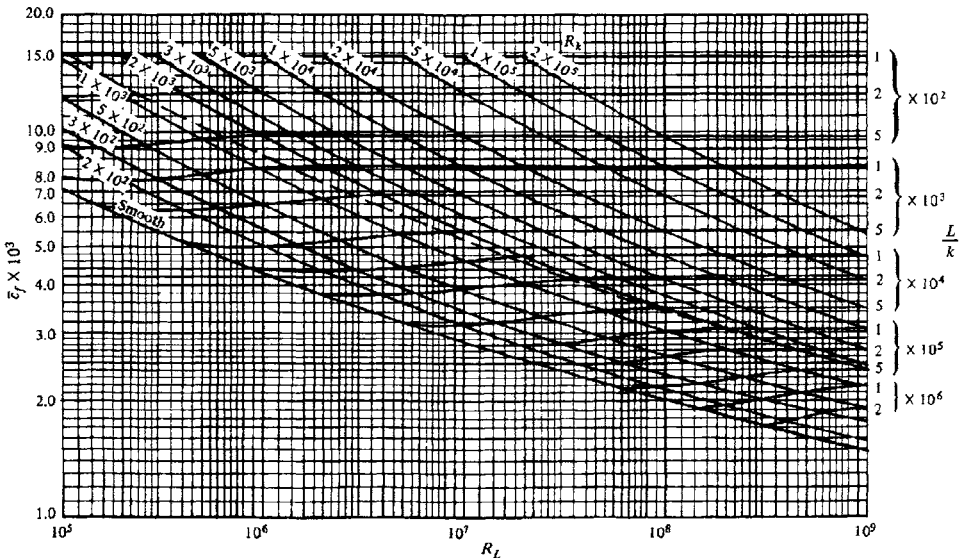


**Fig. 12.7.** Average skin-friction coefficient for a sand-roughened adiabatic flat plate with  $T_w/T_e = 1$ ,  $M_e = 1$ .

based on the wall value of viscosity. The ratio of wall viscosity to freestream viscosity increases as  $M_e$ , increases; so a given value of  $u_e L / \nu_e$  corresponds to a smaller value of  $u_e L / \nu_w$ , and thus a larger  $c_f$ . The effect on  $c_f$  decreases as  $u_e L / \nu_e$  increases because the change of  $c_f$  associated with  $R_L$  is smaller. The effect is absent on fully rough walls.

## 12.6 Numerical Solution of the Boundary-Layer Equations: Differential Method

In parallel with Section 4.5, we now discuss the calculation of two-dimensional flows by a differential method that employs a compressible version of the eddy-viscosity formulation described in subsection 6.3.1.

The governing boundary-layer equations for a two-dimensional laminar and turbulent flow in the absence of body forces, follow from Eqs. (10.5.1a), (10.5.1b), (10.5.2b) and (10.5.2c), and can be written as

$$\frac{\partial}{\partial x} (\rho u) + \frac{\partial}{\partial y} (\bar{\rho} v) = 0, \quad (12.6.1)$$

$$\rho u \frac{\partial u}{\partial x} + \bar{\rho} v \frac{\partial u}{\partial y} = - \frac{dp}{dx} + \frac{\partial}{\partial y} \left( \mu \frac{\partial u}{\partial y} - \rho u' v' \right), \quad (12.6.2)$$

$$\rho u \frac{\partial H}{\partial x} + \bar{\rho} v \frac{\partial H}{\partial y} = \frac{\partial}{\partial y} \left[ u \left( \mu \frac{\partial u}{\partial y} - \rho u' v' \right) + k \frac{\partial T}{\partial y} - \rho v' h' \right], \quad (12.6.3)$$

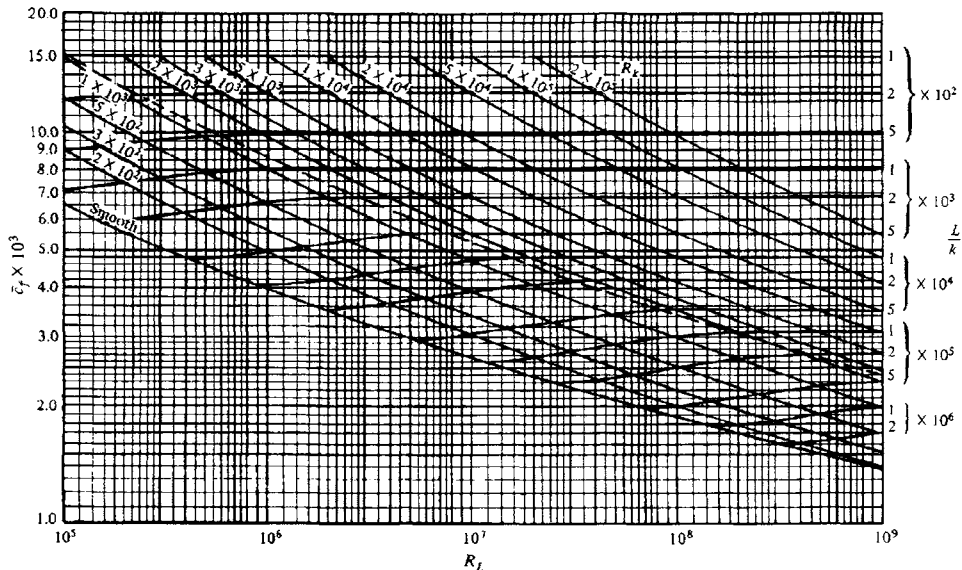


**Fig. 12.8.** Average skin-friction coefficient for a sand-roughened adiabatic flat plate with  $T_w/T_e = 1$ ,  $M_e = 2$ .

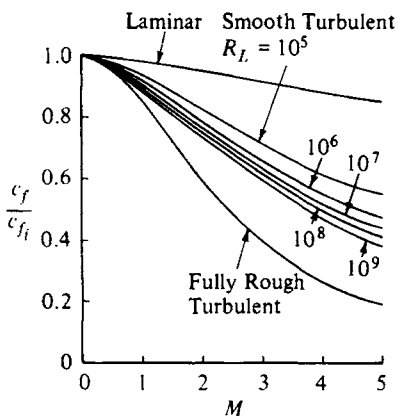


**Fig. 12.9.** Mach number variation of the ratio of the compressible to incompressible values of local skin-friction coefficient for the various types of air flow on an adiabatic flat plate, for given Reynolds number  $u_e L / \nu_e$ .

where, as before,  $\bar{pv}$  is given by Eq. (10.5.2a). With eddy viscosity and turbulent Prandtl number defined by Eqs. (12.2.1) and (12.2.3) and with the use of Bernoulli's equation  $-dp/dx = \rho_e u_e (du_e/dx)$ , Eqs. (12.6.2) and (12.6.3) become

$$\rho u \frac{\partial u}{\partial x} + \bar{pv} \frac{\partial u}{\partial y} = \rho_e u_e \frac{du_e}{dx} + \frac{\partial}{\partial y} \left[ (\mu + \rho \nu_t) \frac{\partial u}{\partial y} \right], \quad (12.6.4)$$

$$\rho u \frac{\partial H}{\partial x} + \bar{pv} \frac{\partial H}{\partial y} = \left[ \left( \frac{k}{c_p} + \rho \frac{\nu_t}{Pr} \right) \frac{\partial h}{\partial y} + u(\mu + \rho \nu_t) \frac{\partial u}{\partial y} \right], \quad (12.6.5)$$

Recalling the definition of Prandtl number  $Pr = \mu c_p / k$  and the definition of total enthalpy for a perfect gas, we can set

$$\left( \frac{k}{c_p} + \rho \frac{\nu_t}{\text{Pr}_t} \right) \frac{\partial h}{\partial y} = \left( \frac{\mu}{\text{Pr}} + \rho \frac{\nu_t}{\text{Pr}_t} \right) \left( \frac{\partial H}{\partial y} - u \frac{\partial u}{\partial y} \right)$$

and write Eq. (12.6.6) as

$$\begin{aligned} \rho u \frac{\partial H}{\partial x} + \bar{\rho} v \frac{\partial H}{\partial y} &= \frac{\partial}{\partial y} \left\{ \left( \frac{\mu}{\text{Pr}} + \rho \frac{\nu_t}{\text{Pr}_t} \right) \frac{\partial H}{\partial y} \right. \\ &\quad \left. + \left[ \mu \left( 1 - \frac{1}{\text{Pr}} \right) + \rho \nu_t \left( 1 - \frac{1}{\text{Pr}_t} \right) \right] u \frac{\partial u}{\partial y} \right\}. \end{aligned} \quad (12.6.6)$$

As in Chapter 11, we use the compressible Falkner–Skan transformation defined by Eq. (11.2.1),

$$d\eta = \sqrt{\frac{u_e}{\nu_e x}} \frac{\rho}{\rho_e} dy, \quad \psi(x, y) = \sqrt{\rho_e \mu_e u_e x} f(x, \eta), \quad (11.2.1)$$

and the definition of stream function that satisfies the continuity equation (12.6.1), so that

$$\rho u = \frac{\partial \psi}{\partial y}, \quad \bar{\rho} v = -\frac{\partial \psi}{\partial x}. \quad (12.6.7)$$

The momentum and energy equations, given by Eqs. (12.6.4) and (12.6.6), can now be written in a form similar to that of Eqs. (11.2.3) and (11.2.4), that is,

$$(bf'')' + m_1 f f'' + m_2 [c - (f')^2] = x \left( f' \frac{\partial f'}{\partial x} - f'' \frac{\partial f}{\partial x} \right), \quad (12.6.8)$$

$$(eS' + f' f'')' + m_1 f S' = x \left( f' \frac{\partial S}{\partial x} - S' \frac{\partial f}{\partial x} \right), \quad (12.6.9)$$

except that now

$$\begin{aligned} b &= C(1 + \nu_t^+), \quad e = \frac{C}{\text{Pr}} \left( 1 + \nu_t^+ \frac{\text{Pr}}{\text{Pr}_t} \right), \\ d &= \frac{Cu_e^2}{H_e} \left[ 1 - \frac{1}{\text{Pr}} + \nu_t^+ \left( 1 - \frac{1}{\text{Pr}_t} \right) \right], \quad \nu_t^+ = \frac{\nu_t}{\nu}. \end{aligned} \quad (12.6.10)$$

Including a transpiration velocity  $v_w$  at the wall, the boundary conditions given by

$$y = 0, \quad v = v_w(x), \quad u = 0, \quad H = H_w(x) \quad \text{or} \quad \left( \frac{\partial H}{\partial y} \right)_w = -\frac{c_{p_w}}{k_w} \dot{q}_w, \quad (12.6.11a)$$

$$y = \delta, \quad u = u_e(x), \quad H = H_e \quad (12.6.11b)$$

can be written in terms of transformed variables as

$$\eta = 0, \quad f' = 0, \quad f_w = \frac{-1}{(u_e \mu_e \rho_e x)^{1/2}} \int_0^x \rho_w v_w dx$$

$$S = S_w(x) \quad \text{or} \quad S'_w = -\frac{c_{p_w}}{k_w} \frac{c_w}{H_e} \frac{x \dot{q}_w}{\sqrt{R_x}}, \quad (12.6.12a)$$

$$\eta = \eta_e, \quad f' = 1, \quad S = 1. \quad (12.6.12b)$$

Note that in the absence of mass transfer, Eq. (12.6.12) is identical to the equations given by Eq. (11.2.5).

As in Section 6.4, we use the eddy-viscosity formulation of Cebeci and Smith, which for compressible flows is given by Eqs. (12.2.9) and (12.2.10). We assume the turbulent Prandtl number  $\text{Pr}_t$  equal to 0.90.

To solve Eqs. (12.6.8) and (12.6.9) subject to the boundary conditions given by Eq. (12.6.12) we follow a similar procedure discussed in Section 4.5 for Eqs. (4.5.4) and (4.5.5). We again write Eqs. (12.6.8) and (12.6.9) and their boundary conditions in terms of a first-order system. For this purpose we introduce new dependent variables  $u(x, \eta)$ ,  $v(x, \eta)$ , and  $p(x, \eta)$  so that the transformed momentum and energy equations can be written as

$$f' = u, \quad (12.6.13a)$$

$$u' = v, \quad (12.6.13b)$$

$$g' = p, \quad (12.6.13c)$$

$$(bv)' + m_1 fv + m_2(c - u^2) = x \left( u \frac{\partial u}{\partial x} - v \frac{\partial f}{\partial x} \right), \quad (12.6.13d)$$

$$(ep + duv)' + m_1 fp = x \left( u \frac{\partial g}{\partial x} - p \frac{\partial f}{\partial x} \right) \quad (12.6.13e)$$

where  $g \equiv H/H_e$  is the total-enthalpy ratio denoted by  $S$  in Eq. (11.2.18). In terms of the new dependent variables, the boundary conditions given by Eqs. (12.6.12) become

$$f(x, 0) = f_w(x), \quad u(x, 0) = 0,$$

$$g(x, 0) = g_w(x) \quad \text{or} \quad p(x, 0) = p_w(x) \quad (12.6.14a)$$

$$u(x, \eta_e) = 1, \quad g(x, \eta_e) = 1 \quad (12.6.14b)$$

We now consider the same net rectangle in the  $x\eta$  plane shown in Fig. 4.8 and the net points defined by Eq. (4.5.10) and express Eqs. (12.6.13) in terms of finite-difference approximations to obtain

$$h_j^{-1}(f_j^n - f_{j-1}^n) = u_{j-1/2}^n, \quad (12.6.15a)$$

$$h_j^{-1}(u_j^n - u_{j-1}^n) = v_{j-1/2}^n, \quad (12.6.15b)$$

$$h_j^{-1}(g_j^n - g_{j-1}^n) = p_{j-1/2}^n, \quad (12.6.15c)$$

$$\begin{aligned} h_j^{-1}(b_j^n v_j^n - b_{j-1}^n v_{j-1}^n) + (m_1^n + \alpha_n)(fv)_{j-1/2}^n - (m_2^n + \alpha_n)(u^2)_{j-1/2}^n \\ + \alpha_n(v_{j-1/2}^{n-1} f_{j-1/2}^n - f_{j-1/2}^{n-1} v_{j-1/2}^n) = R_{j-1/2}^{n-1}, \end{aligned} \quad (12.6.15d)$$

$$\begin{aligned} h_j^{-1}(e_j^n p_j^n - e_{j-1}^n p_{j-1}^n) + h_j^{-1}(d_j^n u_j^n v_j^n - d_{j-1}^n u_{j-1}^n v_{j-1}^n) \\ + (m_1^n + \alpha_n)(fp)_{j-1/2}^n \\ - \alpha_n[(ug)_{j-1/2}^n + u_{j-1/2}^{n-1} g_{j-1/2}^n - g_{j-1/2}^{n-1} u_{j-1/2}^n \\ + f_{j-1/2}^{n-1} p_{j-1/2}^n - p_{j-1/2}^{n-1} f_{j-1/2}^n] = T_{j-1/2}^{n-1}, \end{aligned} \quad (12.6.15e)$$

where

$$\alpha_n = \frac{x^{n-1/2}}{k_n}, \quad (12.6.16)$$

$$R_{j-1/2}^{n-1} = -L_{j-1/2}^{n-1} + \alpha_n[(fv)_{j-1/2}^{n-1} - (u^2)_{j-1/2}^{n-1}] - m_2^n c_{j-1/2}^n \quad (12.6.17a)$$

$$\begin{aligned} L_{j-1/2}^{n-1} = \{h_j^{-1}(b_j v_j - b_{j-1} v_{j-1}) + m_1(fv)_{j-1/2} \\ + m_2(c_{j-1/2} - (u^2)_{j-1/2})\}^{n-1}, \end{aligned} \quad (12.6.17b)$$

$$T_{j-1/2}^{n-1} = -M_{j-1/2}^{n-1} + \alpha_n[(fp)_{j-1/2}^{n-1} - (ug)_{j-1/2}^{n-1}], \quad (12.6.17c)$$

$$\begin{aligned} M_{j-1/2}^{n-1} = [h_j^{-1}(e_j p_j - e_{j-1} p_{j-1}) + h_j^{-1}(d_j u_j v_j - d_{j-1} u_{j-1} v_{j-1}) \\ + m_1(fp)_{j-1/2}]^{n-1}. \end{aligned} \quad (12.6.17d)$$

In order to account for the mixed wall boundary conditions for the energy equation, we write Eq. (12.6.14a) as

$$\alpha_0 g_0^n + \alpha_1 p_0^n = \gamma_0^n \quad (12.6.18)$$

Here for specified wall temperature  $\alpha_0 = 1$ ,  $\alpha_1 = 0$  and since the enthalpy ratio at the surface,  $g_0(x)$ , is given,  $\gamma_0 = g_0(x)$ . For a specified wall heat flux,  $\alpha_0 = 0$ ,  $\alpha_1 = 1$  and  $\gamma_0$  equals the dimensionless total-enthalpy gradient at the wall.

The wall boundary conditions for the momentum and energy equations can be written as

$$f_0^n = 0, \quad u_0^n = 0, \quad \alpha_0 g_0^n + \alpha_1 p_0^n = \gamma_0^n \quad (12.6.19a)$$

and the edge boundary conditions as

$$u_J^n = 1, \quad g_J^n = 1. \quad (12.6.19b)$$

If we assume  $f_j^{n-1}$ ,  $u_j^{n-1}$ ,  $v_j^{n-1}$ ,  $g_j^{n-1}$ , and  $p_j^{n-1}$  to be known for  $0 \leq j \leq J$ , then Eqs. (12.6.15) and (12.6.19) form a system of  $5J + 5$  nonlinear equations for the solution of  $5J + 5$  unknowns  $(f_j^n, u_j^n, v_j^n, g_j^n, p_j^n)$ ,  $j = 0, 1, \dots, J$ . To solve

this nonlinear system, we again use Newton's method discussed in subsection 4.5.2.

This procedure yields a linear system which is again solved with the block-elimination method (subsection 4.5.3). This is discussed in some detail in the accompanying CD-ROM which also gives the computer program for solving the boundary-layer equations for two-dimensional compressible flows.

## 12.7 Shock-Wave/Boundary-Layer Interaction

We now come to one of the most important and outstanding problems in the theory of boundary layers, the response of a turbulent boundary layer to a shock wave generated either by a concave corner on the surface or externally. Normally the structure of the boundary layer has little effect on the external flow unless there are extensive regions of separation, but the situation can be quite different when shocks are involved. For example, the lifting force on airfoils at transonic speeds can be halved, and the shock position moved 20 percent of the chord, by viscous effects even when the Reynolds number is high and the boundary layer is attached. The resolution of the structure of the boundary layer in such flows is still in the development stage and far from complete. It is inappropriate here to attempt to review the enormous amount of work that has been done on this topic. Instead, we refer the reader to the general review by Adamson and Messiter [14], Délery [15, 16] and to the AGARD Conference at Colorado Springs [17], for an assessment of the present state of knowledge. Some comments of a general nature are in order, however, to give the reader an appreciation of the achievements.

The interaction has some general features in common with laminar interactions, principally the formation of a pressure plateau ahead of the shock intersection, but there are important differences. For example, the upstream extent of the interaction is only a few boundary-layer thicknesses, even with a large pressure rise across the shock, and much less than has been observed with laminar flows. Again the pressure rise to provoke separation in a turbulent boundary layer is higher than for laminar flow because the flow speed and dynamic pressure near the wall are larger; a rough rule is that a turbulent boundary layer passing through a normal shock will separate if the Mach number ahead of the shock exceeds 1.3 (this corresponds to a pressure rise of 0.68 of the freestream dynamic pressure, about the same as that needed to separate a low-speed boundary layer in a strong adverse pressure gradient). When the shock is oblique, the pressure rise to separation is roughly the same as for a normal shock.

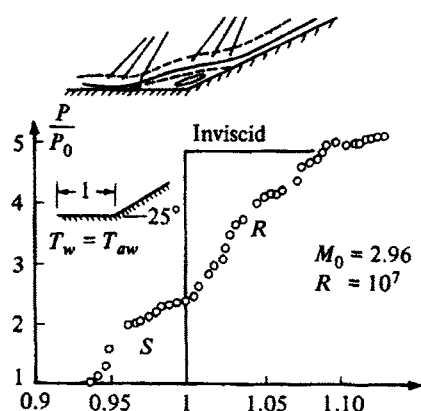
The simplest experimental configuration for examining the nature of the interaction has the shock generated by a ramp on the test surface, and the resulting flow has been studied by many workers during the last 30 years or so. In

Fig. 12.10 we show a comparison between the measured pressure distribution on a  $25^\circ$  ramp at  $M_\infty = 2.96$  and the predictions of inviscid theory (Law [18]), and in Fig. 12.11 we show a photograph of hypersonic flow past a ramp. A large number of measurements of the ramp angle  $\alpha_i$  needed to produce incipient separation have been made, and the results are reviewed by Roshko and Thomke [19]. The trends are displayed in Fig. 12.12. According to inviscid theory, the ramp angle that is required to produce a detached shock increases with Mach number, and so it is not surprising that the critical ramp angle  $\alpha_i$ , for incipient separation, also increases with Mach number, from about  $15^\circ$  at  $M_\infty = 2$  to about  $30^\circ$  at  $M_\infty = 8$ . The variation of  $\alpha_i$  with Reynolds number  $R$  is more interesting. At low values of  $R$ ,  $\alpha_i$  decreases as  $R$  increases, apparently because of the changing outer profile (law of the wake, discussed in Section 12.4). At higher values the trend is reversed due to the profile becoming fuller with consequent decrease of the shape parameter  $H$  and skin-friction coefficient  $c_f$ . For recent results, see Hayakawa and Squire [20].

One of the earliest attempts to describe the details of the interaction is due to Lighthill [21], who used arguments similar to those leading to the establishment of the triple-deck theory of laminar free interactions (Section 11.6). The chief modification is to use the characteristic turbulent profile as initial profile instead of the laminar form, but as Lighthill immediately noticed, the resulting scaling laws [compare Eq. (11.7.10)] are not consistent, the interaction region being thinner than the boundary layer. The most recent precise studies of the interaction ignore the sub-boundary layer [compare Eqs. (11.7.7)–(11.7.9)] and take the velocity upstream of the interaction in the form

$$u_0(y) = u_e \left[ 1 + \varepsilon u_0 \left( \frac{y}{\delta} \right) \right], \quad (12.7.1)$$

where  $u_e$  is the external velocity,  $\varepsilon$  is a small parameter  $O(\log Re)^{-1}$ , and  $\delta$  is the boundary-layer thickness. This form does not satisfy the no-slip condition at the wall and may be thought of as the outer or law-of-the-wake part of the velocity



**Fig. 12.10.** Pressure distribution along a supersonic ramp with a turbulent boundary layer. The freestream Mach number is 2.96 and the Reynolds number is  $10^7$  at the corner. The solid line denotes the inviscid pressure and the symbols experimental results [18].

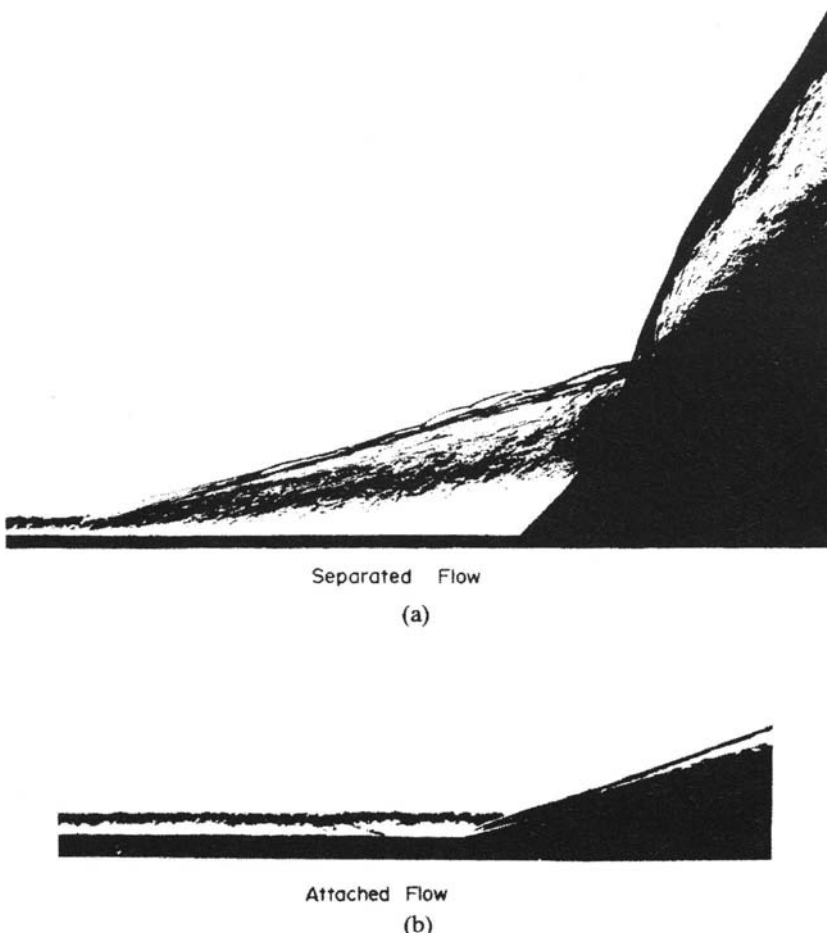


**Fig. 12.11.** Turbulent hypersonic flow at a wedge-compression corner. (a) Separated flow.  
(b) Attached flow.

profile. The interaction of the boundary layer with a shock using  $u_0(y)$  as an approximation to the initial profile is then treated on a largely inviscid basis. The sketch in Fig. 12.13 shows the structure of the interaction. Two features of this procedure are of interest. First it suggests that in numerical studies of weak interactions, the precise form of the law of the wall or the eddy viscosity is not important. This conclusion has been supported by several numerical studies of such interactions, and indeed it seems generally agreed that algebraic eddy-viscosity or mixing-length models give good results provided separation has not occurred. Second, it cannot treat interaction problems in which separation does occur, for a basic assumption is that the important features occur in the outer part of the boundary layer.

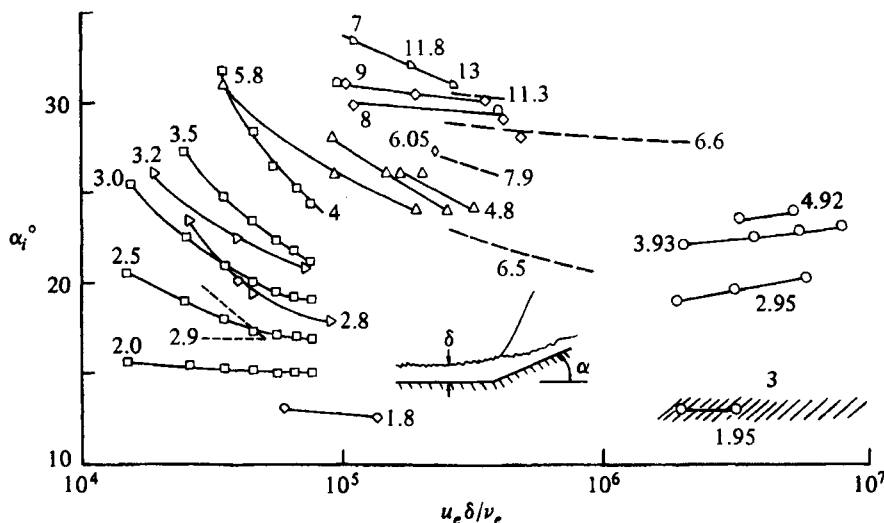


**Fig. 12.12.** Incipient separation of a turbulent boundary layer on a ramp [19]. Labels on curves indicate Mach numbers.

Several attempts, notably by Inger and his associates [22], have been made to account for the sub-boundary layer in a rational way. The basis is the same as Lighthill's and in consequence is subject to the same sort of criticism. Thus the use of laminar equations to describe this layer means that Reynolds stresses are assumed to be relatively unimportant. In fact, Reynolds stresses are significant in the law-of-the-wall region, and the Eq. (10.5.2b),

$$\tau = \mu \frac{\partial u}{\partial y} - \rho \bar{u}' v' \quad (10.5.2b)$$

must be considered in any explanation of the behavior of the wall shear stress  $\tau_w$ . The implication is that even in the interactive region, the pressure gradient and the inertia terms lead to higher-order corrections for  $\tau_w$ . At the present time, therefore, our understanding of the mechanisms that control extensive regions of separated flow is still largely incomplete, and this uncertainty is reflected in

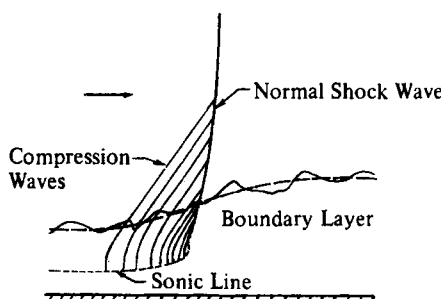


**Fig. 12.13.** Incident normal shock wave with unseparated turbulent boundary layer [21].

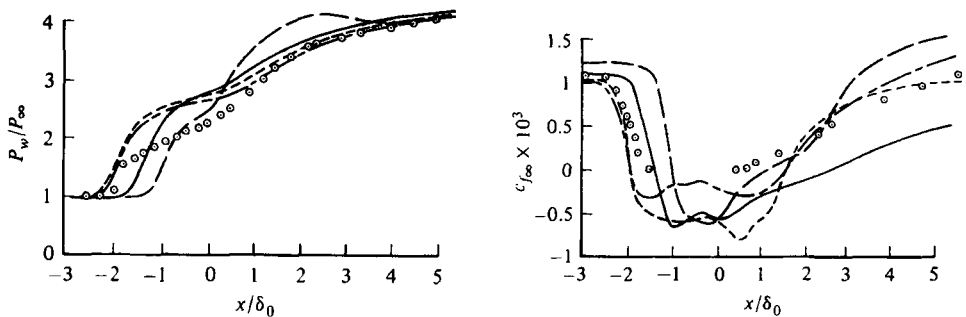


**Fig. 12.14.** Comparison of computation and surface measurements for a supersonic compression corner with shock-wave/boundary-layer interaction. The ramp angle is  $24^\circ$ , the Reynolds number based on boundary-layer thickness is  $1.33 \times 10^6$  and  $M_\infty = 2.8$ . The symbols denote experiment and (—) is obtained using an algebraic eddy-viscosity model, (---) a one-equation turbulence model, (- - -) two-equation Model A, and (- · -) two-equation Model B [22].

the numerical procedure adopted for the calculation of separating interactive flows of practical interest. The use of simple algebraic models for the eddy viscosity, of the type discussed in Section 12.2 predicts the gross features of the flow, even when separation occurs, but not its detailed properties. More complex models have been devised, and it might have been thought that these would permit more accurate predictions. In their review [14], Adamson and Messiter comment that “at the present time it appears that this promise has not been fulfilled, in the sense that it is not possible to choose a given model, with a given set of constants, that gives results more accurate than those given by a simple zero-equation model, for an arbitrary chosen interaction problem.” A typical pair of graphs, due to Viegas and Horstmann [23] for pressure and skin friction, is shown in Fig. 12.14 comparing the predictions, using models of varying complexity, with experiment.

## References

- [1] Cebeci, T.: *Analysis of Turbulent Flows*. Elsevier, London, 2004.
- [2] Cousteix, J., Houdeville, R. and Michel, R.: Couches limites turbulentes avec transfert de chaleur. *La Rech. Aéosp.*, 1974-6, 1974.
- [3] Au poix, B. and Viala, S.: Compressible turbulent boundary layer modelling. In: Kral, L. D., Spina, E. F. and Arakawa, C., eds., *Transitional and Turbulent Compressible Flows*, Vol. 224, pp. 139–146, ASME, Hilton Head Island, 1995.
- [4] Van Driest, E. R.: Turbulent boundary layer in compressible fluids. *J. Aeronaut. Sci.* **18**(3), 145–160 and 216, 1951.
- [5] Catris, S. and Au poix, B.: Density corrections for turbulence models. *Aerospace Sci. Technol.* **4**, 1–11, 2000
- [6] Rotta, J. C.: Turbulent boundary layers with heat transfer in compressible flow. ACARD Rept. 281, 1960.

- [7] Fernholz, H. H.: Ein halbempirisches Gesetz für die Wandreibung in kompressiblen turbulenten Grenzschichten bei isothermer und adiabater Wand. *Z. Angew. Math. u. Mech.* **51**, T146, 1971.
- [8] Spalding, D. B. and Chi, S. W.: The drag of a compressible turbulent boundary layer on a smooth flat plate with and without heat transfer. *J. Fluid Mech.* **18**, 117, 1964.
- [9] Hopkins, E. J. and Keener, E. R.: Pressure gradient effects on hypersonic turbulent skin-friction and boundary-layer profiles. *AIAA J.* **10**, 1141, 1972.
- [10] Cary, A. M. and Bertram, M. H.: Engineering prediction of turbulent skin friction and heat transfer in high-speed flow. NASA TN D-7507, 1974.
- [11] Cary, A. M.: Summary of available information on Reynolds analogy for zero-pressure gradient, compressible turbulent-boundary-layer flow. NASA TN D-5560, 1970.
- [12] Goddard, F. E., Jr.: Effect of uniformly distributed roughness on turbulent skin-friction drag at supersonic speeds. *J. Aero/Space Sci.* **26**, 1–15, 1959.
- [13] Fenter, F. W.: The effect of heat transfer on the turbulent skin-friction of uniformly rough surfaces in compressible flow. The University of Texas, Defense Research Lab Rept. DLR-368, CM-839, April 1956.
- [14] Adamson, T. C. and Messiter, A. F.: Analysis of two-dimensional interactions between shock waves and boundary layers. *Ann. Rev. Fluid Mech.* **12**, 103–138, Annual Reviews, Palo Alto, 1980.
- [15] Délery, J.: Shock phenomena in high speed aerodynamics: still a source of major concern. Lancaster Lecture, The Aeronautical Journal of the Royal Aeronautical Society, Jan. 1999.
- [16] Délery, J.: Shock wave / boundary-layer interactions. In: *Handbook of Shock Waves*, Ben-Dor, D., Igra, O., Elperin, T., eds., Academic Press, 2001.
- [17] Computation of Viscous-Inviscid Interactions. AGARD Conf. Proceedings No. 291, 1981.
- [18] Law, C. H.: Supersonic turbulent boundary-layer separation. *AIAA J.* **12**, 1974.
- [19] Roshko, A. and Thomke, G. J.: Supersonic turbulent boundary-layer interaction with a compression corner at very high Reynolds number. Proc. Symposium on Viscous Interaction Phenomena in Supersonic Hypersonic Flow, USAF Aerospace Research Labs., Wright-Patterson AFB, Ohio, Univ. of Dayton Press, May 1969.
- [20] Hayakawa, K. and Squire, L. C.: The effect of the upstream boundary-layer state on the shock interaction at a compression corner. *J. Fluid Mech.* **122**, 369, 1982.
- [21] Lighthill, M. J.: On boundary layers and upstream influence, II. Supersonic flow without separation. *Proc. Royal Soc. A* **217**, 1953.
- [22] Inger, G. R.: Nonasymptotic theory of unseparated turbulent boundary-layer-shock-wave interaction with application to transonic flows. In: *Numerical and Physical Aspects of Aerodynamic Flows*, Cebeci, T., ed., p. 159, Springer, New York, 1982.
- [23] Viegas, J. R. and Horstmann, C. C.: Comparison of multiequation turbulence models for several shock boundary-layer interaction flows. *AIAA J.* **17**, 811–820, 1979.

## Problems

**12-1.** The turbulence model equation given by Eqs. (12.2.16) and (12.2.17), that is,

$$\rho u \frac{\partial k}{\partial x} + \bar{\rho} v \frac{\partial k}{\partial y} = -\rho \bar{u}' v' \frac{\partial u}{\partial y} - \rho \varepsilon + \frac{\partial}{\partial y} \left[ \frac{\mu_t}{\rho \sigma_k} \frac{\partial \rho k}{\partial y} \right] \quad (\text{P12.1.1})$$

$$\begin{aligned} \rho u \frac{\partial \rho \varepsilon}{\partial x} + \bar{\rho} v \frac{\partial \rho \varepsilon}{\partial y} &= \left( -c_{\varepsilon_1} \rho \bar{u}' v' \frac{\partial u}{\partial y} - c_{\varepsilon_2} \rho \varepsilon \right) \frac{\rho \varepsilon}{k} \\ &\quad + \frac{\partial}{\partial y} \left[ \frac{\mu_t}{\rho^{1/2} \sigma_\varepsilon} \frac{\partial \rho^{3/2} \varepsilon}{\partial y} \right] \end{aligned} \quad (\text{P12.1.2})$$

where

$$\mu_t = \rho c_\mu \frac{k^2}{\varepsilon} \quad (\text{P12.1.3})$$

can be used to study the behavior of the flow in the logarithmic region. Assuming that  $-\rho u' v'$  is constant and equal to  $\tau_w$  and assuming that the Bradshaw hypothesis is valid, i.e.

$$-\rho \overline{u' v'} = 2a_1 \rho k \quad (\text{P12.1.4})$$

where  $a_1$  is a constant and neglecting the convective terms  $\frac{Dk}{Dt}$  and  $\frac{D\rho\varepsilon}{Dt}$  assumed to be negligible because the velocity is small, show that

(a)

$$\frac{\partial u}{\partial y} = \sqrt{\frac{\rho_w}{\rho}} \frac{u_\tau}{\kappa y}, \quad u_\tau = \sqrt{\frac{\tau_w}{\rho_w}} \quad (\text{P12.1.5})$$

(b)

$$c_\mu = (2a_1)^2 \quad (\text{P12.1.6})$$

(c) the law of the wall is verified if

$$(c_{\varepsilon_1} - c_{\varepsilon_2}) \frac{c_\mu^{1/2} \sigma_\varepsilon}{\kappa^2} + 1 = 0 \quad (\text{P12.1.7})$$

**12-2.** In the inner layer (outside the viscous sublayer) the transport terms in the energy equation (10.5.1c) are small and can be neglected. Assuming that  $\tau$  is constant and equal to  $\tau_w$ , from Eq. (10.5.1c) we can write

$$\frac{\partial \dot{q}}{\partial y} = \tau_w \frac{\partial u}{\partial y} \quad (\text{P12.2.1})$$

which states that the next rate of ( $y$ -component) transfer of heat leaving a control volume in the inner layer is equal to the rate at which the fluid in the control volume does work against (shear) stress. Integrating this equation, we get

$$\dot{q} = \dot{q}_w + u \tau_w. \quad (\text{P12.2.2})$$

In a low speed flow the work done is negligible, and  $\dot{q} \simeq \dot{q}_w$ , corresponding to  $\tau = \tau_w$ .

Analogous to Eq. (5.2.2), with  $u_c$  denoted by  $(\tau/\rho)^{1/2}$ , that is,

$$\frac{\partial u}{\partial y} = \frac{(\tau/\rho)^{1/2}}{\kappa y} \quad (\text{P12.2.3})$$

we can write

$$\frac{\partial T}{\partial y} = \frac{-\dot{q}/\rho c_p}{(\tau/\rho)^{1/2} \kappa_h y} \quad (\text{P12.2.4})$$

where  $\kappa_h$ , like  $\kappa$  in Eq. (6.2.3) is a constant. If we divide Eq. (12.2.4) by Eq. (12.2.3), we obtain

$$\frac{\partial T}{\partial u} = \frac{-(\kappa/\kappa_h)\dot{q}}{c_p\tau_w} \quad (\text{P12.2.5})$$

where  $\kappa/\kappa_h$  is the turbulent Prandtl number,  $\text{Pr}_t$ .

(a) Substituting for  $\dot{q}$  from Eq. (12.2.2) and integrating with respect to  $u$ , show that

$$T = -\frac{(\kappa/\kappa_h)\dot{q}_w u}{c_p\tau_w} - \frac{(\kappa/\kappa_h)u^2}{2c_p} + \text{const.} \quad (\text{P12.2.6})$$

Note that, unlike the corresponding equation for laminar flows, Eq. (11.2.22b) for  $\text{Pr} = 1$ , the constant of integration is *not* exactly equal to  $T_w$  because the formulas (P12.2.3) and (P12.2.4) are not valid in the viscous or conductive sublayers, but it is conventionally written as  $c_1 T_w$ , where  $c_1$  is fairly close to unity and is a function of  $\dot{q}_w/\rho_w c_p u_\tau T_w$ ,  $u_\tau/a_w$ , and the molecular Prandtl number  $\text{Pr}$ . That is,

$$T = c_1 T_w - \frac{(\kappa/\kappa_h)\dot{q}_w u}{c_p\tau_w} - \frac{(\kappa/\kappa_h)u^2}{2c_p}. \quad (\text{P12.2.7})$$

(b) Noting that  $\rho = \rho_w T_w / T$ , we can use Eq. (P12.2.7) to eliminate  $\rho$  from Eq. (P12.2.3). Show that the integral required to obtain  $u$  as a function of  $y$  from Eq. (P12.2.3) then becomes

$$\int \frac{dy}{\kappa y} = \int \frac{du/u_\tau}{[c_1 - (\kappa/\kappa_h)\dot{q}_w u/c_p T_w \tau_w - (\kappa/\kappa_h)u^2/2c_p T_w]^{1/2}}. \quad (\text{P12.2.8})$$

(c) Replacing  $(c_p T_w)$  by  $a_w^2/(\gamma - 1)$  and integrating Eq. (P12.2.8), show that the law of the wall for compressible flows, Eq. (12.3.1), is obtained.



# 13

## An Interactive Boundary-Layer Method for Three-Dimensional Flows

### 13.1 Introduction

Equations (10.5.5) to (10.5.12) represent three-dimensional laminar and turbulent compressible boundary layers in a body-oriented coordinate system. Their solution requires boundary and initial conditions together with a turbulence model for the Reynolds stresses and can be obtained either in standard or inverse modes as with the two-dimensional incompressible flows discussed in Chapter 9. For the standard problem, that is for a given external velocity distributions of  $u_e(x, z)$  and  $w_e(x, z)$ , the procedure is similar to that described for three-dimensional incompressible flows in Chapter 7; the main difference relates to the energy equation and whether it is solved together with the continuity and momentum equations or independently from them. In the latter case, the continuity and momentum equations are solved and then the energy equation. The solutions of the velocity and temperature fields are iterated until convergence.

As in two-dimensional flows, the standard method has the drawback that the solutions break down as the streamwise wall shear tends to zero and cannot be used for flows with separation. Thus, the solution of the three-dimensional compressible boundary-layer equations in the inverse mode with an interactive method is considered here. The initial conditions and the turbulence model are described in subsections 13.2.1 and 13.2.2, the interaction law, transformed equations and the numerical method in Sections 13.3, 13.4 and 13.5 and the modeling of viscous effects in inviscid flows is addressed in Section 13.6.

Geometric parameters, such as the metric coefficients and geodesic curvature of the coordinate lines appearing in the boundary layer equations, must be known prior to the boundary layer calculations for given freestream conditions and inviscid velocity distribution. The interface program described in Section 13.7 computes the geometric parameters from the definition of wing geometry together with the nonorthogonal coordinates used in the boundary-layer

method. The interface program also interpolates the inviscid velocity distribution for the boundary-layer grid, which may be different from that calculated by the inviscid method.

The interactive boundary-layer (IBL) method described here has been applied to low speed and transonic flows as discussed in Sections 13.8 and 13.9, respectively. A computer program applicable to three dimensional incompressible and compressible laminar and turbulent flows is described in Appendix C.

For flows over yawed infinite cylinders or with the swept-wing approximation, the spanwise flow is independent of the  $z$ -coordinate and the boundary layer equations for three-dimensional flows simplify. This is discussed in Appendix 13A (Appendix B).

## 13.2 Governing Equations

### 13.2.1 Initial Conditions

For three-dimensional compressible laminar and turbulent flows, the boundary-layer equations for a nonorthogonal system are given by Eqs. (10.5.5) to (10.5.12). As discussed in Section 7.3, they require initial conditions in the  $(x, y)$ -plane at some  $z = z_0$  and in the  $(z, y)$ -plane at  $x = x_0$ . For a wing defined in a Cartesian coordinate system  $\bar{x}, \bar{y}, \bar{z}$  by

$$F(\bar{x}, \bar{y}, \bar{z}) = 0 \quad (13.2.1)$$

where  $\bar{x}$  represents the direction of the airplane longitudinal axis,  $\bar{y}$  the spanwise direction, and  $\bar{z}$  normal to the  $\bar{x}, \bar{y}$  plane, this coordinate system (see subsection 7.2.3) can be chosen by taking  $x$  to denote the coordinates along the lines formed by the intersection of the wing surface and planes representing constant percent semispan,  $z$  the coordinate along the constant percent chordlines which generate the wing surface, and  $y$  the coordinate normal to the wing surface, see Fig. 13.1.

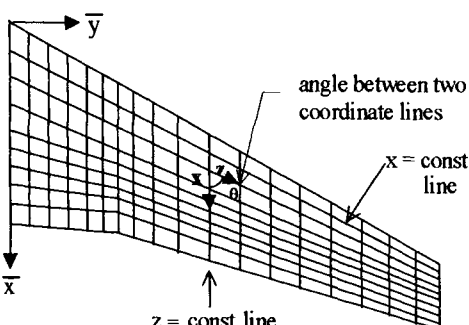


**Fig. 13.1.** The nonorthogonal coordinate system.

Following the same procedure in Section 7.3, the attachment line equations and their boundary conditions can be written as

$$\rho h_2 \sin \theta u_x + \frac{\partial}{\partial x} (\rho w h_1 \sin \theta) + \frac{\partial}{\partial y} (\bar{\rho} v h_1 h_2 \sin \theta) = 0 \quad (13.2.2)$$

$$\begin{aligned} & \rho \frac{u_x^2}{h_1} + \rho \frac{w}{h_2} \frac{\partial u_x}{\partial z} + \bar{\rho} v \frac{\partial u_x}{\partial y} + \rho k_{12} w u_x \\ &= \rho_e \left( \frac{u_{ex}^2}{h_1} + \frac{w_e}{h_2} \frac{\partial u_{xe}}{\partial z} + k_{12} w_e u_{xe} \right) + \frac{\partial}{\partial y} \left( \mu \frac{\partial u_x}{\partial y} - \rho (\bar{u}' v')_x \right) \end{aligned} \quad (13.2.3)$$

$$\begin{aligned} & \rho \frac{w}{h_2} \frac{\partial w}{\partial z} + \bar{\rho} v \frac{\partial w}{\partial y} - \rho \cot \theta k_2 w^2 \\ &= \rho_e \left( \frac{w_e}{h_2} \frac{\partial w_e}{\partial z} - \cot \theta k_2 w_e^2 \right) + \frac{\partial}{\partial y} \left( \mu \frac{\partial w}{\partial y} - \rho \bar{u}' v' \right) \end{aligned} \quad (13.2.4)$$

$$\rho \frac{w}{h_2} \frac{\partial H}{\partial z} + \bar{\rho} v \frac{\partial H}{\partial y} = \frac{\partial}{\partial y} \left[ \frac{\mu}{Pr} \frac{\partial H}{\partial y} + \mu \left( 1 - \frac{1}{Pr} \right) \frac{\partial}{\partial y} \left( \frac{u_t^2}{2} \right) - \rho \bar{v}' H' \right] \quad (13.2.5)$$

$$y = 0; \quad u_x = w = 0, \quad v = v_w, \quad H = H_w(x, z) \text{ or } \left( \frac{\partial H}{\partial y} \right)_w = - \frac{C_{p_w}}{k_w} \dot{q}_w \quad (13.2.6a)$$

$$y = \delta, \quad u_x = u_{xe}(x, z), \quad w = w_e(x, z), \quad H = H_e \quad (13.2.6b)$$

As in Section 7.3. we use the quasi-three-dimensional boundary-layer equations along the wing-fuselage intersection. Neglecting the derivatives with respect to  $z$ , Eqs. (10.5.5) to (10.5.8) can be written as

$$\frac{\partial}{\partial x} (\rho u h_2 \sin \theta) + \frac{\partial}{\partial y} (\bar{\rho} v h_1 h_2 \sin \theta) = 0 \quad (13.2.7)$$

$$\begin{aligned} & \rho \frac{u}{h_1} \frac{\partial u}{\partial x} + \bar{\rho} v \frac{\partial u}{\partial y} - \rho \cot k_1 u^2 + \rho \csc \theta k_2 w^2 + \rho k_{12} u w \\ &= \rho_e \left( \frac{u_e}{h_1} \frac{\partial u_e}{\partial x} - \cot \theta k_1 u_e^2 + \csc \theta k_2 w_e^2 + k_{12} u_e w_e \right) \end{aligned} \quad (13.2.8)$$

$$\begin{aligned} & \rho \frac{u}{h_1} \frac{\partial w}{\partial x} + \bar{\rho} v \frac{\partial w}{\partial y} - \rho \cot k_2 w^2 + \rho \csc \theta k_1 u^2 + \rho k_{21} u w \\ &= \rho_e \left( \frac{w_e}{h_1} \frac{\partial w_e}{\partial x} - \cot \theta k_2 w_e^2 + \csc \theta k_1 u_e^2 + k_{21} u_e w_e \right) \end{aligned} \quad (13.2.9)$$

$$\rho \frac{u}{h_1} \frac{\partial H}{\partial x} + \bar{\rho} v \frac{\partial H}{\partial y} = \frac{\partial}{\partial y} \left[ \frac{\mu}{Pr} \frac{\partial H}{\partial y} + \left( 1 - \frac{1}{Pr} \right) \frac{\partial}{\partial y} \left( \frac{u_t^2}{2} \right) - \rho \bar{v}' H' \right] \quad (13.2.10)$$

The boundary conditions are the same as those given by Eqs. (13.2.6) except that  $u_e$  and  $w_e$  are independent of  $z$ .

### 13.2.2 Turbulence Models

The closure requirements of the boundary-layer equations for compressible turbulent flows, as in incompressible flows, can be satisfied with the turbulence models discussed in Section 6.3 and 7.4. For example, the zero-equation model of Cebeci-Smith described in Section 7.4 can again be represented by Eqs. (7.4.4) to (7.4.6). In Eq. (7.4.4a), the mixing length  $l$  is given by eqs. (6.3.4a) with  $A$  and  $N$  defined by Eq. (12.2.10) with  $u_\tau$  and  $(\frac{\tau_t}{\rho})_{\max}$  given by Eq. (7.4.5). In the energy equation, the turbulent Prandtl number,  $\text{Pr}_t$  is assumed to be constant equal to 0.90.

## 13.3 Interaction Law

The Hilbert integral formula given by Eq. (9.1.4b) can be extended to three-dimensional flows in order to account for the viscous effects. Roget [1] calculates the effects of a perturbation at the wall on inviscid flow solution using Fourier transforms. Equivalently, the presence of viscous effects in the potential flow can also be modelled by a change in boundary condition at the surface ( $y = 0$ ) by imposing a blowing velocity  $v_w(x, z)$  defined in a Cartesian coordinate system by

$$v_w(x, z) = \frac{\partial u_e \delta_x^*}{\partial x} + \frac{\partial w_e \delta_z^*}{\partial z} \quad (13.3.1)$$

where

$$\delta_x^* \equiv \int_0^\delta \left( 1 - \frac{\rho u}{\rho_e u_e} \right) dy \quad (13.3.2a)$$

$$\delta_z^* \equiv \int_0^\delta \left( 1 - \frac{\rho w}{\rho_e w_e} \right) dy \quad (13.3.2b)$$

If the body curvature is small so that a flat surface can be locally assumed, this boundary condition can be replaced by a source distribution of strength  $q_w = 2v_w$  per unit area in the  $y = 0$  plane, so that the potential is

$$F(x, z, 0) = -\frac{1}{4\pi} \int_{x_a}^{x_b} \int_{z_a}^{z_b} \frac{q_w(\sigma, \lambda) d\sigma d\lambda}{\sqrt{(x - \sigma)^2 + (z - \lambda)^2}} \quad (13.3.3)$$

and the corresponding induced velocity is

$$\mathbf{V} = \nabla F \quad (13.3.4)$$

After integration by parts, assuming that  $q_w$  reaches zero on the boundaries of the domain, the perturbation velocity components for an orthogonal coordinate system can be written as

$$\delta u_e(x, z) = -\frac{1}{2\pi} \int_{x_a}^{x_b} \int_{z_a}^{z_b} \frac{\partial(v_w(\sigma, \lambda))}{\partial \sigma} \frac{d\sigma d\lambda}{\sqrt{(x - \sigma)^2 + (z - \lambda)^2}} \quad (13.3.5a)$$

$$\delta w_e(x, z) = -\frac{1}{2\pi} \int_{x_a}^{x_b} \int_{z_a}^{z_b} \frac{\partial(v_w(\sigma, \lambda))}{\partial \lambda} \frac{d\sigma d\lambda}{\sqrt{(x-\sigma)^2 + (z-\lambda)^2}} \quad (13.3.5b)$$

Under the quasi-three-dimensional approach, since all derivatives with respect to  $z$  can be neglected, the integrals for the perturbation velocities become

$$\delta u_e(x, z) = -\frac{1}{2\pi} \int_{x_a}^{x_b} \int_{-\infty}^{+\infty} \frac{\partial(v_w(\sigma))}{\partial \sigma} \frac{d\sigma d\lambda}{\sqrt{(x-\sigma)^2 + (z-\lambda)^2}} \quad (13.3.6a)$$

$$\delta w_e(x, z) = 0 \quad (13.3.6b)$$

so that the boundary condition for  $w_e$  remains unchanged compared with the direct or standard mode. From the potential equation, Eq. (13.3.3), and Eq. (13.3.4), the perturbation velocity  $\delta u_e$  can also be written as

$$\delta u_e(x, z) = -\frac{1}{2\pi} \int_{x_a}^{x_b} v_w(\sigma) \left[ \lim_{a \rightarrow \infty} \frac{\partial}{\partial x} \left( \int_{-a}^a \frac{d\lambda}{\sqrt{(x-\sigma)^2 + (z-\lambda)^2}} \right) \right] d\sigma \quad (13.3.7)$$

Since

$$\int_{-a}^a \frac{d\lambda}{\sqrt{(x-\sigma)^2 + (z-\lambda)^2}} = \left[ \ln \left| \gamma + \sqrt{\gamma^2 + (x-\sigma)^2} \right| \right]_{-a_1}^{a_2} \quad (13.3.8)$$

where  $a_1 = a_2 + z$  and  $a_2 = a - z$ . After differentiating with respect to  $x$  and developing to first order, i.e.

$$\sqrt{a_i^2 + (x-\sigma)^2} = a_i \left( 1 + \frac{(x-\sigma)^2}{2a_i^2} + O\left(\frac{(x-\sigma)^4}{a_i^4}\right) \right), \quad a_i \rightarrow \infty \quad (13.3.9)$$

we get

$$\lim_{a \rightarrow \infty} \frac{\partial}{\partial x} \left( \int_{-a}^a \frac{d\lambda}{\sqrt{(x-\sigma)^2 + (z-\lambda)^2}} \right) = \frac{-2}{x-\sigma} \quad (13.3.10)$$

so that the perturbation velocity in the streamwise direction,  $\delta u_e$  reduces to its value for the two-dimensional case, Eq. (9.1.4).

We shall adopt Eq. (9.1.4) also for three-dimensional flows. Since in three-dimensional flows, unlike the displacement thickness of two-dimensional flows corresponds to a displacement surface, it is clear that the interaction law requires consideration of chordwise and spanwise directions at the same time and with the knowledge that the flow variables are influenced by upstream and downstream conditions in both directions. These features impose special problems since the boundary-layer equations are parabolic with a marching solution procedure, and the interaction procedure must be devised to meet these requirements. A plausible approach used here has the following ingredients. First an initial displacement surface is generated by solving the quasi-three-dimensional boundary-layer equations, Eqs. (13.2.7) to (13.2.10), with the external velocity

distribution obtained from three-dimensional inviscid flow equations. The second step involves interaction between the inviscid flow equations and the quasi-three-dimensional flow equations. As in two-dimensional flows, the solutions of the boundary-layer equations are used to compute distributions of blowing velocity on the surface, which are subsequently used to update the inviscid flow solutions. In step three, the fully three-dimensional boundary-layer equations are solved with the external velocity components resulting from step two. The chordwise edge velocity component is expressed, as in two-dimensional flows, as a sum of inviscid external velocity  $u_e(0)$  and a perturbation velocity  $\delta u_e(x)$  due to viscous effects. The spanwise edge velocity component is assumed to correspond to its inviscid value. The viscous flow solutions are obtained by marching in the spanwise direction at each advancing chordwise location. This represents the first phase in an interactive loop that involves the fully three-dimensional boundary-layer equations. In subsequent phases, as before, the blowing velocity distribution is used to obtain improved inviscid flow solutions so that the fully three-dimensional boundary-layer equations can be solved with this interactive procedure.

The neglect of viscous effects in the spanwise component  $w_e$  is assumed to be second order. This assumption is contrary to the irrotationality condition, but trial calculations involving variations of both velocity conditions suggest that errors were smaller than those associated with convergence.

### 13.4 Transformed Equations

As in incompressible flows, it is again desirable to express the compressible boundary-layer equations in transformed variables. A convenient transformation is the compressible three-dimensional flow version of the Falkner–Skan transformation given by Eqs. (4.2.4), (4.5.3). With  $ds = h_1 dx$ , transformations for the independent variables are

$$x = x, \quad z = z, \quad d\eta = \left( \frac{u_\infty}{\rho_\infty u_\infty s} \right)^{1/2} \rho dy, \quad s = \int_0^x h_1 dx \quad (13.4.1)$$

For the dependent variables  $u, v, w$ , a two-component vector potential is introduced such that

$$\begin{aligned} \rho u h_2 \sin \theta &= \frac{\partial \psi}{\partial y}, & \rho w h_1 \sin \theta &= \frac{\partial \phi}{\partial y} \\ \overline{\rho v} h_1 h_2 \sin \theta &= - \left( \frac{\partial \psi}{\partial x} + \frac{\partial \phi}{\partial z} \right) + \rho_w v_w h_1 h_2 \sin \theta \end{aligned} \quad (13.4.2)$$

together with dimensionless parameters  $f$  and  $g$  defined by

$$\begin{aligned} \psi &= (\rho_\infty \mu_\infty u_\infty)^{1/2} h_2 \sin \theta f(x, z, \eta) \\ \phi &= (\rho_\infty \mu_\infty u_\infty)^{1/2} h_1 \sin \theta g(x, z, \eta) \end{aligned} \quad (13.4.3)$$

where the parameters expressed with subscript  $\infty$  indicate constant reference quantities which are usually taken as corresponding to freestream conditions.

Thus, with the transformations and definitions given by Eqs. (13.4.1) to (13.4.3), together with the eddy viscosity and turbulent Prandtl number definitions, the three-dimensional boundary-layer equations and their boundary conditions, Eqs. (10.5.5) to (10.5.8) and (10.5.13), for compressible laminar and turbulent flows can be written as

$$\begin{aligned} & (bf'')' + f''\theta + m_2(f')^2 + m_5f'g' + m_8(g')^2 + m_{11}c + m_{13}f'' \\ &= m_{10}f'\frac{\partial f'}{\partial x} + m_7g'\frac{\partial f'}{\partial z} \end{aligned} \quad (13.4.4)$$

$$\begin{aligned} & (bg'')' + g''\theta + m_4f'g' + m_3(g')^2 + m_9(f')^2 + m_{12}c + m_{13}g'' \\ &= m_{10}f'\frac{\partial g'}{\partial x} + m_7g'\frac{\partial g'}{\partial z} \end{aligned} \quad (13.4.5)$$

$$\theta' = m_1f' + m_6g' + m_{10}\frac{\partial f'}{\partial x} + m_7\frac{\partial g'}{\partial z} \quad (13.4.6)$$

$$(e_1E')' + E'\theta + e'_2 + m_{13}E' = m_{10}f'\frac{\partial E}{\partial x} + m_7g'\frac{\partial E}{\partial z} \quad (13.4.7)$$

$$\eta = 0, \quad f = g = f' = g' = 0, \quad E_w \text{ or } E'_w \text{ given} \quad (13.4.8a)$$

$$\eta = \eta_e, \quad f' = \bar{u}_e, \quad g' = \bar{w}_e, \quad E = 1 \quad (13.4.8b)$$

Here primes denote differentiation with respect to  $\eta$  and

$$f' = u/u_\infty, \quad g' = w/u_\infty, \quad E = H/H_e, \quad \bar{u}_e = \frac{u_e}{u_\infty}, \quad \bar{w}_e = \frac{w_e}{u_\infty} \quad (13.4.9a)$$

$$b = C(1 + \nu_t^+), \quad C = \frac{\rho\mu}{\rho_e\mu_e}, \quad c = \frac{\rho_e}{\rho}, \quad \nu_t^+ = \nu_t/\nu \quad (13.4.9b)$$

$$\begin{aligned} e_1 &= \frac{C}{\Pr} \left( 1 + \nu_t^+ \frac{\Pr}{\Pr_t} \right), \\ e_2 &= \frac{Cu_\infty^2}{H_e} \left( 1 - \frac{1}{\Pr} \right) [f'f'' + g'g'' + u_e \cos \theta (f'g'' + g'f'')] \end{aligned} \quad (13.4.9c)$$

The coefficients  $m_1$  to  $m_{13}$  are given by

$$\begin{aligned}
m_1 &= \frac{s^{1/2}}{h_1 h_2 \sin \theta} \frac{\partial}{\partial x} (s^{1/2} h_2 \sin \theta), \quad m_2 = -s k_1 \cot \theta, \\
m_3 &= s k_2 \cot \theta, \quad m_4 = -s k_{21}, \quad m_5 = -s k_{12}, \\
m_6 &= \frac{s^{1/2}}{h_1 h_2 \sin \theta} \frac{\partial}{\partial z} (s^{1/2} h_2 \sin \theta), \\
m_7 &= \frac{s}{h_2}, \quad m_8 = -s k_2 \csc \theta, \quad m_9 = -s k_1 \csc \theta, \quad m_{10} = \frac{s}{h_1} \quad (13.4.10) \\
-m_{11} &= m_2 \bar{u}_e^2 + m_5 \bar{u}_e \bar{w}_e + m_8 \bar{w}_e^2 - m_{10} \bar{u}_e \frac{\partial \bar{u}_e}{\partial x} - m_7 \bar{w}_e \frac{\partial \bar{u}_e}{\partial z}, \\
-m_{12} &= m_3 \bar{w}_e^2 + m_4 \bar{u}_e \bar{w}_e + m_9 \bar{u}_e^2 - m_{10} \bar{u}_e \frac{\partial \bar{w}_e}{\partial x} - m_7 \bar{w}_e \frac{\partial \bar{w}_e}{\partial z}, \\
m_{13} &= -\frac{\rho_w v_w}{\rho_\infty u_\infty} \sqrt{\frac{u_\infty s}{\nu_\infty}}
\end{aligned}$$

### 13.4.1 Attachment Line Equations

To transform the attachment-line equations, Eqs. (13.2.2) to (13.2.5), we define the transformed coordinates by

$$x = x, \quad z = z, \quad d\eta = \left( \frac{u_{xe}}{\rho_e \mu_e h_1} \right)^{1/2} \rho dy \quad (13.4.11)$$

the two-component vector potential by

$$\begin{aligned}
\rho u_x h_2 \sin \theta &= \frac{\partial \psi}{\partial y}, \quad \rho h_1 \sin \theta = \frac{\partial \phi}{\partial y}, \\
\overline{\rho v} h_1 h_2 \sin \theta &= -\left( \psi + \frac{\partial \phi}{\partial z} \right) + \rho_w v_w h_1 h_2 \sin \theta \quad (13.4.12a)
\end{aligned}$$

and the dimensionless  $\psi$  and  $\phi$  by

$$\begin{aligned}
\psi &= (\rho_e \mu_e u_{xe} h_1)^{1/2} h_2 \sin \theta f(z, \eta) \\
\phi &= (\rho_e \mu_e u_{xe} h_1)^{1/2} h_1 \sin \theta \frac{u_\infty}{u_{xe}} g(z, \eta) \quad (13.4.12b)
\end{aligned}$$

With these new variables, the attachment-line equations for a laminar flow can be written as

$$(bf'')' + \theta f'' - (f')^2 + m_5 f' g' + c(1 - \bar{w}_e m_5) + m_{13} f'' = m_7 \left( g' \frac{\partial f'}{\partial z} \right) \quad (13.4.13)$$

$$(bg'')' + \theta g'' + m_3 [(g')^2 - (\bar{w}_e)^2 c] + m_{13} g'' = m_7 \left( g' \frac{\partial g'}{\partial z} - c \bar{w}_e \frac{\partial \bar{w}_e}{\partial z} \right) \quad (13.4.14)$$

$$\theta' = f' + m_6 g' + m_7 \frac{\partial g'}{\partial z} \quad (13.4.15)$$

$$(e_1 E')' + \theta E' + e'_2 + m_{13} E' = m_7 \left( g' \frac{\partial E}{\partial z} \right) \quad (13.4.16)$$

Here  $m_3$ ,  $m_5$ ,  $m_6$  and  $m_7$  are:

$$\begin{aligned} m_3 &= h_1 k_2 \cot \theta \frac{u_\infty}{u_{xe}} \\ m_5 &= -h_1 \frac{u_\infty}{u_{xe}} k_{12} - \frac{h_1}{h_2} \frac{u_\infty}{u_{xe}^2} \frac{\partial u_{xe}}{\partial z} \\ m_6 &= \frac{(\rho_e \mu_e u_{xe} h_1)^{-1/2}}{h_2 \sin \theta} \frac{\partial}{\partial z} \left( \sqrt{\rho_e \mu_e u_{xe}} h_1 \sin \theta \frac{u_\infty}{u_{xe}} \right) \\ m_7 &= \frac{h_1}{h_2} \frac{u_\infty}{u_{xe}}, \quad m_{13} = -\frac{\rho_w v_w}{\rho_e u_{xe}} \sqrt{\frac{u_{xe} h_1}{\nu_e}} \end{aligned} \quad (13.4.17)$$

The coefficients  $e_1$  and  $e_2$  are:

$$e_1 = \frac{C}{\Pr} \left( 1 + \nu_t^+ \frac{\Pr}{\Pr_t} \right), \quad e_2 = \frac{Cu_\infty^2}{H_e} \left( 1 - \frac{1}{\Pr} \right) g' g'' \quad (13.4.18)$$

The boundary conditions are:

$$\eta = 0, \quad f = g = f' = g' = 0, \quad E_w \text{ or } E'_w \text{ given} \quad (13.4.19a)$$

$$\eta = \eta_e, \quad f' = 1, \quad g' = \bar{w}_e, \quad E = 1 \quad (13.4.19b)$$

### 13.4.2 Quasi-Three-Dimensional Boundary-Layer Equations

The quasi-three-dimensional boundary-layer equations are obtained from Eqs. (13.4.4) to (13.4.7) by neglecting the partial derivatives of the dependent variables with respect to  $z$ . They are given by

$$(bf'')' + f''\theta + m_2(f')^2 + m_5f'g' + m_8(g')^2 + m_{11}c + m_{13}f'' = m_{10}f' \frac{\partial f'}{\partial x} \quad (13.4.20)$$

$$(bg'')' + g''\theta + m_4f'g' + m_3(g')^2 + m_9(f')^2 + m_{12}c + m_{13}g'' = m_{10}f' \frac{\partial g'}{\partial x} \quad (13.4.21)$$

$$\theta' = m_1 f' + m_6 g' + m_{10} \frac{\partial f'}{\partial x} \quad (13.4.22)$$

$$(e_1 E')' + E'\theta + e'_2 + m_{13} E' = m_{10} f' \frac{\partial E}{\partial x} \quad (13.4.23)$$

The  $m$ 's and  $e$ 's remain the same except

$$m_5 = -k_{12}s\bar{u}_e^{-1}, \quad m_6 = 0 \quad (13.4.24)$$

and  $m_1$ ,  $m_2$  do not have the derivatives of  $\bar{u}_e$  and  $\bar{w}_e$  with respect to  $z$ .

### 13.5 Numerical Method

As in two-dimensional flows, the governing equations discussed in the previous subsections can be solved by using the box schemes discussed in Section 7.4. In the accompanying CD-ROM, Program 11, we discuss the solution procedure and briefly describe a computer program for three-dimensional flows with separation.

### 13.6 Modelling of Viscous Effects in Three-Dimensional Inviscid Flows

Once a solution of the boundary layer equations is obtained for a wing or for a high lift configuration, the viscous effects into a three-dimensional inviscid method can be incorporated by using either the “solid” displacement surface concept or the “transpiration” model concept discussed in Section 9.1 for two-dimensional flows. The transpiration model again is more convenient to adopt and is used in the calculations presented in Section 13.5.

The expression for the blowing velocity again is obtained from the continuity equation by integrating Eq. (10.5.5) from the wall  $y = 0$  to the edge of the boundary layer  $\delta$  for the real flow so that

$$v(\delta) = \frac{-1}{h_1 h_2 \sin \theta} \left[ \int_0^\delta \left( \frac{\partial}{\partial x} (uh_2 \sin \theta) \right) dy + \int_0^\delta \left( \frac{\partial}{\partial z} (wh_1 \sin \theta) \right) dy \right] (\equiv v_e) \quad (13.6.1)$$

Similarly, integrating Eq. (10.5.5) from  $\delta$  to  $y$  for the fictitious flow (in which  $u(y) = u_e$  and  $w(y) = w_e$ ), assuming that the normal velocity component at  $\delta$  is also  $v_e$ , yields

$$v^*(y) = v_e - \frac{(y - \delta)}{h_1 h_2 \sin \theta} \left[ \frac{\partial}{\partial x} (u_e h_2 \sin \theta) + \frac{\partial}{\partial z} (w_e h_1 \sin \theta) \right] \quad (13.6.2)$$

where  $v^*$  is the normal velocity of the fictitious flow.

Substituting  $v_e$  in Eq. (13.6.2) into Eq. (13.6.1) and making use of the definitions of the displacement thickness  $\delta_x^*$  and  $\delta_z^*$  we obtain

$$\begin{aligned} v^*(y) &= \frac{1}{h_1 h_2 \sin \theta} \left[ \frac{\partial}{\partial x} (u_e h_2 \sin \theta \delta_x^*) + \frac{\partial}{\partial z} (w_e h_1 \sin \theta \delta_z^*) \right] \\ &\quad - \frac{1}{h_1 h_2 \sin \theta} \left[ \frac{\partial}{\partial x} (u_e h_2 \sin \theta) + \frac{\partial}{\partial z} (w_e h_1 \sin \theta) \right] \end{aligned} \quad (13.6.3)$$

The value of  $v^*(y)$  in the above equation is the boundary condition that must be applied to the fictitious inviscid flow at a distance  $y$  from the wall in order to account for viscous effects on the inviscid flow. In particular, at  $y = 0$ , the expression for the blowing velocity is obtained from

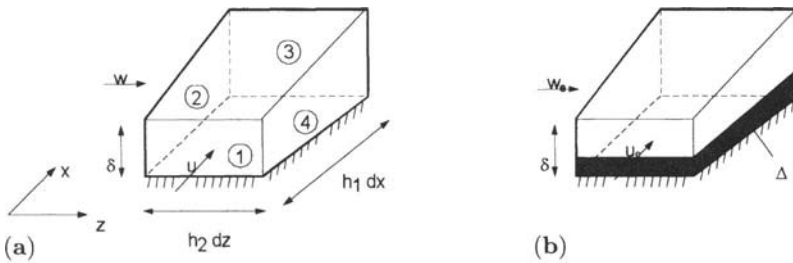


**Fig. 13.2.** Control volume for (a) the real flow and (b) the equivalent fictitious inviscid flow.

$$v_w = \frac{1}{h_1 h_2 \sin \theta} \left[ \frac{\partial}{\partial x} (h_2 u_e \sin \theta \delta_x^*) + \frac{\partial}{\partial z} (h_1 w_e \sin \theta \delta_z^*) \right] \quad (13.6.4)$$

Similarly an equation for the displacement surface,  $\Delta$ , in three-dimensional flows can be obtained by constructing a fictitious inviscid flow (Fig. 13.2b) which has the same mass flow as the real flow (Fig. 13.2a) through the faces 1, 2, 3, 4 of the control volume. As in two-dimensional flows, the fictitious flow has constant properties along a normal to the wall below the line  $y = \delta$ .

Equating the mass flow for real and fictitious flows leads to an equation for displacement surface,

$$\frac{\partial}{\partial x} (h_2 u_e \sin \theta (\Delta - \delta_x^*)) + \frac{\partial}{\partial z} (h_1 w_e \sin \theta (\Delta - \delta_z^*)) = 0 \quad (13.6.5)$$

This equation can be solved by a method of characteristics, i.e. by integrating

$$\frac{dz}{dx} = \frac{w_e h_1}{u_e h_2}, \quad \frac{d\Delta}{dx} = \frac{f(x, z)}{u_e h_2 \sin \theta} \quad (13.6.6)$$

where

$$f(x, z) = \frac{\partial}{\partial x} (h_2 u_e \sin \theta \delta_x^*) + \frac{\partial}{\partial z} (h_1 w_e \sin \theta \delta_z^*) - \Delta \left[ \frac{\partial}{\partial x} (h_2 u_e \sin \theta) + \frac{\partial}{\partial z} (h_1 w_e \sin \theta) \right] \quad (13.6.7)$$

In addition to using the blowing velocity as a boundary condition in the inviscid flow, as in two-dimensional flows, it is also necessary to apply the Kutta condition in the panel method (equal pressure for upper and lower surface at the trailing edge) at the displacement surface. Again, as in two-dimensional flows, the wake viscous effects are modeled by equivalent source distributions.

## 13.7 Interface Program

When a body-oriented coordinate system is used for three-dimensional boundary-layer calculations, it is necessary to compute the geometric parameters of the

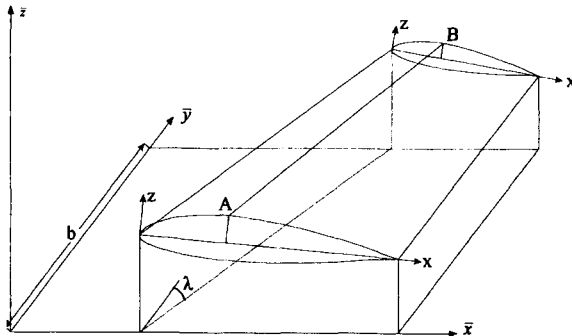


**Fig. 13.3.** Notation for the wing definition.

coordinate system  $(x_1, x_2)$  which correspond to the independent variables  $x$  and  $z$  defined in the boundary-layer equations given by Eqs. (7.2.19) to (7.2.21) for incompressible flows and Eqs. (10.5.5) for compressible flows. To discuss this further, we consider a swept tapered wing which is defined in the Cartesian coordinate system  $\bar{x}, \bar{y}, \bar{z}$  and has a sweep angle  $\lambda$  as shown in Fig. 13.3. Here  $\bar{x}$  is in the direction of the airplane longitudinal axis,  $\bar{y}$  is in the spanwise direction and  $\bar{z}$  is normal to the  $(\bar{x}, \bar{y})$  plane. We assume that the wing definition is given by a number of airfoil sections defined in the  $(x, z)$  coordinate system in planes  $\bar{y} = \text{constant}$ . For simplicity we assume that the root and tip airfoil sections are defined in planes  $\bar{y} = 0$  and  $\bar{y} = b$  and have chord lengths of  $c_r$  and  $c_b$ , respectively.

The relationship between the two coordinate systems  $(\bar{x}, \bar{z})$  and  $(x, z)$  for a point on the defining airfoil section (see Fig. 13.4) is given by the following expressions:

$$\bar{x} = \bar{x}_l + x \cos \alpha + z \sin \alpha \quad (13.7.1a)$$

$$\bar{z} = \bar{z}_l - x \cos \alpha + z \sin \alpha \quad (13.7.1b)$$

where  $\alpha$  is the angle of attack of the defining airfoil section and, with subscripts  $l$  and  $t$  denoting leading and trailing edges, respectively, is given by

$$\alpha = \tan^{-1} \left( \frac{\bar{z}_t - \bar{z}_l}{\bar{x}_t - \bar{x}_l} \right) \quad (13.7.2)$$

Noting that the relation between the local airfoil chord  $c$  and  $\alpha$ , for example,

$$c = \frac{\bar{x}_t - \bar{x}_l}{\cos \alpha} \quad (13.7.3)$$

Eqs. (13.4.1) can be written as

$$\bar{x} = \bar{x}_l + \left( \frac{x}{c} \right) (\bar{x}_t - \bar{x}_l) + \left( \frac{z}{c} \right) (\bar{z}_l - \bar{z}_r) \quad (13.7.4a)$$

$$\bar{z} = \bar{z}_l + \left( \frac{x}{c} \right) (\bar{z}_l - \bar{z}_t) + \left( \frac{z}{c} \right) (\bar{x}_t - \bar{x}_l) \quad (13.7.4b)$$

Since for an airfoil section

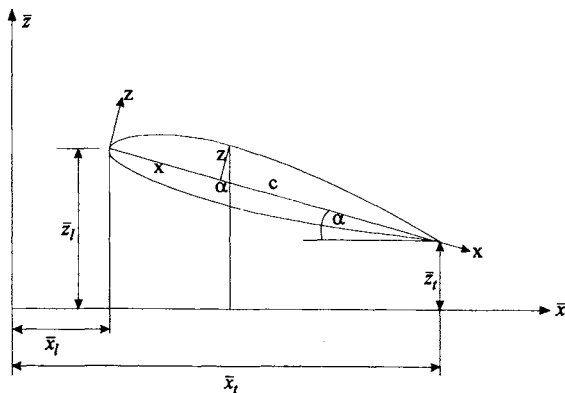


**Fig. 13.4.** Notation for the  $(\bar{x}, \bar{z})$  and  $(x, z)$  coordinate systems.

$$z = z(x)$$

it is clear from Eq. (13.7.4a) that  $\bar{x}$  and  $\bar{z}$  are functions of  $x$  and that they provide a relationship between  $\bar{x}$  and  $x$  and  $\bar{z}$  and  $z$  for a defining airfoil section.

From here on, the  $\bar{x}$  and  $\bar{z}$  coordinates of the defining airfoil sections will be designated by subscripts  $r$  and  $b$ . The sections in between the defining root and tip sections can be obtained for each dimensionless spanwise location  $\bar{y}/b$  by projecting line  $AB$  in Fig. 13.3 into the  $(\bar{x}, \bar{y})$  and  $(\bar{y}, \bar{z})$  planes and by using linear interpolation (see Fig. 13.5).

$$\bar{x} = \bar{x}_r + (\bar{x}_b - \bar{x}_r) \left( \frac{\bar{y}}{b} \right) \quad (13.7.5a)$$

$$\bar{z} = \bar{z}_r + (\bar{z}_b - \bar{z}_r) \left( \frac{\bar{y}}{b} \right) \quad (13.7.5b)$$

Note that in the above equations  $\bar{x}$  and  $\bar{z}$  denote the coordinates of the airfoils in between the root and tip sections and they are distinct from  $\bar{x}$  and  $\bar{z}$  in Eqs. (13.7.4) which represent the coordinates of the root and tip sections. Equations (13.7.5) are the parametric equations of a wing surface which can, in principle, be expressed in the form given by Eq. (13.2.1),

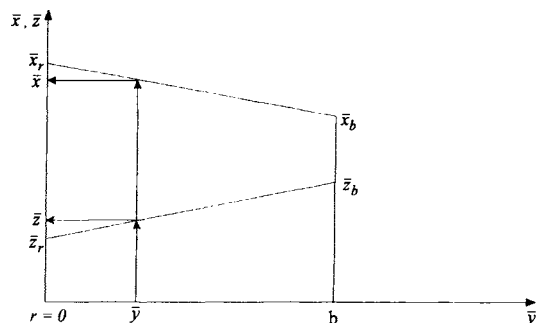


**Fig. 13.5.** Spanwise interpolation for section coordinates  $\bar{x}$  and  $\bar{z}$  along constant percent chord lines ( $x = \text{const}$ ) at fixed  $\bar{y}$ .

$$F(\bar{x}, \bar{y}, \bar{z}) = 0 \quad (13.2.1)$$

Since  $\bar{x}$  and  $\bar{z}$  are functions of  $x$  and  $\bar{y}$ , the surface of the wing can also be defined by coordinates  $(x/c)$  and  $\bar{y}/b$ , and the above relation can be written in the form

$$f\left(\frac{x}{c}, \frac{\bar{y}}{b}\right) = 0 \quad (13.7.6)$$

thus defining a surface coordinate system formed by constant percent chord lines and constant percent spanlines.

The coordinates lines formed by constant  $(x/c)$  values are satisfactory provided the upper and lower surfaces of the wing are treated separately. When the stagnation point of the wing is located on the lower surface, the boundary-layer calculations contain a portion of the lower surface, and the meaning of coordinate  $(x/c)$  becomes ambiguous since  $z/c$  is a dual function of  $x/c$  and has a singularity at  $x/c = 0$ . To avoid this ambiguity and also to stretch the coordinate near the leading edge where flow quantities vary rapidly, we can, for example, relate  $x/c$  to a new coordinate  $x_1$  by

$$\frac{x}{c} = 1 - \cos x_1 \quad (13.7.7)$$

Here  $x_1 = 0$  corresponds to the chordwise coordinate in Fig. 13.3 where  $x_1 = 0$  denotes the leading edge and  $x_1 = \pm \frac{\pi}{2}$  to the trailing edge with positive values of  $x_1$  representing the upper surface and negative values the lower surface.

In general, the surface coordinates  $x_1$  and  $x_2$  ( $\equiv \bar{y}/b$ ) which correspond to the independent variables  $x$  and  $z$  used in Eqs. (10.5.5) to (10.5.8), constitute a nonorthogonal coordinate system embedded in the wing surface.

### 13.7.1 Geometric Parameters of the Coordinate System

To discuss the calculation of the geometric parameters, we write the metric coefficient along a curve in space, with  $P$  denoting an independent parameter, as

$$h^2 = \left(\frac{\partial \bar{x}}{\partial P}\right)^2 + \left(\frac{\partial \bar{y}}{\partial P}\right)^2 + \left(\frac{\partial \bar{z}}{\partial P}\right)^2 \quad (13.7.8)$$

Taking  $P = x_1$  along the curves  $x_2 = \text{const}$ , we obtain

$$h_1^2 = \left(\frac{\partial \bar{x}}{\partial x_1}\right)^2 + \left(\frac{\partial \bar{z}}{\partial x_1}\right)^2 \quad (13.7.9a)$$

Similarly, taking  $P = x_2$  along the curves  $x_1 = \text{const}$ , we get

$$h_2^2 = b^2 + \left(\frac{\partial \bar{x}}{\partial x_2}\right)^2 + \left(\frac{\partial \bar{z}}{\partial x_2}\right)^2 \quad (13.7.9b)$$

where the derivatives in Eqs. (13.7.9) are obtained numerically.

Since the unit tangent vector  $\vec{t}$  along a curve is given by

$$\vec{t} = \frac{d\vec{r}}{ds} = \frac{d\vec{r}}{dP} \frac{1}{(ds/dP)} = \frac{1}{h} \frac{d\vec{r}}{dP} \quad (13.7.10)$$

the unit tangent vector  $\vec{t}_1$  along the curve  $x_2 = \text{const}$  is

$$\vec{t}_1 = \frac{1}{h_1} \left[ \left( \frac{\partial \bar{x}}{\partial x_1} \right) i + \left( \frac{\partial \bar{z}}{\partial x_1} \right) k \right] \quad (13.7.11a)$$

where  $i, j, k$  denote the unit vectors in the coordinate directions  $\bar{x}, \bar{y}, \bar{z}$ , respectively. Similarly, the unit tangent vector  $\vec{t}_2$  along the curve  $x_1 = \text{const}$  is

$$\vec{t}_2 = \frac{1}{h_2} \left[ \left( \frac{\partial \bar{x}}{\partial x_2} \right) i + bj + \left( \frac{\partial \bar{z}}{\partial x_2} \right) k \right] \quad (13.7.11b)$$

The angle between the coordinate lines is then

$$\cos \theta = \vec{t}_1 \cdot \vec{t}_2 = \frac{1}{h_1 h_2} \left( \frac{\partial \bar{x}}{\partial x_1} \frac{\partial \bar{x}}{\partial x_2} + \frac{\partial \bar{z}}{\partial x_1} \frac{\partial \bar{z}}{\partial x_2} \right) \quad (13.7.12)$$

Once the metric coefficients  $h_1$  and  $h_2$  and their derivatives together with coordinate angle  $\theta$  are determined, the curvature parameters are calculated from their definitions in Eqs. (7.2.23).

Once the surface coordinate system is selected, its geometric parameters can be calculated by making use of Eqs. (13.7.9), (13.7.12), (7.2.22) and (7.2.23), and the relation between the Cartesian coordinates  $(\bar{x}, \bar{y}, \bar{z})$  and the surface coordinates  $(x_1, x_2)$  can be written in the form:

$$\bar{x} = \bar{x}(x_1, x_2) \quad \bar{z} = \bar{z}(x_1, x_2) \quad (13.7.13a)$$

$$\bar{y} = bx_2 \quad (13.7.13b)$$

We note that the geodesic curvature of the curve,  $x_1 = \text{const}$ , namely,  $k_2$  given by Eq. (7.2.22b) is zero because of the straight-line development of the wing and that all orders of partial derivatives of  $\bar{y}$  with respect to  $x_1$  and  $x_2$ , except  $\partial \bar{y} / \partial x_2 = b$ , are zero and  $\partial^2 \bar{x} / \partial x_2^2$  and  $\partial^2 \bar{z} / \partial x_2^2$  are also zero because  $\bar{x}$  and  $\bar{z}$  are linear in  $x_2$  (see Eqs. (13.7.5)). Then  $h_1$ ,  $h_2$  and  $\theta$  are calculated from Eqs. (13.7.9) and (13.7.12). With  $k_2 = 0$ , Eqs. (7.2.22a), (7.2.23a) and (7.2.23d) become, with  $h_{12} = h_1 h_2 \cos \theta$ ,

$$k_1 = \frac{1}{h_1 h_2 \sin \theta} \left[ \frac{1}{h_1} \frac{\partial h_{12}}{\partial x_1} - \frac{h_{12}}{h_1^2} \frac{\partial h_1}{\partial x_1} - \frac{\partial h_1}{\partial x_2} \right] \quad (13.7.14a)$$

$$k_{12} = \frac{1}{h_1 h_2 \sin^2 \theta} \left[ (1 + \cos^2 \theta) \frac{\partial h_1}{\partial x_2} - 2 \cos \theta \frac{\partial h_2}{\partial x_1} \right] \quad (13.7.14b)$$

$$k_{21} = \frac{1}{h_1 h_2 \sin^2 \theta} \left[ (1 + \cos^2 \theta) \frac{\partial h_2}{\partial x_1} - 2 \cos \theta \frac{\partial h_1}{\partial x_2} \right] \quad (13.7.14c)$$

The terms appearing in Eqs. (13.7.14) are obtained from Eqs. (13.7.9) and (13.7.12).

$$\frac{\partial h_1}{\partial x_1} = \frac{1}{h_1} \left( \frac{\partial \bar{x}}{\partial x_1} \frac{\partial^2 \bar{x}}{\partial x_1^2} + \frac{\partial \bar{z}}{\partial x_1} \frac{\partial^2 \bar{z}}{\partial x_1^2} \right) \quad (13.7.15a)$$

$$\frac{\partial h_2}{\partial x_1} = \frac{1}{h_2} \left( \frac{\partial \bar{x}}{\partial x_2} \frac{\partial^2 \bar{x}}{\partial x_1 \partial x_2} + \frac{\partial \bar{z}}{\partial x_2} \frac{\partial^2 \bar{z}}{\partial x_1 \partial x_2} \right) \quad (13.7.15b)$$

$$\frac{\partial h_{12}}{\partial x_1} = \frac{\partial \bar{x}}{\partial x_2} \frac{\partial^2 \bar{x}}{\partial x_1^2} + \frac{\partial \bar{z}}{\partial x_2} \frac{\partial^2 \bar{z}}{\partial x_1^2} + \frac{\partial \bar{x}}{\partial x_1} \frac{\partial^2 \bar{x}}{\partial x_1 \partial x_2} + \frac{\partial \bar{z}}{\partial x_1} \frac{\partial^2 \bar{z}}{\partial x_1 \partial x_2} \quad (13.7.15c)$$

$$\frac{\partial h_1}{\partial x_2} = \frac{1}{h_2} \left( \frac{\partial \bar{x}}{\partial x_1} \frac{\partial^2 \bar{x}}{\partial x_1 \partial x_2} + \frac{\partial \bar{z}}{\partial x_1} \frac{\partial^2 \bar{z}}{\partial x_1 \partial x_2} \right) \quad (13.7.15d)$$

To obtain the partial derivatives in Eqs. (13.5.9), (13.5.14) and (13.5.15), we differentiate Eqs. (13.5.5), which are functions of  $x/c$  and  $\bar{y}/b$  and are related to  $x_1$  and  $x_2$  through Eqs. (13.7.7) and (13.7.13b). Also from Eqs. (13.5.1) we can obtain relations between  $\bar{x}$ ,  $\bar{z}$  and  $x$  for the defining root and tip sections, for example, for the root section,  $z$

$$\bar{x}_r = \bar{x}_{tr} + x \cos \alpha_r + z \sin \alpha_r \quad (13.7.16a)$$

$$\bar{z}_r = \bar{z}_{lr} - x \sin \alpha_r + z \cos \alpha_r \quad (13.7.16b)$$

Since  $x$  is related to  $x_1$  through Eq. (13.7.7), and  $z$  is a function of  $x$ , these equations can be used to find the partial derivatives of  $\bar{x}_r$  and  $\bar{z}_r$  with respect to  $x_1$ .

### 13.7.2 Calculation of Inviscid Velocity Components for Boundary-Layer Grid

Since the inviscid flow calculations use a Cartesian coordinate system and the inviscid velocity vector on the wing surface is available in terms of its Cartesian components  $V_{\bar{x}}$ ,  $V_{\bar{y}}$ ,  $V_{\bar{z}}$ ,

$$\vec{V} = iV_{\bar{x}} + jV_{\bar{y}} + kV_{\bar{z}} \quad (13.7.17)$$

it is necessary to express  $\vec{V}$  in the nonorthogonal boundary-layer coordinate system  $(x, z)$ . This can be done by taking a dot product of unit vectors  $\vec{t}_1$  and  $\vec{t}_2$  with Eq. (13.5.17) to obtain the projections of the resultant velocity on the  $x$  and  $z$  axis, respectively.

$$V_x = \vec{V} \cdot \vec{t}_1, \quad V_z = \vec{V} \cdot \vec{t}_2 \quad (13.7.18)$$

The nonorthogonal velocity components for the boundary-layer coordinate system are then obtained from (see Fig. 13.6)

$$u_e = \frac{V_x - V_z \cos \theta}{\sin^2 \theta}, \quad w_e = \frac{V_z - V_x \cos \theta}{\sin^2 \theta} \quad (13.7.19)$$

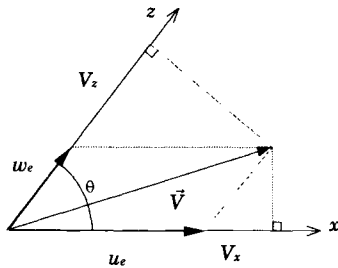


**Fig. 13.6.** Resolution of the inviscid velocity components for a nonorthogonal coordinate system.

where  $\theta$  denotes the angle between the coordinate lines. The resultant inviscid velocity  $u_{te}$  is given by:

$$u_{te}^2 = u_e^2 + w_e^2 + 2u_e w_e \cos \theta \quad (13.7.20)$$

In general, the velocity distribution grid of an inviscid method does not coincide with the grid used in boundary-layer calculations. For this reason, it is necessary to interpolate the inviscid velocity distribution once the velocity components  $u_e$  and  $w_e$  are computed for the inviscid grid. For simplicity, single variable interpolation (first in the  $x$ -direction then in the  $z$ -direction) is used.

## 13.8 Applications of the Interactive Boundary-Layer Method: Subsonic Flows

In this section we discuss the applications of the interactive boundary layer method described in the previous sections to subsonic flows on wings (subsection 13.8.1 and 13.8.2) and multielement wings (subsection 13.8.3). The extension of the applications to transonic flows is discussed in the following section.

Before we discuss the application of the method to subsonic flows, it is useful to describe the calculation procedure in some detail. The calculations begin with an inviscid flow method for a given wing geometry and freestream conditions (Fig. 13.7). Once the external velocity distribution is obtained the input data to the interface program is rearranged so that at first the nonorthogonal coordinate system for the boundary layer program and the geometric parameters appearing in the boundary-layer equations are calculated with the procedure described in subsection 13.7.1. The velocity components  $u_e(x, z)$  and  $w_e(x, z)$  for the boundary-layer grid  $(x, z, \eta)$  are then calculated from the Cartesian components  $V_x, V_y, V_z$  with the procedure described in subsection 13.7.2. Upon the completion of these tasks the upper and lower surfaces of the wing are identified in order to perform the boundary-layer calculations separately for each surface.

As discussed in Section 13.2 the boundary-layer calculations require initial conditions in the  $(z, y)$ -plane at  $x = x_0$  and initial conditions in the  $(x, y)$ -plane at  $z = z_0$ . In the computer program discussed in the accompanying CD-ROM,

those in the  $(z, y)$ -plane are obtained by solving the attachment line equations given by Eqs. (13.4.13) to (13.4.16) subject to their boundary conditions given by Eq. (13.4.19) for laminar flows. The initial conditions in the  $(x, y)$ -plane are obtained by solving the quasi-three-dimensional boundary layer equations given by Eqs. (13.4.20) to (13.4.23) subject to their boundary conditions given by Eqs. (13.4.8) and (9.1.4) for both laminar and turbulent flows at the first spanwise station near the wing-fuselage intersection. At the first cycle the onset of the transition location and the switch location from standard to inverse mode are estimated to be at an  $x$ -location before the pressure peak.

For all the calculations presented in this section the inviscid flow calculations were performed with the panel method by Hess [2], the boundary-layer calculations for  $nz > nz_0$  were performed by solving the quasi-three-dimensional boundary-layer equations. While the characteristic box method in the inverse mode can also be used for this purpose, this method has yet to be developed for flows with negative streamwise velocity component; presently it has only been tested for flows with negative spanwise velocity component.

Once the boundary-layer solutions are obtained for all spanwise and chordwise boundary-layer stations for either input or computed transition locations by making several sweeps in the chordwise direction at each spanwise location, the blowing velocity and displacement surface distributions are calculated for inviscid flow calculations as discussed in Section 13.6. The procedure is then repeated with inviscid flow calculations which now account for the viscous effects. The velocity components  $u_e$  and  $w_e$  and pressure coefficient  $c_p$  distributions are calculated at the displacement surface. Pressures are then integrated to obtain the force coefficients, i.e., lift, moment coefficient and the induced drag coefficients discussed in subsection 13.8.2.

In the next solution (cycle two) of the quasi-three-dimensional boundary-layer calculations, the onset of transition is calculated during the first sweep. It is not computed at each sweep as well as in each cycle to save computer time and effort. Since the linear stability equations do not contain partial derivatives with respect to  $x$  and  $z$ , the laminar boundary-layer profiles obtained by solving the quasi-three-dimensional boundary-layer equations in a nonorthogonal coordinate system must be expressed in an orthogonal coordinate system. With  $\beta$  denoting the positive angle between the  $\bar{x}$  and the  $x$  axis (Fig. 13.8), the  $\bar{u}$  and  $\bar{w}$  profiles in the  $(\bar{x}, \bar{z})$  orthogonal coordinate system are related to the  $u$  and  $w$  profiles in the  $(x, z)$  nonorthogonal coordinate system by

$$\bar{u} = u \cos \beta + w \cos(\theta + \beta) \quad (13.8.1a)$$

$$\bar{w} = u \sin \beta + w \sin(\theta + \beta) \quad (13.8.1b)$$

After the onset of transition is calculated, turbulent flow calculations are performed for one surface for all  $x$ -stations, including the wake. These laminar and turbulent flow calculations are then repeated for all spanwise stations, one

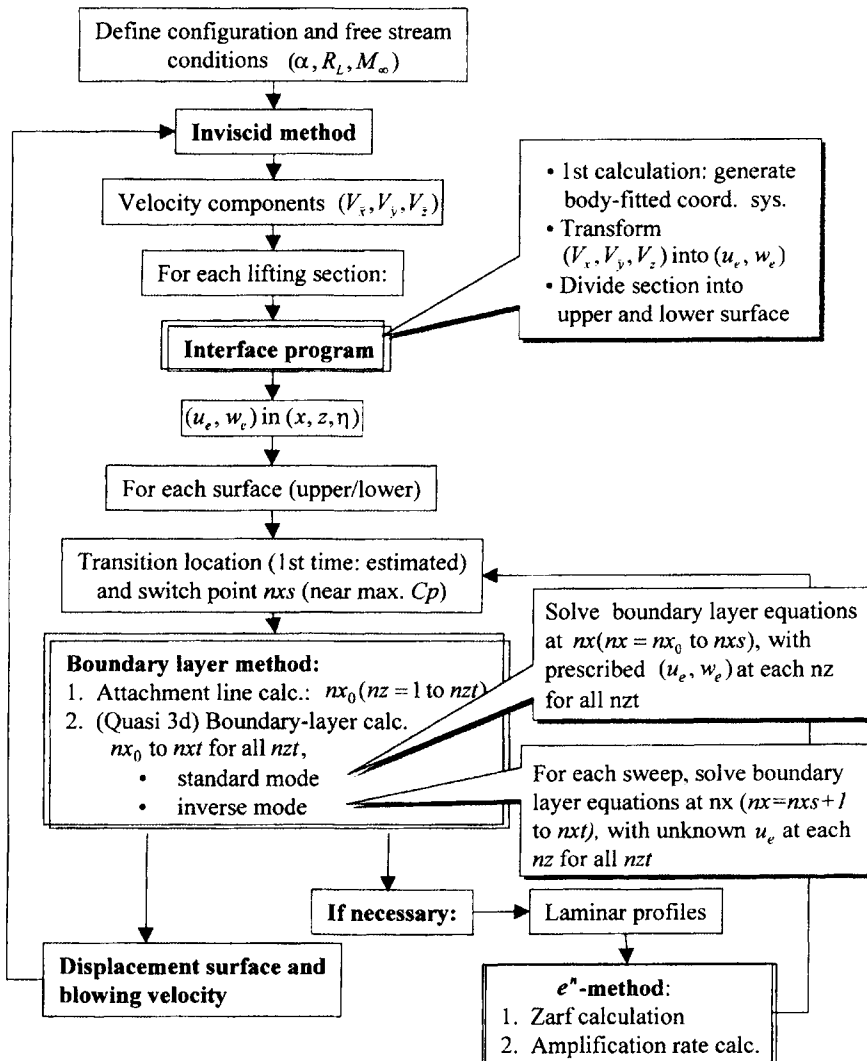


Fig. 13.7. Procedure for inviscid/viscous calculations.

by one until all the boundary-layer solutions on the wing and in the wake are obtained for the upper surface. An identical procedure is then repeated for the lower surface.

### 13.8.1 SAAB Wing

Bertelrud [3] tested the outer part of the wing of a SAAB 32 Lansen in a wind tunnel and measured the distribution of external velocity, pressure, momentum thickness, shape factor, and skin friction coefficient at various locations on the

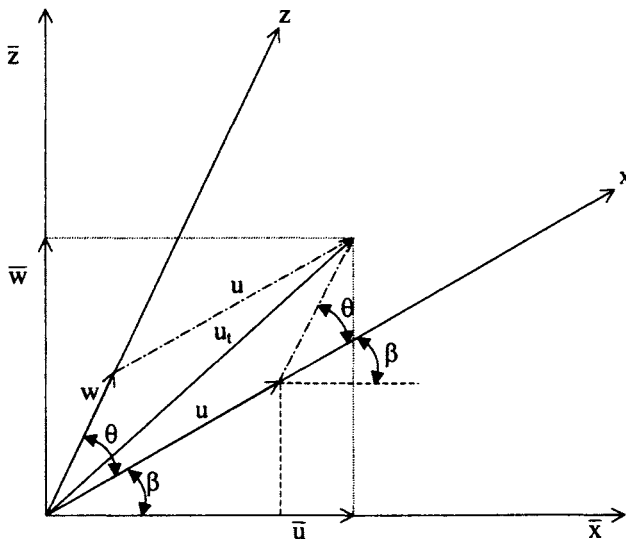


Fig. 13.8. The velocity profiles in  $(x, z)$  and  $(\bar{x}, \bar{z})$  coordinate systems.

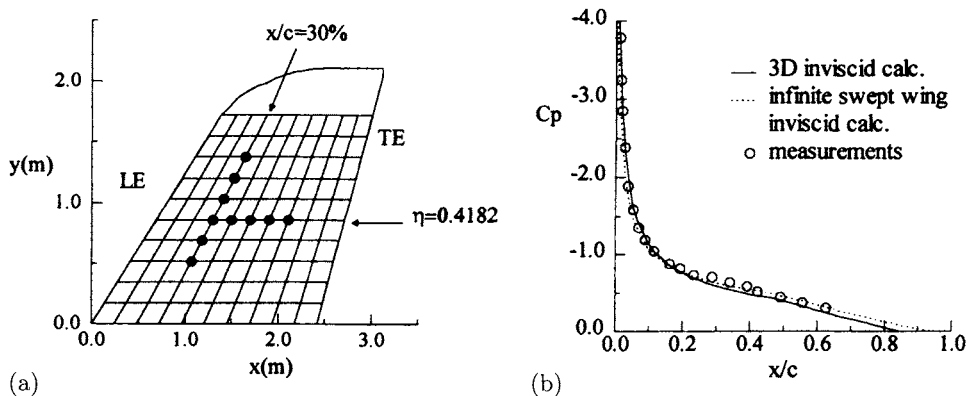


Fig. 13.9. (a) Location of boundary layer measurements. (b) Comparison of measured and calculated pressure distributions  $\eta_b = 0.40$ ,  $\alpha = 14.4^\circ$ .

wing. The wing is symmetric, has an aspect ratio of 2.27, a taper ratio of 0.6 and a leading edge sweep angle of  $39^\circ$ .

Since the exact geometry of the tip of the wing was not precisely described, at first the calculations reported in [4] were performed with various tips to address the effect of the tip shape on the flowfield predictions where measurements were reported, Fig. 13.9a.

Inviscid calculations using the Hess panel method described in [2] were performed for three angles of attack ( $0^\circ$ ,  $4.8^\circ$  and  $14.4^\circ$ ), for which experimental data was available. No noticeable differences in velocity and pressure coefficient distributions were observed at the locations where measurements were reported

for the various tip shapes. Figure 13.9b shows a typical comparison between pressure coefficient measurements and inviscid calculations.

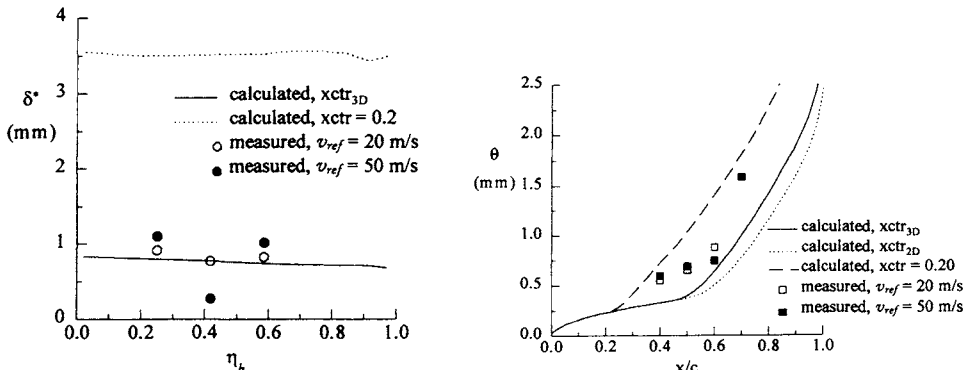
Measurements were made for several freestream velocities;  $u_{\text{ref}} = 20, 40$  and  $50 \text{ m/s}$ . Since most of the data was obtained at  $u_{\text{ref}} = 40 \text{ m/s}$ , all viscous/inviscid calculations reported in [4] were performed at that velocity, which corresponds to a Reynolds number of  $5.6 \times 10^6$  based on the root chord. The transition calculations were initially made for two dimensional flows with the  $e^n$ -method. These calculations were then followed with the  $e^n$ -method for three-dimensional flows with velocity profiles obtained by solving the quasi three-dimensional boundary-layer equations.

Table 13.1 presents a comparison between the transition locations obtained by using the 2D ( $\text{xctr}_{2D}$ ) and 3D ( $\text{xctr}_{3D}$ )  $e^n$ -methods at different spanwise locations and angles of attack. While the differences for the upper surface at  $\alpha = 14.4^\circ$  are minimal, they are relatively small at  $\alpha = 0, 4.8^\circ$ , and rather large at  $\alpha = 14.4^\circ$  for the lower surface due to the growth of crossflow disturbances in the accelerating flow region.

**Table 13.1.** Calculated transition locations on the SAAB wing; (a) upper surface and (b) lower surface.

(a)				(b)			
$\alpha$ (°)	$\eta_b$	$\text{xctr}_{2D}$	$\text{xctr}_{3D}$	$\alpha$ (°)	$\eta_b$	$\text{xctr}_{2D}$	$\text{xctr}_{3D}$
0	0.0843	0.57	0.56	4.8	0.0843	0.65	0.175
	0.2529	0.54	0.452		0.4216	0.64	0.134
	0.4216	0.52	0.441		0.6745	0.65	0.166
	0.6745	0.51	0.461		0.7585	0.65	0.187
	0.9148	0.50	0.445		0.8431	0.70	0.251
4.8	0.0843	0.0833	0.0320	14.4	0.9148	0.75	0.400
	0.2529	0.0612	0.0199		0.0843	0.80	0.109
	0.4216	0.0235	0.0172		0.2529	0.80	0.107
	0.6745	0.0156	0.0163		0.4216	0.80	0.118
	0.9148	0.0156	0.0181		0.6745	0.75	0.1647
14.4	0.0843	0.0015	0.0047		0.9148	0.75	0.186
	0.2529	0.0012	0.0028				
	0.4216	0.0010	0.0025				
	0.6745	0.0004	0.0027				
	0.9148	0.004	0.0029				

Figure 13.10a shows the variation of the calculated and measured streamwise displacement thickness  $\delta^*$  along the span at  $x/c = 0.3$  with transition specified at  $x/c = 0.20$  arbitrarily and at the calculated transition locations ( $\text{xctr}_{3D}$ ). Results demonstrate that the flow is indeed laminar at that chordwise station and that the determination of the transition location is important and should be included in any calculation method, including Navier-Stokes methods, to predict viscous effects accurately.



**Fig. 13.10.** (a) Displacement thickness variation along the span  $x/c = 0.3$  and (b) Momentum thickness variation at  $\eta_b = 0.40$ , both at  $\alpha = 0$ .

Figure 13.10b shows the variation of the streamwise momentum thickness,  $\theta$ , distribution, along the chord at  $\eta_b = 0.40$  at  $\alpha = 0^\circ$  with the specified transition location ( $xctr = 0.20$ ), transition location determined from two- ( $xctr_{2D} = 0.52$ ) and three-dimensional ( $xctr_{3D} = 0.44$ ) calculations. The results obtained with the calculated transition locations agree better with experimental data, although they do not match the data very accurately.

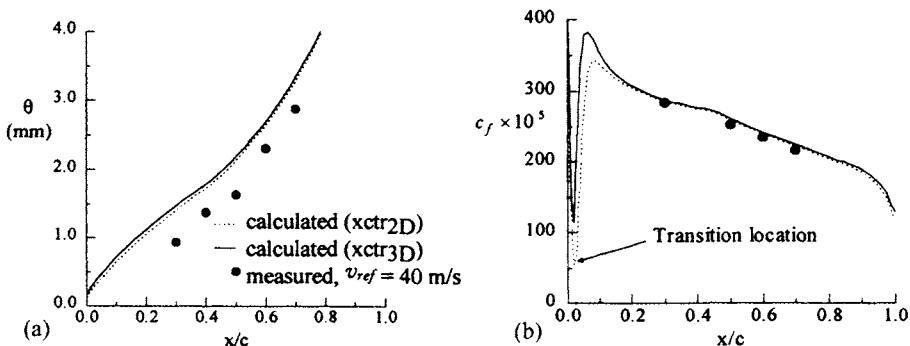
Figure 13.11 shows the results for  $\alpha = 4.8^\circ$  at the same spanwise station. Both total skin friction and streamwise momentum thickness distributions are represented and the agreement between measurements and calculations is good. The effects of transition are limited to the flow near the leading edge only, where no data was available for comparison.

Figure 13.12 shows the results for  $\alpha = 14.4^\circ$ . Again, the agreement between measured and calculated skin friction and momentum thickness distributions is good. A slight improvement is observed with calculated transition locations ( $xctr_{3D}$ ).

### 13.8.2 RAE Wing

The RAE wing, tested by Lovell [5], has an airfoil section having a considerable rear loading with the maximum thickness of 11.7% occurring at 37.5% chord and the maximum camber occurring at 75% chord. It has no twist nor dihedral, but has a quarter-chord sweep angle of  $28^\circ$ , a taper ratio of 1/4 and an aspect ratio of 8.35. The experiments were conducted at a test Reynolds number of  $1.35 \times 10^6$  with one set of measurements corresponding to free transition and with another to fixed transition for a freestream Mach number of 0.223. The wing has a semispan of 1.07 m and a mean aerodynamic chord of 0.26 m.

In one set of Lovell's experiments, transition was set near the leading edge using a series of 0.5 mm diameter wires positioned streamwise around the leading edge from 10% chord on the upper surface to 10% chord on the lower surface.



**Fig. 13.11.** (a) Momentum thickness and (b) skin friction coefficient distributions at  $\alpha = 4.8^\circ$  and  $\eta_b = 0.40$ .

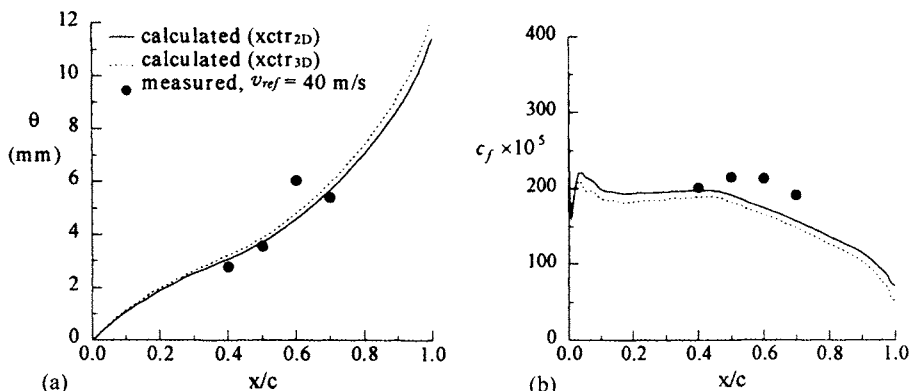


**Fig. 13.12.** (a) Momentum thickness and (b) skin friction coefficient distributions at  $\alpha = 14.4^\circ$  and  $\eta_b = 0.40$ .

Ten wires were equally spaced across each half wing. Measurements showed that the maximum lift coefficient with fixed transition is higher than that with free transition. Lovell noted, however, that “a larger portion is probably caused by the tendency of the streamwise wires to act as vortex generators.” Also, at post stall conditions, the flow became largely unsteady and only average measurements were reported. Therefore, near maximum lift, calculated results with fixed transition should be compared with free transition measurements. Both sets of experimental data are given in Fig. 13.13 which shows the lift coefficient variation with angle of attack. Each calculated lift curve is obtained with the wing described by 10 cross-sections distributed along the span, each cross-section being defined by 63 points with a higher point concentration around the leading and the trailing edges. Calculations were performed with angle of attack increments of  $2^\circ$  until  $10^\circ$ . The increment in angle of attack is reduced to  $1^\circ$  beyond that point. Results indicate that the agreement between measured and calculated lift coefficient is excellent up to  $14^\circ$ . At  $15^\circ$ , the boundary layer

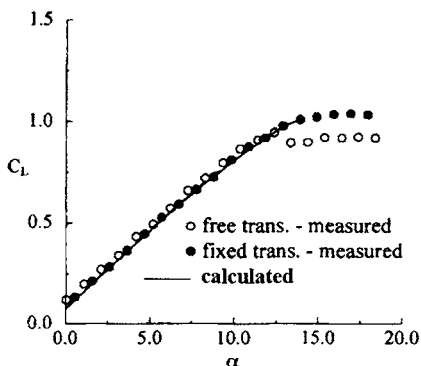


**Fig. 13.13.** Effect of turbulence model on the lift coefficient of the RAE wing.

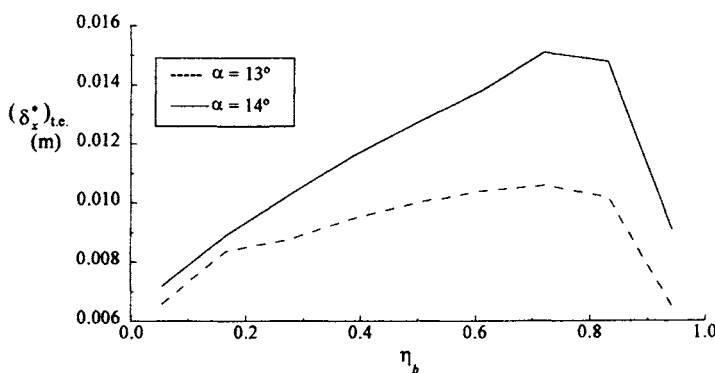


**Fig. 13.14.** Chordwise trailing edge displacement thickness distributions along the span.

calculations at  $\eta_b = 0.7$  do not converge near the trailing edge due to the large separated flow region.

Figures 13.14 and 13.15 show the chordwise trailing edge displacement thickness and flow separation along the span at angles of attack,  $\alpha = 13^\circ$  and  $14^\circ$ . As can be seen, there is a significant increase in the growth of displacement thickness and the amount of flow separation with one degree increase in  $\alpha$ . From  $\alpha = 13^\circ$  to  $14^\circ$  the Maximum  $(\delta_x^*)_{te}$  is multiplied by a factor of 1.6 indicating that the wing is at or very close to stall conditions. The results in Fig. 13.14 also indicate that for a swept non-twisted wing, stall initiates near the tip, at about  $\eta_b = 0.7$ - $0.8$ .

Before we present the comparison between the measured and calculated drag coefficients, it is useful to discuss our approach to the drag calculations. As discussed in [Chapter 10, 2], the fundamental theorems of potential flow state that in three-dimensional cases a body cannot be lifting unless it sheds a vortex wake which represents energy imparted to the fluid, implying a corresponding drag on the body, even in inviscid flow. Since this drag is present only because of the lift, it is often designated drag-due-to-lift or induced drag. Because of the presence of tip vortices, the flow incidence at a given spanwise location, the effective

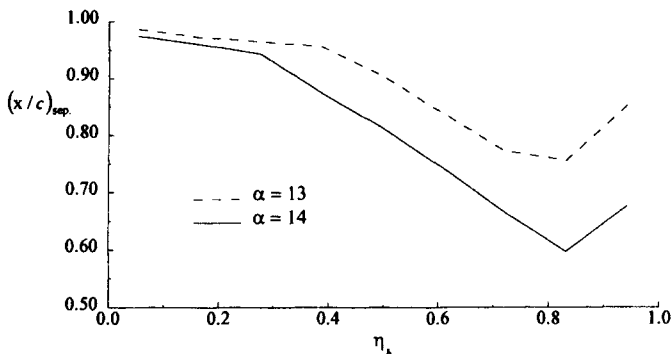


Fig. 13.15. Distribution of flow separation along the span at two angles of attack.

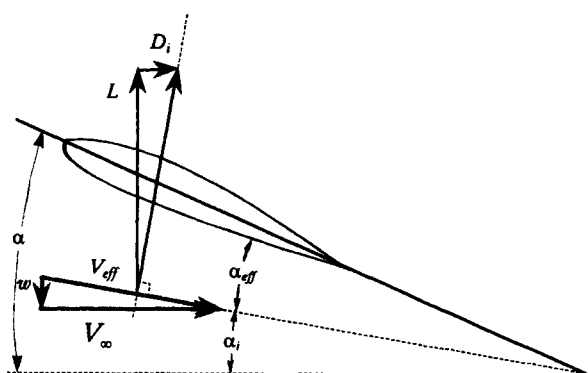
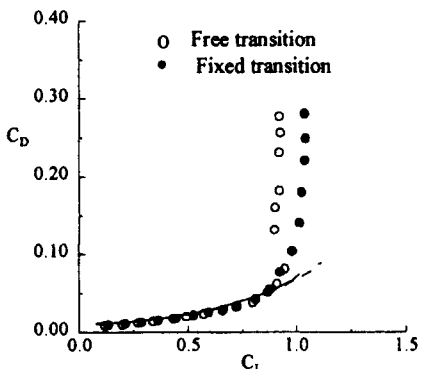


Fig. 13.16. Downwash and induced drag.

angle of attack,  $\alpha_{eff}$ , differs from that of the overall geometry,  $\alpha$  (existence of an induced angle,  $\alpha_i$ , (see Fig. 13.16). The lift force (component normal to the incident flow) generated at that spanwise location is therefore not in the same direction as the lift force of the whole configuration. The offset constitutes the drag due to lift, or induced drag, and can be evaluated by calculating the energy in the wake by a far-wake procedure known as Trefftz-plane analysis [Chapter 10, 2]. Alternatively, the calculated pressures may be integrated over the body panels to give the component of force in the freestream direction. In the limit of a large number of panels these two approaches converge to the same drag. It turns out that the Trefftz-plane analysis approaches its asymptotic value more rapidly with panel number than the pressure integration. In past years, when panel numbers were restricted, the former approach was preferred. Now with more powerful computers, either approach may be used. The agreement between the drags computed by the two procedures is a measure of the accuracy of the calculations. In the calculations reported in [4], far field approach was used to calculate the induced drag.



**Fig. 13.17.** Comparison of calculated and measured drag coefficients for the RAE wing.

For real flows, the viscous effects modify the pressure distribution, thus adding to the pressure drag, so that induced drag and pressure drag do not match any longer. For small to moderate angles of attack, i.e. relatively small induced angles, the drag coefficient for three-dimensional configurations can be calculated by adding the induced drag coefficient  $C_{D_i}$  (due to lift) to the profile drag coefficient,  $c_d$ , (due to viscosity), by

$$C_D = C_{D_i} + \frac{1}{S} \int_0^b c(y)c_d(y) dy \quad (13.8.2)$$

Here  $c$  is the local chord and  $S$  is the reference area used to non-dimensionalize drag. The profile drag coefficient  $c_d$  can be calculated from the Squire-Young formula [2].

$$c_d = 2 \left( \frac{\theta}{c} \right) (\bar{u}_e)^{0.5(H+5)} \quad (13.8.3)$$

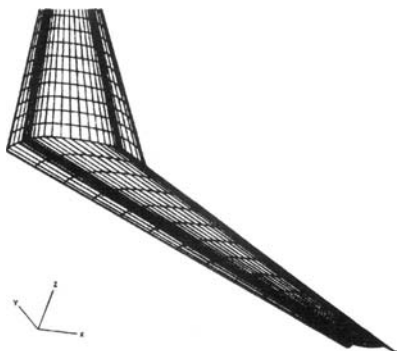
except that here  $\theta$ ,  $H$  and  $\bar{u}_e$  ( $\equiv \frac{u_e}{u_\infty}$ ) are calculated from the velocity profiles in the far wake expressed in an orthogonal coordinate system instead of using the trailing edge values. The boundary layer parameters in the streamwise direction are then calculated and used in Eq. (13.8.3).

Figure 13.17 shows a comparison between the measured and calculated drag coefficients obtained with the above procedure. Again, the agreement between data and calculations is quite satisfactory up to stall.

### 13.8.3 Multielement Wings

The interactive boundary-layer method has also been applied to several high lift configurations of the RAE wing for predicting lift and drag coefficients. The full-span slat was either retracted or deployed at  $25^\circ$  and the full span flap was deployed at either  $10^\circ$  or  $25^\circ$ .

Each element was defined by 13 cross-sections, with each slat cross-section defined by 61 points, each main element cross-section defined by 81 points (slat



**Fig. 13.18.** Multi-element wing paneling with slat and flap deployed at  $25^\circ$  – wakes omitted.

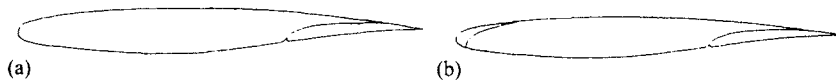


**Fig. 13.19.** Elements of the high lift system (a) main element mid flap when slat is retracted and (b) slat, main element, and flap.

retracted or deployed), and each flap cross-section defined by 71 points. For the Hess panel method, wake shapes were specified. They are generated with the two-dimensional panel method (HSPM program in the accompanying CD-ROM) using an average angle of attack in the range of interest. The variation of the wake shape with angle of incidence and along the span was neglected. Figure 13.18 shows a typical panel distribution with every other panel ignored and wakes omitted for clarity.

In light of the results of the previous subsections, calculations were performed with transition on the upper surface fixed at the leading edge. Also, in order to be able to retract the various elements, surface irregularities (coves) were present on the lower surface of the slat (if deployed) and of the main element (if the flap was deployed). In the calculations presented here, these coves were faired and transition was assumed to take place at the location of the start of the fairing.

Results are first presented for wing-flap configurations, Fig. 13.19a, and are followed by results obtained for slat-wing-flap configurations, Fig. 13.19b. The deflection angles and relative positioning of the elements are described by Lovell [5].

### Wing-Flap Configurations

The cross-section of the wing-flap configuration with the flap deflected at  $10^\circ$  is shown in Fig. 13.20a. The lift coefficient variation with angle of attack and the drag polar are also shown in Figs. 13.20a and 13.20b. The inviscid lift coefficient

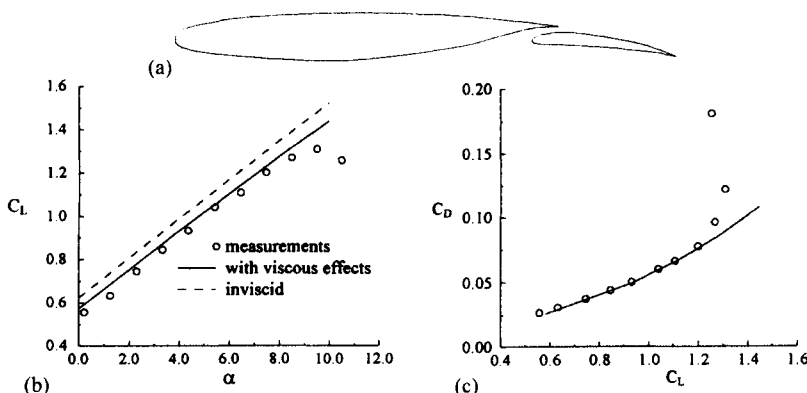


Fig. 13.20. RAE wing with slat retracted and flap deflected at 10°, (a) wing cross-section, (b) lift coefficient, and (c) drag coefficient.

is indicated to show how the introduction of the viscous effects allows for a better prediction of the lift curve. However, the lift coefficient was over-predicted while the drag coefficients, except near stall, were well predicted. Figure 13.20 shows that the flap is positioned very close to the main element. Therefore, merging of the main element wake with the boundary layer developing on the flap upper surface is likely to occur.

This merging, observed in two-dimensional flows, may be the source of the discrepancy since it was not modeled in the present method. Also, several reasons can be advanced to explain why stall was not predicted by the calculation method. One of them is based on prior two-dimensional results. It was shown in [6] that even if the freestream Mach number is low (around 0.2), very high pressure peaks occur at the leading edge of the main element and can lead to locally supersonic flow. Also, a separation bubble is usually present near the pressure peak with transition taking place in that bubble. The stronger pressure gradient when the flap is deployed makes this separation bubble even shorter than for a single wing. The combination of these two phenomena – taking place on such a short distance – makes the calculations in that region a challenging task. At the present time, there is no calculation method which can predict such flows accurately and reliably.

Figure 13.21 shows the results when the flap is deflected at 25°. Observations similar to those in Fig. 13.20 can be made. Agreement between measurements and calculations is satisfactory for both lift and drag coefficients. As expected, the larger flap deflection (25° instead of 10°) causes a larger difference between inviscid and viscous flow calculations.

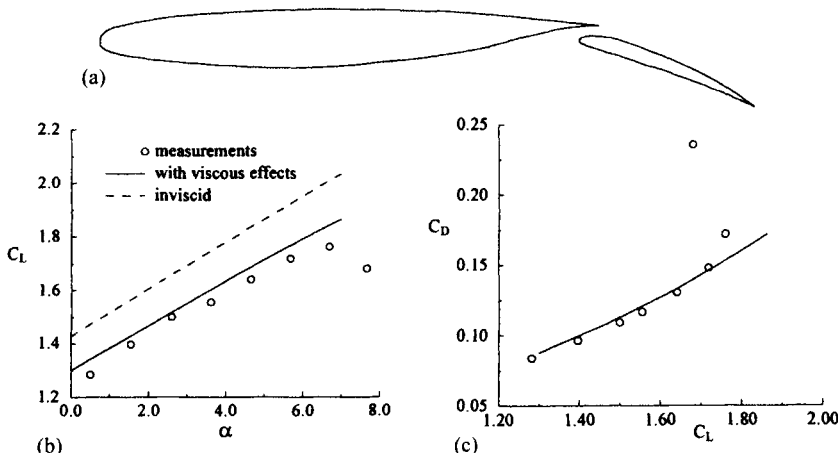


Fig. 13.21. RAE wing with slat retracted and flap deflected at 25°, (a) wing cross-section, (b) lift coefficient, and (c) drag coefficient.

### Slat-Wing-Flap Configurations

Figures 13.22 and 13.23 present results for the same configuration with the slat deflected at 25°, and the flap deflected at 10° and 25°, respectively. Again, the inviscid lift coefficient is indicated to show how the introduction of the viscous effects allows obtaining reasonable predictions of lift and drag coefficients. The discrepancies can be partly explained by the merging of the shear layers which was not accounted for. In addition, the large recirculating flow region in the slat cove – larger at low angles of incidence – was removed with the fairing and may contribute to the disagreement at low angles of attack. Cove calculations, however, could be incorporated by extending the method of [6] to three-dimensional

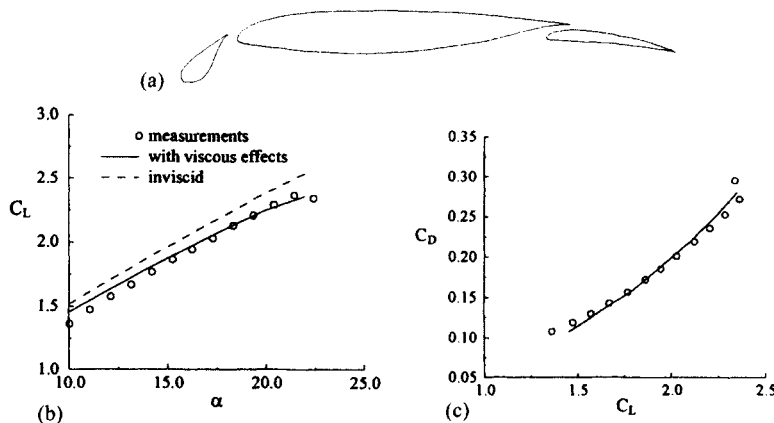
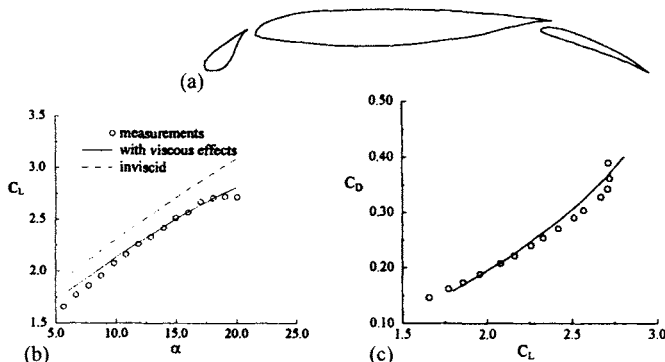


Fig. 13.22. RAE wing with slat deflected at 25° and flap deflected at 10°, (a) wing cross-section (b) lift coefficient, and (c) drag coefficient.



**Fig. 13.23.** RAE wing with both slat and flap deflected at 25°, (a) wing cross-section, (b) lift coefficient, and (c) drag coefficient.

flows. The wake shape, prescribed in the inviscid method, may also be at the source of the discrepancy.

Stall was not captured for the configurations tested. However, it is worthwhile to note that the reliable prediction of stall for slat-wing-flap configurations still offers significant challenges for two-dimensional flows. Unlike for single element and wing-flap configurations, stall can occur without flow separation on the body but may be due instead to a sudden increase of the wake thickness thus reducing the circulation on the entire configuration (see Rogers et al., [7] for an illustration of this phenomenon). Therefore, these results should be viewed as satisfactory.

### 13.9 Transonic Flows

In this section we extend the applications of the interactive boundary layer method to wing and wing/body configurations in transonic flows. The main difference in the calculation method is the replacement of the panel method with an Euler method and use of the compressible version of the boundary-layer method.

There are several Euler methods that can be used to compute the inviscid flow and these are discussed in several references, see for example, [8–12]. Popular and versatile Navier–Stokes codes such as OVERFLOW [13], CFL3D [14, 15], TLNS3D [16] and Full-Aircraft Navier–Stokes Code FANS [17] of Bombardier Aerospace can also be used for this purpose since they all have options for inviscid methods.

The accuracy of the IBL method, as in two-dimensional flows, not only depends on the solutions of the boundary-layer equations and transition prediction, but also on the solutions of the Euler equations, most of which employ either cell-centered schemes or cell-vertex schemes. In the cell-centered scheme,



**Fig. 13.24.** Control volume with (a) cell-centered and (b) cell-vertex schemes. Symbols • and  $\times$  denote grid and flow variable nodes, respectively.

the fluxes across cell surfaces are calculated by making use of the cell-centered solutions of the two neighboring cells adjacent to the cell surface, while in the cell vertex scheme the fluxes across the cell surfaces are calculated by making use of the four nodal solutions of the cell surface. After knowing the fluxes at each cell surface in both schemes, the residuals of the Euler equations are calculated at the centers of each cell. In the cell vertex scheme, the residuals at nodal points are obtained by averaging the cell-centered values of residuals of the surrounding cells. For regular cells, both schemes are equally good in terms of the solution accuracy. For cells with relatively large aspect ratios, the cell vertex scheme seems to introduce smaller truncation errors because of more accurate summation of the fluxes through the surface. However, for surface cells with a high degree of distortion, the cell-centered scheme seems to be more stable, probably because of the avoidance of direct solving for solutions at nodal points on the surface.

To introduce the viscous effects into an Euler method via the blowing velocity approach, it is necessary to modify its surface boundary condition. In the cell-centered scheme, Fig. 13.24a,  $\rho$ ,  $\rho u$ ,  $\rho v$ ,  $\rho w$  and  $\rho e$  are computed at the centers of mesh cells during each time step. Imaginary cells inside the wing surface are used to formulate the flux balance in the surface normal direction and also the dissipation terms near the surface. With flow variables  $\rho$ ,  $\rho u$ ,  $\rho v$ ,  $\rho w$  and  $\rho e$  given at the centers of mesh cells next to the wing surface, and a prescribed blowing velocity distribution on the surface, the flow variables at the centers of imaginary cells can be determined by using a simple linear extrapolation. The normal pressure gradient term on the wing surface is computed according to the prescribed blowing velocity distribution and is then used to evaluate the pressure distribution on the wing surface.

In the cell-vertex scheme, Fig. 13.24b, the blowing velocity distribution is prescribed on the surface, the residual is calculated at the centers of the cells adjacent to the surface, and the pressure distribution on the surface is evaluated directly from the cell-vertex solutions obtained on the surface.

It is clear that the choice of the grid system used in the solution of the Euler equations plays a crucial role, since the grid generation method not only must be able to model the geometry of the configuration accurately, but also be able to resolve the detailed flowfield in high pressure gradient regions, such as along

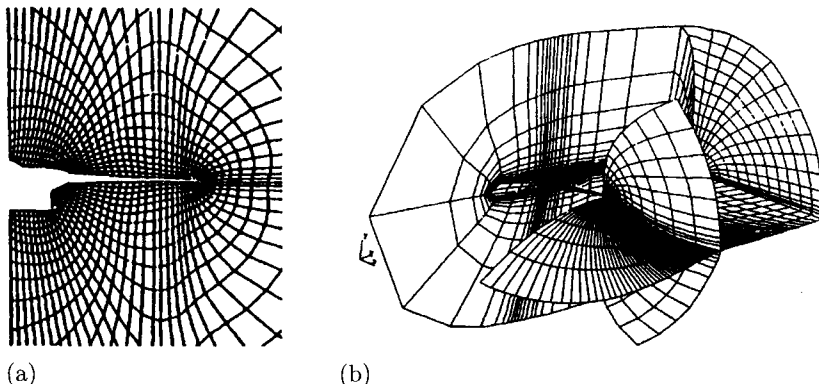


**Fig. 13.25.** (a) A cross-sections view and (b) a global view of the QGRID.

the leading and trailing edges of the body, along the wing/body juncture, and near wing tip and fuselage nose.

The application considered in this section include the ONERA-M6 wing (subsection 13.9.1), Douglas wing/fuselage configuration (subsection 13.9.2) and Challenger wing/fuselage configuration (subsection 13.9.3). The results presented in the first two subsections were obtained by Chen and Bui [18] who used a *C-C-C* grid which they referred to as the QGRID. In this method, based on a hybrid mapping/numerical grid generation scheme, the grid-point distributions near the fuselage surface and in the wing cross-sectional surface are similar to that in the *C-C-H* grid, discussed in [10], but the mesh lines in the wing tip region form a *C*-mesh, as shown in Fig. 13.25a, resulting in a concentration of grid points near the wing tip. A global view of the QGRID is given in Fig. 13.25b, which shows the grid distributions on the body surface, the symmetry plane, and the far-field boundary. With this grid, there is no need to add a fictitious wing extending from the wing tip to the spanwise farfield, as in some other grid systems.

In the following two subsections, we consider two finite-volume Euler methods called FLO-58 and FLO-67, both developed by Jameson [8, 10] using the QGRID discussed above. While FLO-58 uses a cell-centered scheme, FLO-067 uses a cell-vertex scheme, allowing us to evaluate the accuracy of each scheme against data on wing/fuselage and wing-alone configurations in conjunction with the boundary-layer method discussed in previous sections. We assume that the distribution of the onset of transition along the wing span is known. In the third subsection we perform the inviscid flow calculations using Bombardier's FANS code.

### 13.9.1 ONERA-M6 Wing

Figure 13.26 shows a comparison between calculated and measured chordwise pressure distributions at four spanwise stations for the ONERA-M6 wing for

$\alpha = 3.06^\circ$ ,  $M_\infty = 0.84$ . The inviscid flow is computed from FLO-58 and FLO-67. This wing has a  $30^\circ$  leading-edge sweep and a  $15.8^\circ$  trailing-edge sweep. Its wing tip is closed by a half body of revolution. The test data was obtained with free transition, and pressure data was obtained using seven rows of pressure taps located from 20% to 99% semispan. The Euler calculations with the QGRID used a total of  $193 \times 25 \times 33$  grid points. The location of transition was fixed at  $x/c = 0.03$  on the upper surface. On the lower surface its location varied, being at  $x/c = 0.66$  at the root and 0.50 at the tip. As can be seen, the interactive solutions in which the inviscid flow solutions obtained with two different Euler methods are essentially the same and agree well with measured values.

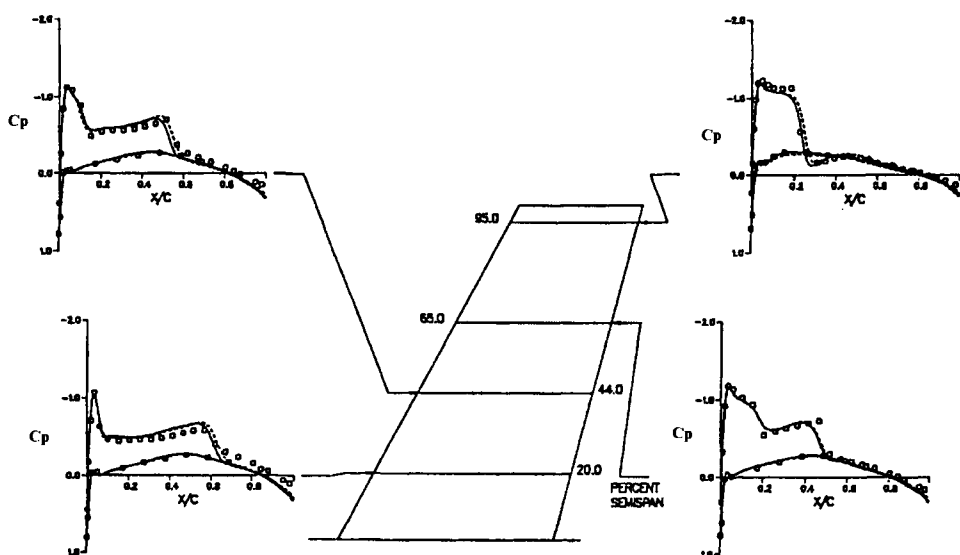


**Fig. 13.26.** Comparison of interactive boundary-layer solutions with the experimental data for the ONERA-M6 wing for  $\alpha = 3.06^\circ$ ,  $M_\infty = 0.84$ . Symbols denote data and solid and dashed lines denote the interactive flow solutions in which the inviscid flow solutions are obtained from FLO-58 and FLO-67 codes, respectively.

### 13.9.2 Douglas Wing/Fuselage Configuration

Figure 13.27 shows a comparison between the solutions of the calculation method and experimental data for a Douglas wind-tunnel model LB 488 for  $M_\infty = 0.80$ ,  $\alpha = 2.30^\circ$ ,  $Re = 5.4 \times 10^6$ . Again the inviscid flow calculations used the QGRID and two Euler methods, as in the wing-alone case, for a total of  $193 \times 25 \times 25$  grid points, and the distribution of transition locations was specified. Unlike the wing-alone case, however, the calculated solutions for the inviscid flow computed with two Euler codes using different numerical schemes

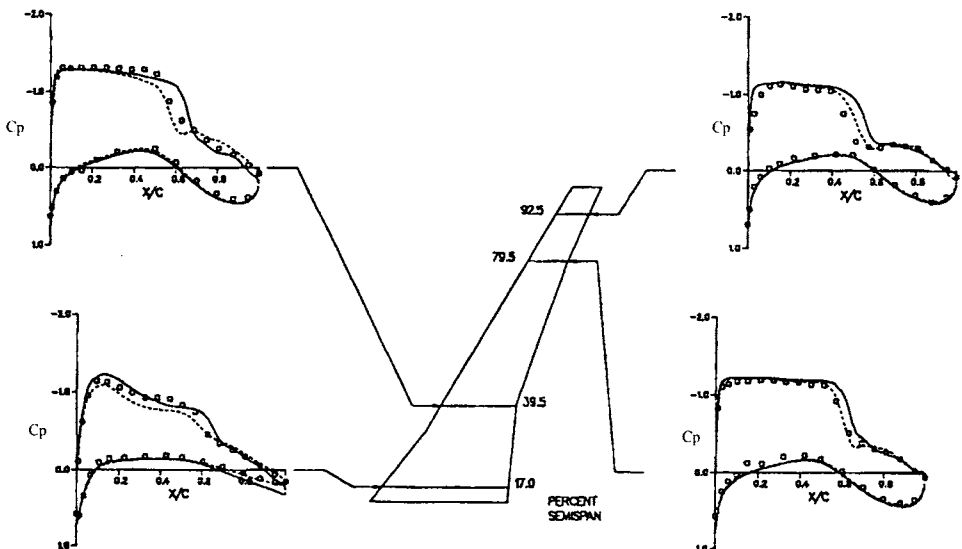


**Fig. 13.27.** Comparison of interactive boundary-layer solutions with the experimental data for the LB-488 wing/body configurations for  $\alpha = 2.30^\circ$ ,  $M_\infty = 0.80$ ,  $Re = 5.4 \times 10^6$ . Symbols denote data and solid and dashed lines denote the interactive flow solutions in which the inviscid flow solutions are obtained from FLO-58 and FLO-67 codes, respectively.

differ from each other. Those computed with FLO-67 (cell-vertex scheme) predict a weaker shock near the wing root and are not in good agreement with experimental data in the inboard region of the wing, but are in good agreement with data in the outboard region. The calculations performed with FLO-58 (cell-centered scheme) agree well with measurements in the inboard region but predict a stronger shock in the outboard region. Additional calculations performed for wing/body configurations show that even though the FLO-67 solutions are better for predicting the correct shock, the predictions of FLO-67 are consistently poor in the wing-root region, and overall Euler solutions using the cell-centered scheme produce results which, when used in the calculation method, yield much better agreement with data, including the outboard region.

### 13.9.3 Challenger Wing/Body Fuselage Configuration

In [19], Laurendeau and Mokhtorion applied this IBL method to Bombardier's Challenger wing/fuselage configuration and compared the predictions with experiment and with those computed with FANSC, which solves the Euler/Navier Stokes equations on a multi-block structured computational domain with arbitrary boundary conditions. They first applied the method by using the option in which the boundary-layer equations were solved for the standard problem (direct coupling) on the wing surface, thus limiting the solutions to attached flows,

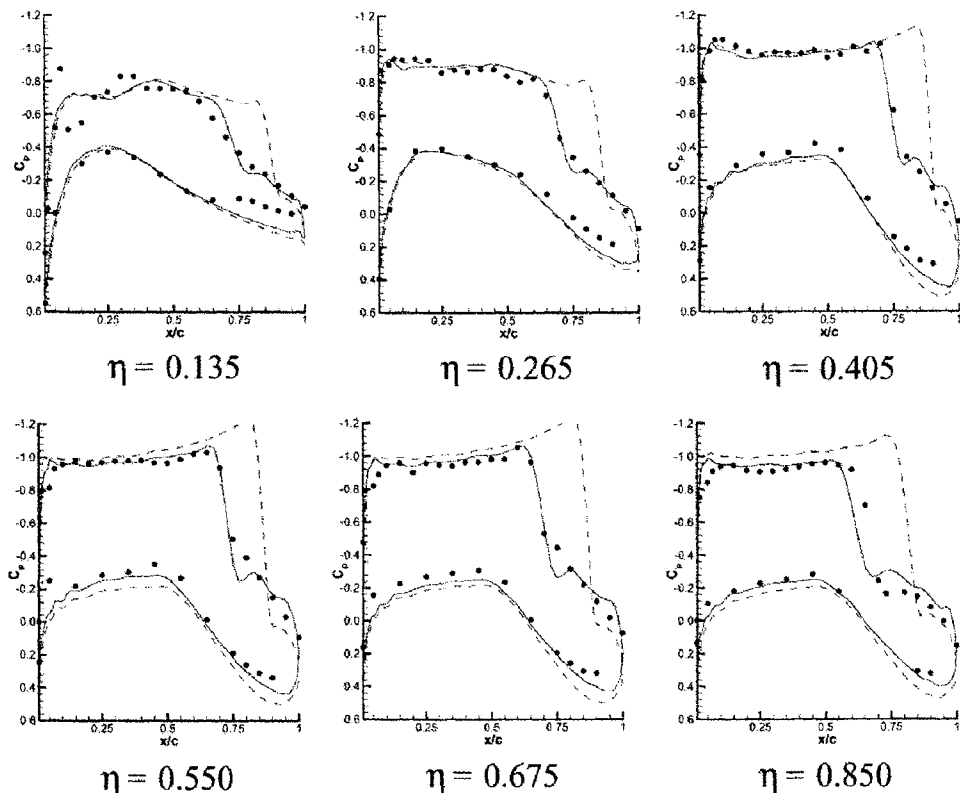


**Fig. 13.28.** Direct coupling results for the Challenger wing-fuselage configuration,  $M_\infty = 0.82$ ,  $\alpha = 1.5^\circ$  (Euler results shown with dashed line).

and the blowing velocity distributions were calculated, thus removing the need to regenerate the body-conforming grid after each viscous calculation. Blowing velocities were kept constant equal to the previous attached flow value when trailing edge separations were encountered.

The results obtained with this procedure show the importance of modeling viscous effects on the Challenger wing/body configuration, Fig. 13.28. When compared to inviscid Euler flow solutions at constant angle-of-attack and constant Mach number, the predicted upper surface shock-wave position moved forward with viscous effects, in agreement with the experimental location. The effects of viscosity are also seen in the cove region, where the inviscid solver overestimates the lower surface pressure coefficients by as much as 0.2, whereas the viscous/inviscid procedure reduces this number to 0.1. As expected, there is good agreement in regions where the boundary layer is thin, such as in the leading edge region of the wing.

The predictions close to the trailing edge viscous results were, however, inadequate for design, particularly when the wing form drag was calculated from the Squire-Young formula, Eq. (13.8.3). Significant errors in wing form drag are

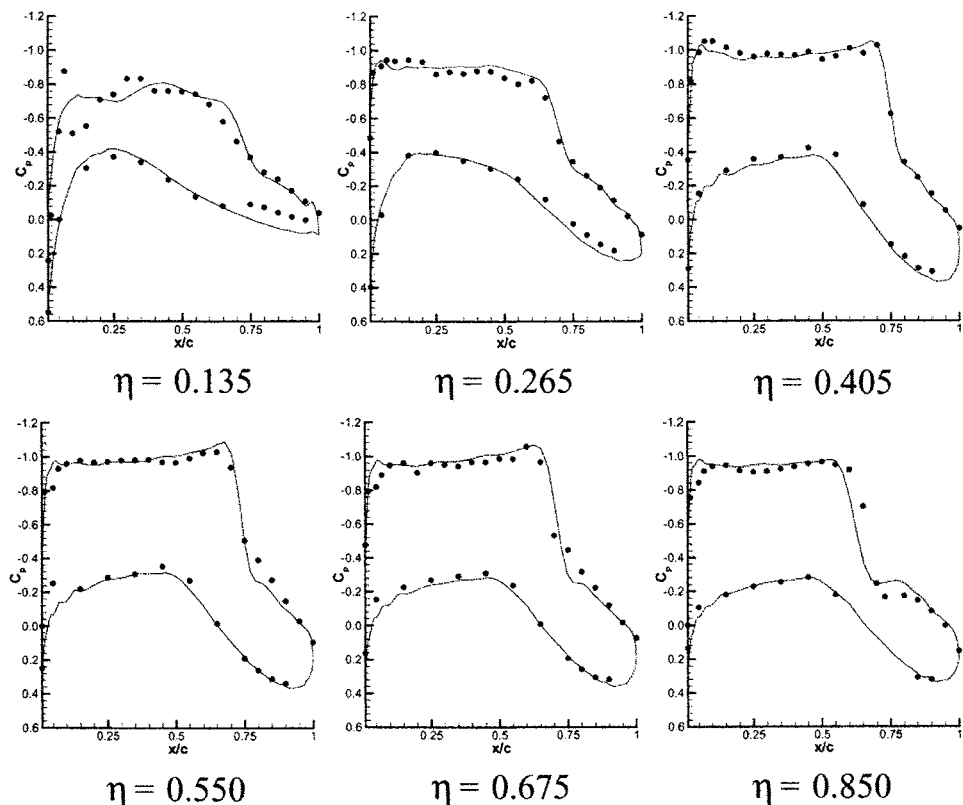


**Fig. 13.29.** IBL results for the Challenger wing-fuselage configuration  $M_\infty = 0.82$ ,  $\alpha = 1.5^\circ$ .

introduced when the trailing-edge boundary-layer properties are in error and most importantly, when the external trailing edge velocities are not properly computed.

All of these physical requirements were dealt with by the use of the interactive boundary-layer option of the program in which the boundary-layer solutions were obtained with the inverse method on the wing surface and into the wake of the wing. This ensured accurate results when separated flow regions are encountered and maintained the strongly coupled nature of the inviscid and viscous flows in the trailing edge region. The results obtained with the IBL method are shown in Fig. 13.29 where the surface pressure distributions are shown for the same flow conditions of Fig. 13.28. In these calculations, the IBL method used the Baldwin-Lomax turbulence model. The trailing edge pressures are significantly improved, especially with regard to the evaluation of the form drag and the improvements in the cove pressures are due to proper consideration of coupling rather than to separation, as there was none in this case. Improvements at the foot of the upper surface shock wave can also be seen, this time due to quality

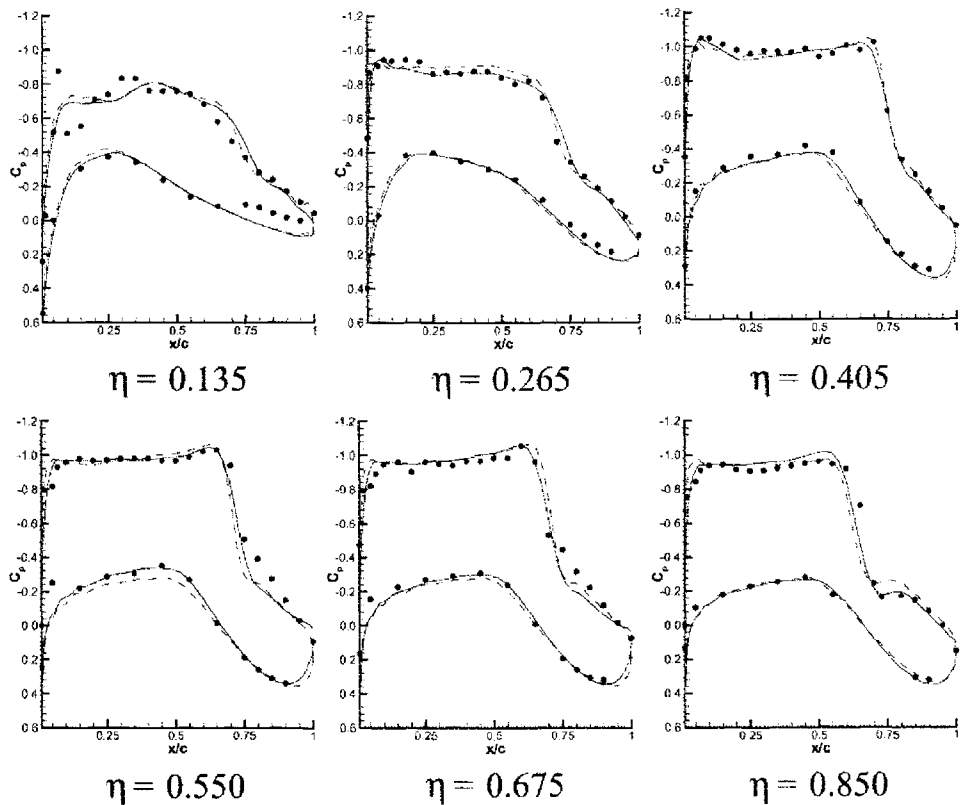


**Fig. 13.30.** NS (solid lines), IBL (dashed lines) and experimental (circles) for the Challenger wing-fuselage configuration  $M_\infty = 0.82$ ,  $\alpha = 1.5^\circ$ .

of the indirect viscous flow solver as shock-induced separation occurred at this buffet flow condition.

To verify the accuracy of the IBL method, Navier-Stokes calculations were performed with the FANSC code [17], for the same flow conditions. The turbulent eddy viscosity was computed with the SA turbulence model. The surface pressure distributions calculated by FANSC together with the IBL results and experiments are shown in Fig. 13.30 and the agreement is excellent. The discrepancy at the inboard lower-surface region is due to the different wing-body fairing of the experimental model and those in the upper surface shock wave region are due to the intensity of the shock-wave/boundary-layer interaction. The differences between the results of the two calculation methods are very small, and more so when the difficult buffet-flow conditions are considered.

## References

- [1] Roget, C.: "Structures asymptotiques et calculs d'écoulements sur des obstacles bi- et tridimensionnels." Thèse de l'Université Paul Sabatier.

- [2] Cebeci, T.: *An Engineering Approach to the Calculation of Aerodynamics Flows*. Horizons Publ., Long Beach, Calif. and Springer, Heidelberg, Germany, 1999.
- [3] Bertelrud, A.: "Measurements on a Three-Dimensional Swept Wing at Low Speeds." The Aeronautical Research Institute of Sweden, Rept No. 131, Stockholm, 1977.
- [4] Besnard, E.: "Prediction of High Lift Flows with Separation." Ph.D. Dissertation, California State University, Long Beach, 1998.
- [5] Lovell, D. A.: "A Wind-Tunnel Investigation of the Effects of Flap Span and Deflection Angle, Wing Planform and a Body on the High-Lift Performance of a 28° Swept Wing." RAE CP 1372, 1977.
- [6] Cebeci, T. and Besnard, E.: "An Efficient and Accurate Approach for Analysis and Design of High Lift Configurations." *Canadian Aeronautics and Space J.* **44**, 212–222, 1998.
- [7] Rogers, S., Menter, F. and Durbin, P. and Mansour, N.: "A comparison of turbulence models in computing multi-element airfoil flows." AIAA Paper No. 94-0291, 1994.
- [8] Jameson, A., Schmidt, W. and Turkel, E.: "Numerical Solutions of the Euler Equations by Finite-Volume Methods Using Runge-Kutta Time-Stepping Schemes." AIAA Paper No. 81-1259, June 1981.
- [9] Rizzi, A.: "Damped Euler-Equation Method to Compute Transonic Flow Around Wing-Body Combinations." *AIAA J.* **20**, 1321–1328, Oct. 1982.
- [10] Jameson, A. and Baker, T. J.: "Multigrid Solution of the Euler Equations for Aircraft Configurations." AIAA Paper No. 84-0093, Jan. 1984.
- [11] Jameson, A. and Yoon, S.: "Multigrid Solution of the Euler Equations Using Implicit Schemes." *AIAA J.* **24**, 1737–1743, Nov. 1986.
- [12] Roe, P. L.: "Characteristic-Based Schemes for the Euler Equations." *Annual Review of Fluid Mechanics* **18**, 337–365, 1986.
- [13] Buning, P. G. et al.: "OVERFLOW User's Manuel" Version 1.7r. NASA Ames Research Center, Moffett Field, CA, 1996.
- [14] Thomas, J. L., Taylor, S. L. and Anderson, W. K.: "Navier-Stokes Computations of Vortical Flows Over Low Aspect Ratio Wings." AIAA Paper No. 87-0207, Jan. 1987.
- [15] Krist, S. L., Biedron, R. T. and Rumsey, C. L.: "CFL3D User's Manual." NASA Langley Research Center, Hampton, VA, 1996.
- [16] Vatsa, V. N. and Wedan, B. W.: "Development of an Efficient Multigrid Code for 3-D Navier-Stokes Equations." AIAA Paper No. 89-1791, June 1989.
- [17] Laurendeau, E. and Boudreau, J.: FANSC Structured Multiblock, AIAA 2<sup>nd</sup> Drag Prediction Workshop, <http://aaac.larc.nasa.gov/tsab/cfdlarc/aiaa/-dpw/workshop2>
- [18] Chen, L. T. and Bui, M. N.: "An interactive scheme for transonic wing/body flows based on Euler and inverse boundary-layer equations." AIAA Paper No. 90-1586, June 1990.
- [19] Laurendeau, E. and Mokhtarian, F.: "Coupled Euler/boundary-layer methods with the FANSC code." Canadian Aeronautics and Space Institute (CASI) Aerodynamic Symposium, Toronto, April 29–May 2, 2001.

# 14 Transition in Three-Dimensional Compressible Flows

## 14.1 Introduction

The approach and many of the ideas presented for stability and transition in Chapters 5 and 8 for incompressible flows remain the same for compressible flows. Again the linear and parabolized stability equations can be obtained from the Navier–Stokes equations with procedures similar to those for incompressible flows, subsection 14.2.1, and the inviscid stability equations from the linear stability equations by neglecting viscous effects, subsection 14.2.2. The resulting equations reveal the differences between incompressible and compressible forms and contribute to understanding of compressible stability theory. For example, inviscid stability increases with Mach number and the mean flow relative to the disturbance phase velocity can be supersonic as discussed in subsection 14.4.2.

There are several factors that can influence the onset and evolution of transition in compressible flows, as in incompressible flows, and include noise, wall temperature, nose bluntness, surface roughness and leading edge contamination as discussed in Section 14.3. The onset of transition in compressible flows can again be determined by solving in the linear or parabolized stability equations together with the  $e^n$  method. Section 14.4 describes the method for the linear stability equations with the Cebeci and Stewartson eigenvalue formulation and Section 14.5 describes the applications of the  $e^n$  method.

## 14.2 Linear Stability Theory

In this section we extend the discussion on linear stability theory for incompressible flows to compressible flows. In subsection 14.2.1 using the small disturbance theory, we discuss the derivation of the linear stability equations for three-dimensional compressible flows with three-dimensional disturbances, and

in subsection 14.4.2 we discuss the inviscid theory for the linear stability equations.

### 14.2.1 Stability Equations

The derivation of the linear stability equations in a Cartesian coordinate system for a compressible flow is discussed in [1]. It is assumed that as in the procedure used for incompressible flows, the velocity components  $u$ ,  $v$  and  $w$ , pressure  $p$ , temperature  $T$ , density  $\rho$  represent the instantaneous components of the flow properties in the compressible Navier–Stokes equations, and these components are divided into a mean term and a fluctuating term so that the instantaneous flow properties can be expressed as

$$\begin{aligned} u &= \bar{u} + u', & v &= \bar{v} + v', & w &= \bar{w} + w' \\ p &= \bar{p} + p', & T &= \bar{T} + T', & \rho &= \bar{\rho} + \rho' \end{aligned} \quad (14.2.1a)$$

In addition, it is assumed that thermal conductivity  $k$ , dynamic viscosity  $\mu$ , and second viscosity  $\lambda$ , are functions of temperature only and are written as

$$\begin{aligned} k &= \bar{k} + k', & k' &\equiv \frac{dk}{d\bar{T}} T' \\ \mu &= \bar{\mu} + \mu', & \mu' &\equiv \frac{d\mu}{d\bar{T}} T' \\ \lambda &= \bar{\lambda} + \lambda', & \lambda' &\equiv \frac{d\lambda}{d\bar{T}} T' \end{aligned} \quad (14.2.1b)$$

It is also assumed that the mean-velocity and pressure terms satisfy the Navier–Stokes equations for a steady laminar flow.

Next the Navier–Stokes equations are examined with instantaneous flow properties and transport coefficients expressed in terms of the relations given by Eq. (14.2.1). Since  $u'$ ,  $v'$ ,  $w'$ ,  $p'$ ,  $T'$ ,  $\mu'$ ,  $k'$ ,  $\lambda'$  are small, their squares and products can be neglected. Noting that the mean velocity, pressure and temperature satisfy the Navier–Stokes equations, the equations simplify further. They are, however, still complicated and can be further simplified by noting that all velocity and temperature fluctuations and derivatives are of the same order of magnitude, and by assuming that the mean flow velocities  $\bar{u}$  and  $\bar{w}$ , density  $\bar{\rho}$  and temperature  $\bar{T}$  are a function of  $y$  only and  $\bar{v}$  is zero, that is,

$$\bar{u} = \bar{u}(y), \quad \bar{w} = \bar{w}(y), \quad \bar{\rho} = \bar{\rho}(y), \quad \bar{T} = \bar{T}(y), \quad \bar{v} = 0 \quad (14.2.2)$$

The assumption in Eq. (14.2.2) is the *parallel flow approximation* discussed in Section 5.3. Before proceeding further, again all the fluctuating and steady-state velocity components are normalized by  $u_e$  and all lengths by a reference length  $L$ . The fluctuating and steady-state pressure, density, and temperature are normalized by  $p_e$ ,  $\rho_e$  and  $T_e$  respectively. Both viscosities are normalized

by  $\mu_e$ , and heat conductivity by  $c_p \mu_e$ . A Reynolds number,  $R$ , a Mach number,  $M_e$ , and a Prandtl number,  $\text{Pr}$ , are also defined by

$$R = \frac{u_e L}{\nu_e}; \quad M_e = \frac{u_e}{\sqrt{\gamma \tilde{R} T_e}}, \quad \text{Pr} = \frac{c_p \mu}{k} \quad (14.2.3)$$

with  $\gamma = c_p/c_v$  and  $\tilde{R}$  denoting the universal gas constant. The resulting nondimensional disturbance flow equations and the equation of state

$$p = \rho R T \quad (14.2.4)$$

form a set of coupled partial-differential equations whose solutions describe how disturbances originate near the surface  $y = 0$  and spread out through the boundary layer and beyond as they are convected along the local streamlines. To study the properties of these equations, we again assume that the small disturbance is a sinusoidal travelling wave and write the three-dimensional disturbance  $q'$  given by Eq. (5.3.14). The small disturbance equations then can be written as

Continuity

$$i\gamma_1 \hat{v} + \rho \left[ \frac{d\hat{v}}{dy} + i(\alpha \hat{u} + \beta \hat{w}) \right] + \frac{d\rho}{dy} \hat{v} = 0 \quad (14.2.5)$$

Momentum equation parallel to the wave number vector

$$\begin{aligned} & \rho \left[ i\gamma_1 (\alpha \hat{u} + \beta \hat{w}) + \left( \alpha \frac{du}{dy} + \beta \frac{dw}{dy} \right) \hat{v} \right] \\ &= -i\gamma_2^2 \frac{\hat{p}}{\gamma M_e^2} + \frac{\mu}{R} \left\{ \left( \alpha \frac{d^2 \hat{u}}{dy^2} + \beta \frac{d^2 \hat{w}}{dy^2} \right) + \gamma_2^2 \left[ i \frac{d\hat{v}}{dy} - 2(\alpha \hat{u} + \beta \hat{w}) \right] \right\} \\ &+ \frac{2 \lambda - \mu}{3R} \gamma_2^2 \left[ i \frac{d\hat{v}}{dy} - (\alpha \hat{u} + \beta \hat{w}) \right] + \frac{1}{R} \frac{d\mu}{dT} \left( \alpha \frac{d^2 u}{dy^2} + \beta \frac{d^2 w}{dy^2} \right) \hat{T} \\ &+ \frac{1}{R} \left[ \left( \frac{d\mu}{dT} \frac{d\hat{T}}{dy} + \frac{d^2 \mu}{dT^2} \frac{dT}{dy} \hat{T} \right) \left( \alpha \frac{du}{dy} + \beta \frac{dw}{dy} \right) \right] \\ &+ \frac{1}{R} \frac{d\mu}{dT} \frac{dT}{dy} \left[ \left( \alpha \frac{d\hat{u}}{dy} + \beta \frac{d\hat{w}}{dy} \right) + i\gamma_2^2 \hat{v} \right] \end{aligned} \quad (14.2.6)$$

Momentum equation normal to the wave number vector

$$\begin{aligned} & \rho \left[ i\gamma_1 (\alpha \hat{w} - \beta \hat{u}) + \left( \alpha \frac{dw}{dy} - \beta \frac{du}{dy} \right) \hat{v} \right] \\ &= \frac{\mu}{R} \left[ \left( \alpha \frac{d^2 \hat{w}}{dy^2} - \beta \frac{d^2 \hat{u}}{dy^2} \right) - \gamma_2^2 (\alpha \hat{w} - \beta \hat{u}) \right] \\ &+ \frac{1}{R} \left[ \frac{d\mu}{dT} \frac{dT}{dy} \left( \alpha \frac{d\hat{w}}{dy} - \beta \frac{d\hat{u}}{dy} \right) + \frac{d\mu}{dT} \left( \alpha \frac{d^2 w}{dy^2} - \beta \frac{d^2 u}{dy^2} \right) \hat{T} \right. \\ &\quad \left. + \left( \frac{d\mu}{dT} \frac{d\hat{T}}{dy} + \frac{d^2 \mu}{dT^2} \frac{dT}{dy} \hat{T} \right) \left( \alpha \frac{dw}{dy} - \beta \frac{du}{dy} \right) \right] \end{aligned} \quad (14.2.7)$$

$y$ -Momentum equation

$$\begin{aligned} i\rho\gamma_1\hat{v} = & -\frac{1}{\gamma M_e^2}\frac{d\hat{p}}{dy} + \frac{\mu}{R}\left[2\frac{d^2\hat{v}}{dy^2} + i\left(\alpha\frac{d\hat{u}}{dy} + \beta\frac{d\hat{w}}{dy}\right) - \gamma_2^2\hat{v}\right] \\ & + \frac{2}{3}\left(\frac{\lambda-\mu}{R}\right)\left[\frac{d^2\hat{v}}{dy^2} + i\left(\alpha\frac{d\hat{u}}{dy} + \beta\frac{d\hat{w}}{dy}\right)\right] + \frac{1}{R}\left\{i\frac{d\mu}{dT}\left(\alpha\frac{du}{dy} + \beta\frac{dw}{dy}\right)\hat{T}\right. \\ & \left.+ 2\frac{d\mu}{dT}\frac{dT}{dy}\frac{d\hat{v}}{dy} + \frac{2}{3}\frac{d}{dT}(\lambda-\mu)\frac{dT}{dy}\left[\frac{d\hat{v}}{dy} + i(\alpha\hat{u} + \beta\hat{w})\right]\right\} \end{aligned} \quad (14.2.8)$$

Energy equation

$$\begin{aligned} \rho\left[i\gamma_1\hat{T} + \frac{dT}{dy}\hat{v}\right] = & -(\gamma-1)\left[\frac{d\hat{v}}{dy} + i(\alpha\hat{u} + \beta\hat{w})\right] + \frac{\gamma\mu}{\text{Pr}R}\left\{\frac{d^2\hat{T}}{dy^2}\right. \\ & - \gamma_2^2\hat{T} + \frac{1}{k}\left[\frac{dk}{dT}\frac{d^2T}{dy^2} + \frac{d^2k}{dT^2}\left(\frac{dT}{dy}\right)^2\right]\hat{T} + \frac{2}{k}\frac{dk}{dT}\frac{dT}{dy}\frac{d\hat{T}}{dy}\Big\} \\ & + \gamma\frac{(\gamma-1)}{R}M_e^2\left\{2i\mu\left(\alpha\frac{du}{dy} + \beta\frac{dw}{dy}\right)\hat{v} + \frac{d\mu}{dT}\left[\left(\frac{du}{dy}\right)^2 + \left(\frac{dw}{dy}\right)^2\right]\hat{T}\right. \\ & + \frac{2\mu}{\gamma_2^2}\left[\left(\alpha\frac{du}{dy} + \beta\frac{dw}{dy}\right)\left(\alpha\frac{d\hat{u}}{dy} + \beta\frac{d\hat{w}}{dy}\right)\right. \\ & \left.\left. + \left(\alpha\frac{dw}{dy} - \beta\frac{du}{dy}\right)\left(\alpha\frac{d\hat{w}}{dy} - \beta\frac{d\hat{u}}{dy}\right)\right]\right\} \end{aligned} \quad (14.2.9)$$

$$y=0, \quad \hat{u}=\hat{v}=\hat{w}=\hat{T}=0 \quad (14.2.10a)$$

$$y \rightarrow \infty, \quad \hat{u}, \hat{v}, \hat{w}, \hat{T} \rightarrow 0 \quad (14.2.10b)$$

where

$$\gamma_1 = \alpha u + \beta w - \omega, \quad \gamma_2^2 = \alpha^2 + \beta^2 \quad (14.2.11)$$

### 14.2.2 Inviscid Stability Theory

A detailed account of the inviscid stability theory for compressible flows and of results is given by Mack [2]. The results of this theory are very important because even a flat plate flow has an inviscid instability at a finite Reynolds number.

The governing equations can be obtained by taking the limit of the linear stability equations, Eqs. (14.2.4) to (14.2.8), when the Reynolds number goes to infinity,

$$i\gamma_1\hat{p} + \rho\left[\frac{d\hat{v}}{dy} + i(\alpha\hat{u} + \beta\hat{w})\right] + \frac{d\rho}{dy}\hat{v} = 0 \quad (14.2.12a)$$

$$\rho\left[i\gamma_1(\alpha\hat{u} + \beta\hat{w}) + \left(\alpha\frac{du}{dy} + \beta\frac{dw}{dy}\right)\hat{v}\right] = -i\gamma_2^2\frac{\hat{p}}{\gamma M_e^2} \quad (14.2.12b)$$

$$\rho \left[ i\gamma_1(\alpha\hat{w} - \beta\hat{u}) + \left( \alpha \frac{dw}{dy} - \beta \frac{du}{dy} \right) \hat{v} \right] = 0 \quad (14.2.12c)$$

$$i\rho\gamma_1\hat{v} = -\frac{1}{\gamma M_e^2} \frac{d\hat{p}}{dy} \quad (14.2.12d)$$

$$\rho \left[ i\gamma_1\hat{T} + \frac{dT}{dy}\hat{v} \right] + (\gamma - 1) \left[ \frac{d\hat{v}}{dy} + i(\alpha\hat{u} + \beta\hat{w}) \right] = 0 \quad (14.2.12e)$$

To show the importance of compressibility in inviscid flow theory, we introduce a Mach number  $\tilde{M}$  defined by

$$\tilde{M} = \frac{\gamma_1 M_e}{\gamma_2 T^{1/2}} \quad (14.2.13)$$

which, for a temporal neutral wave, is real and has a physical meaning. To show this, we write

$$\tilde{M} = (u_\psi - c_r) \frac{M_e}{T^{1/2}} \quad (14.2.14)$$

with

$$u_\psi = u \cos \psi + w \sin \psi, \quad c_r = \frac{\omega_r}{|\vec{k}|} \quad (14.2.15)$$

The angle  $\psi$  is the angle between the wave number vector  $\vec{k}$  and the  $x$ -axis so that  $u_\psi$  is the orthogonal projection of the local mean velocity on the direction of the wave number vector and  $c_r$  is the phase velocity of the wave. Using physical quantities, we have

$$\tilde{M} = \frac{u_\psi^* - c_r^*}{a^*} = M_\psi - \frac{c_r^*}{a^*} \quad (14.2.16)$$

where  $M_\psi$  is the local Mach number of the mean flow in the direction of the wave number,  $c_r^*$  is the phase velocity and  $a^*$  is the speed of sound. For a temporal neutral wave, Eq. (14.2.16) shows that  $\tilde{M}$  is the Mach number of the local mean flow in the direction of the wave number relative to the phase velocity. By extension, even in the case of a non neutral wave,  $\tilde{M}$  is called the *relative Mach number*.

From Eqs. (14.2.12a, 14.2.12b, 14.2.12d, 14.2.12e), we can determine a set of coupled first order differential equations for  $\hat{v}$  and  $\hat{p}$

$$\frac{d}{dy} \left( \frac{\hat{v}}{\gamma_1} \right) = i \frac{1 - \tilde{M}^2}{\tilde{M}^2} \frac{\hat{p}}{\gamma} \quad (14.2.17a)$$

$$\frac{d}{dy} \left( \frac{\hat{p}}{\gamma} \right) = -i\gamma_2^2 \tilde{M}^2 \frac{\hat{v}}{\gamma_1} \quad (14.2.17b)$$

from which second order differential equations for  $\hat{v}$  and  $\hat{p}$  are obtained

$$\frac{d^2}{dy^2} \left( \frac{\hat{v}}{\gamma_1} \right) + \frac{d}{dy} \left[ \ln \frac{\tilde{M}^2}{|1 - \tilde{M}^2|} \right] \frac{d}{dy} \left( \frac{\hat{v}}{\gamma_1} \right) - \gamma_2^2 (1 - \tilde{M}^2) \frac{\hat{v}}{\gamma_1} = 0 \quad (14.2.18a)$$

$$\frac{d^2 \hat{p}}{dy^2} - \frac{d}{dy} [\ln \tilde{M}^2] \frac{d \hat{p}}{dy} - \gamma_2^2 (1 - \tilde{M}^2) \hat{p} = 0 \quad (14.2.18b)$$

The boundary conditions are  $\hat{v}(0) = 0$  and  $\hat{v}$  is bounded as  $y \rightarrow \infty$ .

The value of the relative Mach number with respect to 1 plays an important role. It can be negative if the phase velocity of the wave is larger than the local velocity (in the direction of the wave number). If  $|\tilde{M}| > 1$ , the perturbation is said *locally* supersonic. If  $|\tilde{M}| = 1$ , the perturbation is locally sonic and if  $|\tilde{M}| < 1$ , the perturbation is locally subsonic.

In the freestream, we have

$$\tilde{M}_e = M_{\psi e} \left( 1 - \frac{c_r}{u_{\psi e}} \right) \quad (14.2.19)$$

For two-dimensional waves,  $\psi = 0$  and  $M_{\psi e} = M_e$ ,  $u_{\psi e} = 1$ . It will be seen that the waves with a subsonic freestream relative Mach number are important. These waves are such that the phase velocity is in the range

$$1 - \frac{1}{M_e} < c_r < 1 + \frac{1}{M_e} \quad (14.2.20)$$

The limit  $c_r = 1 + 1/M_e$  means that the wave propagates downstream relative to the freestream with the freestream celerity of sound. The limit  $c_r = 1 - 1/M_e$  means that the wave propagates upstream relative to the freestream with the freestream celerity of sound.

A detailed study of the inviscid stability equations is given by Lees and Lin [3]. It is assumed that the mean flow is two-dimensional ( $w = 0$ ) and that the waves are also two-dimensional ( $\beta = 0$ ). The results are obtained with the temporal theory ( $\omega$  is complex and  $\alpha$  is real). In the results given below, the waves are said subsonic, sonic or supersonic if the relative Mach number  $\tilde{M}_e$  in the freestream is such that  $\tilde{M}_e < 1$ ,  $\tilde{M}_e = 1$  or  $\tilde{M}_e > 1$ .

1. A necessary and sufficient condition for the existence of a neutral subsonic wave ( $\tilde{M}_e < 1$ ) is that there is a point in the boundary-layer at distance  $y_s$  such that

$$u(y_s) > 1 - \frac{1}{M_e} \text{ and } \frac{d}{dy} \left[ \frac{1}{T} \frac{du}{dy} \right]_{y_s} = 0 \quad (14.2.21)$$

The phase velocity  $c_{rs}$  of this wave is equal to  $u(y_s)$ .

These results are an extension of the Rayleigh condition valid in incompressible flow. The point  $y_s$  is called the generalized inflection point.

The sufficient condition of this theorem is demonstrated by assuming that the wave is locally subsonic everywhere in the boundary-layer. Then, it is shown that there is only one wave number  $\alpha_s$  corresponding to the phase velocity  $c_{rs}$  for the neutral subsonic wave.

2. A sufficient condition for the existence of a subsonic ( $\tilde{M}_e < 1$ ) unstable wave is that condition (14.2.21) is satisfied.

This sufficient condition of instability requires also that the relative Mach number  $\tilde{M}$  is subsonic everywhere in the boundary-layer.

For a flat plate boundary-layer in compressible flow on a adiabatic wall, the velocity profile has a generalized inflection point satisfying condition (14.2.21). Such boundary-layers have an inviscid instability. In incompressible flow, the velocity profile of a flat plate boundary layer has a zero second derivative at the wall and there is no inviscid instability.

3. There exists a neutral sonic wave ( $\tilde{M}_e = 1$ ) with the eigenvalues  $\alpha = 0$ ,  $c_r = 1 - 1/M_e$ .

Other important results were discovered by Mack when the waves are locally supersonic. At first, it has been observed, numerically, that the most unstable waves are always subsonic ( $\tilde{M}_e < 1$ ). Then, according to the results of Lees and Lin, if the relative Mach number is subsonic everywhere in the boundary-layer, there is a unique wave number corresponding to the phase velocity  $c_{rs}$  of the neutral subsonic wave. However, the relative Mach number can be supersonic near the wall. Mack demonstrated the possibility of multiple solutions, i.e. the possibility of an infinite sequence of wave numbers corresponding to the value of the phase velocity of the neutral subsonic wave. The analytical proof is provided by an approximate solution obtained at large value of the wave number. In Eq. (14.2.18a) the term with the first derivative of  $\hat{v}_1/\gamma_1$  can be neglected and the equation becomes

$$\frac{d^2}{dy^2} \left( \frac{\hat{v}}{\gamma_1} \right) - \gamma_2^2 (1 - \tilde{M}^2) \frac{\hat{v}}{\gamma_1} = 0 \quad (14.2.22)$$

It is clear that the mathematical nature of the equation depends on the value of the relative Mach number with respect to unity. When the relative Mach number is supersonic, Eq. (14.2.22) is a wave equation whose solution is an oscillating function and it is expected that there is an infinite sequence of wave numbers for which the boundary conditions are satisfied. The interesting case is when the relative Mach number is supersonic near the wall and subsonic in the outer part of the boundary layer. Because of the supersonic region, the solution is oscillating near the wall and decays exponentially in the subsonic region. In addition, there is an infinite sequence of eigenvalues for the wave number. In these circumstances, the Lees and Lin result that there is only one wave number  $\alpha_s$  corresponding to the phase velocity  $c_{rs}$  for the neutral subsonic wave does not hold because the relative Mach number is not subsonic everywhere.

Figure 14.1 shows results obtained by Mack [2] according to the inviscid theory for two-dimensional waves in a two-dimensional flat plate boundary-layer developing on an adiabatic wall. The evolution of the wave number  $\alpha_{sn}$  corresponding to neutral subsonic waves is plotted as a function of the Mach

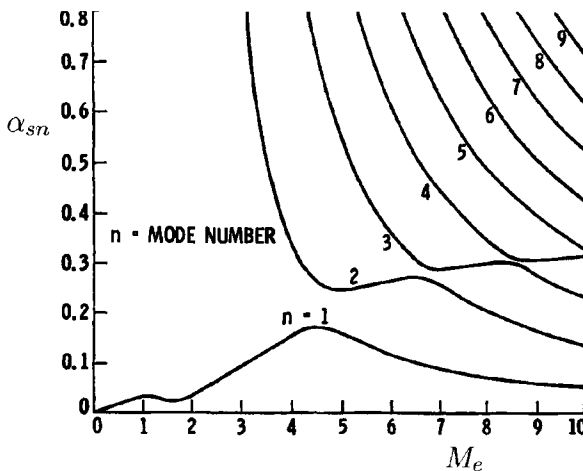


**Fig. 14.1.** Multiple modes of two-dimensional inflectional neutral waves in inviscid theory. Adiabatic wall. [2]

number  $M_e$ . The evolution of the wave numbers is in agreement with the analysis of Eq. (14.2.22) except for the wiggles shown by the curves. The behaviour of results obtained numerically with the full stability equations (at finite Reynolds number) is also well explained by this analysis.

Numerically, the inflectional multiple solutions have been detected in a flat plate boundary-layer on an adiabatic wall for Mach numbers larger than 2.2. This is explained by the location of the relative sonic point which moves out in the boundary-layer when the Mach number  $M_e$  increases.

Except for certain particular modes, the higher modes are interpreted as sound waves which reflect back and forth between the wall and the sonic line of the relative flow at  $y = y_a$  in the boundary-layer.

Mack found also multiple solutions corresponding to noninflectional neutral waves. These waves are subsonic ( $\tilde{M}_e < 1$ ) and their phase velocities are such that

$$1 \leq c_r \leq 1 + \frac{1}{M_e} \quad (14.2.23)$$

The case  $c_r = 1$  means that the wave is at rest with respect to the freestream. The case  $c_r = 1 + 1/M_e$  means that the wave propagates downstream relative to the freestream with the freestream celerity of sound. In the freestream, the necessary condition for the existence of a subsonic neutral wave is satisfied. If the condition  $\tilde{M}^2 > 1$  is satisfied somewhere, the existence of multiple solutions is possible. The waves with  $c_r = 1$  are important because in the absence of a generalized inflection point in the boundary-layer, these waves are associated to unstable waves with  $c_r < 1$ . This means that a compressible boundary-layer with a region of supersonic relative Mach number has an inviscid instability.

### 14.2.3 Examples of Results

#### Two-Dimensional Waves

Figures 14.2 to 14.5 show the results obtained by Arnal [4] who solved the full stability equations according to the spatial theory. The stability diagrams are computed for two-dimensional waves ( $\psi = 0^\circ$ ) for a mean flow which is a flat plate boundary-layer developing on an adiabatic wall. The Reynolds number  $R_{\delta^*}$  is based on the displacement thickness  $\delta^*$ , on the freestream velocity  $u_e$  and on the freestream kinematic viscosity. The wave number  $\alpha_r$  and the amplification coefficient  $-\alpha_i$  are made dimensionless with the displacement thickness.

In the range of Reynolds number shown in the figures, the general shape of the stability diagrams does not change much when the Mach number  $M_e$  increases from 0 to 1.3. No sign of inviscid instability is detected. In this range of Mach number, the instability is essentially viscous for a wide range of Reynolds number; at very large Reynolds number, however, the characteristics of instability become inviscid. A local maximum of the amplification coefficient is observed at a finite Reynolds number and curves of iso-amplification enclose this maximum. The values of the maximum amplification coefficient decrease when the Mach number increases. At low Mach numbers this result is of importance because a two-dimensional wave has the largest amplitude ratio at any Reynolds number but this conclusion is no longer true above a Mach number of about 1. In transonic and supersonic flows, an oblique wave can become more unstable than a two-dimensional wave. In addition, the instability becomes strongly dependent upon the behaviour of the higher modes when the Mach number is increased. Except at low Mach numbers, the stability of boundary-layers, even for the flat plate, must be examined by taking into account the oblique waves and the higher modes.

Increasing the Mach number from the low subsonic case, it is observed that the inviscid instability comes into play. At large but finite Reynolds numbers, the iso-amplification coefficient curves are nearly parallel to the Reynolds number axis and an unstable range of wave numbers is expected at infinite Reynolds number. This feature is visible in the figures corresponding to  $M_e > 2.2$ . The inviscid instability occurs because of the existence of a generalized inflection point which moves away from the wall as the Mach number increases.

When the Mach number increases, the higher modes are present. The second mode appears at lower and lower wave numbers and is clearly seen in the stability diagram for  $M_e = 4.5$ . If the Mach number increases again, the two unstable regions join together. This does not mean that the higher modes disappear but their detection is more subtle.

The results shown in Fig. 14.6 are obtained from the temporal inviscid theory for two-dimensional waves [2]. The dimensionless maximum amplification coefficient is plotted as a function of the freestream Mach number for a flat

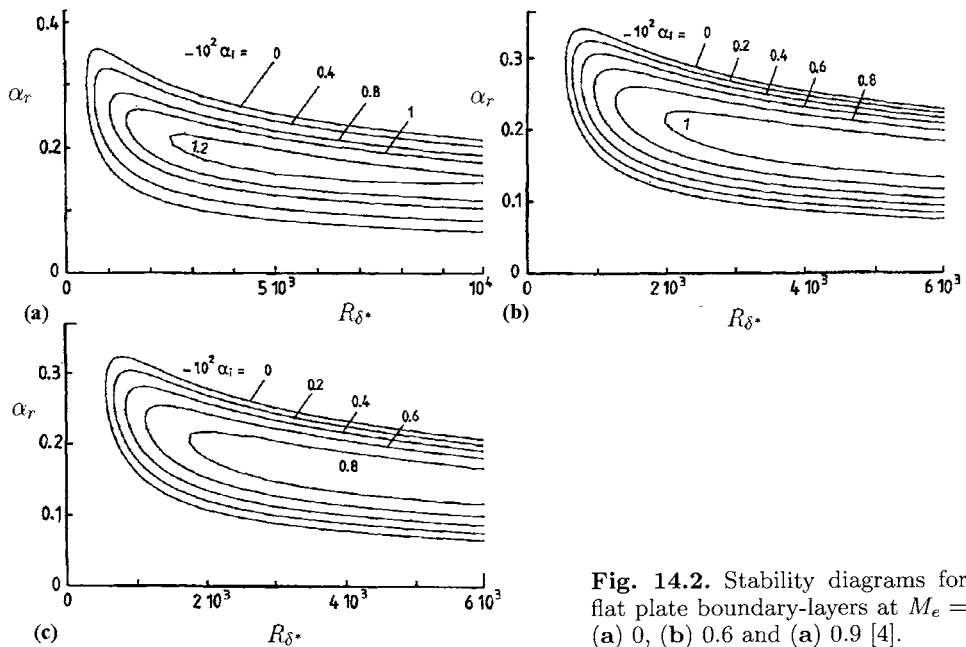


**Fig. 14.2.** Stability diagrams for flat plate boundary-layers at  $M_e =$  (a) 0, (b) 0.6 and (a) 0.9 [4].

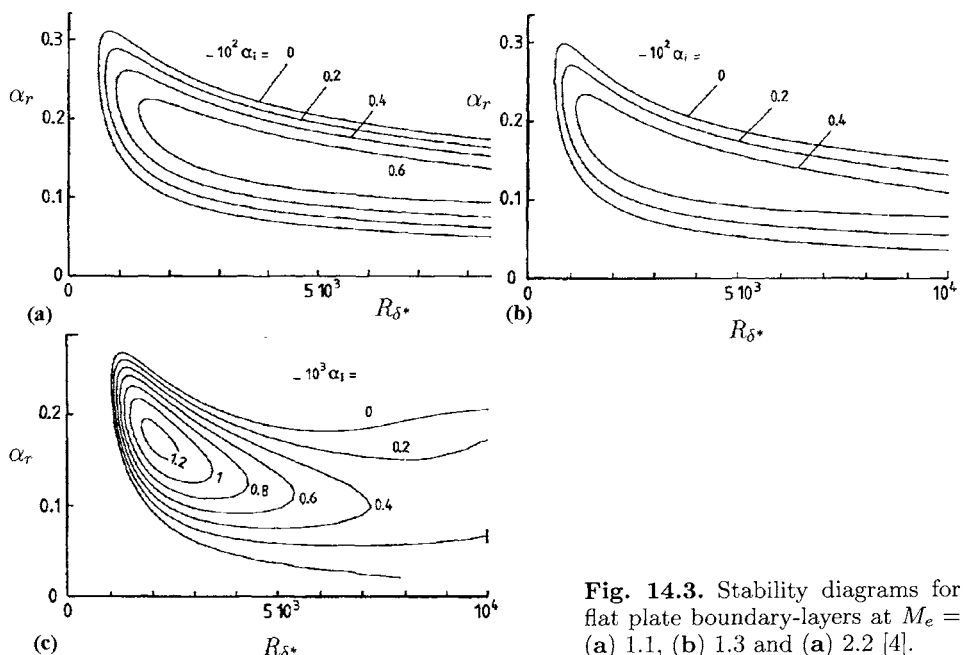


**Fig. 14.3.** Stability diagrams for flat plate boundary-layers at  $M_e =$  (a) 1.1, (b) 1.3 and (a) 2.2 [4].

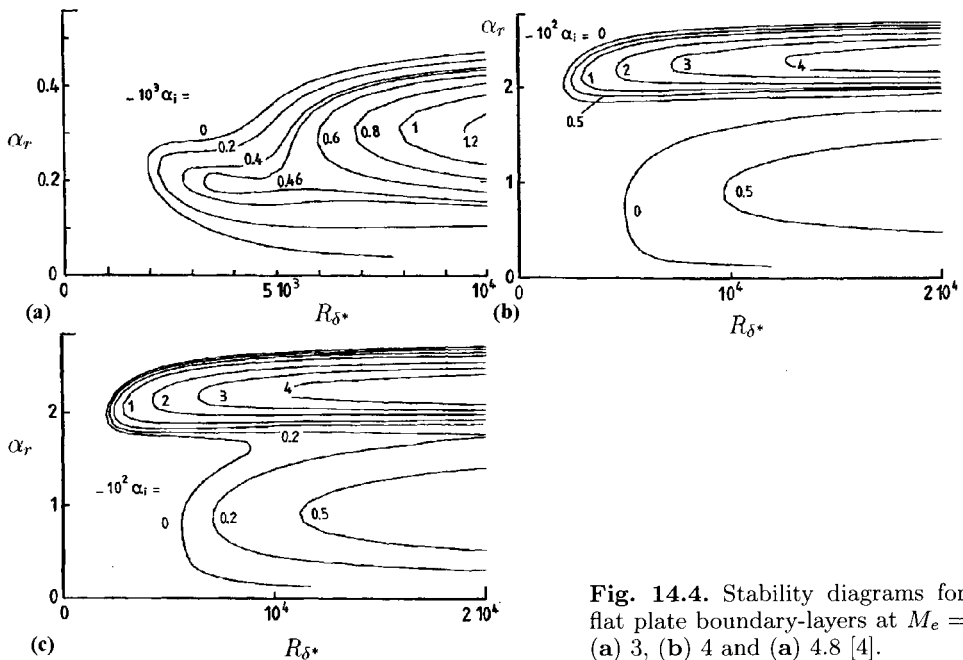


Fig. 14.4. Stability diagrams for flat plate boundary-layers at  $M_e =$  (a) 3, (b) 4 and (a) 4.8 [4].

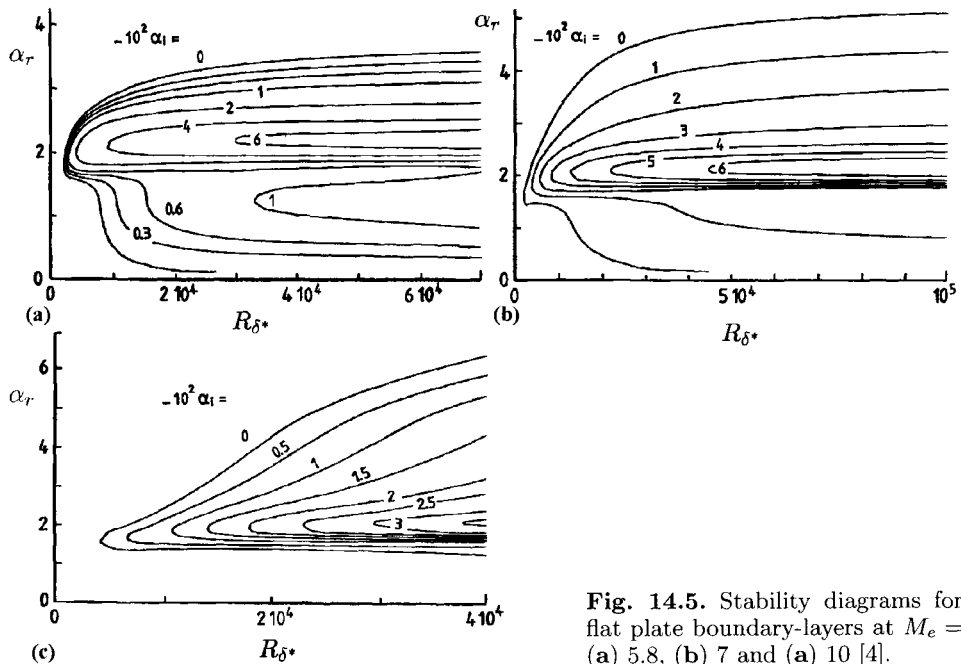
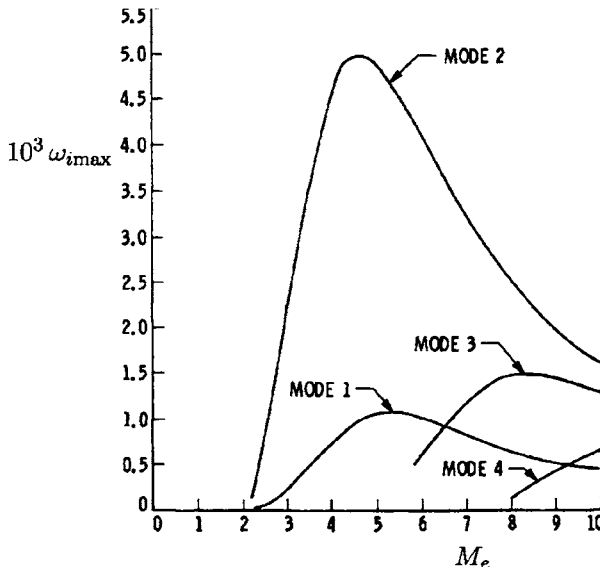


Fig. 14.5. Stability diagrams for flat plate boundary-layers at  $M_e =$  (a) 5.8, (b) 7 and (a) 10 [4].



**Fig. 14.6.** Flat plate on adiabatic wall [2]. Maximum amplification rate of two-dimensional waves in temporal inviscid theory. The reference length is  $(\nu_e x / u_e)^{1/2}$ .

plate boundary-layer developing on an adiabatic wall. In these calculations the reference length is  $(\nu_e x / u_e)^{1/2}$ . This figure shows that below  $M_e = 2.2$  there is no inviscid instability. In the range  $M_e < 10$ , the second mode is always more unstable than the first mode and above  $M_e = 6.5$  the third mode is even more unstable than the first mode.

### Effect of wave direction

In a compressible flow it is very important to consider oblique waves even if the mean flow is two-dimensional and even in the transonic regime. For example, Fig. 14.7 [4] shows the evolution of the maximum amplification coefficient at given Reynolds numbers as a function of the wave direction  $\psi$  and of the freestream Mach number  $M_e$ ; these results are obtained for a flat plate boundary-layer on an adiabatic wall. It is seen that for  $M_e = 1.1$  and  $M_e = 1.3$  the maximum amplification coefficient occurs for oblique waves around  $\psi = 40^\circ$  at  $M_e = 1.1$  and around  $\psi = 50^\circ$  at  $M_e = 1.3$ .

At larger Mach numbers, the higher modes are present and the effect of wave direction depends on the considered mode. Figure 14.8 [4] shows two stability diagrams for  $M_e = 4.5$ , one corresponds to two-dimensional waves and the other to a wave direction  $\psi = 60^\circ$ . The instability of the first mode is increased for the oblique wave whereas the second mode is very stable for this wave direction. These results confirm the inviscid calculations of Mack. Figure 14.9 [2] shows that for  $M_e = 4.5$ , the second mode is more unstable than the first mode; the

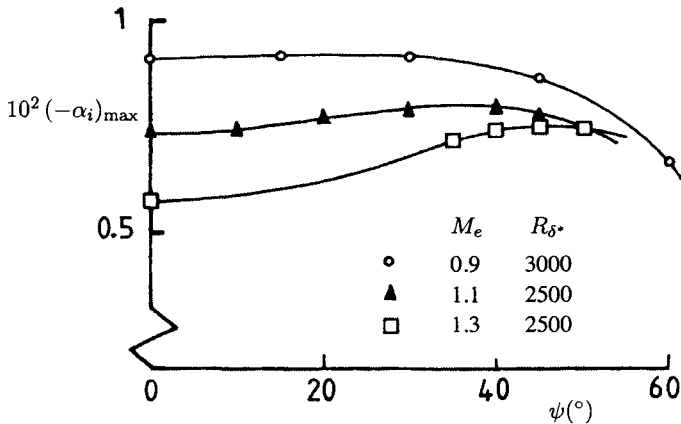


Fig. 14.7. Effect of wave direction on the maximum amplification rate in transonic flow [4]. The reference length is  $\delta^*$ .

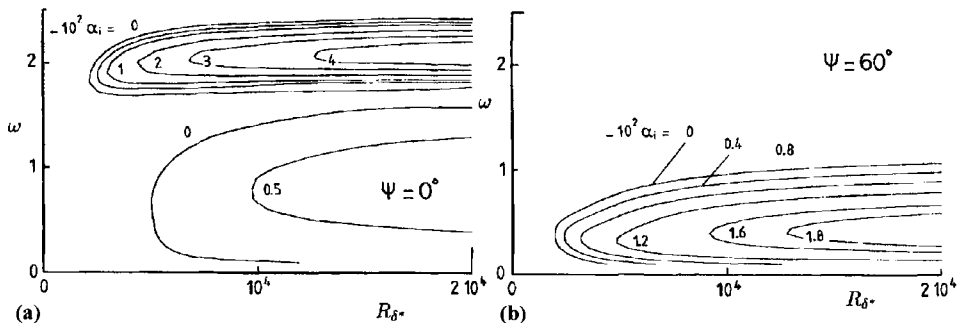
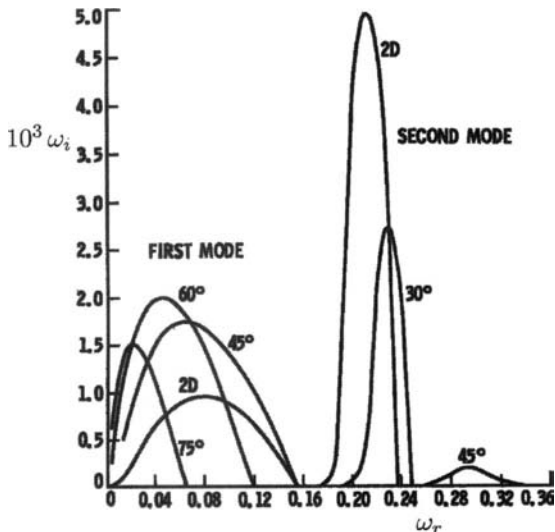


Fig. 14.8. Effect of wave direction on the amplification rate in a flat plate boundary-layer on adiabatic wall ( $M_e = 4.5$ ), spatial theory [4]. The reference length is  $\delta^*$ .

instability of the first mode is maximum for an oblique wave ( $\psi = 60^\circ$ ) whereas the instability of the second mode is maximum for a two-dimensional wave.

### Effect of Wall Cooling

The effect of wall temperature on the stability of a flat plate flow, obtained by Arnal [4], is shown in Fig. 14.10. The results are shown for two-dimensional waves at  $M_e = 7$  and for two wall temperatures  $T_w/T_{aw} = 1$  and  $T_w/T_{aw} = 0.3$ . It is seen that wall cooling tends to separate the second mode from the first mode. The instability of the first mode is lowered whereas the instability of the second mode is enhanced. In fact, the condition (14.2.21) of a generalized inflection point is no longer satisfied when the wall is cooled, then the inviscid instability disappears and it is observed that the first mode vanishes even for oblique waves. However, the wall cooling is not able to eliminate the region of supersonic relative flow and higher modes persist. Actually, the second mode is



**Fig. 14.9.** Effect of wave direction on the amplification rate in a flat plate boundary-layer on an adiabatic wall, inviscid temporal theory ( $M_e = 4.5$ ) [2]. The reference length is  $(\nu_e x / u_e)^{1/2}$ .

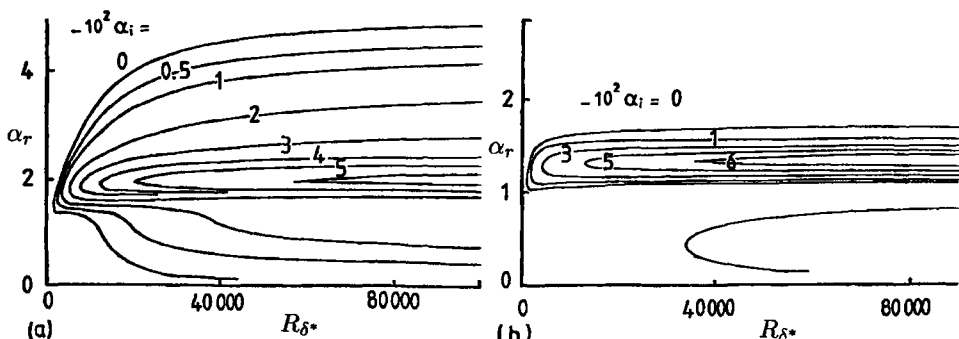


**Fig. 14.10.** Effect of wall temperature on the stability of a flat plate boundary-layer ( $M_e = 7$ ,  $\psi = 0^\circ$ ). a)  $T_w/T_{aw} = 1$  b)  $T_w/T_{aw} = 0.3$  [4]. The reference length is  $\delta^*$ .

destabilized by wall cooling. Such comments however depend on the reference length because the evolution of the dimensionless amplification coefficient is not the same if the reference length is  $\delta^*$  or  $(\nu_e x / u_e)^{1/2}$ .

### 14.3 Factors that Influence Transition

#### 14.3.1 Effects of Noise

In supersonic flow a mysterious effect of unit Reynolds number in wind tunnel has been the subject of a debate for a long time. Correlations have been

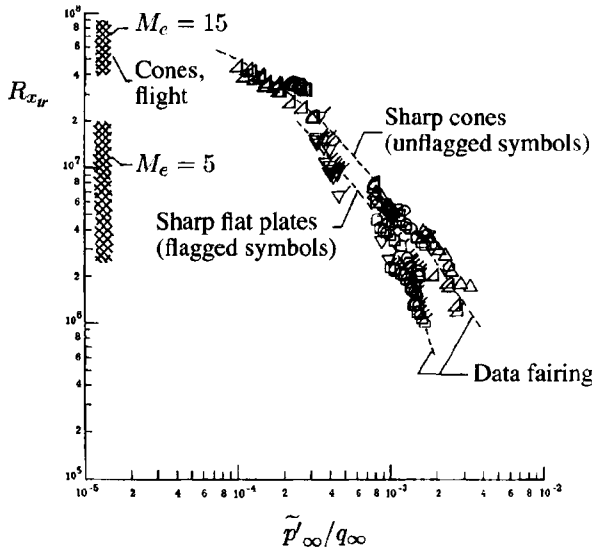


Fig. 14.11. Effect of noise on transition [5].

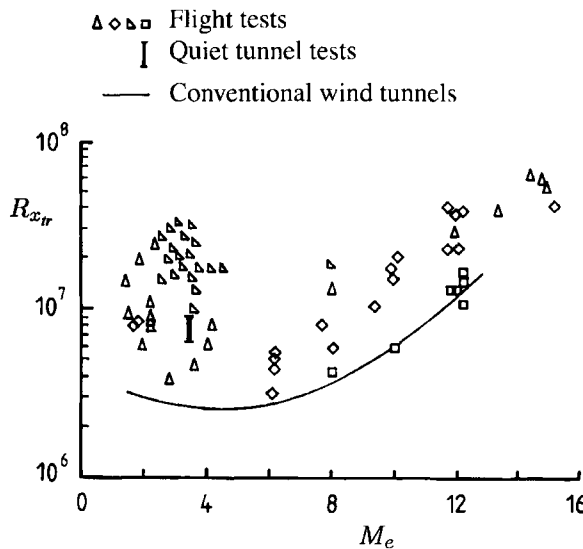


Fig. 14.12. Transition on cones [6, 7].

proposed to relate the transition Reynolds number on a flat plate to the unit Reynolds number  $u_e/\nu_e$  and also to the size of the wind tunnel. Nowadays, it is accepted that transition in a supersonic flow is dominated by the noise, i.e. the pressure fluctuations. This is illustrated in Fig. 14.11 [5] which shows a correlation between the transition Reynolds number  $R_{x_{tr}}$  and the level of pressure fluctuations in the Mach number range  $4 < M_e < 23$ . The noise is generated upstream of the test section in the freestream and is also radiated by the turbulent boundary-layer developing along the walls of the wind tunnel. This is

consistent with the early observations on the effect of unit Reynolds number. For a larger wind tunnel the nozzle walls are farther from the model and it is expected that the noise radiated by the boundary-layer is lower at the location of the model.

In fact, the unit Reynolds number effect is a combination of many parameters such as the radiated noise, the bluntness of the flat plate or of the cone, the receptivity of the boundary-layer to external disturbances which depends on the characteristics of the boundary-layer developing on the model. For example, consider a flat plate boundary-layer; if the unit Reynolds number is increased, the boundary-layer is thinner and its receptivity to the freestream disturbances is modified in the sense that the range of unstable frequencies is changed, then the transition Reynolds number varies.

A quiet wind tunnel has been developed at NASA Langley for a Mach number  $M = 3.5$  [6, 7]. To eliminate the noise radiated by the nozzle turbulent boundary-layer the wind tunnel has been specially designed to have a laminar boundary-layer along the walls of the nozzle. In the best conditions, the transition Reynolds numbers measured on a  $5^\circ$  half-angle sharp cone are two or three times larger than in conventional wind tunnels. The results are in much better agreement with available flight experiments (Fig. 14.12); a precise comparison is difficult however because the wall temperature in flight tests is not known. With the same restriction about the possible effect of wall temperature, it seems that the transition Reynolds number has a local maximum around  $M_e = 3$  and a local minimum around  $M_e = 5$ .

### 14.3.2 Effects of Wall Cooling

Figure 14.13 shows experimental results collected by Potter [8]. The transition Reynolds number  $R_{x_{tr}}$  is reduced by its value  $R_{x_{tr0}}$  for an adiabatic wall at the same Mach number. At a given Mach number, all the data correspond to the same unit Reynolds number  $u_e/\nu_e$  but at different Mach numbers the unit Reynolds number is not the same. It is possible that the effect of unit Reynolds number (noise) is not negligible even if the transition Reynolds number is reduced by its adiabatic value. The two curves for a flat plate boundary-layer at  $M_e = 8$  are obtained for two unit Reynolds numbers, the upper curve is for the lower unit Reynolds number. With this reservation, the general trend is that wall cooling delays transition. Exceptions are observed in this behaviour but the reason is not understood.

### 14.3.3 Effects of Nose Bluntness

In supersonic flow, experiments are often carried out by using flat plates or cones. If the leading edge of the flat plate or the apex of the cone are not

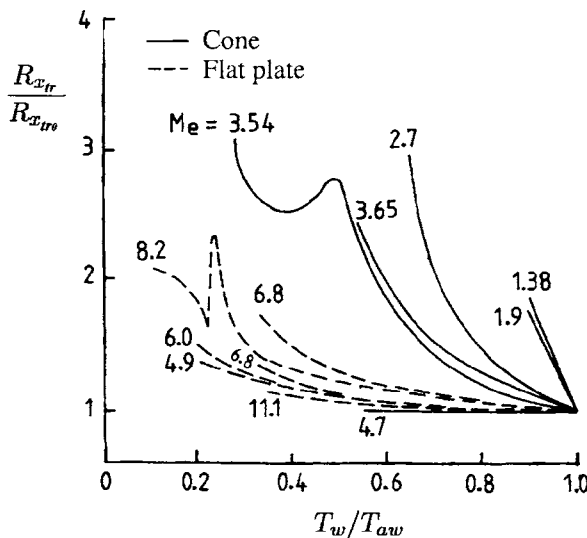


Fig. 14.13. Effect of wall cooling on transition [8].

perfectly sharp, significant variations of the transition Reynolds number are observed.

Figure 14.14 shows the variation of the transition Reynolds number on blunted cones as a function of the Reynolds number  $R_r = u_e r / \nu_e$  where  $r$  is the radius of the spherical nose [9].

With blunted cones, the flow is modified by the existence of a bow shock wave in front of the cone. The streamlines which cross this bow shock wave have a different entropy jump according to the local slope of the shock wave with

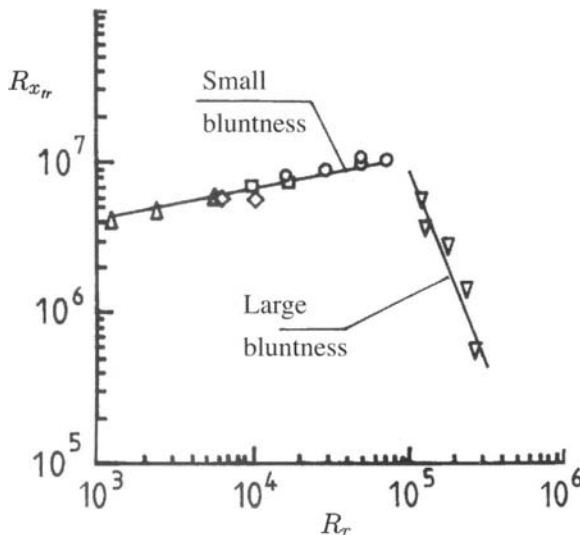


Fig. 14.14. Effects on bluntness on transition on a cone [9].

respect to the freestream. Downstream of the shock wave, in inviscid flow, the entropy is not constant as it varies from streamline to streamline. The entropy variations are observed in a region which wraps the cone near the wall. Due to mass conservation, the thickness of the layer of variable entropy decreases downstream. This phenomenon is called entropy swallowing. Even if the wall pressure distribution is not dramatically changed away from the nose, the flow characteristics are modified sufficiently to have a significant effect on transition mechanisms.

For small bluntness, a stabilizing effect is observed since disturbances which are observed on a sharp cone are no longer detected (Stetson et al. [10, 11]). For larger bluntness, Stetson et al. measured large amplitude disturbances outside the laminar boundary-layer which seems to indicate the existence of an inviscid instability associated with the variations of the mean flow.

#### 14.3.4 Effects of Surface Roughness

When the roughness elements are large enough, it can be expected that their effect will dominate the transition process so that the effects of other parameters such as noise will be less.

Consider the evolution of transition as a function of the size of an isolated roughness element, everything being the same otherwise. If the size is very small the flow is locally modified around the roughness but the transition location is not affected. For a *critical size*, there is a rapid movement of the transition location towards the roughness but this movement is more and more gradual as the Mach number increases. Transition takes place in a wedge like region behind the roughness element. The apex of the wedge is at a certain distance  $L$  from the roughness. For roughness elements larger than the *effective roughness* size, the distance  $L$  does not change very much. In fact, this distance is a function of the Mach number and increases as the Mach number increases. In incompressible flow, the apex of the wedge is practically at the roughness location.

There is no general criterion giving the effective roughness size. For the flow on a cone the Van Driest-Blumer [12, 13] criterion is

$$R_{k_{\text{eff}}} = K \left[ 1 + \frac{\gamma - 1}{2} M_e^2 - 0.81 \frac{T_{aw} - T_w}{T_e} \right] R_{x_k}^{1/4}, \quad K = 33.4 \quad (14.3.1)$$

where the Reynolds numbers are based on the freestream velocity  $u_e$  and the freestream kinematic viscosity  $\nu_e$ . The effective roughness  $k_{\text{eff}}$  is the height of the roughness for which the apex of the transition wedge is at distance  $L$  from the roughness and  $x_k$  is the roughness distance from the nose of the cone. The correlation given by Eq. (14.3.1) is applicable for Mach numbers less than 4.

For a flat plate boundary-layer the coefficient  $K$  is multiplied by a factor between 2 and 3.

### 14.3.5 Leading Edge Contamination

Consider a swept wing and the region in the vicinity of the attachment line. As in Section 8.2,  $x$  is the surface coordinate normal to the leading edge and  $z$  is the coordinate parallel to the attachment line. The Reynolds number  $R$ , Eq. (8.2.3), is now defined with the kinematic viscosity at the boundary-layer edge

$$R = \frac{w_e}{\nu_e} \left[ \frac{\nu_e}{(du_e/dx)_{x=0}} \right]^{1/2} \quad (14.3.2)$$

To analyze the available experimental data on leading edge contamination, Poll [14] introduced a transformed Reynolds number

$$R^* = R \left( \frac{\nu^*}{\nu_e} \right)^{1/2} \quad (14.3.3)$$

where  $\nu^*$  was calculated from a reference temperature  $T^*$

$$T^* = T_e + 0.1(T_w - T_e) + 0.6(T_{aw} - T_e) \quad (14.3.4)$$

In the range  $0 < M_e < 6$ , the leading edge contamination criterion is  $R^* = 245 \pm 35$ . With this Reynolds number, no effect of Mach number, unit Reynolds number, wall temperature is observed.

## 14.4 $e^n$ -Method for Compressible Flows

The  $e^n$ -method discussed in Chapters 5 and 8 for two- and three-dimensional incompressible flows can also be used for two- and three-dimensional compressible flows. The procedure is essentially similar to that for incompressible flows. For three-dimensional flows we now solve the compressible stability equations, Eqs. (14.2.4) to (14.2.9), rather than the equations for incompressible flows with velocity and temperature profiles obtained either from the solution of the compressible laminar boundary-layer or Navier–Stokes equations. Either one of the eigenvalue formulations discussed in subsection 8.3.1 can be used for compressible flows. Here we use the eigenvalue formulation of Cebeci and Stewartson and briefly discuss the numerical solution of the stability equations with the box method discussed for the incompressible stability equations.

Similar to the procedure used for the Orr–Sommerfeld equation in Section 5.6, Eqs. (14.2.21) to (14.2.25) can be expressed as a first-order system by defining the following new variables with primes denoting differentiation with respect to  $y$ ,

$$\begin{aligned} z_1 &= \alpha \hat{u} + \beta \hat{w}, & z_2 &= \alpha \hat{u}' + \beta \hat{w}', & z_3 &= \hat{v}, & z_4 &= \frac{\hat{p}}{\gamma M_e^2} \\ z_5 &= \hat{T}, & z_6 &= \hat{T}', & z_7 &= \alpha \hat{w} - \beta \hat{u}, & z_8 &= \alpha \hat{w}' - \beta \hat{u}' \end{aligned} \quad (14.4.1)$$

In terms of these new variables, Eqs. (14.2.11) to (14.2.15), for a three-dimensional compressible flow can be written as

$$\begin{aligned} z'_1 &= z_2 \\ z'_2 &= b_{21}z_1 + b_{22}z_2 + b_{23}z_3 + b_{24}z_4 + b_{25}z_5 + b_{26}z_6 \\ z'_3 &= b_{31}z_1 + b_{33}z_3 + b_{34}z_4 + b_{35}z_5 \\ z'_4 &= b_{41}z_1 + b_{42}z_2 + b_{43}z_3 + b_{44}z_4 + b_{45}z_5 + b_{46}z_6 \\ z'_5 &= z_6 \\ z'_6 &= b_{62}z_2 + b_{63}z_3 + b_{64}z_4 + b_{65}z_5 + b_{66}z_6 + b_{68}z_8 \\ z'_7 &= z_8 \\ z'_8 &= b_{83}z_3 + b_{85}z_5 + b_{86}z_6 + b_{87}z_7 + b_{88}z_8 \end{aligned} \quad (14.4.2)$$

where the coefficients  $b_{ij}$  ( $i, j = 1, 2, \dots, 8$ ) are

$$\gamma_3 = \alpha \frac{du}{dy} + \beta \frac{dw}{dy}, \quad \gamma_4 = \alpha \frac{dw}{dy} - \beta \frac{du}{dy}, \quad d = \frac{\lambda}{\mu} \quad (14.4.3a)$$

$$b_{21} = \frac{iR}{\mu T} \gamma_1 + \gamma_2, \quad b_{22} = -\frac{1}{\mu} \frac{d\mu}{dT} \frac{dT}{dy} \quad (14.4.3b)$$

$$b_{23} = \frac{R\gamma_3}{\mu T} - \gamma_2 \frac{i}{\mu} \frac{d\mu}{dT} \frac{dT}{dy} - \frac{1+2d}{3} \gamma_2 \frac{i}{T} \frac{dT}{dy} \quad (14.4.3c)$$

$$b_{24} = \frac{iR}{\mu} \gamma_2 - \frac{1+2d}{3} \gamma M_e^2 \gamma_2 \gamma_1 \quad (14.4.3d)$$

$$b_{25} = \frac{1+2d}{3T} \gamma_1 \gamma_2 - \frac{1}{\mu} \frac{d\mu}{dT} \left( \alpha \frac{d^2 u}{dy^2} + \beta \frac{d^2 w}{dy^2} \right) - \frac{1}{\mu} \frac{d^2 \mu}{dT^2} \frac{dT}{dy} \gamma_3 \quad (14.4.3e)$$

$$b_{26} = -\frac{1}{\mu} \frac{d\mu}{dT} \gamma_3, \quad b_{31} = -i, \quad b_{33} = \frac{1}{T} \frac{dT}{dy}, \quad b_{34} = -i \gamma M_e^2 \gamma_1 \quad (14.4.3f)$$

$$b_{35} = \frac{i}{T} \gamma_1, \quad E = \frac{R}{\mu} + \frac{2}{3} i (2+d) \gamma M_e^2 \gamma_1, \quad (14.4.3g)$$

$$b_{41} = -\frac{i}{E} \left[ -2b_{22} + \frac{2}{3} (2+d) b_{33} \right] \quad (14.4.3h)$$

$$b_{42} = -\frac{i}{E} \quad (14.4.3i)$$

$$b_{43} = \frac{1}{E} \left[ -\gamma_2 + \frac{2(2+d)}{3\mu T} \frac{d\mu}{dT} \left( \frac{dT}{dy} \right)^2 + \frac{2(2+d)}{3T} \frac{d^2 T}{dy^2} - \frac{iR}{\mu T} \gamma_1 \right] \quad (14.4.3j)$$

$$b_{44} = -\frac{2i}{3E} (2+d) \gamma M_e^2 (-\gamma_1 b_{22} + \gamma_3 + b_{22} \gamma_1) \quad (14.4.3k)$$

$$b_{45} = \frac{i}{E} \left[ \frac{1}{\mu} \frac{d\mu}{dT} \gamma_3 + \frac{2(2+d)}{3T} (-b_{22} \gamma_1 + \gamma_3) \right] \quad (14.4.3l)$$

$$b_{46} = \frac{2i}{3ET} (2+d) \gamma_1, \quad b_{62} = -2(\gamma - 1) \text{Pr} M_e^2 \left( \frac{\gamma_3}{\gamma_2} \right) \quad (14.4.3m)$$

$$b_{63} = \frac{\text{Pr}R}{\mu} b_{33} - 2i(\gamma - 1)\text{Pr}M_e^2 \gamma_3, \quad b_{64} = -\frac{i}{\mu}(\gamma - 1)\text{Pr}RM_e^2 \gamma_1 \quad (14.4.3n)$$

$$\begin{aligned} b_{65} &= i \frac{\text{Pr}R}{\mu T} \gamma_1 + \gamma_2 - \frac{1}{k} \frac{dk}{dT} \frac{d^2T}{dy^2} - \frac{1}{k} \frac{d^2k}{dT^2} \left( \frac{dT}{dy} \right)^2 \\ &\quad - (\gamma - 1)\text{Pr}M_e^2 \frac{1}{\mu} \frac{d\mu}{dT} \left( \frac{d^2u}{dy^2} + \frac{d^2w}{dy^2} \right) \end{aligned} \quad (14.4.3o)$$

$$b_{66} = -\frac{2}{k} \frac{dk}{dT} \frac{dT}{dy}, \quad b_{68} = -\frac{2(\gamma - 1)}{\gamma_2} \text{Pr}M_e^2 \gamma_4, \quad b_{83} = \frac{R}{\mu T} \gamma_4 \quad (14.4.3p)$$

$$b_{85} = -\frac{1}{\mu} \frac{d\mu}{dT} \left( \alpha \frac{d^2w}{dy^2} - \beta \frac{d^2u}{dy^2} \right) - \frac{1}{\mu} \frac{d^2\mu}{dT^2} \frac{dT}{dy} \gamma_4 \quad (14.4.3q)$$

$$b_{86} = -\frac{1}{\mu} \frac{d\mu}{dT} \gamma_4, \quad b_{87} = \frac{iR}{\mu T} \gamma_1 + \gamma_2, \quad b_{88} = b_{22} \quad (14.4.3r)$$

The boundary conditions become

$$\begin{aligned} y = 0, \quad z_1 &= z_3 = z_5 = z_7 = 0 \\ y \rightarrow \infty, \quad z_1, z_3, z_5, z_7 &\rightarrow 0 \end{aligned} \quad (14.4.4)$$

In terms of these new variables, Eqs. (14.4.2) and (14.4.4) can be written as

$$\tilde{z}' = B\tilde{z} \quad (14.4.5)$$

Here  $\tilde{z} = (z_1, z_2, \dots, z_8)$  and  $B$  is an  $8 \times 8$  coefficient matrix defined by

$$B = \begin{vmatrix} 0 & 1 & 0 & 0 & 0 & 0 & 0 & 0 \\ b_{21} & b_{22} & b_{23} & b_{24} & b_{25} & b_{26} & 0 & 0 \\ b_{31} & 0 & b_{33} & b_{34} & b_{35} & 0 & 0 & 0 \\ b_{41} & b_{42} & b_{43} & b_{44} & b_{45} & b_{46} & 0 & 0 \\ 0 & 0 & 0 & 0 & 0 & 1 & 0 & 0 \\ 0 & b_{62} & b_{63} & b_{64} & b_{65} & b_{66} & 0 & b_{68} \\ 0 & 0 & 0 & 0 & 0 & 0 & 0 & 1 \\ 0 & 0 & b_{83} & 0 & b_{85} & b_{86} & b_{87} & b_{88} \end{vmatrix} \quad (14.4.6)$$

with its nonzero elements defined by Eqs. (14.4.3a) to (14.4.3r).

The solution of the system given by Eqs. (14.4.4) and (14.4.5) is obtained with the numerical method described in Section 8.4.

In [1] a commercial software for calculating transition in compressible and incompressible flows on wings with and without suction is described. The software uses the  $e^n$ -method and the Cebeci–Stewartson saddle-point method described here and in Section 8.4. It includes an interface program, a stability-transition program and a boundary layer program for incompressible and compressible flows. The boundary layer program is formulated in such a way that it can also be used to calculate separated flows as described in Chapter 13.

## 14.5 Applications of the $e^n$ -Method

### AS 409 Infinite Swept Wing

As in incompressible flows, the  $e^n$ -method with various eigenvalue formulations discussed in subsection 8.3.1 has also been applied to three-dimensional compressible flows [1]. Here, with the eigenvalue formulation of Cebeci and Stewartson we discuss its application for the AS 409 infinite swept wing data of [15, 16]. Similar calculations using the eigenvalue formulation of Mack and Arnal have also been carried out as discussed in [1]. The measurements for this 15-degree swept tapered wing were conducted in the cryogenic wind tunnel T2 of ONERA/CERT at very low stagnation temperatures [15]. The wing, with a chord of 0.228 m at the root and 0.145 m at the tip, had a span of 0.39 m with an AS409 cross-section and a trailing-edge sweep angle of three degrees. It also had wavy surfaces less than 0.05 mm (from peak to valley) for a chordwise extent of about 2 cm. In order to avoid the need to perform fully three-dimensional stability/transition calculations, the measurements discussed in [15] and summarized in [16] were carried out under infinite swept wing conditions with the wing having a mean sweep angle of 13 degrees at an angle of attack of 0.3 degrees. The mean chord for computations was stated to be 0.196 m.

Calculations with the Cebeci and Stewartson formulation have been performed for runs 42 and 79 having stagnation temperatures of 145 K and 165 K and stagnation pressures of 2.0 and 2.5 bar, respectively. Here we present a brief summary of the predictions for these runs.

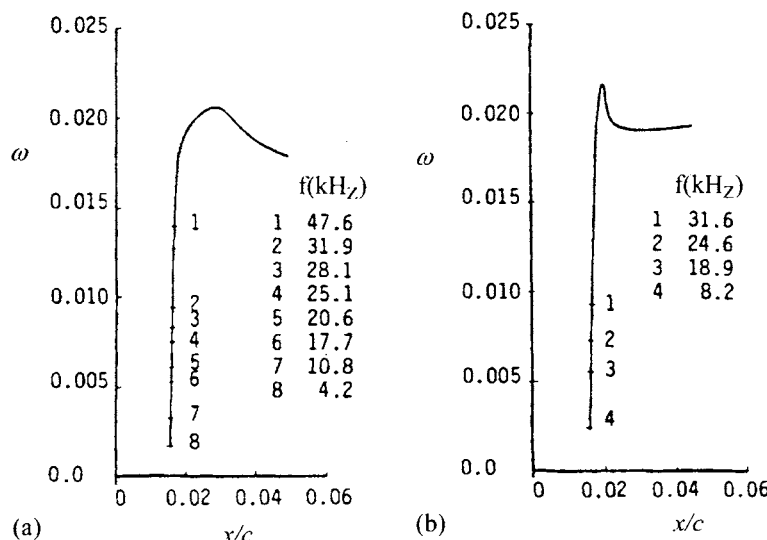


Fig. 14.15. Zarfs for run 42 for (a) adiabatic and (b) measured wall temperature distributions.

Figure 14.15 shows the zarfs for run 42 for an adiabatic and measured wall temperature distributions at a Reynolds number of  $12.8 \times 10^6$ . As can be seen, the frequencies originate at nearly the same location (on a vertical line) and vary drastically one from another. Figure 14.16 shows the computed  $n$  factors for the zarfs of Fig. 14.15. The results demonstrate that for adiabatic wall conditions, the maximum value of  $n$  for the experimental transition location is around 6.2; the corresponding value for the measured wall temperature is 6.7. What is more important, however, is the fact that in the latter case the computed transition location agrees very well with the observed location, considering that the  $n$ -value for transition in this tunnel lies between 7 and 8.

Figure 14.17 shows the zarfs for run 79 with wall conditions corresponding to adiabatic temperature and Fig. 14.18 shows a comparison between the zarfs obtained under adiabatic and measured wall temperature conditions. Again the steep rise in frequencies close to a single  $x/c$ -location is noted. The zarf calculations were performed for a very fine  $x/c$ -grid, since most of the frequencies begin to exhibit amplification in an interval of  $1/1000^{\text{th}}$  of chord around 0.015. Figure 14.17 also shows zarfs away from the leading edge. These zarfs have low

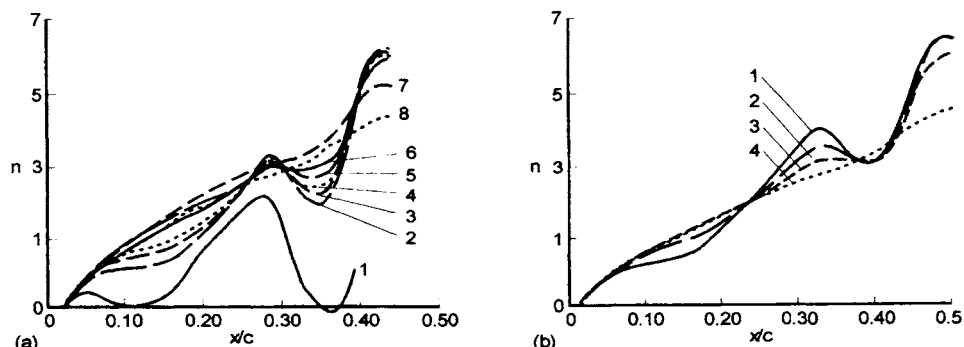


Fig. 14.16. Computed  $n$ -factors for run 42 for (a) adiabatic and (b) measured wall temperature distributions.

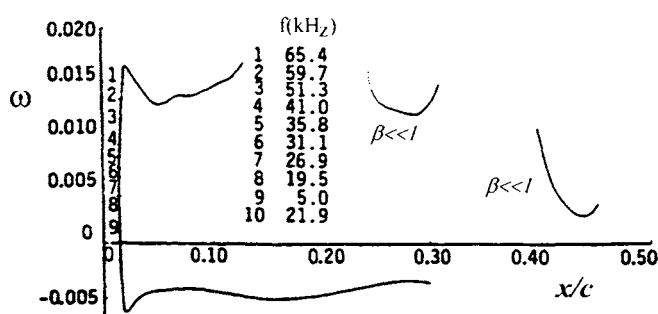


Fig. 14.17. Zarfs for run 79 for adiabatic wall temperature distribution.

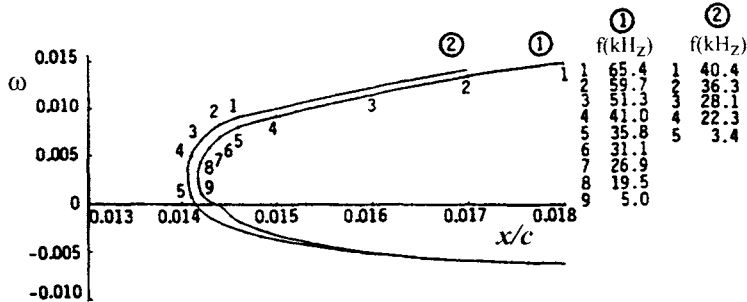


Fig. 14.18. Comparison between zarfs of run 79 for (1) adiabatic and (2) measured wall temperature distributions.

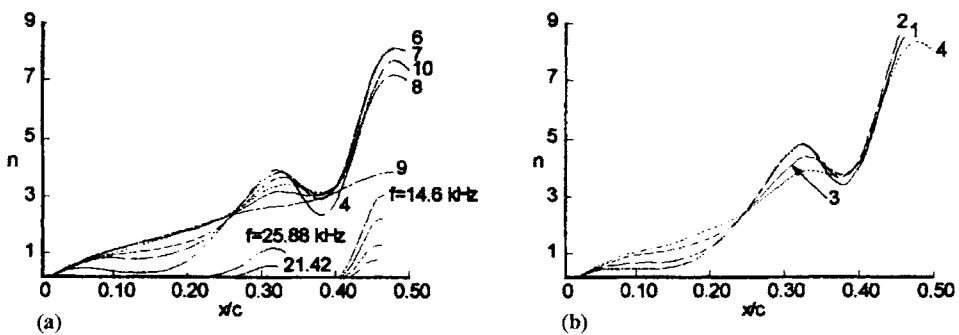


Fig. 14.19. Computed  $n$ -factors for run 79 for (a) adiabatic and (b) measured wall temperature distributions.

values of  $\beta_r$  around  $10^{-2}$ , occur in an almost zero pressure gradient region and do not lead to amplification rates that grow significantly.

Figure 14.19 shows the computed  $n$  factors for run 79 with stability calculations performed for the adiabatic and measured wall temperature conditions. For this flow, the  $n$ -value is much higher than those in run 42. For an adiabatic wall, it reaches a maximum value of around 8 and a value of around 9 for the measured wall temperature case. If we take the  $n$  value to be 7.5 (a mid- $n$  value of the expected  $n$ -value range for this wind tunnel) then transition occurs at  $x/c = 0.46$  for adiabatic wall conditions and  $x/c = 0.47$  for measured wall temperature conditions. This compares well with the inferred transition location of  $x/c = 0.47$ .

### Effect of Mach Number

Figure 14.20 [17] shows an application of the  $e^n$ -method to a flat plate boundary-layer developing on an adiabatic wall. The transition Reynolds number  $R_{x_{tr}}$  is plotted as a function of the Mach number  $M_e$  at the edge of the boundary-layer. It is assumed that transition occurs for a fixed value of the  $n$ -factor.

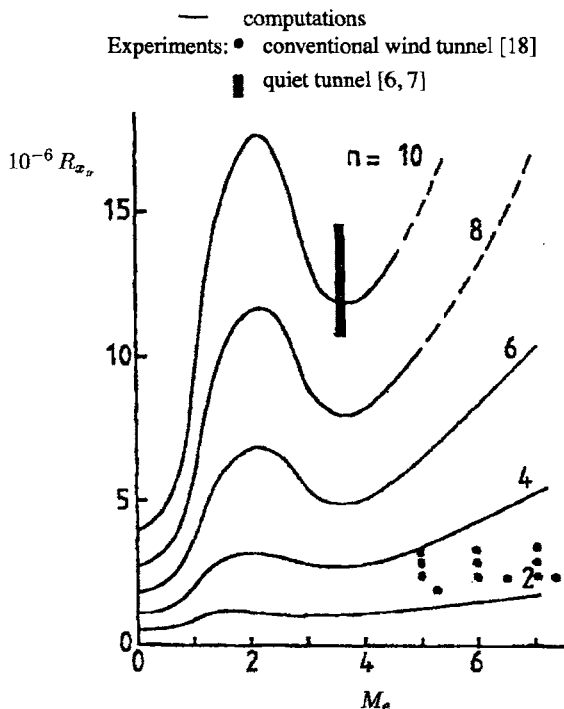


Fig. 14.20. Effect on Mach number for a flat plate boundary layer on an adiabatic wall.

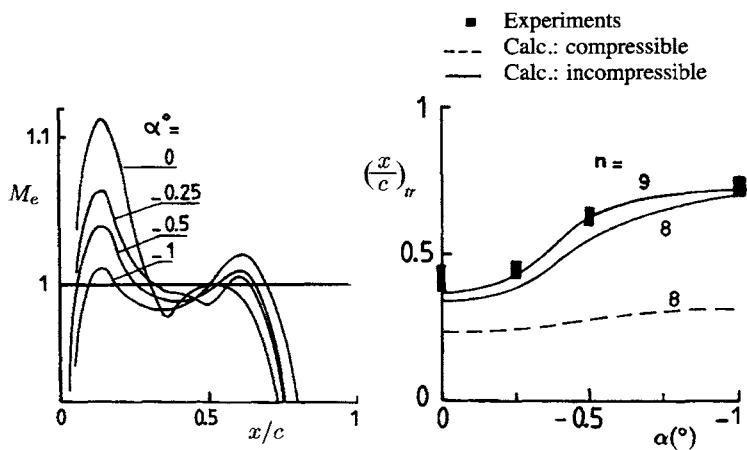


Fig. 14.21. Transition on an airfoil in transonic flow.

The transition location has been calculated for different values of  $n$  in order to simulate the quality of the flow in wind tunnel. It is observed that the transition Reynolds number has a local maximum for a Mach number around  $M_e = 2$  and a local minimum around  $M_e = 3.5$ . The comparison with the data obtained in a conventional wind tunnel (solid circles) indicates low values of the  $n$ -factor,

between 2 and 4, which probably means that transition is dominated by the noise in the wind tunnel. The hatched bar refers to data obtained in the quiet tunnel at NASA Langley [6, 7]. The corresponding  $n$ -factor is much higher, of the order of 10, indicating that reducing the noise in the nozzle is very effective.

Figure 14.21 shows an application of the  $e^n$ -method to the transition on an airfoil in transonic flow. The experimental distribution of the Mach number  $M_e$  was determined from the wall pressure distribution and is given for different angles of attack [18]. The evolution of the transition location as a function of the angle of attack is well reproduced by the  $e^n$ -method with  $n = 9$  [15]. The dotted line shows the results of transition prediction with incompressible stability calculations. The difference with the curves calculated from the compressible stability theory shows a strong stabilizing effect of the Mach number in transonic flow.

### Effect of Wall Temperature

Figure 14.22 [4] shows another application of the  $e^n$ -method to a flat plate boundary-layer. The objective was to investigate the effect of wall cooling at different Mach numbers. In these calculations, it is assumed that transition occurs when the  $n$ -factor reaches  $n = 9$ . The transition Reynolds number  $R_{x_{tr}}$  is reduced by its value  $R_{x_{T0}}$  for an adiabatic wall and it must be remembered

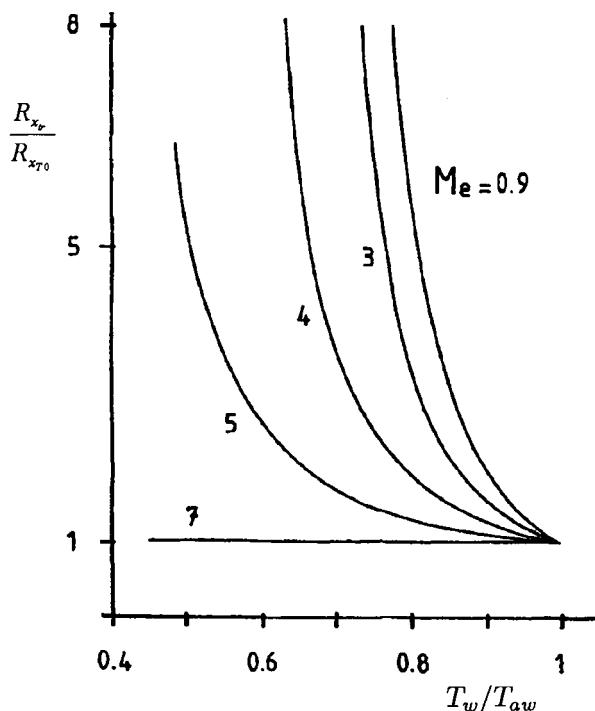


Fig. 14.22. Application of the  $e^9$ -method to the influence of wall temperature on transition location on a flat plate.

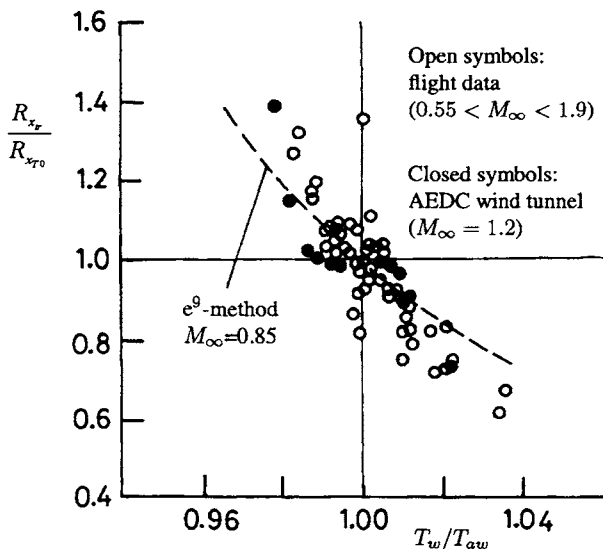


Fig. 14.23. Influence of wall temperature on transition location on a cone.

that  $R_{x_{T0}}$  depends on the Mach number  $M_e$  at the edge of the boundary-layer. Comparatively, the effect of wall cooling is more spectacular at low Mach number than in hypersonic flow. In particular, there is practically no effect of wall cooling on transition for  $M_e = 7$ .

The effects of wall cooling and heating on transition was studied in flight on a cone mounted on the nose of an F-15 aircraft and tested in the range of Mach numbers 0.5-2 [19]. In Fig. 14.23, the transition Reynolds number  $R_{x_T}$  is reduced by the value  $R_{x_{T0}}$  of the transition Reynolds number for an adiabatic wall ( $T_w/T_{aw} = 1$ ). The experimental data in the AEDC wind tunnel follow the same trend as the flight data. The theoretical curve calculated by the  $e^n$ -method [19] with  $n = 9$  is in good agreement with data. It is shown that a small variation of the wall temperature moves significantly the transition location.

## References

- [1] Cebeci, T.: *Stability and Transition: Theory and Application*. Horizons Pub., Long Beach, Calif. and Springer, Heidelberg, 2004.
- [2] Mack, L. M.: Boundary-Layer Linear Stability Theory. In *Special Course on Stability and Transition of Laminar Flow*. AGARD-R-709, 1984.
- [3] Lees, L. and Lin, C. C.: Investigation of the stability of the laminar boundarylayer in a compressible fluid. TN 1115, NACA, 1946.
- [4] Arnal, D.: Laminar-Turbulent Transition Problems in Supersonic and Hypersonic Flows. In *Special Course on Aerothermodynamics of Hypersonic Vehicles*. AGARD-R-761, 1989.
- [5] Harvey, W. D.: Influence of Freestream Disturbances on Boundary-Layer Transition. NASA TM 78635, 1978.

- [6] Beckwith, I. E.: Development of a high Reynolds number quiet wind tunnel for transition research. *AIAA J.* **13**(3), 1975.
- [7] Beckwith, I. E., Creel, T. R., Jr, Chen, F. J. and Kendall, J. M.: Freestream Noise and Transition Measurements on a Cone in a Mach 3.5 Pilot Low-Disturbance Tunnel. NASA TP 2180, 1983.
- [8] Potter, J. L.: Review of the influence of cooled walls on boundary-layer transition. *AIAA J.* **18**(8), 1980.
- [9] Softley, E. J., Graber, B. C. and Zempel, R. C.: Experimental observation of transition on the hypersonic boundary-layer. *AIAA J.* **7**(2), 257–263, 1969.
- [10] Stetson, K. F., Thompson, E. R., Donaldson, J. C. and Siler, L. G.: Laminar Boundary-Layer Stability Experiments on a Cone at Mach 8. Part 1: sharp cone. AIAA Paper 83-1761, 1983.
- [11] Stetson, K. F., Thompson, E. R., Donaldson, J. C. and Siler, L. G.: Laminar Boundary-Layer Stability Experiments on a Cone at Mach 8. Part 1: blunt cone. AIAA Paper 84-0006, 1984.
- [12] Van Driest, E. R. and Blumer, C. B.: Boundary-layer transition at supersonic speeds. Three-dimensional roughness effects (Spheres. *J. Aero. Sci.* **29**(8), 1962.
- [13] Van Driest, E. R. and Blumer, C. B.: Boundary-layer transition at supersonic speeds; Roughness effects with heat transfer. *AIAA J.* **6**(4), 603–607, 1968.
- [14] Poll, D. I. A.: The development of intermittent turbulence on swept attachment line including the effects of compressibility. *The Aer. Quart.*, XXXIV, 1983.
- [15] Arnal, D. and Juillen, J. C.: “Three-Dimensional Transition Studies at ONERA/CERT,” AIAA Paper No. 87-1335, 1987.
- [16] Cebeci, T., Chen, H. H. and Arnal, D.: “A Three-Dimensional Linear Stability Approach to Transition on Wings at Incidence,” AGARD Symposium on Fluid Dynamics of Three-Dimensional Turbulent Shear Flows and Transition, Cesme, Turkey, 3–6 October 1988.
- [17] Arnal, D.: Boundary-Layer Transition: Predictions Based on Linear Theory. In *Special Course on Progress in Transition Modelling*. AGARD-R-793, 1989.
- [18] Blanchard, A., Mignosi, A., Dor, J. B. and Séraudie, A.: Essais de profils cast 7 ety cast 10 dans la soufflerie cryogénique à parois adaptables T2. étude de l'effet reynolds en transition naturelle et déclenchée. 22ème Colloque d'Aérodynamique Appliquée, Lille, 1985.
- [19] Fisher, D. F. and Dougherty, N. S., Jr.: In-Flight Transition Measurements on a 10° Cone at Mach Numbers from 0.5 to 2. NASA TP 1971, 1982.

## Problems

**14-1. Squire theorem.** Consider the stability equation, Eq. (5.3.15)), in incompressible flow and in the temporal theory, for a two-dimensional mean flow. The following change of variables is defined

$$\omega^* = \frac{\omega}{\cos \psi}, \quad \alpha^* = \frac{\alpha}{\cos \psi}, \quad \beta^* = \frac{\beta}{\sin \psi}, \quad \phi^* = \frac{\phi}{\cos \psi}, \quad R^* = R \cos \psi$$

with

$$\tan \psi = \frac{\beta}{\alpha}$$

Write the stability equation with the starred variables. Deduce that the critical Reynolds number is obtained for a two-dimensional wave.

**14-2.** *Stuart theorem.* Consider the stability equation, Eq. (5.3.15), in incompressible flow and in the temporal theory, for a three-dimensional mean flow. The following change of variable is defined

$$\alpha^* = \frac{\alpha}{\cos \psi}, \quad \beta^* = \frac{\beta}{\sin \psi}$$

$$u^* = u \cos \psi + w \sin \psi, \quad w^* = -u \sin \psi + w \cos \psi$$

$$\phi^* = \phi, \quad \omega^* = \omega, \quad R^* = R$$

with

$$\tan \psi = \frac{\beta}{\alpha}$$

Write the stability equation with the starred variables. Deduce that the study of an oblique wave can be carried out from the study of a two-dimensional wave.



# Appendix A

## Computer Programs

### on the Accompanying CD-ROM

The CD-ROM accompanying this book contains both source and executable computer programs and test cases. They are listed below.

*Prior to running the test cases, it is necessary to save the executable files and input data on the hard drive in the same directory. The reader can then double click executable file and run the program with instructions given on the screen.*

#### Program 1: Shooting Method

##### A.1 Shooting Method for $f''(0) \geq 0$

1. Compile p100shooting.f (Shooting Method) and generate PC executable file p100shooting.exe.
2. Test:
  - $m = 0$   
Input file: p100a\_inp.txt  
Output file: p100a\_out.txt and p100a\_out.pdf
  - $m = 0.5$   
Input file: p100b\_inp.txt  
Output file: p100b\_out.txt and p100b\_out.pdf
  - $m = 1$   
Input file: p100c\_inp.txt  
Output file: p100c\_out.txt and p100c\_out.pdf

##### A.2 Shooting Method for $f''(0) < 0$

1. Compile p5\_5shooting.f (Shooting Method) and generate PC executable file p5\_5shooting.exe.

2. Test:  $f''(0) = 0$ ,  $m = -0.09043$

Input file: p5\_5ainp.txt

Output file: p5\_5aout.txt and p5\_5aout.pdf

$f''(0) = -0.02699$ ,  $m = -0.08940$

Input file: p5\_5binp.txt

Output file: p5\_5bout.txt and p5\_5bout.pdf

$f''(0) = -0.06569$ ,  $m = -0.08271$

Input file: p5\_5cinp.txt

Output file: p5\_5cout.txt and p5\_5cout.pdf

$f''(0) = -0.08998$ ,  $m = -0.0707$

Input file: p5\_5dinp.txt

Output file: p5\_5dout.txt and p5\_5dout.pdf

Result summary: Results\_Summary.pdf

### Program 2: Thwaites' Method

Compile thwaites.f (Thwaites' Method) and generate PC executable file thwaites.exe

Test case: This case involves Programs 2, 4 and 7. [Click here to see the details](#)

### Program 4: Hess-Smith Panel Method

Compile HSPM.f (Hess-Smith Panel Method) and generate PC executable file HSPM.exe

Test Cases NACA0012 Airfoil,  $M = 0.1$

1.  $\alpha = 0$  degree angle of attack.

Input file: deg00\_inp.txt

Output file: deg00\_Out.txt

2.  $\alpha = 8$  degree angle of attack.

Input file: deg08\_Inp.txt

Output file: deg08\_Out.txt

3.  $\alpha = 16$  degree angle of attack.

Input file: deg16\_Inp.txt

Output file: deg16\_Out.txt

### Program 7: Head's Method

Compile head.f (Head's Method) and generate PC executable file head.exe

Test case: This case involves Programs 2, 4 and 7. [Click here to see the details](#).

# **Appendix B**

## **Computer Programs**

### **Available from the First Author**

#### **Program 3: Boundary-Layer Program (BLP2D) for Two-Dimensional Incompressible Flows**

Compile boundary-layer program `blp2d.f` and generate PC executable file `blp2d.exe`

Test case: This case involves Programs 3, 4 and 6. [Click here to see the details.](#)

#### **Program 5: Matrix Solver Algorithm**

#### **Program 6: Stability-Transition Program (STP)**

Compile stability-transition program ( $e^n$ -method) `stp2d.f` and generate PC executable file `stp2d.exe`

Test case: This case involves Programs 3, 4 and 6. [Click here to see the details.](#)

#### **Program 9: Subroutine IVPT**

#### **Program 10: Boundary-Layer Program (BLP3D) for Three-Dimensional Incompressible Flows**

Compile `BLP3D.f` (Boundary-Layer Program for Three-Dimensional Incompressible Flows) and generate PC executable file `BLP3D.exe`

Test case: Input files: `input.txt` and velocity profile `fort.1`. Output file: `Out.txt`

**Program 11: Boundary-Layer Program (BLP2C) for Two-Dimensional Compressible Flows**

Compile **BLP2C.f** (Boundary-Layer Program for Two-Dimensional Compressible Flows) and generate executable file **BLP2C.exe**

Test Case: upper part of NACA0012 airfoil.

Input file: **pr11\_2Inp.txt**

Output files: **pr11\_20ut.txt** and summary: **pr11\_20ut.pdf**

**Appendix 7A: Application of the Characteristic Box to a Model Problem****Appendix 13A: Boundary-Layer Equations for Restricted Three-Dimensional Flows**

# Appendix C

## A Boundary-Layer Program for Three-Dimensional Compressible Flows on Wings

This CD-ROM contains a source and PC-executable computer program and a test case for compressible laminar and turbulent flows, including separation on wings. The location of the onset of transition and external velocity distribution are assumed to be given. The quasi three-dimensional boundary-layer equations are solved for a nonorthogonal system in the inverse mode by using the interaction law described in detail in [1] and briefly in Section C6.0. The boundary-layer calculations are performed on the wing and along the wake (optional) and chordwise displacement thickness and blowing velocity distributions needed to incorporate viscous effects into the inviscid flow method are calculated together with other parameters discussed in Section C5.0.

This computer program has been applied to transonic flows as well as subsonic flows as described in [1]. Its application to transonic flows is also described in [2] and in Section C9.0. A sample of calculations for the Challenger wing/body fuselage configuration is given below.

In [2], Laurendeau and Mokhtorion applied this method to Bombardier's Challenger wing/fuselage configuration and compared the predictions with experiment and with those computed with FANSC, which solves the Euler/Navier Stokes equations on a multi-block structured computational domain with arbitrary boundary conditions. They first applied the method by using the option in which the boundary-layer equations were solved for the standard problem (direct coupling) on the wing surface, thus limiting the solutions to attached flows, and the blowing velocity distributions were calculated, thus removing the need to regenerate the body-conforming grid after each viscous calculation. Blowing velocities were kept constant equal to the previous attached flow value when trailing edge separations were encountered.

The results obtained with this procedure show the importance of modeling viscous effects on the Challenger wing/body configuration, Fig. C1. When compared to inviscid Euler flow solutions at constant angle-of-attack and con-

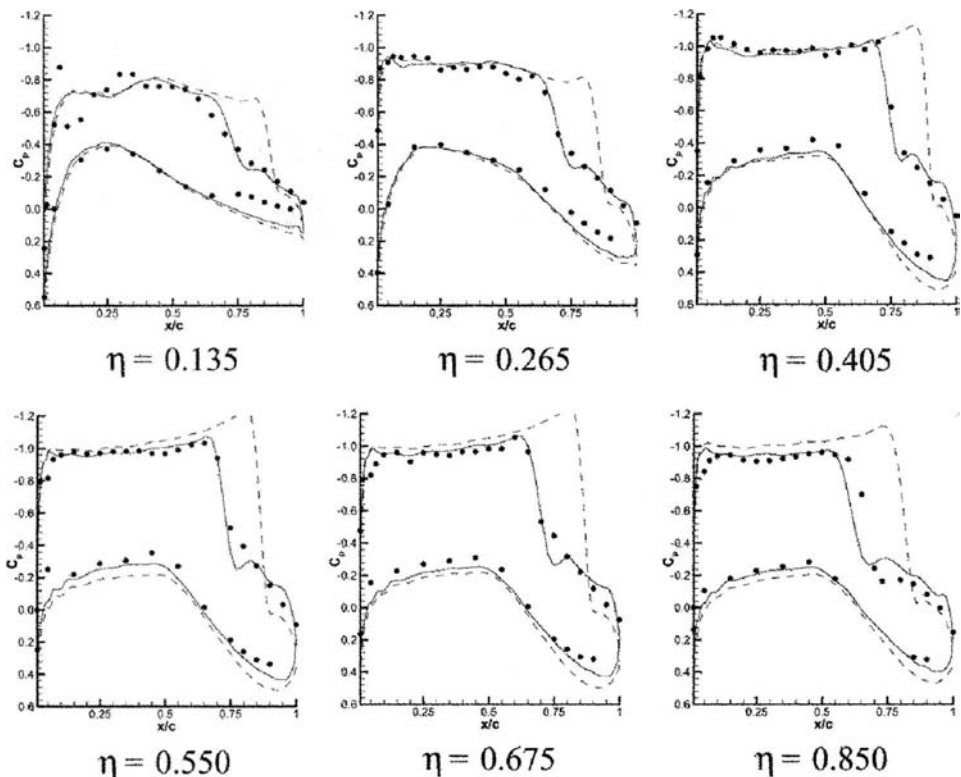


**Fig. C1.** Direct coupling results on challenger wing-fuselage configuration  $M_\infty = 0.82$ ,  $\alpha = 1.5^\circ$  (Euler results shown with dashed line).

stant Mach number, the predicted upper surface shock-wave position moved forward with viscous effects, in agreement with the experimental location. The effects of viscosity are also seen in the cove region, where the inviscid solver overestimates the lower surface pressure coefficients by as much as 0.2, whereas the viscous/inviscid procedure reduces this number to 0.1. As expected, there is good agreement in regions where the boundary layer is thin, such as in the leading edge region of the wing.

The predictions close to the trailing edge viscous results were, however, inadequate for design, particularly when the wing form drag was calculated from the Squire-Young formula[1]. Significant errors in wing form drag are introduced when the trailing-edge boundary-layer properties are in error and most importantly, when the external trailing edge velocities are not properly computed.

All of these physical requirements were dealt with by the use of the interactive boundary-layer option of the program in which the boundary-layer solutions were obtained with the inverse method on the wing surface and into the wake of the wing. This ensured accurate results when separated flow regions are encoun-

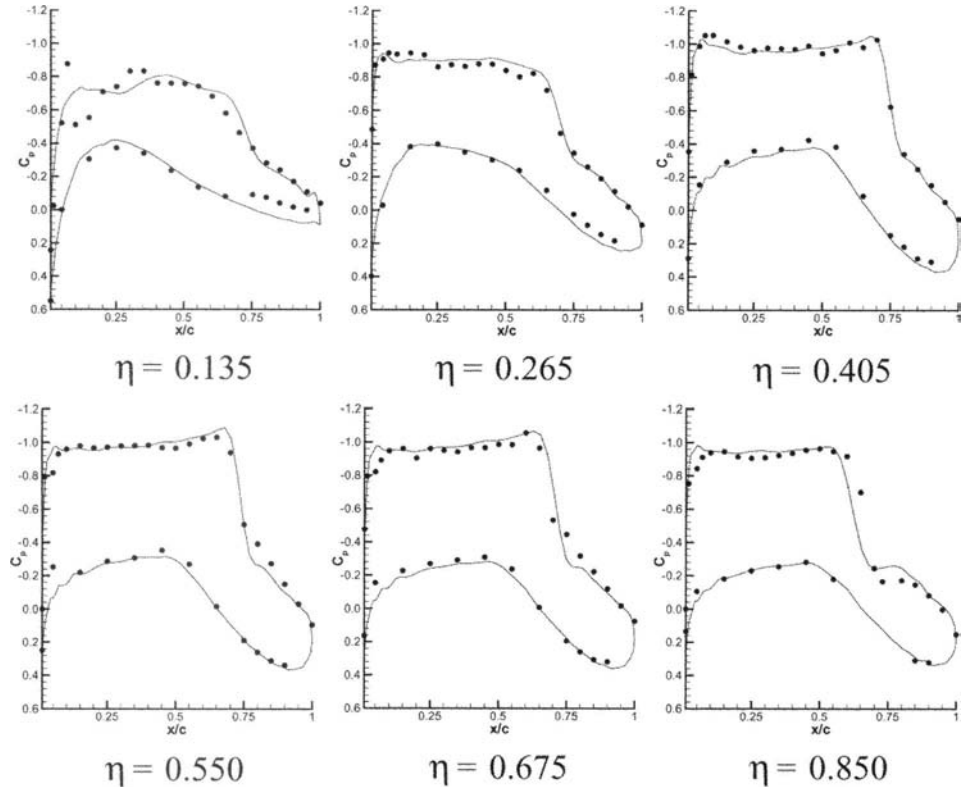


**Fig. C2.** IBL results on challenger wing-fuselage configuration  $M_\infty = 0.82$ ,  $\alpha = 1.5^\circ$ .

tered and maintained the strongly coupled nature of the inviscid and viscous flows in the trailing edge region. The results obtained with this IBL method are shown in Fig. C2 where the surface pressure distributions are shown for the same flow conditions of Fig. C1. In these calculations, the IBL method used the Baldwin-Lomax turbulence model [2, 3]. The trailing edge pressures are significantly improved, especially with regard to the evaluation of the form drag and the improvements in the cove pressures are due to proper consideration of coupling rather than to separation, as there was none in this case. Improvements at the foot of the upper surface shock wave can also be seen, this time due to quality of the indirect viscous flow solver as shock-induced separation occurred at this buffet flow condition.

To compare the IBL prediction with the NS prediction, calculation with the Spalart-Allmaras turbulence model [2, 3] were performed with FANS for the some flow conditions. The turbulent eddy viscosity was frozen after 200 fine mesh iterations. The surface pressure distributions calculated by FANS are shown in Fig. C3 with the IBL results. Note the excellent agreement between the numerical and experimental results. The discrepancy in the inboard lower

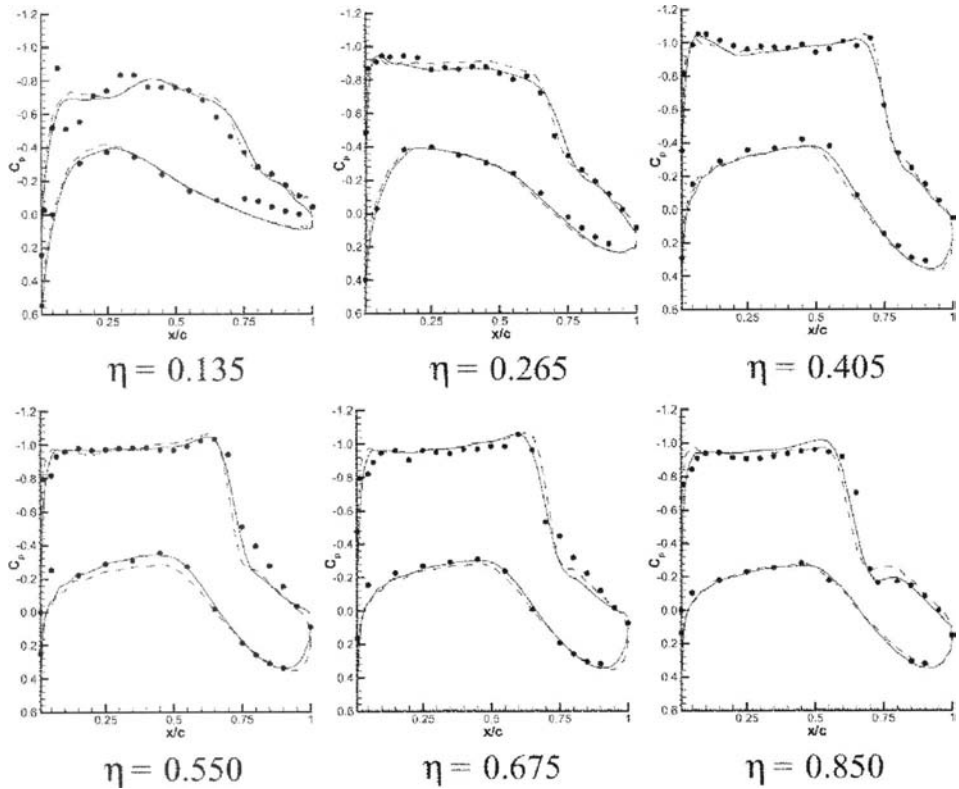


**Fig. C3.** Comparison of NS (solid lines) and IBL (dashed lines) for challenger wing-fuselage configuration  $M_\infty = 0.82$ ,  $\alpha = 1.5^\circ$ .

surface region is due to the fact that the geometry had a different wing-body fairing than the experimental model. Differences can also be seen in the upper surface shock wave region, due to the intensity of the shock-wave/boundary-layer interaction.

To verify the accuracy of the IBL method, Navier-Stokes calculations were performed with the FANSC code [2], for the same flow conditions. The turbulent eddy viscosity was computed with the SA turbulence model. The surface pressure distributions calculated by FANSC together with the IBL results and experiments are shown in Fig. C3 and the agreement is excellent. The discrepancy at the inboard lower-surface region is due to the different wing-body fairing of the experimental model and those in the upper surface shock wave region are due to the intensity of the shock-wave/boundary-layer interaction. The differences between the results of the two calculation methods are very small, and more so when the difficult buffet-flow conditions are considered.

## References

- [1] Cebeci, T.: An Engineering Approach to the Calculation of Aerodynamic Flows. Horizons Pub., Long Beach, CA and Springer, Heidelberg, 1999.
- [2] Laurendeau, E. and Mokhtarian, F.: "Coupled Euler/boundary-layer methods with the FANS code." Canadian Aeronautics and Space Institute (CASI) Aerodynamic Symposium, Toronto, April 29–May 2, 2001.
- [3] Cebeci, T.: Turbulence Models and Their Application. Horizons Pub., Long Beach, CA and Springer, Heidelberg, 2004.

# Subject Index

- Algebraic eddy-viscosity formulation 163
- Amplification factor 8
- Application of the  $e^n$ -method to three-dimensional flows 275
  - infinite swept wing 275
  - prolate spheroid 278
- Applications of the boundary-layer program
  - airfoil flow 74
  - ellipse flow 75
  - external flow 73
  - prolate spheroid flow 77
- Applications of the interactive boundary-layer theory
  - airfoils at high Reynolds numbers 327
  - airfoils at low Reynolds numbers 329
  - effects of Reynolds number 329
  - multielement airfoils 333
  - separation bubble 330, 333
  - stall angle 332
  - trailing edge of a flat plate 322
  - wake 326
  - wake effect 327
- Applications of the inverse boundary-layer method 320
  - flows with separation 320
  - interactive boundary-layer theory 321
  - trailing edge singularity 320
  - trailing-edge flow 320
  - triple-deck theory 321
- Applications of the three-dimensional interactive boundary-layer method
  - subsonic flows 431
  - multielement wings 440
  - transonic flows 444
- Arnal's method 119
- Asymptotic suction profile 52, 83
- Attachment flow on an infinite swept wing 253
- Attachment line equations 217, 253
  - initial conditions 254
  - quasi-three-dimensional flow conditions 219
- Axisymmetric flows 30
  - momentum-integral equation 30
- Axisymmetric wake 85
- Blasius equation 48
- Blowing velocity 314, 338
  - in three-dimensional flow 338, 424
- BLP2 (boundary-layer program) 73, 96, 97
- BLP3 (boundary-layer program for three-dimensional flows) 247, 248
- Block-elimination method 72
- Body of revolution 254
- Body-oriented coordinate system 215
  - boundary conditions 217
  - geometric curvature parameters 215
  - nonorthogonal coordinate system 215
- Boundary condition for  $v$  35
- Boundary initial conditions 34
  - boundary initial conditions 34
  - calculation domain 34
  - heat conduction equation 34
  - influence domain 34
  - parabolic partial differential equations 34
  - propagation of disturbances 34
- Boundary-layer approximation 27
  - laminar flow 27
  - turbulent flow 29
- Boundary-layer equations 29
  - axisymmetric flows 30
  - boundary and initial conditions 34
  - dimensionless quantities 41
  - laminar flows 27, 28, 29
  - numerical solution 66
  - second-order 102
  - turbulent flows 29
  - two-dimensional flow 29
- Boundary-layer equations for compressible flow 351
  - axisymmetric flow 352
  - three-dimensional flow 352
  - two-dimensional flow 351

- Boundary-layer equations for three-dimensional flows
  - body-oriented coordinate system 215
  - calculation of geometric parameters 233
  - Cartesian coordinate system 211
  - characteristic box scheme 227, 251
  - domain of dependence 225
  - domain of influence 225
  - geodesic curvatures 213
  - initial conditions 217
  - numerical solution 225
  - standard box 228
  - streamline coordinate system 213
  - transformed equations 223
- Boundary-layer program (BLP2) 73
- Boundary-layer program for three-dimensional flows (BLP3) 247
  
- Calculation of geometric parameters 233
  - geodesic curvature 233
  - geometric curvatures 234
  - local Cartesian axis-system 235
  - metric coefficients 234
  - tangential curvatures 234
- Calculation of inviscid velocity components for boundary-layer grid 430
- Calculation of three-dimensional turbulent boundary layers
  - full three-dimensional flows 243
  - infinite swept wing flows 236
- Cartesian coordinate system 211
  - boundary conditions 212
  - infinite swept wing equations 212
- Cebeci-Smith turbulence models 178
- Characteristic box 231
  - CFL condition 232
  - flow reversal 231
- Characteristic time of viscosity 41
- Closure problem 21
- Coles formula 172
  - law-of-the-wake 172
- Composite nature of a turbulent boundary layer 163
- Compressible flows
  - Crocco integral 361
  - Falkner-Skan transportation 358
  - Illingworth-Stewartson transportation 359
  - nonsimilar flows 367
  - relation between compressible and incompressible boundary-layer parameters 363
  - similar flows 362
  - transformed energy equation 361
  - transformed momentum equation 361
  
- Computer program for stability 144
- Computer program for three-dimensional boundary-layers 247
- Conservation equations 17
  - mass 17
  - momentum 17
- Conservation form 24
- Convection time 28
- Critical Reynolds number 115
- Cross-flow instability 8
- Crossflow transition criterion 297
  
- Damping parameter 174
- Differential method 163, 195
  - Cebeci-Smith algebraic eddy viscosity 196
- Direct numerical simulation (DNS) 20
- Displacement surface 257
- Displacement thickness 33, 256, 336
- Displacement thickness in three-dimensional flows 256
- Dissipation function 347
- Divergence form 24
- Domain of influence 42
- Drag reduction 131
  - momentum drag 133
  - optimum suction 132
  - ram drag 133
  - sink drag 133
  - suction drag 131, 133
  - suction drag coefficient 131
  
- Eddy viscosity concept 176, 219
- Eigenvalue procedure for transition 274
- Eigenvalue procedure for zarf 272
  - eigenvalues of the zarf 274
  - saddle-point method 272
- Empirical formulas 163
  - calculating boundary-layer parameters 163
  - rough surfaces 163
  - smooth surfaces 163
- $e^n$ -method 119
- $e^n$ -method for three-dimensional flows 265
  - absolute neutral curve 268
  - eigenvalue formulations 266
  - group velocity 266
  - saddle point method 266
  - saddle-point 266
  - spatial amplification theory 266
  - stationary phase method 267
  - wave packet 267
  - zarf 268
- Ensemble average 20
- Entrainment velocity 38, 42

- Entrance region 36  
Envelope method 120  
– neutral stability curve 120  
Evaluation of a turbulence model 235  
– boundary-layer separation 239  
– infinite swept wing flows 236  
– turbulence models 239
- Factors that influence transition  
– freestream turbulence and noise 122  
– heat transfer 127  
– pressure gradient 124  
– suction 130  
– surface curvature 135  
– surface roughness 133
- Factors that influence transition in compressible flow  
– effects of noise 466  
– effects of nose bluntness 468  
– effects of surface roughness 470  
– effects of wall cooling 468
- Falkner-Skan equation 44  
– dimensionless pressure-gradient parameter 45  
– similarity variable 44
- Falkner-Skan transformation 44, 95
- Falkner-Skan-Cooke equations 224  
– yawed infinite cylinder 225
- Flat-plate flow 49  
– displacement thickness 49  
– local skin-friction coefficient 49  
– shape factor 50
- Flat-plate turbulent boundary-layer 186
- Flow separation 74  
– axisymmetric flows 77  
– BLP2 76  
– ellipse flow 75  
– NACA 0012 airfoil 74  
– prolate spheroid flow 76
- Flow with suction 91
- Free shear layer 35
- Free shear layer in turbulent flow 196  
– axisymmetric jet 196  
– power laws for similar free shear layers 201  
– two-dimensional wake 199
- Free-shear flows 53  
– axisymmetric jet 53
- Freestream turbulence 122
- Friction velocity 164, 203
- Fully developed region 36
- Generalization of the CS eddy-viscosity formulation 221
- Global momentum equation 38
- Goldstein singularity 307, 321, 342
- Granville's method 118, 156  
– point of instability 118
- Group velocity 152
- Half jet 59
- Heat transfer 227
- Hess-Smith panel method (HSPM) 73  
– NACA 0012 airfoil 73
- Hiemenz flow 50
- $H\!-\!R_x$  method 121
- HSPM (Hess-Smith panel method) 73
- Hybrid laminar flow wings 7
- Independence principle 212, 225
- Infinite swept wing 252
- Influence of Reynolds number 41
- Initial conditions 217  
– initial boundary conditions 217
- Inner layer: rough surface 166  
– fully rough flow 168  
– hydraulically smooth condition 168  
– intercept 167  
– law-of-the-wall 166  
– roughness Reynolds number 167  
– turbulence velocity scale 167
- Inner layer: smooth surface 164
- Integral equation of continuity 259
- Integral equation for the  $x$ -momentum 260
- Integral equation for the  $z$ -momentum 260
- Integral equations for three-dimensional flows 259  
– continuity 259  
–  $x$ -momentum 260  
–  $z$ -momentum 260
- Integral equations for compressible flow 350  
– continuity equation 353  
– energy equation 355  
– momentum equation 354
- Integral form 62
- Integral methods for laminar boundary-layers  
– Pohlhausen method 62  
– Thwaites' method 64
- Integral methods for turbulent boundary-layers 192  
– entrainment velocity 162  
– Green's “lag-entrainment” method 194  
– Head's method 192  
– Onera's method 193  
– skin-friction law given by Ludwieg and Tillmann 193
- Integral momentum equation  
– axisymmetric flow 33

- two-dimensional flow 32
- Interaction problem 313, 314
- blowing or suction velocity 314
- displacement surface 314
- interactive boundary-layer scheme 314
- Kutta condition 314
- Interactive boundary-layer theory 310
  - boundary conditions 312
  - generalized expansion 310
  - model 312
  - model for an outer irrotational flow 313
  - numerical procedure 315
- Interactive theory 310
- Interactive three-dimensional boundary-layer
  - interaction law 418
  - transformed equations 420
- Interface program 425
- Intermittency factor 177
- Inverse boundary-layer method 315
  - computer program 320
  - discretization approximation to the Hilbert integral 316
  - Flügge-Lotz Reyhner approximation 318
  - FLARE 318
  - numerical method 317
  - transformed equations: general form 317
- Inverse problem 308
- Inviscid flow equations 22
  - Bernoulli equation 22
  - Euler equation 22
  - irrotational 23
- Inviscid flow equations for compressible flow 350
- $k-\varepsilon$  model 206, 222, 257
- $k-\omega$  model 207
- Kutta-Joukowski condition 23
- Laminar flow control 1
  - adjustment of pressure gradient by shaping 4
  - hybrid laminar-flow control 6
  - natural laminar flow 4
  - suction through slotted or perforated surfaces 5
- Laminar mixing of two streams 85
- Laplacian operator 20
- Law of the wall 164
- Leading edge contamination 263
  - delay the leading edge contamination 264
  - Gaster bump 264
- leading edge contamination criterion 264
- spanwise Reynolds number 263
- suction 264
- Linear stability equation 153
- Linear stability theory 109
  - boundary conditions 112
  - critical layer 117
  - $e^n$ -method 109
  - disturbance stream function 111
  - linear stability equations 109
  - Orr-Sommerfeld equation 111
  - Orr-Sommerfeld equation for a three-dimensional flow 112
  - parallel flow approximation 110
  - radian (circular) frequency 110
  - relative phase angle 111
  - separation of variables 110
  - small-disturbance theory 109
  - stability diagrams 114
  - Tollmien-Schlichting waves 111
  - two-dimensional disturbance 110
  - two-dimensional incompressible 109
  - wave number 111
  - wavelength 111
- Linear stability theory for compressible flow
  - equations 455
  - examples 461
  - inviscid stability theory 456
  - locally subsonic or supersonic perturbation 458
  - Mack's modes 459
  - relative Mach number 457
- Local nonsimilarity equations 95
- Local skin-friction coefficient 33
- Logarithmic law 170
- Logarithmic law of the wall 165
  - buffer zone 166
  - linear sublayer 166
- Longitudinal curvature 102
- Mangler transformation 39, 95
- equivalent two-dimensional flow 31
- Mass-weighted averaging 355
- Mathematical nature of three-dimensional boundary-layer equations 259
  - characteristic determinant 259
  - characteristic roots 259
  - characteristic surfaces 259
  - subcharacteristics 259
  - system is parabolic 259
- Matrix solver algorithm 73
- Michel's method 117, 156
- von Mises' transformation 81
- Mixing layer 59

- Mixing length 176  
Mixing-length formulations 222  
Models for Reynolds shear stress 175–186  
Momentum integral equation 31–33  
Momentum thickness 33  
Multielement wings 11
- NACA 0012 airfoil coordinates 88  
Natural laminar flow wings 7  
Navier-Stokes equations 18  
– continuity equation 18  
– differential and integral forms 29  
– momentum equation 18  
– viscous stresses 18  
Navier-Stokes equations for compressible flow 346  
– continuity equation 346  
– energy equation 347  
– heat flux 347  
– momentum equation 346  
– viscous stresses 346  
Newton's method 70  
– amplification rate 120  
Noise 122  
– acoustic perturbations 123  
Nonconservation form 24  
Normal shear stresses 19  
*N*-type of transition 127  
Numerical solution of the boundary-layer equations for three-dimensional flows 225  
– box method 227  
– characteristic box scheme 227  
– Courant, Friedrichs, Lewy (CFL) condition 226  
– domain of dependence 226  
– general principles 225  
– region of influence 225  
– transformed equations 227  
Numerical solution of the boundary-layer equations for two-dimensional flows 66  
– block-elimination method 72  
– Falkner-Skan transformation 67  
– finite-difference approximation 69  
– linear system 71  
– Newton's method 70  
– numerical formulation 69  
– similarity variables 67  
– transformed coordinates 67  
Numerical solution of the Orr-Sommerfeld equation 136  
– boundary conditions 137  
– box scheme 136  
– eigenfunctions 137  
– eigenvalue problem 139  
– eigenvalue procedure for transition 143  
– eigenvalues 137  
– Newton's method 138, 141  
– numerical scheme 137  
– variational equations 140
- Order-of-magnitude analysis 27  
– boundary-layer approximation 27  
Origin of crossflow 210  
– crossflow 210  
– curvature of the external streamline 210  
– pressure-driven three-dimensional boundary-layers 211  
Orr-Sommerfeld equation 111, 153, 157  
– amplification rates 111  
– boundary conditions for the Orr-Sommerfeld equation 153  
– critical Reynolds number 111  
– effects of wall temperature 155  
– heat transfer effects 157  
– neutral stability curve 111  
– small disturbance waves 111  
– stability equations 154  
– three-dimensional incompressible flows 154  
– Tollmien-Schlichting waves 111  
Outer Layer 169  
– intermittency 169  
– length scale 169  
– velocity scale 169  
Overlap layer 170  
– buffer layer 171  
– equilibrium boundary-layer flows 171  
– fully turbulent wall region 171  
– law-of-the-wall 171  
– sublayer 171  
– velocity-defect law 170
- Panel method 7, 12, 73  
Parabolic equations 30  
Parabolized stability equations 286  
– derivation of equations 299  
– initial conditions 289  
– *n*-factor calculations 288  
– sample calculations 291  
Perfect gas law 348  
Power laws for similar free shear layers 61  
Power-law assumption 189  
Practical formulas for turbulent boundary layer 187  
– smooth flat plate 187  
– streamwise-average skin friction 188  
Prandtl number 348  
Prediction of maximum lift condition 11

- Prediction of transition
  - airfoil flow 147
  - effect of free-stream turbulence 120
  - eigenvalue procedure 143
  - ellipse flow 148
  - empirical correlations 117
  - $e^n$ -method 119
  - flat-plate flow 146
  - Granville's method 118
  - Michel's method 117
  - Wazzan et al.'s method 121
- Prediction of transition in compressible flow
  - applications of the  $e^n$ -method 474–479
  - $e^n$ -method 471
- Prediction of transition in three-dimensional flows 265
  - eigenvalue procedure 265, 274
  - $e^n$ -method 266
  - saddle-point method 267
  - zarpf 268, 272
- Pressure difference rule 12
- Prolate spheroid 278
- Propagation of perturbation 258
- Properties of an integral method 339
  - boundary-layer separation 340
  - inverse approach 340
- Properties of the Orr–Sommerfeld equation 113
  - eigenfunctions 113
  - eigenvalue problem 113
  - eigenvalues 113
  - spatial amplification 114
  - temporal amplification 114
- PSE equations 300, 301
- Qualitative effects of mass transfer 156
- Rayleigh equation 116
- Rayleigh theorem 116
- Reynolds stress 21
- Reynolds stress models 184
  - wall effects 185
- Reynolds-averaged Navier–Stokes (RANS) equations 17, 20, 21
- Reynolds-averaged Navier–Stokes equations for compressible flow 349
- Rough flat plate 190
  - equivalent sand roughness 190
- Roughness effect 157
- Second-order boundary-layer equations 102
- Separating velocity profile 51
- Separation point 46
- Shape factor 33
- Shock-wave/boundary-layer interaction 408
- Shock-wave/shear-layer interaction 370
  - free interaction and upstream influence 375
  - Lighthill's scaling laws 377
- Shooting method 48, 60
  - computer program
- Similar flows
  - adverse pressure gradient 46
  - axisymmetric jet 53
  - Blasius equation 48
  - centerline velocity for free shear layers 61
  - external flows 44
  - Falkner–Skan equation 44
  - favorable pressure gradient 46
  - free-shear flows 53
  - Hiemenz equation 48
  - incipient separation 46
  - lower branch solutions 47
  - mixing layer 59
  - separating velocity profile 51
  - separation 46
  - similarity concept 44
  - sink flow 51
  - two-dimensional stagnation flow 48
  - two-dimensional wake 56
  - wedge-flow 47
  - zero-pressure gradient 46
- Similarity solutions of turbulent free shear flows 163
- Singularity of boundary layer equations 307, 308
  - coupling 308, 309
  - singular behavior of boundary-layer equations 308
- Sink flow 82
- Skin-friction drag reduction 3
- Solution of the Orr–Sommerfeld equation 136
  - boundary conditions 137
- Solution of the turbulent boundary-layer equations 163
- Solutions of the Falkner–Skan equation 48, 50
  - Blasius equation 48
  - flat plate at zero incidence 48
  - Hiemenz equation 48
  - normal velocity component 49
  - sink flow 50
  - two-dimensional stagnation flow 48
- Squire's theorem 480
- Stability diagrams
  - Blasius flow 114, 115
  - critical Reynolds number 115

- Falkner-Skan flows 159
- homotopy continuation method 159
- neutral curve 114
- neutral stability curve 161
- Poiseuille flow 161
- Stability diagrams 114
- Stability diagrams for Blasius flow 145
  - BLP2 114
  - Falkner-Skan flows 114
  - neutral stability diagrams 145, 146
  - STP 144
- Stability diagrams for similar flows 124
  - critical Reynolds number 124
- Stability equations 152, 154
  - with heat transfer 158
- Stability theorems 116
  - critical layer 117
  - profiles with a point of inflection 117
- Stability-transition program (STP) 144
  - boundary-layer program (BLP2) 144
  - eigenvalues on the lower branch 144
  - neutral stability curves 144
  - onset of transition 144
  - onset of transition in two-dimensional external flows 144
  - Orr-Sommerfeld equation 144
- Stagnation point 82
- Standard box 228
  - block-elimination method 231
  - Newton's method 231
- STP (Stability-transition program) 144
- Strain tensor 19
- Streamline coordinate system 213
  - geodesic curvatures 213
  - metric coefficients 213
  - small cross-flow equations 214
- Stress tensor 21
- Stuart theorem 481
- Substantial derivative 23
- Suction 9
- Suction drag 83
- Surface curvature 135
- Surface roughness 133
  - isolated roughness 134
- Sutherland's law 348
- Taylor-Görtler instability 195
- Tensor notation 19, 21
- Thwaites' method 64
- Time scales 28
- Tollmien-Schlichting instabilities 262
- Tollmien-Schlichting waves 106
- Transition in three-dimensional flows 262
  - correlation formulas 262
  - crossflow instabilities 262
  - $e^n$ -method 262
- leading edge contamination 263
- prediction of transition 262
- streamwise instability 261
- Transition in two-dimensional flows 105
  - $e^n$ -method 105
  - direct numerical simulation 105
  - parabolized stability equations 105
- Transition prediction 146–149
  - airfoil flow 147
  - amplification rate calculations 147
  - BLP2 147–149
  - envelope of the amplification rates 146
  - flat-plate flow 146
  - prolate spheroid flow 148
  - STP 146, 148
- Transition process 106
  - eigenfunctions 137
  - eigenvalue procedure 139
  - eigenvalues 137
  - intermittency 108
  - numerical solution 136
  - spots 107
  - spots of turbulence 106
  - Tollmien-Schlichting (TS) waves 106
  - turbulent spot 107
- Transverse-curvature effect 99
- Triple-deck flow structure 442
- Triple-deck theory 321
  - strong coupling 321
  - triple-deck region 321
  - upstream influence 321
- Turbulence amplifier 86
- Turbulence models
  - Cebeci-Smith eddy viscosity 176
  - $k-\epsilon$  model 181
  - $k-\omega$  model 207
  - Reynolds-stress models 184
  - Spalart-Allmaras model 180
  - three-dimensional boundary layers 219
  - zero equation models 176
- Turbulence models for compressible flow
  - Cebeci-Smith model 390
  - eddy diffusivity 389
  - eddy viscosity 389
  - inner layer 393
  - $k-\epsilon$  model 393, 413
  - turbulent Prandtl number 389
- Turbulence velocity scale 164
  - length scale 164
  - turbulence length scale 165
  - turbulence velocity scale 165
  - velocity scale 164
- Turbulent boundary layer in compressible flow
  - numerical methods 403
  - Reynolds analogy factor 400

- skin-friction formulas on rough surfaces 401
- skin-friction law 397
- Van Driest II formula 398
- Van Driest transformation 395
- Turbulent boundary layer on a flat plate 186
- Turbulent boundary layer on a rough flat plate 190
- Turbulent free shear layers 196
  - axisymmetric jet 196
  - centerline velocity 201
  - two-dimensional wake 199
- Two-dimensional jet 84
- Two-dimensional laminar flows 43
- Two-dimensional stagnation point 253
- Two-dimensional wake 56
- Two-equation models 181
  - $k-\varepsilon$  model 181
  - two-layer method 182
  - wall functions 181
- Velocity-defect law 170
  - effect of roughness 170
  - mean flow time scale 170
  - turbulence time scale 170
- Viscous stress 21
- Viscous-inviscid coupling 433
  - blowing velocity 309
  - Hilbert integral 309
- Von Mises transformation 81
- Wall shear layer 35
- Wall suction 37, 83
  - suction drag coefficient 83
  - uniform suction 83
- Whitfield's formula 175
- Whole layer 171
- Zero-equation models 176
  - mixing length 176
- Zig-zag scheme 231